Spinel and garnet textures in mantle peridotite xenoliths and lunar dunite: a micro-CT study

Spinel and Garnet Textures in Mantle Peridotite Xenoliths and Lunar Dunite: A Micro-CT study

Krishan Kumar Bhanot

PhD Dissertation

Department of Earth and Planetary Science

Birkbeck, University of London

Supervisors:

Hilary Downes, University of London, Birkbeck.

Chiara Maria Petrone, Natural History Museum, London.

Emma Humphreys-Williams, Natural History Museum, London.

Word count: 62728

Author's Declaration

I declare that the work in this dissertation was carried out in accordance with the requirements of the University's Regulations and Code of Practice for Research Degree Programmes and that it has not been submitted for any other academic award. Except where indicated by specific reference in the text, the work is the candidate's own work. Work done in collaboration with, or with the assistance of, others, is indicated as such. Any views expressed in the dissertation are those of the author.

Krishan Bhanot

23 August 2022

Acknowledgements

Firstly, I would like to take this opportunity to thank Hilary Downes for help, guidance, and more notably her kindness to me during this project. Her enthusiasm is and remains a source of inspiration to me. I would also like to thank Chiara Maria Petrone and Emma Humphreys-Williams for their support and encouragement during this project.

I wish to thank my wife, Archa Bhanot and my children, Kanav, Nandini and Shivani Bhanot for their support and consideration without which completion of this project would have been impossible. I would also take this opportunity to thank my family for their encouragement.

I also extend my gratitude to members at Birkbeck and the Natural History Museum who have offered me advise. I would also like to thank my teachers and educators for inspiring from an early age in the world of science and to the words and music of Bob Dylan which act to inspire and motivate me.

I would like to extend my appreciation to Brett Clark at the X-Ray CT scan facility at the Natural History Museum, London for CT data collection and help and advice provided in data processing and Hilary Downes, Dimitri Ionov, Theo Ntaflos, Emma Humphreys-Williams and Pamela Kempton for providing mantle xenolith samples for this project (the latter samples being curated at the NHM). I would also like to thank Ryan Zeigler (NASA) for providing the lunar samples and Harrison Schmitt for collecting them on the Apollo 17 mission. I wish to express my gratitude to Andy Beard for thin-section preparation and help and advice he provided with microprobe analysis. I am also grateful to Maz Iqbal for CT sample preparation.

This project was funded by Rigaku for which I am very grateful.

Dedication

This dissertation is dedicated to my mother and father, Surinder (Rano) Kumari Bhanot and Kewal Krishan Bhanot. They have both been an inspiration to me and a source of strength. They are deeply missed.

Contents

List of Figures

List of Tables

Abstract

This study uses Micro-CT scanning to investigate spinel and garnet textures in terrestrial and extra-terrestrial mantle xenoliths. Terrestrial studied sample are from: (1) Massif Central, France; (2) Lanzarote, Canary Islands; (3) Calatrava, central Spain; (4) Pali Aike, Patagonia; (5) Vitim, Siberia, and (6) Kimberley, South Africa. Xenoliths from the Massif Central showing typical textural types were analysed to provide a record of examples of protogranular, porphyroclastic and equigranular textures. Micro-CT analysis of xenoliths from Massif Central, Lanzarote and Calatrava revealed a range of spinel textures from <2 mm microcrystals which can be either spatially concentrated or distributed more evenly throughout the rock, to large 4-12 mm individual spinel-pyroxene clusters with complex vermicular textures in random orientation. These clusters are the result of a transition of shallow lithospheric mantle from the garnet stability field to the spinel stability field. We predict that such textures would only occur in the mantle beneath regions that show evidence of thinning of the lithospheric mantle. Metasomatic reactions around spinel-pyroxene clusters in some Lanzarote xenoliths indicate that metasomatism post-dated cluster formation.

Micro-CT scanning was also used to examine the textures of garnet-spinel clusters and the relationship between garnet and spinel in garnet-spinel peridotite mantle xenoliths from Pali-Aike and Vitim. A xenolith from the Kaapvaal craton provided an example of a typical garnet peridotite and thus provided a reference to compare and contrast 3D structures in garnet and garnet-spinel peridotites from Vitim and Pali-Aike. These xenoliths record a complex tectonic history, in which the original garnets in garnet peridotites were transformed to spinel-pyroxene clusters in spinel peridotites, via lithospheric thinning, but returned to garnet during cooling.

Spinel symplectite textures occur in lunar dunite clasts collected during the Apollo 17 mission. Micro-CT analysis confirms that spinel forms complex structures of varying size, shape and texture. Four types of symplectite with different compositions of spinel were identified. Based on texture and spinel mineral chemistry, we propose that the four textural types have different origins. Each type represents a different stage in the history of the lunar dunite. The oldest were formed from decompression of garnet brought up from ~420 km depth by convective overturn, and thus this is a piece of the lunar mantle. Two small symplectite types are related to melts in the lunar mantle. The youngest type has a shallower origin with interaction of olivine and decompression melts forming anorthite-bearing symplectites. This texture most likely formed from impact melts during the Serenitatis event.

Chapter 1

Introduction to the lithospheric mantle

This thesis consists of several studies which describe and interpret the textural characteristics of lithospheric mantle xenoliths including grain size, shape, orientation, distribution, and mineral compositions in mantle xenoliths from a variety of tectonic settings, including sub-oceanic mantle, Phanerozoic "off craton" sub-continental mantle, and cratonic sub-continental mantle. Textures in an Apollo sample that is potentially derived from the Moon's mantle has been also studied to provide a direct comparison with those of the terrestrial samples, thus offering an insight to lunar mantle processes.

1.1 The nature of the lithosphere.

It is important to explain some of the terms used in this thesis. In simple terms, the lithosphere is the rigid outer layer of the Earth. A more rigorous definition includes a wider variety of aspects based on flexural, thermal, seismic or compositional properties (White 1988). Upwelling of hot mantle material at divergent plate boundaries forms new oceanic lithosphere which migrates away from the spreading centre. The depth of the seafloor away from the spreading centre increases by a factor of the square root of the age of the lithosphere (Parsons and Sclater, 1977). This increase in seafloor depth is attributed to an increase in density governed by cooling over time during which the asthenospheric mantle converts to lithosphere by cooling (White, 1988). Therefore, a definition for the thermally controlled lithosphere comes from the cooling behaviour of the mantle beneath oceanic basins: the lithosphere is the outer shell of the Earth where there is a conductive temperature gradient, overlying the well mixed adiabatic interior (White, 1988). Conduction dominates in regions that are cold and cannot be deformed over geological timescales (Jaupart and Mareschal, 2007). Lithospheric temperature varies through conduction, in contrast to the deeper parts of the upper mantle which cool by convection. The crust and upper mantle can thus be separated into three regions (Fig. 1.1):

- The convecting asthenospheric mantle (well-mixed adiabatic interior) where the Rayleigh number (combined properties of a fluid which explain onset of convection and mathematically describes conditions under which convection occurs) is above a critical value, the potential temperature, or the temperature it would have if brought to the surface adiabatically without melting (dotted line, Fig. 1.1), being within 1280 ±20 °C (White, 1988).

- The thermal boundary layer (TBL) of small-scale convection with a local Rayleigh number close to the critical value.
- The mechanical boundary layer (MBL) with a Rayleigh number much less than critical.

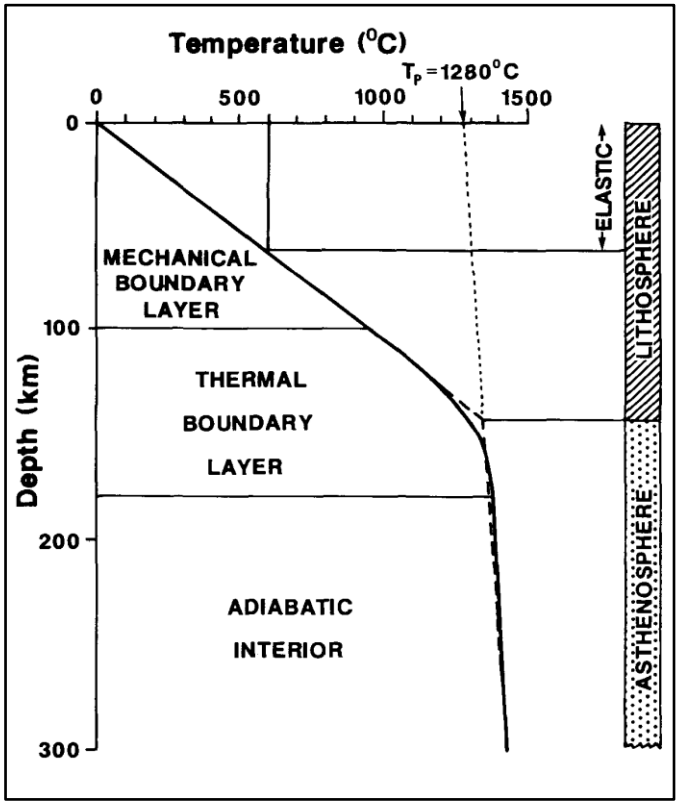

Figure 1.1. Upper mantle temperature gradient and mantle solidus, from White (1998).

In attempting to define the lithosphere, a definition of its base is essential (Artemieva, 2011), but there are several different definitions of the nature of its base. Changes in geophysical properties of mantle rocks provide a basis for various definitions, but they differ significantly, depending on the parameter under consideration. Most properties of the upper mantle change gradually with depth and do not exhibit sharp boundaries that could be uniquely associated with the lithospheric base (Artemieva, 2011). Geophysical studies centring on different properties of the lithosphere result in different lithospheric thicknesses and thus four thicknesses can be defined, i.e.

- Elastic-layer, based on the rheological strength which responds isostatically to loads.
- Thermal region, where heat transfer is conductive and lies above the well mixed convecting mantle whose depth is largely defined by the 1300 °C isotherm.
- Seismic-layer, defined as a high-velocity layer above the low-velocity zone (LVZ), i.e., a zone registering a high thermal gradient brought on by partial melting.

- Electrical-layer, based on resistivity, i.e., a high resistive upper layer lying above a highly conductive asthenosphere. Increase in conductivity is due to small melt fractions and/or the presence of graphite.

1.2 Sub-oceanic and sub-continental lithospheric mantle

The thermal regime of the Earth provides critical information on its evolution through geological history (Artemieva, 2011). Interior heat is transmitted to its surface by three mechanisms: radiation, advection, and conduction. In the Earth's lithosphere, conduction of heat generally dominates among these mechanisms (Clauser and Huenges, 1995). Surface heat flow shows a high degree of variability. Overall, higher heat flow is detected in young structures both on continents and in the oceans, with the mean heat flux on continents being 65 mWm^{-2} and in the oceans 101 mWm^{-2} (Stein, 1995). The oceanic TBL thickness is controlled by the conductive cooling, i.e., the half-space lithosphere cooling model (movement of oceanic plate from mid-ocean ridge) where the thickness of the lithosphere is related to the age of the lithosphere (Humphreys and Niu, 2009). The half-space cooling model predicts a linear variation of depth with the square root of seafloor age and thus applies to "young" seafloor (Carlson and Johnson, 1994). For oceanic lithosphere older than 80 Ma, bathymetry is shallower than is predicted by the half-space cooling model. In such old oceanic lithosphere, the plate model, i.e., a slab of constant thickness moving with a constant velocity (McKenzie, 1967), explains the ocean bathymetry and oceanic lithospheric thickness. Humphreys and Niu (2009) stated that oceanic lithosphere reaches its full thickness at ~70 Ma and assumed a constant thickness of ~90 km for older lithosphere. The base of the oceanic lithosphere would approximate to the ~1250 °C isotherm of Parsons and Sclater (1977) and is consistent with a mantle potential temperature of 1315 °C (McKenzie et al., 2005). One study in this thesis investigates the response of 120 Ma sub-oceanic lithospheric mantle to the impact of a mantle plume (Lanzarote, Canary Islands).

Like oceanic lithosphere, continental lithosphere also thickens with age but does not follow any simple relationship (Artemieva, 2011). Archean cratons older than 3 Ga have a 200-250 km thick lithosphere. Archean cratons younger than 3 Ga may have preserved 300-350 km thick lithospheric roots and the thickness of the continental TBL decreases to younger terranes, i.e., Paleoproterzoic, 200 ± 50 km, Meso-Neoproterozoic 140 ± 50 km, Palaeozoic 100-120 km and in tectonically active Cenozoic regions it is between 60 and 80 km in thickness (Artemieva, 2011). This thesis includes a study of thickened sub-continental lithospheric mantle beneath Siberia and Patagonia.

This study includes mantle xenoliths from both the continental and oceanic domains. Important differences between the sub-continental and sub-oceanic mantle exist (Artemieva, 2011). This distinction is the consequence of mantle melting and to some extent the age of the lithosphere. Hence, the chemical boundary layer (CBL) can be regarded as a region dominated by the residue which remains following melt extraction. Major element composition of the CBL is governed by the multiple factors, (1) initial mantle composition, (2) melt composition, (3) the pressure range of decompression melting and (4) degree of melting. With the extraction of basaltic melt, the residue is higher in Mg (increasing Mg# (Mg# = 100 Mg/[Mg+Fe_{total}])) with high Mg/Si, Fe/Al, Cr/Al and Ca/Al ratios (Cr# = 100 Cr/[Cr+Al]). At low initial melting pressure (2-3 GPa), the residual harzburgite is depleted in Al_2O_3, whereas at higher initial pressures >3 GPa the residual harzburgites yield a constant MgO but with higher Al_2O_3, SiO_2 and lower FeO. Initial melting at high pressures in the range of 7-10 GPa accompanied by large amount extracted melt produces residual harzburgite strongly depleted in Al_2O_3. Cratonic peridotites display chemical signatures consistent with melting at high pressure (>3Pa) and thus deep mantle compared to oceanic peridotites which display chemical signatures concordant with melting initiating at low pressure and mantle depth. Since the Mg# of olivine reflects the degree of mantle depletion of basaltic components, different settings defined by melt extraction and mantle depletion display a narrow range of Mg#. The asthenosphere has a Mg# in the order of 88-89, whereas the oceanic residues represented by abyssal peridotites, ophiolite tectonites and some alpine peridotites are characteristically olivine-rich with Mg#s of 90.5-91.5 (Boyd 1989), fertile continental mantle has a Mg# of approximately 90 and cratonic mantle highly depleted by melt extraction yields Mg# >92.

Boyd (1989) showed that modal and chemical data for variably depleted peridotites of oceanic origin, together with estimates of the composition of fertile parental peridotite, defined an oceanic trend. The oceanic residues may have formed in a variety of tectonic environments but are of relatively shallow origin (Boyd 1989). Comparison of mantle peridotites from cratonic settings (Boyd and Nixon, 1975; Boyd and Nixon, 1978; Pearson et al., 2003) and sub-oceanic regions (Clague, 198); Neumann et al., 1995) highlight the chemical difference between continental and oceanic mantle brought on by melting at different pressures. Mg-rich peridotite xenoliths from continental areas marginal to Archaean cratons have compositions that fit the oceanic trend (Boyd, 1989) through the possibility of the accretion of oceanic mantle to Archean lithosphere and sub-continental magmatic events at low pressure and thus depth. The Archaean cratonic peridotites have had a history that differs from those forming oceanic lithosphere and it is conjectured that they are high-pressure residues of komatiite formation.

Representative chemical analyses from cratonic and oceanic mantle xenoliths are shown in Table 1. The compositions of low-temperature peridotites from Udachnaya, both spinel and garnet facies, closely resemble those from the Kaapvaal craton but differ markedly from oceanic peridotites (Boyd et al. 1997) that follow the oceanic trend (Figure 1.2a). Low-temperature <1100 °C) Udachnaya peridotites have an average Mg# is 92.6. and similar Mg#s are reported in the Kaapvaal peridotites (92.7). Low-temperature peridotites from both cratons have markedly higher Mg#s than depleted oceanic peridotites which range around 90.5-91.5. Figure 1.2b is a plot of the olivine Mg# against the modal amount of olivine, it also shows the oceanic trend (Boyd 1989) i.e., the compositional trend from fertile lherzolite to depleted oceanic harzburgite and also that the high-temperature peridotites (equilibration temperatures >1100 °C) in both the Udachnaya and Kaapvaal xenolith suites have lower Mg#s than the low-temperature peridotites. High-temperature peridotites from both cratons scatter above and below the oceanic trend (Boyd, 1989).

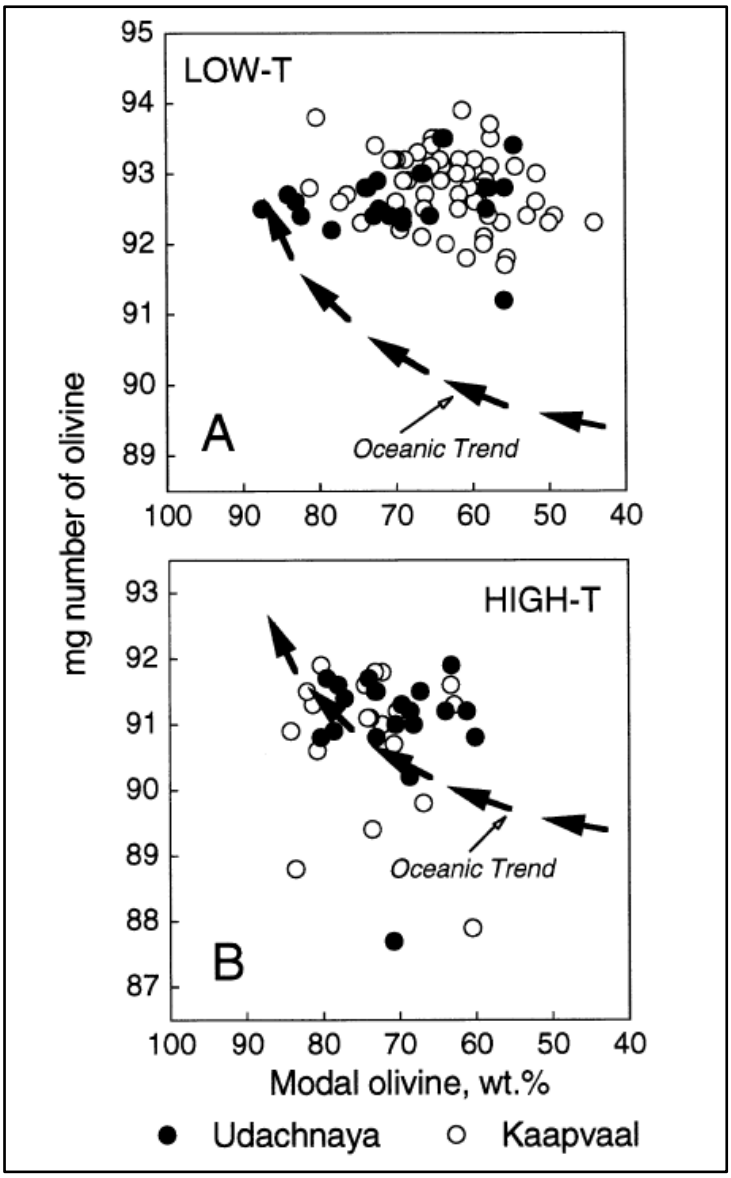

Figure 1.2. Plots of Mg# of olivine against modal olivine for Udachnaya and Kaapvaal peridotite xenoliths (Boyd et al, 1997).

Table 1.1. (A) representative mineral analysis of a spinel peridotite from a cratonic setting (wt% oxide). (B) representative mineral analysis of a spinel peridotite from a a oceanic setting (wt% oxide).

1A. Cratonic peridotites (Boyd et al. 1997).

Udachnaya Spinel Peridotite (Uv 34/93)

	Olivine	Enstatite	Diopside	Spinel
SiO_2	40.7	56.3	53.6	0.02
TiO_2	0.01	0.03	0.04	0.03
Al_2O_3	-	2.84	2.63	39.1
Cr_2O_3	-	0.59	1.03	30.1
Fe_2O_3	-	-	-	2.75
FeO	6.5	4.46	1.43	10.3
NiO	0.41	0.08	0.04	0.11
MnO	0.08	0.1	0.06	0.45
MgO	51.8	35	17	18.1
CaO	0.01	0.59	23.2	0.01
Na_2O	-	0.03	0.66	-
Total	99.51	100.02	99.69	100.97
Mg#	93.42	93.33	95.49	75.8
Cr#				34.06

Udachnaya Garnet-Spinel Peridotite (Uv 76/93)

	Olivine	Enstatite	Diopside	Garnet	Spinel
SiO_2	40.8	57	55.1	41.7	0.03
TiO_2	-	0.01	0.01	0.01	0.03
Al_2O_3	-	1.1	1.04	19.7	12
Cr_2O_3	0.01	0.49	1.18	5.9	58.7
Fe_2O_3	-	-	-	-	2.77
FeO	7.48	4.59	1.5	7.51	13.2
NiO	0.41	0.1	0.05	0.01	0.09
MnO	0.07	0.11	0.08	0.5	0.85
MgO	51.4	35.8	17.9	19.3	13.2
CaO	0.01	0.48	22.5	6.52	0.01
Na_2O	-	0.04	0.83	0.01	-
Total	100.18	99.72	100.19	101.16	100.88
Mg#	92.45	93.29	95.51	82.08	64.06
Cr#	-	-	-	-	77.00

Modal Mineralogy (volume)

Olivine	54.9
Enstatite	41.9
Diopside	2.5
Spinel	0.7

Olivine	59.0
Enstatite	36.7
Diopside	0.7
Garnet	3.4
Spinel	0.2

1B, Oceanic peridotites (Neumann et al. 1995).

Lanzarote spinel harzburgite (LA1-7/LA1-10)

Oxide	Olivine	Enstatite	Diopside	Spinel
SiO_2	40.07	55.31	54.05	-
TiO_2	-	0.01	0.01	0.02
Al_2O_3	-	2.09	2.29	25.06
Cr_2O_3	-	0.8	0.74	42.91
Fe_2O_3	-			5.43
FeO	8.28	5.24	2.7	5.43
NiO	0.1	0.13	0.12	0.13
MnO	51.61	34.02	18.76	16.54
MgO	0.4	0.11	0.07	0.2
CaO	0.05	1.83	22.28	-
Na_2O	-	-	0.22	-
Total	100.51	99.54	101.02	95.72
Mg#	91.74	92.05	92.53	84.45
Cr#	-	-	-	53.46

Modal Mineralogy (vol %)	
Olivine	76
Enstatite	22
Diopside	1.5
Spinel	0.8

1.3 Lithospheric Thinning.

In this thesis, several of the suites of xenoliths examined come from lithosphere which has been thinned due to rifting. The intra-plate volcanism in which mantle xenoliths are usually found is often linked to continental rift zones (Witt and Seck, 1987; Ziegler, 1992; Ionov et al., 1993; Lenoir et al., 2000; Babuška et al., 2002) and hot-spot volcanism associated with mantle plumes originating from deep within the mantle (Wilson (1963) and Morgan (1971)). Rifting can be either active or passive (Fig. 1.3). In the first, the mantle plays an active role, convection plumes dome up and crack the lithosphere, whereas in the second the horizontal movements of plates give rise to extension of the lithosphere and induce rifting (Sengŏr and Burke, 1978). The passive model requires that extension predates any uplift and magmatism, while in the active model, uplift should precede magmatism and extension (Wilson, 1993). For passive rifting, McKenzie (1978) described a simple model of the behaviour of the lithosphere when stretched. This stretching of the lithosphere results in the passive upwelling of hot asthenosphere that results in a thermal perturbation of hot asthenospheric

material. Under an active rifting regime, the base of the lithosphere is acted upon by a hot mantle plume. Partial melting, heating by conduction, and convecting heating associated with the asthenosphere can thin and weaken the lithosphere with a result of isostatic uplift.

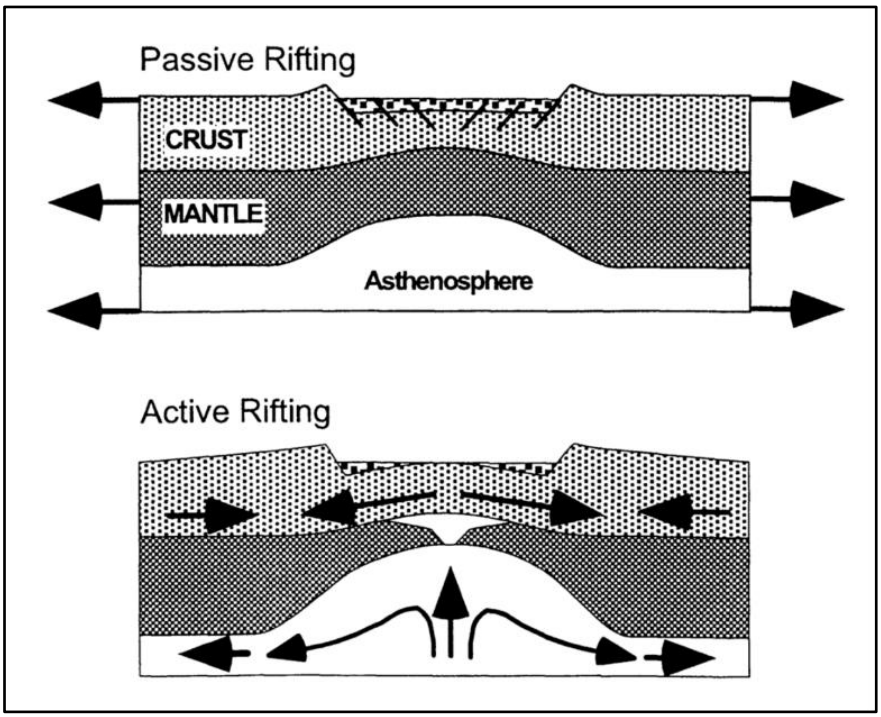

Figure 1.3. Sketch of passive and rifting models based on Sengör and Burke (1978). Passive rift model extensional stresses leading to the passive upwelling of hot asthenospheric material. Active rift model, plume impingement leads to uplift and rifting (Huismans et al, 2001).

1.4 Upper mantle mineralogy.

The lithospheric mantle is composed of ultramafic rocks, mostly ranging from lherzolites (olivine + orthopyroxene + clinopyroxene ± garnet ± spinel) to harzburgites (olivine + orthopyroxene) and dunites (olivine). This compositional range is usually interpreted in terms of the progressive removal of basaltic components during partial melting (Griffin et al., 2008). The process of partial melting of the mantle is one of chemical differentiation. Regions that have not undergone differentiation are termed “primitive” or “fertile”, whereas regions which show a decrease in basaltic elements are termed “depleted”. Some regions may have acquired a re-enrichment by means of metasomatism. Mantle peridotites rich in clinopyroxene are referred to as fertile, in contrast to depleted mantle rocks which are poor in clinopyroxene (Artemieva, 2011).

Three conditions exist in which samples of the upper mantle can be brought to the Earth’s surface: - (1) xenoliths in mafic alkaline magmas, i.e., volcanic rocks such as alkali basalts and kimberlites, (2) ophiolites and orogenic peridotite massifs which are tectonically emplaced sections of the Earth’s

mantle (sub-oceanic in the case of ophiolites and sub-continental in orogenic massifs) and (3) serpentinized peridotite fragments dredged or drilled from mid-ocean ridges (i.e., sub-oceanic). Almost all mantle samples come from the conductively cooled lithosphere from depths <200 km (Frost 2008). A peridotite is an ultramafic rock consisting of >40% olivine. The modal mineralogy of the three most abundant mineral phases, i.e., olivine, orthopyroxene and clinopyroxene, is used to classify peridotites (Figure 1.4).

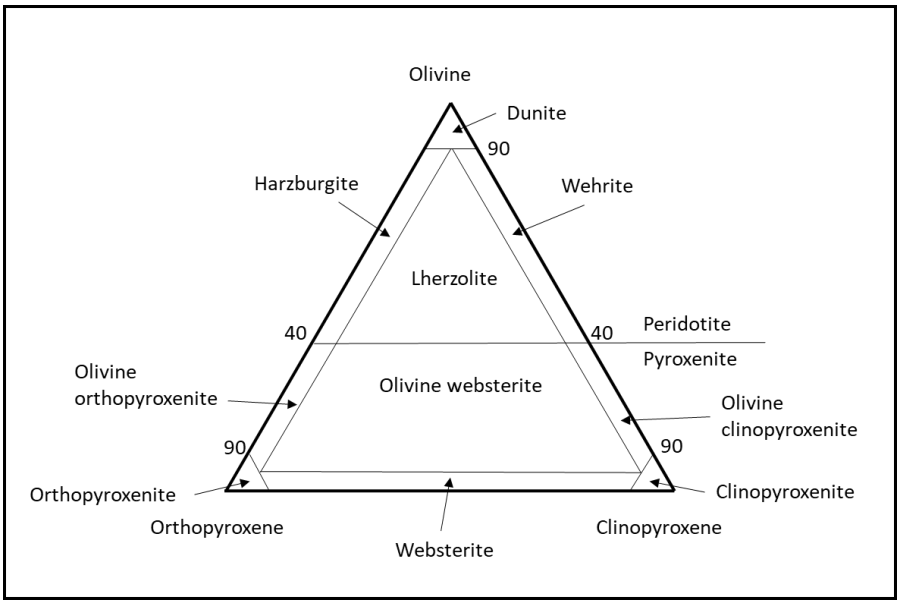

Figure 1.4. IUGS classification of ultramafic rocks, adapted from Streckeisen (1974).

Petrological data of mantle xenoliths provide a detailed insight into the mineralogy and composition of the mantle and thus a snapshot of the lithospheric mantle beneath a region at the time of eruption (Pearson 2003). However, geochemistry of the mantle xenoliths can be altered by reaction to the host magma. Volcanic eruptions are brief events compared to the time taken to emplace tectonic massifs and will thus freeze the mineralogy and textures of the xenoliths, whilst samples from massifs will display a tendency to re-equilibrate texturally and mineralogically during emplacement into the crust. There is a marked difference in xenoliths from stable cratonic and circum-cratonic regions (i.e., xenoliths on and around craton margins) and non-cratonic areas (i.e., away from cratons, often in areas of lithospheric thinning). Continental xenoliths are further divided by the age and tectonic history of the overlying crust. The non-cratonic suite of mantle xenoliths which is dominated by the spinel peridotite facies is largely composed of lherzolites with lesser amounts of harzburgite and dunite; garnet peridotites are uncommon. Cratonic xenoliths are mainly sampled from kimberlite diatremes and have erupted through Precambrian crust with a low geothermal gradient. These xenoliths are more refractory than those from younger regions and have also often undergone metasomatic reactions. This study investigates mantle xenoliths from cratonic and non-cratonic regions, including those which have experienced varying degrees of depletion and metasomatism.

In addition to the main three phases, xenoliths also contain an aluminous phase. aluminous phase which is determined by pressure and temperature of equilibration. With increasing pressure, the stable Al phase changes from plagioclase (<30 km) to spinel (30-70 km) and then garnet (>70 km). Figure 1.5 is a pressure vs temperature diagram which shows the stability fields of the Al-phase in the upper mantle. Equations 1 and 2 represent the Al-phase changes for the plagioclase – spinel facies transition and spinel – garnet facies transition. This study includes samples which have experienced mainly the spinel-garnet transition, as well as those in both the spinel and garnet facies.

Experimental studies on phase changes of the major minerals of the Earth's upper mantle have been carried out by several authors (Kushiro and Yoder, 1966; Green and Ringwood, 1967; Green and Hibberson, 1970; O'Hara et al., 1971; Macgregor, 1974; Zhang and Herzberg, 1994). Kushiro and Yoder (1966) concluded that olivine and anorthite are stable at low pressures (< 8 kbar, 1100^{O} C) and that increasing pressure leads to further change in the mineral assemblage in which anorthite disappears and spinel and pyroxenes become stable (>8 kbar, 1200^{O} C). The reaction is shown in equation 1 (Kushiro and Yoder, 1966).

$$Olivine + Plagioclase + Cr-Spinel \leftrightharpoons Orthopyroxene + Clinopyroxene + Al-Spinel \quad Equ\ 1$$

$$Olivine + Garnet \leftrightharpoons Orthopyroxene + Spinel \qquad Equ\ 2$$

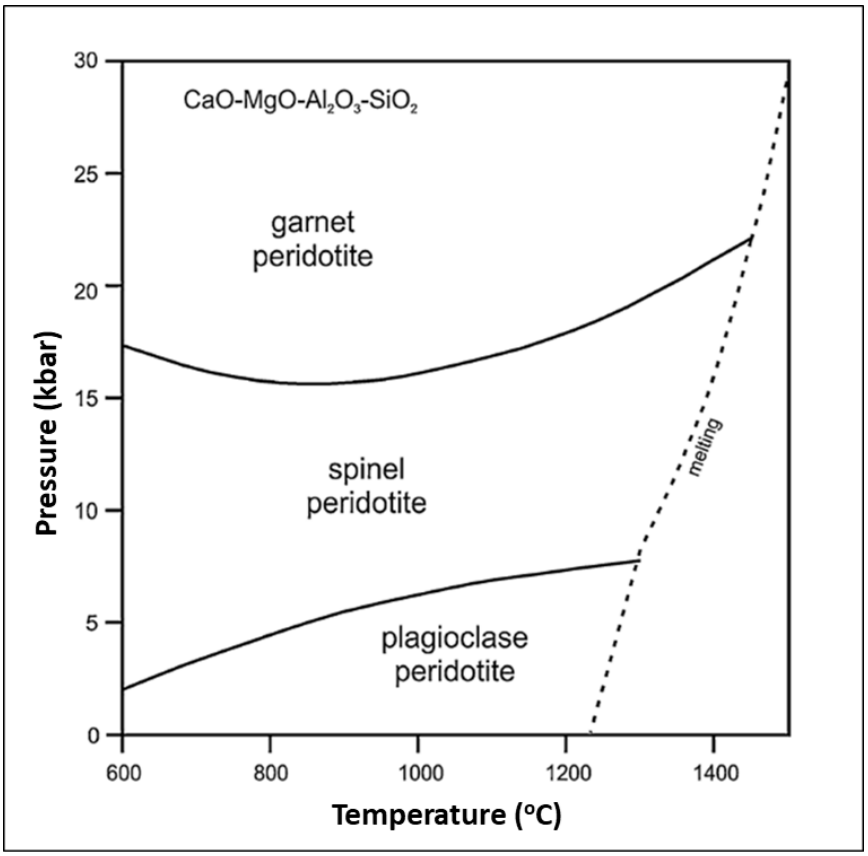

Figure 1.5. Pressure temperature phase diagram displaying the Al stability fields in the upper mantle (adapted from Perkins and Anthony (2011).

Partial melting and melt extraction are processes which alter the mineralogy of upper mantle rocks. The effect on the modal mineralogy of peridotite as melt extraction proceeds is a decrease in clinopyroxene whereas the percentage of olivine increases, i.e., with increasing melt extraction a trend exists from lherzolite through harzburgite to dunite, as shown in Figure 1.6. Major element

changes accompany the transition from lherzolite to dunite, including increases in MgO and NiO along with decreases in CaO, Al_2O_3, Na_2O, SiO_2 and TiO_2.

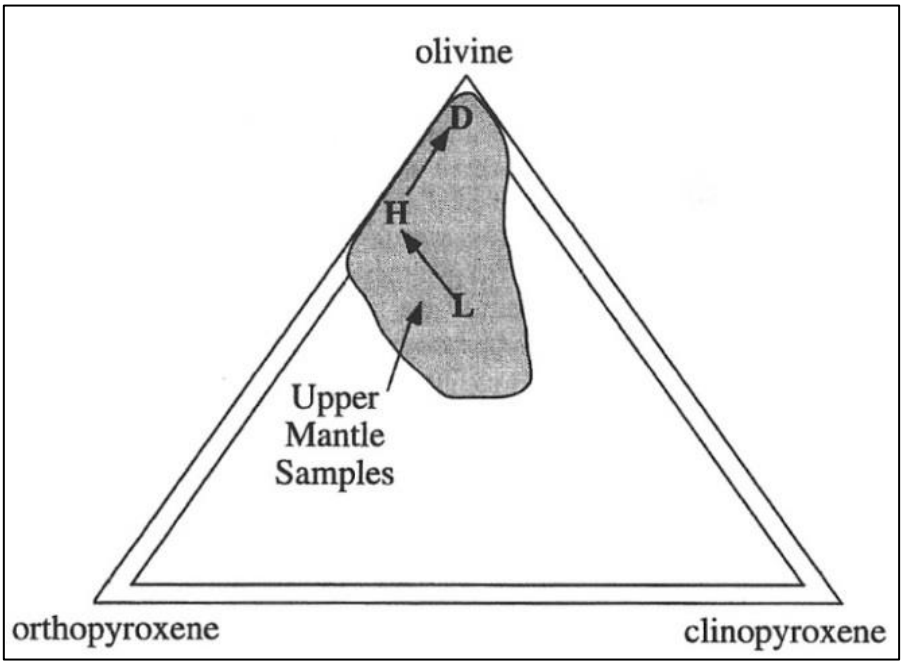

Figure 1.6. Melt extraction trend (McDonough and Rudnick 1998). D = dunite; H = harzburgite; L = lherzolite.

Mineral chemistry for the major minerals of mantle xenoliths is provided by Pearson (2003) and summarised below.

Olivine (ol). $(Mg,Fe)_2SiO_4$

- Over 40% modal proportions by definition and a major host for Mg, Fe and Ni.
- Mg# is 88-94 (88-92 for off-craton xenoliths and 91-94 on-craton)

Orthopyroxene (opx). $(Mg,Fe)_2Si_2O_6$

- Mg# values are broadly similar to olivine.
- CaO varies between 0.2 and 2.0 wt %, depending on temperature of equilibrium and bulk rock composition, i.e., increasing with temperature.
- Al_2O_3 content varies considerably and is dependent on temperature and pressure of equilibrium and the bulk rock composition. In spinel peridotites, content varies between 1 and 6 wt %. In garnet facies content is <2 wt %, being dependant on both temperature and pressure. Harzburgites have low Al_2O_3 contents in opx. Cr_2O_3 content is <0.6 wt %.

Clinopyroxene (cpx). $Ca(Mg,Fe,Al)(Si,Al)_2O_6$

- Mg# values are somewhat higher than olivine.
- Major host for Ca, Cr, Na and Ti. Ca content is temperature-dependant.
- Al_2O_3 varies from 1 to 7 wt % and displays a positive correlation with temperature and bulk composition.
- Cr_2O_3 is <3 wt %. Molar Cr/Al is similar to bulk composition and there is a positive correlation with the degree of depletion.

Spinel (sp). $(Fe,Mg)(AlCr)_2O_4$

- Mg# and Cr# reflect degree of depletion of bulk rock and the temperature and pressure of equilibrium.
- Spinel varies in composition between 4 endmembers, i.e., spinel, hercynite, magnesio-chromite and chromite.

Garnet (gt). $(Mg,Fe,Ca,Mn)_3Al_2Si_3O_{12}$

- Mg# values range from 0.75 to 0.90 and are sensitive to temperature-dependant exchange with coexisting olivine.
- A positive correlation of CaO and Cr_2O_3 results from the complex relationship with pressure, temperature, bulk composition and reciprocal solid-solution effects between the Ca-Mg-Fe and Al-Cr end-member components.

Arai (1994) outlined how the Mg# in olivine - Cr# (Cr# = 100 Cr/[Cr+Al]) in spinel values can help to constrain the origin of spinel peridotite xenoliths. Spinel lherzolites and spinel harzburgites have a limited range of Mg# - Cr# values, forming the olivine - spinel mantle array (OSMA). Spinel peridotites (harzburgites and lherzolites), of both massif and xenolithic derivations, plot in a narrow band, the olivine-spinel mantle array, in terms of Fo of olivine and Cr# of chromian spinel. The Cr# of spinel grows rapidly within the olivine-spinel mantle array with a slight increase of Fo (Arai, 1984). Spinel peridotites from various tectonic settings occupy distinctive regions (Figure 1.7). Harzburgites reside in the high Cr# (> 0.5) field, whilst lherzolites occur in the low Cr# field. Dunites plot both within and outside the mantle array.

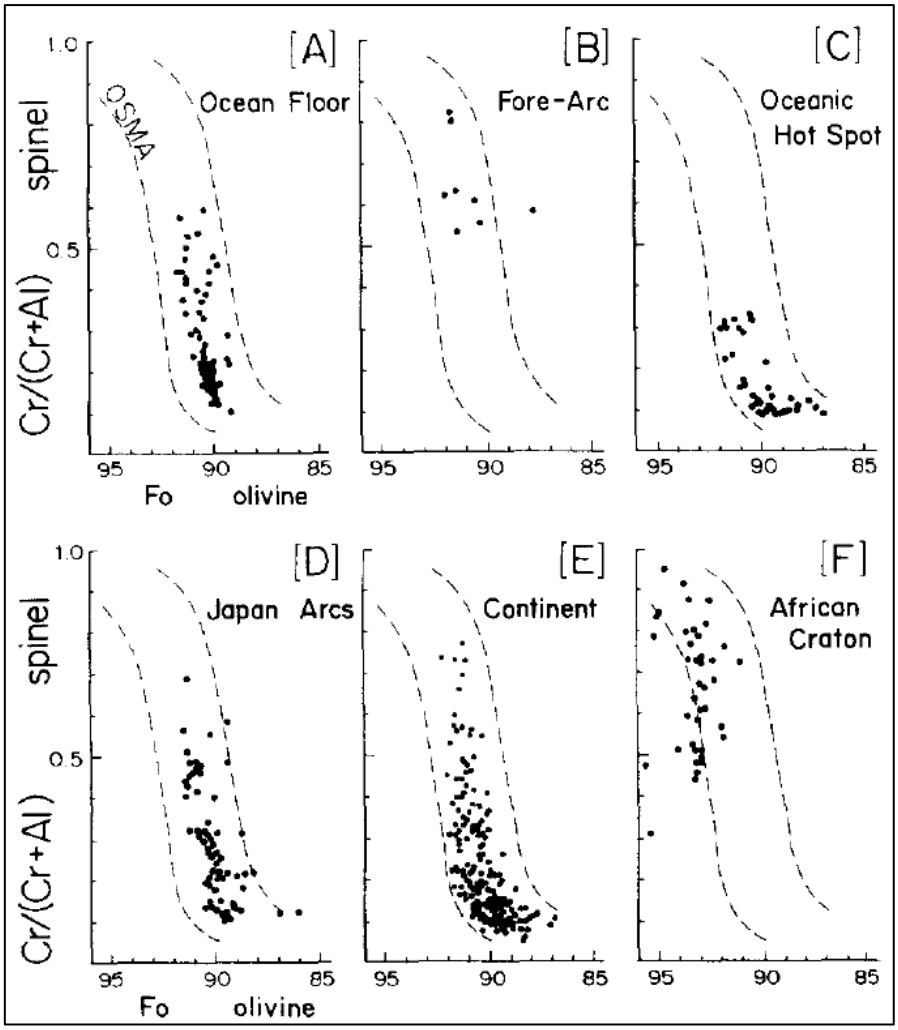

Figure 1.7. Olivine – spinel mantle array, the Mg# in olivine - Cr# in spinel relationships of spinel peridotites from known tectonic settings (Arai 1994).

1.5 Mantle Metasomatism

Metasomatism is a chemical change, whereby a pre-existing mineral or rock is converted to another composition. It usually refers to a solid-state transformation, with material transfer through a vapour or fluid, without melting (Bailey, 1982). Mantle metasomatic processes are described as either modal metasomatism or cryptic metasomatism. Modal metasomatism is a process in which mantle rock displays the addition of new minerals. Harte (1983) described peridotite xenoliths entrained in kimberlites from South Africa which show the presence of chemical and mineralogical changes in the form of late-stage alteration features such as development of phlogopite associated with kelyphite rims mantling garnets. Harte (1983) defined modal metasomatism as the introduction of mineral species not present in the rock previously, e.g., phlogopite, ilmenite and barium titanite containing large amounts of K, Ti and Ba which are not abundant in the rocks previously and thus suggest an infiltration metasomatic event in which the rocks have been penetrated by a moving fluid

of distinct composition. Amphibole and apatite are also common metasomatic minerals. The study by O'Reilly and Griffin (1998) of ultramafic xenoliths included volatile samples rich in amphibole ± mica ± apatite from Western Australia and looked at the effects of metasomatic processes on the chemical and isotopic composition of the sub continental lithosphere. Volatile phases are considered metasomatic in origin. Figure 1.8 is a backscattered electron image of a spinel peridotite from this study where amphibole has been added to clinopyroxene in a spinel-pyroxene cluster.

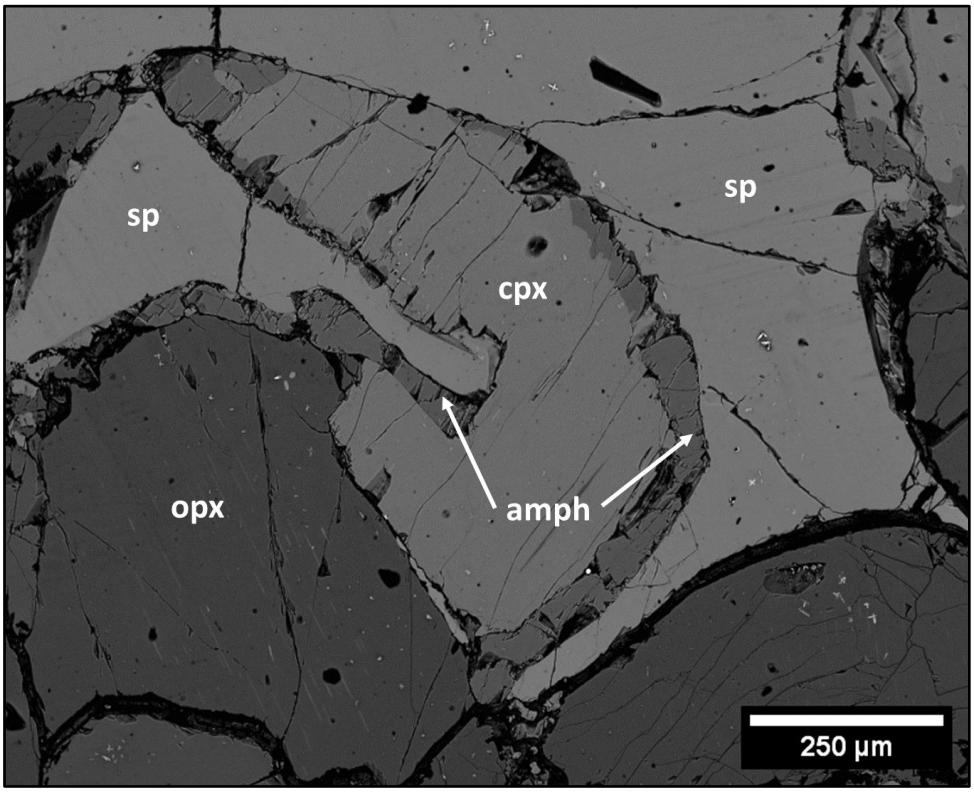

Figure 1.8. BSE image of a spinel peridotite (sample 1EHW1248, Calatrava, Spain) showing metasomatic textures. Amphibole has been added within a spinel-pyroxene cluster due to reaction of metasomatic agents. Sample from this study. Scalebar is 250 µm.

Cryptic metasomatism is a process experienced by existing minerals in which changes to their trace-element composition occur without formation of new phases. Most descriptions of mantle metasomatism deduce the introduction of some or all of the following elements: H, C, F, Na, Al, P, S, Cl, K, Ca, Ti, Fe, Rb, Y, Zr, Nb, Ba, rare earths (Bailey, 1987; Gibson et al., 2020). Bailey (1970) showed that in xenoliths entrained in alkaline magmas, the Al-Fe-Ti-rich assemblages are products of mantle metasomatism. The chondrite-normalised patterns for average and median compositions (Fig. 1.9) display relatively coherent LREE-enriched trends and flat HREE abundances (McDonough, 1990). The study by Downes et al. (2003) into the trace element composition of clinopyroxenes in spinel peridotites from the northern and southern domains in the Massif Central, France, revealed the different trace element compositions between the two distinct domains and that the mantle

lithosphere in both domains has experienced episodes of metasomatism. Figure 1.9 shows REE figure for clinopyroxenes from two samples from Montboissier, Massif Central (MB1 and MB57).

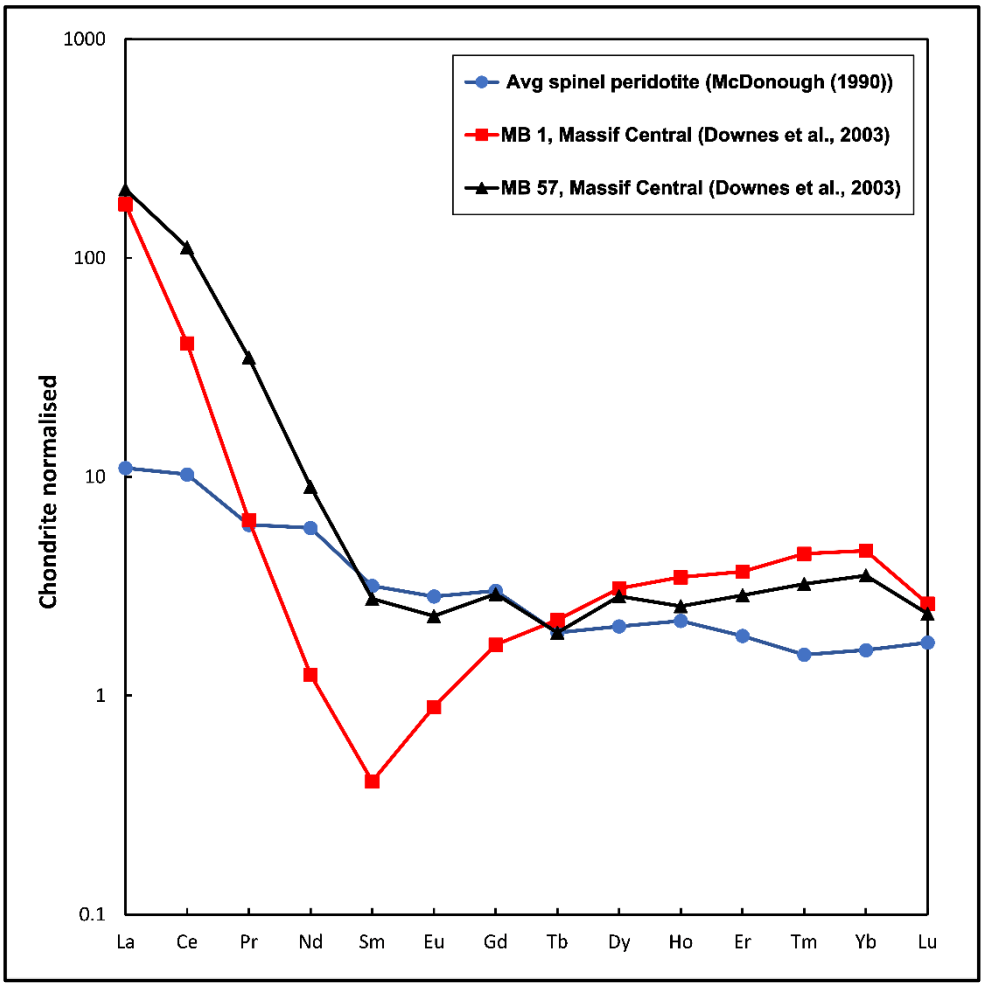

Figure 1.9. Comparison of C1 chondrite normalized REE patterns measured on clinopyroxenes from spinel peridotites from the northern Massif Central, France (data from Downes et al. 2003) and of the REE pattern for the average spinel peridotite (data from McDonough). This study includes samples from the northern Massif Central.

A wide range of fluid types are involved in metasomatic reactions and include silicate melts ranging from mafic to ultramafic; carbonatite melts; sulphide melts; C-O-H fluids ranging from water to CH_4 and CO_2; dense brines and hydrosilicic fluids; and hydrocarbon-bearing fluids (O' Reilly and Griffin, 2013). Fluid movement through the mantle is controlled by two main processes, i.e., crack propagation and grain-boundary infiltration. During crack propagation, large volumes of metasomatic liquid will move instantaneously and thus accounts for large scale intrusions in the mantle and magma ascent. Many metasomatised xenoliths contain planar veins of secondary phases such as amphibole and mica less than 0.1 mm to more than 10 cm wide (O' Reilly and Griffin, 2013). Fluid movement via grain boundary infiltration is a major process for cryptic metasomatism. During grain boundary infiltration original solid-solution minerals remain but are changed in composition,

e.g., clinopyroxene may become more Fe-rich (Best, 2003). This thesis will include several examples of metasomatism in peridotite xenoliths.

1.6 Mantle xenolith textures.

Mercier and Nicolas (1975) presented a classification of mantle xenoliths and analysis of flow mechanisms operating in the upper mantle by examination of textural types coupled with plastic flow and recrystallization with samples from Cenozoic alkali basalt volcanoes of Western Europe and Hawaii. The mantle peridotites are imprinted with tectonic and metamorphic textures, which were observed in two-dimensions by studying thin-sections of xenoliths. In this current study, this has been expanded to studying mantle xenoliths in three dimensions, via computerised tomography (CT) scanning of cores drilled from xenoliths.

Mercier and Nicolas (1975) distinguished three groups of lherzolite xenoliths based on texture, fabric and the paragenetic relations of minerals, chiefly spinel, and described the structural groups in order of their natural sequence. The first structural group, the protogranular one, can be viewed as the oldest texture largely resulting from recrystallization occurring during partial melting. The second structural group is the porphyroclastic one, resulting from the protogranular texture grading into the porphyroclastic texture due to plastic flow, and the third structural group (equigranular) is formed from the complete recrystallization of the porphyroclastic texture. Below is a summary of textural groups. Figure 1.10 shows an example of a protogranular spinel harzburgite (RP83-68) from the Massif Central, France.

In the protogranular textural type, olivine and orthopyroxene are coarse-grained >2 mm. Olivine crystals display kink bands, polygonization and crystallisation of larger crystals (Mercier and Nicolas, 1975). In general, both olivine and orthopyroxene grains display curvilinear grain boundaries. Thus, the principal texture for a protogranular mantle xenolith is in which olivine grains are equant and globular with curvilinear boundaries. Grains display a weak fabric with no foliation or lineation but may exhibit evidence of straining. Clinopyroxene and spinel grains are <2 mm in size. Spinel can display a vermicular texture forming inside orthopyroxene or between orthopyroxene and clinopyroxene grains. Porphyroclastic texture comprises of large strained elongated olivine and orthopyroxene grains (porphyroclasts) and small (~0.5mm) polygonal strain-free crystals (neoblasts). Porphyroclasts display signs of deformation i.e., displaying kink bands and a degree of polygonization. The spinel displays a characteristic holly-leaf shape, surrounded by olivine, and is flattened parallel to the porphyroclasts defining a strong foliation, and by their elongation in this plane, a mineral lineation, thus, the fabric of the porphyroclasts is strong (Mercier and Nicolas,

1975). Clinopyroxene and spinel form small grains scattered in the rock. Primary porphyroclastic textures are thus described by two types of olivines: (1) porphyroclasts which display a xenomorphic and heavily strained texture and strong fabric and (2) small strain-free polygonal grains. Spinel commonly appears between olivines and exhibit a holly-leaf shape due to deformation. Spinel is both seen in contact with pyroxenes and scattered. The porphyroclastic texture derives from the protogranular type by intense recrystallisation as demonstrated by the occurrence of some generally rare remnants of porphyroclasts (Mercier and Nicolas, 1975). Equigranular textural types are divided into two subgroups: tabular and mosaic. Grains are fine-grained <0.7 mm and equant, boundaries are rectilinear and converge at 120° triple points. Clinopyroxene and spinel grains are <0.2 mm in size and are distributed throughout the rock with spinel residing as inclusions inside olivine. Mosaic subgroup textural types display a strong fabric.

This study will attempt to characterise these three classic textural types in 3-D using CT scanning.

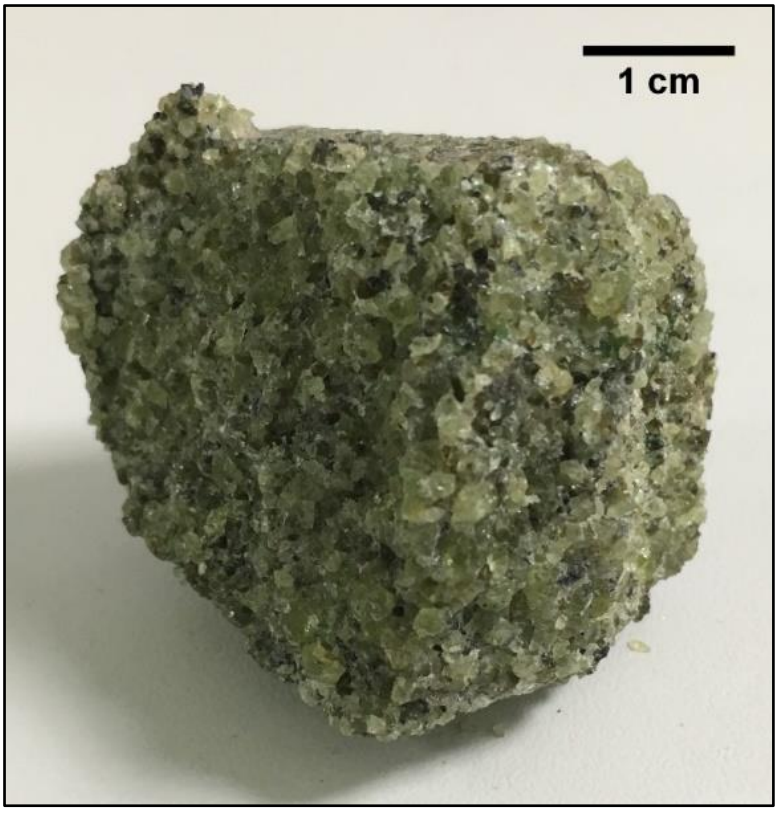

Figure 1.10. Protogranular spinel harzburgite (RP83-68, Ray Pic, Massif Central).

Tabor et al. (2010) provided a method for quantitative characterization of textures in spinel peridotites. They stated that all the textural descriptions were based on a qualitative assessment of textural features in thin-sections which provide two-dimensional objects for measurement. Although intuitively these can be expected to reflect the three-dimensional structure of the rock, the 2D to 3D

relationship is not simple. Distributions of grains in thin-section are a combination of the size distribution of minerals being sectioned and a distribution produced by the random sectioning plane (Tabor et al. 2010). These authors showed that textures in spinel peridotites can be quantified, and a linear relationship exists between mean grain-section area and standard deviation of the grain-section area size. Protogranular and equigranular peridotites which under Mercier and Nicolas (1975) are considered textural end-members, are readily characterised with porphyroclastic peridotites tending to overlap protogranular ones at larger grain-section areas and equigranular ones at smaller grain-section areas, suggesting that spinel peridotite textures form a continuum rather than being discrete entities (Tabor et al., 2010). This study showed the necessity for examining mantle textures in three-dimensions, as opposed to two-dimensional investigations of thin-sections.

However, mantle xenoliths modal abundances can be heterogeneous particularly of the aluminous phase which can vary from thin section to thin section of the same sample. In some rare examples, (Downes et al., 1992; Tabor and Downes, 2019) thin sections display a variation in texture, as shown in Fig. 1.11C in which a mantle xenolith exhibits adjacent protogranular and equigranular textures and in Fig. 1.11D in which a xenolith displays grain size banding. In general, the scale of textural heterogeneity is greater than the scale of a single hand specimen, which in turn is greater than the scale of a single thin section or 2D slice. Therefore, it is uncommon to find a thin section in which two different textural types can be recognised. Pyroxene distribution is also not uniform with grains even in thin-section showing regions of concentration. Variation in modal mineralogy is confirmed in 2D slice images of the 3D data. Grain size is also an important factor. For samples with grain sizes and structures >5mm, although individual grains are visible, any relationship to other grains of similar size could potentially be lost when viewed in a single thin-section (and 2D slice image). This also applies to the chosen standard sample size of a 25mm cylindrical core for CT scanning of a mantle xenolith. Thus, sample size is an important consideration. Experiments of micro-CT scanning whole rock samples is an option but there remains the risk of poor data due to beam hardening. Overall, characterisation of mantle xenolith textures based on thin-section analysis remain the most accurate. This classification can be complemented by analysing larger samples through micro-CT analysis helping to identify larger structures and variation in high density phases and identify any lineation.

The association of spinel between coexisting olivines and pyroxenes ranges from strain blebs and vermicular textures with orthopyroxene and clinopyroxene and inclusions in olivine's. Mercier and Nicolas (1975) proposed that the formation of vermicular spinel and pyroxene texture (spinel-

pyroxene cluster) is a result of exsolution from a previous Al-Ca-rich orthopyroxene. Figure 1.11 shows the vermicular spinel and orthopyroxene texture (spinel-pyroxene clusters); spinel is clearly visible in close association with orthopyroxene and clinopyroxene which forms a clear cluster.

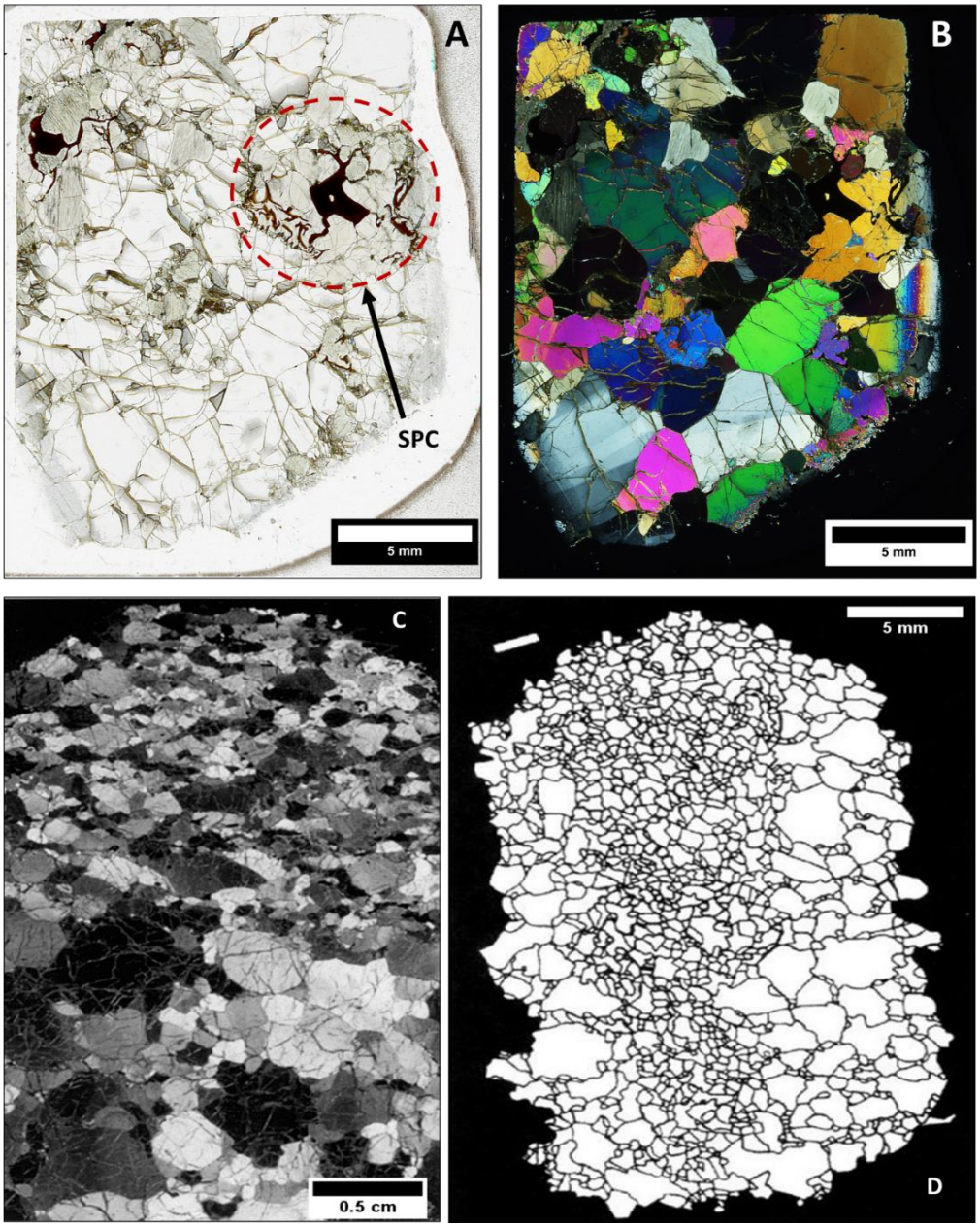

Figure 1.11. (A) PPL photomicrograph of spinel peridotite CH11 (Massif Central), protogranular textural type with vermicular spinel associated with a spinel-pyroxene cluster. Scalebar is 5 mm. (B) Same view in crossed polars. (C) XPL image of a composite mantle xenolith showing adjacent protogranular (lower part) and equigranular (upper part) textures (SZT1068, Hungary. (Downes et al., 1992)). Scalebar 0.5cm. (D) Thin-section skeleton of a spinel peridotite xenolith with a grain size banding texture (D8 Eifel, Germany (Tabor and Downes, 2019)). Scalebar 5mm.

1.7 2D Thin section analysis and 3D analysis of Mantle xenoliths.

Analysis of (2D) thin sections of mantle xenoliths allow for the identification of primary textures, classification of structural types based on the work of Mercier and Nicolas (1975) and identification of mineral phases. 2D analysis can easily resolve the silicate-silicate boundaries differentiating grain size, shape, position relative to other grains, the nature of grain boundaries (e.g., curvilinear, or polygonal) and the existence of any foliation/layering or preferred orientation along with identification of the stress regime experienced by individual grains. All this information is vital in correctly classifying any sample. Figure 1.12 is an image of a thin section in ppl and xpl of a protogranular spinel-pyroxene bearing spinel lherzolite. Coarse olivine grains with curvilinear grain boundaries are easily identified along with the vermicular intergrowth of the sp+ opx+cpx (spc) cluster.

In contrast, 3D analysis (micro-CT) provides information on the density of a sample which is dependent on the mean Z of an element e.g., spinel and garnet due to the Cr content have a higher attenuation of X-rays compared with silicates and thus this density difference allows for the identification of the size, shape, and distribution of these phases throughout the sample. However, when attenuation of minerals is similar as is the case with the silicate phases differentiating individual silicate phases is extremely difficult if not lost in the 3D data set altogether. However, the 2D slice images in a 3D data can yield information on silicate grain boundaries even if individual grain identification can only be at best insinuated. 3D data provides very high spatial resolution, ability visualise any orientation between grains and structures not directly in contact with each other, e.g., the relationship of spinel-pyroxene clusters or garnet grains which are not evenly distributed throughout a sample and provide precise linear, angular and volume measurements.

A major drawback for both 2D and 3D analysis is the size of coarse grains and structures leading to the position where a sample core (or thin-section) size is not able to capture the true extent of a texture or structure or only partially capturing a coarse grain and thus losing any information of relationship to other similar grains distributed throughout the sample from which a representative core was extracted. One advantage the 3D data set provides is the ability to combine single 2D slice images and view how the mineral distribution varies throughout the thickness of the sample along a particular axis or chosen orientation. This is demonstrated in Fig 1.13 (A-D) which shows individual slice images of spinel harzburgite, with spinel forming part of a spinel-pyroxene cluster. With increasing distance along the Z axis, the structure of the vermicular intergrowth of the cluster can be seen to vary from slice to slice.

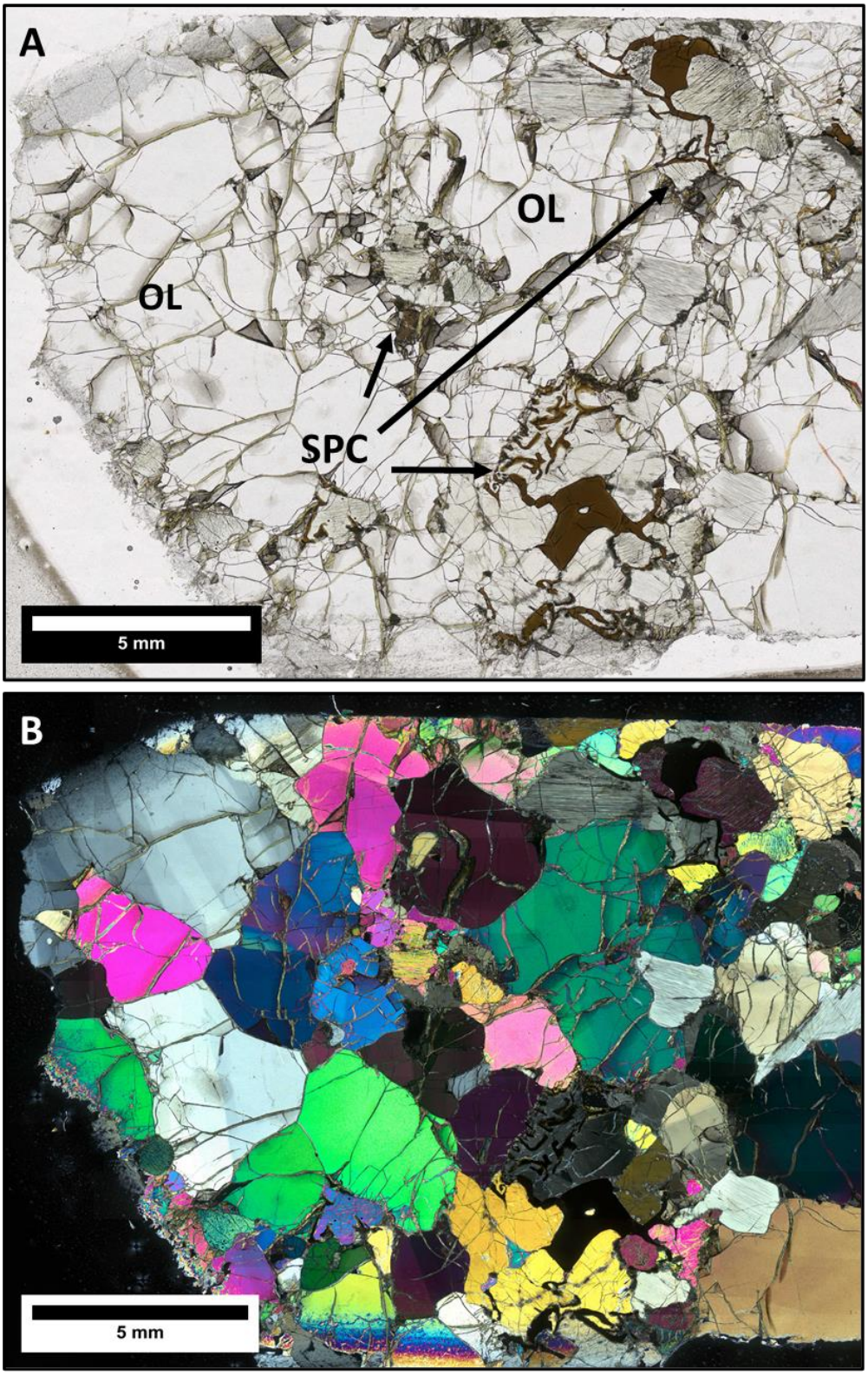

Figure 1.12. (A) PPL image of a protogranular spinel lherzolite (CH11) from the Massif Central. Visible is coarse grained, curvilinear olivine grains with several vermicular intergrowths of spinel+opx+cpx. Scalebar is 5 mm. (B) XPL image of same sample showing strain twinning and exsolution. Scalebar is 5 mm.

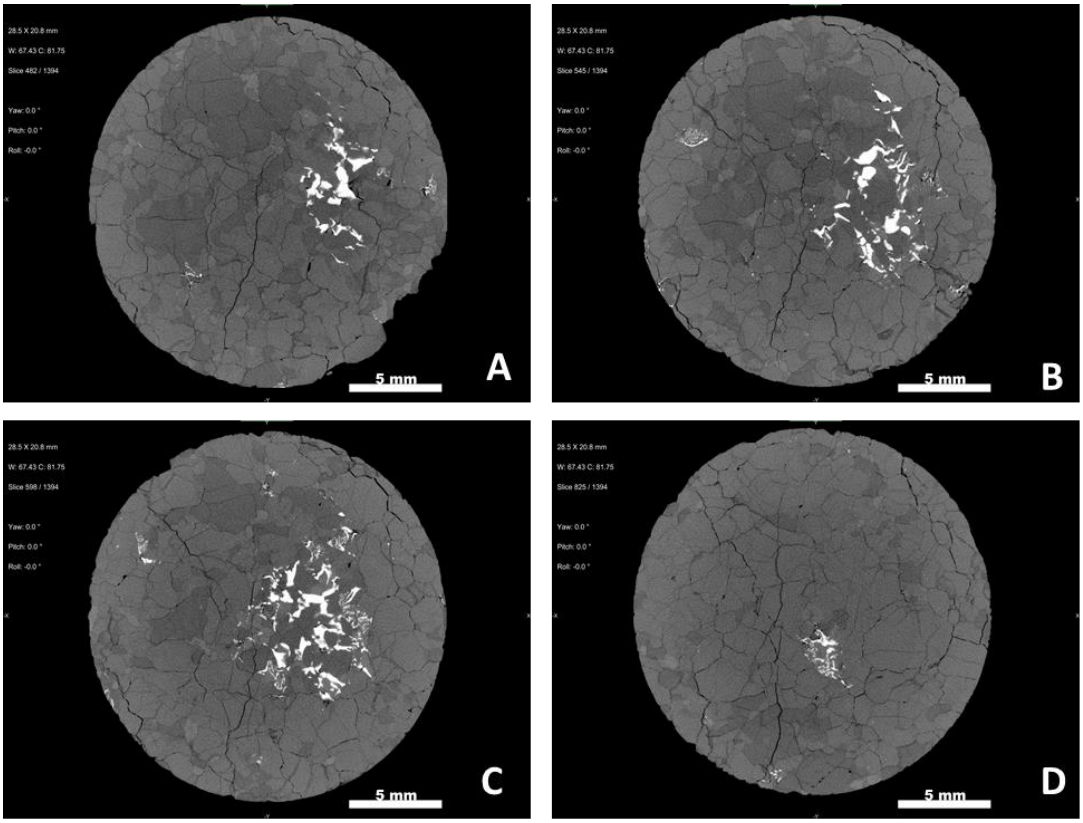

Figure 1.13. (A-D) Series of 2D slice images of vermicular interstitial spinel (white) forming part of a spinel-pyroxene custer in protogranular spinel harzburgite (EC6) from Lanzarote. Silicate ((ol,opx,cpx, (grey)). Scalebar is 5 mm.

1.8 Outline of the thesis

The aims of the thesis are to understand the textures of well-known suites of mantle peridotite xenoliths in three dimensions, rather than in traditional 2-D thin-section analyses, and to understand the processes involved in forming the observed textures. In the upper mantle, the Al-phase phase will change from plagioclase to spinel and then to garnet with increasing pressure. Phase changes in the upper mantle are brought about by tectonic processes. Decompression, deformation, heating and cooling are all processes effecting the nature of the upper mantle. Thus, this study will investigate textures brought about by changes in the thickness of the lithosphere and the consequent changes in the nature of the Al-phase. Investigation of spinel-pyroxene clusters, garnet-spinel clusters, and garnets in peridotites from different tectonic settings will thus provide accurate representations of the solid-state reactions involving olivine and the upper mantle Al-phase. In addition to CT scanning of samples, studies will be made of textures via Back-scattered Electron (BSE) imaging, and mineral compositions will be made by Electron Probe Microanalyser (EMPA). These methods will be described in detail in Chapter 2.

This thesis will investigate the textures and compositions in mantle peridotite xenoliths from various tectonic settings both terrestrial and extra-terrestrial. It will concentrate mainly on 3-D

representations obtained by CT-scanning applied to xenoliths from the protogranular-porphyroclastic-equigranular groups of Mercier and Nicolas (1975), xenoliths which show vermicular spinels in spinel-pyroxene clusters (Fig 1.12), xenoliths which contain both garnet and spinel and hence represent a transition between garnet- and spinel-facies (Fig. 1.14), some examples of garnet-only peridotites, and a suite of fragments of dunite 72415 from the Moon which will provide an opportunity to contrast and compare spinel textures from both terrestrial and extra-terrestrial settings. Samples include xenoliths from the oceanic crust (Lanzarote), young sub-continental lithosphere (France, Spain), older more complex sub-continental lithosphere (Siberia, Patagonia), and Archean lithosphere (South Africa).

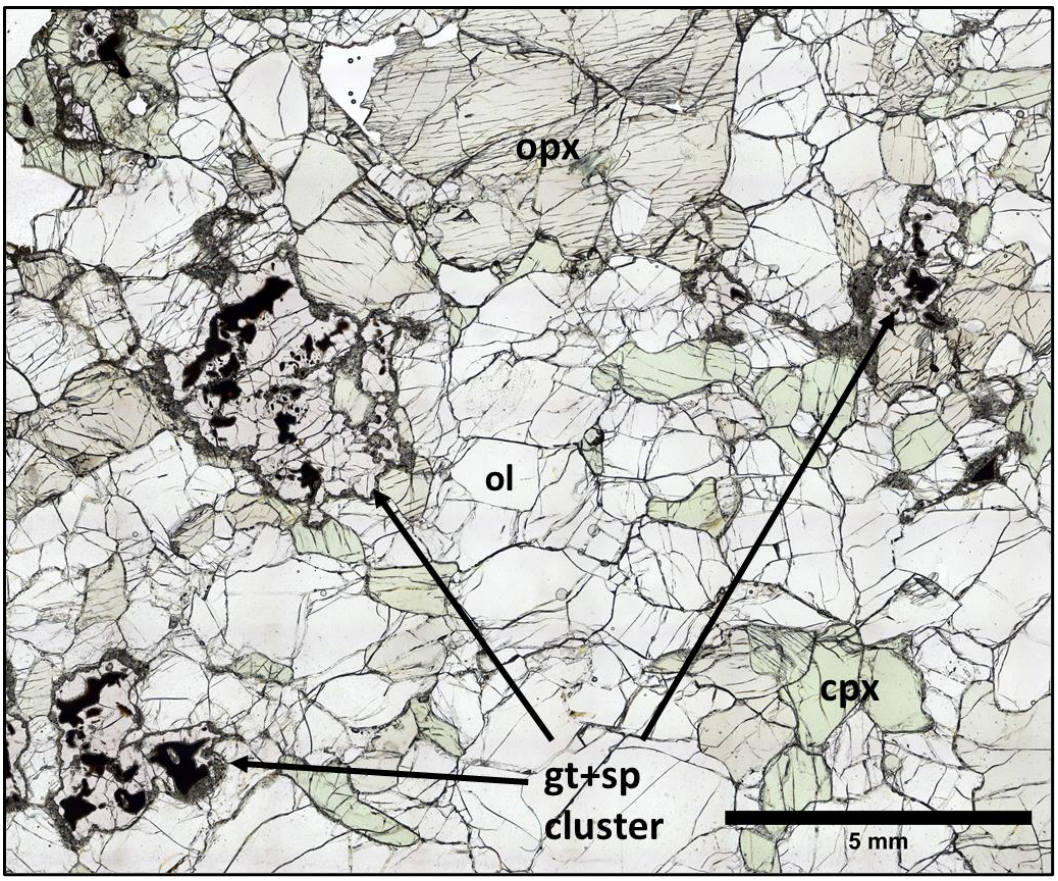

Figure 1.14. Photomicrograph under PPL of a garnet-spinel peridotite (PA-16) from Pali-Aike. Scalebar is 5 mm.

Chapter 2

Methodologies used in this study

This chapter contains details of the methodologies used in this study, including petrographic thin sections, X-Ray Tomography of cored samples (Section 2.1), Electron Microprobe Analysis of the chemical composition of minerals and glass in polished thin-sections (Section 2.2).

Prior to data collection, a thin section of each sample was investigated to characterise it in terms of grain size and shape, and to carry out mineral compositional analysis. Modal mineralogy was calculated using a square grid superimposed over a photomicrograph of a thin section in ppl. Minerals occupying more than 50% of an individual square were assigned to a particular mineral. Based on modal mineralogy, each sample was then characterised based on the melt extraction trend from lherzolite through harzburgite to dunite.

Thin-section analyses of grain size of the silicate minerals, polygonization and evidence of kink bands in olivine, along with spinel texture and grain size, helped to characterise each sample into one of the structural groups of Mercier and Nicholas (1975). Measurements of grain size in thin-section and distribution of spinel-pyroxene clusters, garnet-spinel structures and garnet within the thin section is important information when considering the size of a core for 3D analysis. For example, features >5 mm in size would be underrepresented in a small (~10 mm diameter) core. Thin-section analysis is also vital to identify textures such metasomatic reactions affecting mineral grains. Since these textures are easily seen in thin-section and EMPA data, 3D analysis can be used to investigate their signature and texture within a whole rock sample via the segmentation process. Tailored smaller cores can be made to allow high resolution 3D data of finer textures. Characterisation was based on a single thin section of the sample due to financial considerations. Ideally, more than one section should be used, especially in garnet peridotites, in which the sectioning process can miss both large garnets and small spinels. Figure 2.1A and B are photomicrographs in both PPL and XPL of a protogranular garnet-spinel lherzolite from Pali-Aike. Images reveal coarse grained olivine with linear grain boundaries and large garnet-spinel clusters and vermicular spinel. The XP image (Fig2.1B) shows evidence of strain in ol grains in the form of kink banding.

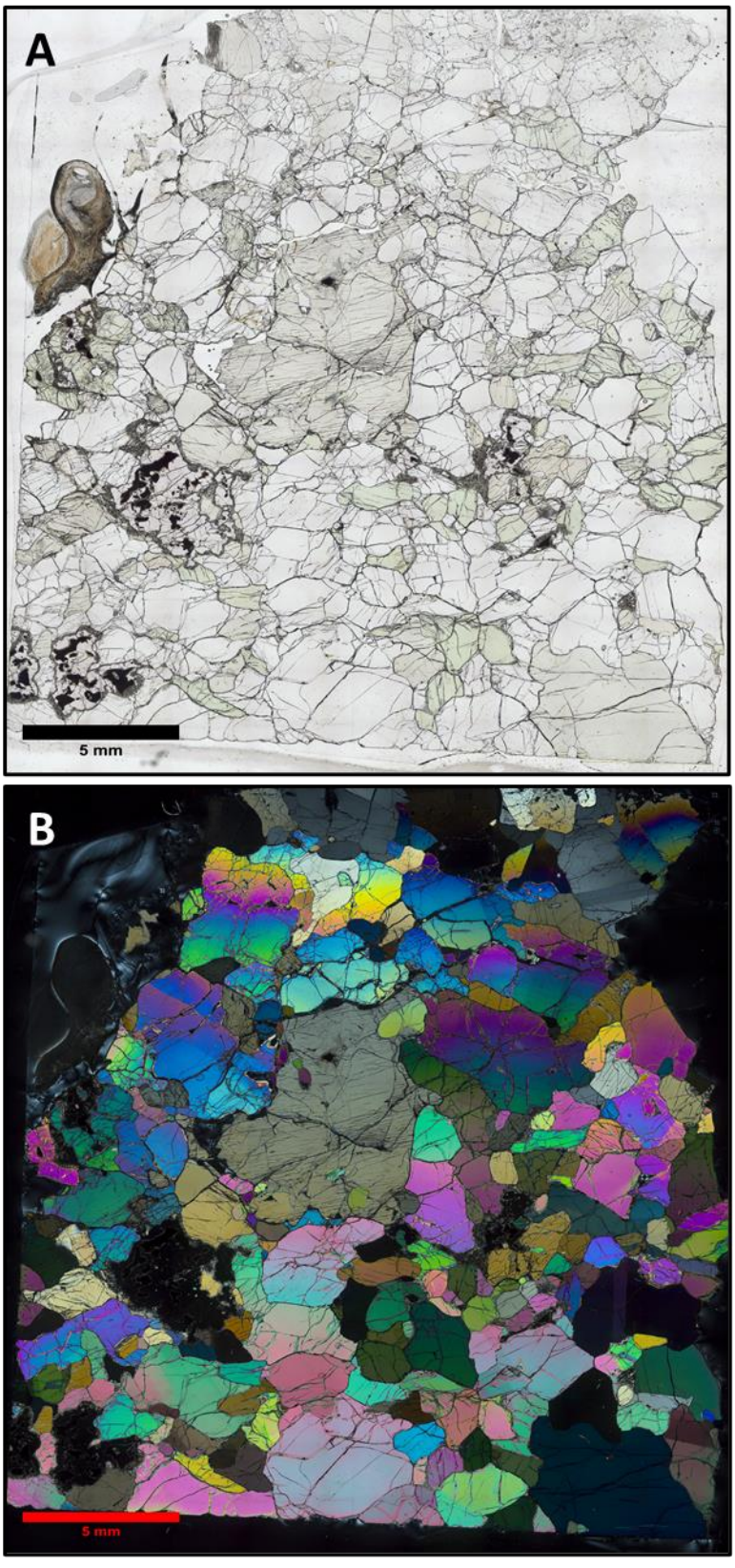

Figure 2.1. (A) Photomicrograph in PPL of a protogranular garnet-spinel lherzolite from Pali-Aike (PA16) with coarse grained ol (1-3 mm) grains. Ol grains display linear grain boundaries. Several gt-sp sites are visible with the largest 4.3 x 3.2 mm is size. Scalebar 5mm.

2.1 X-Ray Computed Tomography

X-Ray computed tomography (CT) is a non-destructive technique in which a series of 2D images (radiographs) characterising variations of X-Ray interaction due to density differences of the subject matter are mathematically combined provide a high-resolution 3D visualisation of the object. The 3D data set provides access to internal features which would normally be obscured, thus allowing for direct measurement and evaluation. CT scanning techniques have been applied to material analysis. Micro-CT (µ-CT) is a technique also used in geological studies, e.g., the examination of rare specimens. The capacity of 3D CT data to yield a scale of resolution in order of microns is significant in exploring the textural analysis of geological samples and quantification of mineral phases within a rock specimen. A range of CT systems can be used; the choice of system employed is dictated by the size of subject matter and desired spatial resolution. Table 2.1 outlines the general classification of CT systems highlighting the scale of resolution.

Table 2.1. Classification of CT systems and Resolution (Adapted from Carlson et al., 2003).

Type	Scale of observation	Scale of resolution
Medical	m	mm
High - Resolution	dm	100µm
Ultra-high resolution	cm	10µm
Micro-CT (µ-CT)	mm	3-125µm
Nano-CT	mm	0.2-2µm

2.1.2 X-Ray Generation.

The chief components of X-ray generators are a high voltage generator, electron gun (cathode), a metal target (anode), commonly made of Cu, Mo or Cr. X-rays exit the tube via a beryllium window. Figure 2.2 shows an image of an X-Ray tube and its major components. This assembly is kept under high vacuum. X-rays are produced when a cathode tungsten filament emits electrons which are then accelerated toward the anode, the convergence and intensity of the electron beam is controlled, and the focused beam of electrons produces a line focus or spot on the target with a diameter or width in the order of 100 µm.

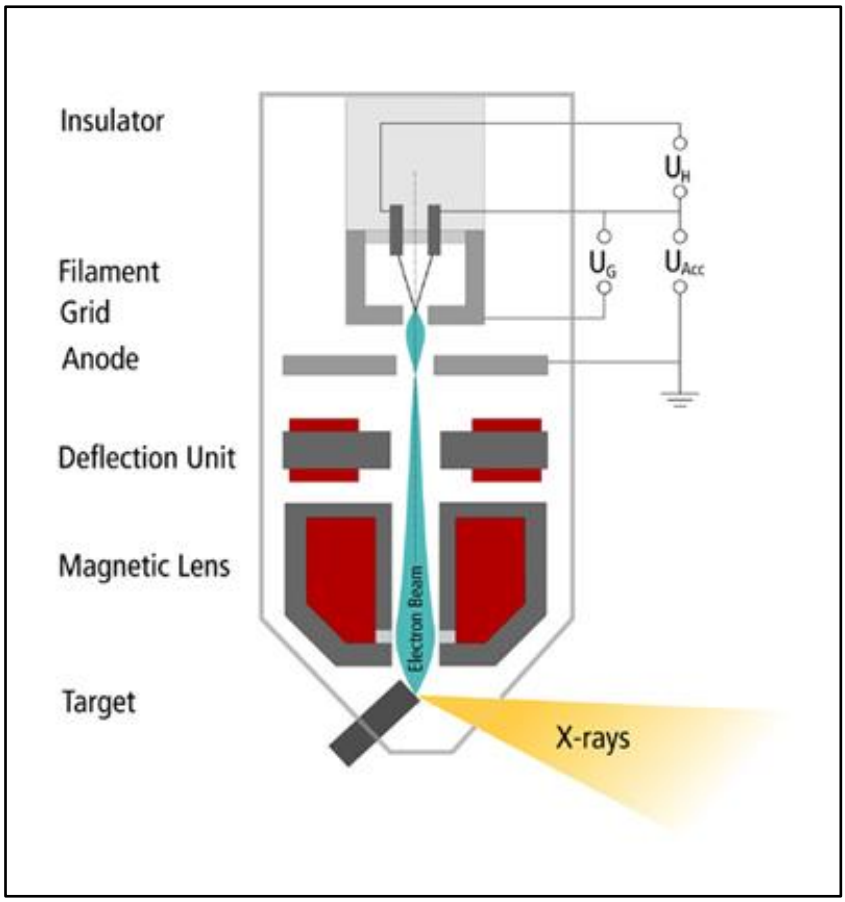

Figure 2.2 .X-Ray tube major components. (Kruth et al. 2011).

High voltage (50 -225 kV) supplied to the cathode ensures continuous electron emission from the filament surface, the rate of which is dictated by the filament current and is defined as the number of electrons travelling between the cathode and the anode. The beam current (μA) is responsible for X-ray intensity but does not affect the beam quality (penetration power), the beam voltage (kV) affects both energy distribution of the X-rays and intensity (Kruth et al., 2011). The spectrum of X-rays produced is in the form of Bremsstrahlung and characteristic radiation (Fig. 2.3).

Bremsstrahlung radiation produces a continuous background energy from low energies up to the maximum energy which is equal to the applied kV. This is due to the electrons interacting with the target atoms and the resulting X-ray emission equates to the amount of energy lost during collision. Characteristic radiation spectra are the result of electrons interacting with the target (Fig. 2.2). When an incident electron hits the target with the sufficient kinetic energy to overcome the binding energy of the electron shells, an electron is ejected and so an electron vacancy is generated. This leads to an unstable atom, so electrons from outer shells fill the K shell vacancy, this results in a discrete energy X-ray photon whose energy is equal to the difference in binding energies, the emitted X-ray energies are characteristic of the element (Seibert, 2004).

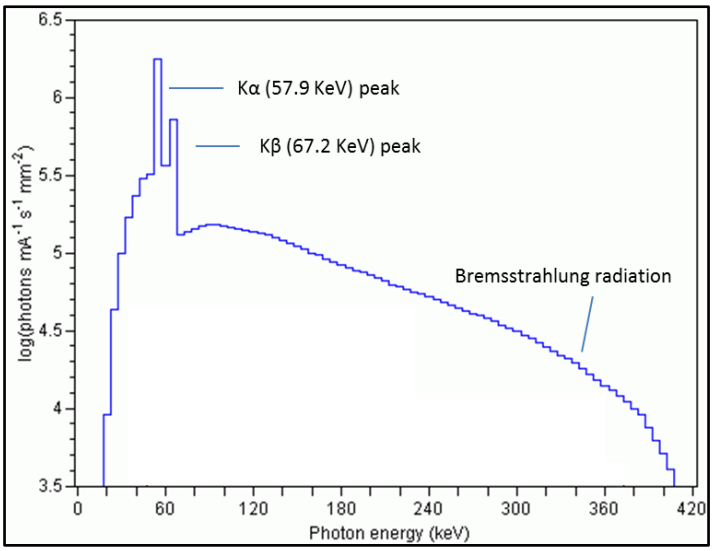

Figure 2.3. Tungsten X-ray spectra (Ketcham 2004).

2.1.3 X-Ray Attenuation.

X-rays travelling through a medium will experience an increasing reduction in intensity due to the X-rays becoming absorbed and scattered. The degree of attenuation is represented by equation 2.1 which is based on Lambert Beer law. Figure 2.4 is a graphic representation of an incident beam and the transmitted beam having passed through a material with reduced intensity. Equation 2.1 shows that X-rays penetrating a material of distance x is a logarithmic function of the absorptivity of that material.

$$I = I_o e^{-\mu x} \qquad Equation\ 2.1$$

Where I = transmitted beam, I_o = Intensity of incident beam, μ = the linear attenuation coefficient, X = distance travelled by beam through material

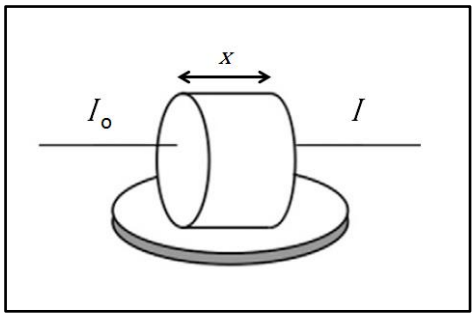

Figure 2.4. Graphic showing relative intensities of a beam of X-rays travelling through a material (adapted from Landis and Keane 2010).

The linear attenuation coefficient (μ) is defined as the proportion of the X-ray beam that is reduced per unit thickness of material and is dependent on density of the attenuating material. If a material's density was to decrease, i.e., volume increased, the effect of this density reduction would lead to a

lowering of linear attenuation coefficient. In order to obtain an attenuation coefficient that is not dependent on density, the linear attenuation coefficient must be divided by the density of material to yield the mass attenuation coefficient (μ_m, equation 2.2). The path length of the beam (x) of the material is replaced by a new quantity called the mass thickness (x_m). For a material with mass (m) has a uniform cross section area (A) and length x, the density ρ (mass/volume) is defined as:

$$\rho = \frac{m}{A\,x} \qquad Equation\ 2.2$$

When equation 2.2 and 2.3 are substituted into equation 2.1, this yields equation 2.4.

$$\mu_m = \frac{\mu}{\rho} \qquad Equation\ 2.3$$

$$I = I_o e^{-\mu_m x_m} \qquad Equation\ 2.4$$

There are three principal methods in which attenuation of an X-ray beam is explained as the beam is transmitted through a material, namely photoelectric adsorption, Compton scattering and pair production. The process of photoelectric adsorption involves the total energy of the incident photon is transferred to the inner shell electron causing that electron (photoelectron) to become ejected (ionization) with an energy equal to the energy of the incident photon minus the binding energy of the electron (equation 2.5).

$$E_e = hf - E_b \qquad Equation\ 2.5$$

Where E_e = energy of the ejected photoelectron, hf = energy of the incident photon, E_b = inner shell electron binding energy.

The process of attenuation through Compton scattering is an interaction with the incident photon and outer electrons, with the incident photon losing only a portion of its energy. The resultant photon loses energy and is of a longer wavelength. In pair production, the photon interacts with a nucleus and is transformed into a positron-electron pair; any excess photon energy is transferred into kinetic energy in the particles produced (Ketcham and Carlson, 2001). Figure 2.5 shows the principal mechanisms of X-ray generation. Electron path 1, 2, and 3 depict incident electrons interacting with a nucleus so producing bremsstrahlung radiation. Electron path 4 demonstrates production of characteristic radiation emission.

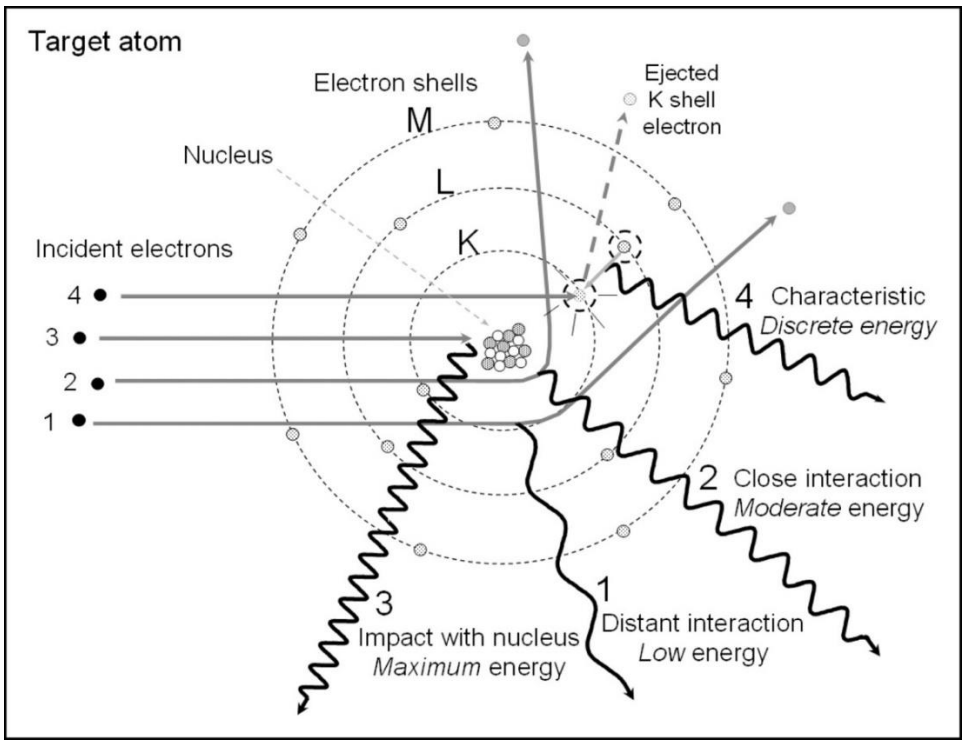

Figure 2.5. Principal mechanisms of x-ray generation by energy conversion (Seibert 2004).

For geological specimens, the photoelectric effect is the principal process under which signal is becomes attenuated at low X-ray energies (50-100 keV), whilst Compton scattering is the principal process of attenuation up to high X-ray energies (2-10 MeV). Beyond 10 MeV energies, pair production will prevail. Therefore, only photoelectric adsorption and Compton scattering are relevant due to the X-rays energies involved unless the geological samples are exposed to high energy X-rays.

The practical importance of the distinction between mechanisms is that photoelectric adsorption is proportional to Z^{4-5} (Z = atomic number), whereas Compton scattering is proportional only to Z (Ketcham and Carlson, 2001). The significance of this difference is that low energy X-rays are more sensitive to differences in composition compared to higher energy X-Rays (Ketcham and Carlson, 2001). Geological samples are composed of multiple minerals and thus densities and so it is important to understand how a geological sample will react to exposure to an X-Ray beam. Figure 2.6 is a plot of linear attenuation coefficient against X-ray energy for minerals quartz, orthoclase, calcite and almandine. (From Equation 3, mass attenuation coefficient x density = linear attenuation coefficient).

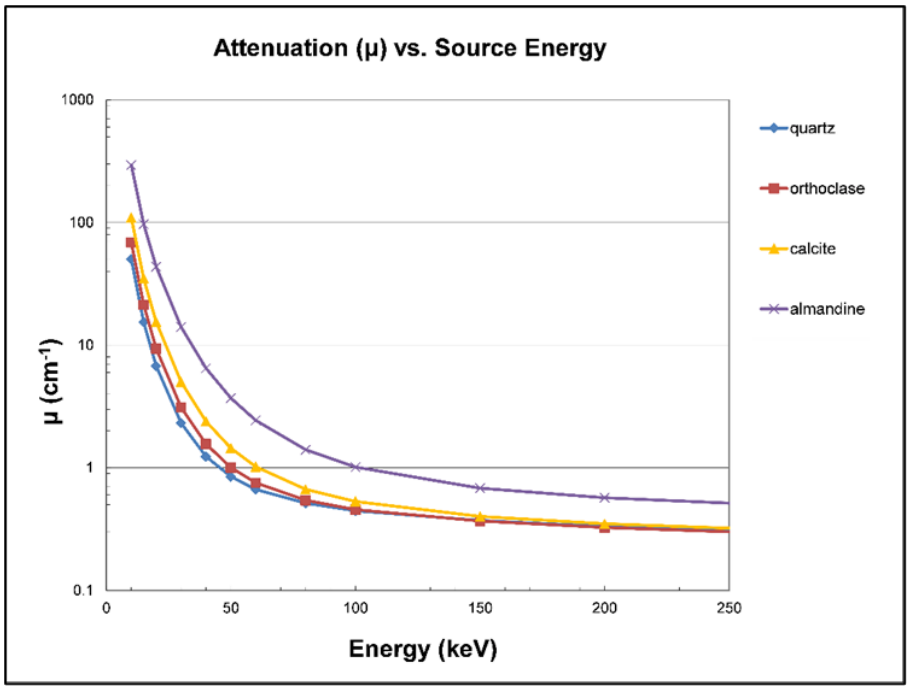

Figure 2.6. Plot of linear attenuation coefficient against X-ray energy for minerals quartz, orthoclase, calcite and almandine (adapted from Ketcham and Carlson, 2001; (MuCalcTool. http://www.ctlab.geo.utexas.edu/software).

Mass densities for the minerals, quartz, orthoclase, almandine and calcite in Figure are 2.5 g cm^{-3}, 2.57 g cm^{-3}, 4.31 g cm^{-3} and 2.71 g cm^{-3}, respectively. The curves for quartz and orthoclase whose densities are comparable and at low energy (50 keV) their linear coefficients show a small difference with orthoclase demonstrating higher linear attenuation coefficient which is related to the presence of K (a higher Z element) in orthoclase. At higher energies, the linear attenuation coefficient is seen to converge (Ketcham and Carlson, 2001). Calcite, whose density is marginally higher compared to quartz and orthoclase, has a higher linear attenuation coefficient, and so experiences a greater degree of attenuation caused by the high Z of the element Ca. The high density and high Z mineral almandine displays a high linear attenuation coefficient across the whole range of X-ray energies. Analysing the attenuation characteristics is significant because it allows prediction of the ability to differentiate between minerals in CT images (Ketcham and Carlson, 2001).

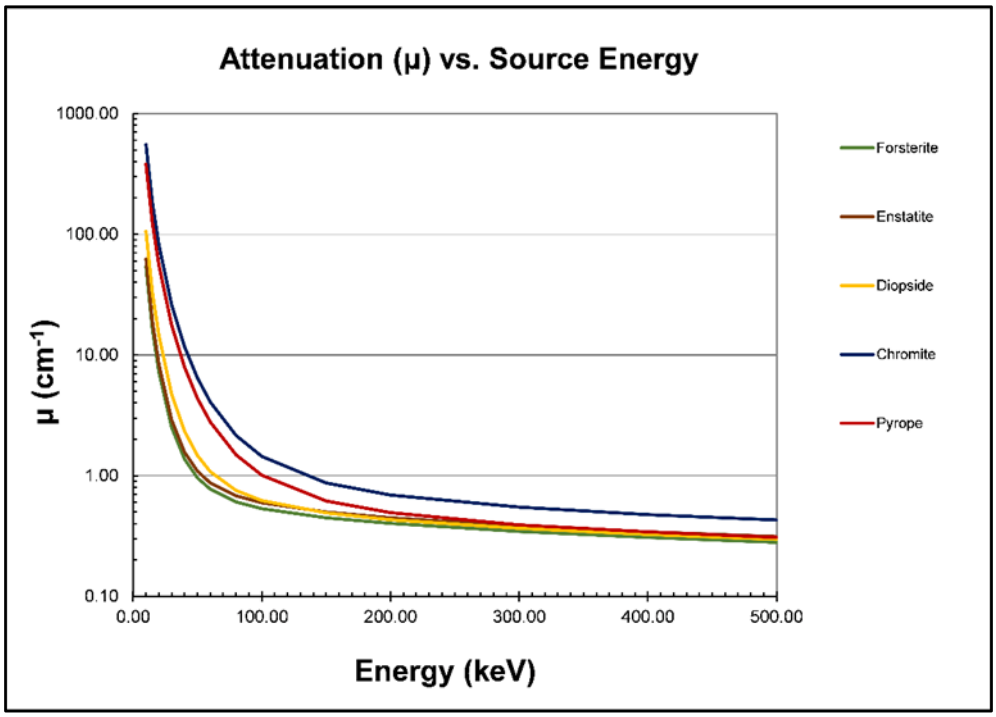

Figure 2.7. Attenuation coefficient as a function of X-ray energy of the major minerals associated with peridotite. (MuCalcTool. http://www.ctlab.geo.utexas.edu/software).

Figure 2.7 shows the attenuation of the major minerals associated with peridotite, i.e., olivine (forsterite), orthopyroxene (enstatite), clinopyroxene (diopside) and spinel (chromite). The mass densities for these minerals are 3.22 g cm^{-3}, 3.58 g cm^{-3}, 3.39 g cm^{-3} and 5.08 g cm^{-3}, respectively. The attenuation curves for forsterite and enstatite are similar across the whole range of energies; this makes distinguishing between the two minerals extremely problematic. At low energies (50 keV), clinopyroxene shows a higher attenuation factor compared to the other silicates due to the high *Z* of Ca and so allows distinction of clinopyroxene in CT images. Spinel with a high density and high linear attenuation coefficient across the whole range of energies is easily distinguishable from the silicates.

2.1.3 Detectors

Flat panel detectors (FPD) are widely used in the acquisition of CT images. FPDs are based on amorphous silicon thin film transistor (TFT) photodiode arrays coupled with scintillating material sensitive to X-ray signal (indirect detectors). The principal method which captures an image is X-ray photons transmitted through a sample interacting with a layer of scintillating material which converts X-ray photons to visible light. Visible light photons then interact with an array of photodiodes producing electrons which interact with the pixels in the amorphous silicon TFT array, this process generates electronic signal which is converted to an image. Figure 2.8 shows the exploded sections of an FPD and its interaction with an X-ray signal.

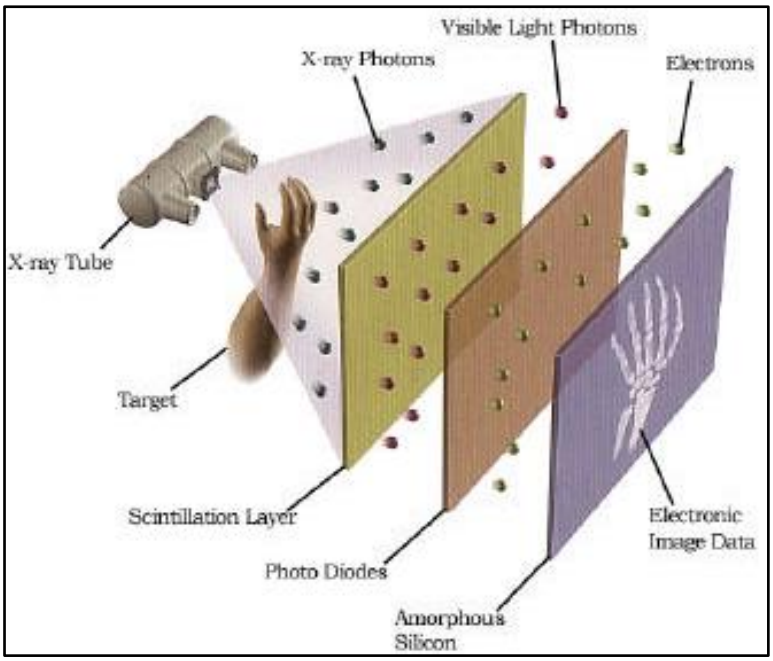

Figure 2.8. Flat panel detector individual sections. (http://atlas.physics.arizona.edu).

Three principal metrics are used to quantify Detector Image Quality (www.teknologisk.dk):

- Sensitivity - a measure of the detector signal output as a function of number of exposure quanta per unit area.

- The Modulation Transfer Function (MTF) – the measure of the transfer of modulation (or contrast) from the input to the detector output. i.e., a measure of how well the imaging system transfers detail of resolution from the object to the image produced by the detector.

- Detective Quantum Efficiency (DQE) - measure of the efficiency with which a detector passes signal to noise ratio from its input to its output. DQE is the principal objective measurement used to determine imaging performance.

2.1.5 CT Data collection

The principal configuration for CT data acquisition involves a stationary X-ray source, rotational sample stage and a detector which is sensitive to the X-ray signal.

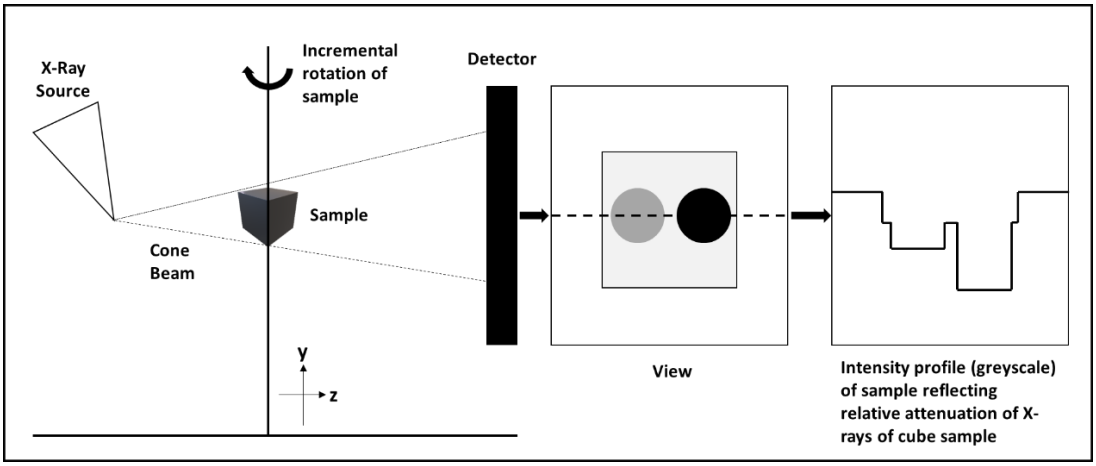

Figure 2.9. Principal configuration for CT data acquisition. (Author's own image).

During data collection a specimen is mounted onto the rotational sample stage in-line with the X-ray source and detector as seen in Figure 2.9. The geometry of the specimen and X-ray source will dictate the CT image resolution. This relationship is explained in Figure 2.10 whereby reducing the specimen to X-ray source distance along the magnification axis (Z) a higher magnified and more resolved image is captured at the detector when compared with the specimen with a greater distance away from the X-ray source, however higher magnified images incur the possibility of introducing blurring to the image as shown in Figure 2.10.

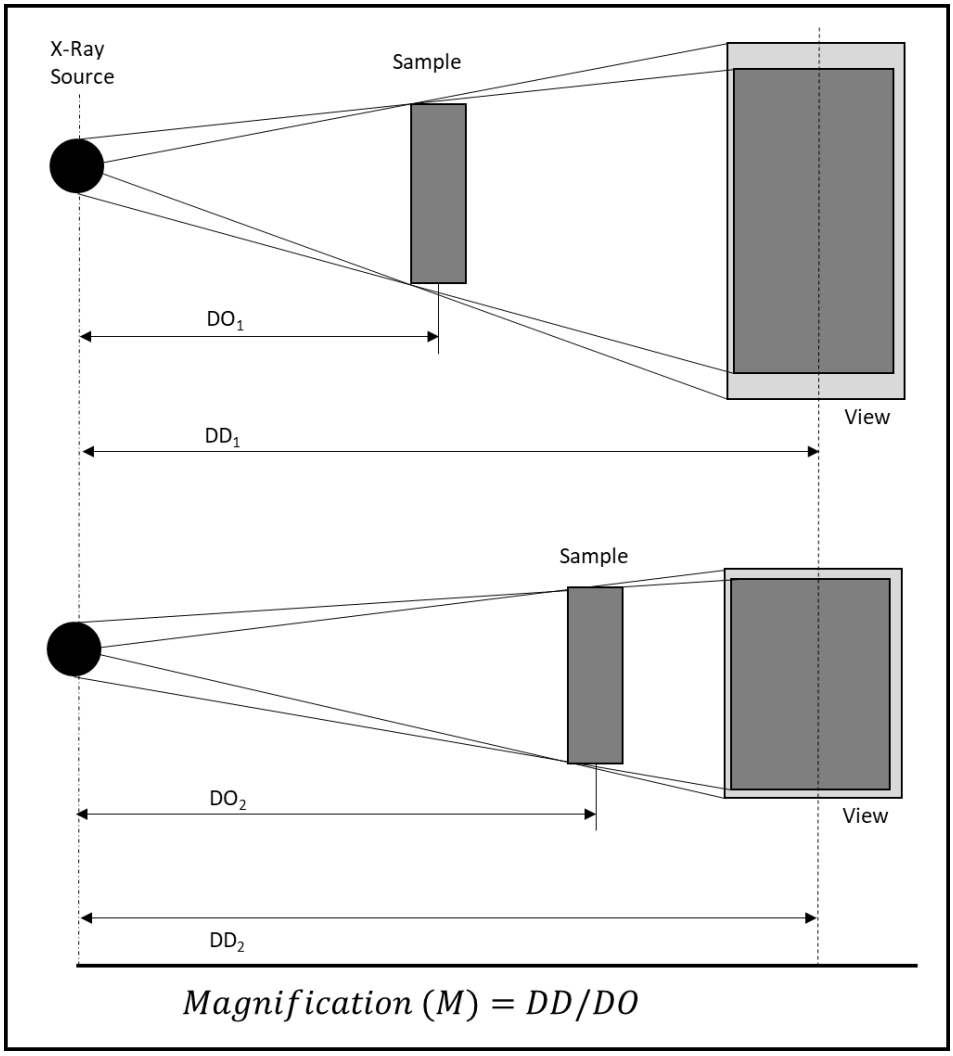

Figure 2.10. Sample magnification and image blur. (Adapted from Kruth et al., 2011).

Data acquisition involves the specimen rotating about the sample stage allowing multiple sets of images (views) to be captured over the desired range of rotation and thus forming 2D projections of the specimen. The process in which 2D slice images are reconstructed from the raw intensity data into a 3D digital image is a mathematical process, one of which is filtered back projection. The input for the reconstruction is the grey value profiles along the pixels located on one line of the detector, i.e. pixels lying in the XZ section of the object (Kruth et al., 2011) as show in Figure 2.11. The process of filtered back projection involves data which is first convolved with a filter and each view is successively superimposed over a square grid at an angle corresponding to its acquisition angle. During the reconstruction process raw intensity data is converted to CT values and map linearly to the effective attenuation coefficient of the material in each voxel (Ketcham and Carlson 2001). A single tomographic slice is defined as a cross-sectional layer of a subject matter and is comprised of smaller divisions characterised as volume elements (voxels). In a digital image each voxel dimensions

are related to the size of a pixel and also to the degree of the sum of attenuation with respect to the X-ray path. Figure 2.12 is an illustration of a tomographic slice.

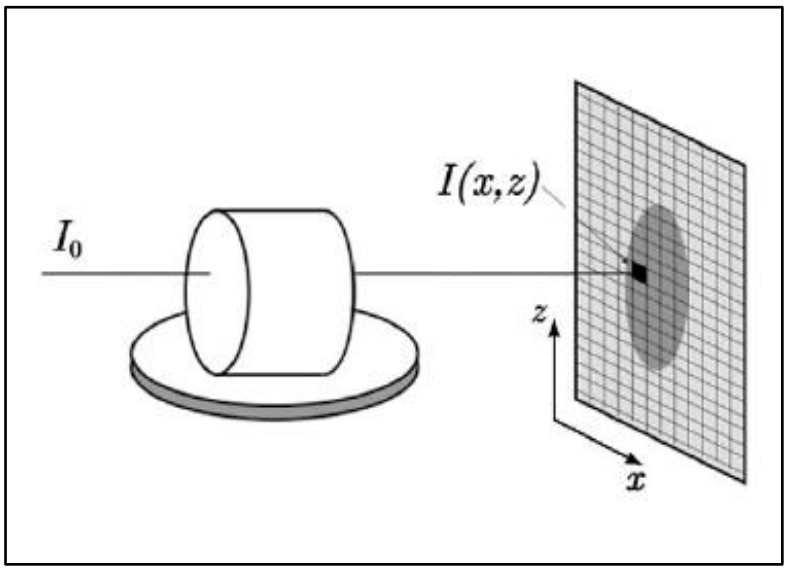

Figure 2.11. Grey value profiles along the pixels located on one line of the detector (Landis and Keane, 2010).

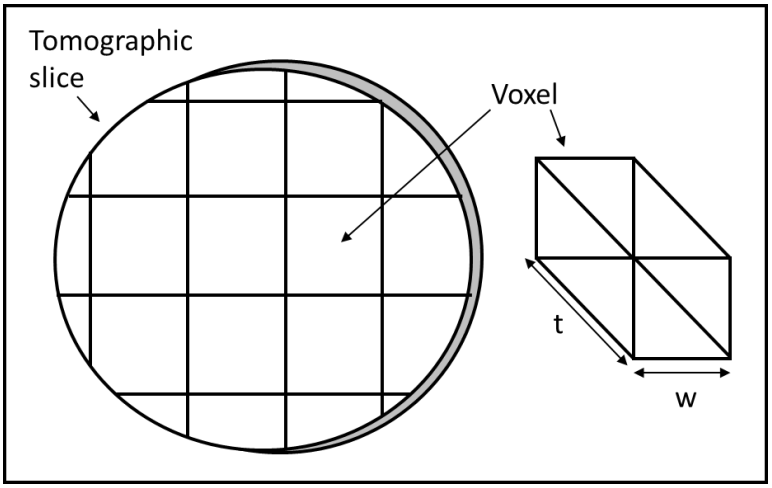

Figure 2.12. Illustration of a tomographic slice and individual voxel. (Author's own image).

The series images in Figure 2.13 show the result of three aligned balls which were reconstructed from scans with increasing angular positions. The series of images shows that with small number angular positions, e.g., four, the resulting reconstruction is unclear and ill-defined and results in what appears to be a 3 x 3 grid of square objects. As the views are increased, the reconstructed slices increasingly improve and with sufficient slices reveal an accurate image of the aligned balls.

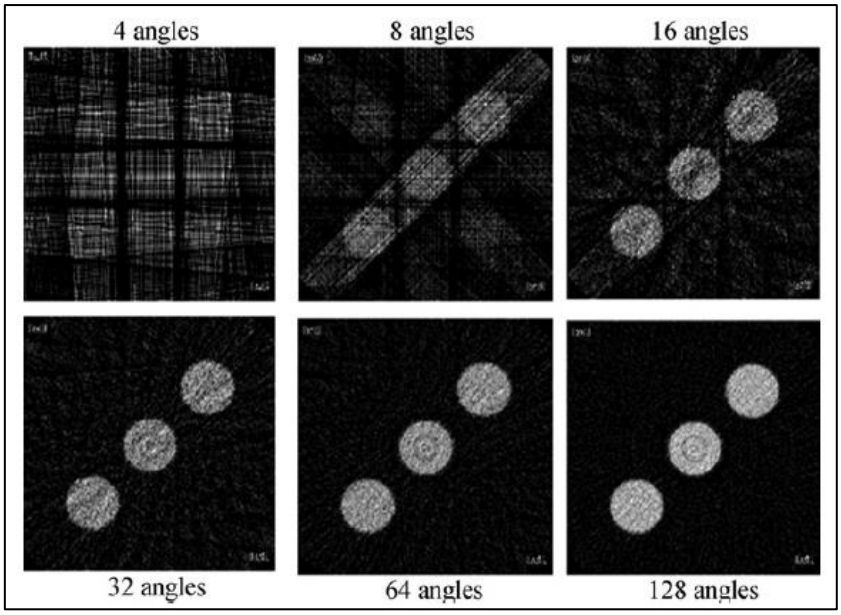

Figure 2.13. Reconstructed from scans with increasing angular positions (Kruth et al 2011).

Resolution of the measurement and reconstruction is influenced by pixel size, number of pixels within each grey value profile, number of pixel or slices in the Y direction and number of angular positions (Kruth et al., 2011). Figure 2.14 is an illustration outlining the major processes involved in the production of a 3D image using CT scanning techniques.

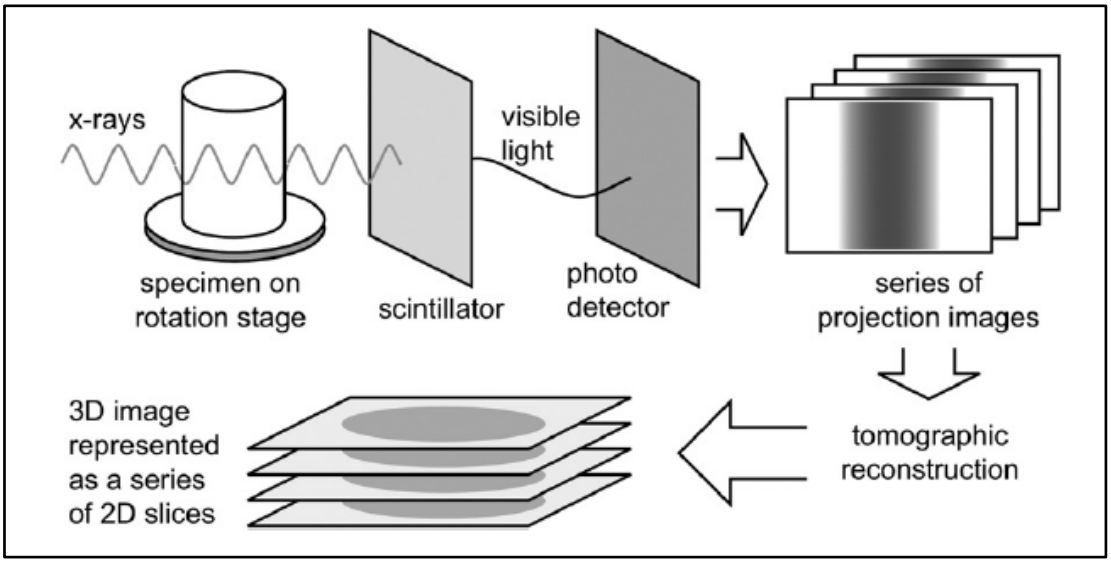

Figure 2.14. Graphic outlining CT major processes in producing 3D images. (Landis and Keane, 2010).

2.1.5 Data processing.

Since X-ray absorption is a measure of material density, its distribution within 3D images provides an insight into the internal structures and distribution of phases within a specimen. This division between density differences represented in a 2D image is illustrated in Figure 2.15. In Figure 2.15a

and b the images are of a reconstructed slice image and a 3D image of garnet peridotite. The attenuation difference and hence density difference between minerals is revealed as a disparity in grey scale intensities, thus separating distinct phases within the sample material, i.e., bright regions representing high absorption/density phases and dark intensities representing low absorption/density phases. Raw 3D data is processed using multiple software suites. The two data processing and segmentation software used in this study is Drishti, Avizo and Dragonfly. Analysis of individual slice images was done using the ImageJ software suite.

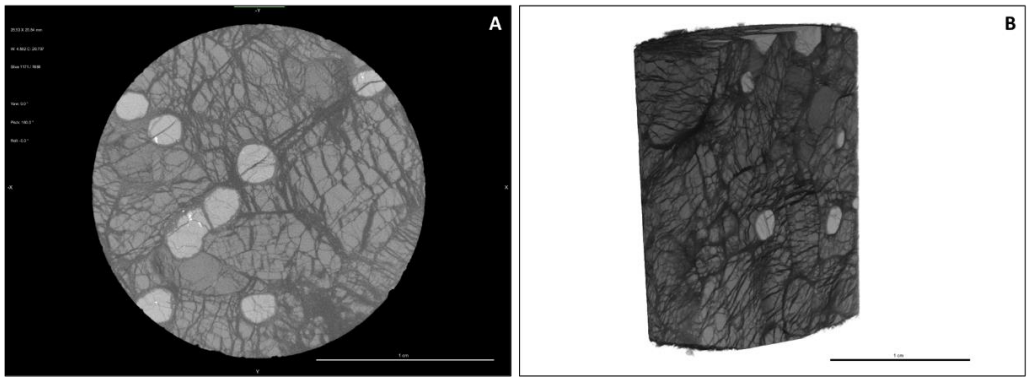

Figure 2.15. Images of mantle xenoliths from this study. (A). 2D slice Garnet peridotite (DB1). Scalebar 1 cm. (B) 3D multiphase image. Garnet peridotite (DB1). Scalebar 1 cm. Author's own image.

Phase analysis for 2D and 3D images is carried out by utilising the voxel intensity histogram, which plots the frequency of voxels at a particular intensity and so permits the separation (segmentation) of an image into distinct phases. This examination of the histogram is further illustrated in Figure 2.16a and c. Here the histogram for a garnet peridotite core (DB1) is shown with peaks corresponding to different phases clearly distinguishable, i.e., air and solid material. Figure 2.16 provides an example of segmentation where voxel intensities less than a value chosen as a distinction between two phases and in which values less than that phase boundary is set to 0 (black) and intensities greater to 1 (white). This manipulation of the histogram yields the grey scale image (Fig. 2.15).

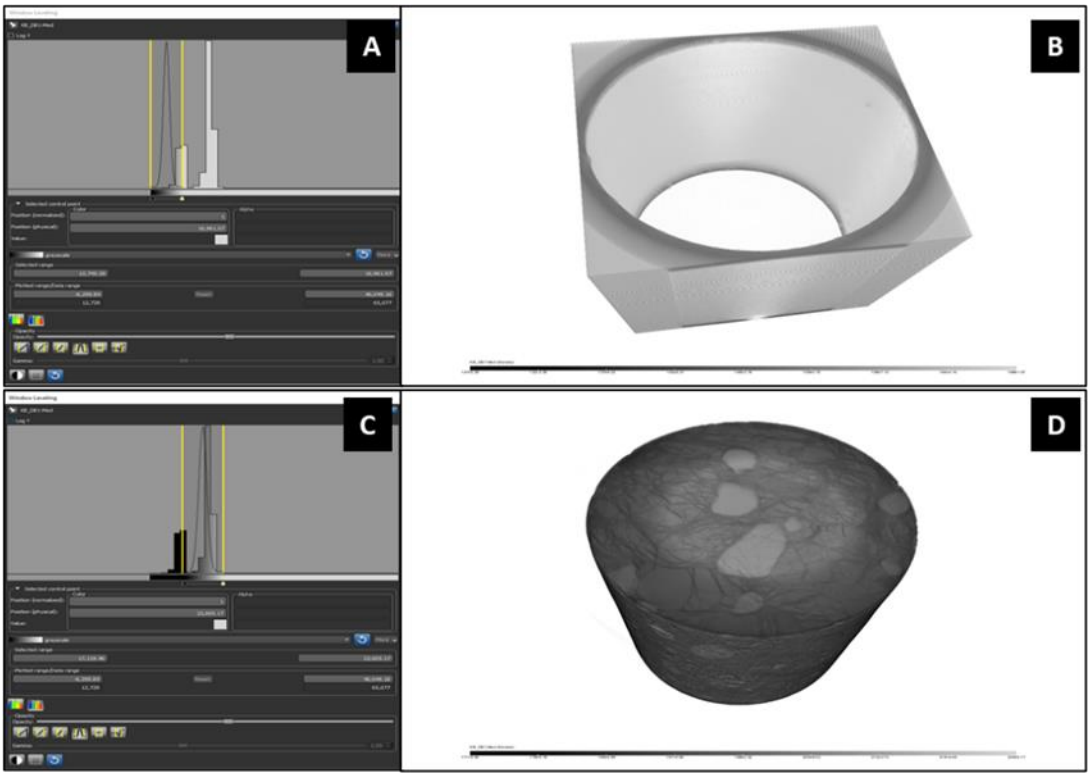

Figure 2.16. (A) Voxel intensity histogram isolating region relating to air and low-density sample holder. (B) 3D image rendered of low-density region of sample data including air. based on phase identification. (C) Voxel intensity histogram isolating region relating to air and low-density sample holder. (D) 3D image rendered of high-density (rock) region of sample data. Author's own image.

One major factor that must be considered when evaluating voxel intensity histograms taken from multiphase data is overlapping intensities of the different phases. Careful consideration must be applied in identifying an accurate phase boundary. Figure 2.17a is an illustration of a histogram of a multi-phase material in which overlapping intensities are present and where the phase boundary is set to the minimum overlap. Figure 2.17b is a 3D image of the multiphase material and c, d and e are rendered images of the individual phases of the multi-phase material (cement). In this study, similar images will be obtained for minerals in mantle xenoliths to reveal the three-dimensional nature of their textures. Segmented images can be displayed in single 2D images, or the 3D data can be converted into a movie which rotates the sample and individual phases can be highlighted and viewed displaying a true representation of a particular phase and its relation within the sample.

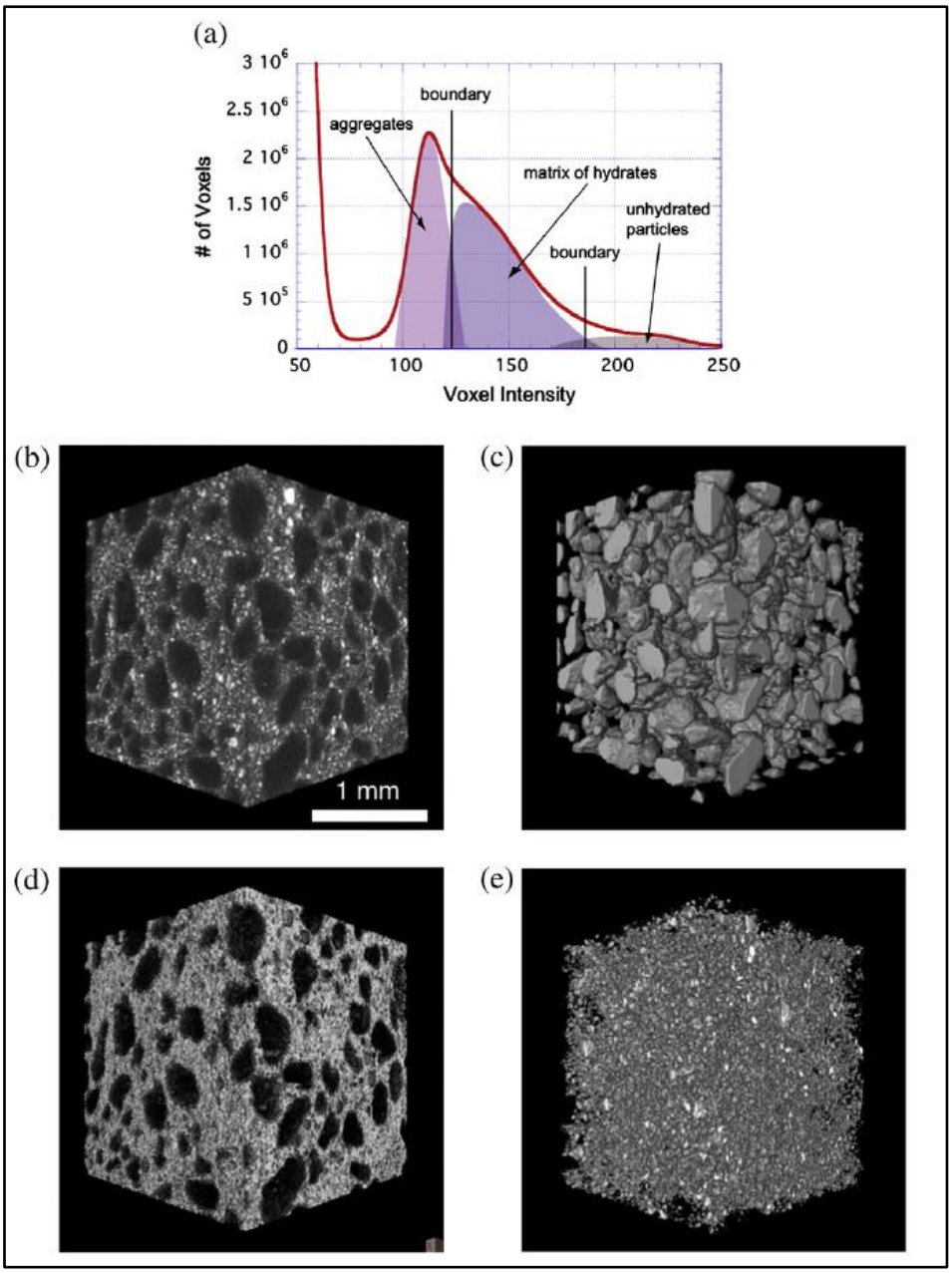

Figure 2.17. (A) Illustration of a histogram of a multi-phase material in which overlapping intensities are present and where the phase boundary is set to the minimum overlap. Figure 2.17b is a 3D image of the multiphase material and 2.17c, d and e are rendered images of the individual phases of the multi-phase material (cement). (Landis and Keane, 2010).

2.1.6 Artifacts

CT scan data can be affected by artifacts which can compromise the quality of any 3D rendered volume. Beam hardening is an example of one such artefact in which the edges of an image appear more intense when compared to its centre. Beam hardening artifacts in multi-component geological samples will impact identification of mineral phases. Beam hardening is caused by the increase in mean X-ray energy, i.e., hardening of the X-ray beam travelling through a medium. It occurs because the X-ray beam is polychromatic and attenuation is greater for photons of lower energy and the

energy distribution hardens as it passes through the material (Ramakrishna et al., 2006). Several techniques can be employed to minimise the effect of beam hardening; one technique is to use an attenuation filter before the X-ray beam interacts with the sample, thus reducing low energy X-rays. Cu or Al are examples of the composition of filters used.

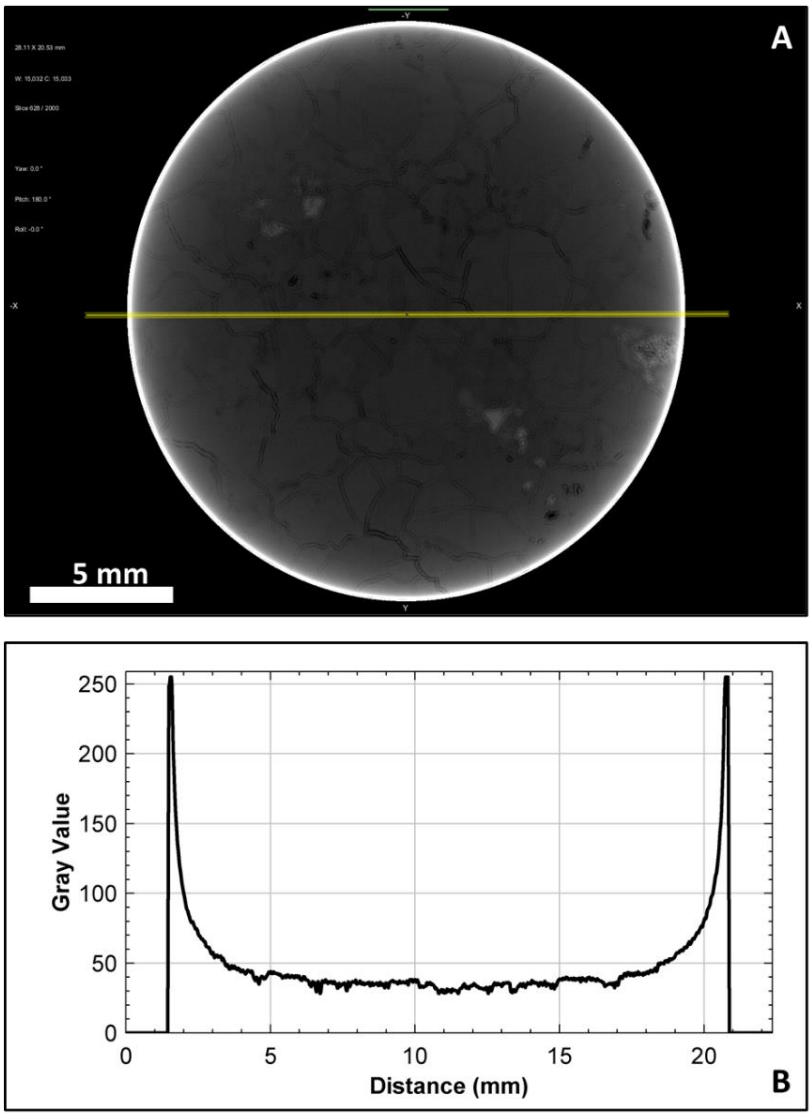

Figure 2.18. (A) 2D slice image of a garnet peridotite (Vitim) slice exhibiting beam hardening and corresponding grey value profile along the arrow line. Scalebar is 5 mm. Data collected using Cu filter 1 mm thickness. (B) Grey scale intensity plot across diameter of sample. Data taken from this study.

Figure 2.18 is an image which shows beam hardening in a single slice image of a garnet peridotite (from Vitim) and the associated grey value profile where the outer portion of the material is more intense when compared to its centre. Figure 2.19 A and B compares the effect of beam hardening on a sample with the use of an attenuation filter. Figure 2.19A displays the more intense outer rim and associated high grey values. Image B is the same material scanned but using an attenuation filter in

between the X-ray beam and sample, Image B clearly shows a more even grey scale and the intense outer rim displayed in image A is drastically reduced.

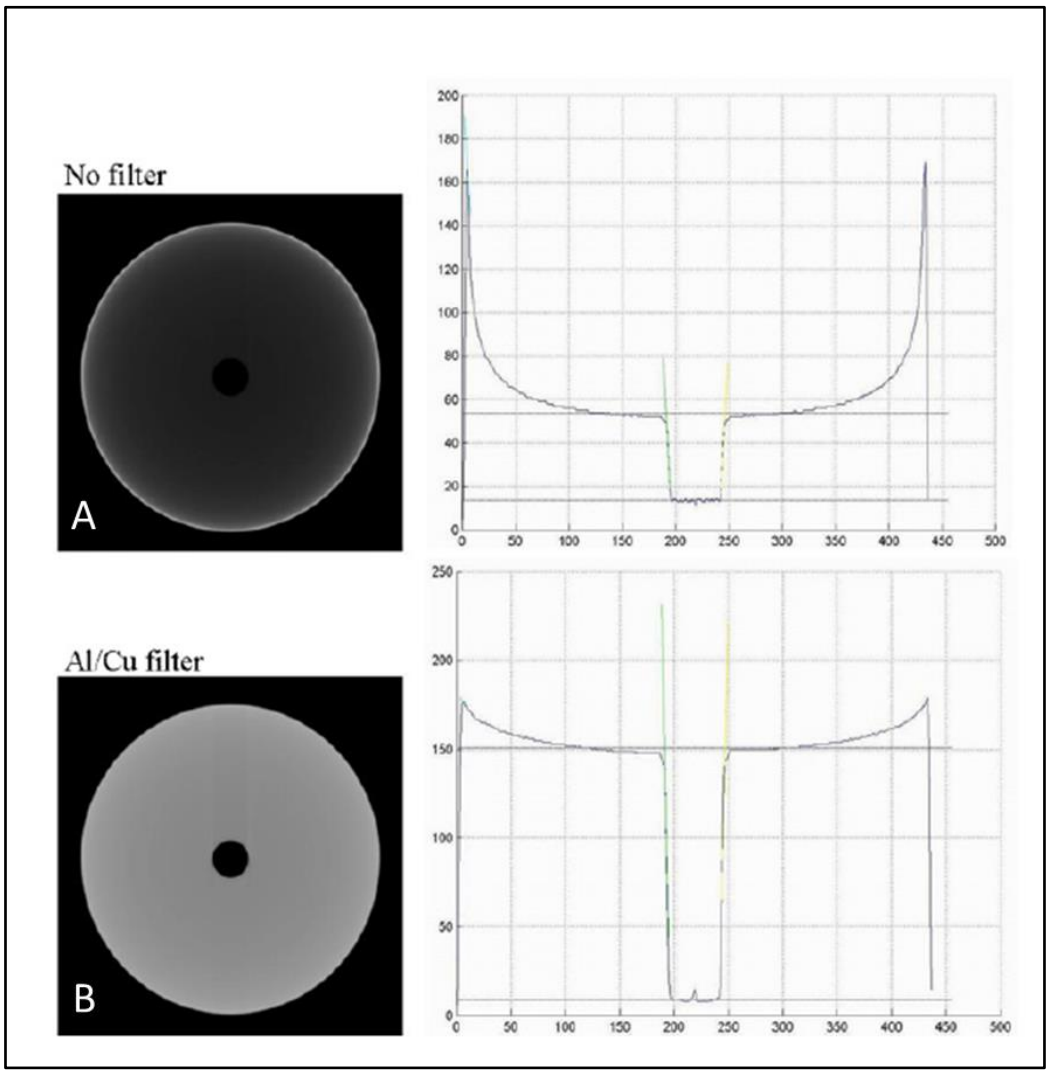

Figure 2.19. Beam hardening and its reduction with the use of an attenuation filter (Kruth et al., 2011).

Partial volume effects can become visible in a multi-phase material since for a sample, a voxel represents an attenuation value but when the voxel is composed of multiple materials of different attenuation values, then the voxel attenuation value will be an average of the attenuation values. This results in boundary edges being blurred and not sharply defined. The presence of artifacts must be considered prior to data collection of geological samples in order to minimise their effect and associated loss in image quality in the 3D rendered volume.

CT scanning has been used in numerous studies to studies into the textures of mantle rocks and meteorites. Carlson (2006) and Ketcham and Carlson (2001) studies provided detailed descriptions into the application of CT scanning for the textural analysis of geological samples. Jerram et al (2009)

used CT analysis to investigate olivine populations in kimberlites. Griffin et al (2012) and Hezel et al. (2013) studies investigated meteorite textures.

Numerous studies have investigated meteorite and mantle xenolith textures using micro-CT analysis e.g., Cnudde et al., (2006); kimberlites (Jerram et al., 2009); lunar and martian fragments (Nascimento-Dias et al., 2019); Allende and Mokoia meteorite (Griffin et al., 2012; Hezel et al., 2012) and xenoliths from the Pannonian Basin (Patkó, et al., 2020). Each study demonstrated that micro-CT analysis is a powerful tool in investigating rock textures in three dimensions.

2.1.7 Micro-CT sample preparation, data collection and analysis

X-Ray computed tomography (CT) is a non-destructive technique in which a series of 2D images (radiographs) characterising variations of X-Ray interaction due to density differences of the subject matter, when combined provide a high-resolution 3D visualisation of the subject matter. The attenuation characteristics allow us to predict the possibility of differentiating between different minerals in CT images (Ketcham and Carlson, 2001). The attenuation curves for forsterite and enstatite are similar across the whole range of energies, which makes it very difficult to distinguish these two silicate minerals. Clinopyroxene has a higher attenuation factor at low energies (50 KeV) because of the high Z of Ca, and so allows clinopyroxene to be distinguished in CT images. Spinel with high density and a high linear attenuation coefficient across the whole range of energies is easily distinguishable from the silicates. Thus, during segmentation, the spinel and garnet phases can be viewed in isolation. Segmentation of spinel with a higher density due to its Cr content is relatively straightforward compared with garnet. Garnet Cr content (and hence density) varies with tectonic setting with craton peridotites (e.g., South Africa) having ~5 wt% Cr_2O_3 in garnet, compared with <2 wt% Cr_2O_3 in garnet from non-cratonic continental peridotites (e.g., Vitim and Pali-Aike). The effect of this is that, even in a 25 mm diameter core, beam hardening makes segmentation of garnets throughout the sample data difficult, principally due to two factors. Firstly, grey scale values for similar density material are lower in the centre compared with the outer portion and secondly, lower Cr content in garnets reduces density and, with low-Cr garnets from Vitim, the grey scale values are closer to those of the silicate phases. Figure 2.20 shows plots of greyscale value versus distance across a sample core showing the relative intensities of spinel and garnet peridotites from different tectonic settings and how these vary against the silicate background of each core.

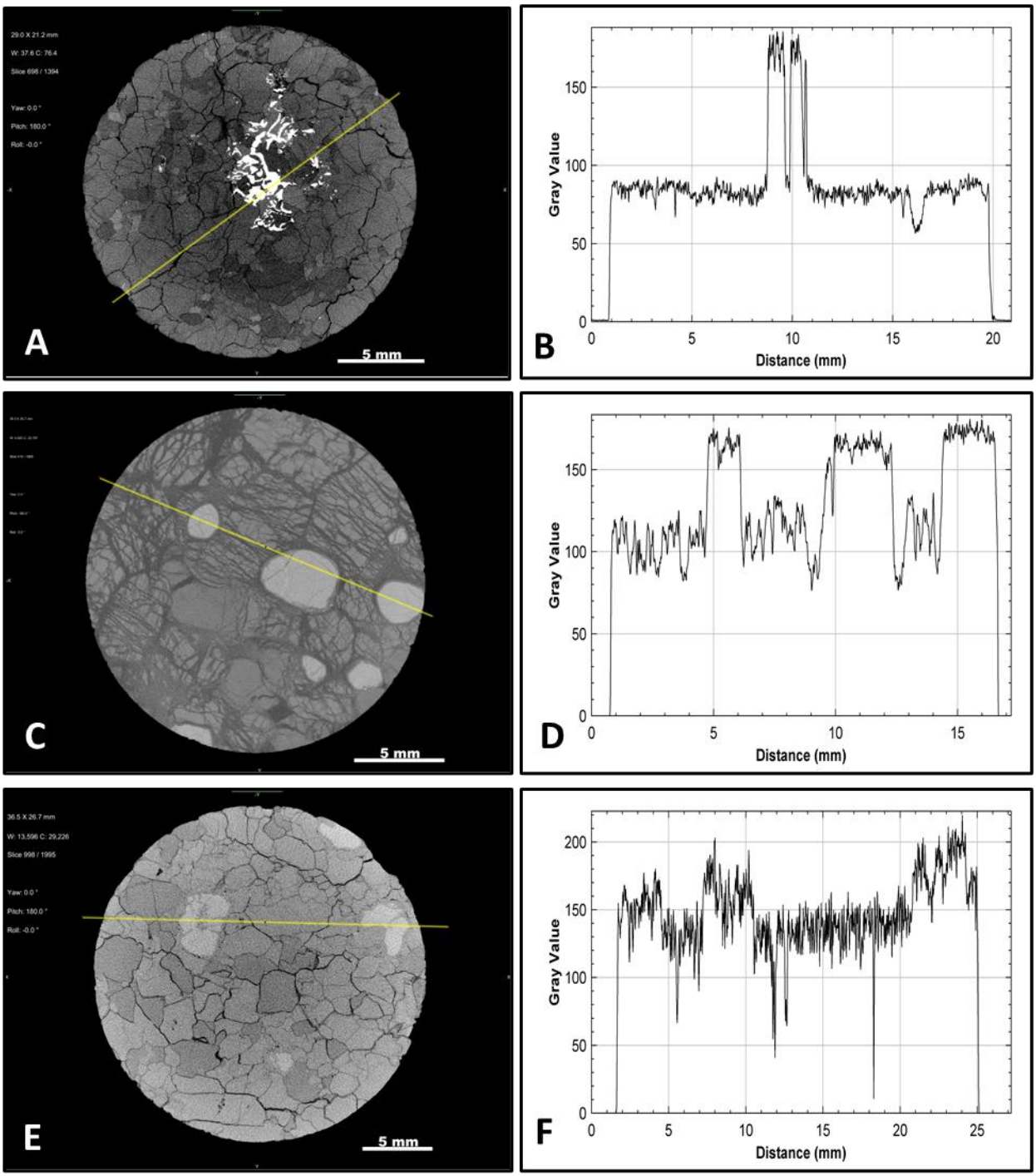

Figure 2.20. (A) 2D slice image of a spinel peridotite core from Lanzarote. (B) Plot profile of grey scale intensity across spinel peridotite core from Lanzarote. (C) 2D slice image of a Garnet peridotite core from South Africa. (D) Plot profile of grey scale intensity across spinel peridotite core from South Africa. (C) 2D slice image of a Garnet-spinel peridotite core from Vitim. (D) Plot profile of grey scale intensity across spinel peridotite core from Vitim.

The 3-D rendered visualisations detail the spinel grain size, shape, and distribution throughout the whole rock core with high accuracy, allowing a complete visualisation of the progress of spinel texture from a protogranular textural type to an equigranular texture. Several factors must be considered for imaging a geological sample. In this study the spinel peridotites and garnet-bearing peridotites are protogranular textural type i.e., coarse grained with olivine grain size >2 mm.

Although the technique is described as “non-destructive”, 25 mm diameter cylindrical cores of each sample must be made. The shape and size of the cores were chosen to ensure equal X-ray absorption and penetration of the X-ray beam, thus limiting the introduction of false artifacts into the final 3D rendered volume. During initial imaging, it was shown that artifacts including beam hardening can adversely affect the data quality. Greyscale values at the edges of the sample can be higher than those towards the centre in the same material, making 3D segmentation inaccurate. In this scenario 2D slice images in greyscale can provide information on the internal structure of the sample but 3D segmentation is difficult due to similar material/grains having differing greyscale values across the image. Thus, there is a balance to be considered between grain size and sample size. For instance, cores of 10 mm diameter would provide higher resolution but because of the coarse grain-size of peridotites, almost all useful information on grain shape and relationship would be lost. 10 mm diameter cores would be useful if the core were derived from a larger previously analysed core and a 10 mm core would then represent a specific site of interest, e.g., a region of metasomatic reaction. In this study, samples were cored to a diameter of 25 mm and height of 25 mm, except for the lunar material. The 25 mm diameter rock core, coupled with the random selection of a region of the sample to core, caused some problems particularly with garnet peridotites where the garnet grain-size is > 5mm and the distance between garnet grains can be > 15 mm. This can lead to the core not being representative of the original sample with cores capturing regions devoid of garnets or only partially capturing garnet grains on the edges of the core. This is exaggerated when the 3D data set was cropped to accommodate beam hardening.

Several samples of garnet and spinel peridotites were analysed without coring. This data provided a test and a limit into the size of sample for which accurate data can be obtained. Samples chosen to be analysed were generally spherical in shape with a diameter of <100 mm. Micro-CT data did suffer from beam hardening, rendering 3D segmentation difficult. However, 2D slice images captured information on the distribution of high-density phases of spinel and garnet. The advantage of imaging a whole rock sample is that a more accurate display of spinel and garnet is obtained but, if the raw data is cropped, this effectively results in the loss of data and reduces the sample size thus eliminating wider mineral distribution. Figure 2.21 shows 2D slice images and 3D rendered images of a whole rock scan of a spinel lherzolite from Calatrava (Fig. 2.21E). Dimensions of the sample are 69.6 x 62.1 x 52.6 mm. Figure 2.21B shows distribution of spinel throughout the sample but, due to beam hardening, spinel greyscale values are higher on the outer portion compared with the centre. This is most notable in the silicate phase and Figure 2.21D which displays how silicate greyscale values vary across the width of the data set within a material of equal density.

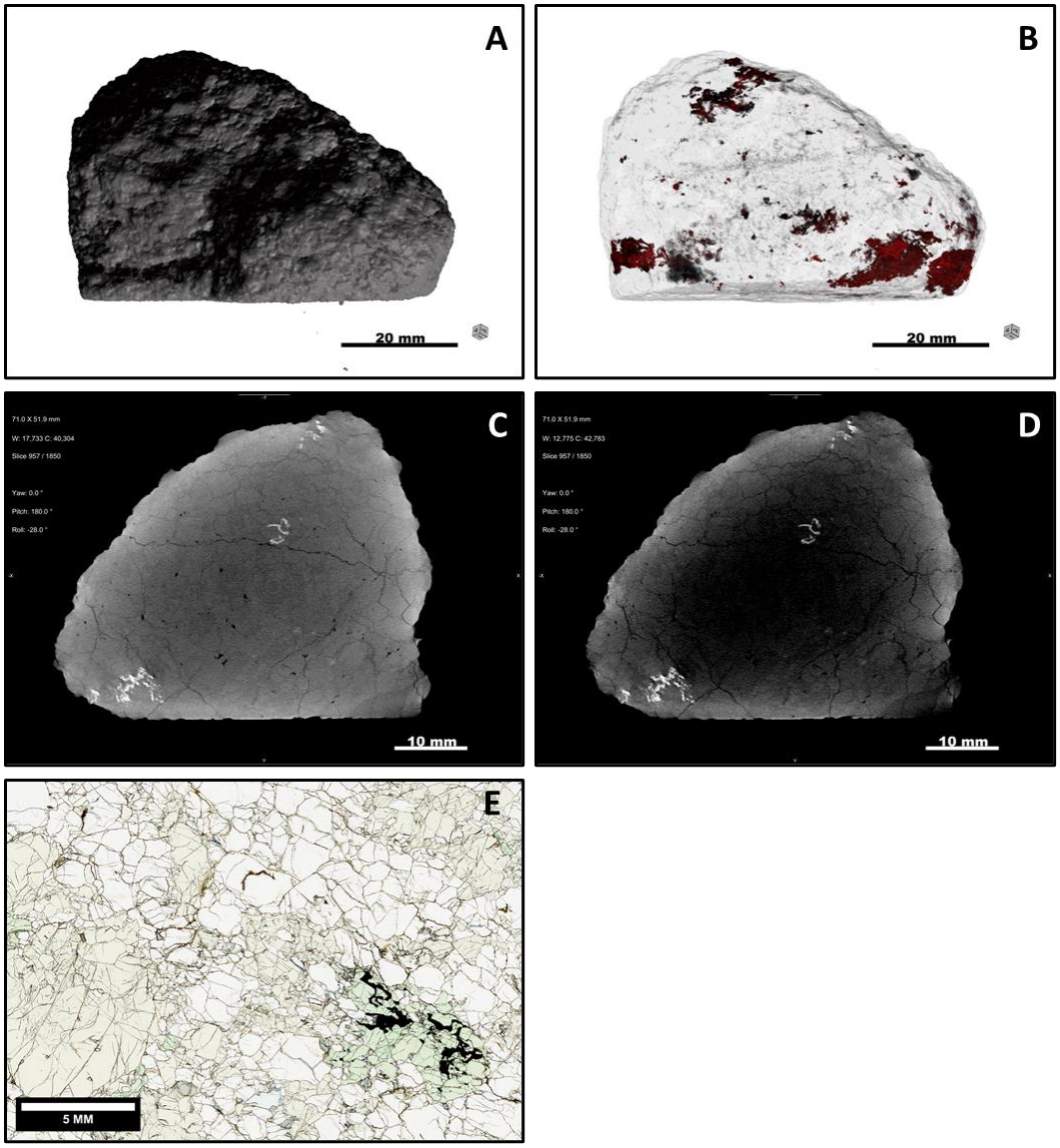

Figure 2.21. (A) 3D solid rendered image of a spinel lherzolite (Calatrava), Dimensions of the sample are 69.6 x 62.1 x 52.6 mm. Scalebar 20 mm. (B) 3D rendered image of a spinel lherzolite (1EHW03, Calatrava) with silicate phases set to semi-transparent. Scalebar 20 mm. (C) 2D slice image of a spinel lherzolite (1EHW03, Calatrava) showing the silicate phases (grey) and spinel (white). Scalebar 10 mm. (D) 2D slice image of a spinel lherzolite (1EHW03, Calatrava) showing the silicate phases (grey) and spinel (white) with reduced histogram selection showing loss of data in sample centre caused by beam hardening. Scalebar 10 mm. (E) Photomicrograph in ppl of a spinel lherzolite (1EHW03, Calatrava). Scalebar 10 mm.

For micro-CT data collection, the rock cores were mounted onto oasis foam to ensure stability housed on a translation stage where the sample was centred inside the X-ray enclosure, and precession reduced. Filters were added at the X-ray source exit. These filters act to effectively harden the beam prior to interacting with the sample. The distance of the sample to source was checked on a single view to ensure maximum magnification without introducing blurred edges. The rock cores were scanned with 0.1° rotation, forming a total of 3142 projections for a complete rotation and an exposure time typically of 708 ms. Raw image data was then imported into 3D software analysis software for 2D slice analysis and 3D segmentation. Before the 3D data set was segmented, 2D slice images were viewed to identify structures and begin the process of 3D

segmentation. The 3D representation will display accurately the size, shape and relative position of grains and structures within the core. On this visual basis any information on orientation is obtained. Measurements of grain size and structures were made on the individual 2D slices.

2.2 Electron Microprobe

Electron microprobe analysis (EMPA) is an analytical technique which involves the interaction of a finely focused electron beam with a solid sample material (Fig. 2.22). The incident electrons have a kinetic energy of 5-30 keV and penetrate the sample to a depth of the order of 1 µm, spreading out laterally to a similar distance (Reed, 1993).

Major components of the electron probe include electron gun, which houses the W filament (cathode), electromagnetic condenser and focus coils which focus and condition the electron beam onto the sample hosed on a X, Y, Z translation stage. Several detectors are positioned to collected characteristic X-rays and electron signals emitted from the solid sample. These include WDS (wavelength-dispersive X-ray spectroscopy) spectrometers, EDS (energy-dispersive X-ray spectroscopy) and backscatter electron (BSE) detectors.

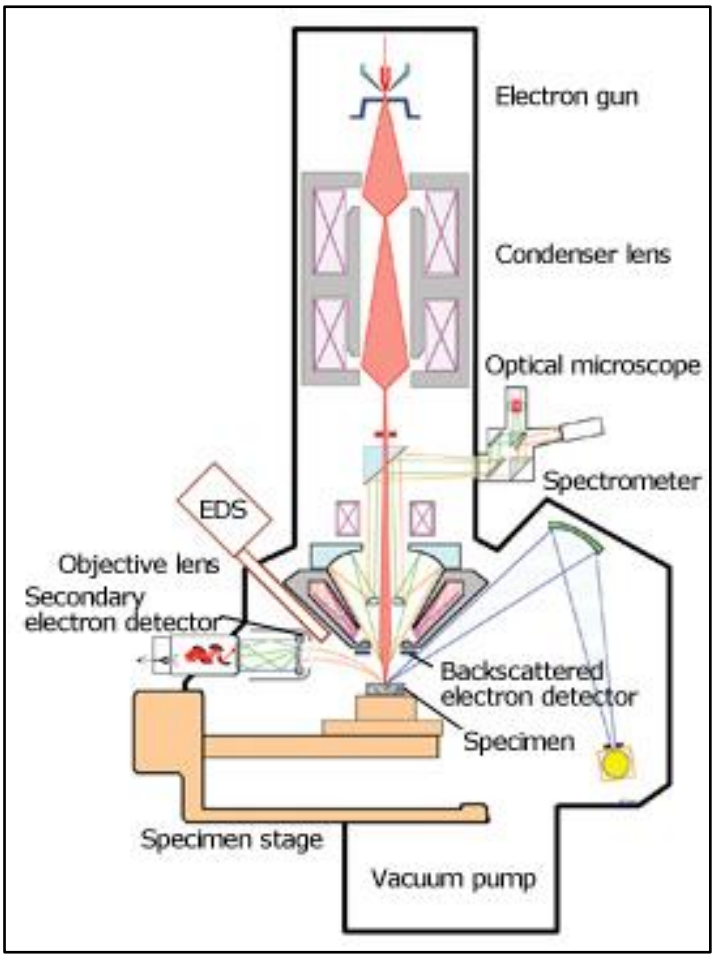

Figure 2.22. Electron microprobe block diagram (https://www.jeol.co.jp/en/science/epma.html).

Interaction of electron beam and atoms of the sample involves production of signals by undergoing two types of scattering i.e., elastic, and inelastic scattering. Electrons also simply pass through the material with no interaction. The electron beam kinetic energy does not significantly change during elastic scattering and, if the elastic scattering angle is > 90^{o}, then it produces backscatter electrons. Inelastic scattering electron beam energy is transferred to atoms of the sample material, and this leads to the production of characteristic X-rays, bremsstrahlung, Auger electrons and secondary electrons (Fig. 2.23).

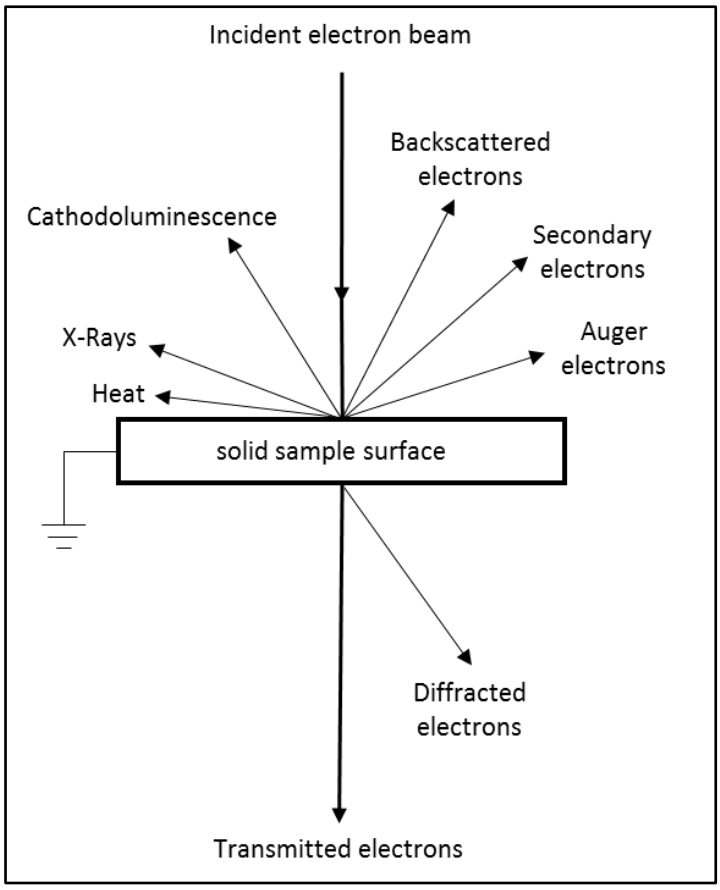

Figure 2.23.Types of signals recorded from the interaction of a finely focused high kinetic energy beam of electrons with a solid sample material (adapted from Potts et al., 2012).

2.2.1 Wavelength Dispersive Spectroscopy (WDS)

WDS measurements of the sample area require an electron beam which impinges the sample yielding characteristic X-ray wavelengths of individual elements. The characteristic wavelength signal is interpreted and thus provides quantitative analyses of the elemental composition of the subject material. Characteristic X-ray intensity emitted by an element in a compound is proportional to mass concentration of that element (Reed, 1993). Following production of characteristic x-rays, the X-ray beam passes through a specified analytical crystal (Figs. 2.24 and 2.25) based on its lattice (d) spacings. The geometry of the sample and analysing crystal is such that a constant angle is maintained. X-rays interact with the crystal and those X-rays which satisfy the Bragg condition (equ. 2.6) are transmitted and registered on the detector. To record other elements the orientation of an analytical crystal must be changed to allow the change in Bragg condition from the different element. Multiple analysing crystals are utilised in a WDS spectrometer to allow for a complete range of compositional analysis. The configuration of the sample crystal and detector is such that all three components (sample, analysing crystal and detector) lie on a common circle, the Rowland

circle (Fig. 2.24). X-ray intensities counted at the detector require correction to account for the effects of matrix effects, i.e., atomic number (Z), absorption (A) and fluorescence (F). RAW signal for individual elements is compared to standards and processing software applies the ZAF correction and intensities are then reported as weight % of the oxides or elements.

$$n\lambda = 2d \sin \theta \qquad \text{Equ 2.6.}$$

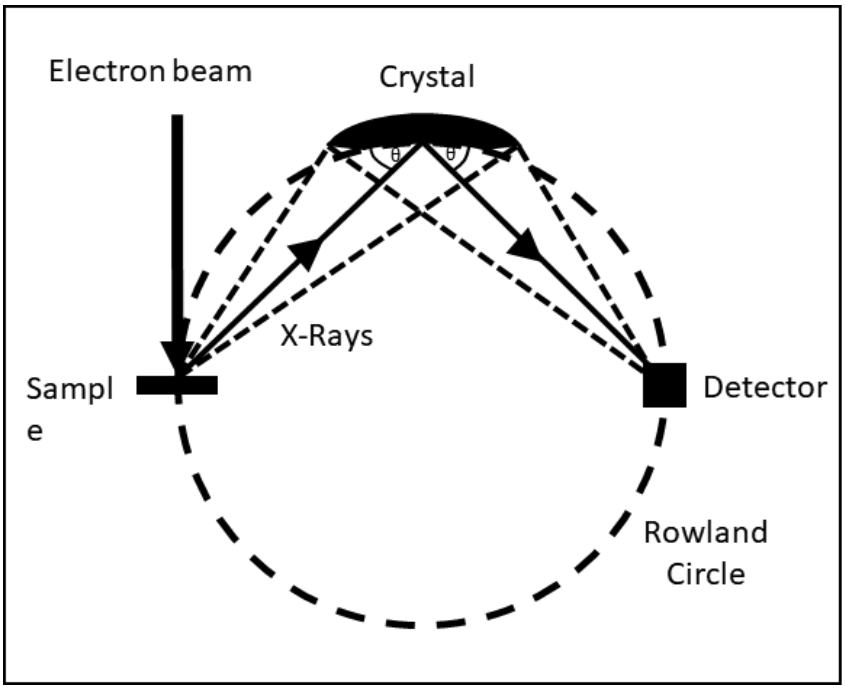

Figure 2.24. WDS sample, detector and detector geometry and Rowland sphere. (Adapted from Henry D. 2021. Wavelength-Dispersive X-Ray Spectroscopy (WDS) https://serc.carleton.edu/research_education/geochemsheets/wds.html).

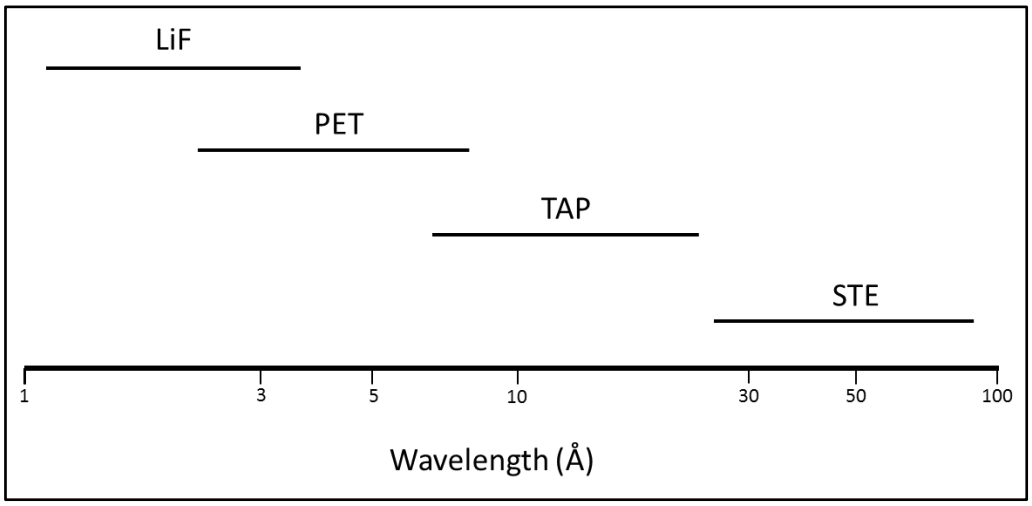

Figure 2.25. Typical WDS Analysing crystals. (lithium fluoride (LIF) Short wavelengths < 3 Å, pentaerythritol (PET) Intermediate wavelengths, thallium acid pthalate (TAP) long wavelengths and lead stearate (STE) (Adapted from Reed, 1993).

2.2.2 Energy-Dispersive X-Ray Spectroscopy (EDS)

The energy-dispersive (ED) type records X-rays of all energies effectively simultaneously and produces an output in the form of a plot of intensity versus X-ray photon energy (Reed, 2005). Incoming X rays promote electron-hole production in a semiconducting lithium-drifted silicon (Si (Li)) or germanium detector. An electric current is produced which is proportional to the incoming X-ray energy which is analysed by a multichannel analyser yielding the intensity versus X-ray photon energy plot. Elements above Z=4 (Be) are measured. EDS provides the chemical composition of a sample, and it is used in creating elemental maps.

2.2.3 Backscatter electron (BSE) imaging

Backscattered electrons have higher energies than secondary electrons and the fraction of incident electrons that are backscattered is known as backscattered coefficient (η) and varies with atomic number (Reed, 1993). Therefore, contract of BSE images is linked to the atomic number. High Z compounds are displayed as brighter portions of a BSE image and shown as grey values ranging from 0 to 255 (Fig 2.26).

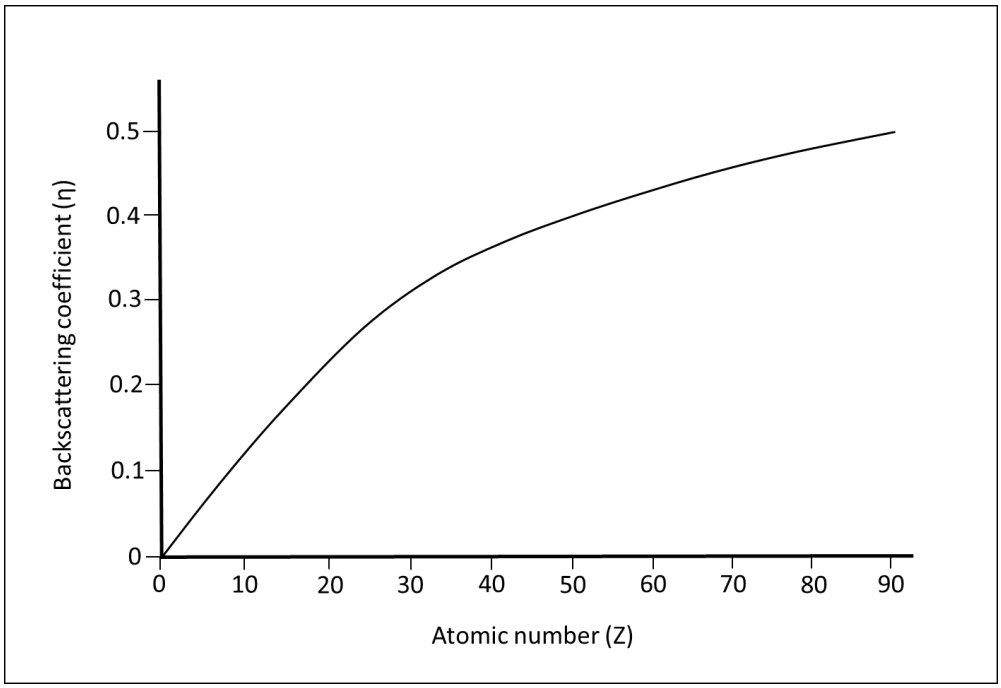

Figure 2.26. Sketch of backscatter coefficient versus atomic number (adapted from Reed, 1993).

The slope of backscatter coefficient vs atomic number (Fig. 2.26) at low atomic number is steep but shallows as atomic number increases. Therefore, the contrast between low atomic numbers is higher than in comparison to high atomic numbers. BSE images (Fig. 2.27) and EMPA data provide a

high degree of chemical textural and analysis samples. This technique will be used to determine mineral compositions to constrain the degree of depletion and the nature of metasomatism.

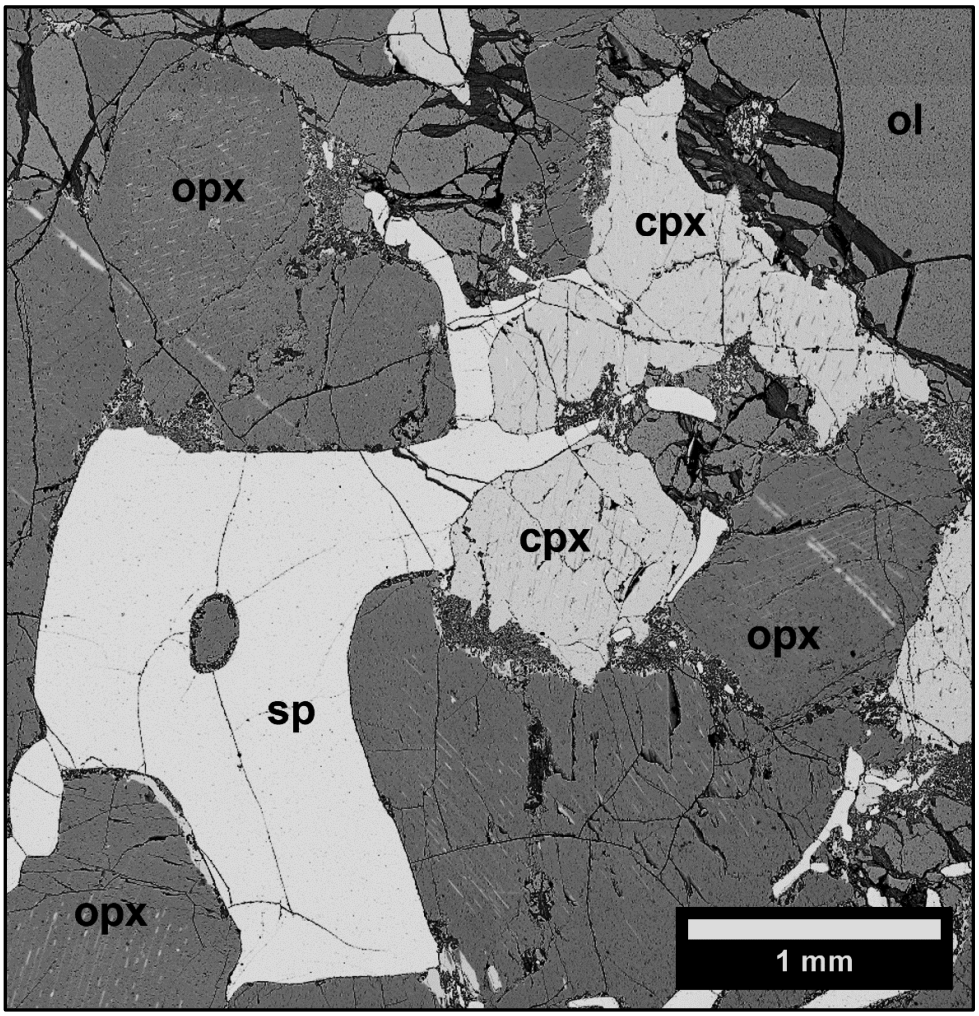

Figure 2.27. BSE image of a spinel pyroxene cluster from a spinel peridotite. High density spinel is shown as light grey in greyscale image with less dense silicate phases showing as darker grey. Image from this study.

2.2.4 Comparison of EDS and WDS data

In EMPA the incident electron beam generates an X Ray signal from the rock sample being analysed. EDS detects the energy of the emitted X Rays whilst WDS records the wavelength. The ability to generate a finely focused beam (1 µm spot size) allows for small areas to be detected. EMPA analysis allows for both qualitative analyses i.e., in which elements are identified and quantitative analysis intensity is measured (peak and background yielding net intensity), i.e., measurement of a characteristic peak of each element present in the 'unknown' sample and comparing this with measurements on one or more standards under identical instrumental conditions (Reed, 1997). EDS data provides high quality qualitative analysis, and a complete spectrum is simultaneously collected

in a short time. However poor resolution in EDS can lead to overlapping peaks. The higher peak to background ratio obtained in WDS analysis provides better data quality for low concentrations also, the resolution of WDS data provides better peak separation and identification of elements which appear overlapped in EDS data. EDS can be set up to produce elemental mapping of the elemental concentration of a region of interest in a short time. Reed (1993) highlighted the advantages and disadvantages of both EDS and WDS analysis and Table 2.2 summarises these points. Reed (1997) stated that it is desirable to have both types of spectrometers and it is beneficial to combine both forms of analysis, using EDS data for major elements and WDS data for minor and trace elements.

Table 2.2. Comparison between EDS and WDS data collection (adapted from Reed (1997)).

Data collection parameter	EDS	WDS
X ray collection efficiency	High	Low
Data recording mode	Parallel	Serial
Count-rate capability	Low	High
Spectral resolution	Low	High
Peak to background ratio	Low	High

All analyses in this study were calibrated against standards of natural silicates, oxides and Specpure® metals with the data corrected using a ZAF (atomic number, absorption, and fluorescence) correction program. EDS analysis was carried out using an accelerating voltage of 15 kV, a current of 10 nA and a beam diameter of 1 µm. The counting times for all elements were 40 s. The instrument was standardised using a Co secondary standard. EDS analysis was carried out on USGS standard BCR2_G. Data collected over the period of analysis in this study allows for a check on the precision and accuracy of the instrument. Results of 96 analyses of BCR2_G are shown in Table 2.3, with the calculated lower limit of detection (LLD) set at 3 x the one-sigma standard deviation.

Table 2.3. Lower Limit Detection (LLD) and standard sample analysis (EDS) of USGS sample BCR2_G.

Standard Sample: BCR2_G (USGS Basalt, Colombia river, artificial glass).					
Oxide	**Minimum**	**Maximum**	**Average (n=96)**	**Sigma**	**LLD**
SiO_2	54.94	56.37	55.60	0.31	0.94
TiO_2	2.10	2.29	2.21	0.04	0.13
Al_2O_3	14.59	15.78	15.00	0.26	0.77
FeO	12.13	12.73	12.53	0.10	0.29
MnO	0.16	0.24	0.20	0.02	0.05
MgO	3.37	3.86	3.69	0.10	0.31
CaO	6.95	7.24	7.16	0.04	0.13
Na_2O	1.41	1.93	1.83	0.07	0.22
K2O	1.73	1.83	1.80	0.02	0.06
P_2O_5	0.22	0.31	0.26	0.02	0.05
Total	99.25	101.00	100.28	0.39	-

Secondary mineral and metal standards of a known chemical composition are analysed prior to every WDS data collection. Table 2.4 shows analysis of standards by WDS, highlighting detection limits (LLD) for individual elements. The LLD values by WDS are much lower than by EDS.

Table 2.4. Lower Limit Detection limits for WDS analysis on a JXA8100 microprobe.

JXA8100	
Acc Vol =	15kv
Spot dia.	1 um
LLD	Lower limit detection
Peak count time	40 sec
BG+	20 sec
BG-	20 sec

Oxide	**Std**	**LLD (Wt.%)**
SiO_2	K-feldspar	0.03
TiO_2	Rutile	0.01
Al_2O_3	Corundum	0.02
FeO	Olivine	0.02
MnO	Metal Mn	0.01
NiO	metal Ni	0.03
Cr_2O_3	Metal Cr	0.02
CaO	Wollastonite	0.03
MgO	Olivine	0.02
Na_2O	K-feldspar	0.02
K_2O	K-feldspar	0.03
P_2O_5	Apatite	0.03

Both EDS and WDS data analysis were used in this project. The main factor in deciding which technique to use for analysis of mantle peridotites was time, specifically when data analysis can be conducted. For EDS analysis there was relatively easy access to the Birkbeck probe which allows weekend working and provides the opportunity to obtain a large amount of data very quickly, whereas WDS data analysis was largely undertaken on the NHM probe which can only be accessed during the week. Therefore, due to the limited amount of time available during normal office hours, this option was largely for data for publication. One powerful tool in EMPA is elemental mapping in which within a selected region of interest the elemental distribution is measured and displayed in false colour. These images can be mixed or added together creating an image which aids in characterising mineral phases. Elemental mapping will be used to characterise fine detail with small regions such as metasomatic reactions sites and kelyphite rims. EMPA mineral data formula recalculation will be calculated using the mineral chemistry spreadsheets form GabbroSoft (https://www.gabbrosoft.org).

Chapter 3

Textures in Spinel Peridotite Mantle Xenoliths: examples from Canary Islands, France, Spain*

** Part of this chapter has been published as "Bhanot K K, Downes H, Petrone C M and Humphreys-Williams E., 2017. Textures in Spinel Peridotite Mantle Xenoliths using Micro-CT scanning: examples from Canary Islands and France. Lithos v 276, 90-102. https://doi.org/10.1016/j.lithos.2016.08.004*

3.1 Introduction

Mantle xenoliths are metamorphic tectonites whose textures reflect the temperature, pressure and differential stress conditions under which they were accidently sampled by their host magma. Petrological data of mantle xenoliths provide insights into the mineralogy and composition of the mantle and thus a snapshot of the state of the underlying lithospheric mantle at the time of eruption (Pearson et al., 2003). Textures in mantle xenoliths are related to three major factors: grain size, grain shape, and contact relationships of the grains (Tabor et al., 2010). However, analyses of mantle xenoliths in most previous studies have usually been two dimensional via thin-sections. Distributions of crystals in thin-section are a combination of the size distribution of minerals in the rock and a distribution produced by the random sectioning plane (Tabor et al., 2010). Therefore, this study extends analysis of textures to three dimensions through the use of micro-computed tomography (micro-CT).

Several studies have categorised mantle xenolith textures, e.g., Boullier and Nicolas (1975), Pike and Schwarzman (1977) and Harte (1977), although the textural terminology formulated by the authors differed. Mercier and Nicolas (1975) presented a classification of mantle peridotite textural types by examination of xenoliths from Western Europe and Hawaii. They distinguished three structural groups of xenoliths (termed "protogranular", "porphyroclastic" and "equigranular") based on texture, fabric and the paragenetic relations of minerals, chiefly spinel, and described the textural groups in order of their assumed sequence. The protogranular group was characterised by grain sizes for both olivine and orthopyroxene (enstatite) as coarse-grained (>4mm) with finer-grained clinopyroxene (diopside) and spinel (1mm) in direct contact with large orthopyroxene grains. Locally the diopside occurs in microcrystals in peripheral parts of the enstatite and the spinel commonly has a vermicular form inside the enstatite or between the enstatite and diopside microcrystals. Thus spinel-pyroxene clusters were originally considered by Mercier and Nicolas (1975) as a major textural feature of the protogranular texture. However, many protogranular xenoliths lack spinel-pyroxene

clusters. Lenoir et al (2000) later distinguished two major subgroups of the protogranular texture: the first being the spinel-pyroxene cluster-bearing 'protogranular' subgroup, and the second being characterised by a scattered distribution of pyroxene and spinel and a lack of exsolution features, and termed 'coarse-granular' peridotites.

Numerous studies have recorded the presence of spinel-pyroxene clusters (SPCs) in mantle xenoliths and ultramafic massifs but at times they have been ignored or misidentified. Studies reporting the presence of spinel-pyroxene clusters in xenoliths include those from the Massif Central, France (Nicolas et al., 1987; Lenoir et al., 2000), Pannonian Basin, Hungary (Falus et al., 2000), Kozakov, Czech Republic (Ackerman et al., 2007), Rhön, Germany (Witt-Eickschen et al., 1997), South Africa and Lesotho kimberlites (Dawson and Smith, 1975; Grégoire et al., 2005), Northern Patagonia (Bjerg et al., 2009), Wangqing, NE China (Xu et al., 1997), Tallante, Spain (Rampone et al., 2010), Canary Islands, Spain (Neumann et al., 1995; Hansteen et al., 1991; Neumann and Wulff-Pedersen, 1997), Cape Verdes (Shaw et al., 2006), Mexico (Luhr et al., 1997), British Columbia, Canada (Ross, 1983), New Mexico, USA (Smith, 1977), and Calatrava, Spain (Humphreys, 2011). Studies of peridotite massifs reporting the presence of SPCs include Andaman Islands (Ghosh et al., 2013), Bay of Islands, Canada (Suhr, 1993), northern Italy (Obata and Morten, 1987), New Caledonia ophiolite (Secchiari et al., 2019) and the Horoman peridotite complex, Japan (Morishita and Arai, 2003; Odashima et al., 2007).

A number of authors have investigated the origin of SPCs and put forward various hypotheses for their formation. Mercier and Nicolas (1975) stated that spinel and diopside formed by exsolution of a previous Al-Ca-rich enstatite. Nicolas et al. (1987) proposed melting in rising diapir which is initiated in the garnet stability field, forms melt pockets at the site of garnets and subsequent cooling yields the crystallisation of SPCs. In general, and in this study, SPCs are considered to be the product of garnet breakdown with the transition from the garnet stability field to the spinel stability field being represented by equation 3.1 (Smith, 1977):

olivine + garnet = orthopyroxene + clinopyroxene + spinel. ……. (equ 3.1)

$$2Mg_2SiO_4 + CaAl_2Si_2O_8 = 2MgSiO_3 + CaMgSi_2O_6 + MgAl_2O_4$$

Transition from garnet to spinel is possible by either an increase in temperature or a decrease in pressure. In order to understand the unusual samples which, contain SPCs, we have undertaken a 3D investigation of xenoliths which contain such clusters using micro-CT scanning techniques to determine their three-dimensional textures and structures.

In order to fully understand the texture of spinel in SPC-bearing samples from the Massif Central and Lanzarote, a Micro CT and EMPA study on samples from Ray Pic, Massif Central was also undertaken to identify and record the textural types as described by Mercier and Nicolas (1975). SPC-bearing spinel peridotites from a third location in Calatrava were also studied using EMPA and Micro CT. These samples provide a comparison to the SPC textures observed in spinel peridotites from the Massif Central and Lanzarote and lend weight to the hypothesis that SPC textures in spinel peridotites are a distinct textural type.

3.2 Sample Localities

Our samples are from four localities (1) Montboissier (MB) in the Limagne graben of the northern Massif Central, France, representing thinned off-craton continental lithosphere, and (2) Ray Pic (RP) in the southern Massif Central, France, representing thinned off-craton continental lithosphere and representative spinel peridotite textures as defined by Mercier and Nicolas (1975), (3) the El Cuchillo (EC) maar in western Lanzarote, Canary Islands, representing sub-oceanic mantle lithosphere and (4) Calatrava (IEWH), located in the Calatrava volcanic province situated some 150 km south of Madrid, Spain, representing thinned off-craton continental lithosphere

Many previous studies have been made of textures and petrology of mantle xenoliths from the Massif Central, e.g., Hutchison et al. (1975), Coisy and Nicolas (1978), Nicolas et al. (1987), Downes and Dupuy (1987), Zangana et al. (1997; 1999), Lenoir et al. (2000) and Downes et al. (2003). Previous studies of textures and petrology of Lanzarote mantle xenoliths include those of Neumann (1991), Neumann et al. (1995; 1997 and 2002) and Siena et al. (1991). Neumann et al. (1995) showed that ultramafic xenoliths from Lanzarote are mostly spinel harzburgites and spinel dunites with rare examples of spinel lherzolite and spinel plagioclase dunite. Numerous studies of mantle peridotite textures from Calatrava have been made, e.g., Bianchini et al. (2010), Villaseca et al. (2010) and Puelles et al. (2016).

The French Massif Central is an uplifted plateau of continental lithosphere associated with Tertiary-Quaternary volcanic activity related to asthenospheric upwelling (Wilson and Downes, 1991). Products of this volcanism contain large numbers of mantle-derived peridotite xenoliths (Downes and Dupuy, 1987; Lenoir et al., 2000). The Massif Central is divided into three distinct domains of differing lithosphere thickness: the western (100-140 km), the north-eastern (100 km) and southern (60-80 km) domains. Babuška et al. (2002) modelled the lithosphere thickness and structure based on spatial variations of P wave delay times and shear wave splitting relief profiles across 5 transects across the Massif Central. They showed that the lithosphere is significantly thinned (i.e., 75 km)

under the Limagne graben whilst the adjacent lithosphere-asthenosphere boundary records a depth of >100 km. Lenoir et al (2000) considered that the Massif Central region appears to be underlain by two texturally and chemically distinct shallow subcontinental lithospheric mantle (SCLM) domains assembled during the Variscan orogeny. They showed that SPC-bearing xenoliths occur exclusively north of latitude 45°30', whereas `coarse-granular' peridotites which lack SPCs occur south of latitude 45°30'. Our main sample locality of Montboissier lies in the northern domain.

Lanzarote is located in the eastern part of the Canary Islands, an archipelago close to the continental margin off the NW coast of Africa. Carracedo et al. (1998) proposed that the Canary Islands formed from an asthenospheric plume. The thickness of oceanic lithosphere beneath the islands is 90 km (Humphreys and Niu, 2009) and thus the base of the lithospheric mantle lies within the garnet peridotite facies. Neumann et al. (1995) concluded that Lanzarote rests on "normal" sub-oceanic lithospheric mantle similar to that found under the most western part of the Canary Islands El Hierro. They reported a high geothermal gradient underneath the Canary Islands, indicating lithospheric thinning due to plume upwelling. Neumann et al. (1995) showed that the pressure and temperature of the lithospheric mantle under Lanzarote is associated with a high geothermal gradient compared with "normal" sub-oceanic lithospheric mantle of Jurassic age. Neumann et al. (1995) also suggested that hotter conditions exist in the mantle under the eastern Canary Islands than under the western islands, possibly related to the proximity to the West African continental margin in which enhanced thermal erosion may be caused by small-scale convection of hot plume material.

The Late Miocene-Quaternary Calatrava Volcanic Province (CVP) of Central Spain forms a series of scattered vents and outcrops of lava flows and pyroclastic deposits in a domain of some 4000 km^2 within the Iberian Hercynian Massif and the nearby external sectors of the Alpine Betic cordilleras (López-Ruiz et al., 1993). The CVP is situated some 150 km south of Madrid, and outcrops in an area characterized by a Hercynian basement covered by late Cenozoic sediments. The Palaeozoic rocks are predominantly lower Palaeozoic sedimentary strata variably affected by Hercynian deformations, resulting in a series of NW-SE to W-E orientated folds. This basement is unconformably overlain by upper Miocene to Quaternary fluvial and lacustrine sediments. These were deposited within a series of fault-bounded Tertiary-Quaternary sedimentary basins that formed as a result of extensional tectonics, beginning by late Miocene time. The bulk of the Calatrava Volcanic Province magmatic activity does not lie within the Hercynian blocks but fills extensional Late Miocene-Pliocene basins (López-Ruiz et al., 1993). The volcanic products were erupted in an area where geophysical data highlighted significant crustal thinning, down to 30 km (Bianchini et al., 2010). Volcanic vent distribution does not follow a clear spatial pattern and their geodynamical setting is controversial

with volcanic clustering related to asthenospheric mantle upwelling (hot-spot or diapir instabilities) in a pre-rifting stage (Villaseca et al., 2010)

3.3 Methodology

Thin-section preparation and analysis was performed at Birkbeck, University of London. For the Massif Central samples, polished thin-sections were provided by Hilary Downes, Birkbeck, University of London. For the Lanzarote samples, cylindrical cores were first drilled and micro-CT-scanned and then thin-sections were prepared from the cores. Samples from Calatrava were provided by Emma Humphrey-Williams, Natural History Museum (NHM), London. Polished thin-section for these were prepared at the Natural History Museum, London. The cylindrical cores were prepared at the NHM, London.

BSE images and elemental mapping was conducted at the NHM London using a Zeiss EVO 15LS Scanning electron Microprobe (SEM). Major element mineral analyses were obtained using a Jeol JXA8100 Superprobe (WDS) with an Oxford Instruments INCA system (EDS) at Birkbeck. EDS analysis was carried out using an accelerating voltage of 15 kV, current of 10 nA and a beam diameter of 1 µm. The counting times for all elements were 20 seconds on the peak and 10 seconds each on the high and low backgrounds. EDS analyses were calibrated against standards of natural silicates, oxides and Specpure® metals with the data corrected using a ZAF (atomic number, absorption and fluorescence) correction program. Additional analyses of samples from Lanzarote were conducted at the NHM, using WDS on a Cameca SX-100 electron microprobe.

Cores of 25 mm diameter and approximately 25 mm length were drilled from nine spinel peridotite xenoliths (6 from Lanzarote; 3 from the northern Massif Central) and scanned using micro-CT. The circular shape and size of the sample was chosen to ensure equal absorption and penetration of the X-ray beam, thus reducing artifacts into the final 3D rendered volume. Micro-CT scans were collected at the NHM on the Metris X-Tek HMX ST 225 scanner coupled with a 4-megapixel Perkin Elmer XRD 1621 AN3 HS detector panel. Detector pixel size was 0.2 mm. The power setting for data collection for a polychromatic X-ray beam (cone beam projection) with a Cu target (reflection target) and Cu filter (thickness 1.5 mm) was 215 kV and 190 µA. Resolution of the 3D rendered volumes ranged from 13 to 17 µm. Calatrava samples were both cored (1 cm diameter) and whole rock measurement. The whole rock sample had a generally rounded shape. Micro-CT data was collected on both the NHM on the Metris X-Tek HMX ST 225 scanner and Versa Zeiss scanner.

The rock cores were mounted inside the X-ray enclosure and housed on a translation stage. The distance of the sample to source was set to ensure maximum magnification without introducing

blurred edges. The cores were scanned with 3142 projections (single projection equivalent to 0.1^{o} rotation) and an exposure time of 708 ms. Both the Drishti and ORS Dragonfly software suite were used for 3D segmentation and volume rendering. The data sets were analysed, segmented and rendered, and three phases were identified, i.e., air, silicate minerals and higher density spinel. Geological samples consist of multiple minerals of different densities, and it is important to understand how such samples will react to exposure to the X-Ray beam. Attenuation characteristics allow us to predict the possibility of differentiating between different minerals in CT images (Ketcham and Carlson, 2001). However, the attenuation curves for forsterite and enstatite are similar across the whole range of energies, which makes it very difficult to distinguish the two minerals. Clinopyroxene has a higher attenuation factor at low energies (50 keV) because of the high atomic number of Ca, and so clinopyroxene can be distinguished in CT images. Spinel, with high density and a high linear attenuation coefficient across the whole range of energies is easily distinguishable from the silicates. Thus, during segmentation, the spinel and silicate phases can be viewed in isolation, as can Ca-rich minerals such as clinopyroxene. With the spinel and silicate phases isolated, the 3D rendered visualisations show the grain size, shape and distribution of spinel and clinopyroxene throughout each rock core. Figure 3.1 shows a sequence of images displaying 3D rendered volumes of a cored xenolith from Lanzarote (EC5) and the separate phases that can be identified.

SPC modal mineralogy was calculated using back-scattered electron (BSE) and elemental maps (Mg, Ca and Cr) imported into the Fiji (ImageJ) software (Schindelin et al., 2012). Elemental map images of SPCs were first converted from RGB (colour) to an 8-bit image. All elemental images were cropped to the same dimensions using the pixel x, y positions identified in the image. Using the threshold utility in Fiji, individual phases were isolated based on greyscale and the percentage of the phase isolated was shown, thus allowing accurate calculations of modal mineralogy (Table 3.1).

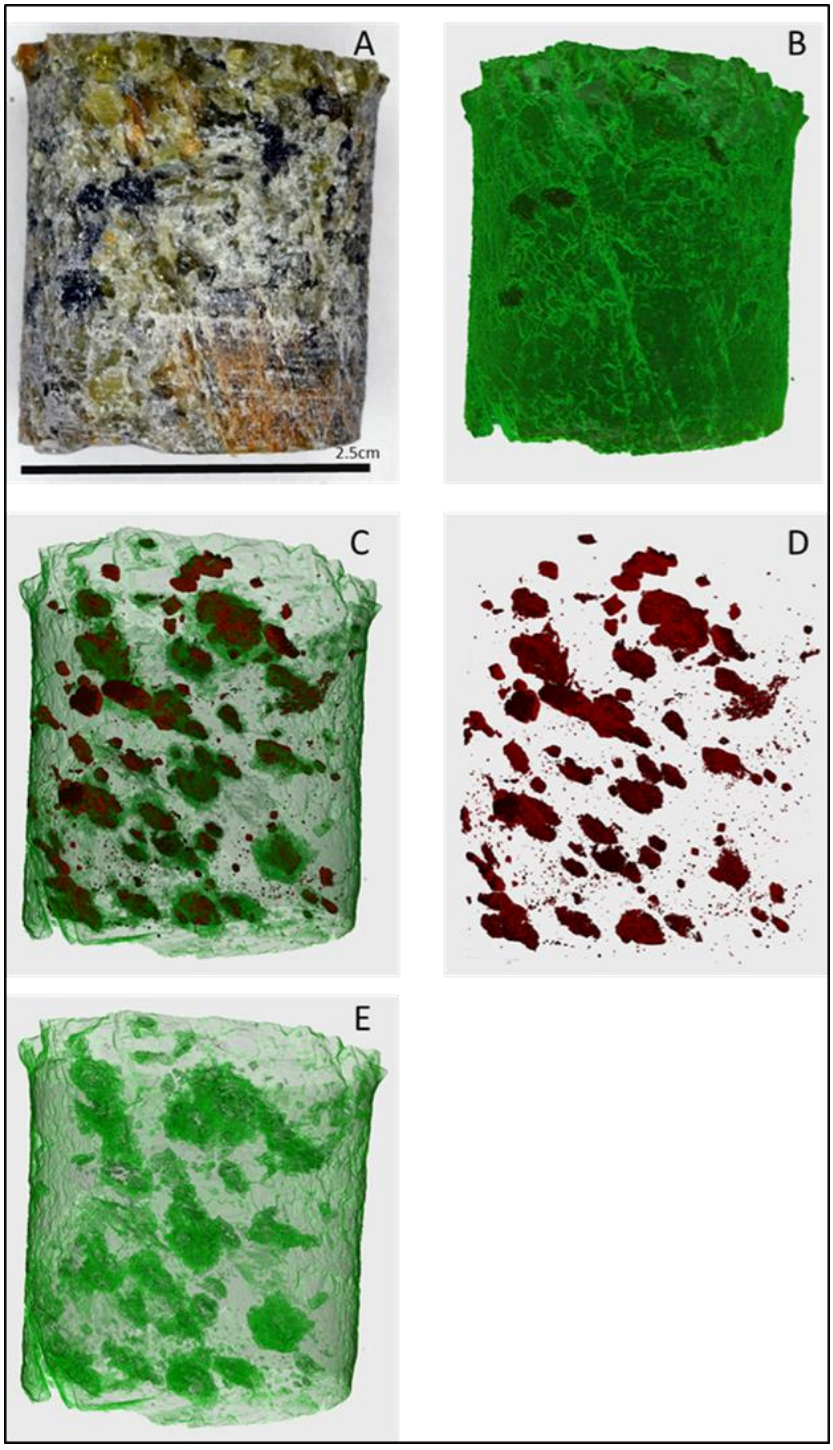

Figure 3.1. (A) Image of an example of a spinel peridotite core 2.5 × 2.5 cm prepared for data collection (sample EC5); (B) 3D rendered image showing the silicate and spinel phase of the rock core; (C) 3D rendered image showing the spinel phase along with the silicate phase set to semi-transparent; (D) image of 3D rendered volumes of the spinel viewed in isolation; (E) image of 3D rendered volume of silicate phases (glass, ol and cpx).

3.4 Results

3.4.1 Textural analysis

Figure 3.2 shows micro-CT scan images of samples from Ray Pic, chosen as examples of the three structural types as classified by Mercier and Nicolas (1975). The protogranular sample (Fig. 3.2a) displays concentrations of blebs of spinel 2 mm in size, distributed throughout the sample with a strong preferred orientation. The porphyroclastic sample (Fig. 3.2b) displays a smaller spinel grain size <2mm and more evenly distributed throughout the sample with holly leaf texture, a weaker preferred orientation is also visible. Figure 3.2c displays a peridotite with a porphyroclastic to equigranular texture. Here the spinel is smaller and more evenly distributed throughout the rock, but preferred orientation is weaker.

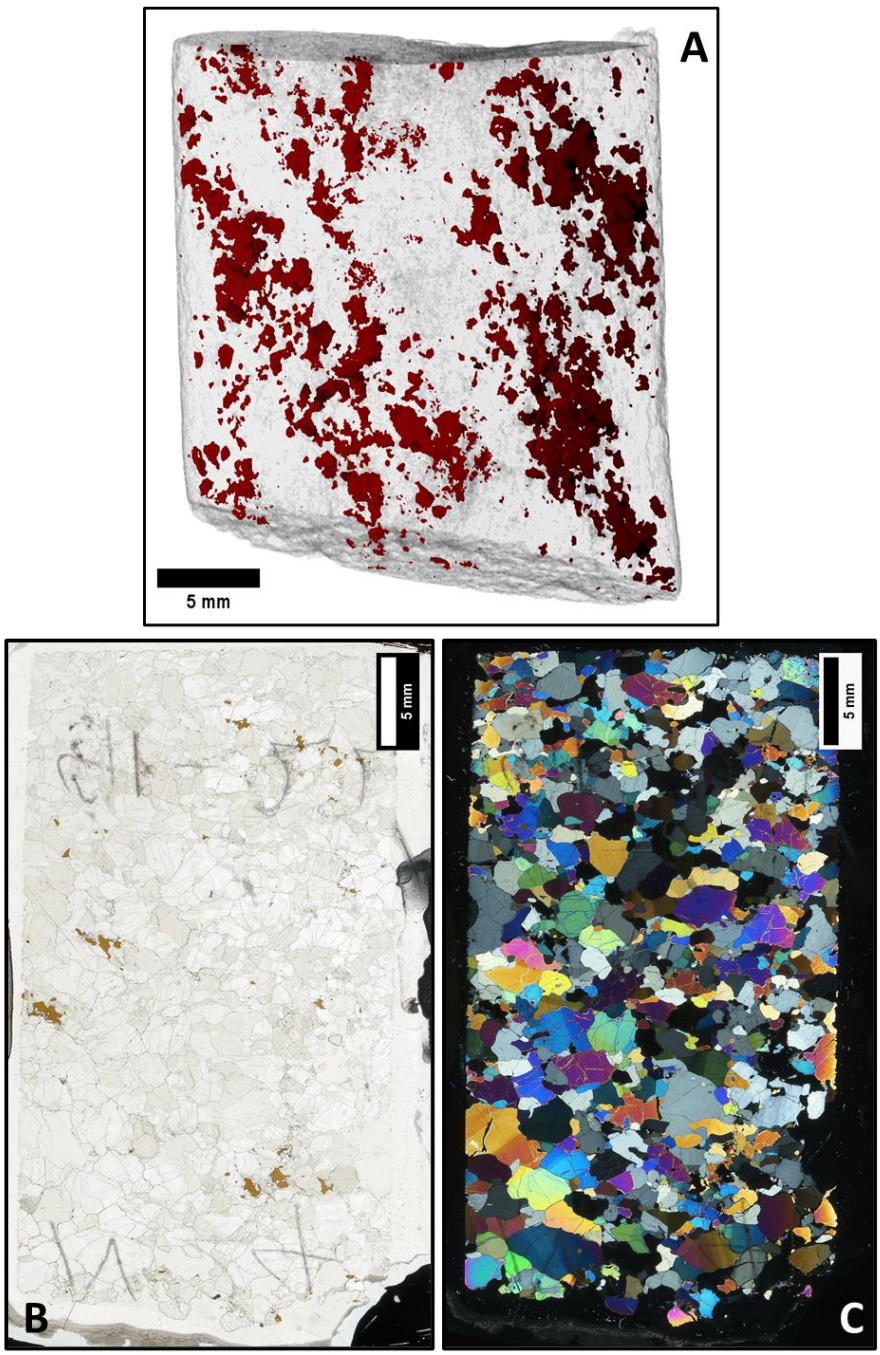

Figure 3.2. (A) 3D rendered image of a protogranular spinel peridotite xenolith (RP91_22) from Massif Central. The spinel reveals elongate spatially concentrated features with a preferred orientation. Much of the spinel relates to the linear features. Large portions of the xenolith are devoid of spinel. (B). Photomicrograph under PPL of same sample (RP91_22). Coarse ol and opx grains. Sp forms large blebs in random distribution with a weak orientation. Scalebar is 5 mm. (C) Photomicrograph under XPL of sample RP91_22. Coarse ol grains display evidence of strain. Scalebar is 5 mm.

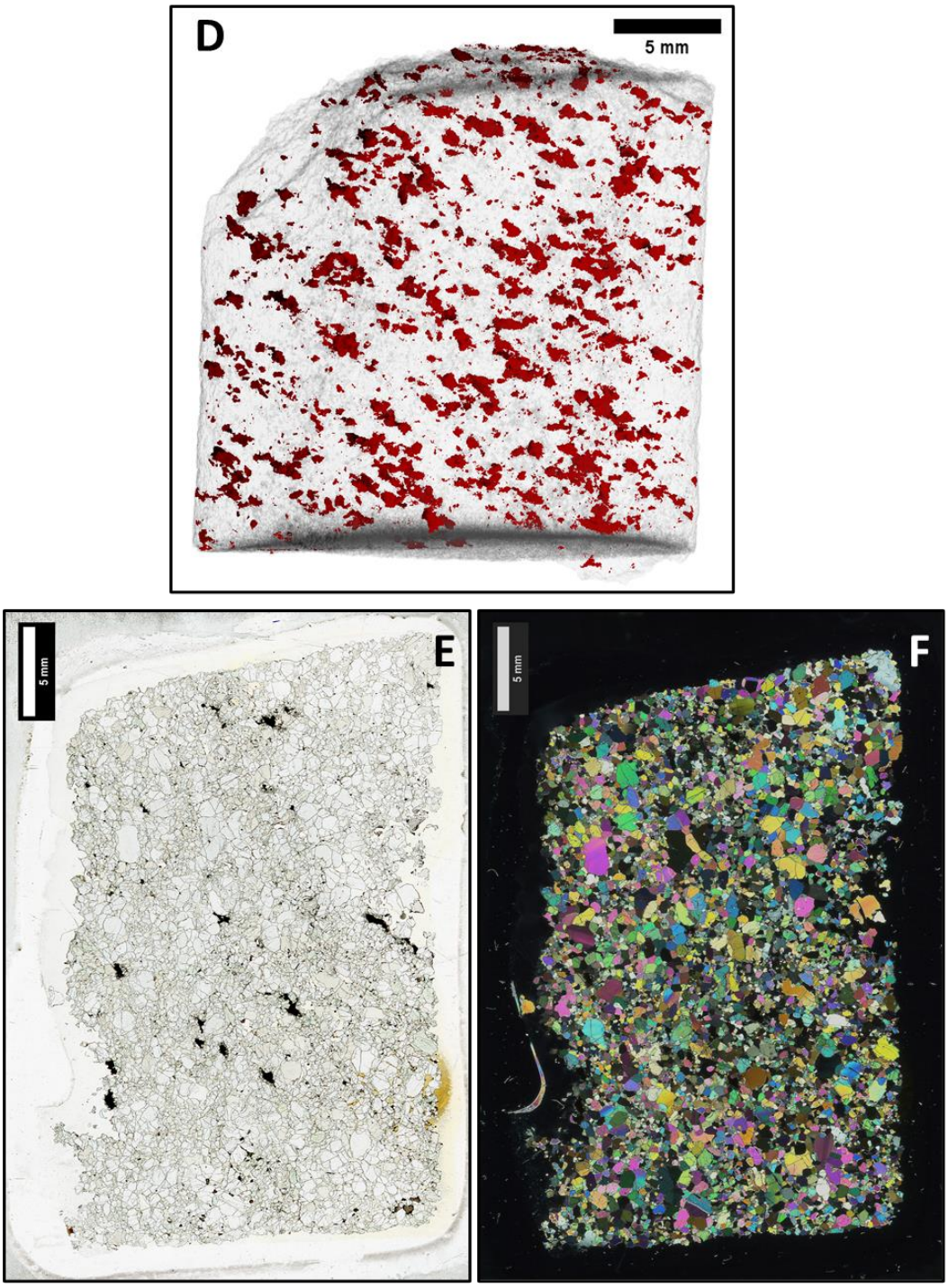

Figure 3.2 Continued. (D) 3D rendered image of a porphyroclastic spinel peridotite xenolith (RP91_11) from Massif Central. Spinel shows elongate spatially concentrated features with a preferred orientation. Much of the spinel relates to these linear features. Large portions of the xenolith are devoid of spinel. (E) Photomicrograph under PPL of porphyroclastic spinel peridotite xenolith (RP87_4) from Massif Central. Coarse ol and opx grains. Sp forms large blebs in random distribution with a weak orientation. Scalebar is 5 mm. (F) Photomicrograph under XPL of same sample (RP87_4). Coarse ol grains display evidence of strain. Scalebar is 5 mm.

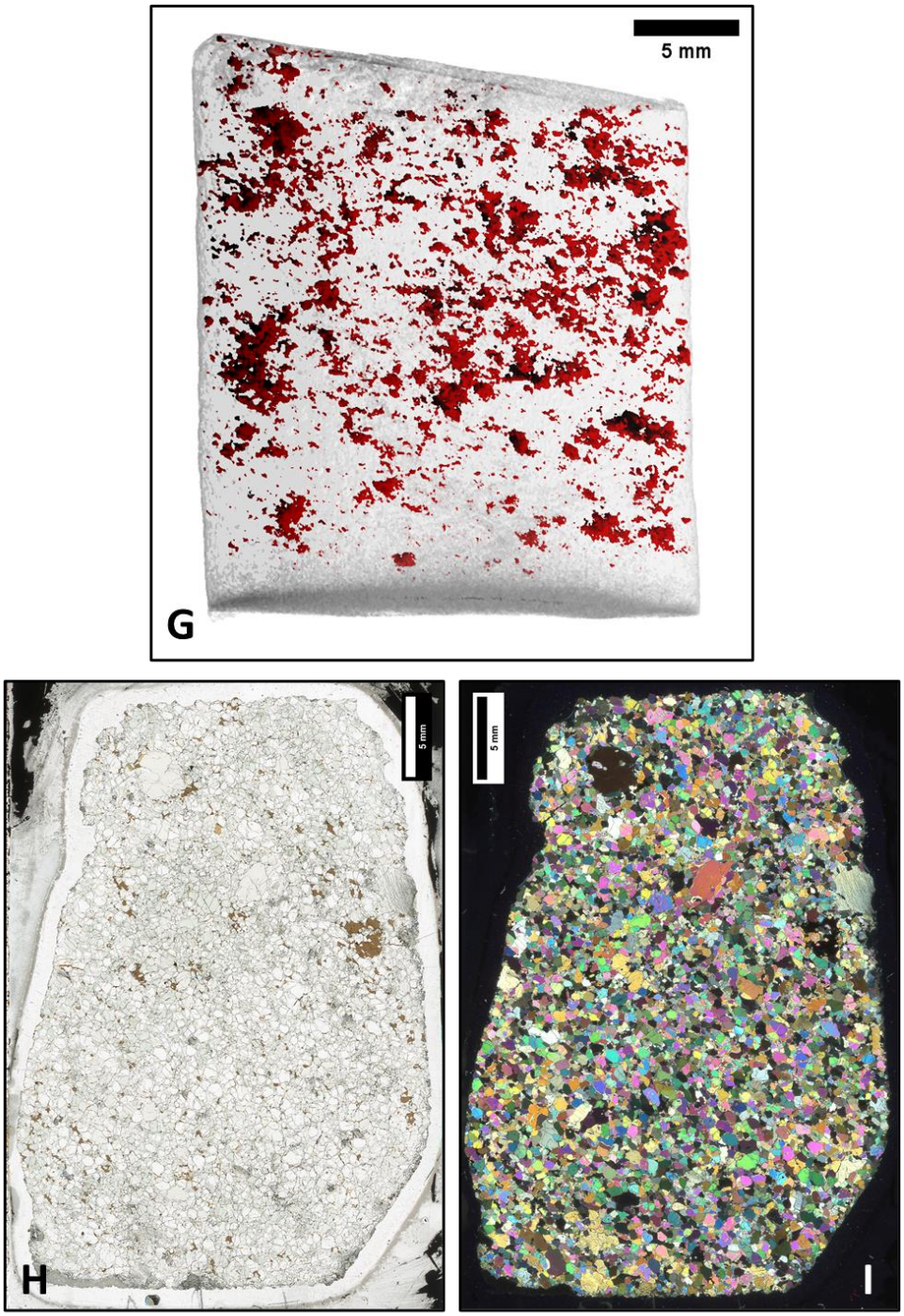

Figure 3.2 Continued. (G) 3D rendered image of a porphyroclastic to equigranular spinel lherzolite (VP92) from Massif Central. The spinel is fine grained with holly leaf texture and evenly distributed throughout the rock. Several larger blebs are visible in the 3D volume. Sp is red. Silicate phase(grey) set to semi-transparent. Scale bar is 5 mm. (H). Photomicrograph under ppl of same sample. (I) Photomicrograph under xpl of same sample. Scalebar is 5 mm.

3.4.2 Modal analysis

Modal mineralogy for spinel peridotites used in this study are summarised in Table 3.1. Downes et al. (2003) reported that among xenoliths from the northern domain of the Massif Central, harzburgites are as common as lherzolites; however only one of our eight samples is a harzburgite. Our samples from Lanzarote are mostly harzburgites, in agreement with Neumann et al (1995), but in addition one (EC5) is a dunite and one (EC3) is a wehrlite. Except for this sample, there is much less clinopyroxene in the Lanzarote samples than those from the Massif Central, suggesting a greater degree of melt depletion in the sub-oceanic lithosphere compared to the sub-continental mantle. Samples from Calatrava are lherzolites.

The SPCs consist of equant, anhedral orthopyroxene and clinopyroxene with interstitial spinel (Fig. 3.3 and 3.4). Spinel appears both as microcrystals and in a vermicular texture. Olivine does not form any part of an SPC. Maximum size of the clusters in thin-section is 6 mm. Spinel is broadly limited to SPCs whereas pyroxenes crystals are present throughout the sample and cannot be related with spinel. Modal mineralogies for SPCs are given in Table 3.1.

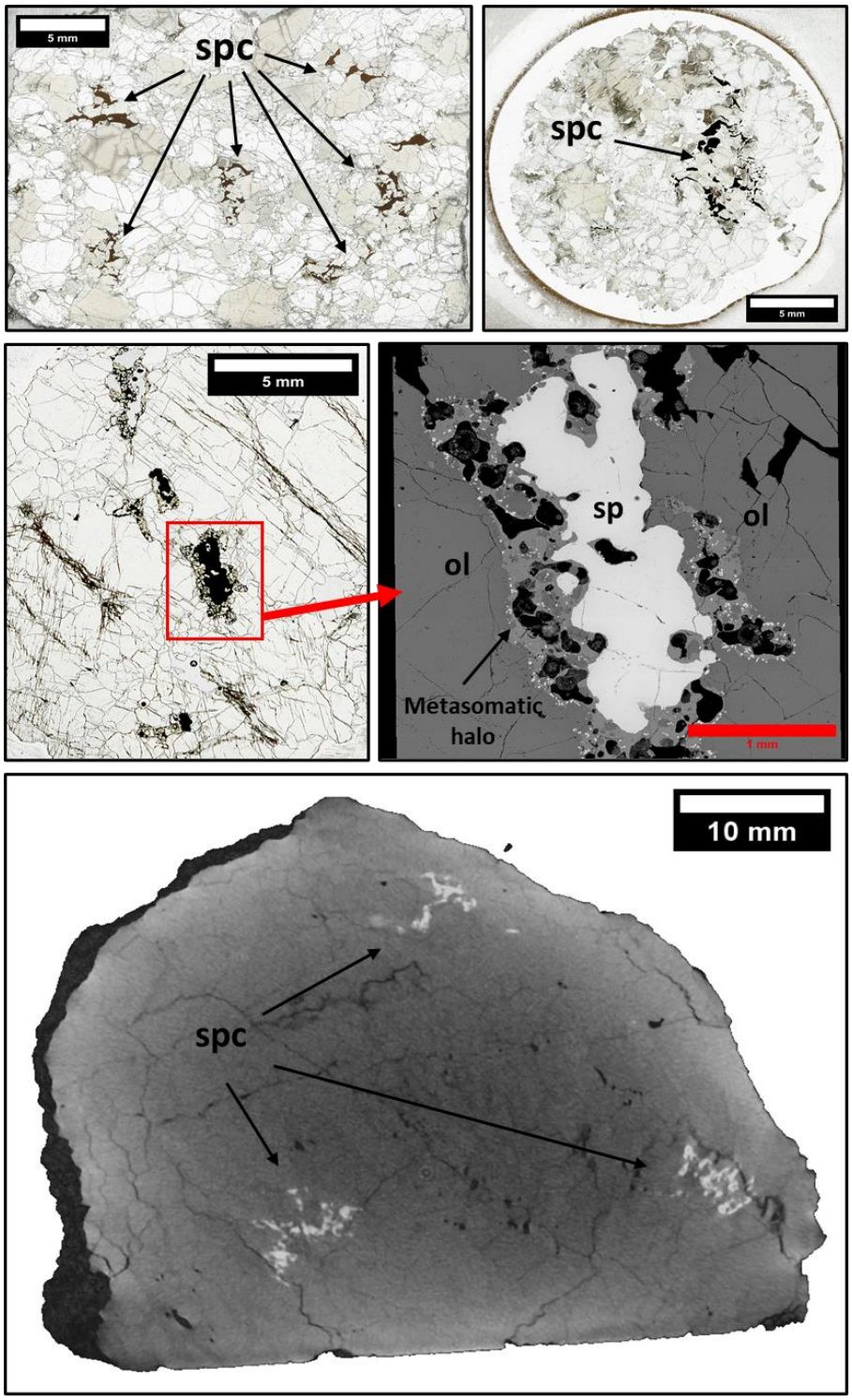

Figure 3.3. (A) Thin-section photograph (PPL) of a protogranular spinel peridotite xenolith from the Massif Central (MB1) showing spinel–pyroxene clusters. (B) Thin section photograph (PPL) of a protogranular spinel peridotite xenolith from Lanzarote (EC6) showing spinel–pyroxene clusters and associated metasomatic halos. (C) Thin section photograph (PPL) of a protogranular spinel peridotite xenolith from Lanzarote (EC5) spinel and associated metasomatic halo. (D) 3D rendered image of protogranular spinel peridotite xenolith from Calatrava (IEHW03) of SPC sites and associated silicate phases.

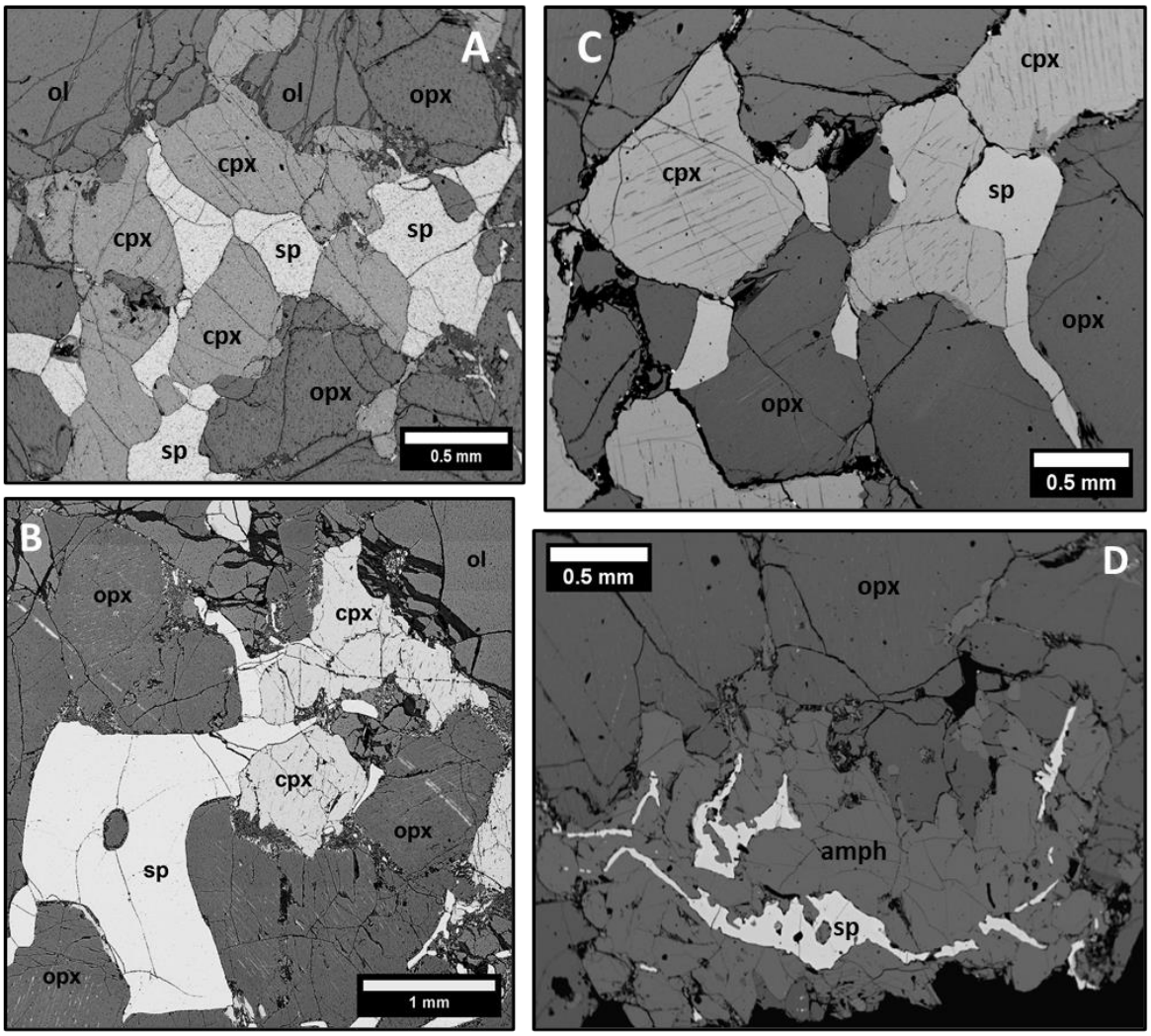

Figure 3.4. Figure 3.4. (A) BSE image of a spinel–pyroxene cluster from the Massif Central (MB1), SPC cpx with exsolution lamellae. Scale bar 0.5 mm. (B) BSE image of a spinel–pyroxene cluster from Massif Central (Ch11). Scale bar 0.5 mm.(C) BSE image of a spinel–pyroxene cluster from the Calatrava (1EWH02). Scalebar 0.5 mm. (D) BSE image of a site of an original spinel-pyroxene cluster in which metasomatic reactions has formed a spinel-amphibole cluster where spinel is wholly encased in amphibole. Sample from Calatrava (IEWH02) Scalebar 0.5 mm.

Table 3.1. Modal compositions and textural groups of spinel peridotites from Massif Central Northern domain (MCN), Massif Central Southern domain (MCS), Lanzarote (Lanz) and Calatrava (Cal). Modal mineralogy of SPCs associated with metasomatic reaction halos not calculated. MCS modal variation taken from Zangana et al (1995).

		Whole Rock							SPC		
Sample	location	ol%	opx%	cpx%	Sp%	Amph%	Textural type	Sp texture	opx%	cpx%	sp%
EC3	Lanz	86.1	1.9	9.0	3.0	-	Protogranular spinel dunite.	Coarse Blebs with sponge texture	-	-	-
EC4	Lanz	83.8	5.1	2.5	8.6	-	Protogranular spinel harzburgite	Coarse Vermicular	34.8	28.3	36.9
EC6	Lanz	77.0	14.0	3.5	5.5	-	Protogranular spinel harzburgite	Coarse Vermicular	35.9	31.9	32.2
EC5	Lanz	95.3	2.6	1.6	0.5	-	Protogranular spinel dunite	Coarse Blebs with sponge texture	-	-	-
EC21	Lanz	78.0	10.6	3.8	7.6	-	Protogranular spinel harzburgite	Coarse Blebs with sponge texture	-	-	-
CH11	MCN	74.4	12.6	7.1	6.0	-	Protogranular spinel lherzolite	Coarse Vermicular	57	15	28
MB1	MCN	60.8	23.7	6.9	8.6	-	Protogranular spinel lherzolite	Coarse Vermicular	50.1	32.6	17.3
MB9	MCN	65.9	21.1	10.7	2.3	-	Protogranular spinel lherzolite	Coarse Vermicular	41.1	26.1	16.7
MB50	MCN	74.5	13.5	8.7	3.3	-	Protogranular spinel lherzolite	Coarse Vermicular	32.4	44.2	23.4
MB57	MCN	77.4	16.8	3.4	2.4	-	Protogranular spinel harzburgite	Coarse Vermicular	-	-	-
MB63B	MCN	58.8	31.9	6.1	3.2	-	Protogranular spinel lherzolite	Coarse Vermicular	-	-	-
MB64	MCN	45.4	32.3	8.6	13.7	-	Protogranular spinel lherzolite	Coarse Vermicular	-	-	-
ST2	MCN	69.7	12.2	14.3	3.8	-	Protogranular spinel lherzolite	Coarse Vermicular	-	-	-
RP87_6*	MCS	61.5	19.0	16.1	3.5	-	Protogranular to porphyroclastic spinel lherzolite	Coarse sp blebs with orientation	-	-	-
RP91_11*	MCS	72.9	17.2	7.4	2.5	-	Porphyroclastic to equigranular spinel lherzolite	Coarse holly leaf sp and fine blebs	-	-	-
RP91_22*	MCS	66.4	21.4	10.8	1.5	-	Protogranular spinel lherzolite	Coarse holly leaf sp and fine blebs	-	-	-
VP92	MCS	52.0	34.4	10.7	3.0	-	Porphyroclastic to equigranular spinel lherzolite	Coarse holly leaf sp and fine blebs	-	-	-
02	Cal	60.7	25.3	1.0	2.4	10.7	Protogranular spinel lherzolite	Coarse blebs with linear channels	-	-	-
03	Cal	41.4	37.9	1.0	1.2	18.5	Protogranular spinel lherzolite	Coarse blebs with linear channels	-	-	-
05	Cal	58.6	32.7	7.0	1.7	-	Protogranular spinel lherzolite	Coarse blebs	-	-	-

BSE images of spinel peridotites from Lanzarote and the northern Massif Central (Fig. 3.4) show exsolution features associated with pyroxenes. Orthopyroxene crystals exhibit exsolution lamellae of clinopyroxene and spinel. Clinopyroxenes exhibit exsolution lamellae of orthopyroxene and/or spinel. The exsolution lamellae in pyroxenes are restricted to the core of the crystal whilst the rims are devoid of exsolution lamellae. The long thin shape and fine nature of the exsolution lamellae makes accurate microprobe analysis unreliable. Several Lanzarote samples display a 'halo' of olivine, clinopyroxene, amphibole and silicate glass surrounding the SPCs; inside the halos, spinel cores are surrounded by micro-crystals of spinel. BSE images of two samples from the Massif Central (MB57 and ST2) show that they have also been affected by metasomatic reactions. BSE images of spinel peridotites from Calatrava (Fig. 3.4) show exsolution features associated with pyroxenes. Clinopyroxene crystals exhibit exsolution lamellae of orthopyroxene. Orthopyroxene crystal exhibit exsolution lamellae of orthopyroxene (IEHW03). The SPC sites have also undergone reaction to metasomatic agents with the addition of amphibole. Other samples show the SPCs have undergone a greater degree of reaction, with spinel wholly encased in amphibole. (Fig 3.4D).

3.4.2 Electron microprobe analysis

Microprobe analyses of samples from Massif Central, Lanzarote and Calatrava obtained in this study (Tables 3.2, 3.3 and 3.4) show a similar range of mineral compositions as found in previous studies from the three regions (Hutchison et al., 1986; Werling and Altherr, 1997; Downes et al., 2003; Neumann et al., 1995; Neumann and Wulff-Pedersen, 1997; Bianchini et al., 2010; Puelles et al., 2016). Mg#s (Mg# = Mg/(Mg+Fe)x100) for olivine, orthopyroxene and clinopyroxene from the three localities are broadly similar and range from 89-92, whereas the spinel Cr# (Cr# = Cr/(Cr+Al)x100) are higher in Lanzarote samples (38-44) than in Massif Central (14-22) and Calatrava (4-11). There is no significant difference in the composition of olivine's, orthopyroxene and clinopyroxenes between SPC and non-SPC crystals (Table 3.2). Orthopyroxenes all three localities are enstatites. Their Mg# are 90-91 (Massif Central), 91.3-91.5 (Lanzarote) and 86.9-90.0 wt% (Calatrava). Al_2O_3 contents are 3.5-4.4 wt% (Massif Central), 3.2-3.6 wt% (Lanzarote) and 3.6-5.1 wt% (Calatrava). Clinopyroxenes are diopside with Mg# of 90-92 (Massif Central) and 91-92 Lanzarote) and 90.1-90.8 wt% (Calatrava). CaO content varies from 21.2 to 24.0 wt% in all three localities. Al_2O_3 contents are 3.5-4.4 wt% (Massif Central), 3.2-3.6 wt% (Lanzarote) and 5.3-7.2 wt% (Calatrava). Calatrava diopsides are also associated with spongy reaction halos. However, the olivine's and spinels, pyroxenes from the sub-oceanic Lanzarote mantle show more depleted compositions than those from beneath the Massif Central and Calatrava (Table 3.2 and 3.4). Amphiboles (Calatrava) are pargasite. Mg# is 86-88, with 15 wt% Al_2O_3, 11 wt% CaO and 3 wt% Na_2O.

In several Lanzarote samples (e.g., EC3, EC5), the SPCs exhibit halos consisting of olivine + clinopyroxene ± amphibole and interstitial glass, but lacking orthopyroxene (Fig. 3.5). Within these SPCs, spinel cores are surrounded by microcrystals of spinel, known as sponge-texture (Carpenter et al, 2002) (Fig. 3.5). Thickness of the spinel-sponge texture is ~ 50 µm. SPCs in sample EC5 also exhibit reaction halos; however, the spinel rims lack the sponge texture but contain smaller satellite microcrystals within the halo. Spinel microcrystals within the halos have Cr#s in the range 32-41, whilst the spinel microcrystals from the sponge texture have Cr#s of 46–51 and are also richer in TiO_2 compared to the cores (Table 3.3). There is negligible compositional difference between clinopyroxene within the halo and non-halo clinopyroxene, but a compositional variation occurs between olivine within the halo (Mg#=89-91) and outside (90-92).

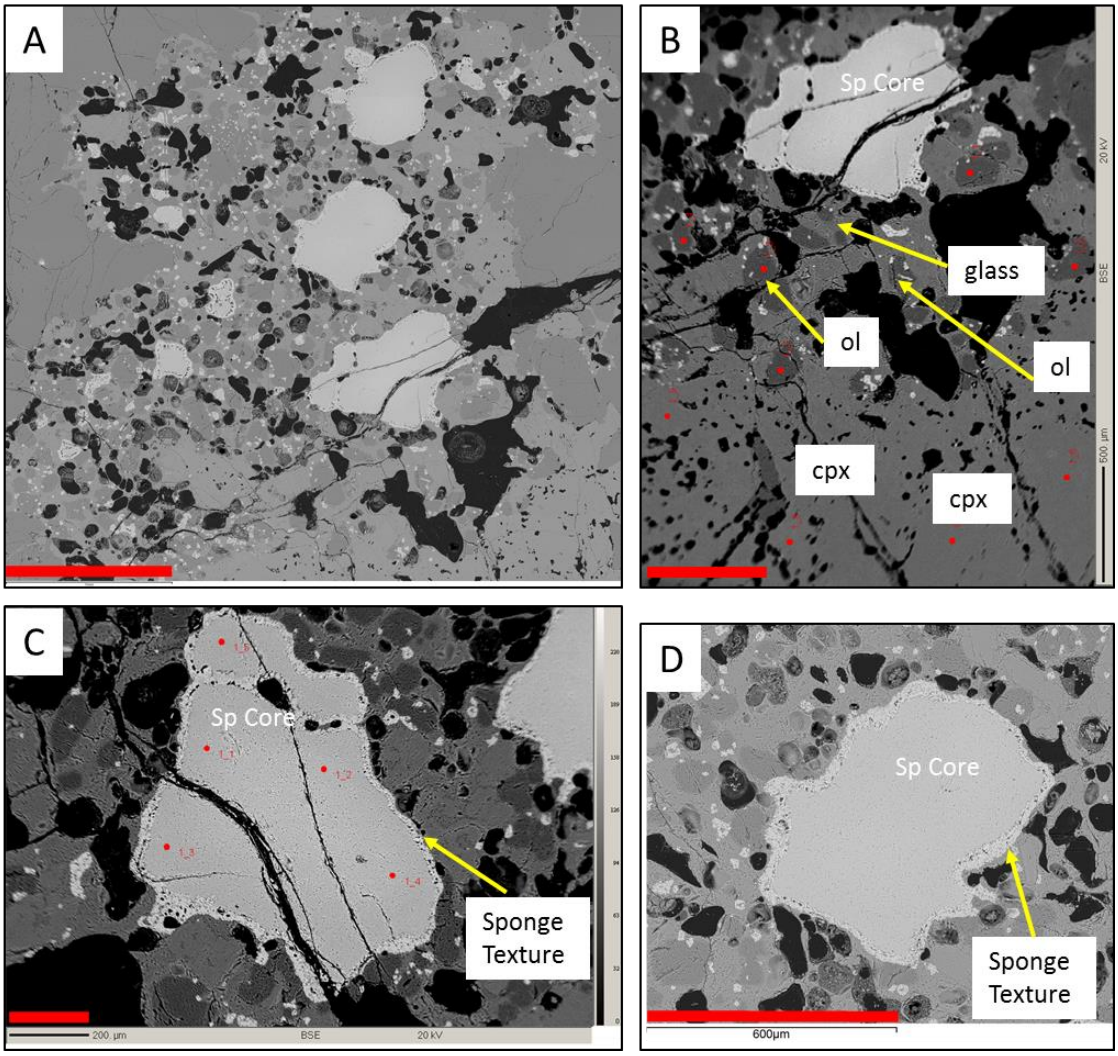

Figure 3.5. (A) BSE image (EC3) of a spinel–pyroxene cluster site with metasomatic reaction rim, Lanzarote (EC3). 2 mm scale bar. (B) Magnified BSE image (EC3) showing spinel core and metasomatic halo. 500 µm scale bar. (C) Spinel grain mantled with spinel sponge texture (EC3). 200 µm scale bar. (D) Spinel grain mantled with spinel sponge texture (EC5). 600 µm scale bar.

Table 3.2. Representative microprobe analysis (EDS) of minerals present in the clusters and those outside the clusters from peridotite xenoliths from the Massif Central (MB), northern domain and Lanzarote (EC), (wt% oxide).

Location	Sample	Mineral	SiO_2	FeO	MnO	NiO	MgO	Total	Mg#	no
Cal	5	ol	41.05	10.14	0.09	0.18	48.93	100.39	89.59	7
Cal	12548	ol	40.78	10.09	0.16	0.37	48.46	99.84	89.54	12
Lanz	EC4B	ol	41.11	8.85	0.17	0.38	50.25	100.76	91.01	4
Lanz	EC6	ol	40.58	8.52	0.20	0.32	49.72	99.28	91.23	3
MCN	MB1	ol	40.44	9.64	0.14	0.39	47.89	98.51	89.86	9
MCN	MB64	ol	42.42	9.45	0.11	0.47	48.15	100.60	90.09	4

Location	Cal	Cal	Lanz	Lanz	MCN	MCN
Sample	5	12548	EC4B	EC6	MB1	MB64
Mineral	sp	sp	sp	sp	sp	sp
Al_2O_3	54.83	56.35	30.44	33.02	45.13	50.85
Cr_2O_3	10.38	10.10	34.99	31.82	19.80	17.32
Fe_2O_3	4.21	2.98	6.41	6.24	4.73	1.78
FeO	9.72	9.42	11.52	10.96	11.30	10.81
MnO	0.31	0.19	0.24	0.30	0.19	0.15
MgO	19.86	20.37	16.68	17.17	18.21	19.13
Total	99.31	99.38	100.28	99.83	99.64	100.10
Mg#	75.29	83.42	67.36	68.96	70.74	75.93
Cr#	11.27	10.74	43.54	39.26	22.74	18.59
Al	1.70	1.73	1.04	1.12	1.46	1.59
Cr	0.22	0.21	0.80	0.72	0.43	0.36
Fe(iii)	0.08	0.06	0.14	0.14	0.10	0.04
Fe(ii)	0.21	0.20	0.28	0.26	0.26	0.24
Mn	0.01	0.00	0.01	0.01	0.00	0.00
Mg	0.78	0.79	0.72	0.74	0.74	0.76
Total	3.00	3.00	3.00	3.00	3.00	3.00
no. of points	12	7	7	6	5	4

Location	Sample	site	Mineral	SiO_2	TiO_2	Al_2O_3	Cr_2O_3	FeO	MnO	MgO	CaO	Na_2O	Total	Mg#
Cal	05	spc	opx	54.80	-	3.95	0.33	6.62	0.17	32.44	1.44	0.11	99.85	89.73
Cal	05	nspc	opx	55.06	-	4.17	0.30	6.79	0.20	33.00	0.52	0.09	100.07	89.65
Cal	12548	spc	opx	54.83	-	3.95	0.36	6.51	0.30	33.21	0.63	0.07	99.70	90.10
Cal	12548	nspc	opx	55.14	-	4.96	0.58	6.71	0.33	32.99	0.56		100.96	89.76
Lanz	EC4B	spc	opx	55.14	0.02	3.16	0.47	5.58	0.20	33.85	0.63	0.45	99.50	91.53
Lanz	EC4B	nspc	opx	55.04	0.02	4.06	0.43	6.40	0.26	33.26	0.59	0.20	100.06	90.26
Lanz	EC6	spc	opx	55.00	0.02	4.04	0.41	6.43	0.24	33.13	0.73	0.18	100.02	90.17
Lanz	EC6	nspc	opx	54.41		4.17	0.91	5.63	0.13	33.48	0.80	0.46	100.00	91.38
MCN	MB1	spc	opx	54.62	0.06	4.26	0.59	6.49	0.19	33.09	0.56	0.39	100.24	90.08
MCN	MB1	nspc	opx	55.12	0.09	3.86	0.33	6.40	0.15	33.08	0.79	0.40	100.20	90.21
MCN	MB64	spc	opx	54.87	0.07	4.06	0.46	6.44	0.17	33.09	0.67	0.39	100.22	90.15
MCN	MB64	nspc	opx	52.14	0.07	4.34	0.72	2.95	0.07	16.61	22.45	0.60	99.96	90.94
Cal	05	spc	cpx	51.78	-	5.58	0.92	3.25	0.18	15.14	21.25	1.06	99.11	89.26
Cal	05	nspc	cpx	51.87	-	6.05	1.06	3.26	0.13	15.44	21.18	1.06	100.00	89.41
Cal	12548	spc	cpx	51.90	-	5.60	0.69	3.20	0.13	15.75	21.41	0.87	99.50	89.77
Cal	12548	nspc	cpx	52.11	-	6.27	0.78	2.94	0.17	15.36	21.34	0.98	99.81	90.32
Lanz	EC4B	spc	cpx	52.83	0.04	3.49	0.92	2.77	0.10	17.01	21.87	1.11	100.10	91.63
Lanz	EC4B	nspc	cpx	52.75	0.20	3.44	0.89	2.87	0.12	17.97	20.75	1.03	100.00	91.78
Lanz	EC6	spc	cpx	52.91	0.10	3.45	0.86	2.54	0.10	17.16	22.56	0.75	100.40	92.34
Lanz	EC6	nspc	cpx	52.65		3.38	0.91	2.56	0.11	17.24	22.43	0.88	100.14	92.32
MCN	MB1	spc	cpx	51.58	0.10	3.89	0.74	2.81	0.13	16.45	24.03	0.72	100.43	91.25
MCN	MB1	nspc	cpx	51.62	0.09	3.73	0.70	2.74	0.11	16.36	23.97	0.70	100.02	91.41
MCN	MB64	spc	cpx	52.04	0.13	4.34	0.76	2.90	0.11	16.75	22.35	0.61	99.95	91.16
MCN	MB64	nspc	cpx	52.14	0.07	4.34	0.72	2.95	0.07	16.61	22.45	0.60	99.96	90.94

Table 3.2. Continued from previous page. Representative microprobe analysis (EDS) of amphibole in Calatrava xenoliths

Location	Sample	Mineral	SiO_2	Al_2O_3	Cr_2O_3	FeO	MnO	MgO	CaO	Na_2O	Total	Mg#
Cal	05	Amph	42.27	14.41	0.78	4.85	0.15	17.17	10.84	2.82	93.28	86.33
Cal	12548	Amph	43.09	14.94	1.15	4.35		17.82	10.84	3.00	95.53	87.68
Location	**Sample**	**Mineral**	**Si**	**Al**	**Cr**	**Fe(ii)**	**Mn**	**Mg**	**Ca**	**Na**	**Total**	**no.**
Cal	05	Amph	6.34	2.55	0.09	0.61	0.02	3.84	1.74	0.82	16.00	3
Cal	12548	Amph	6.21	2.62	0.14	0.55	0.00	3.89	1.67	0.91	16.00	3

Table 3.3. Representative microprobe analysis (WDS) of metasomatic (halo and spinel sponge texture) and non-halo mineral phases from peridotite xenoliths from Lanzarote (EC).

Location	Lanz	Lanz	Lanz	Lanz	Lanz	Lanz
Sample	EC3	halo	EC5	EC5	EC21	EC21
Mineral	ol	ol	ol	ol	ol	ol
Site	Core	Halo	Core	Halo	Core	Halo
SiO_2	41.06	40.74	40.61	40.48	40.98	40.85
FeO	8.44	7.94	10.43	8.79	8.45	7.57
MnO	0.13	0.12	0.36	0.37	0.13	0.12
NiO	0.41	0.41	0.03	0.16	0.39	0.32
MgO	50.42	49.85	48.67	49.71	50.36	51.22
Total	100.69	99.71	100.51	100.15	100.31	100.45
Mg#	91.41	91.79	89.27	90.98	91.40	92.34
no.	6	11	19	9	18	3

Location	Lanz	Lanz	Lanz	Lanz
Sample	EC3	EC3	EC5	EC5
Mineral	cpx	cpx	cpx	cpx
Site	core	Halo	core	Halo
SiO_2	53.14	52.00	52.52	51.48
TiO_2	0.37	0.72	0.77	0.91
Al_2O_3	4.59	4.03	2.80	2.71
Cr_2O_3	1.07	1.28	1.05	1.11
FeO	2.78	2.64	3.26	3.11
MnO	0.08	0.07	0.08	0.07
MgO	16.45	16.90	17.29	16.82
CaO	20.94	21.81	22.04	22.95
Na_2O	1.42	0.68	0.56	0.39
Total	100.85	100.12	100.37	99.55
Mg#	91.35	91.93	90.44	90.59
Wo	45.46	45.97	46.45	47.00
En	49.71	49.58	50.70	47.94
Fs	4.83	4.44	2.85	5.06
Si	1.90	1.88	1.90	1.88
Ti	0.01	0.02	0.02	0.03
Al	0.19	0.17	0.12	0.12

Cr	0.03	0.04	0.03	0.03
Fe(ii)	0.08	0.08	0.10	0.10
Mn	0.00	0.00	0.00	0.00
Mg	0.88	0.91	0.93	0.92
Ca	0.80	0.85	0.85	0.90
Na	0.10	0.05	0.04	0.03
Total	4.00	4.00	4.00	4.00
No.	7	9	8	6

Location	Lanz	Lanz	Lanz	Lanz	Lanz	Lanz
Sample	EC3	EC3	EC5	EC5	EC 21	EC21
Mineral	sp	sp	sp	sp	sp	sp
Site	core	sponge rim	bleb	Halo	Bleb	sponge rim
SiO_2	0.10	0.61	0.05	0.19	0.05	0.32
TiO_2	0.52	1.00	1.32	1.64	0.12	0.24
Al_2O_3	31.50	25.04	17.14	18.49	38.06	29.87
Cr_2O_3	33.84	39.49	8.88	8.39	27.28	37.32
Fe_2O_3		4.30	43.90	41.52	4.88	3.65
FeO	15.64	12.19	14.44	14.94	10.04	10.07
NiO	0.27	-	-	0.24	0.13	0.14
MnO	0.14	0.15	0.20	0.22	0.28	0.18
MgO	16.97	16.23	13.83	13.80	17.98	17.46
Total	99.18	99.18	99.76	99.42	98.82	99.26
Mg#	65.91	67.19	41.88	42.25	72.38	72.63
Cr#	41.89	51.41	25.80	23.55	32.47	45.60
Si	0.00	0.04	0.00	0.01	0.00	0.02
Ti	0.01	0.02	0.03	0.04	0.00	0.01
Al	1.08	0.89	0.63	0.68	1.27	1.01
Cr	0.78	0.93	1.09	1.03	0.61	0.88
Fe(iii)	0.11	0.06	0.21	0.20	0.10	0.06
Fe(ii)	0.27	0.34	0.38	0.39	0.24	0.27
Mn	0.00	0.00	0.01	0.01	0.00	0.00
Mg	0.74	0.71	0.65	0.65	0.76	0.75
Total	3.00	3.00	3.00	3.00	3.00	3.00
No.	25	10	5	4	7	5

In samples from Ray Pic, the olivine, orthopyroxene and clinopyroxene compositions were analysed using WDS analysis (Table 3.4). Mg#s for olivine, orthopyroxene and clinopyroxene are broadly similar to those from the northern Massif Central. Spinel Cr#s range from 12-16. Orthopyroxenes are enstatites with Mg#s from 90 to 91. Their Al_2O_3 content varies from 4.0 to 4.3 wt%. Clinopyroxenes are diopside with Mg# of 89-90, 19.7-20.0 wt% CaO and 5.9-7.3 wt% Al_2O_3.

Table 3.4. Representative WDS microprobe analysis of major rock-forming minerals from peridotite xenoliths from Ray Pic (RP), Massif Central, southern domain (SMC).

Location	Sample	Mineral	SiO_2	FeO	MnO	NiO	MgO	Total	Mg#	no.
SMC	RP87 6	ol	40.86	9.82	0.16		48.50	99.33	99.33	8
SMC	RP9122	ol	40.60	9.25	0.13	0.38	49.04	99.72	99.40	11

Location	Sample	Mineral	SiO_2	TiO_2	Al_2O_3	Cr_2O_3	FeO	MnO	MgO	CaO	Na_2O	Total	Mg#
SMC	RP87 6	opx	54.30	0.06	4.15	0.27	6.30	0.14	32.73	0.88	0.08	98.90	90.26
SMC	RP91 22	opx	54.82	0.06	4.02	0.37	5.96	0.14	32.71	0.79	0.12	99.01	90.72

Location	Sample	Mineral	Wo	En	Fs	Si	Ti	Al	Cr	Fe(ii)	Mn	Mg	Ca	Na	Total	no.
SMC	RP87 6	opx	1.71	88.53	9.76	1.89	0.00	0.17	0.01	0.18	0.00	1.70	0.03	0.01	4.00	3
SMC	RP91 22	opx	1.55	89.13	9.33	1.91	0.00	0.17	0.01	0.17	0.00	1.70	0.03	0.01	4.00	10

Location	Sample	Mineral	SiO_2	TiO_2	Al_2O_3	Cr_2O_3	FeO	MnO	MgO	CaO	Na_2O	Total	Mg#
SMC	RP87 6	cpx	51.78	0.30	6.21	0.67	3.35	0.09	15.75	20.02	1.15	99.32	89.35
SMC	RP91 22	cpx	51.41	0.32	6.17	0.91	3.12	0.10	15.57	19.74	1.29	98.62	89.88

Location	Sample	Mineral	Wo	En	Fs	Si	Ti	Al	Cr	Fe(ii)	Mn	Mg	Ca	Na	Total	no.
SMC	RP87 6	cpx	45.18	49.47	5.36	1.88	0.01	0.27	0.02	0.10	0.00	0.85	0.78	0.08	4.00	7
SMC	RP91 22	cpx	44.95	49.33	5.72	1.88	0.01	0.27	0.03	0.10	0.00	0.85	0.77	0.09	4.00	13

Location	Sample	Mineral	SiO_2	TiO_2	Al_2O_3	Cr_2O_3	Fe_2O_3	FeO	MnO	MgO	Total	Mg#	Cr#
SMC	RP87 6	sp	0.20	0.10	55.57	11.72	2.04	10.00	0.12	20.28	100.04	76.79	12.40
SMC	RP91 22	sp	0.20	0.10	52.57	14.92	1.94	10.00	0.13	19.90	99.74	76.54	15.99

Location	Sample	Mineral	Si	Ti	Al	Cr	Fe(iii)	Fe(ii)	Mn	Mg	Total	no.
SMC	RP87 6	sp	0.01	0.00	1.70	0.24	0.04	0.22	0.00	0.79	3.00	6
SMC	RP91 22	sp	0.01	0.00	1.64	0.31	0.04	0.22	0.00	0.78	3.00	4

The olivine-spinel mantle array (OSMA) shows the compositional differences between spinel peridotites from different tectonic settings (Arai, 1994). Coexisting olivine (Mg#) and spinel (Cr#) plot on the olivine-spinel mantle array (OSMA) where spinel peridotites from a particular tectonic setting lie, on average, in their particular area. Majority of fertile lherzolites (Cr# <20) from subcontinental settings generally lie in the high Mg# and low Cr# region of the OSMA. Whilst oceanic hot-spot peridotites resemble a fertile group of subcontinental peridotites (Arai, 1984), harzburgite peridotites from oceanic peridotites occupy the high Mg# and High Cr# region of the OSMA. Olivine and spinel pairs from xenoliths analysed in this study plot within the OSMA (Fig. 3.6) with Massif Central and Lanzarote samples lying within the continental and oceanic hotspot regions, respectively. Samples from Lanzarote are considerably more depleted in elements CaO, Al_2O_3, Na_2O and TiO_2 associated with melt extraction than those from the Massif Central and Calatrava, in keeping with the generally more depleted nature of the sub-oceanic mantle lithosphere. Olivine and spinel pairs from Calatrava plot within the OSMA lying within the continental region (Fig 3.6), similar to those from the southern domain of the Massif Central.

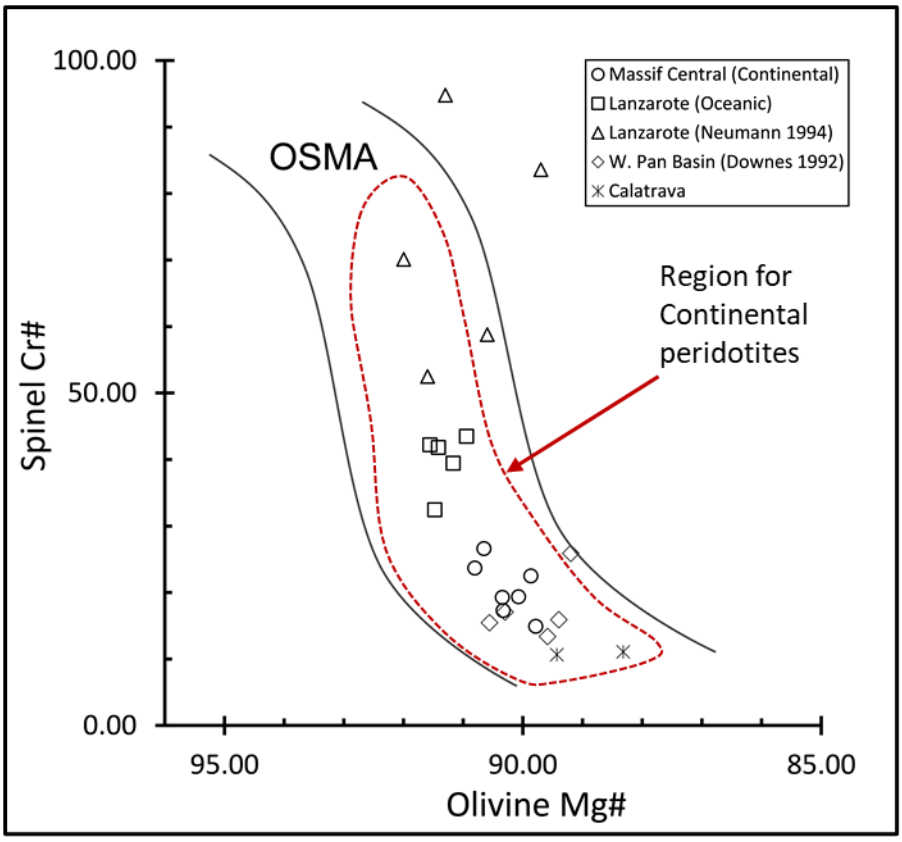

Figure 3.6. Mg# in olivine versus Cr# in spinel (OSMA), showing the compositional variation in the spinel peridotites from Massif Central, northern domain, Massif Central, southern domain, Lanzarote and Calatrava.

3.4.3 Micro-CT results

3D micro-CT scans of Lanzarote xenoliths revealed two distinct textures; small individual bleb-like spinels (Fig. 3.7 A, B) and large individual complex vermicular spinel clusters which range up to 4-12 mm (Fig. 3.6D, E, F and 3.8). Samples EC4 and EC6 (Fig. 3.7 C, D) show good examples of the large complex clusters with spinel displaying vermicular texture. Measurements taken via the Drishti software (Limaye, 2012) show that the dimensions of the complex structure in sample EC6 are 11.5 x 6.6 x 3.3 mm, and 15.2 x 11.8 x 2.5 mm in EC4. Their shape is therefore that of an ellipsoid. Fig. 3.8 shows an enlarged image of a single large complex structure from xenolith EC6. Individual spinel branches are in contact with adjacent branches thus forming a single crystal of spinel. The interstitial texture of spinel within SPCs is visible in Figure 3.8, which shows voids where the shapes and sizes of associated pyroxene crystals are imprinted on the individual vermicular branches of the spinel complex.

In samples EC20 and EC21 the spinels show fewer complex structures (Fig. 3.7 E, F and 3.9), however in EC21 a large complex structure is surrounded by a halo of high atomic number material, interpreted as the olivine + cpx + glass material seen in thin-section. In thin-section distribution of spinel within the individual samples is concentrated in cluster sites and there is an absence of spinel outside the cluster sites. Therefore, spinels within this halo are considered to be the remnants of a single large complex SPC which has been altered by metasomatic reactions.

Sizes of individual spinel blebs in samples EC3 and EC5 (Fig. 3.7A and B) vary from 0.5 to 3 mm and may be either spatially concentrated or distributed throughout the rock with a strong lineation. Several smaller regions of concentrated spinel blebs are visible in sample EC3 (Fig. 3.7A). Almost all the spinel is associated with these SPCs. Spinel blebs within the concentrated region show a preferred orientation forming discrete bands. Sample EC5 displays uniform size elongate blebs whose dimensions are on average 2.5 x 1.5 x 0.8 mm. The spinel blebs are distributed throughout the rock and display a preferred orientation. They are interpreted as remnants of SPCs which have been altered by metasomatic reactions and in addition experienced deformation.

The Massif Central micro-CT data sets also show two distinct SPC textures, which differ from those seen in Lanzarote samples. The SPCs occur as relatively small <4 mm complex vermicular structures (MB8, Fig. 3.10A) which are evenly distributed throughout the rock, and also as larger 5-9 mm clusters with complex vermicular textures (MB64, Fig. 3.10B) evenly distributed but showing a strong preferred orientation. Similarly, to the Lanzarote samples, almost all the spinel is associated with these SPCs, with large portions of the rocks being devoid of spinel. The shape of the small complex

spinel cluster textures in sample MB8 is an ellipsoid with dimensions 3.5 x 2.46 x 0.75 mm. Spinel inside these structures displays a strong vermicular texture but is largely confined to the outer portion of the complex structure with the central region having less spinel (Fig. 3.11). These small complex structures display no lineation and their distribution throughout the rock core is random. In contrast, the large complex SPC textures in sample MB64 (Fig. 3.9B) are flattened elongate structures with dimensions 5.5 x 8.8 x 2-3 mm. Strongly vermicular spinel is evenly distributed within the structures with higher spinel concentrations compared with the structures in sample MB8. Micro-CT images of a large spinel complex structure (MB64) also shows a preferred orientation. No reaction halos were detected in the micro-CT data for Massif Central samples.

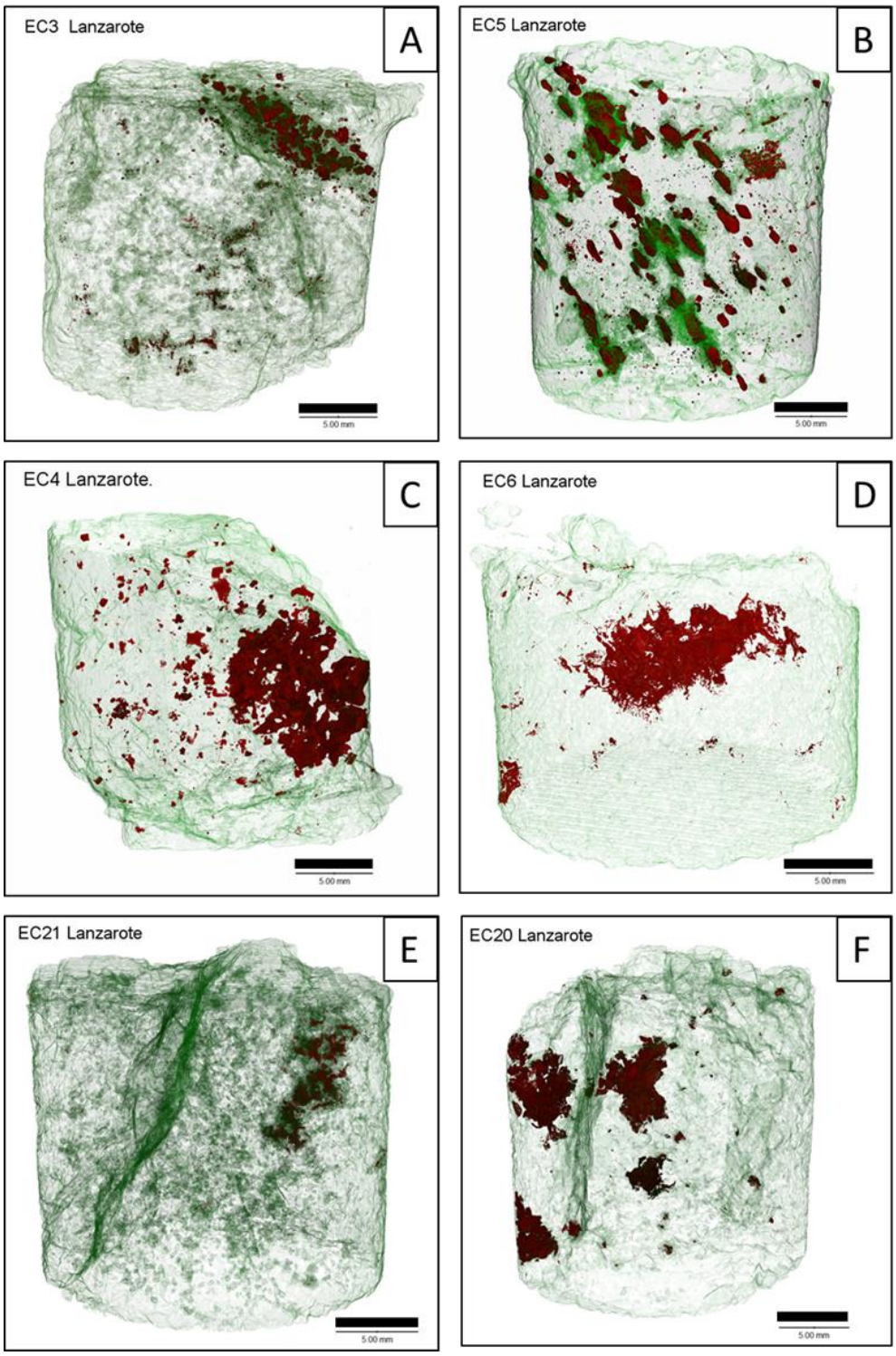

Figure 3.7. (A–F) Spinel peridotite micro-CT 3D rendered volumes from Lanzarote (EC3, EC5, EC4, EC6, EC21 and EC20). 5 mm scale bar.

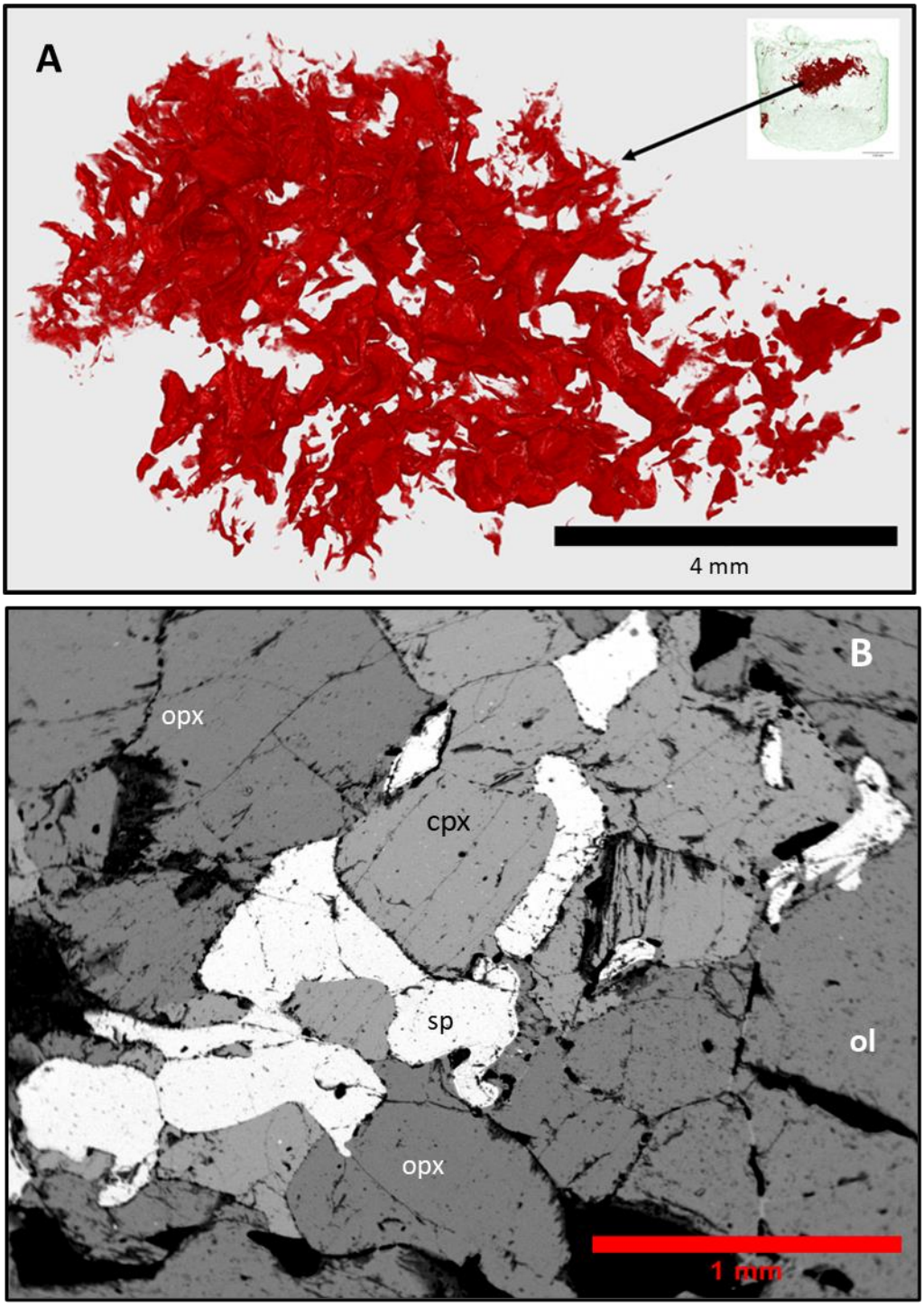

Figure 3.8. (A) Spinel texture of a large single individual cluster site in higher resolution and greater magnification (EC6). 4 mm scale bar. Voids represent the shapes and sizes of associated pyroxene crystals which are imprinted on the individual vermicular branches of the spinel complex. (B) BSE image showing the texture of large single individual cluster site with pyroxene grains and interstitial spinel (EC6). 1 mm scale bar.

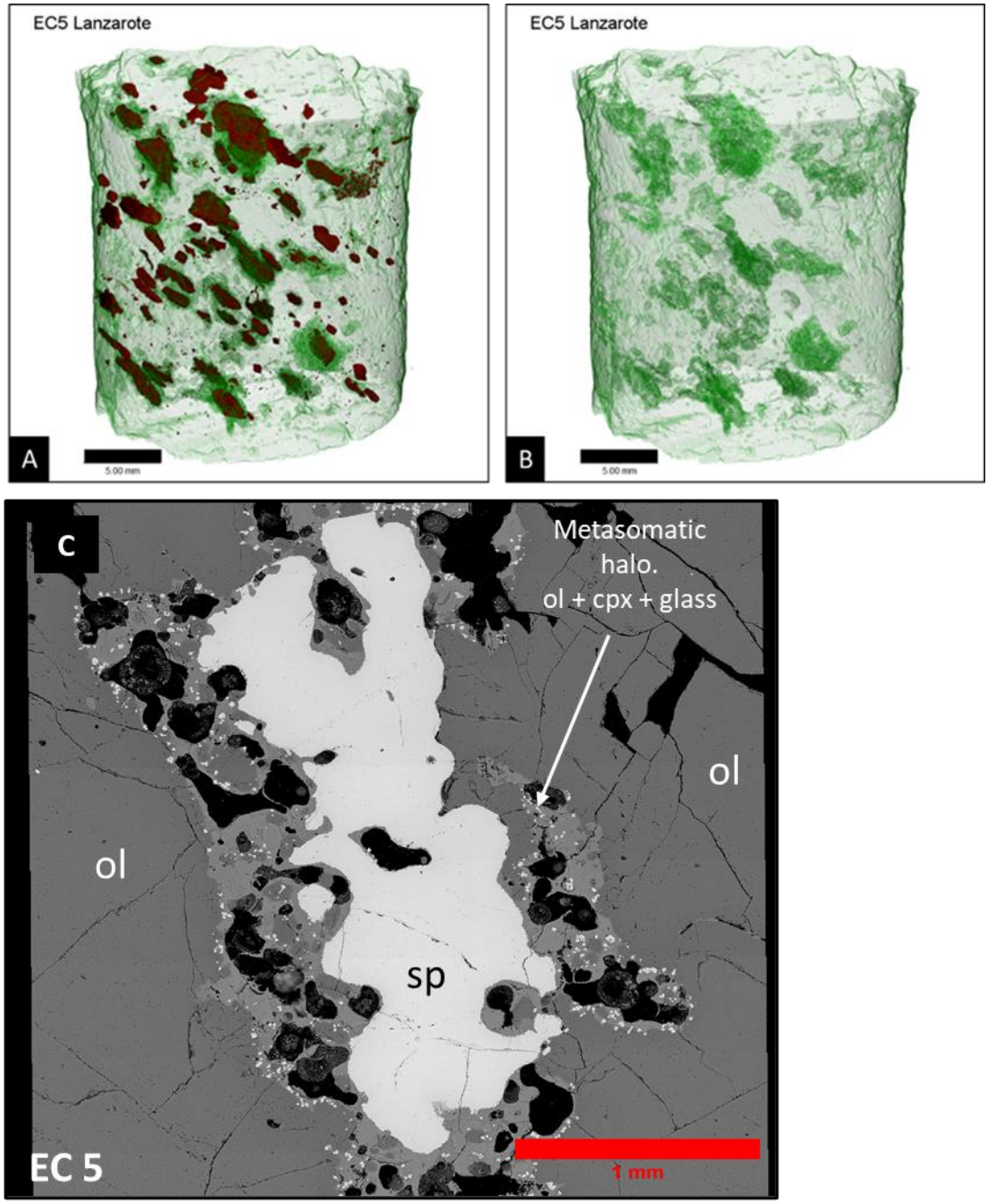

Figure 3.9. (A and B) Spinel peridotite (EC5). Micro-CT 3D rendered volumes from Lanzarote B. Spinel phase removed leaving silicate and metasomatic reaction zones in 3D rendered images. 5 mm scale bar. (C) BSE image of a spinel surrounded by a metasomatic halo comprising of ol+cpx+glass. Scalebar is 1 mm

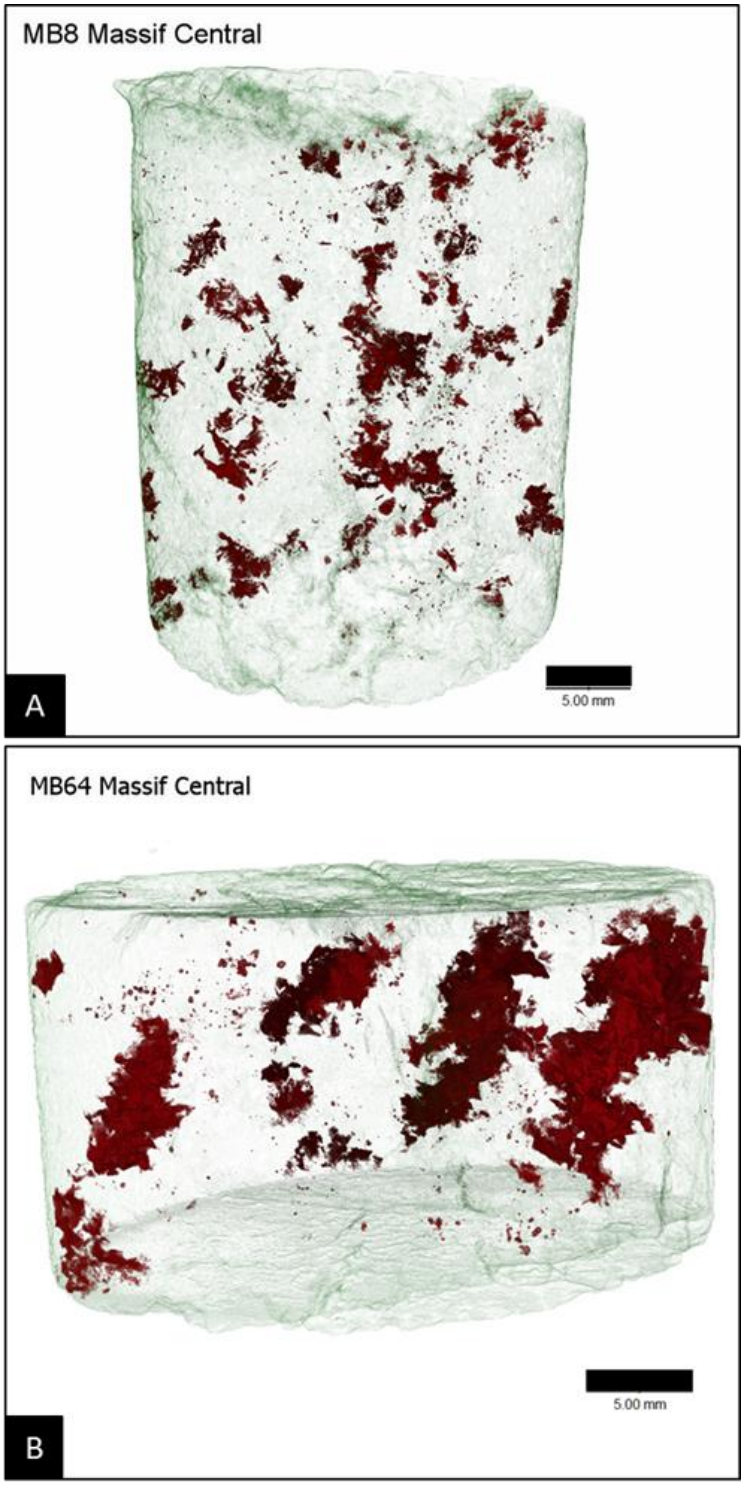

Figure 3.10. (A and B) Spinel peridotite micro-CT 3D rendered volumes from Montboissier, Massif Central (MB8 and MB64). 5 mm scale bar.

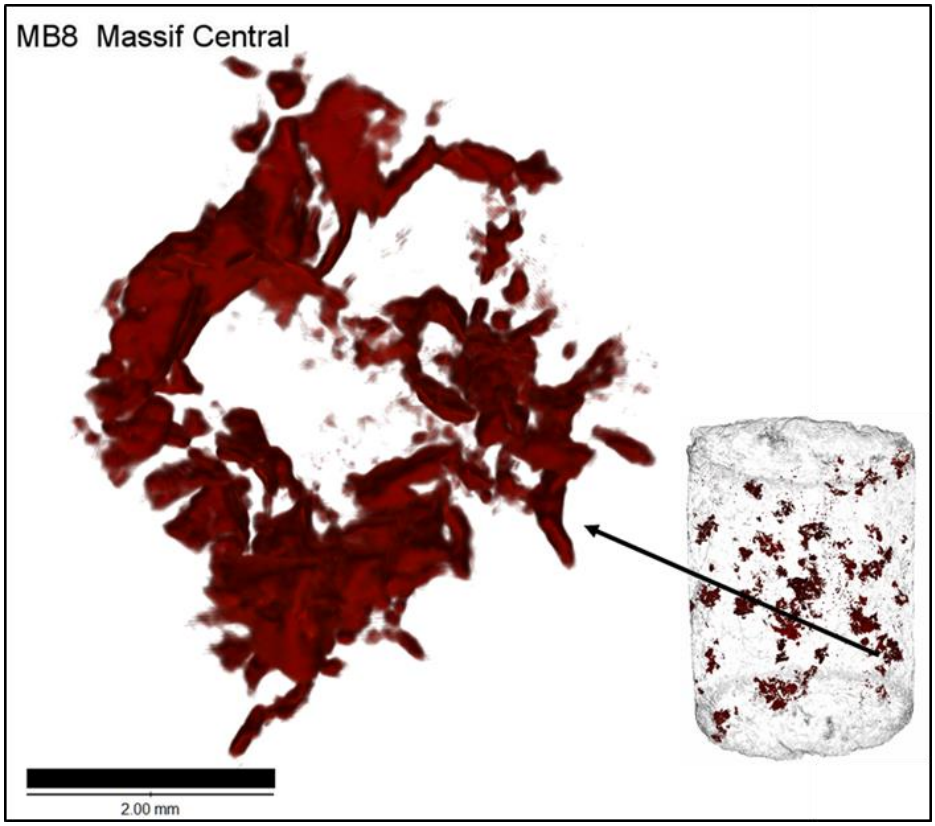

Figure 3.11. Texture of large single individual cluster site in higher resolution and greater magnification (MB8). 2 mm scale bar.

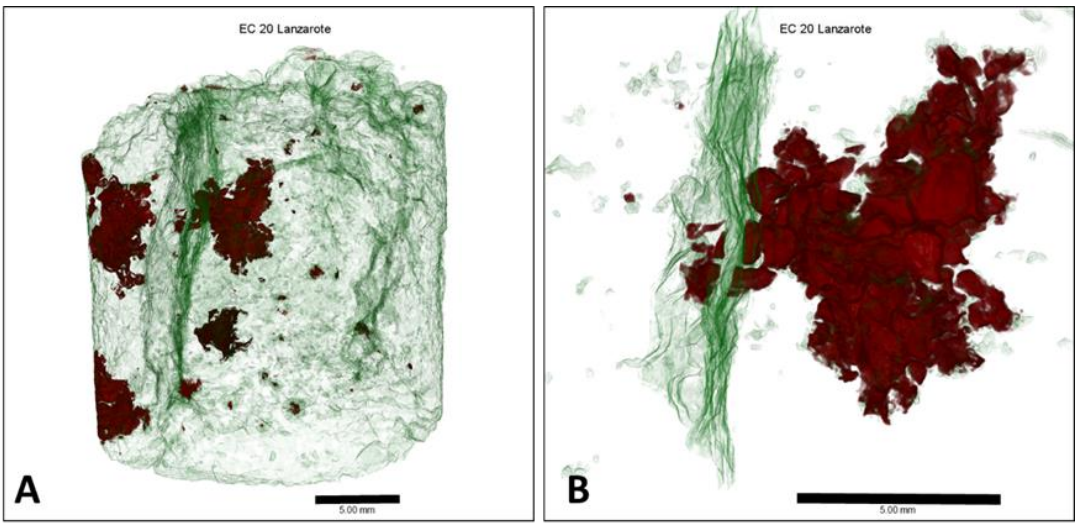

Figure 3.12. (A) Spinel peridotite micro-CT 3D rendered volume from Lanzarote. 5mmscale bar. (B) The texture of a melt channel in higher resolution and greater magnification (EC20) extracted from a 3D data set. 5 mm scale bar.

Micro-CT scans of three spinel peridotites from Calatrava (Fig. 3.13) reveal two main spinel textures. Type 1 is a large individual complex vermicular spinel clusters which range up to 15.73 x 5.36 mm in size. The complex structures are ellipsoidal in shape with an aspect ratio (AR) of 2.93 (Fig. 3.13 A and B). Type 1 complex spinel structures are very similar shape, size and AR to those described from Lanzarote spinel peridotites (Bhanot et al., 2017). The spinel clusters display a lineation along the

longest axis (Fig. 3.13A). In the second (type 2), spinel (Fig 3.13 C and D) occurs as locally isolated complex structures in which spinel displays channel-like branches connected to large flat plate-like structures. Long channel-like structures (Fig. 3.13D) are relatively straight due to formation along cracks.

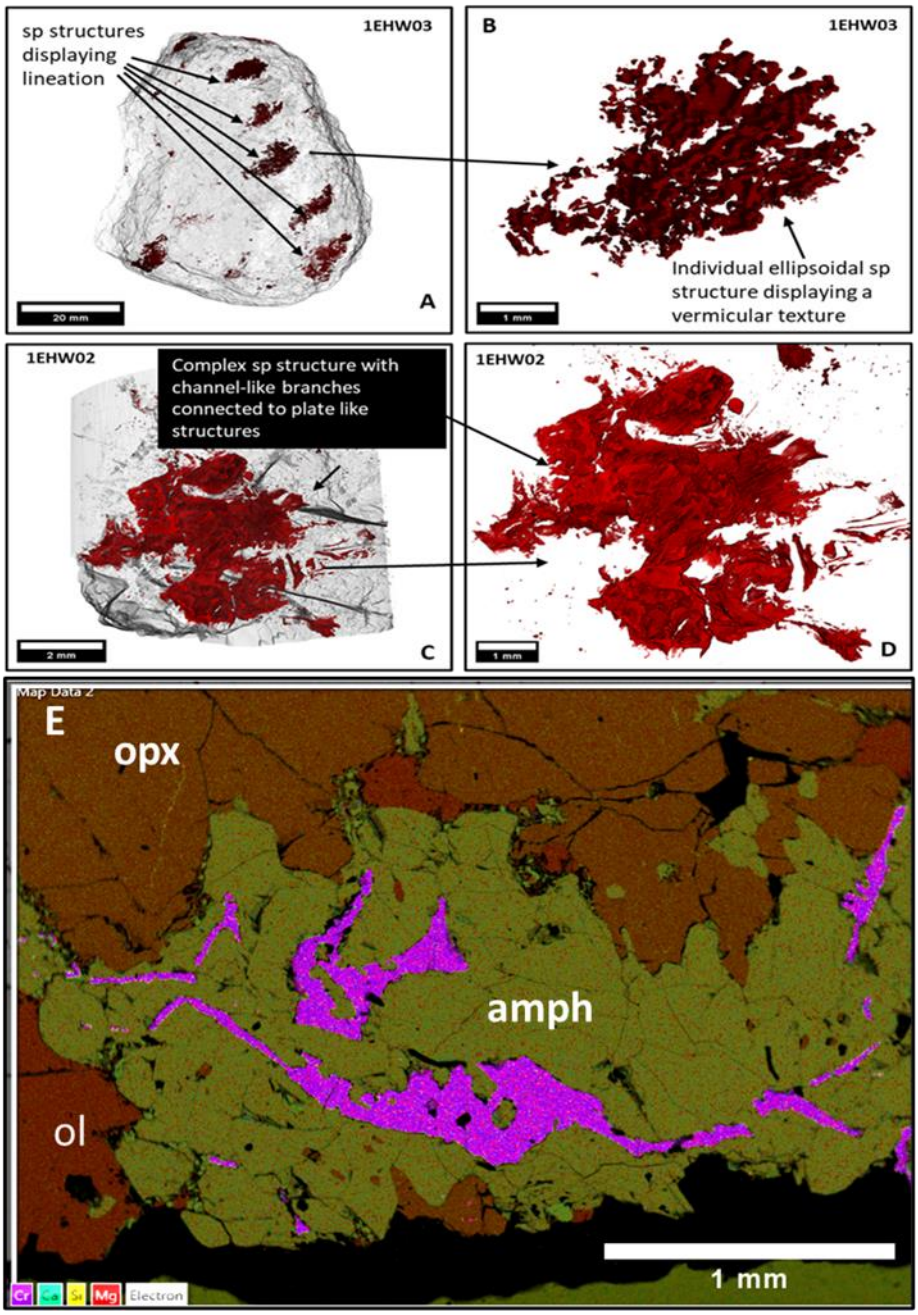

Figure 3.13. (A) 3D rendered image of spinel textures found in spinel-amphibole structure from a spinel peridotite (IEWH03) from Calatrava. Scalebar is 20 mm. (B) 3D rendered image of and individual type 1 complex vermicular structure from a spinel peridotite (IEWH03) from Calatrava. Scalebar is 1 mm. (C) 3D rendered image of a type 2 complex structure from a spinel peridotite (IEWH02) from Calatrava. Scalebar is 2 mm. (D) Enhanced 3D rendered image of a single sp type 2 complex structure from a spinel peridotite (IEWH02, Calatrava) showing channel and flat plate structures. Scalebar is 1 mm. (E) False colour image of spinel texture in a spinel peridotite form Calatrava (1EHW02). Spinel (purple) forms long channels running through an amphibole (light green) structure. This texture has been interpreted has the result of a metasomatic reaction. Scalebar is 1 mm.

3.5 Discussion

3.5.1 Typical spinel peridotite textural types

Micro-CT analysis of spinel textures from spinel peridotite xenoliths from Ray Pic have provided accurate representations of the three structural types and their major characteristics as defined by Mercier and Nicolas (1975). Micro-CT data reveals that spinel grain size decreases from protogranular through to equigranular textured peridotites. From the protogranular to the equigranular rock cores shown in Figure 3.2 spinel is more evenly distributed from the protogranular to the equigranular samples (3.2 A-C). However, protogranular (Fig. 3.2A) and porphyroclastic (Fig. 3.2B) textures reveal that they are not distinct examples of each textural type but more a texture transitioning from one to another, i.e., a protogranular texture transitioning to porphyroclastic as seen in Fig. 3.2A and a porphyroclastic texture transitioning to equigranular texture as seen in Fig. 3.2A with increasing deformation. Photomicrographs of a spinel lherzolite (VP92) in Figure 3.2C shows the transition occurring in one peridotite in which a porphyroclastic to equigranular is visible in this section. spinel is fine grained with holly leaf texture and evenly distributed throughout the rock. Several larger blebs are clearly visible along with several large ol grains. Suggestion that spinel peridotite textures form a continuous series rather than distinct groups is in agreement with Tabor et al. (2010). Spinel also shows that in both protogranular and porphyroclastic texture types of spinel shows a lineation. It is my opinion that this is another example of a transitional texture from one textural type to another with increasing deformation. Another key characteristic is spinel association with olivine> this texture is most visible in the porphyroclastic texture in which holly-leaf shaped spinels typically are encircled by olivine grains.

3.5.2 Formation of SPCs

Our microprobe data show compositional uniformity between the minerals present in the clusters and those outside the clusters (Table 3.2). This is in agreement with Smith (1977) who proposed that any textural explanation of SPCs must account for their compositional uniformity. Several hypotheses that account for the formation of SPCs were discussed by Smith (1977) and Falus et al. (2000) and are as follows:

1. crystallisation from pools of melt concentrated during partial fusion or original crystallisation.
2. deformation, leading to the accumulation of both spinel and pyroxene followed by subsequent annealing.
3. exsolution of spinel and clinopyroxene from aluminous orthopyroxene.
4. Reaction of aluminous orthopyroxene with olivine or a reaction between garnet and olivine.

Hypothesis 1 fails to account for the absence of olivine in the SPCs. BSE images of SPCs from Massif Central, Lanzarote and Calatrava samples unaffected by metasomatism show that olivine does not form part of the cluster and thus provides support to Smith's (1977) dismissal of this hypothesis. In regard to hypothesis 2, there is no evidence that the fracture and breakup of grains results in the concentration of grains that are more resistant to deformation. Mercier and Nicolas (1975) outlined how, with increasing deformation, spinel develops a holly-leaf texture and smaller grain size and becomes distributed throughout the xenolith. 3D volumes of both Massif Central, Lanzarote and Calatrava show that the spinel is restricted to SPCs and spinel texture of the SPC is highly vermicular and lacks the deformation-related holly-leaf texture and spinel grain size remains coarse. In terms of hypothesis 3, Smith (1977) highlighted that spinel and pyroxene have different cation/oxygen ratios and that solid solution between spinel and pyroxene would be non-stoichiometric. High spinel/pyroxene ratios in SPCs would require improbably high degrees of non-stoichiometric reactions. For hypothesis 4, transition from garnet to spinel is possible by an increase temperature or a pressure decrease (Smith 1977). Several studies record the garnet-olivine reaction, where the breakdown of garnet led to radiating spinel–pyroxene symplectites or with spinel-pyroxene coronas around garnets in contact with olivine (Reid and Dawson 1972; Aoki and Shiba 1973; Wallace 1975). Smith (1977) concluded that the SPC texture reflects transport of a garnet peridotite through the garnet-spinel transition at depths < 90 km, brought about by a decrease pressure.

Smith (1977) cites studies by Obata (1976) and O'Hara et al. (1971) which concluded that the transition from garnet to spinel peridotite is unaffected at temperatures 1000–1200 °C and that pyroxene exsolution lamellae textures observed in SPCs in peridotite xenoliths from Green Knobs, New Mexico, are produced by slow cooling and therefore indicate a pressure-induced reaction. Exsolution textures from the Massif Central, Lanzarote and Calatrava (Fig. 3.4) are also a result of slow cooling and suggest that the garnet–spinel transition beneath these areas is the result of reduction in pressure.

Reid and Dawson (1972) studied garnet peridotite xenoliths from the Lashaine volcano, Tanzania. Reaction coronas <1.5 mm thickness surround the garnet (Mg-rich chrome pyrope). They divided the reaction rims into 3 zones. Zone 1 is in contact with the outermost portion of the garnet and is composed of a microcrystalline aggregate. Zone 2 is a fine-grained acicular crystallite in a feathery aggregate, oriented approximately normal to the garnet margin, whereas zone 3 which is in contact with olivine and is wider compared to zones 1 and 2, coarser grained with equant and largely euhedral spinel and clinopyroxene surrounded by orthopyroxene. Reid and Dawson (1972) considered that the phase transition from garnet to spinel (Eq. 3.1) starts in the region of 20 kb and 900–1300 °C and the reaction rims are the product of this reaction. They suggest that, if the reaction had gone to completion, all the garnet would have reacted, and a spinel-bearing assemblage would have resulted. The original garnet peridotite assemblage would be converted to spinel peridotite containing SPCs. Reid and Dawson (1972) reported that pyroxenes within the reaction rims are Al-rich in comparison to independent pyroxenes. Textures identified in 3D volumes (Figs. 3.7, 3.8, 3.9, 3.10 3.11 3.12 and 3.13) of our Massif Central, Lanzarote and Calatrava samples also indicate sufficient time for the completion of the garnet + olivine (Eq. 3.1) reaction. Microprobe data (Table 3.2) for Massif Central, Lanzarote and Calatrava samples shows no major differences in mineral compositions between SPC and non-SPC sites, indicating equilibrium texture in the SPCs, rather than the reaction texture of a radiating halo around a small garnet. Thus, the SPCs likely represent mantle that has reacted and equilibrated. Smith (1977) concluded that the sub-solidus olivine–garnet reaction is the probable explanation for the origin of SPCs and, given that mineral compositions for both cluster sites and non-clusters sites from Massif Central, Lanzarote and Calatrava are similar, this observation gives support to Smith's hypothesis 4.

Morishita and Arai (2003) investigated variations in SPCs (symplectites) in the Horoman peridotite complex, Japan, brought about by the phase transition from the garnet to spinel. Geochemical and textural characteristics of SPCs in the Horoman Complex vary with sample locality such that the grain size of SPC minerals increases gradually upwards in the massif and represents differences in thermal

history during exhumation and textural variations result from differences in the decompression histories. The basal section of the Horoman complex experienced a lower temperature decompression path yielding less chemical modification by diffusion during decompression whereas the higher part of the complex experienced a relatively high temperature decompression path, which resulted in chemical equilibration among samples by diffusion, accompanied by coarsening of the SPC minerals (Morishita and Arai, 2003). Morishita and Arai (2003) considered that the Horoman peridotite ascended as a mantle diapir from the garnet peridotite stability field. A similar explanation may apply to the Massif Central xenoliths analysed in this study, in which there is a difference in the size of SPCs in different xenoliths. Samples showing smaller cluster sizes may have been formed at shallower depths. The micro-CT data for Massif Central xenoliths also showed two distinct SPC textures; both show complex vermicular structures, but one has a strong lineation. The large complex spinel cluster structures display a strong lineation interpreted as a response to deformation.

Odashima et al. (2007) also studied SPC formation and deformation in Horoman, focusing on a porphyroclastic spinel lherzolite with a strong foliation and lineation. The SPCs are described as having an elliptic outline and are mantled by a lenticular seam of orthopyroxene with minor clinopyroxene and spinel, thus differing from the samples in our study. They proposed a multi-stage process for formation and deformation of SPCs. The sequence of formation involves (1) an initial stable garnet crystal surrounded by olivine in the garnet stability field; (2) decompression into spinel stability field resulting in garnet beginning to react with olivine, forming a reaction rim composed of an intergrowth of spinel and pyroxenes; (3) with continuing decompression and rise through the spinel stability field, reaction rim growth due to recrystallization, coarsening and deformation; (4) deformation with a relict rigid garnet in the centre; (5) growth of SPC; and (6) deformation of the surrounding mineral aggregate and the SPC. Odashima et al. (2007) considered that simultaneous growth of spinel and pyroxenes entangling with each other starting from their nucleation at limited sites on the garnet surface is a plausible mechanism for garnet decomposition.

Falus et al. (2000) also considered decompression to be the major driving force in forming SPCs in xenoliths from Hungary, following the reaction of garnet and olivine. This implies that the lithospheric mantle experienced upwelling and thinning beneath that region, consistent with the geophysical evidence for thinned crust and lithosphere beneath the Pannonian Basin. A minimum of 50–60 km vertical movement for the SPC-bearing xenoliths was calculated by Falus et al. (2000), thus transporting mantle material from conditions where garnet was stable to a depth range where spinel is present. Both the northern Massif Central and Lanzarote are regions that have experienced

significant lithospheric thinning (Babuška et al., 2002; Neumann et al., 1995). The process provides a mechanism for the sub-solidus reaction of olivine + garnet = orthopyroxene + clinopyroxene + spinel by providing a change in pressure conditions. We suggest that the spatially constrained lithospheric thinning in both regions results in restricted occurrences of the SPCs in both localities.

3.5.3 3D textures and structure of SPCs

Lanzarote xenoliths show two distinct SPC textures, one consisting of large clusters with complex vermicular textures in the shape of an ellipsoid (Fig. 3.7C and D), and the other being small anhedral "bleb-like" spinels showing a lineation (Fig. 3.7A and B). These two types of SPC occur in different samples from the Lanzarote xenoliths. The ellipsoid shape displayed in Figs. 3.7C and D must have been formed by flattening of originally spherical structures formed by replacement of large, originally equant, garnets with an SPC, whereas the anhedral spinel blebs are always surrounded by metasomatic halos. This strongly suggests that the bleb-like spinels are relics of vermicular spinels that have been strongly attacked by metasomatic fluids.

Micro-CT images of a large spinel complex structures (MB 64) show that deformation can modify spinel within the SPC with a lineation, however BSE (Fig. 3.4A and B) suggests that silicate minerals appear unaffected by deformation. The textural variation seen in the 3D volumes of spinel within SPCs in the Massif Central would indicate a difference in the decompression histories of the peridotites likely indicating different source regions within the lithospheric mantle. Fig. 3.10A displays the relatively small complex vermicular structures and it is likely that this sample experienced a different decompression path compared to the coarse SPCs in the 3D images in Fig. 3.10B.

Calatrava xenoliths reveal SPC textures similar to those observed in Lanzarote, i.e., one consisting of large clusters with complex vermicular textures (Fig. 3.13A and B), i.e., large ellipsoidal clusters with complex vermicular textures. Samples from Calatrava (Fig. 3.13D) similar to those seen in Lanzarote show evidence spinel reacting with metasomatic fluids forming a more fluid-like texture with multiple flat channels and a less vermicular complex structure.

Kelyphite is a well-known metamorphic reaction texture (corona) developed around garnet typically in mantle-derived garnet peridotites and eclogites. Obata and Ozawa (2011) studied the reaction mechanism and kinetics of kelyphite textures of garnet peridotites from the Czech Republic and western Norway. They proposed that the reaction (Eq. 3.1) following decompression initiates at original interfaces between garnet and olivine. It is unlikely, however, that all the product phases, orthopyroxene, clinopyroxene and spinel, nucleated simultaneously. Obata and Ozawa (2011)

proposed that orthopyroxene is the first phase to nucleate with each orthopyroxene domain developing from a single orthopyroxene nucleus. Nucleation of orthopyroxene on garnet would cause subsequent nucleation of spinel and clinopyroxene. Once nucleation occurred, the orthopyroxene–spinel assembly simply grows eutectoidally, replacing garnet and maintaining the initial topotaxic (crystallographic) relationship established at the nucleation stage.

The sub-solidus reaction series following Eq. 3.1 proposed by Obata and Ozawa (2011) provides a likely explanation for the formation of SPCs in Massif Central, Calatrava and Lanzarote xenoliths. The modal mineralogy of the SPC with the high proportion of orthopyroxene coupled with the complex vermicular texture of the interstitial spinel viewed in the 3D volumes (Fig. 3.4) lends weight to the proposal that orthopyroxene is the first phase to form with spinel and clinopyroxene forming subsequently. Several Lanzarote samples display reaction halos surrounding spinel at SPC sites in thin-section and BSE images (Fig. 3.5). The origin of reaction textures (halos), i.e., olivine + clinopyroxene + glass + sponge-textured spinel, has been debated over numerous studies. Carpenter et al. (2002) proposed that they result from fluid-induced melting in the mantle. Bonadiman et al. (2005) considered that they are a result of metasomatism by melts in the lithospheric mantle, but Shaw et al. (2006) demonstrated that the same textures identified in harzburgitic mantle xenoliths from Sal, Cape Verde show clear evidence of reaction with the host magma during xenolith transport. Neumann et al. (1995) proposed that the reaction zones are due to infiltration by Fe-Ti-rich silicate melts, whereas El-Rus et al. (2006) proposed that xenoliths entrained in hot magma during ascent experience partial melting due to decompression and heating and the formation of spongy spinel.

When the reaction halos in Lanzarote xenoliths are viewed in 3D without the spinel phase, their shapes are very similar to the spinel blebs which they enclose (Fig. 3.7). Furthermore, the halos in sample EC5 (Fig. 3.7) appear isolated and unconnected to each other. These reaction halos provide strong textural evidence that the SPCs experienced a metasomatic reaction in the mantle, rather than via melt infiltration during eruption. Images captured from the 3D volume of sample EC3 (Fig. 3.7A) show local concentrations of small blebs of spinel, forming bands. In sample EC3 the metasomatic reaction halo encases the spinel microcrystals but in addition discrete channels in contact with the reaction halo (Fig. 3.7A). We interpret this feature as a result of melt infiltration and the spinel microcrystals, spinel sponge texture and metasomatic halos of ol + cp x+ glass are the product of metasomatic reactions between a melt and a large complex SPC. Metasomatic reaction channels have also been identified in 3D volumes of sample EC20 and EC21 (Figs. 3.7E, F and 3.12). The 3D volumes reveal that the metasomatic reactions show two textures associated with SPCs. The

individual SPCs surrounded by the metasomatic reaction halos indicate reactions occurring in isolation, whereas the second texture shows linear channels in contact with cluster sites and as linear features running through the rock core, indicating melt infiltration.

3.6 Conclusions

Micro-CT analysis of samples of spinel peridotites from Ray Pic in the southern domain of the Massif Central, has provided accurate representations of typical spinel peridotite xenolith textures. These provide examples of the three main structural groups (protogranular, porphyroclastic and equigranular) of spinel mantle xenoliths as defined by Mercier and Nicolas (1975). 3D visualisations were used as a reference in comparison to spinel textures in SPC-bearing peridotites to compare and contrast these textures and record the unique nature of the spinel textures in SPC-bearing peridotites. Protogranular spinel textures observed in 3D images from Ray Pic revealed spinel, which is coarse grained, concentrated and also displaying a lineation. The spinel grain size distribution throughout the protogranular samples showed that the spinel graded into the second structural group i.e., the porphyroclastic textural type. Grain size, shape and distribution of spinel from protogranular through porphyroclastic to equigranular grain size is increasingly finer and spinel distribution becomes more evenly distributed in the fine grained equigranular textural type.

The 3D rendered volumes provide accurate representations of the shape and form of spinel–pyroxene clusters in xenoliths from Lanzarote, northern domain of the Massif Central and Calatrava, with identification of variations in cluster sizes, shapes, and textures. 3D visualisation of textures in samples that have experienced metasomatic events and deformation is clearly distinguished and thus illustrates evidence of mantle processes than can be obtained in 2D visualisations. The spinel cluster textures identified in the 3D rendered volumes are textural evidence of the sub-solidus reaction of garnet + olivine whose products yield orthopyroxene + clinopyroxene + spinel (Eq. (3.1)). Large complex vermicular structures and localised nature of the individual spinel, shape and form (sometimes branched) display a common origin and therefore each spinel structure can be regarded as composed of an individual spinel crystal. Smaller less complex vermicular spinel structures have also been characterised from the 3D datasets and therefore variations in the size of the spinel complex structures and thus size of spinel–pyroxene clusters imply different source regions within the lithospheric mantle that have followed different thermal histories.

SPC spinel textures observed in 3D images from Lanzarote, Massif Central and Calatrava reveal that SPC- bearing peridotites form a distinct textural type from the protogranular type described by Mercier and Nicolas (1975). When comparing the Ray Pic protogranular xenolith with SPC-bearing spinel peridotites, the spinel is more evenly distributed throughout the sample and TS data reveal some association with olivine grains. Samples from SPC-bearing peridotites the TS and 3D data reveal concentrated regions of spinel with regions of the sample outside the spinel concentration almost devoid of spinel. These textures occur in regions of the upper mantle that have experienced

lithospheric thinning and thus are limited to these regions. The identification of SPC textures forming a distinct textural type for coarse mantle xenoliths is in agreement with Lenoir et al. (2000).

Our results are in agreement with Smith (1977) in terms of the lack of compositional change in mineral chemistry between cluster and non-cluster crystals. The large individual spinel clusters with complex vermicular texture show that locally the spinel is highly concentrated. This texture may well conserve evidence for lithospheric mantle from the garnet stability field to the spinel stability field by pressure reduction. We predict that such textures would only occur in the mantle beneath regions that show tectonic evidence of lithospheric thinning. The metasomatic reactions displayed around the spinel–pyroxene clusters in some Lanzarote xenoliths suggest that this occurred after the formation of the cluster texture. No metasomatic reaction halos were detected from the micro-CT data for samples from the Massif Central.

Chapter 4

Micro-CT investigation of garnet-spinel clusters in mantle peridotite xenoliths*

* Part of this chapter has been published as "Bhanot K K, Downes H, Petrone C M, Humphreys-Williams E and Clark B (2019). Lithos v352-353. https://doi.org/10.1016/j.lithos.2019.105250

4.1 Introduction

Garnet-bearing peridotite mantle xenoliths are rare in off-craton alkali basaltic areas and are only reported from a few alkali basaltic provinces such as Patagonia (Skewes & Stern, 1979; Kempton et al, 1999), Siberia (Murav'yeva et al., 1987) and China (Cao & Zhu, 1987; Ionov, 2004). In studies of spinel-garnet peridotite xenoliths, Ionov et al. (1993), Ionov (2004) and Stern et al. (1999) concluded that the garnets were formed at the expense of spinel and pyroxenes in a sub-solidus reaction. This sub-solidus transition from the spinel stability field to the garnet stability field is caused by either a decrease in temperature or an increase in pressure, and is represented by the reversible equation 4.1 (Smith, 1977):

orthopyroxene + clinopyroxene + spinel ↔ olivine + garnet ---------- Equ 4.1

This study will test the hypothesis that garnets formed from spinel and pyroxenes in suites of garnet-spinel peridotite xenoliths by using micro-CT scanning to determine their three-dimensional textures and the relationships between garnet and spinel. Micro-CT 3D volumes provide accurate and high-resolution representations of both garnet and spinel phases in peridotites. Analysis of the 3D volumes will allow comparison of garnet-spinel textures in samples from the two localities, including their aspect ratios. We will compare these with 3D textures of spinel-pyroxene clusters in spinel peridotite mantle xenoliths (Bhanot et al., 2017) which provide textural evidence of the reverse of the reaction shown in Equ 4.1. Garnet peridotite xenoliths from South Africa will also be used for comparison.

4.2 Sample localities

Our samples are from two well-known off-craton continental mantle xenolith localities: Pali-Aike (PA) in South America, and Vitim (VI) in eastern Russia. The Pali-Aike volcanic field forms part of the Patagonian plateau lavas and is ≤4 Ma in age. The western margin of South America is a convergent plate boundary

between the South American, Nazca and Antarctic plates (Skewes and Stern 1979). The Pali-Aike host basalts are alkali-olivine basalts generated by partial melting of the mantle in response to tectonic changes of the South American, Nazca and Antarctic plate triple junction.

The Vitim plateau is composed of Cenozoic alkali basaltic lava flows and pyroclastic deposits, located ~ 250 km east of Lake Baikal. Tectonic and geophysical studies (e.g., Petit et al., 1998) have found no evidence for large-scale lithospheric thinning beneath the Vitim plateau (Ionov, 2002). Because the Vitim plateau is clearly distinct from the Baikal rift in terms of its relief and tectonic setting, it may be more appropriate to consider it as part of the broad diffuse area of Cenozoic alkali basaltic volcanism between the Siberian and North China cratons (Ionov, 2004).

Textures and petrology of mantle xenoliths from Pali-Aike have been previously studied by Skewes and Stern (1979), Douglas et al. (1987), Stern et al. (1999), Kempton et al. (1999) and Wang et al. (2008). They are high-temperature (>970^{o}C) peridotites, mostly protogranular garnet-spinel harzburgites and garnet lherzolites. Low temperature spinel peridotites were not studied. Previous studies of textures and petrology of Vitim mantle xenoliths include those of Ionov et al. (1993), Ionov (2004), Ionov et al. (2005) and Ionov and Hoffman (2007). Xenoliths from Vitim are protogranular garnet-spinel or garnet lherzolites.

Garnet peridotite xenoliths (DB1 and TE201) from the Kaapvaal craton, South Africa, are chosen to represent a typical garnet peridotite, i.e., the stating material for the decompression solid state reaction of olivine and garnet yielding a spinel-pyroxene cluster. Sample DB1 is a coarse-grained granular garnet peridotite from Kimberly. The Kaapvaal craton extends over an area 1.2 million km^2. Its age is considered to be between 3.7 and 2.6 Ga. Based on P-T calculations, its thickness is ca. 250 km (Rudnick and Nyblade, 1999). Peridotites from Kaapvaal are commonly garnet-facies peridotites, coarse grained and entrained in kimberlites. Bulk compositions of garnet peridotites are typically highly depleted in Fe, Ca and Al but enriched in Mg (Pearson et al., 2003). Six large kimberlite diatremes (Kimberley, De Beers, Wesselton, Dutoitspan, Bultfontein and Kamfersdam) are clustered together in or near the city of Kimberley (Wagner, 1914; Boyd and Nixon, 1978). Xenoliths erupted in kimberlites include two groups of garnet peridotites that can be categorised by differences in estimated equilibrium conditions (Boyd, 1987). Low temperature (coarse-grained, granular) peridotites have calculated equilibrium temperatures at <1100 ^{o}C, olivine Mg#s between 92and 93 and are depleted in basalt-forming elements

(Fe and Ti). High temperature (deformed) peridotites have equilibrium temperatures >1100 ^{o}C with ol Mg#s >91.5 and are enriched in Fe and Ti.

4.3 Methodology

Thin-section preparation and electron microprobe analysis (EMPA) were performed at Birkbeck, University of London. The modal mineralogy was calculated by point-counting from scanned images of thin-sections. BSE images, elemental mapping and major element mineral analyses were obtained using a Jeol JXA8100 Superprobe with an Oxford Instruments Aztec energy dispersive system (EDS) at Birkbeck. EDS analysis was carried out using an accelerating voltage of 15 kV, a current of 10 nA and a beam diameter of 1 µm. EDS analyses were calibrated against standards of natural silicates, oxides and Specpure® metals with the data corrected using a ZAF (atomic number, absorption and fluorescence) correction program.

Cylindrical cores of 25 mm diameter and approximately 25 mm length were drilled from the peridotite xenoliths for CT scanning. The shape and size of the cores were chosen to ensure equal absorption and penetration of the X-ray beam, thus reducing artefacts in the final 3D rendered CT volume. One sample (VI 313-1270) was analysed without being cored; this made little difference to the processed CT results but provided a larger volume for analysis.

Micro-CT scans were collected at the NHM on the Metris X-Tek HMX ST 225 scanner coupled with a 4-megapixel Perkin Elmer XRD 1621 AN3 HS detector panel. The power setting for data collection for a polychromatic X-ray beam (cone beam projection) with a tungsten target (reflection target) and Cu filter (thickness 1.0 mm) was 190 kV and 210 µA. Resolution of the 3D rendered volumes ranged from 13 to 19 µm. The rock cores were mounted inside the X-ray enclosure and housed on a translation stage. The distance of the sample to source was set to ensure maximum magnification without introducing blurred edges. The cores were scanned with 3142 projections and an exposure time of 1000 ms.

CT scans can be affected by various artifacts which can compromise the quality of the 3D rendered volume. Beam hardening is an artefact in which the edges of an image appear more intense compared to its centre (Ramakrishna et al. 2006). To minimise this effect, we tried both Cu and Al attenuation filters with varying thickness before the X-ray beam interacted with the sample, to reduce the low energy X-rays, and found that a Cu filter with a thickness of 1 mm provided the optimum conditions.

The Avizo software suite was used for 3D segmentation and volume rendering. The data sets were analysed, segmented and rendered, and four phases were identified, i.e., air, silicate minerals, garnet and spinel. Initial data sets of garnet peridotite cores yielded data highly susceptible to beam hardening. The result was that, although the spinel was easily segmented, the garnet phase could not be accurately segmented from the other silicate phases. The scan conditions were varied in order to optimise data collection. Different X-ray tube power settings and the sample-to-source distances were tested. Although beam hardening could not be completely removed, the optimum machine conditions are as shown above. The effect of beam hardening poses a problem in segmenting similar material at the edge of the data set compared to its centre, because mean grey values for garnets at the edge appear higher than mean grey values at the centre of the 3D data set. To overcome this, the data set was cropped into a rectangular box and only the central portion was selected. A major disadvantage is that, since the large garnets are often clustered and unevenly distributed, whole garnets were often also cropped, thus reducing our ability to truly image the garnet texture. Two samples from Vitim suffered from this effect and were omitted from the data set.

One of the tools for manual segmentation in the Avizo software suite is the “region-growing” utility (called a “magic wand”) in which different material can be manually selected in the individual slice images based on defined grey value range of voxels for all connected voxels, which can be assigned to that material automatically. Care must be taken that other materials are not selected and assigned incorrectly, since the attenuation coefficients for garnet are close to other silicates for samples from Vitim and Pali-Aike because of the low Cr_2O_3 content (<2 wt %) in the garnets. Garnet and other silicate phases overlap in the 3D slice histogram and use of the region-growing can lead to errors in segmentation.

The “Volume Fraction” tool in Avizo was used to calculate the volume fraction for garnet and spinel in samples from Vitim and Pali Aike. The volume fraction tool works by comparing the number of voxels of a selected material with the total number of voxels of the sample. Volume fractions are listed in Table 4.1. The aspect ratio (AR) of garnets and garnet-spinel clusters were obtained from the raw 3D volume data by using ImageJ software to measure the longest and shortest axes. For comparison, the same methodology was applied to garnets in cratonic garnet peridotite xenoliths and to spinel-pyroxene clusters in xenoliths from Massif Central and Lanzarote (Bhanot et al., 2017). Videos and images of 3D volumes are available in the Supplementary data.

4.4 Results

4.4.1 Textural and modal analyses in thin-section

The Kaapvaal samples were provided by Hilary Downes, Birkbeck, University of London. Polished thin-section were prepared at the Natural History Museum, London. Samples from Vitim were provided by Dimitri Ionov, University of Montpellier, France and Theo Ntaflos, Department of Lithospheric Research, University of Vienna. Polished thin-sections were prepared at Birkbeck, University of London. Pali-Aike samples were provided by the Natural History Museum, London, from the collection donated by Pamela Kempton. Polished thin-section were prepared at Birkbeck, University of London. The modal mineralogy for all samples from both localities were calculated by point-counting from optically scanned images of thin-section slides.

The modal mineralogy of the mantle xenoliths in thin-section (Table 4.1) shows that the samples from Vitim and Pali-Aike include both garnet-spinel peridotites and garnet peridotites, but no pure spinel peridotites. All the xenoliths are coarse-grained and protogranular following the classification of Mercier and Nicolas (1975). Mineralogy consists of olivine (forsterite), orthopyroxene (enstatite), clinopyroxene (diopside), ± spinel and garnet (pyrope). Garnet-spinel peridotites from Pali-Aike are largely harzburgites whilst those from Vitim are mostly lherzolites (Table 4.1). Garnet peridotites from Pali-Aike are also mostly harzburgites whereas those from Vitim are largely garnet lherzolites with one harzburgite. This suggests that samples from Pali Aike have experienced more depletion than those from Vitim. Figure 4.1 shows images of thin-sections of a garnet lherzolite from Vitim, Kaapvaal and a garnet-spinel lherzolite from Pali-Aike. The samples from Vitim showed a surprising lack of spinel (Table 4.1).

BSE images of garnet-spinel peridotites and garnet peridotites from Vitim and Pali-Aike show coarse-grained anhedral garnets which vary in size (Fig. 4.2). They have irregular but generally circular grain shapes and often contain olivine inclusions. Garnets are often not randomly distributed but appear to be clustered. Spinels in garnet-spinel peridotites are associated with garnets and often occur as inclusions within garnets (Fig. 4.2a), where they form the central core surrounded by garnet. Spinel shapes vary from small blebs to large vermicular grains. The spinel content in thin-sections of samples from Vitim is <1% whilst in those from Pali-Aike spinel content is <3% (Table 4.1). Garnets display no chemical zoning but are commonly mantled with a kelyphite rim (Fig. 4.2b) composed of garnet, cpx and spinel. Spinel and cpx grains in kelyphite rims in Vitim samples can be zoned. The contacts between garnet and spinel

inclusions are also mantled with a kelyphite rim showing a similar texture to the rim surrounding the garnet.

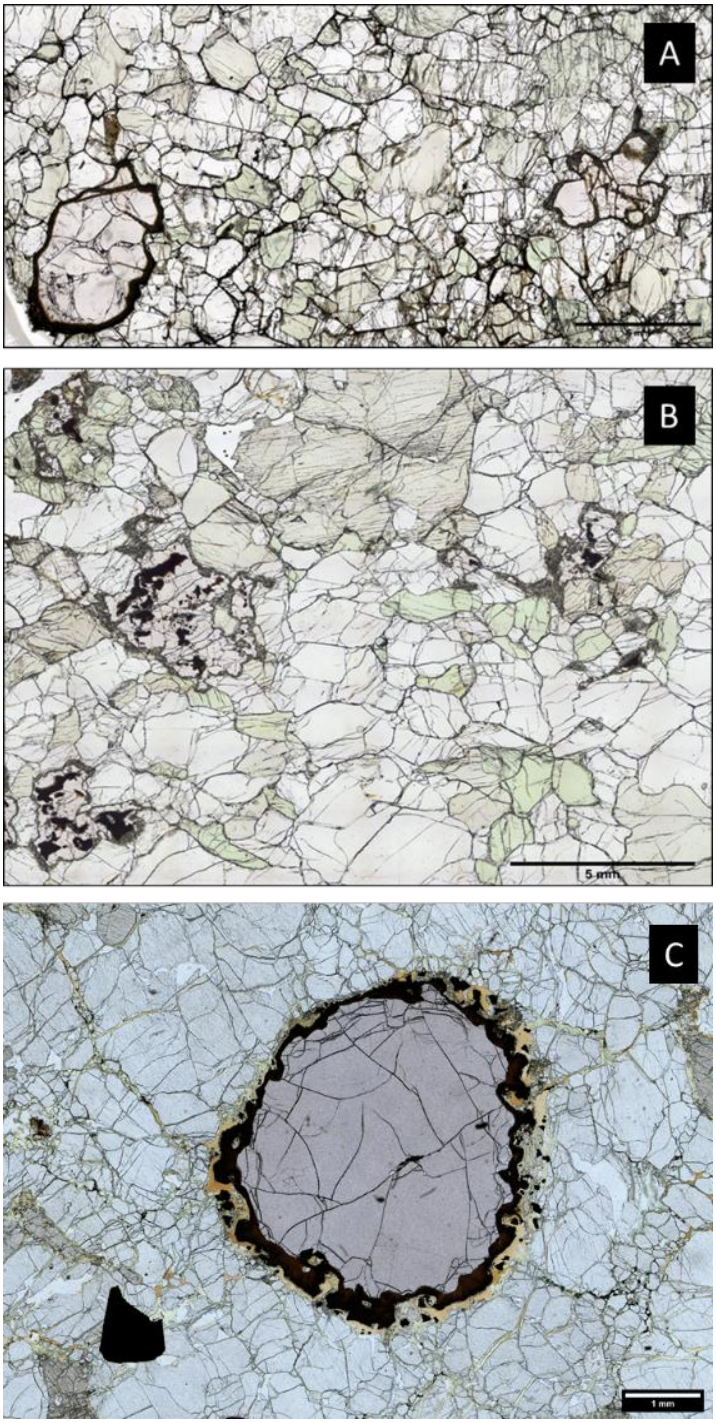

Figure 4.1. (A). Garnet peridotite thin-section PPL image (VI 313 532). Garnet grains are mantled by kelyphite rims. Scalebar is 5 mm. B. Garnet-spinel peridotite thin-section PPL image (PA 16). Garnet-spinel clusters display complex vermicular structures and are mantled by a kelyphite rim. Scalebar is 5 mm. (C) Representative example of a garnet in a Garnet peridotite (Kaapvaal, craton) thin-section PPL image (TE201). Garnet display complex mantled by a kelyphite rim. Scalebar is 1 mm.

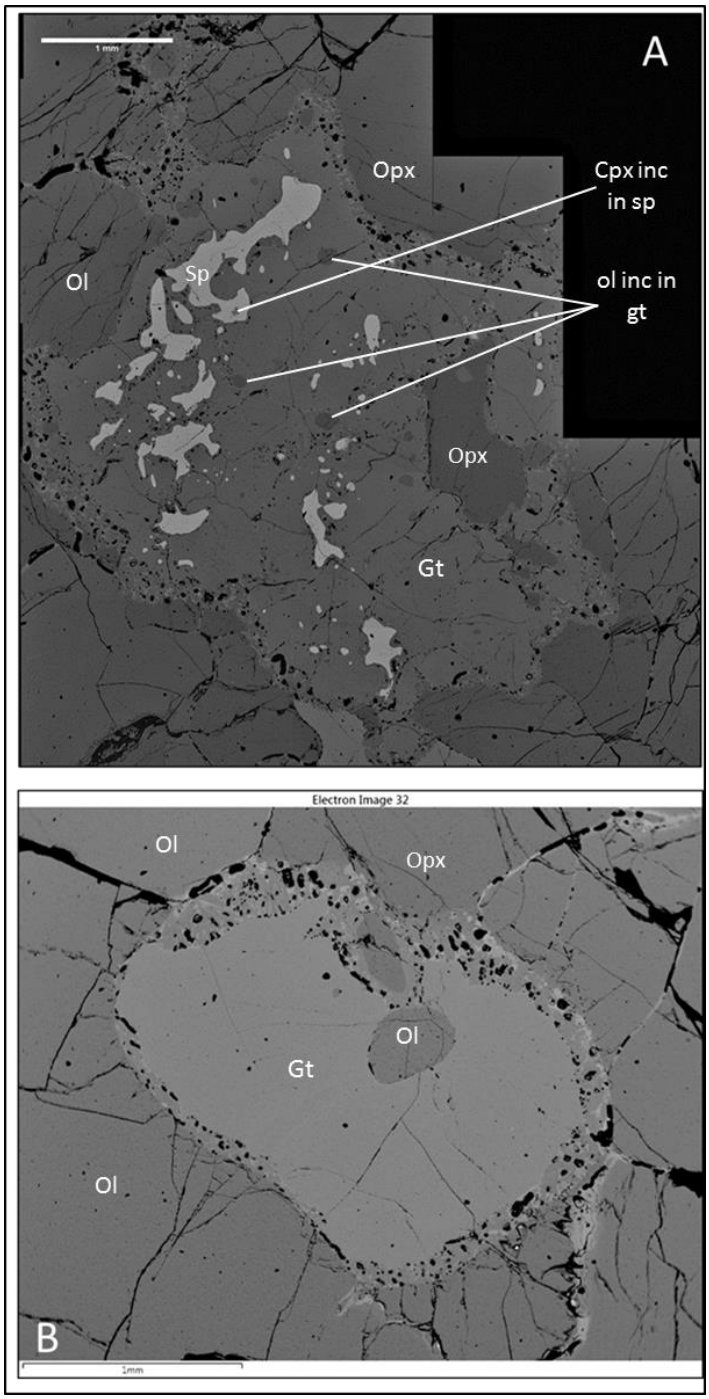

Figure 4.2. (A) BSE image of garnet-spinel cluster and kelyphite rim (PA 16). (B) BSE image of garnet with olivine inclusion and kelyphite rim in a garnet peridotite (PA 18). Scale bar 1 mm.

Table 4.1. Modal mineralogy and nomenclature of garnet peridotites and garnet-spinel peridotites from Pali-Aike and Vitim. [1] Classification of garnet lherzolite based on point counting on a thin-section. Analysis of 3D volume shows presence of spinel. [2] Classification of garnet lherzolite based on point counting on a thin-section. Analysis of 3D volume shows presence of garnet-spinel clusters and reveals sample to be a garnet-spinel lherzolite. [3] Average modal composition of a low temperature garnet lherzolite (Boyd and Mertzman, 1987).

Sample	Ol%	Opx%	Cpx%	Gt%	Sp%	Textural type
Pali-Aike						
BM 2004 PA 10	69.2	23.1	1.5	3.5	2.7	Protogranular garnet-spinel harzburgite
BM 2004 PA 13	71.2	16.6	1.0	10.7	0.5	Protogranular garnet-spinel harzburgite
BM 2004 PA 16	58.2	21.2	11.2	5.8	3.6	Protogranular garnet-spinel lherzolite
BM 2004 PA 18	58.9	34	1.1	6	-	Protogranular garnet harzburgite
Vitim						
VI 20	54.1	15.4	3.0	26.7	0.8	Protogranular garnet-spinel harzburgite
VI 313 116	66.6	19.7	9.3	4.3	0.1	Protogranular garnet-spinel lherzolite
VI 313 148[1]	59.5	13.2	6.8	20.5	-	Protogranular garnet lherzolite
VI 313 532[2]	58.1	18.6	17.0	6.3	-	Protogranular garnet lherzolite
VI 313 1270	67.5	10.8	15.7	6.0	-	Protogranular garnet lherzolite
VI 313 1278	52.4	23.6	9.0	14.2	0.8	Protogranular garnet-spinel lherzolite
Kaapvaal						
Gt peridotite [3]	62	31	2	5	-	Protogranular garnet lherzolite
DB1	60.9	26.1	-	13.0	-	Protogranular garnet harzburgite

4.5.2 Garnet-spinel peridotites

Garnets in garnet-spinel clusters from Vitim vary in size from <5 mm weakly elliptical to highly elliptical vermicular structures. In samples from Pali-Aike the garnet-spinel clusters are also highly elliptical, >4 mm in length and <3 mm in width and display a vermicular texture. In thin-section, spinels vary from blebs with a mild vermicular texture inside the garnets to complex vermicular structures. Volume of spinel can vary from small individual blebs to larger complex structures forming a larger percentage of the garnet-spinel complex (sample PA 10).

4.5.3 Garnet peridotites

Garnets from Kaapvaal peridotites (DB1 and TE201) vary from ~4 mm to < 2mm and are generally rounded (Fig.4.1). Garnet content in thin-sections of garnet peridotites ranges from 4 to 26% in xenoliths from Vitim and from 3 to 6% in Pali-Aike samples. Garnets in Vitim samples (Fig. 4.1) vary from ~2 mm rounded grains to highly elliptical vermicular grains >4 mm in length (e.g., VI 313 1278). Garnets from Pali-Aike are largely equant and approximately 2 mm in diameter (e.g., PA 18). Garnets from both locations often contain small, rounded inclusions of olivine (Fig. 4.2b).

4.5.4 Mineral chemistry

Microprobe analyses of samples from Pali-Aike and Vitim in this study (Table 4.2) are similar to previous studies from the two regions (Skewes and Stern, 1979; Stern et al., 1999; Ionov et al., 1993). Both garnet-spinel peridotites and garnet peridotites have a similar mineral composition. Mg#s (Mg# = Mg/(Mg + Fe) x 100) for olivine, orthopyroxene and clinopyroxene from the two localities are similar in the range of 88-90. Spinel Cr#s (Cr# = Cr/(Cr+Al) x 100) are higher in Pali-Aike samples (21-32) than in Vitim (19-20). Al_2O_3 contents in spinel are 36-47 wt%, Cr_2O_3 is 17-27 wt%, MgO is 16-20 wt% and FeO is 12-18 wt%. Orthopyroxenes from both localities are enstatites with 3.5-4.4 wt% Al_2O_3. Clinopyroxenes are diopside containing 17-19 wt% CaO, 5-11 wt% Al_2O_3 and <1.5 wt% Cr_2O_3. Garnets are pyrope with Mg#s 81-85. Their Al_2O_3 content is 23 wt%, Cr_2O_3 is 1.1 wt%, MgO is 20 wt%, CaO is 5 wt% and FeO is 8 wt%. Garnets in several samples from both localities contain olivine inclusions with Mg#s of 89-90, identical to olivines outside garnets. Garnet harzburgite (DB1) from the Kaapvaal craton the olivine Mg# is 94. Orthopyroxene is enstatite and Mg# for orthopyroxene is 95 with 0.7 wt% Al_2O_3. Garnets are pyrope with Mg# 89. Their Al_2O_3 content is 21.5 wt%, Cr_2O_3 is 4.0 wt%, MgO is 23.1 wt%, CaO is 3.7 wt% and FeO is 5.3 wt%.

Arai (1994) outlined how the values of Mg# in olivine and Cr# in spinel can constrain the origin of spinel peridotites. Spinel lherzolites and spinel harzburgites have limited ranges of $Mg\#_{olivine}$ and

$Cr\#_{spinel}$ values, forming the olivine - spinel mantle array (OSMA). Since we have no xenoliths which are purely spinel-bearing, we have used EMPA analysis of spinel peridotites from Vitim (Ionov et al., 1995) and Pali Aike (Skewes and Stern, 1979; Wang et al., 2008) (Fig 4.3a). Comparing our data to previous results for spinel peridotites from the same locations, Vitim samples have higher spinel Cr#s than in spinel peridotites, but Pali Aike samples show the opposite. Olivine Mg#s for Vitim and Pali Aike are 90 and 89, respectively. All analysed spinel Cr#s from Vitim and Pali Aike are much lower than those of cratonic spinel peridotite xenoliths (Fig. 4.3a).

Garnet compositions from Vitim and Pali Aike (PA) have Cr#s of 3.4-3.5 which are much lower than those of garnet and garnet-spinel peridotites from Udachnaya (Ionov et al., 2010), Lashaine (Reid et al., 1975; Gibson et al., 2013) and Kaapvaal (Carswell et al. (1979); Grégoire et al. (2003); Simon et al. (2003)) which vary from 11 to 33 (Fig 4.3b). Mg#s of Vitim garnets are higher than those of Pali Aike at 82-84 and 81, respectively.

Kelyphite rims around garnets have an average thickness of 100 µm, which is uniform in samples from both Vitim and Pali Aike. Kelyphite rims display a sharp contact with garnet cores. BSE images of reaction rims arounds garnets in this study show that the kelyphite symplectite microstructures, often associated with coronae mantling garnet peridotite (Godard and Martin, 2000), are largely absent in Pali Aike and Vitim samples. However, one sample does show a partial portion displaying a fibrous symplectite texture. Kelyphite rims from Pali Aike and Vitim are composed of cpx and spinel and a secondary garnet which is more Mg-rich (Mg# 85) but with lower Al_2O_3 and CaO than the garnet cores. A third garnet exists in small regions in sharp in contact with the garnet core (PA 16). This garnet is more Ca-rich with 14 wt% CaO. Both Mg# (60) and Cr# (0.8) are considerably lower than the garnet core. Spinel and cpx in the kelyphite rims can be zoned (e.g., VI 313-1278). The contact between garnet and spinel inclusions are also mantled with a kelyphite rim displaying a similar texture to the rim surrounding garnet. The presence zoning in grains in the kelyphite rim and the absence of the kelyphite texture from the cores implies that the kelyphite rim is a secondary texture and is thus independent of the sub-solidus reaction shown in Equ 4.1. In fact, it is the reverse reaction (gt_1+ol goes to sp+pyx+gt_2) and is related to exhumation.

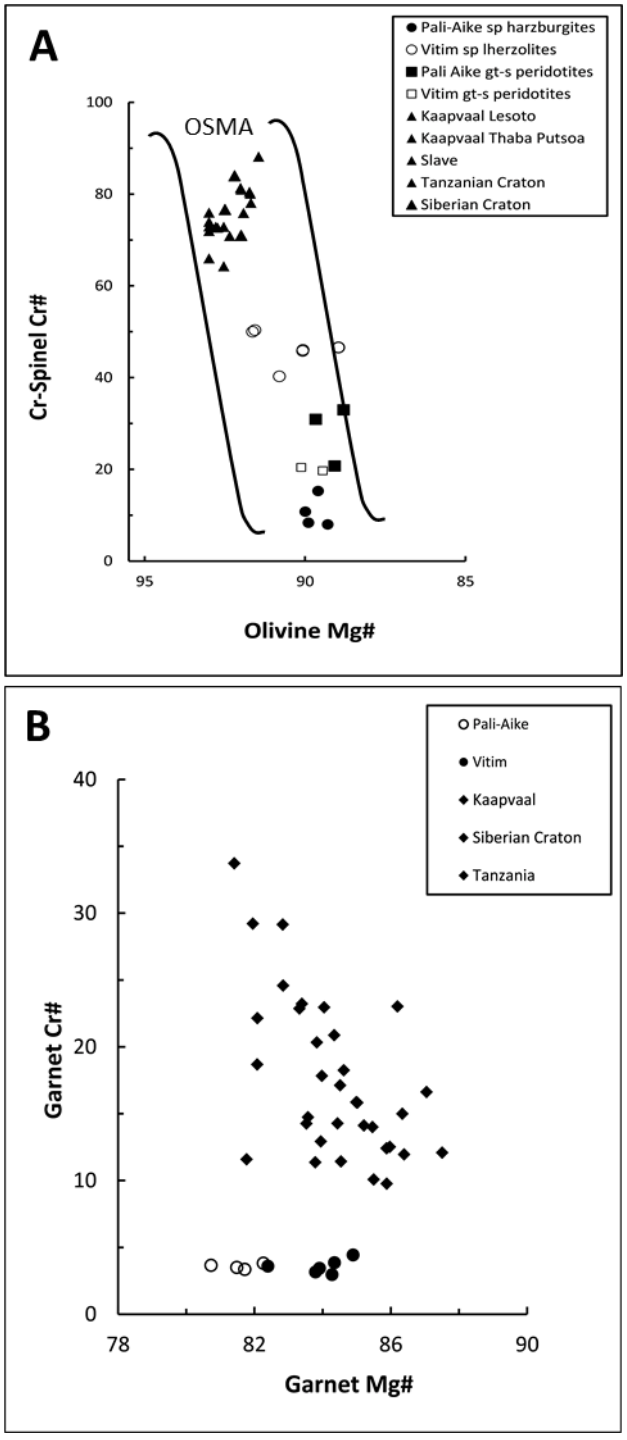

Figure 4.3. (A) OSMA diagram for spinel peridotites and garnet-spinel peridotites from Vitim, Pali-Aike and cratonic peridotites. Data taken from this study and Ionov et al. (2005); Ionov et al. (2010); Gibson et al. (2013) and Simon et al. (2003). Cratonic peridotites are shown as solid diamonds, Pali Aike spinel harzburgites as solid circles, Vitim spinel lherzolites as open circles, Pali Aike garnet-spinel peridotites as solid squares and Vitim garnet-spinel peridotites as open squares. (B) Cr# vs mg# in garnets in Vitim (open circles) and Pali Aike (solid circles) xenoliths compared with cratonic peridotites (solid diamonds). Cratonic peridotite data taken from Carswell et al. (1979); Grégoire et al. (2003); Ionov et al. (2010); Gibson et al. (2013); Reid et al. (1975) and Simon et al. (2003).

Table 4.2. Representative EMPA (WDS) analysis of garnet peridotite from Pali-Aike and Vitim (wt% oxide).

Sample	locality	Mineral	SiO_2	FeO	MnO	NiO	MgO	Total	Mg#	no.
PA18	PA	ol	41.10	10.85	0.13	0.42	47.82	100.32	88.71	6.00
VI48	VIT	ol	40.59	9.70	0.13	0.36	48.45	99.22	89.90	4.00
VI48	VIT	ol (inc)	41.23	10.05	0.12	0.39	48.86	100.64	89.75	2.00

Sample	locality	Mineral	SiO_2	TiO_2	Al_2O_3	Cr_2O_3	FeO	MnO	MgO	CaO	Na_2O	Total	Mg#	Cr#
PA18	PA	gt	41.73	0.28	23.34	1.27	8.22	0.32	20.29	5.09	0.03	100.58	81.48	3.51
VI48	VIT	gt	42.18	0.19	23.58	1.08	6.87	0.29	20.62	4.99	0.02	99.84	84.24	2.99

Sample	locality	Mineral	Al	An	Gr	Pyr	Spe	Uva	Si	Ti	Al	Cr	Fe^{2+}	Mn	Mg	Ca	Total	no.
PA18	PA	gt	13.79	0.61	8.85	72.48	0.66	3.61	2.95	0.02	1.95	0.07	0.47	0.02	2.14	0.39	8.0	3
VI48	VIT	gt	13.87	0.00	9.65	72.87	0.57	3.04	2.98	0.01	1.96	0.06	0.42	0.02	2.17	0.38	8.0	5

Sample	locality	Mineral	SiO_2	FeO	MnO	NiO	MgO	Total	Mg#	no.
PA18	PA	ol	41.10	10.85	0.13	0.42	47.82	100.32	88.71	6.00
VI48	VIT	ol	40.59	9.70	0.13	0.36	48.45	99.22	89.90	4.00
VI48	VIT	ol (inc)	41.23	10.05	0.12	0.39	48.86	100.64	89.75	2.00

Sample	locality	Mineral	SiO_2	TiO_2	Al_2O_3	Cr_2O_3	FeO	MnO	MgO	CaO	Na_2O	Total	Mg#
PA18	PA	opx	55.26	0.26	3.56	0.50	6.87	0.13	32.02	0.79	0.10	99.62	89.25
VI48	VIT	opx	53.90	0.15	5.18	0.56	5.97	0.13	31.44	1.15	0.18	98.76	90.37

Sample	locality	Mineral	Wo	En	Fs	Si	Ti	Al	Cr	Fe^{2+}	Mn	Mg	Ca	Na	Total	no.
PA18	PA	opx	1.56	87.66	10.78	1.93	0.01	0.15	0.01	0.20	0.00	1.67	0.03	0.01	4.0	9
VI48	VIT	opx	2.32	88.09	9.59	1.89	0.00	0.21	0.02	0.17	0.00	1.64	0.04	0.01	4.0	3

Table 4.3. Representative EMPA (WDS) analysis of garnet-spinel peridotite from Pali-Aike (PA) and representative EMPA (EDS) analysis of garnet-spinel peridotite from Vitim (VIT) (wt% oxide).

Sample	locality	Mineral	SiO_2	FeO	MnO	NiO	MgO	Total	Mg#	No.
PA16	PA	ol	40.70	10.03		0.44	48.85	100.02	89.67	4
PA16	PA	ol (inc)	40.60	9.71		0.46	48.84	99.61	89.97	3
VI1278	VIT	ol	40.23	10.25	0.58	0.09	48.91	99.95	89.48	6

Sample	locality	Mineral	SiO_2	TiO_2	Al_2O_3	Cr_2O_3	FeO	MnO	MgO	CaO	Na_2O	Total	Mg#	Cr#
PA16	PA	gt	41.92	0.20	22.83	1.35	7.89	0.43	20.53	4.95	0.07	100.13	82.26	3.82
VI1278	VIT	gt	42.00	0.33	22.26	1.34	7.32	0.29	21.63	4.93	0.03	100.11	84.05	3.87

Sample	locality	Mineral	Alm	And	Gro	Pyr	Spe	Uva	Si	Ti	Al	Cr	Fe^{2+}	Mn	Mg	Ca	Total	no.
PA16	PA	gt	13.47	1.29	7.54	73.00	0.87	3.82	2.97	0.01	1.91	0.08	0.44	0.03	2.17	0.38	7.98	5
VI1278	VIT	gt	10.10	3.59	5.19	76.75	0.58	3.78	2.97	0.02	1.85	0.07	0.07	0.36	0.02	2.28	8.01	10

Sample	locality	Mineral	SiO_2	TiO_2	Al_2O_3	Cr_2O_3	FeO	MnO	MgO	CaO	Na_2O	Total	Mg#
PA16	PA	opx	55.03	0.11	3.33	0.57	6.30	0.19	33.39	0.65	0.14	99.70	90.43
VI1278	VIT	opx	53.71	0.31	5.22	0.61	6.46	0.25	31.91	1.26	0.17	99.86	89.80

Sample	locality	Mineral	Wo	En	Fs	Si	Ti	Al	Cr	Fe^{2+}	Mn	Mg	Ca	Na	Total	no.
PA16	PA	opx	1.25	89.07	9.68	1.90	0.00	0.14	0.02	0.18	0.01	1.72	0.02	0.01	4.0	6
VI1278	VIT	opx	2.47	87.26	10.27	1.86	0.01	0.21	0.02	0.19	0.01	1.65	0.05	0.0	4.0	6

Sample	locality	Mineral	SiO_2	TiO_2	Al_2O_3	Cr_2O_3	FeO	MnO	MgO	CaO	Na_2O	Total	Mg#
PA16	PA	cpx	52.44	0.41	5.22	1.15	3.10	0.23	15.33	19.49	1.52	98.89	89.82
VI1278	VIT	cpx	51.01	0.90	6.88	1.19	3.96	0.30	16.87	17.39	1.50	99.79	88.37

Sample	locality	Mineral	Wo	En	Fs	Si	Ti	Al	Cr	Fe^{2+}	Mn	Mg	Ca	Na	Total	no.
PA16	PA	cpx	44.86	49.08	6.06	1.96	0.15	0.02	0.03	0.10	0.01	0.85	0.78	0.11	4.0	4
VI1278	VIT	cpx	39.36	53.14	7.50	1.84	0.02	0.29	0.03	0.12	0.01	0.91	0.67	0.10	4.0	3

Sample	locality	Mineral	Al_2O_3	Cr_2O_3	Fe_2O_3	FeO	MnO	MgO	Total	Mg#	Cr#
PA16	PA	sp	39.79	26.54	3.70	11.65	0.27	17.45	99.84	70.01	30.91
VI1278	VIT	sp	47.15	17.23	6.03	8.53	0.33	20.29	100.08	76.29	19.69

Sample	locality	Mineral	Al	Cr	Fe^{3+}	Fe^{2+}	Mn	Mg	Total	no.
PA16	PA	sp	1.32	0.59	0.08	0.27	0.01	0.73	3.00	4
VI1278	VIT	sp	1.49	0.37	0.12	0.19	0.01	0.81	3.00	3

4.5.5 Micro CT results

Modal abundances for garnet and spinel calculated from the 3D volume fraction and measured in thin-section by point counting show significant differences (Table 4.1). Garnet modal values from Vitim are generally higher in the micro-CT volume, but the reverse is true for samples from Pali Aike. In most cases, the spinel modal abundance is much lower in the 3D volume than in thin-section. However, in the cores of two of the Vitim xenoliths, very little garnet was found despite it being present in the thin-sections. This suggests that neither method accurately represents the actual modal abundances of these very coarse-grained rocks, but since the volume being analysed by CT-scanning is much greater than the area represented by a thin-section, the CT scans probably yield a more accurate result.

4.5.6 Pali-Aike

In the Pali-Aike xenoliths, spinel is generally found in clusters with garnet, with a few exceptions in which spinels are found as individual isolated crystals. Micro-CT scans of garnet-spinel clusters reveal a range of textures including (a) randomly orientated large elliptical (>2 mm) garnet grains, (b) large elliptical (>2 mm) garnet grains encasing small individual spinel blebs, (c) large (<4 mm) garnet grains encasing large complex spinel structures, (d) complex and highly elongate garnet-spinel clusters displaying a strong lineation. Distribution of garnets through the cores is often random but the garnets also occur as clusters with large volumes of the sample devoid of garnet. The individual spinel blebs form a small volume of the garnet-spinel cluster whereas the complex, highly vermicular spinel structures form a much higher volume of the garnet-spinel cluster.

The different samples from Pali-Aike show slightly different features. In PA 10, a garnet-spinel harzburgite (Fig. 4.4A and B), the individual garnet-spinel structures vary from <10 mm in length and <2 mm in width to small garnet-spinel clusters <2 mm in the longest dimension. Their average aspect ratio (AR) is 2.3. Spinel forms much of the volume of these structures, whilst several spinel crystals have no associated garnet. Individual garnet-spinel structures often show a strong lineation (Fig. 4.4).

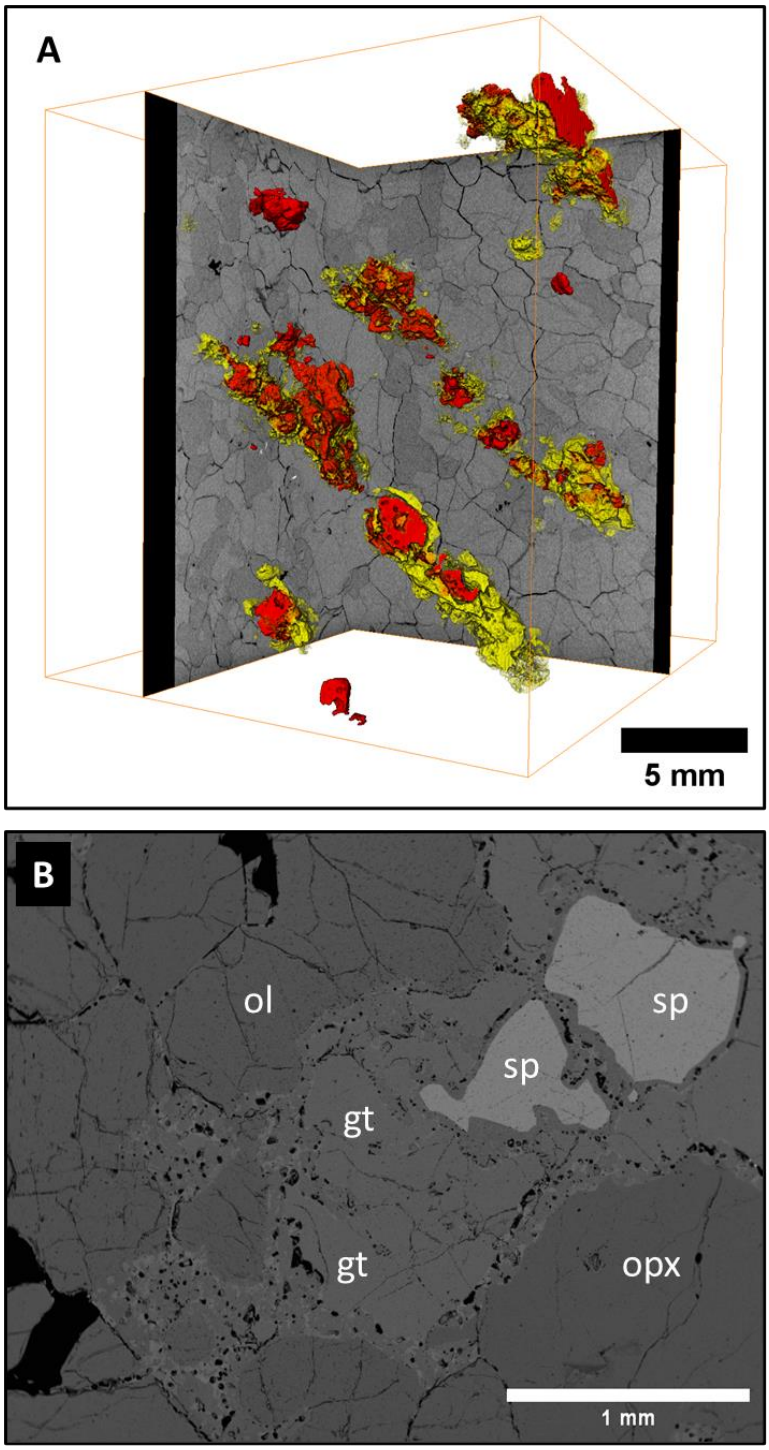

Figure 4.4. 3D rendered image of garnet-spinel cluster in sample PA 10. Garnet coloured yellow; spinel shown as red. Scalebar is 10 mm. (B) BSE image of garnet-spinel cluster in sample PA 10. Scalebar is 1 mm.

Garnet-spinel harzburgite **s**ample PA 16 (Fig. 4.5A-C) shows examples of the individual large complex garnet-spinel clusters displaying the ellipsoidal garnet shapes and vermicular spinel texture within the cluster. The garnet-spinel clusters are individual ellipsoidal structures which measure <4 mm (Fig. 4.5A-F) in length and <2 mm in width, with a mean AR of 1.9. Garnet displays a vermicular texture, and all spinel is associated with garnet. Spinel forms much of the volume of these

structures. Spinel also forms complex and highly vermicular features enclosed within the garnet. The large complex spinel structure shows individual spinel branches which are in contact with adjacent branches, thus forming a single crystal of spinel.

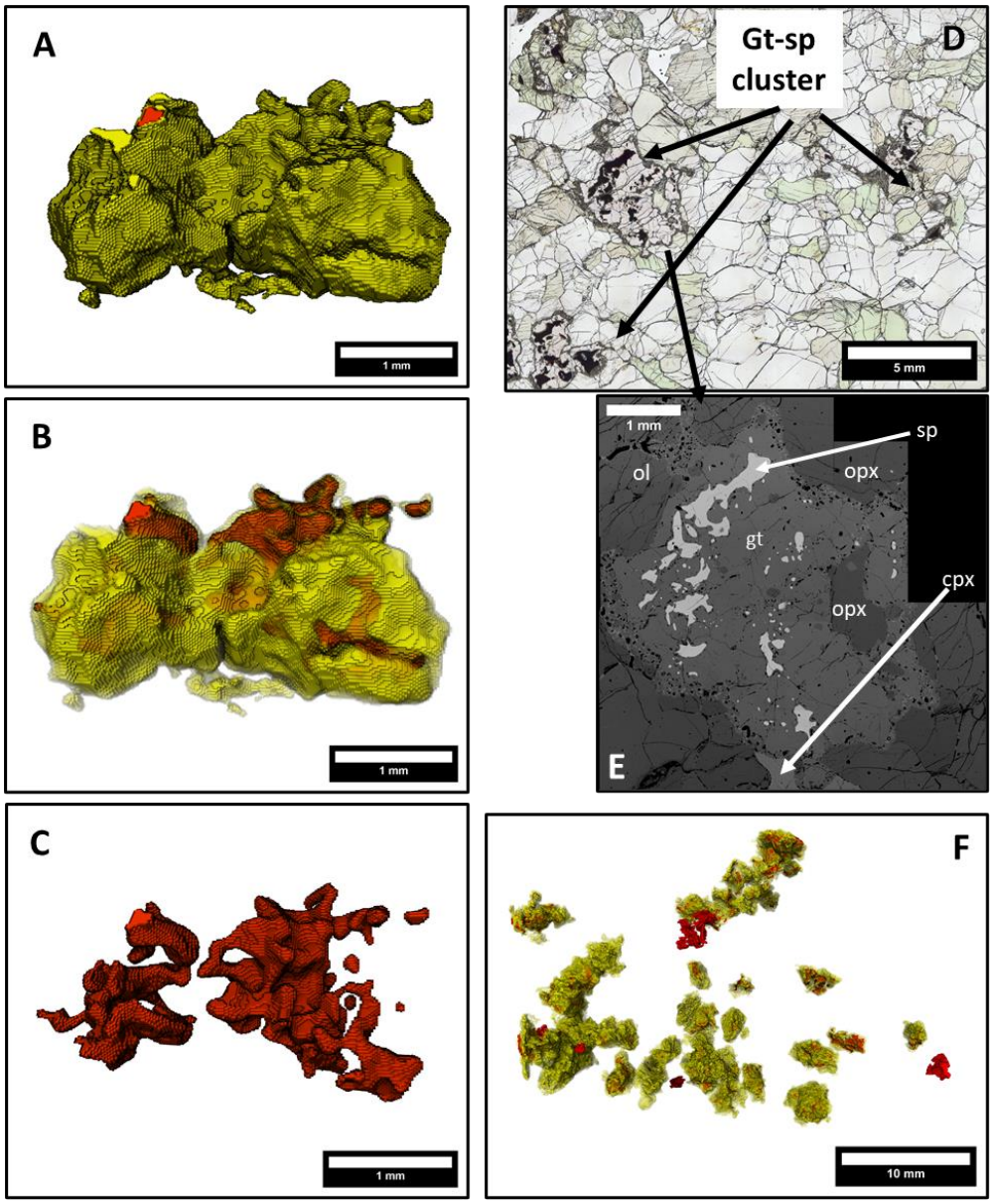

Figure 4.5. (A-C) Series of 3D rendered images of garnet-spinel cluster from Pali-Aike (PA 16) with increasing garnet transparency. Garnet coloured yellow; spinel shown as red. Scale bar is 1 mm. (D) Photomicrograph under PPL of protogranular garnet peridotite xenolith Pali-Aike (PA 16) highlighting several gt-sp clusters. Scalebar is 5 mm. (E) BSE image of a garnet-sp cluster in Pali-Aike (PA 16). Scalebar is 1 mm.(F) 3D rendered image of gt-sp cluster in protogranular garnet peridotite xenolith Pali-Aike (PA 16). Garnet is yellow and spinel is red. Scalebar is 10 mm.

Sample PA 13 (Fig. 4.6) is a good example where garnet grains are clustered but show no alignment. The 3D rendered volume shows much of the sample is devoid of garnet and spinel. Garnets in PA 13 are large individual grains that measure <4 mm in length and <2 mm in width, with a mean AR of 1.9. Several garnets grains are clustered in the sample core with large volumes free of both spinel and garnet. Spinel forms a low volume compared to garnet and exists as small blebs <1 mm. All spinel is associated with garnet.

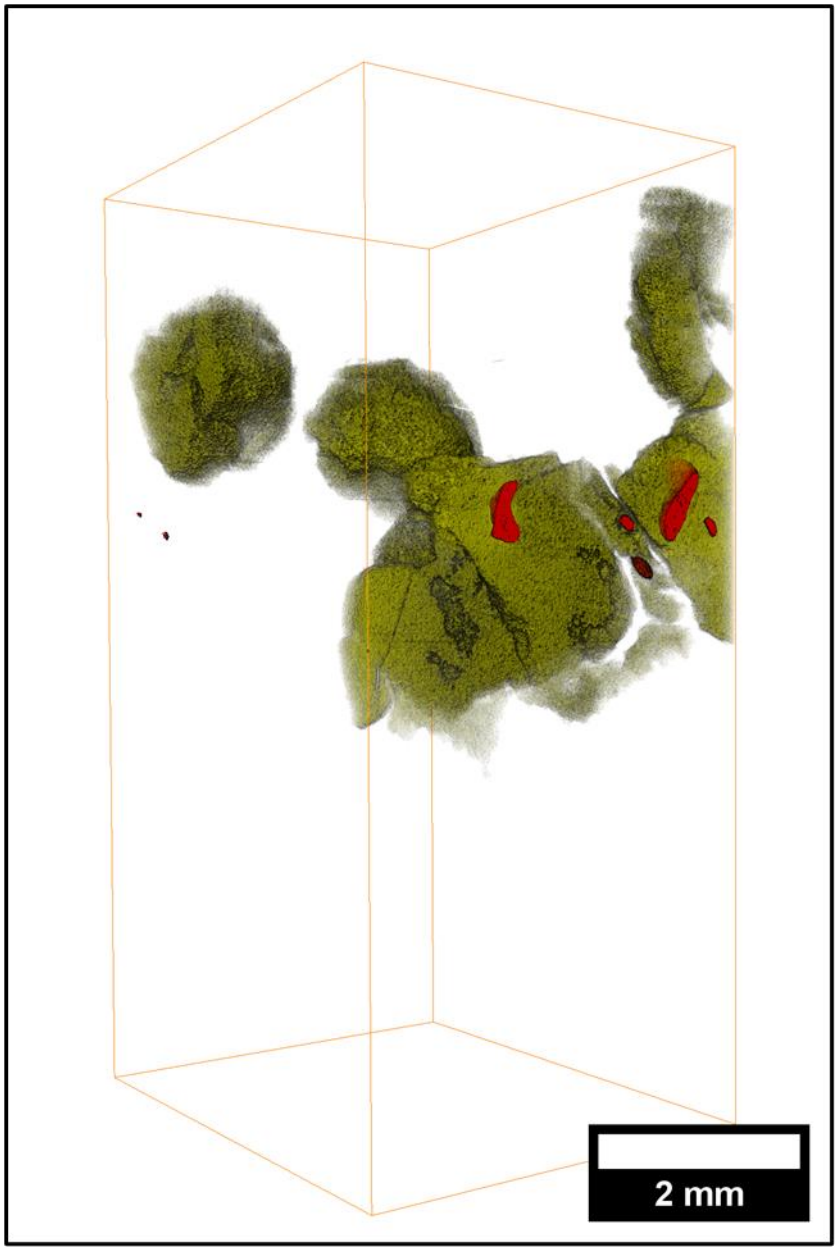

Figure 4.6. 3D rendered image of garnet-spinel cluster from Pail-Aike (PA 13). Garnet coloured yellow and set to semi-transparent; sp shown as red. Silicate phase removed. Sp forms small blebs with a less complex texture compared with sample PA16 (Fig. 4.5). Scalebar is 2 mm.

Garnets in garnet harzburgite sample PA 18 (Fig. 4.7) are large individual grains that measure between <4 mm in length and <2 mm in width to <2 mm in diameter and are more spherical in

shape (mean AR = 1.4). Garnets are randomly distributed throughout the core but regions with a higher density of garnet are visible where individual garnet grains are clustered. Spinel forms a very low volume compared to garnet and exists as small blebs <1 mm only in several grains, with most of the garnet being spinel-free. Spinel is not limited to garnet-spinel clusters, but several small blebs are visible in the core in garnet-free regions.

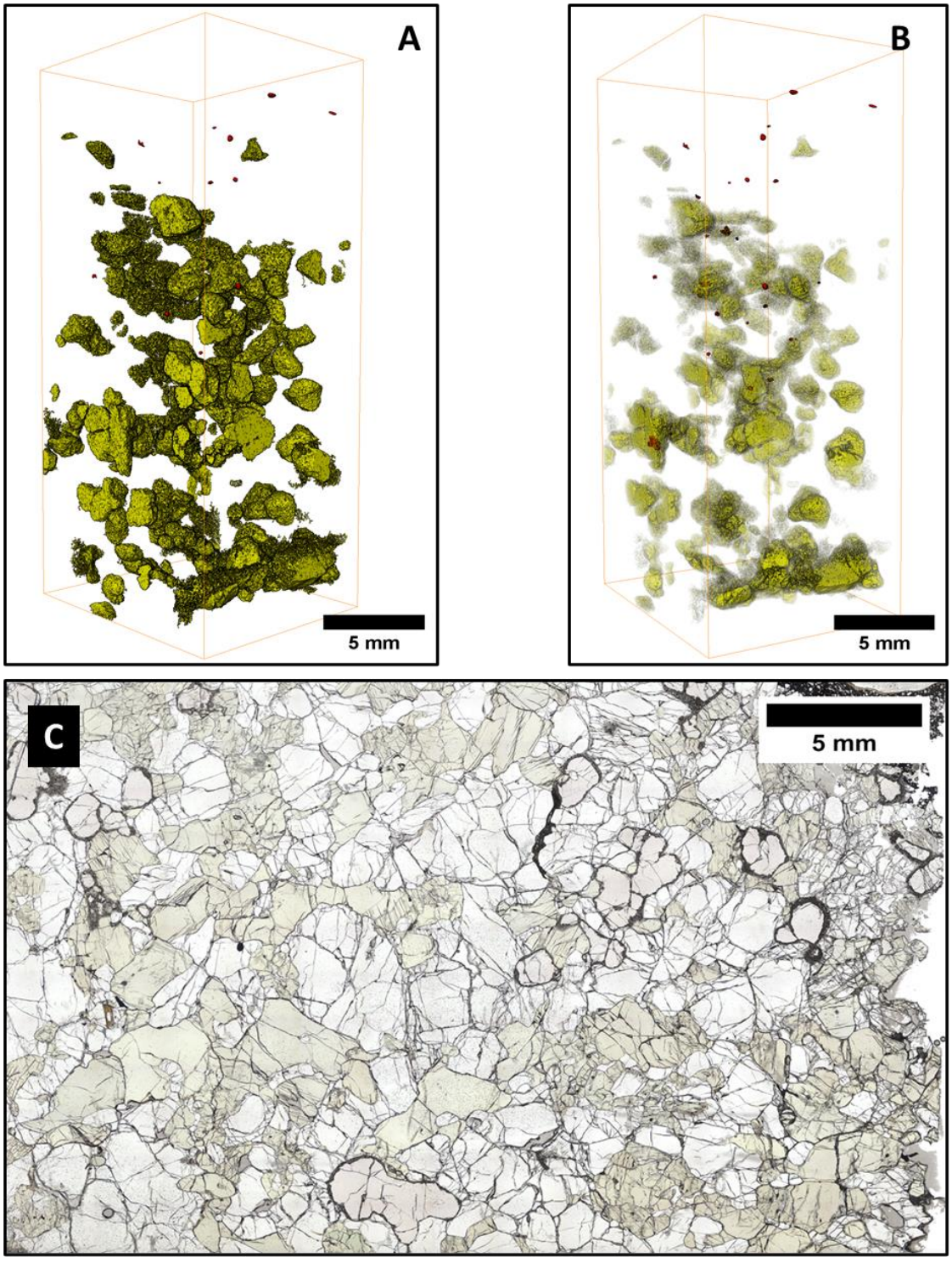

Figure 4.7. (A) 3D rendered image of garnet grains and garnet-spinel clusters in a gt-sp peridotite from Pali-Aike (PA 18). Garnet coloured yellow; spinel shown as red. Silicate phases removed. Scalebar is 5 mm. (B) 3D rendered image of garnet-spinel cluster (PA 18). Garnet coloured yellow is set to semi-transparent; spinel shown as red. Scalebar is 5 mm. (C) Photomicrograph under ppl of gt-sp peridotite from Pali-Aike (PA 18). Scalebar is 5 mm.

Sample PA 31 (Fig. 4.8A-E) is a garnet-spinel peridotite. Garnet grains are randomly distributed throughout the core and vary in shape from complex vermicular grains with no spinel to spherical <4 mm size garnet-spinel structures (mean AR = 2.2). Large ellipsoidal spinel blebs <4 mm in size with a strong vermicular texture are not associated with garnet but are also randomly distributed throughout the core. In PA 31, garnet-free spinel blebs are surrounded by a halo of high atomic number material which is less dense than both the garnet and spinel phases (Fig. 4.8A and D). There is enough density contrast in the halo (Fig 4.8D and E) for it to be resolved from the silicate phase and is interpreted has a secondary product of either metasomatic reactions similar to metasomatic halos in spinel-pyroxene clusters from Lanzarote spinel harzburgite xenoliths (Bhanot et al., 2017) or reactions with melt and formation of kelyphite rims mantling garnet grains.

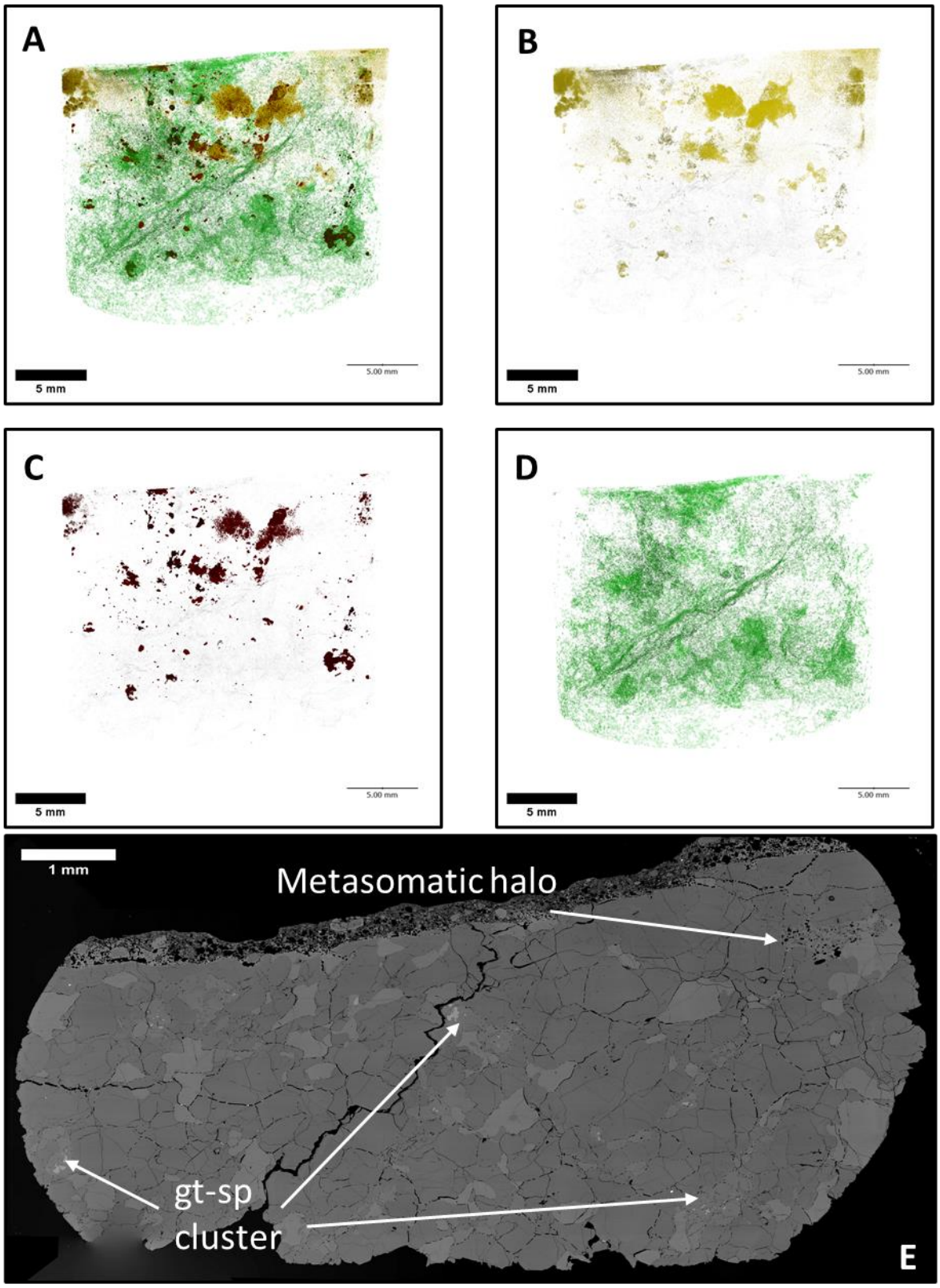
A
5 mm
5.00 mm
B
5 mm
5.00 mm
C
5 mm
5.00 mm
D
5 mm
5.00 mm
1 mm
Metasomatic halo
gt-sp
cluster
E

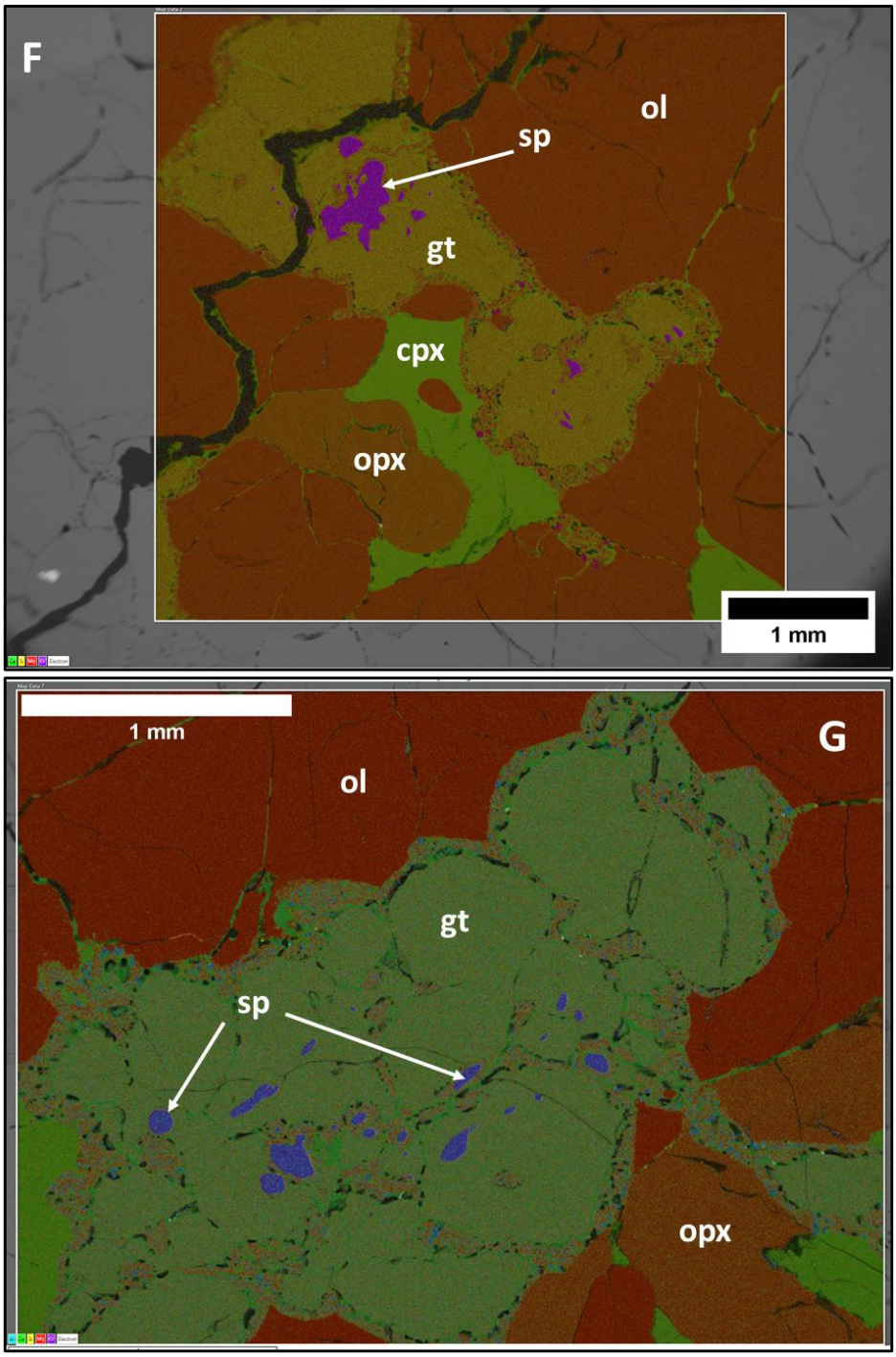

Figure 4.8. (A). 3D rendered image of garnet-spinel peridotite from Pali-Aike (PA 31). Garnet coloured yellow; spinel shown as red and metasomatic halo is green. Scale bar is 5mm mm. (B) 3D rendered image of garnet-spinel peridotite from Pali-Aike (PA 31). Garnet coloured yellow; spinel and metasomatic halo removed. Scale bar is 5mm mm. (C) 3D rendered image of garnet-spinel peridotite from Pali-Aike (PA 31). Spinel coloured red; garnet and metasomatic halo removed. Scale bar is 5 mm. (D) 3D rendered image of garnet-spinel peridotite from Pali-Aike (PA 31). Metasomatic halo coloured green: garnet and spinel halo removed. Scale bar is 5 mm. (D) 3D rendered image of garnet-spinel peridotite from Pali-Aike (PA 31). Metasomatic halo coloured green: garnet and spinel halo removed. Scale bar is 5 mm. (E) BSE image of garnet-spinel peridotite from Pali-Aike (PA 31) showing gt-sp cluster and metasomatic halo. Scale bar is 5 mm. (F) Elemental map of ar-s cluster in garnet-spinel peridotite from Pali-Aike (PA 31). Spinel is purple and gr is light brown. Scale bar is 5 mm. (G) Elemental map of metasomatic halo in garnet-spinel peridotite from Pali-Aike (PA 31). Spinel is purple and gt is green. Scale bar is 5 mm.

4.5.7 Vitim

Micro-CT scans of garnet-spinel clusters in samples from Vitim show large ellipsoidal (>2 mm) garnet grains encasing individual spinel blebs and large (<4 mm) garnet grains enveloping complex spinel structures with a strong vermicular texture. Distribution of garnets through the cores is random but the garnets are often clustered such that large volumes of the core are devoid of garnet, as in the Pali-Aike samples. Also, like samples from Pali-Aike, individual spinel blebs form a small volume of the garnet-spinel cluster whilst the complex, high vermicular spinel structures form a higher volume of the complex. The large complex spinel structures are ellipsoidal and individual spinel branches are in contact with adjacent branches, thus forming a single crystal of spinel.

Garnet lherzolite VI 313 1270 was the only sample that was CT-scanned without being cored and so it provided the largest imaged volume of any studied xenolith. It is also the only sample which did not contain any spinel in the 3D scan (Table 4.1). Fig. 4.9A shows that the garnets are large individual grains that measure between <4 mm in length and <2 mm in width to <2 mm in diameter and are more spherical (mean AR = 1.3). Garnets are randomly distributed throughout the core but regions with a higher density of garnet are visible where individual garnet grains are clustered.

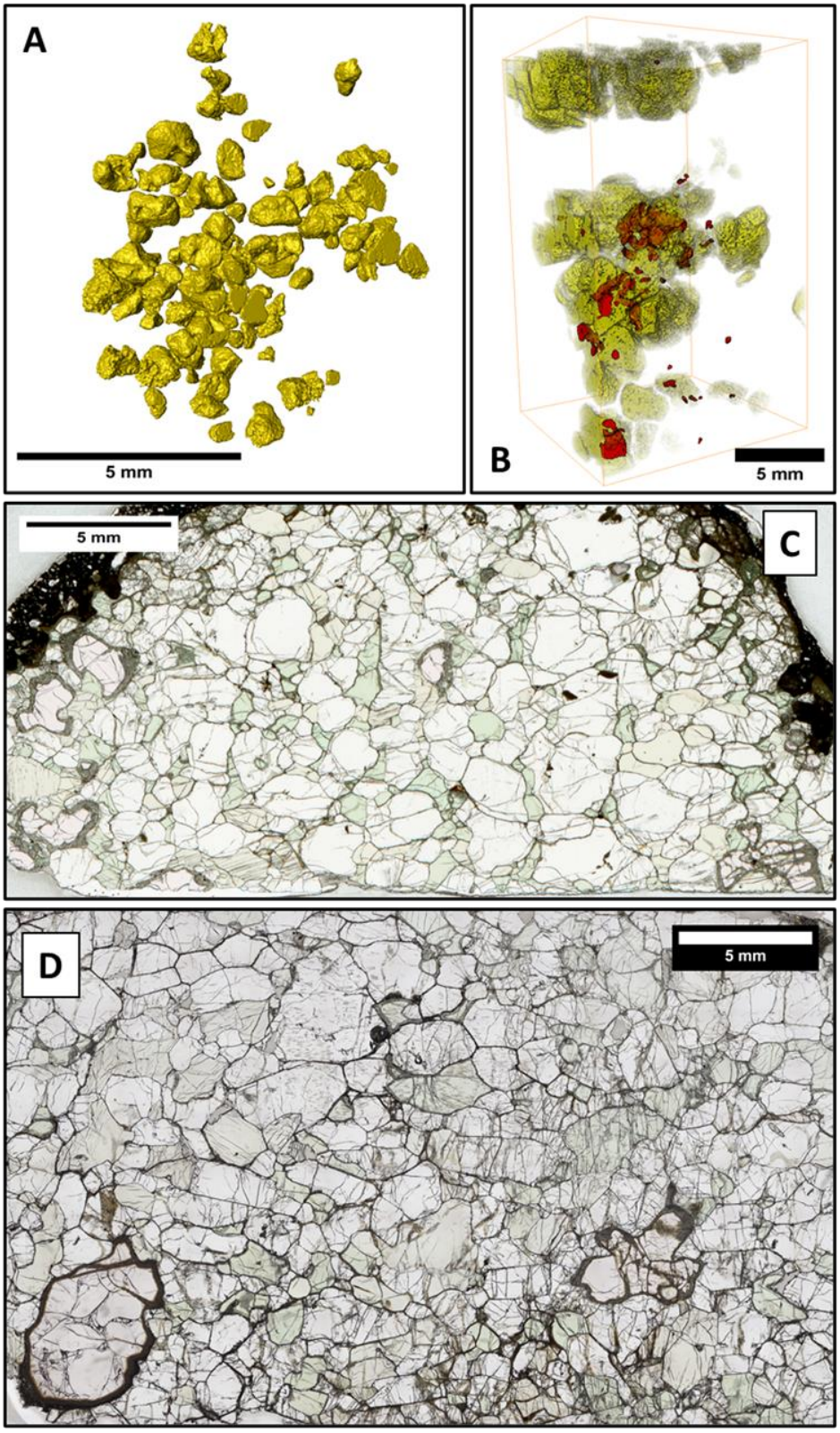

Figure 4.9. (A) 3D rendered image of garnet grains in garnet peridotite VI 313 1270. Garnet coloured yellow. Silicate phase removed. Scale bar is 10 mm. (B) 3D rendered image of garnet-spinel cluster (VI 313 532), garnet coloured yellow and set to semi-transparent. Spinel is red. Scale bar is 5 mm. (C) Photomicrograph under PPL of garnet peridotite VI 313 1270. Scale bar is 5mm. (D) Photomicrograph under PPL of garnet peridotite VI 313 532. Scale bar is 5 mm.

4.5.8 Kaapvaal Craton

Sample DB1 from Kimberley is a typical garnet peridotite xenolith from the cratonic mantle. Garnets in DB1 (Fig. 4.10A-D) are large individual grains are spherical to ellipsoidal in shape. Individual grain is <4.5 mm in length and <3.4 mm in width. Aspect ratios of individual grains ranges from 1.05 to 1.38. Garnets are randomly and evenly distributed throughout the core but there does appear to be some clustering of garnet grains. Spinel is visible in BSE images but is limited to within the kelyphite rim (Fig 4.10D) and the 3D volume, in which spinel is largely limited to garnet grains, however, 2D slice images reveal this phase is closely associated with cracks in garnet grains, but rare fine grains are visible in the sample core not associated with garnet. Elemental maps reveal phase visible in cracks is a sulphide.

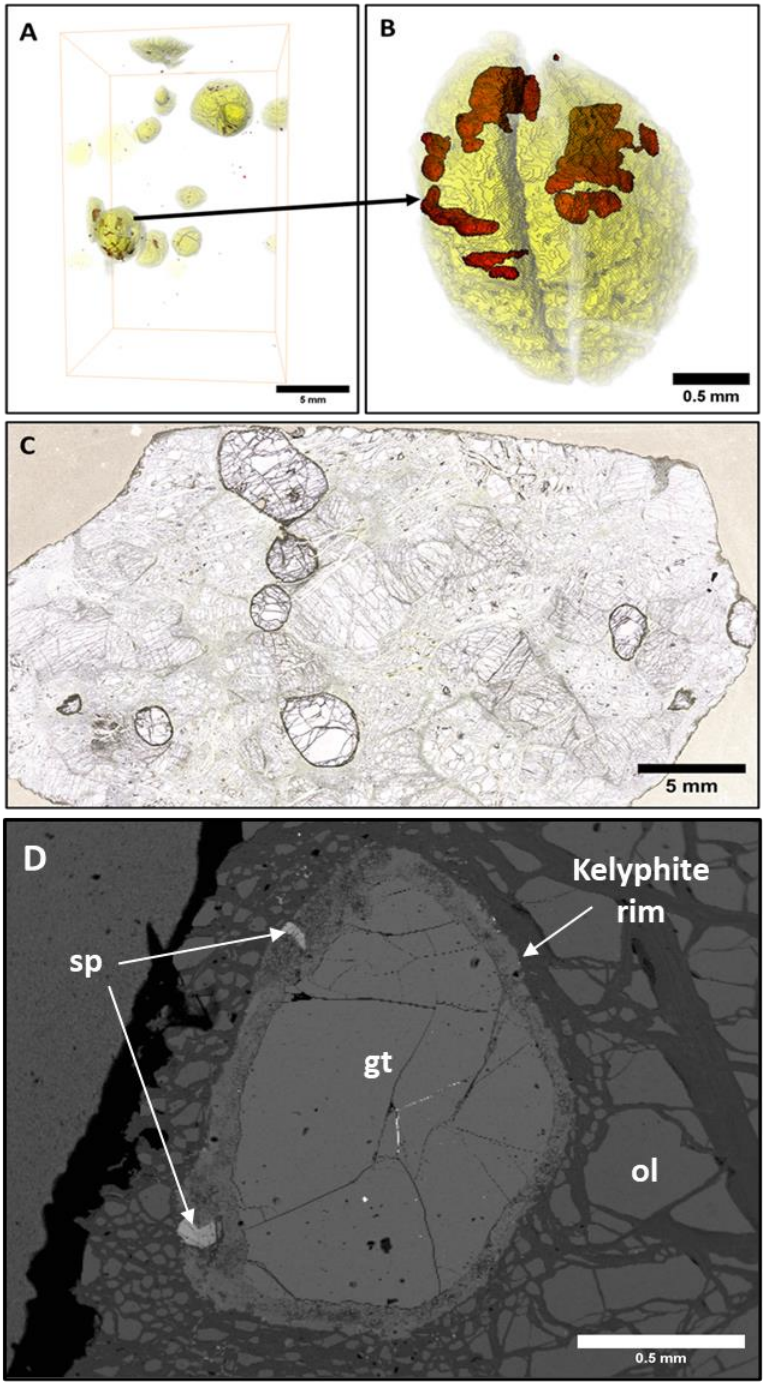

Figure 4.10. (A) 3D rendered image of a garnet peridotite from South Africa (DB1). Garnets (yellow) are generally circular in shape with a low (<1.5) AR. Scalebar is 20 mm. (B) 3D rendered image of an isolated garnet isolated from a garnet peridotite from South Africa (DB1). Scalebar is 0.5mm. Garnet is yellow. High density phase sulphide phase is red. Scalebar is 0.5 mm. (C) Photomicrograph under ppl of a garnet peridotite from South Africa (DB1). Garnets are circular to elliptical in shape and are randomly distributed with evidence of clustering. Scalebar is 5 mm. (D) BSE image of garnet grain in a garnet peridotite form South Africa. Small blebs of spinel are visible within the garnet kelyphite rim. Scalebar is 0.5 mm.

4.5.9 Garnet grains and garnet-spinel aspect ratios

Modal mineralogy based on thin-section analysis revealed sample VI 313 532 to be a garnet lherzolite (Fig 4.9). However, analysis of the 3D volume revealed the presence of garnet-spinel clusters. Spinel forms a low volume compared to garnet and exists as blebs <5 mm and complex, vermicular structures with an ellipsoidal shape. Spinel is not limited to garnet-spinel clusters, but several small blebs (<1 mm) are also visible. Garnets in garnet-spinel peridotite VI 313 532 (Fig. 4.9B) are large individual ellipsoidal grains that measure <5 mm in length and <4 mm in width. Garnets are randomly and evenly distributed throughout the core. There is no spinel visible in the scan of the core of this sample, although some had been found in thin-section (Table 4.1).

Mean ARs for garnet in garnet peridotites from Vitim and Pali-Aike are between 1.2 and 1.4. In contrast, garnets from garnet-spinel peridotites display a broader range of mean ARs ranging from 1.7 to 2.3. Mean ARs for garnet and garnet-spinel peridotites are shown in Fig. 4.11, where they are compared to ARs for cratonic garnet peridotites and in spinel-pyroxene clusters in spinel peridotite xenoliths.

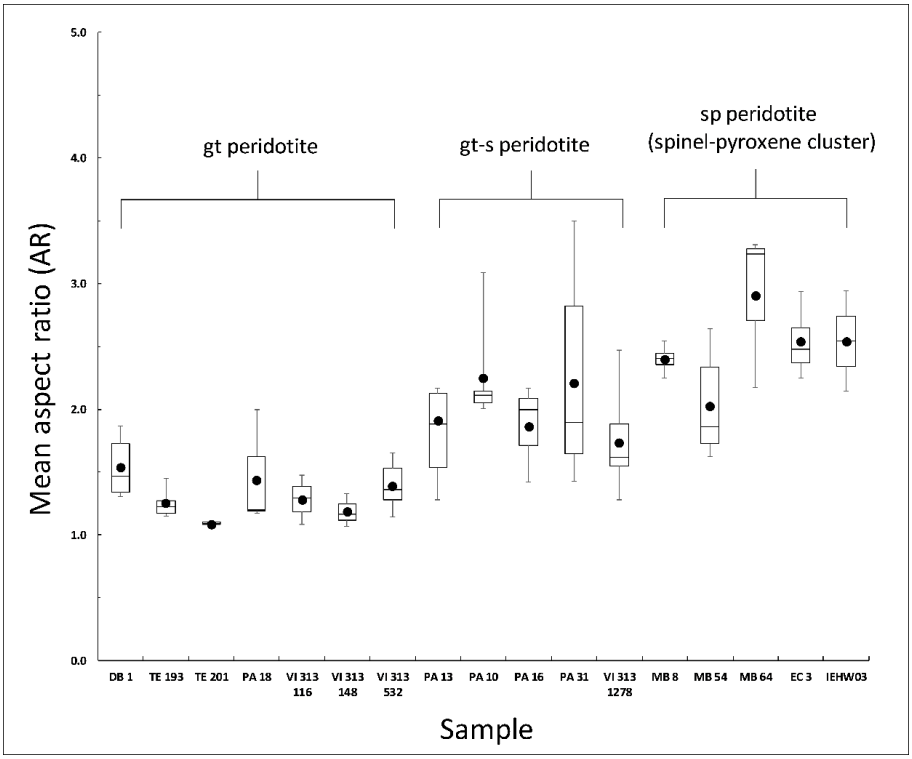

Figure 4.11. Box and whisker plot of aspect ratios (AR) for spinel peridotites from Massif Central (France), Lanzarote (Spain) and Calatrava (Spain) containing spinel-pyroxene clusters, and for garnet peridotites and garnet-spinel peridotites from Vitim and Pali Aike. Aspect ratios for garnet in garnet peridotites from Kaapvaal craton included for comparison. Mean ARs are shown as a solid black circle.

4.6 Discussion

4.6.1 Modal abundances of garnet and spinel

CT-scanning produces 3D volumes of garnet-spinel and garnet peridotite xenoliths which may offer a more accurate classification of samples. Calculating modal mineralogy from thin-sections alone may not provide the most accurate classification since clustering of garnets can lead to sections of the sample being devoid of garnet. Also, garnet-spinel clusters can co-exist with spinel-free garnets and some samples contain no interstitial spinel. Therefore, if the 3D volume is representative of a peridotite, analysis of the slice images and 3D rendered volumes can be used to better characterise a xenolith as a garnet or garnet-spinel peridotite. Figure 4.12 (A-B) shows images of thin-sections of garnet peridotites under PPL with garnets free of spinel whilst images in Fig. 4.12 (C-D) are 3D rendered images of cores of the same samples where there is evidence of the presence of spinel in close association with garnet grains.

Variation of garnet content seen in the 3D volumes is due to clustering of garnet grains in the sample and since the garnets are general ellipsoidal in shape, the position of the slice image affects the volume of garnet observed. Based on point counting on a thin-section, sample VI 313 532 was characterised as a garnet peridotite (Table 1) but based on the 3D volume slice images, it is clearly a garnet-spinel peridotite due to the presence of significant spinel volume in several garnet-spinel clusters. Modal mineralogy of sample VI 313 148 also shows a similar presence of a small volume of spinel in the CT scan.

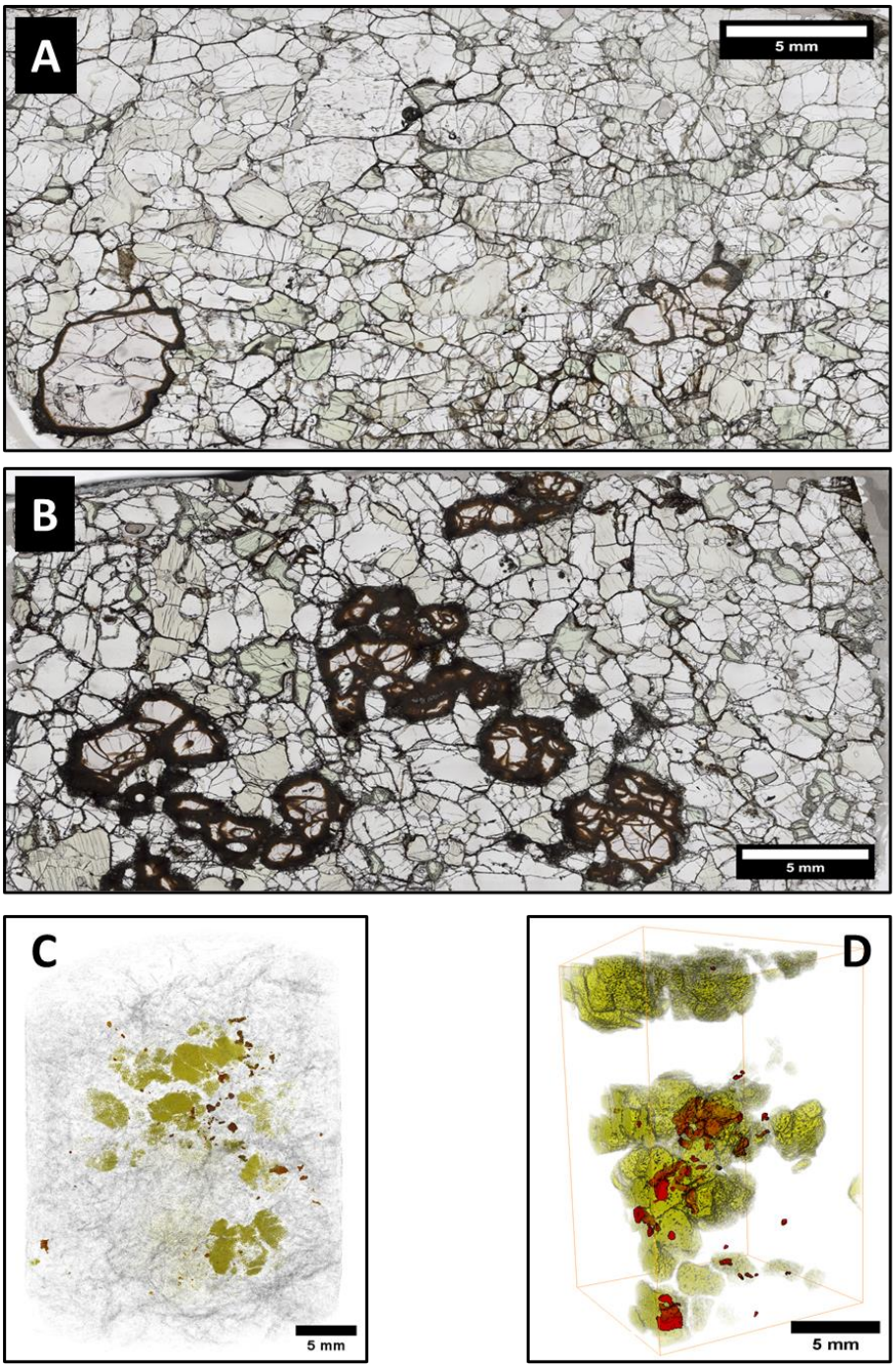

Figure 4.12. (A) Photomicrograph under PPL of protogranular garnet peridotite xenolith (VI313532). Garnets show no associated spinel, so the TS peridotite is classified as a garnet peridotite. Scalebar is 5 mm. (B) Photomicrograph under PPL of protogranular garnet peridotite xenolith (VI48). Garnets show no associated spinel, so TS peridotite is classified as a garnet peridotite. Scalebar is 5 mm. (C) 3D rendered image of sample VI148, Image shows garnet (yellow) set to semi-transparent with several grains free of sp (red) and presence of sp blebs associated with gt. Silicate phases (grey) semi-transparent. Scalebar 5 mm. (D). 3D rendered image of sample VI313532, Image shows garnet (yellow) set to semi-transparent with several grains free of sp (red) and others forming complex gt-sp structures. Silicate phases removed. Scalebar 5 mm.

4.6.2 Garnet-spinel cluster textures

Micro-CT images of garnet-spinel clusters in peridotite xenoliths reveal the complex relationship between garnet and spinel (Figs. 4.4-4.9). Spinel is not just simply an inclusion in garnet but both minerals form complex structures. Slice images of the garnet grains have also revealed low density silicate inclusions. EMPA and BSE images of such inclusions in samples VI 313 116 and PA 18 (Fig. 3B) confirmed that they are olivine. Thus, they record the solid-state reaction of pyroxene and spinel converting to garnet and olivine (equ 4.1).

The lineation seen in the garnet-spinel structures (Fig. 4.4) and the ellipsoidal shape of garnet grains and garnet-spinel clusters point to deformation which probably occurred while the rock was garnet-free. Fig. 4.11 shows that the highest mean aspect ratios are found in spinel-pyroxene clusters whilst the lowest are found in garnet peridotites. Garnet grains in the studied garnet peridotites are somewhat ellipsoidal (AR = 1.2-1.4) but their overall grain shape is much more spherical compared with the garnet-spinel structures (AR = 1.7-2.3), which in turn are more similar to the shape of spinel-pyroxene clusters in mantle xenoliths from Lanzarote and the Massif Central (Bhanot et al., 2017). The micro-CT study of a garnet peridotite from Kaapvaal craton shows an average garnet AR of 1.3, remarkably similar to those in spinel-free garnet peridotites. Thus, we conclude that the garnet growth occurred after deformation. This may also account for the clustered nature observed in the garnets.

The mineral compositions of the garnet-free peridotites are not systematically different from those of the garnet peridotites and, therefore, the difference in mineral assemblage must depend on the difference in physical conditions under which these peridotites recrystallized (Kushiro and Yoder, 1966). The boundary between the spinel and garnet-lherzolite mineral facies is strongly curved between 1300^{o}C and 1450^{o}C; below 1200^{o}C it lies almost parallel to the temperature axis on a P-T diagram (O'Hara et al., 1971). Experimental studies of the spinel to garnet transition show that it occurs at ~ 1.6 GPa at 1000°C in the CMAS (CaO-MgO-Al_2O_3-SiO_2) system (Jenkins & Newton, 1979; Ionov et al., 1999; Klemme and O'Neill, 2000). However, the experiments of Robinson and Wood (1998) demonstrated that the minimum pressure at which garnet is stable on the anhydrous solidus of fertile peridotite is 2.8 GPa, corresponding to a depth of about 85 km and the spinel to garnet transition, which is 0.1–0.2 GPa wide, deepens as melt is extracted from the solid residue and solidus temperatures increase. Perkins and Anthony (1999) used bulk rock compositions to calculate equilibrium phase diagrams to calculate the conditions in which mineral assemblages are stable in the upper mantle. This approach requires consideration of the 7-component system SiO_2-Al_2O_3-Cr_2O_3-FeO-MgO-CaO-Na_2O, internally consistent thermodynamic data for end-members, and reliable

mixing models for all mineral solutions. They showed that a specific mineral assemblage is stable over a range of P-T conditions and that the compositions of the individual minerals vary with changing P-T conditions, with the ol + cpx + opx + sp + gt five-phase assemblages having a very restricted stability field, i.e., ~0.5 kbar at 1100 ^{O}C.

The pressure interval where garnet and spinel coexist in the peridotite mantle beneath Vitim appears to be rather narrow (Ionov et al., 1993), when uncertainties of the geobarometry (Brey & Kohler, 1990) are considered. The garnet-spinel peridotites yield pressure estimates ranging from 1.6 to 1.95 GPa (980°C< T< 1045°C). This indicates a 'garnet-in' pressure of 1.6-1.7 GPa and a 'spinel-out' limit (for fertile peridotites) of ~2.0 GPa for Vitim xenoliths. Figure 4.13 is a pressure-temperature (P-T) graph of equilibrium temperatures and pressures for garnet and garnet-spinel peridotites from Vitim and Pali-Aike. The graph shows a distinction between phase assemblages where garnet peridotites from Vitim plot in the high pressure (garnet) stability field whilst garnet-spinel peridotites plot in the relatively cooler and lower pressure region. Garnet-spinel peridotites from Pali-Aike plot at a higher pressure than gt and gt-sp peridotites from Vitim.

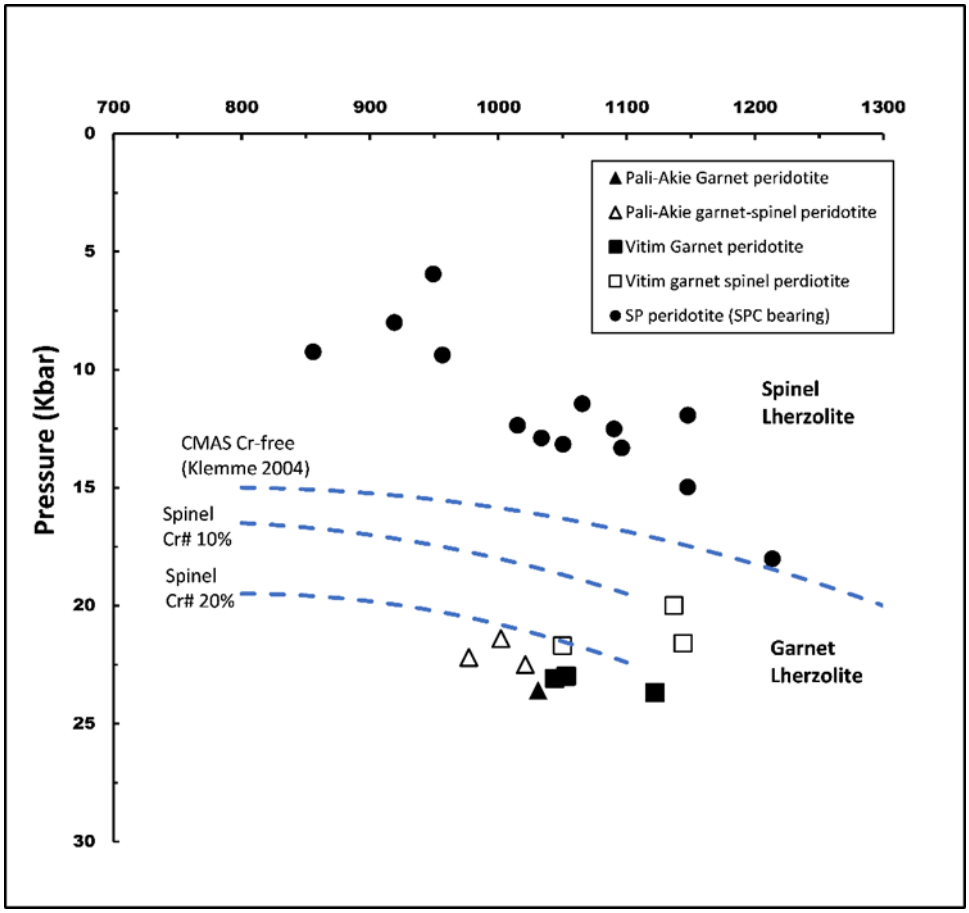

Figure 4.13. Graph of equilibrium temperatures and pressures for garnet and garnet-spinel peridotites from Vitim and Pali-Aike. Data from this study. Representative garnet-spinel transition from Klemme (2004). Vitim garnet lherzolites, solid squares, Vitim garnet-spinel lherzolites, open squares, Pali Aike garnet lherzolites, solid triangle. Pali Aike garnet-spinel lherzolites, open triangle. Temperatures and pressures calculated using Brey and Kŏhler (1990) Ca-in-Opx thermometer and Nickel and Green (1985) Gt-opx barometer. Sp peridotite (spc bearing) solid circle. Temperatures and pressures calculated for spc bearing spinel peridotites (Massif central, Lanzarote and Calatrava) using Putirka (2008) RiMG (The Mineralogical Society of America two pyroxene spreadsheet http://www.minsocam.org/msa/rim/RiMG069/RiMG069_Ch03_two-pyroxene_P-T.xls).

Mantle xenoliths record the fact that different continental settings display mineralogical variations in relation to the age of the overlying crust; older sub-continental lithospheric mantle shows an increasing level of depletion indicated by low values of CaO and Al_2O_3 in bulk rocks. Thus, Archean lithospheric mantle has a high Mg# (generally 93-95) coupled with low CaO and Al_2O_3 contents. In contrast Protozoic and Phanerozoic sub-continental lithospheric mantle shows intermediate Mg# values and higher CaO and Al_2O_3 bulk rock compositions. Depletion trends in mantle xenoliths thus record the mean level of depletion in the sub-continental lithospheric mantle from the Archean to the Phanerozoic (Artemieva, 2011). In garnet peridotite xenoliths, the Cr_2O_3 content of garnet is correlated with generally accepted measures of depletion in basaltic components and high-Cr garnets are found in refractory rocks with high Mg#, low CaO and Al_2O_3, whereas low-Cr garnets are found in more fertile peridotites (Griffin et al., 1999). Cr_2O_3 content of garnets from Vitim and Pali Aike are low, with a mean Cr# of 3.4 for both Vitim and Pali Aike, whereas cratonic garnet Cr#s are

generally higher at 11 (Boyd et al., 1993). CaO content in garnets from Vitim and Pali Aike range between 4.8-5.1 wt% and are thus distinct from the Cr- and Ca-rich garnets found in Kaapvaal-type (cratonic) peridotites.

In Fig. 4.3A, Vitim and Pali Aike peridotites plot within the lower part of the mantle array whilst cratonic peridotites occupy the more depleted (higher Cr# and Mg#) part of the array. Comparison of garnet Mg# and Cr# (Fig. 4.3A) reveals a distinct difference between the more depleted cratonic garnets and the low-Cr garnets of the younger lithosphere beneath Pali Aike and Vitim. Based on modal cpx content and the mantle array diagram, the Pali Aike mantle is more depleted than the lithospheric mantle of Vitim.

Estimated equilibration temperatures and pressures for Vitim and Pali Aike were calculated using the Ca-opx thermometer of Brey and Köhler (1990) and the barometer of Nickel and Green (1985) and presented in the P-T diagram in Figure 4.14, with additional data for Vitim from the study by Ionov et al. (2005) and for Pali Aike from Wang et al. (2008). Garnet spinel peridotites from both Pali Aike and Vitim occupy a region close to the oceanic geotherm (65 mW/m^2) and show a narrow range of pressure and temperature, i.e., 18.4-23.2 kbar and 965-1121 ^oC. Cratonic peridotites from Kaapvaal (Simon et al., 2003) plot at greater depth (~ 125 km), display a wider range in temperature and pressure in comparison to both Vitim and Pali Aike, and plot close to the continental geotherm estimated at 40 mW/m^2. Ionov et al. (2005) stated that, assuming that temperature gradually increases with depth, the relative positions of the rock types in the lithospheric cross-section beneath Vitim can be inferred. Garnet-spinel peridotites coexist with spinel peridotites in the depth range ~60–70 km (18–21 kbar). Spinel peridotites, garnet-spinel and garnet peridotites occur together in the depth range ~70–75 km (21–22 kbar). At pressures greater than 22 kbar, garnet peridotite begins to dominate.

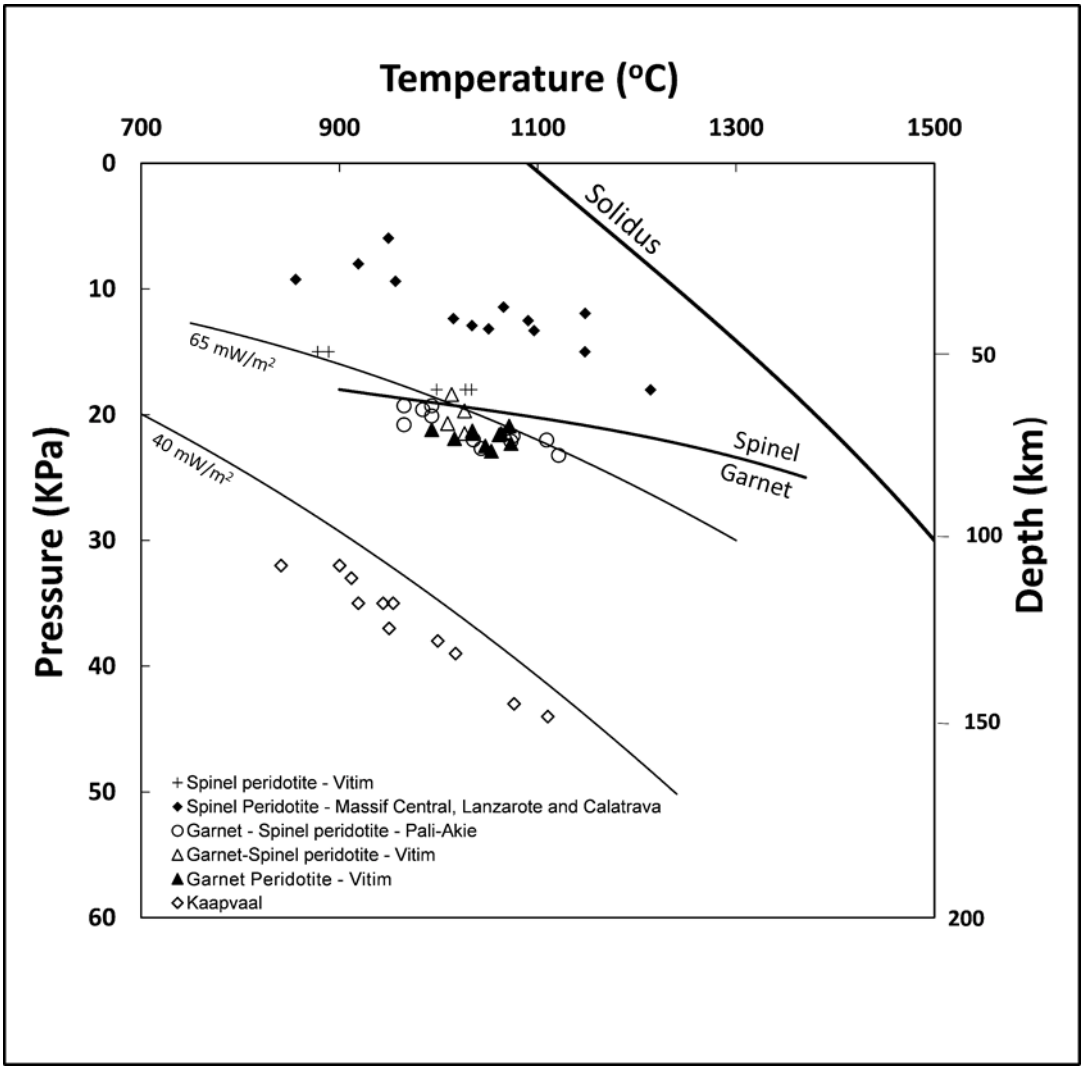

Figure 4.14. P-T diagram comparing mantle peridotites from Pali-Aike (open squares) and Vitim (open circles), spinel peridotites (Vitim, crosses) and spinel peridotites from Calatrava, Massif Central, (northern domain) and Lanzarote, solid diamonds, with cratonic mantle xenoliths (open diamonds). Data from Simon et al. (2003); Ionov et al. (2005) and Wang et al. (2008). Temperatures and pressures calculated using Brey and Köhler (1990) Ca-in-Opx thermometer, and Nickel and Green (1985) Al-in-Opx barometer. Garnet-spinel transition from Green and Ringwood (1967) is representative only, as this varies in depth according to the composition of the mantle.). Temperatures and pressures calculated for MCN, Lanz and Calatrava sp peridotites using Putirka (2008) RiMG (The Mineralogical Society of America two pyroxene spreadsheet http://www.minsocam.org/msa/rim/RiMG069/RiMG069_Ch03_two-pyroxene_P-T.xls).

Garnet, garnet-spinel and spinel peridotites can coexist at pressures of 18–22 kbar because of differences in their bulk major element compositions, since the spinel–garnet phase transition takes place at greater depths in more refractory rocks (Ionov et al., 2005). Robinson and Wood (1998) also pointed out that the spinel to garnet transition deepens as melt is extracted from the solid residue and solidus temperatures increase. This is probably why Pali Aike garnet-spinel peridotite samples plot at higher pressures than those from Vitim (Fig. 4.14).

The 3D volume of sample PA 31 from Pali-Aike displays a halo which surrounds spinel but not garnet. The halo is a phase denser than the silicate phase but significantly less dense than spinel and less

dense than garnet. The halos are not isolated but appear to connect to channels and provide textural evidence of metasomatic reactions affecting the mantle. This phase is composed of phases high in Cr, Al, Mg and Si (Fig. 4.8) and mineral phases interpretated has ol, cpx, gt and sp.

Textures of single spinel-pyroxene complex structures in spinel peridotites from Lanzarote and Massif Central were investigated by Bhanot et al. (2017). Sizes of these structures range from 4 to 12 mm in the longest dimension. Their AR values range from 2.0 to 2.9. Their ellipsoid shape is attributed to flattening of originally spherical structures formed by replacement of large, originally equant, garnets with a spinel-pyroxene cluster (Bhanot et al., 2017). Garnet-spinel structures from Vitim and Pali-Aike display a similar ellipsoidal shape. Garnet grains in garnet peridotites from Pali-Aike, Vitim and Kaapvaal (Figs. 4.7, 4.9A and 4.10) also show ellipsoidal shapes but with a lower AR. The ellipsoidal shape of the garnet-spinel structures reflects the shape and size of the original deformed spinel-pyroxene clusters, whereas the newly grown garnets have a more spherical shape.

Garnet and the associated complex spinel structure are very similar to spinel textures observed in spinel peridotite xenoliths from Massif Central and Lanzarote (Bhanot et al., 2017), albeit the spinel structures in Pali Aike and Vitim are less vermicular. Thus, they are considered to be relics of the original more vermicular spinel complex in a spinel-pyroxene cluster. Based on this observation, it is likely that the textures are related and thus act as examples of the garnet + olivine reaction with garnet (± olivine inclusions) and spinel-pyroxene clusters are examples of the reversible sub-solidus reaction (sp + opx + cpx ↔ ol + gt) going to completion, whereas the garnet-spinel textures seen in this study represent the transition stage of that reaction.

In addition, the size and texture of the spinel is relative to the degree of completion of the reaction, with less complex vermicular spinel textures representing the reaction near to completion (along with olivine inclusions) relative to the more complex and more substantial spinel volume of the garnet-spinel cluster (PA 16). 3D rendered images of garnet grains show no concentric pattern, garnet appears as a single crystal. The upper mantle beneath both Vitim and Pali-Aike has been subjected to cooling and Ionov (2004) and Stern et al (1999) have proposed cooling of the lithosphere as the driving force for the development garnet and garnet-spinel peridotite textures. The 3D rendered volumes of both garnet peridotites and garnet-spinel peridotites reveal that there is no interaction between the kelyphite rim and conversion of the original spinel-pyroxene cluster to garnet. Therefore, this process of kelyphite rim reaction forms no part of the garnet-spinel cluster formation process.

4.7 Conclusions

Micro-CT scanning of garnet peridotite xenoliths from the Kaapvaal craton provides an accurate representation of garnet textures and serves as a reference to which garnet and garnet-spinel textures mantle peridotites from Vitim and Pali-Aike can be compared and contrasted. Garnets in samples form Kaapvaal are spherical in shape with a low AR. DB1 (South Africa) 2D slice images and the 3D volumes show that the garnet distribution is random but unevenly spread throughout the sample.

Micro-CT scanning of garnet-spinel and garnet peridotite xenoliths from Vitim and Pali-Aike also provides accurate representations of the textures of the constituent garnets and spinels. The complex textures shown in the 3D volumes reveal the tectonic histories of the upper mantle beneath the two localities. Garnets containing olivine inclusions and complex garnet-spinel structures are considered to be the products of the reaction between pyroxene and spinel (sp + opx + cpx ↔ ol + gt). We have interpreted the textures to be evidence of a multi-stage process affecting the upper mantle. This process involves several stages (Fig. 4.15). Firstly, the original garnet-bearing mantle was decompressed due to lithospheric thinning and followed the reverse reaction in equ 3.1 such that the garnet (and olivine) was transformed into spinel-pyroxene clusters. These clusters then experienced a period of deformation which changed their shapes to ellipsoids with aspect ratios of 2.0-2.9, similar to those of spinel-pyroxene clusters in other mantle xenoliths. We interpret the lineation of garnet-spinel clusters seen in sample PA 10 as deformation formed during the garnet-free phase and retained as the garnets regrew. The final stage involves cooling and/or thickening of the lithosphere (Fig. 4.14) which transformed the spinel-pyroxene clusters back to garnet and olivine. Garnet-spinel clusters are interpreted to represent the incomplete conversion of a spinel-pyroxene cluster to garnet + olivine. Following conversion of spinel to garnet, garnet-spinel peridotites experienced metasomatic reactions as seen in the halo textures in sample PA 31. Finally, garnets were mantled with kelyphite rims due to increased heating prior to exhumation. We predict that the garnet-spinel cluster textures seen in Vitim and Pali-Aike garnet-spinel peridotites will form in regions which have experienced lithospheric thinning followed by isobaric cooling of the lithosphere.

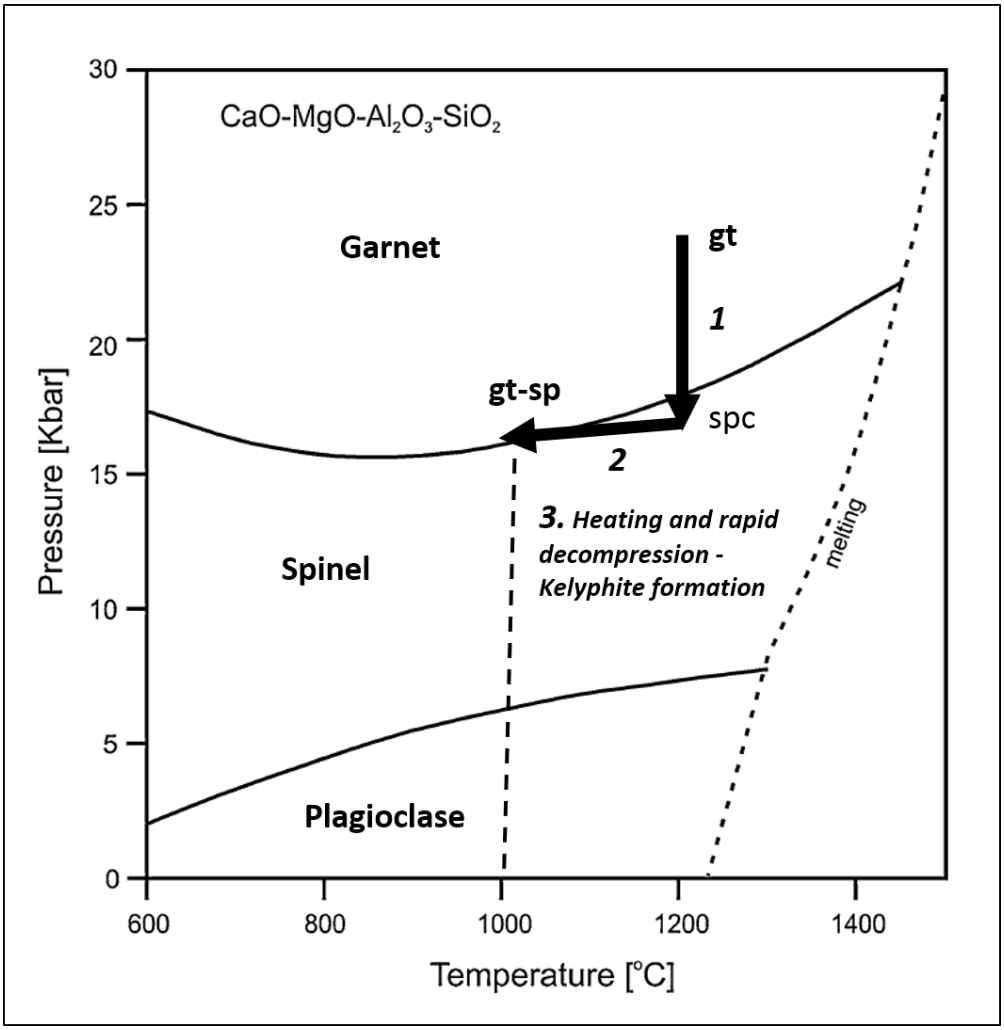

Figure 4.15. Mantle facies diagram showing schematic transition of spinel peridotite to garnet peridotite stability field by a decrease in pressure (1) followed by isobaric cooling (2) and exhumation (3). Heating brought on by host magma, rapid decompression and kelyphite formation. Adapted from Perkins and Anthony (2011).

Chapter 5

Spinel symplectite textures in Lunar Dunite 72415 and 72417

5.1 Introduction

5.1.1 Lunar spinel symplectites

Spinel symplectites have been reported in dunites collected by astronauts on the Apollo 17 mission to the Taurus–Littrow valley on the south-eastern edge of Mare Serenitatis. Several studies have discussed the origin of the dunites and their symplectites (Dymeck et al., 1975; Bell and Mao, 1975; Bell et al., 1975; Albee et al., 1975; Laul and Schmitt 1975; Ryder, 1992; Schmitt 2016). The interpretations fall into two major categories: shallow formation as olivine cumulates in the lunar crust, and deep formation within the lunar mantle. This study will investigate the various types of spinel symplectite textures in Apollo 17 dunite samples 72415,4 and 72417,9003 and will discuss the different hypotheses of their formation.

Micro-CT imaging will be used to establish the variations in three-dimensional texture of the symplectites and the relationships between symplectites and the olivine grains. EPMA analysis will investigate spinel mineral compositions and determine whether there is any variation in mineral composition between symplectite types. The textures will be compared with spinel textures in terrestrial peridotites (Bhanot et al., 2017). A short introduction to the Moon is given below.

5.1.2 Nature of the Moon

The Earth and Moon have followed very different evolutionary paths in their 4.6 billion-year histories (Zuber et al., 2006). The Moon's surface is composed of two distinct types of terrain, one a bright (high albedo) highland region (known as "terra") composed of anorthosite and the second darker (low albedo) basaltic plains (known as "maria"). Ferroan anorthosites make up 80% of the lunar crust and the remaining surface is composed of mare basalts (Shearer et al., 1999). The bedrock of the maria typically extends only hundreds of meters below the surface and locally reaches depths of about 5 km. In contrast, the highland bedrock is feldspathic (plagioclase-rich) material. Seismic data indicate that highland material forms a crust 45 to 60 km thick in the west-central nearside (Nakamura, 1981). Bombardment of the lunar surface has pulverised the surface rocks into a fine-grained mass of "regolith" which consists of single mineral grains and rock fragments cemented by impact-generated glass.

Three processes were particularly important in the evolution of the Moon: impact cratering (in particular, the formation of large multi-ringed basins), mare volcanism, and tectonic activity which formed linear rilles and mare ridges (Solomon and Head, 1980). Wilhelms (1987) divided the lunar geological timescale into the following periods: (1, oldest) the Pre-Nectarian period; (2) the Nectarian system, all landforms produced between the formation of the Nectaris impact basin and the formation of the Imbrian impact basin, including the Serenitatis basin; (3) Imbrium period; (4) the Eratosthenian and (5) the Copernican system (Table 5.1).

Table 5.1. Lunar timescale and defining events (Stöffler et al., 2001).

Period		Major Events
Copernican		Formation of Copernicus crater. Includes present day
Eratosthenian		Less clearly defined then the other systems and includes Mare plains that are much less extensive than the upper Imbrian.
Imbrian	**Upper Imbrian**	Landforms between formation of Orientale – the youngest impact basin and a upper boundary defined by diameter of largest crater eroded to 1^{o} interior slopes. Two thirds of Mare lavas are in the Upper Imbrian with extensive mare lavas forming the Serentartis, Tranquilities and Crisium.
	Lower Imbrian	Landforms between formation of the Imbrian basin and the formation of the Orientale impact basin.
Nectarian		Landforms produced between the formation of the Nectarian impact basin and the formation of the Imbrian impact basin. Serenitatis and Crisium are also Nectarin basins.
Pre-Nectarian		Lunar magma ocean. All landforms older than the Nectarin basin. Oldest recognised basin is Procellarum. South Pole Atkin is high probability impact origin and is the oldest, deepest and largest basin (?) Pre Nectarian land forms are dominantly of impact origin. No volcanic landforms, faults or folds recognised. Pre Nectarian terrain is predominant on the lunar far side.

The chemical composition and mineralogy of the Apollo 11 basalts and soils led the first investigators of lunar samples to formulate the hypothesis that the Moon was covered by a deep magma ocean that solidified and underwent chemical differentiation (Wood et al. 1970; Grove and Krawczynski, 2009). Cooling of the magma ocean would cause crystals of olivine and pyroxene to form and sink, forming the ultramafic mantle at its base (Stöffler et al. 2001). Further crystallisation would lead to the appearance of plagioclase, which would ultimately float and form the anorthositic crust. Late-stage ilmenite-rich (dense) cumulates would be unstable and might sink (e.g., Kesson and Ringwood, 1976), producing limited mixing of the cumulate layers (Snyder et al., 1992) or full-scale overturn of the cumulate pile (e.g., Hughes et al., 1988; Hess and Parmentier, 1995).

Beneath the highland crust and constituting all or most of the remaining lunar volume, is the ultramafic lunar mantle. No samples of the lunar mantle have yet been unambiguously identified in the Apollo sample collection, the lunar meteorite collection, or by remote sensing techniques. Thus, the lunar mantle must be studied through indirect means. Seismological data place some constraints on the interior profile (Wieczorek 2009), revealing that the lunar mantle is composed primarily of olivine and orthopyroxene with lesser amounts of clinopyroxene and garnet.

Goins et al. (1978) provided an estimate of the seismic velocity structure of the lunar mantle. The nearside crust reaches a depth of 60 km. Below this, mantle P and S-wave velocities are ~ 7.8 km/s and 4.6 km/s, respectively, with a decrease in both P and S wave velocities at 400 km, thus defining the lower portion of the lunar upper mantle (Fig. 5.1). Between 400 and 480 km, a transition zone occurs between the upper and lower mantle. The lower mantle extends to 1100 km. The pressure regime of the lunar interior is much lower than those of the Earth's interior. Lunar pressures can be calculated using equation 5.1 (Elkins-Tanton et al., 2011). Hence, in the lunar mantle, ~ 400 km depth is equivalent to 22 kbar.

$$P(r) = (-1.522\ x\ 10\text{^}(-6))\ r\text{^}2 + (-8.963\ x\ 10\text{^}(-5)\ )r + 4.76 \quad \text{Equ. 5.1}$$

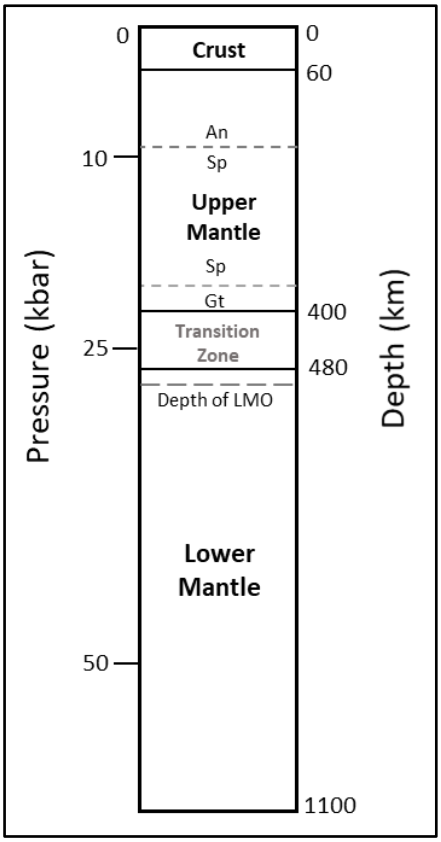

Figure 5.1. Sketch of the lunar upper mantle (Adapted from Goins et al., 1981).

Numerous studies (Longhi, 2003; Taylor and Jakes, 1974; Snyder et al., 1992; Tonks and Melosh, 1993; Elkins-Tanton et al, 2011) have modelled the crystallisation of the lunar magma ocean (LMO). Estimates of the extent of initial lunar melting range from a shallow magma ocean (~250 km) up to whole Moon melting (Warren, 1985; Pritchard and Stevenson, 2000; Longhi, 2006; Shearer and Papike, 1999: Elardo et al, 2011). However, a deep lunar magma ocean (LMO) (>500 km) is consistent with geophysical models of the lunar interior (Taylor and Jakes 1974; Shearer and Papike, 1999). Crystallisation of the LMO created a chemically stratified Moon consisting of an anorthositic crust and magma ocean cumulates overlying the primitive lunar interior. Shearer and Papike (1999) state that, in a dynamically simple LMO, the most probable crystallization sequence is olivine → ± orthopyroxene ± olivine → clinopyroxene ± plagioclase → clinopyroxene + plagioclase → clinopyroxene + plagioclase + ilmenite. Thus, the last liquids to crystallize formed dense, ilmenite-rich cumulates. The underlying olivine-orthopyroxene cumulates would also be stratified with later crystallised, denser, more Fe-rich compositions at the top (Hess and Parmentier, 1995). Soon after the crystallisation of most of the LMO, the cumulate pile experienced large-scale gravitational overturn (Hess and Parmentier, 1995). This resulted in transport of late-forming cumulates into the deep lunar mantle and mixing of LMO cumulates on a variety of scales (Ryder, 1991; Shearer and Papike, 1999).

The Moon has a lower mean density (3.34 g cm^{-3}) than the Earth, however, the lunar mantle has a higher Fe^{2+} content compared to Earth's upper mantle (Basaltic Volcanism Study Project (1981). The Mg# of Earth's upper mantle is ~ 89, based on studies of terrestrial mantle peridotites, whereas estimates of the Mg# of the Moon's mantle range from 87 to 91 (Warren, 1986), and even 93 (Elardo et al., 2011) although an early estimate by Buck and Toksoz (1980) suggested an Mg# of 70.

The evidence for garnet in the lunar mantle is consistent with both the predicted range of thermodynamically stable phase assemblages with depth and the lunar seismic data (e.g., Anderson 1975; Wieczorek et al., 2006). Predicted seismic velocities showed that garnet should be a significant phase (8-13 mol%) in the lower mantle between depths of ~500 and 1260 km. Garnet has been predicted to be thermodynamically stable in the mantle above the 500 km seismic discontinuity for certain compositional models and temperature profiles (Kuskov 1995; Khan et al. 2006). Based on the modeling of Kuskov (1995), up to 4 vol% garnet could be stable at a depth of 400 km, whereas Khan et al. (2006) found that ~15 wt% garnet may be present between depths of ~200 and 600 km. Neal (2001) modelled the composition of lunar basaltic glasses using a mantle source containing 5 vol% garnet.

5.1.3 Impact basins

The numerous multi-ring basins identified on the Moon were caused by the impact of asteroids. On the Moon, the mean impact velocity is ~20 kms^{-1} (Shoemaker, 1977; Spudis 1999). Over 40 multi-ring basins are recorded on the Moon. The formation of multi-ring basins (Fig. 5.2) involves cratering, volcanism, tectonism, ballistic sedimentation and endogenic modification (Spudis, 1999). A basin-forming impact redistributes vast amounts of crustal materials (Spudis 1999). The impactor imparts its kinetic energy to the surface which results in a shockwave which propagates deep into the impacted body, leading to compression. As the shockwave travels, it is preceded by a rarefaction (decompression) wave. When the decompression waves encounter the free surface of the impacted body, material will be ejected forming a crater (Fig. 5.2). Material that was the last to be mobilised is deposited first close to crater rim whilst debris flung out in the initial stages of impact and with the highest velocities is deposited further from the crater rim. Inside the newly formed crater, the floor experiences rebound which forms a central peak (Fig. 5.2). As basin evacuation proceeds, the surrounding area experiences deformation and crustal adjustment that produce basin rings.

Rocks at the impact site will undergo shock metamorphism. The shockwave intensity dissipates radially away from site of impact, so rocks experience a range of shock damage throughout the impact site. Rocks closest to impact experience peak pressures and potential vaporisation. Away from the centre of impact, high pressures can cause melting and formation of impact melt. Further away, rocks experience lower shock pressures with damage to minerals such as surface dislocations, formation of diaplectic glass and partial melting along grain boundaries (Spudis, 1999).

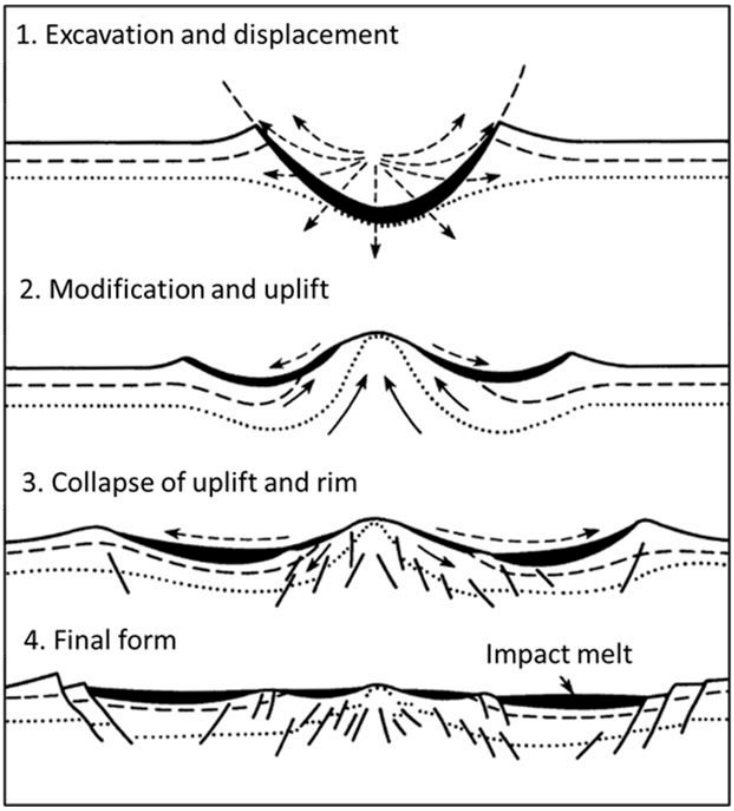

Figure 5.2. Sketch of the major stages in the formation of multi ringed impact basins, (1) excavation and displacement, (2) modification and uplift, (3) collapse of uplift and rim and (4) final form (adapted from Grieve et al., 1981; Heiken et al. 1991).

There are eight major circular maria on the Moon: Orientale, Serenitatis, Humorum, Crisium, Nectaris, Imbrium, Smythii and Grimaldi (Fig. 5.3). All were formed by volcanic infilling of a multi-ringed basin, and all are associated with mascons (Muller and Sjogren, 1968; Solomon and Head, 1980; Melosh et al., 2013; Neumann et al., 2015). Mascons are attributed in part to the upward displacement of the crust-mantle interface (Neumann et al., 2015), so they occur in regions in which the lithosphere has been thinned.

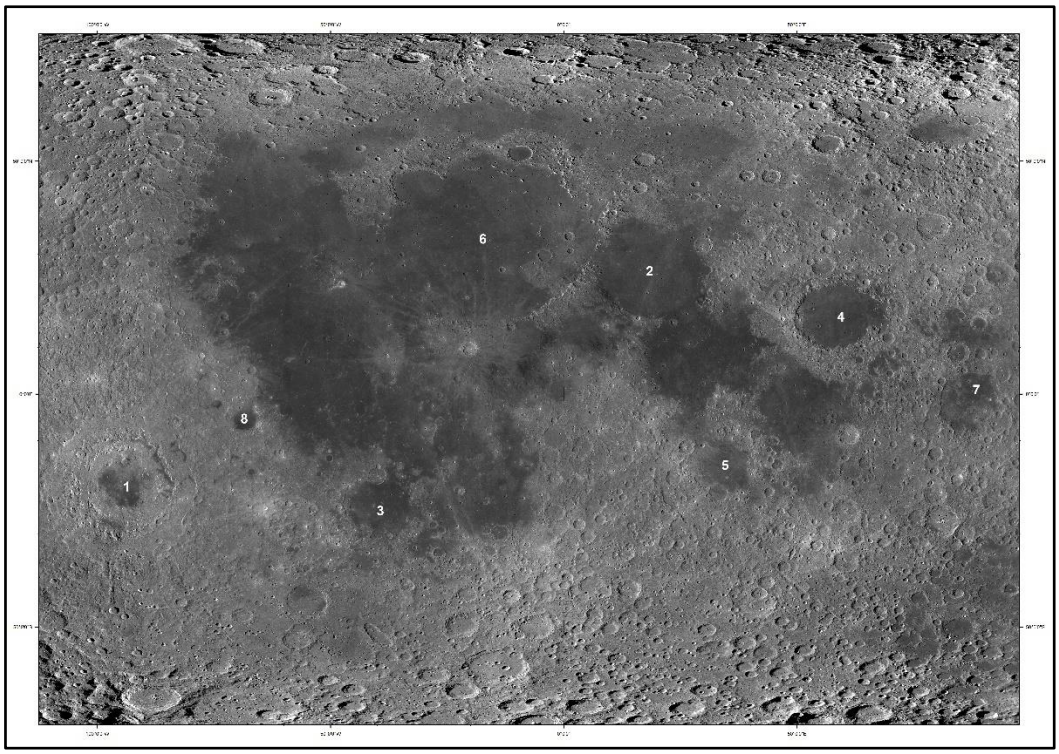

Figure 5.3. Major ringed impact basins Orientale (1), Serenitatis (2), Humorum (3), Crisium (4), Nectaris (5), Imbrium (6), Smythii (7) and Grimaldi (8). (USGS, https://astrogeology.usgs.gov/search/map/Moon/LRO/LROC_WAC/Lunar_LRO_LROC-WAC_Mosaic_global_100m_June2013.

The Serenitatis multi-ring basin (Fig. 5.4) was the landing site of Apollo 17. Its western sector has been nearly destroyed by formation of the Imbrium basin, and its north rim is covered by hummocky Imbrium ejecta. Yet the basalt lavas filling Mare Serenitatis are unaffected by the Imbrium deposits, and so considerable time must have intervened after the Serenitatis basin formed and before basaltic eruptions filled it (Wilhems, 1987). Serenitatis is associated with four ring structures and a faint fifth ring, with rings diameters of 410, 620, 920, 1300 and 1800 km (Spudis 1999). The main highland ring (920 km) is considered to be the rim of the transient cavity. The main Serenitatis basin rim is defined by highland scarps and isolated massifs rising in places above 2 km.

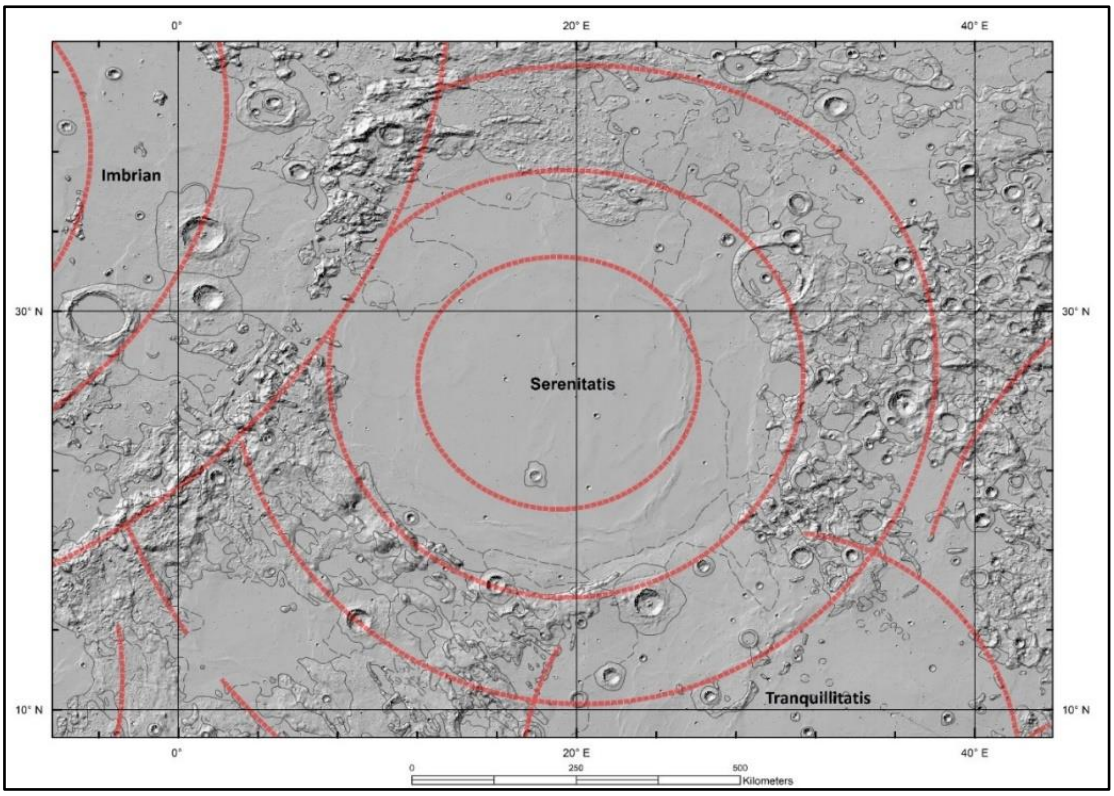

Figure 5.4. Serenitatis impact basin and location of rings. LOLA Grayscale Shaded Relief map, USGS (https://astrogeology.usgs.gov/search/map/Moon/Geology/Lunar_Geologic_GIS_Renovation_March2013).

5.2 Geological Setting of Apollo 17 landing site, Taurus-Littrow Valley

Apollo 17 astronauts Cernan and Schmitt landed in the Taurus-Littrow valley (20°9'55" N 30°45'57" E; 20.19° N 30.77°E (Hasse et al., 2019)) on December 11,1972. The major objectives for observation and sampling during the mission were (l) highlands, (2) dark mantling deposits, and (3) sub-crater floor material (Wolfe et al., 1981).

The rover excursions made by astronauts Cernan and Schmitt around the Taurus-Littrow Valley are shown in Figure 5.5, and a detailed geological map of the area is shown in Figure 5.6. The Taurus-Littrow valley is a graben that is radial to Mare Serenitatis, partially filled by ~1400 m of basaltic lava (Wolfe et al., 1975). It formed 3.97 Ga ago, during the Serenitatis impact event. Much of the original ~60 km thick crust may have been excavated by the Serenitatis impact (Dence et al., 1976; Spudis, 1999). It abuts against the large, blocky East Massif (Fig. 5.7).

Toward the south, a narrow outlet partially blocked by a large crater leads off to another valley. On the west side of this outlet, a second blocky mountain called the South Massif forms the southwestern wall of Taurus-Littrow (Fig. 5.7). North of the East Massif, across an outlet into another small valley, the Sculptured Hills and farther to the west, the North Massif form the

remaining walls of Taurus-Littrow. Between the North and South Massifs, the main exit from the valley leads out toward Serenitatis. This exit is about 7 km wide and is partially blocked by a 1 km high hill (Family Mountain) and also by a fault scarp (Lee-Lincoln scarp) that stretches between the North and South Massifs (Fig. 5.8). A bright deposit, called the light mantle, extends across the valley floor from the foot of South Massif (Fig. 5.8). It consists of breccias similar to those of the massif and is interpreted as a land-slide generated on the massif slopes (Team, A.F.G.I., 1973; Magnarini et al., 2021). The massifs are composed of feldspar-rich breccia (Wolfe et al 1975) and basalt underlies unconsolidated materials of the valley floor. The North and South Massifs rise to heights of 2000 and 2300 m, respectively, and represent the major structural boundaries of the valley, and their faces contain intermittent exposures of thick sections of pre-mare crustal rocks.

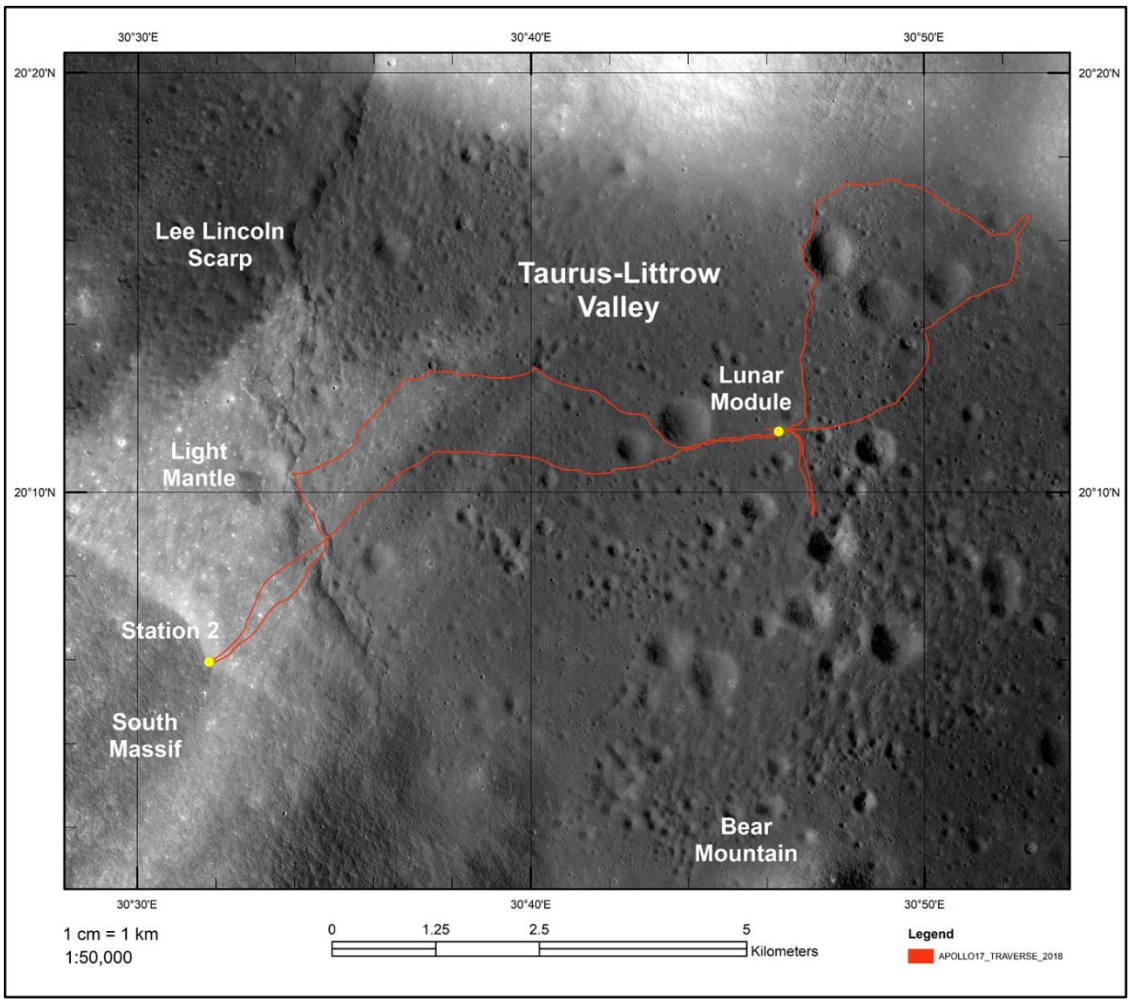

Figure 5.5. Apollo 17 landing site map, showing the traverses performed by the astronauts (red line) and station 2, south massif, Taurus-Littrow Valley (Apollo 17). Moon Apollo 17 LROC NAC Orthomosaic 50cm v1. https://astrogeology.usgs.gov/search/map/Moon/Apollo/Traverse/Apollo17/Taurus-Littrow%20Valley%20Apollo%2017%20Orthomosaic%2050cm (Haase et al., 2018).

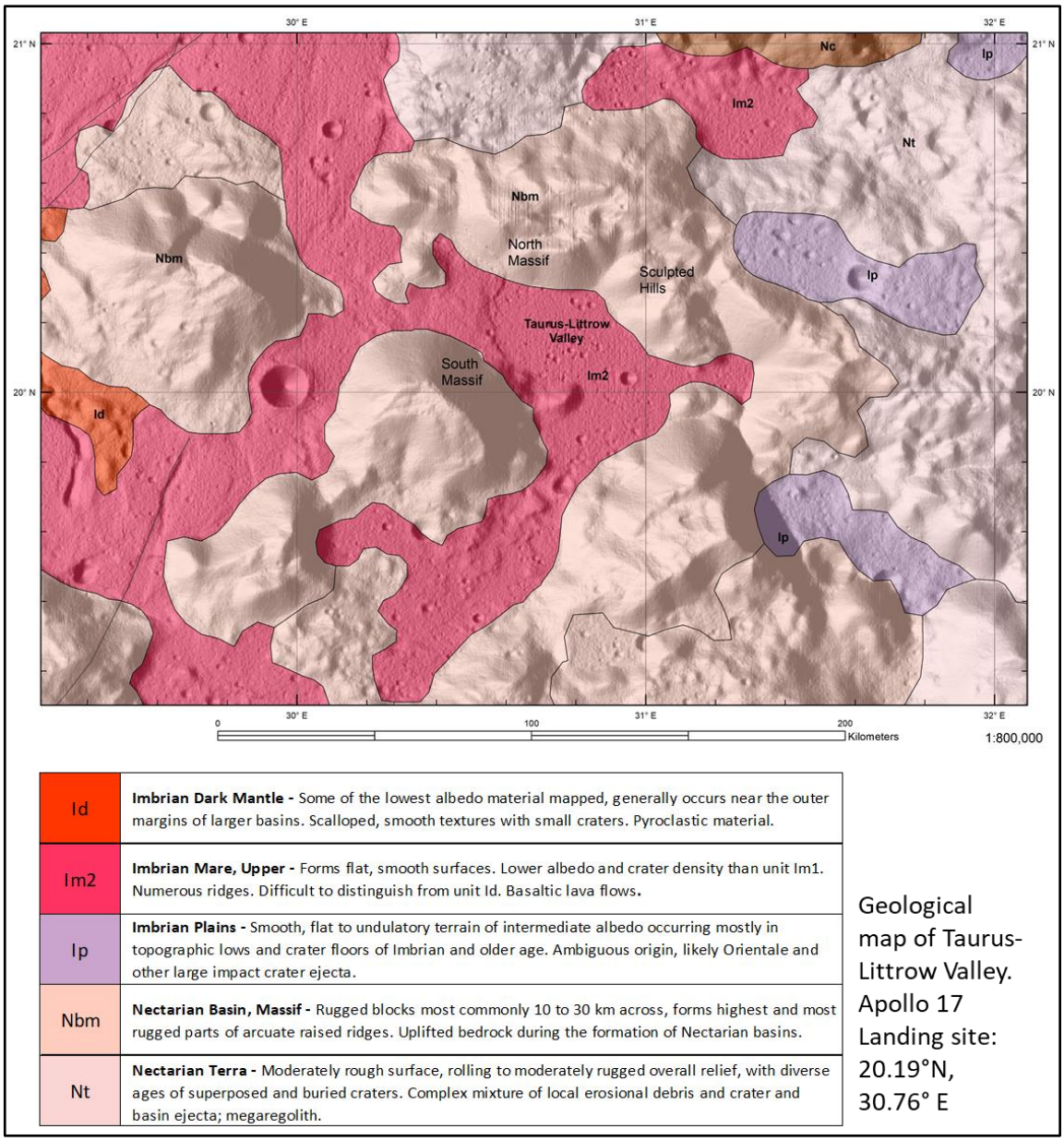

Figure 5.6. Geological map of Taurus-Littrow Valley (USGS. Unified Geologic Map of the Moon, 1:5M, 2020, base map shaded-relief products derived from SELENE Kaguya terrain camera stereo (equatorial, ~60 m/pix (https://astrogeology.usgs.gov/search?pmi-target=moon))

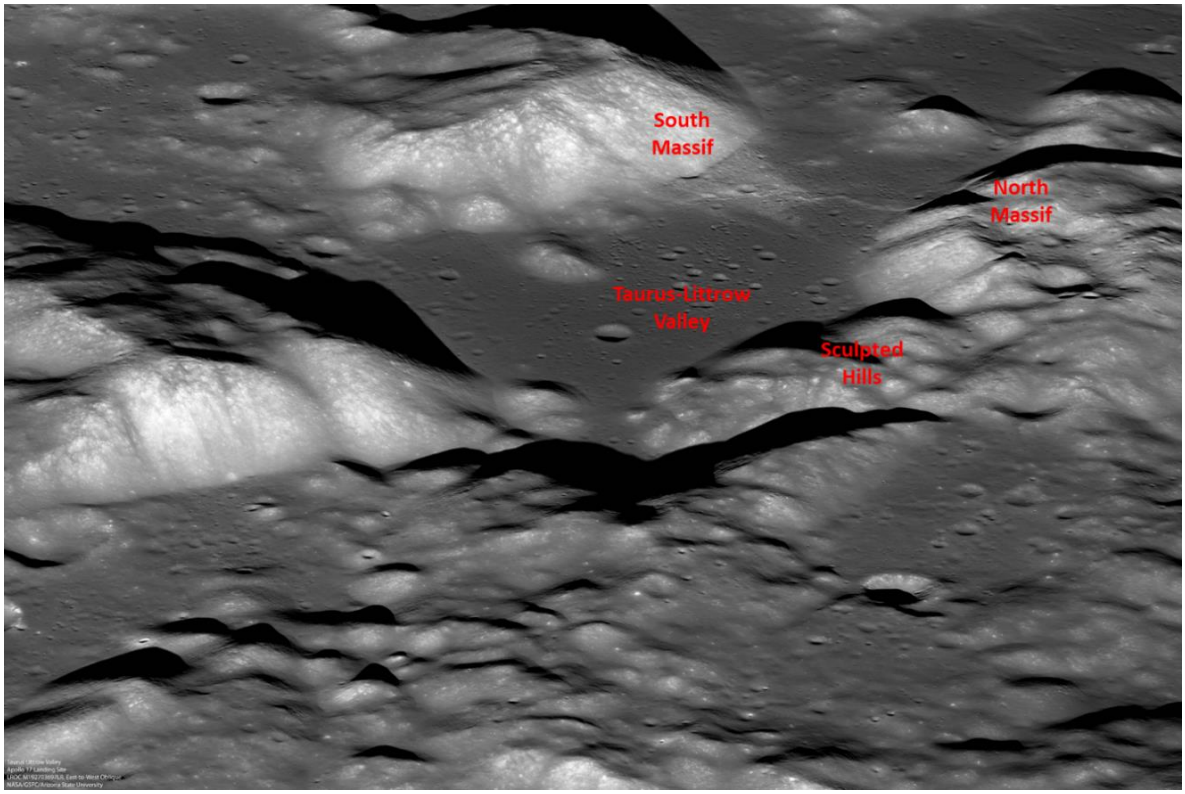

Figure 5.7. Image of valley of Taurus-Littrow. Image M192703697LR (NASA/GSFC/Arizona State University).

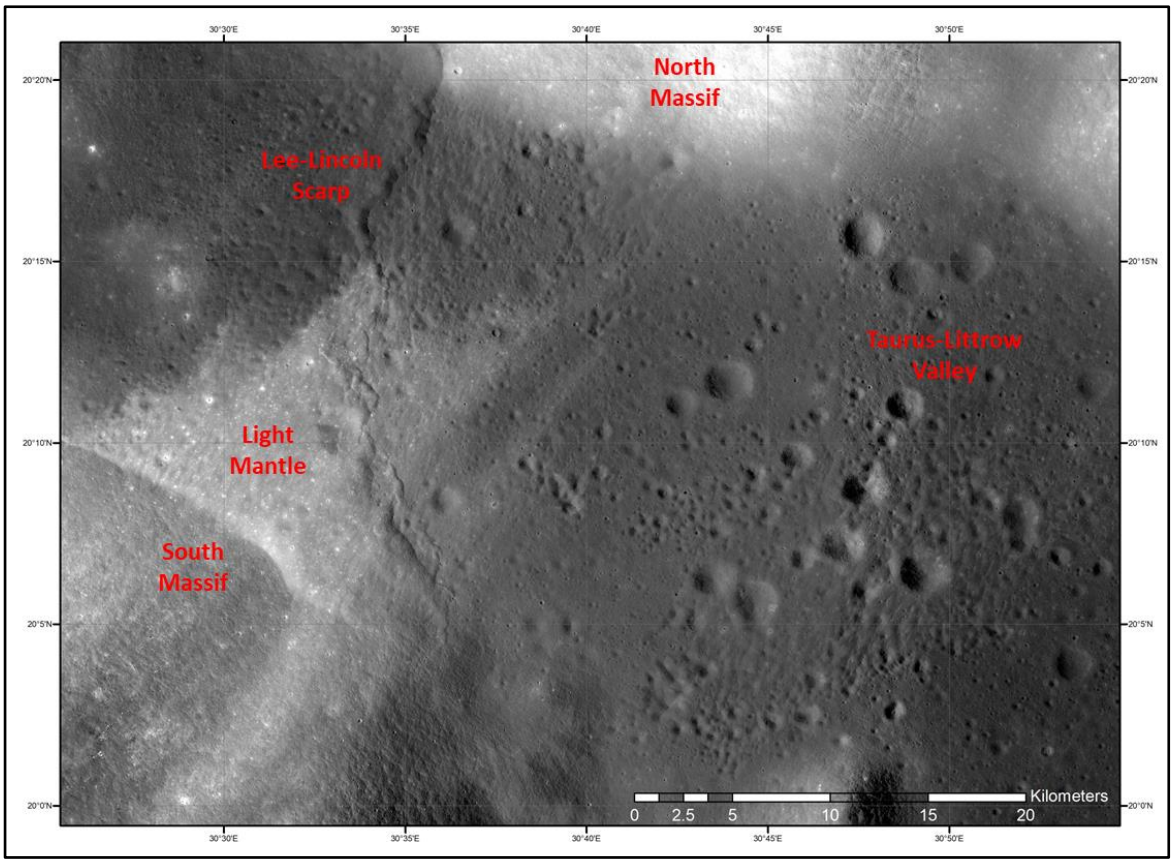

Figure 5.8. Image of Light Mantle region, Taurus-Littrow valley (Moon Apollo 17 LROC NAC Orthomosaic 50cm v1. https://astrogeology.usgs.gov/search/map/Moon/Apollo/Traverse/Apollo17/Taurus-Littrow%20Valley%20Apollo%2017%20Orthomosaic%2050cm).

Numerous fields, or "source-crops" of boulders are present on the upper parts of both the South and North Massifs, from which they have rolled into the valley. Several blocks were the prime field objectives (Schmitt, 1973). The large boulder investigated at station 6 (Fig. 5.5) has a well-defined track above it and appears to have originated from the lowermost source-crop band about one-third of the way up the slope. Figure 5.9 shows a cross-section of the Taurus-Littrow valley, explaining the local derivation of the boulders.

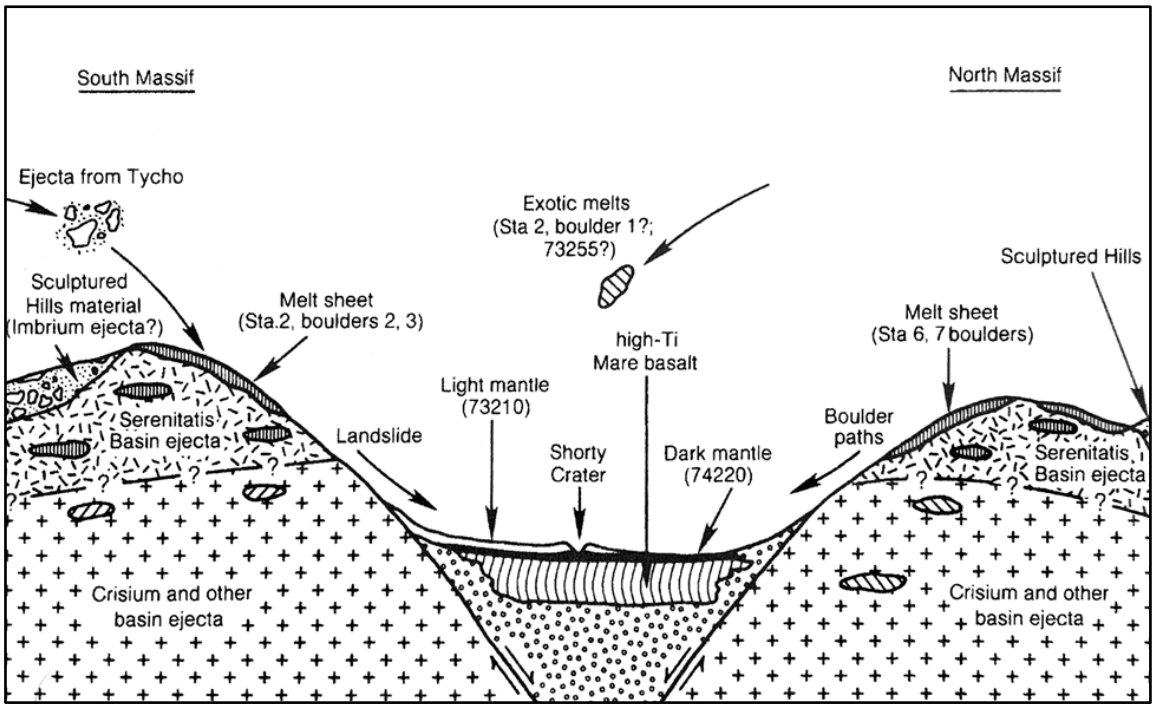

Figure 5.9. Taurus-Littrow cross section (Heiken et al., 1991: Spudis, 1999)

The stratigraphy and historical sequence of events in the Taurus-Littrow area were thought to be understood before the Apollo 17 mission. This sequence as then understood, from older to younger events, is shown in Table 5.2. The Taurus-Littrow highlands are partially embayed by mare basalts and discontinuously mantled by pyroclastic deposits associated with mare flooding (Heikin et al., 1974; Spudis 1991).

According to Spudis (1991), the regional composition of the Taurus-Littrow highlands is distinctly different from those around the Crisium and Nectaris basins. Spudis and Davis (1993) showed that extensive norite deposits occur within the rim units of the Serenitatis basin. Norite is the major rock type and constitute 90% of the basin. Anorthite is a minor constituent with <2% abundance (Ryder, 1981b; Spudis, 1999). These observations have major implications for the geology of the Serenitatis basin and the lunar highlands. The impactor that formed the Serenitatis basin struck in an area mostly comprised of Mg-suite rocks. This suggests either an anorthite layer was not formed in this region (Ryder, 1981) or was removed prior to the Serenitatis impact. The Serenitatis impact occurred into a highland region that was petrological distinct from typical lunar crust and volcanism had possibly begun before the impact (Simonds et al., 1974; Ryder et al., 1974; Spudis, 1999); thus, the lunar surface may have had a partial covering of basalt leading to inclusion of basalt fragments in impact ejecta.

Table 5.2. Major stratigraphic and historical events concerning the Taurus-Littrow valley (Schmitt, 1973).

Time Scale	Event	Description
Oldest	**Pre-Serenitatis**	Evolution of the lunar crust and subsequent impact processes. Rock types composed of breccias or of previously melted materials, and products of formation of large basins. Igneous processes not ruled out by the available evidence.
	Serenitatis	Formation of major mountain ring of uplifted crustal rocks and initial formation of Taurus-Littrow valley. Major breccia units created during Serenitatis impact event.
	Nectaris and Crisium	Possible ejecta blankets of breccia that extended across the Taurus- Littrow area.
	Imbrium	Imbrium impact event contributed ejecta to the area, may have accented formation of grabens like Taurus-Littrow that are radial to both the Imbrium and Serenitatis impact basins.
	Post-Imbrium	Materials partially filled and levelled the valley floor after graben formation was complete or near completion. These materials formed coherent blocks in the walls of craters and were thought to be either breccia or basalt.
	Cratering event	Older craters (e.g., Camelot) exposed post-Imbrium materials in the valley floor. Young craters less mantled by dark material.
	Dark mantle deposition	Mantling of older features on a regional scale. The deposits interpreted as likely pyroclastic in origin with a relatively young age of deposition, < 1 Ga.
	Lee-Lincoln scarp formation	Superposed on North Massif talus. The age relation of this fault or flow scarp to the dark mantle material remains uncertain
	Light mantle deposition	Located at the base of the south massif, superposed on the dark mantle and Lee-Lincoln scarp. May be an avalanche deposit of massif materials covering older materials on the valley floor
	young cratering events	craters Shorty and Van Serg, created small and relatively sharp craters in the older surfaces of the dark and light mantles
Youngest	**Regolith and talus formation**	Ongoing formation of impact-generated regolith formed on all exposed surfaces. Accumulation of talus which is forming continuously at the base of all steep slopes.

5.2.1 Taurus-Littrow Valley, Station 2, South Massif

Station 2 was established at the foot of South Massif on the light mantle region near the south eastern rim of Nansen Crater. The light mantle is a deposit of pale predominantly fine-grained unconsolidated material with finger-like projections that extend 6 km across the valley floor from the South Massif (Wolfe et al., 1981). It has been interpreted as the deposit of an avalanche triggered, perhaps, by the impact on the South Massif of secondary projectiles from Tycho and is approximately 100 Ma old (Wolfe et al., 1981). Most of the rock samples collected from the lower slopes of South Massif were chipped from three boulders (Fig. 5.10).

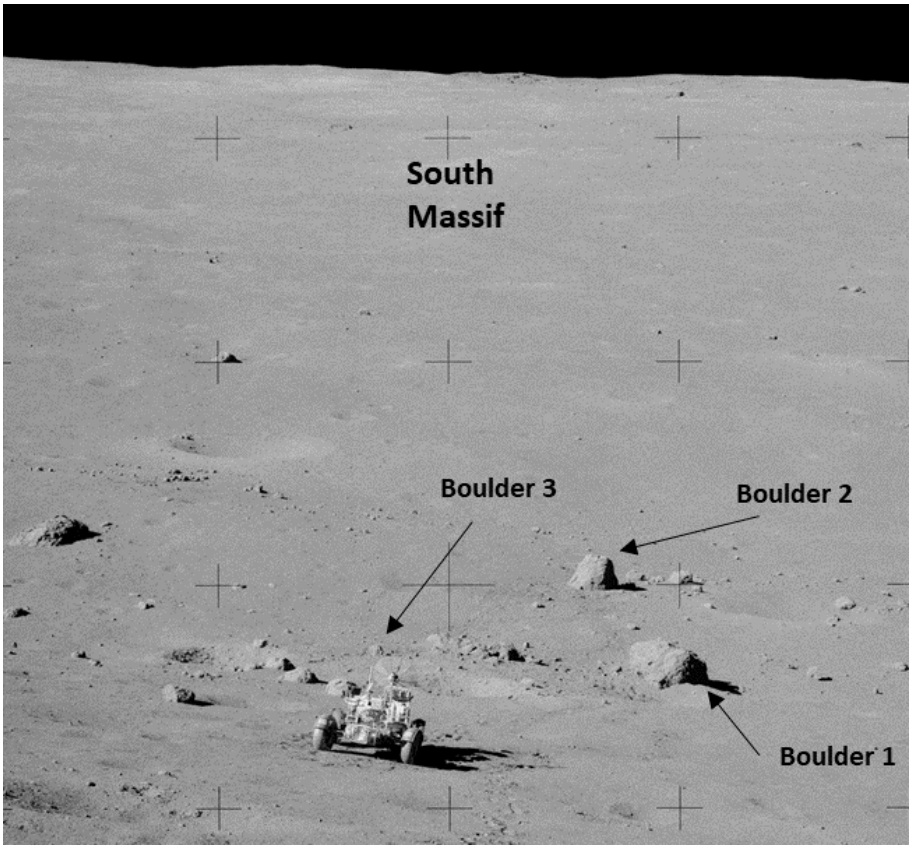

Figure 5.10. Location of Boulder 3, Station 2 on the lunar surface. Image AS17-138-21072HR (Apollo Image Library, https://www.hq.nasa.gov/alsj/a17/images17.html#MagI).

Samples collected from the South and North Massifs include crystalline mafic and some ultramafic rocks. Of the three boulders sampled at station 2, boulder 3 was the smallest and likely rolled down the slopes of the South Massif. It is an equant, 40 cm subangular block (Fig. 5.10 and Fig. 5.11) with clasts up to 10 cm. It contained a prominent 10 cm pale-coloured clast; several pieces were collected from it and subsequently named samples 72415 to 72418 (Fig. 5.11). Astronaut Schmitt recognized the clast as being composed of light pastel green material in an even paler matrix and suggested that

it was "olivine and something." This greenish crystalline clast proved to be composed largely of olivine.

The Lunar Sample Compendium (Meyer, 2011) categorises the samples as cataclastic dunite made up of 93% olivine (Fo_{86-89}), 4% plagioclase (An_{85-97}) and 3% pyroxene ($En_{84}Wo_3Fs_{10}$ and $En_{50}Wo_{42}Fs_4$). It also includes minute blebs of symplectite. It was determined to be 4.55 Ga old and considered to be the product of the primary differentiation of the Moon (Papanastassiou and Wasserburg 1975; Dymek et al. 1975). It is this clast which is the object of the study reported here. Samples for this study were provided by NASA (Apollo curation team). Samples included several small fragments of lunar dunite 72415,4 and 72417,9003. In addition, thin-section 72415,52 was also provided for EMPA analysis.

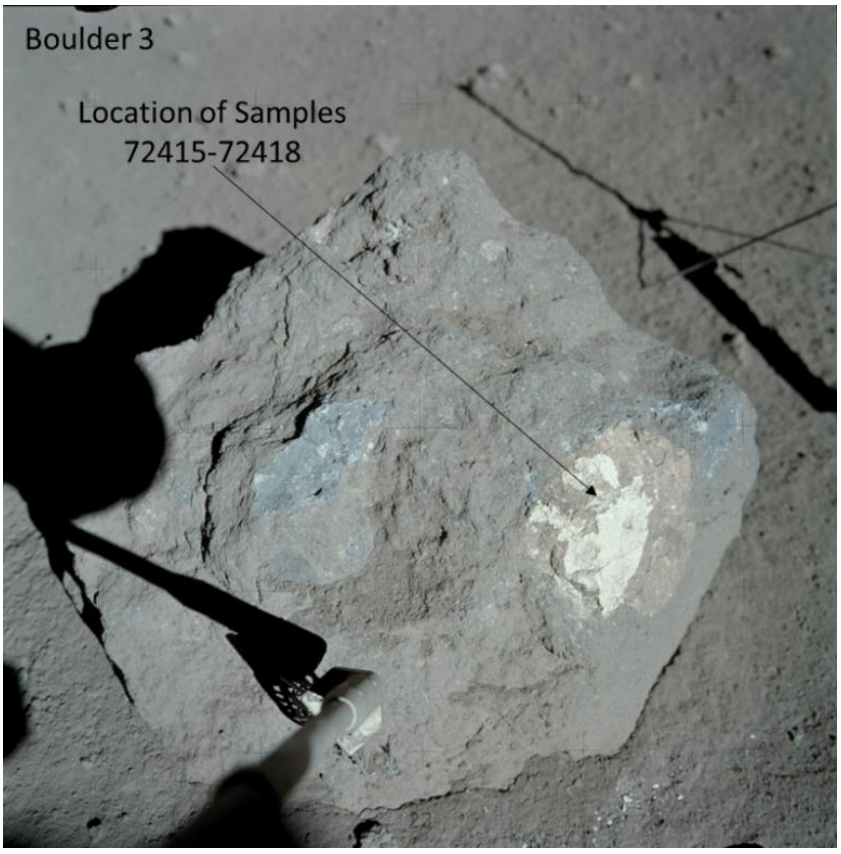

Figure 5.11. Image of Boulder 3 taken by astronaut Cernan (AS17-137-20971HR). Boulder 3 is an equant, 40 cm subangular block with an overall dull blue-grey colour (Apollo Image Library, https://www.hq.nasa.gov/alsj/a17/images17.html#MagI).

5.3 Results

5.3.1 Textural analysis, thin-section 72415,53

Thin-section analysis was performed at Birkbeck, University of London and the Natural History Museum, London. Thin-section 72415,53 was examined using an optical microscope in plane-polarised light (Fig. 5.12) and in crossed polars (Fig. 5.13). The sample is a breccia composed mainly of olivine clasts in a very fine-grained matrix. Olivine grains show a range of sizes, with the largest clasts measuring 0.6-1.7 mm, smaller olivine clasts range in size from 0.4 to 0.1 mm and fine clasts measuring ~50 µm. In addition to olivine, tiny (~100 µm) spinel symplectites are visible when magnified (Fig. 5.14).

Most of the olivine clasts are angular, but a few have more rounded edges. They often show fractures which terminate at their edges and do not continue into the matrix. These are probably the "irregular fractures" described by Snee and Ahrens (1975) who attributed them to impact shock. Some olivine grains show undulose extinction and mosaicism, but most show unit extinction (Fig. 5.12 and 5.13). These features are also probably a result of shock metamorphism, as suggested by Snee and Ahrens (1975). Carter et al. (1968) provided a classification of the degree of shock deformation in silicates of stony meteorites and stated that very distinctive textural changes take place with increasing shock pressure: (1) well-developed fracturing and local undulatory extinction at 0.15-0.2 Mb, (2) a pervasive mosaic structure at 0.25 to >0.5 Mb, and (3) abundant recrystallization at 1.0 Mb, with all gradations between. The identification of irregular fractures, undulose extinction and mosaicism would indicate that this sample experienced shock pressures ~ 0.5 Mb (50 GPa) which agrees with the study by Snee and Ahrens (1975) who suggested shock pressures of 33 GPa to 44 GPa.

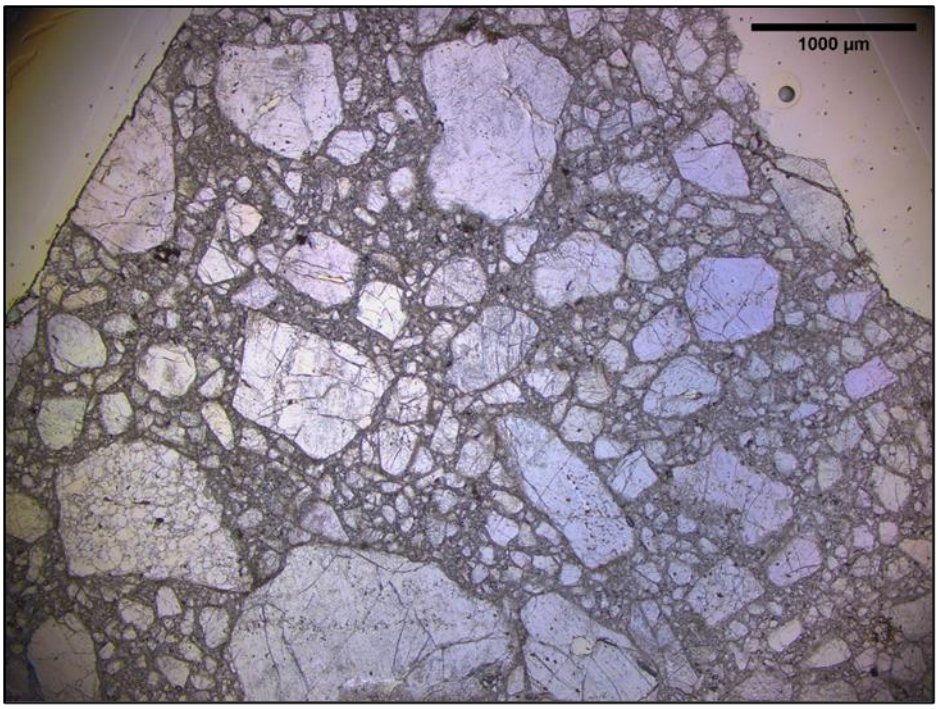

Figure 5.12. Photomicrograph of thin-section of lunar dunite TS72415,53 in plane-polarised light, showing colourless olivine clasts in a darker fine-grained matrix. Very small black minerals are Fe-Ni metal grains. Scalebar is 1000 µm. Image taken on a Zeiss Primo optical microscope, Petrology Teaching Laboratory, Birkbeck College.

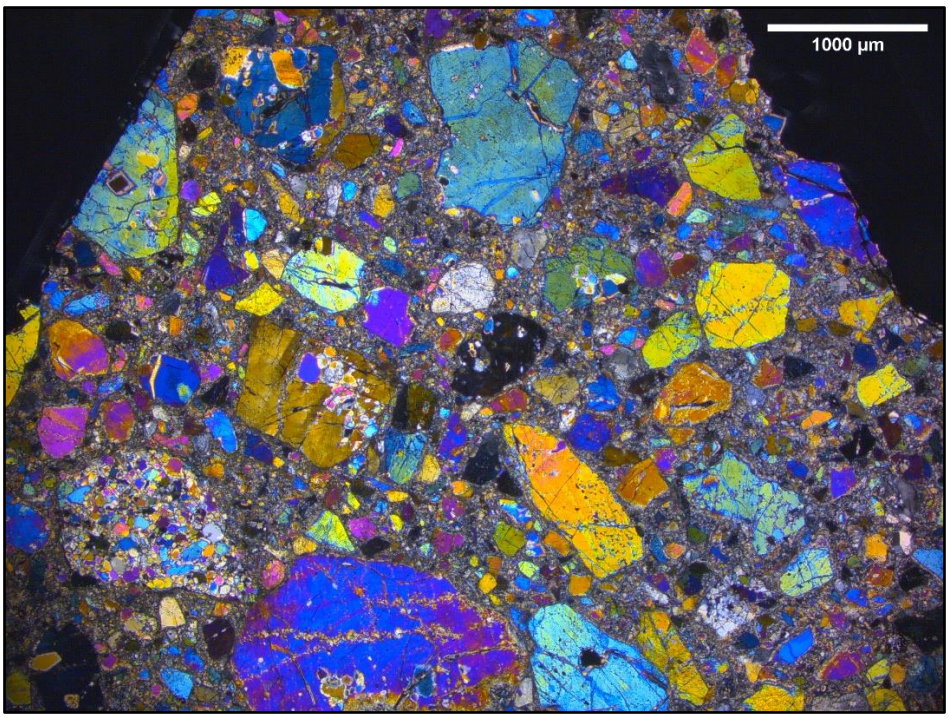

Figure 5.13. Photomicrograph of thin-section of lunar dunite TS72415,53 in crossed polars. Olivine clast in bottom left shows mosaicism; clast to the left of centre shows undulose extinction. Scalebar is 1000 µm. Image taken on a Zeiss Primo optical microscope, Petrology Teaching Laboratory, Birkbeck College.

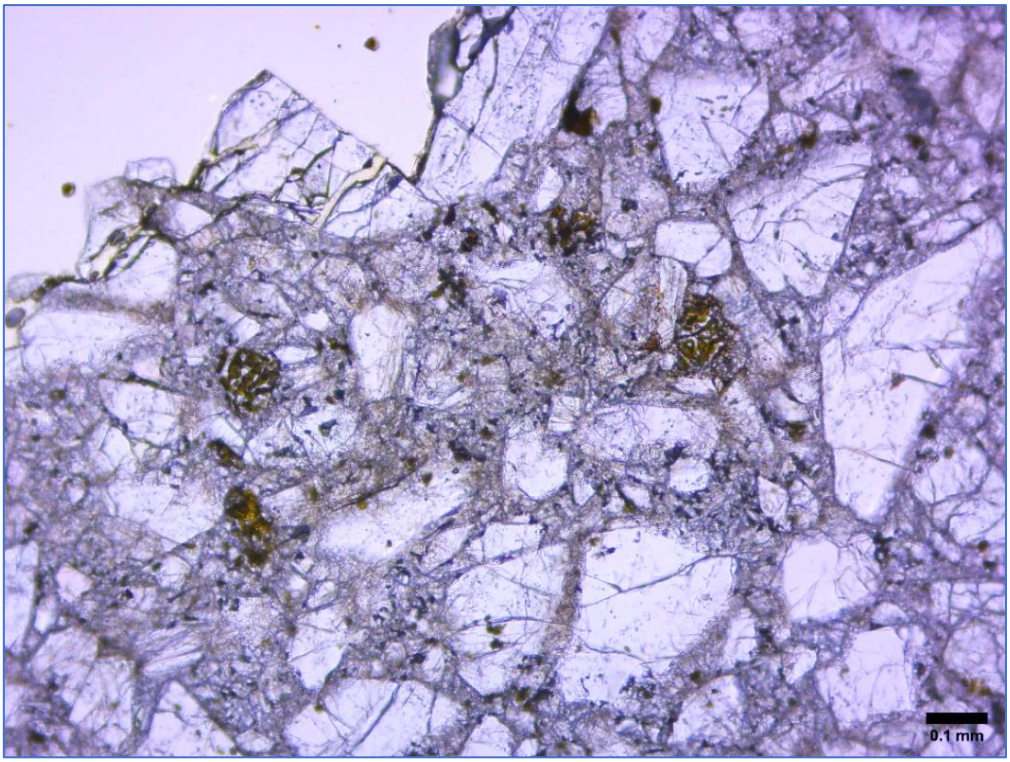

Figure 5.14. Photomicrograph of thin-section of lunar dunite TS72415,53 in plane-polarised light, showing spinel symplectite blebs. Very small black minerals are Fe-Ni metal grains. Scalebar is 0.1 mm. Image taken on a Zeiss Primo optical microscope, Petrology Teaching Laboratory, Birkbeck College.

A BSE image of thin-section 72415,53 (Fig. 5.15) confirms its brecciated texture of angular to sub-angular olivine fragments, with a size range from < 1 mm to > 100 μm set in a fine-grained matrix.

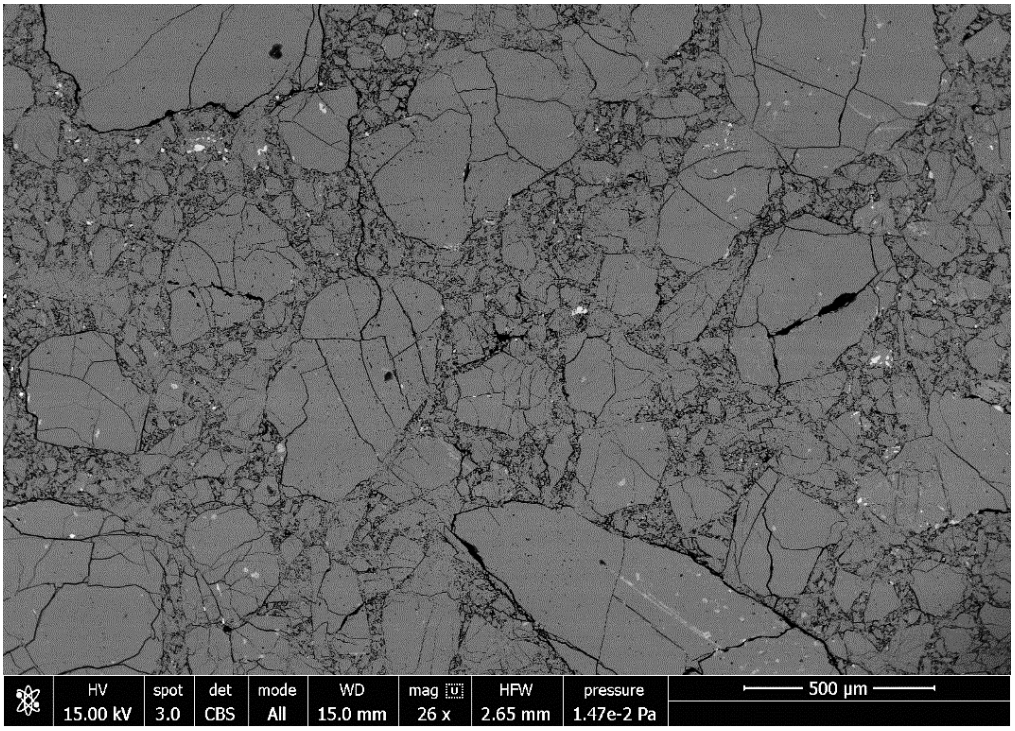

Figure 5.15. BSE of lunar dunite TS72415,53 with a brecciated texture. Large olivine clasts (medium grey) set in a fine-grained olivine matrix. Scalebar is 500 µm. Bright flecks are Fe-Ni metal; black areas are holes. Image taken on a Zeiss EVO 15LS analytical scanning electron microscope (SEM), Imaging suite, NHM London.

A false-colour electron image (Fig. 5.16) shows that the mineralogy of 72415,53 consists mostly of olivine with rare anorthite. Spinel, apatite, clinopyroxene, orthopyroxene and Fe-Ni metal are minor components. Anorthite is unevenly distributed and occurs as fine-grained lath-shaped inclusions in some of the large olivine grains. Several olivine grains have anorthite inclusions present throughout the entire grain, whilst other grains have anorthite inclusions only in portions of the grain.

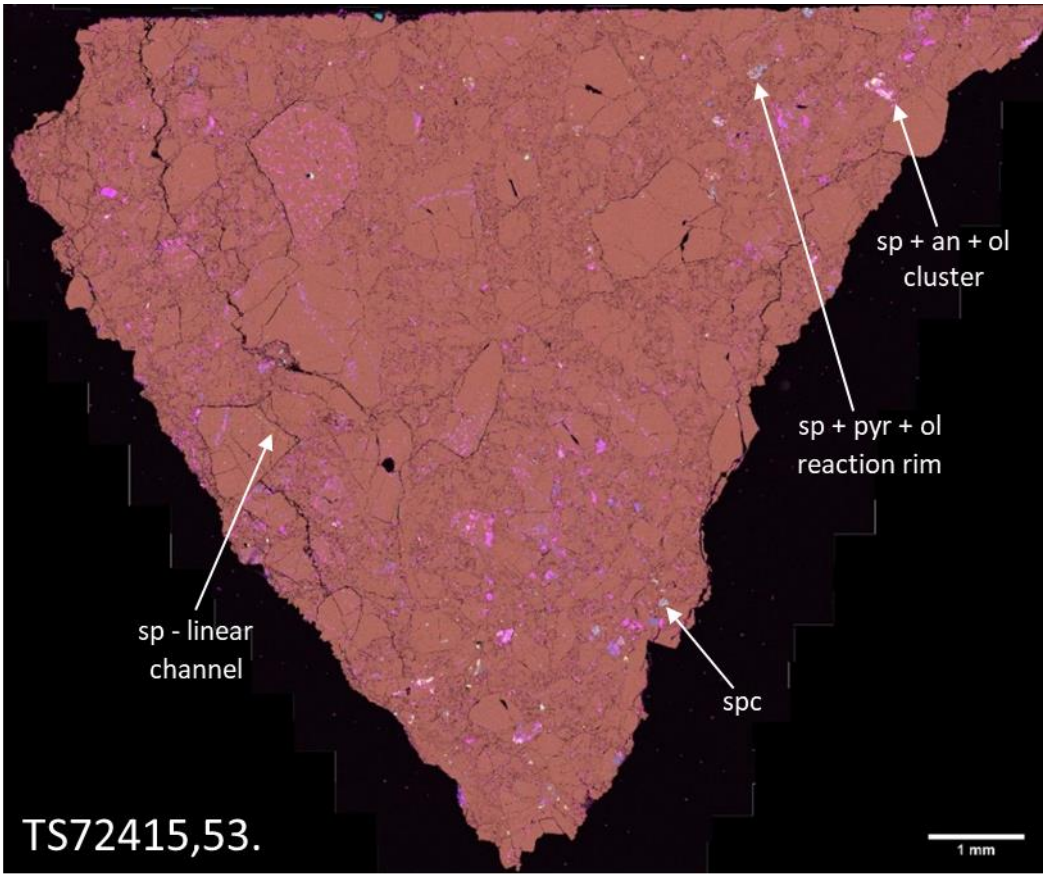

Figure 5.16. False colour montage of TS72415,53. Anorthite inclusions (pink) inside large olivine clasts (brown), spinel (yellow), pyroxene (blue) and Fe/Ni metal (green). Scalebar = 1 mm. Image taken on a Zeiss EVO 15LS analytical scanning electron microscope (SEM), Imaging suite, NHM London.

Distributed randomly through thin section 72415,53 are clasts showing symplectite textures (Fig. 5.16). Several types of spinel symplectites have been identified, varying in size and mineral associations. One common symplectite type (Type A) is between spinel + diopside ± enstatite ± Fe-Ni metal (Fig. 5.17), whereas another (Type B) is between spinel + anorthite and is closely associated with olivine (Fig. 5.18). A third type of symplectite (Type C) is only found inside olivine clasts and is composed of spinel + diopside ± enstatite (Fig. 5.19). The size of these intergrowths is ~30 µm, so they are referred to as "micro symplectite spinel-pyroxene inclusions" in this study. A fourth type of symplectite (Type D) is also only found inside olivine clasts either as linear channels running through the olivine clast or spinel blebs isolated on a single region on the rim of an olivine clast. Type D structures are composed of spinel ± diopside (Fig. 5.23).

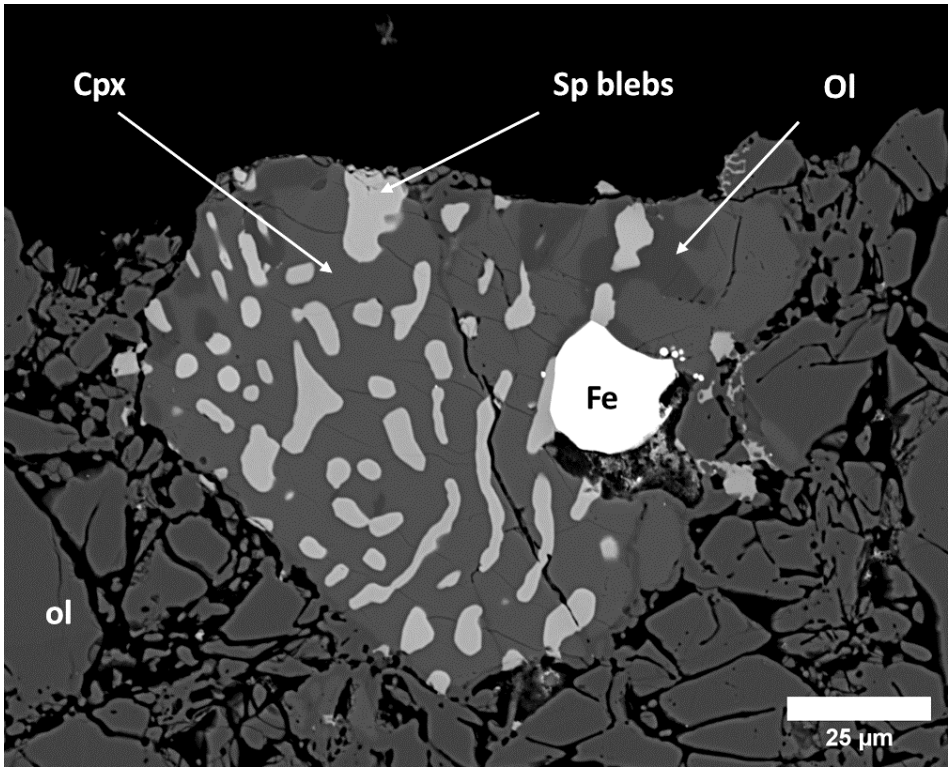

Figure 5.17. BSE of a Type A spinel-pyroxene symplectite clast in lunar dunite TS72415,53. Scalebar is 25 µm. White mineral is spinel. Bright grey mineral is clinopyroxene. Dark grey mineral is orthopyroxene. Bright white mineral is Fe/Ni metal. Image taken on a Jeol JXA8100 Superprobe, Department of Earth and Planetary Sciences, Birkbeck College.

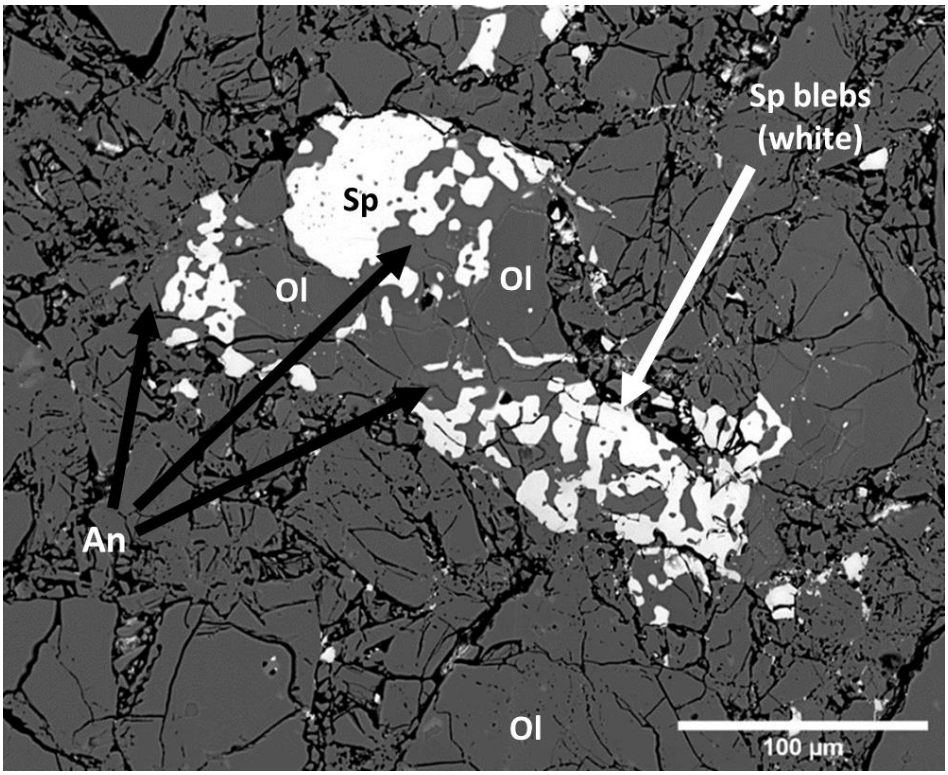

Figure 5.18. BSE image of Type B spinel-olivine texture in lunar dunite TS72415,53. Scalebar is 100 µm. Bright mineral is spinel. Image taken on a Jeol JXA8100 Superprobe, Department of Earth and Planetary Sciences, Birkbeck College.

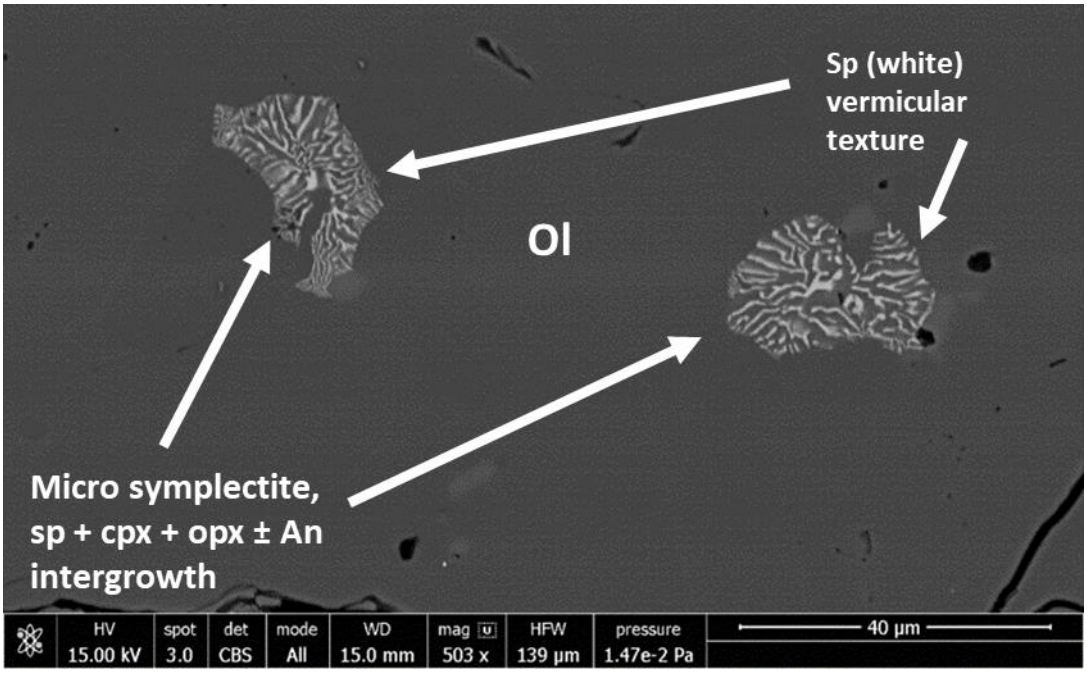

Figure 5.19. BSE of a Type C micro-symplectite in a large olivine clast in lunar dunite TS72415,53. Scalebar is 40 µm. Bright mineral is spinel. Image taken on a Zeiss EVO 15LS analytical scanning electron microscope (SEM), Imaging suite, NHM London.

The different types of spinel textures identified in 72415,53 are best displayed in false-colour X-Ray maps. Type A are found as individual clasts formed by clusters of spinel + diopside ± enstatite (Fig. Fig. 5.20). Spinel displays a strong vermicular texture with elongate branches throughout the clast. The Type B texture is a cluster formed of spinel + anorthite + olivine (Fig. 5.21). Spinel and anorthite are closely associated with olivine forming one complex structure. The spinel is much less vermicular in texture compared to that in Type A and forms blocky grains both connected with other grains and in isolation. The Type C texture is found as abundant inclusions of a micro-symplectite of spinel + diopside ± enstatite only found inside single olivine clasts and is much smaller than Type A and B (<30 µm in size) (Fig. 5.22). Spinel in these micro-symplectites inclusions displays a strong vermicular texture. Spinel-pyroxene structures are also visible on single edges of several large olivine clasts where they form large lobate arms (Fig. 5.22A). TS72415,53 contains a single example of apatite (Fig. 5.24), which forms along cracks and larger blebs within olivine clasts.

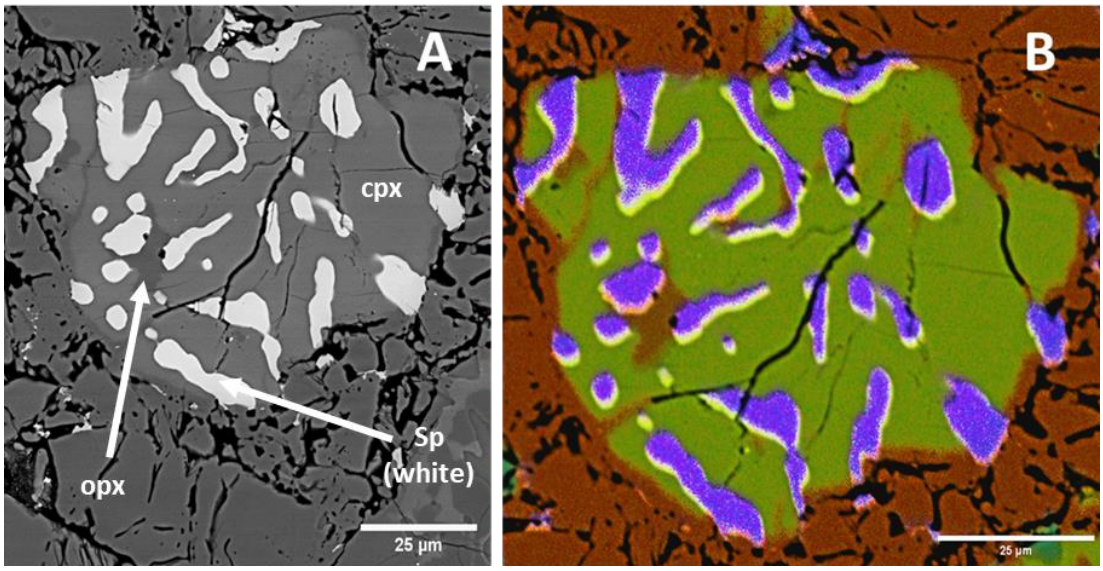

Figure 5.20. (A) BSE and (B) false colour image of a Type A spinel texture with vermicular texture. spinel (purple) + clinopyroxene (green) + orthopyroxene (light brown) symplectite (Type 1a) clast from TS 72415,53. Scalebar = 25 µm. Image taken on a Jeol JXA8100 Superprobe, Department of Earth and Planetary Sciences, Birkbeck College.

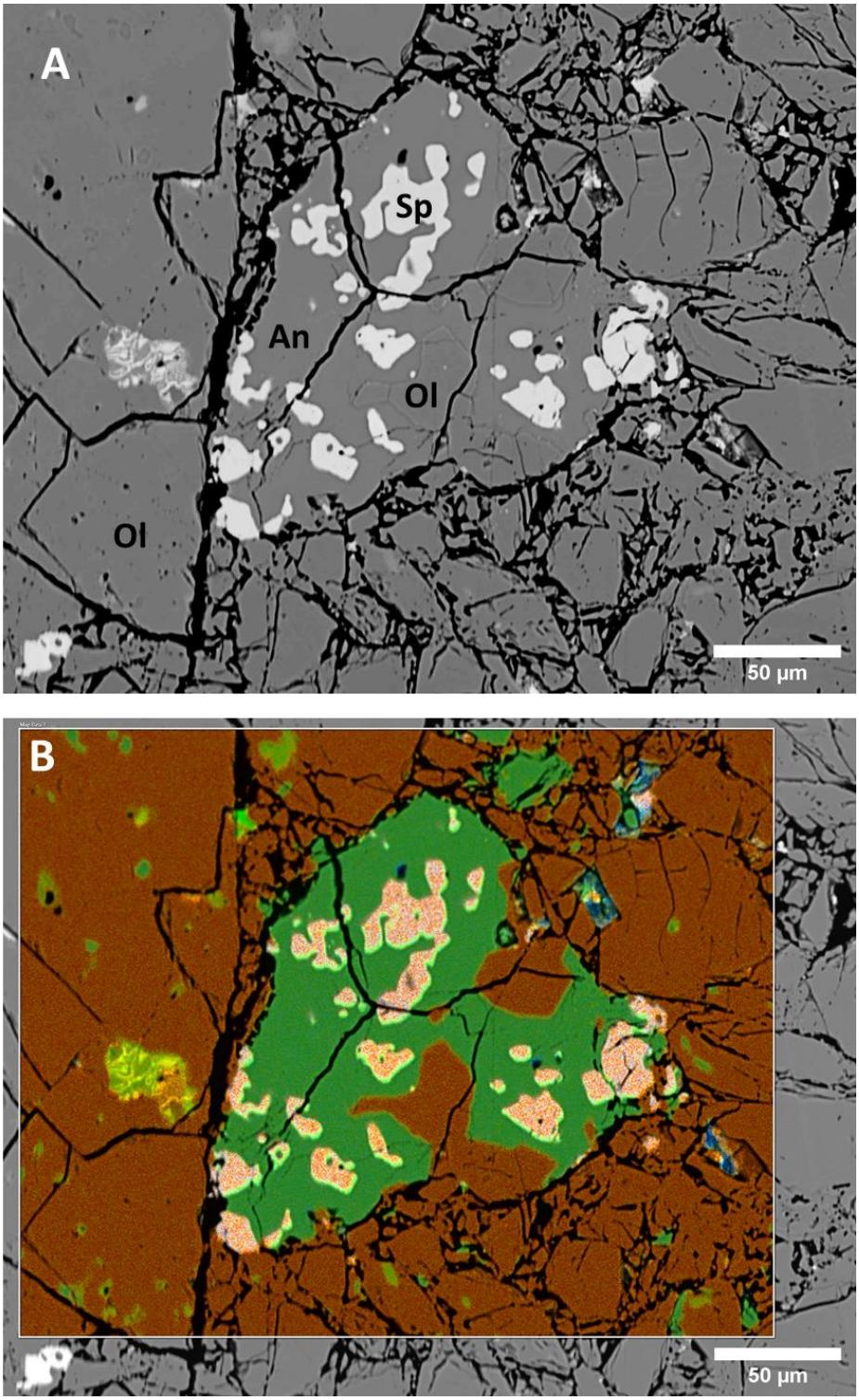

Figure 5.21. (A) BSE and (B) false colour image of a Type B spinel texture. Spinel (pink) + anorthite (dark green) + olivine (brown) symplectite clast in TS 72415,53. Scalebar = 50 µm. Image taken on a Jeol JXA8100 Superprobe, Department of Earth and Planetary Sciences, Birkbeck College.

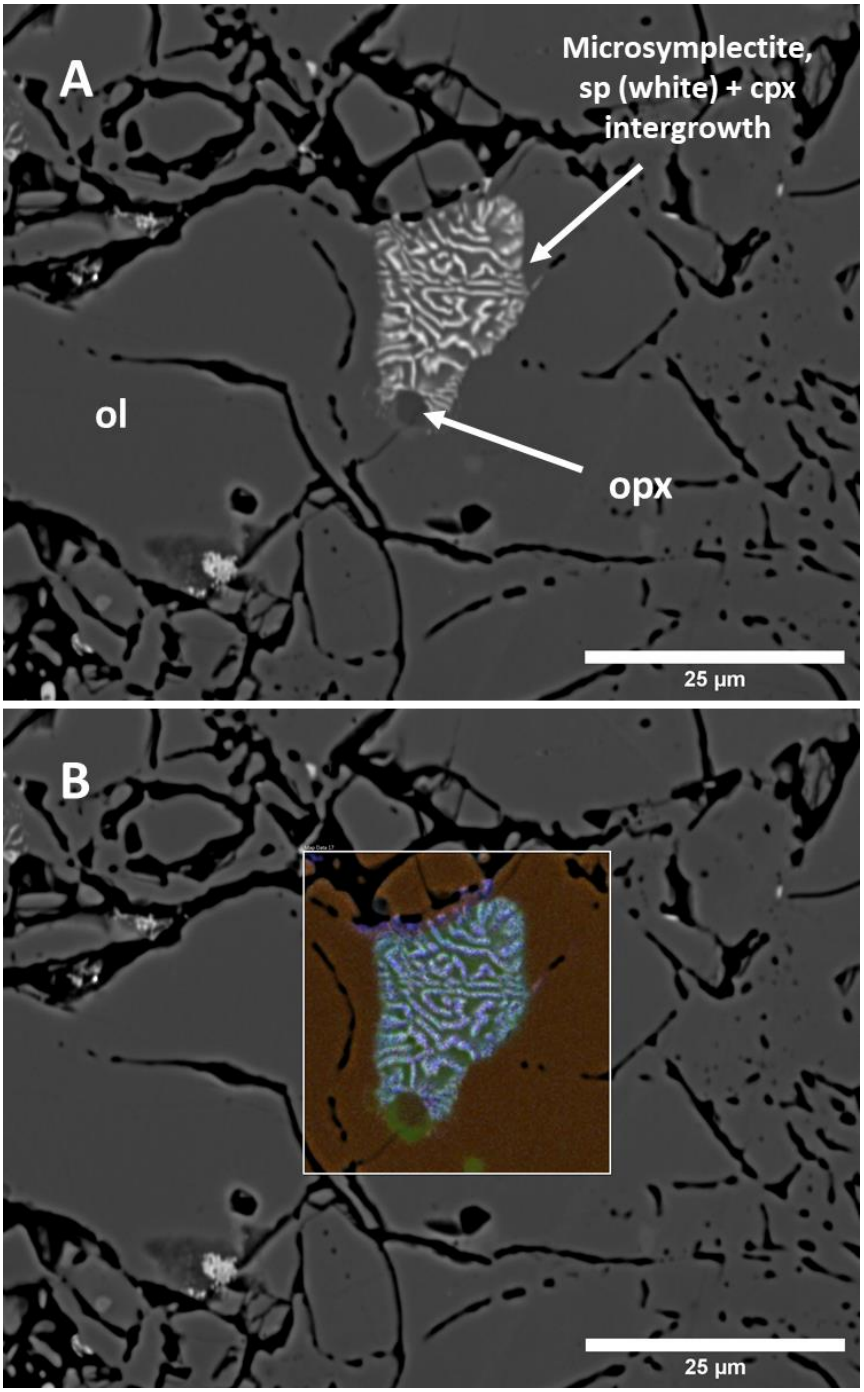

Figure 5.22. (A) BSE and (B) false colour image of a symplectite (Type C) only found inside single olivine clasts, composed of spinel (purple) + diopside (green) ± enstatite (light brown). Scalebar =25 µm. Image taken on a Jeol JXA8100 Superprobe, Department of Earth and Planetary Sciences, Birkbeck College.

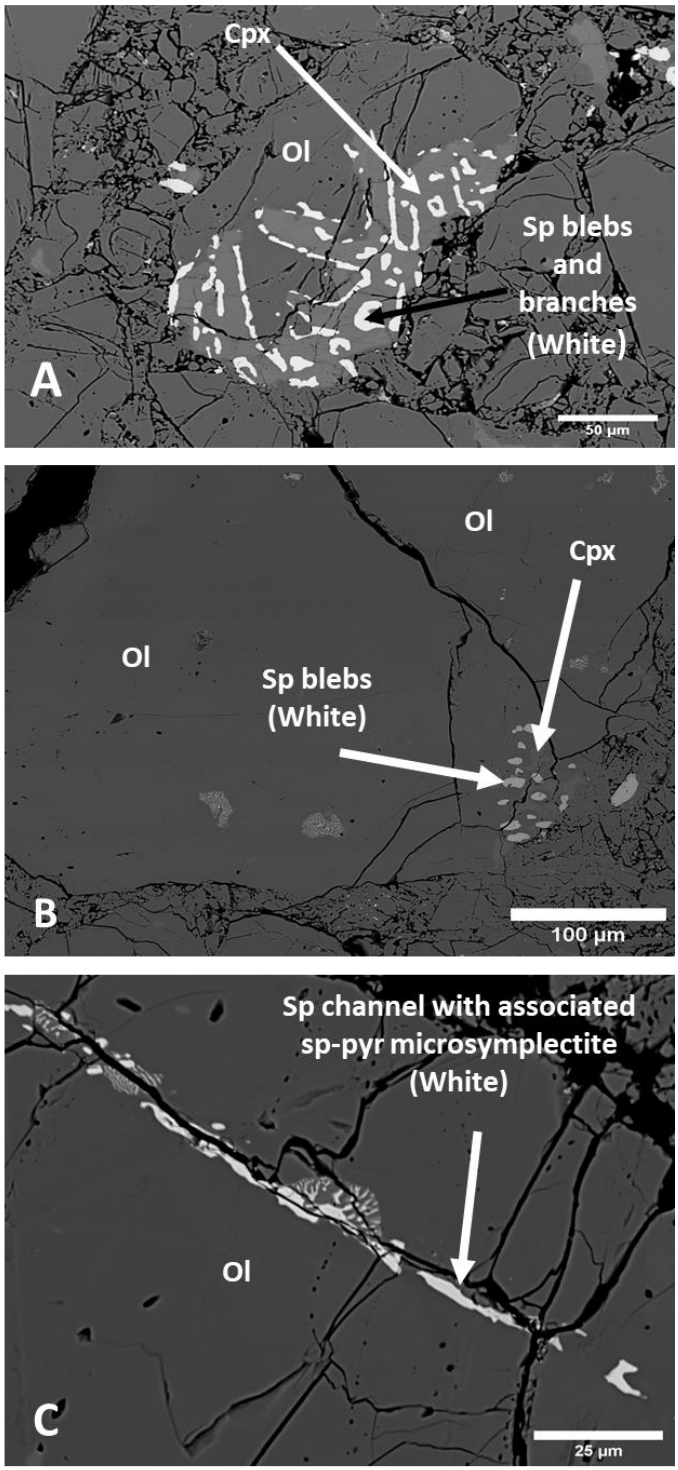

Figure 5.23. (A) BSE image of a type D spinel texture on the rim of an olivine clast. Spinel with vermicular texture. Spinel + cpx structure forms large lobate arms. Spinel (white) + clinopyroxene (grey) + olivine (dark grey) clast from TS 72415,53. Scalebar = 50 µm. Image taken on a Zeiss EVO 15LS analytical scanning electron microscope (SEM), Imaging suite, NHM London. (B) BSE image of a type D spinel texture on isolated rim of an olivine clast. Spinel with block texture. spinel (white) + clinopyroxene (grey) + olivine (dark grey) clast from TS 72415,53. Scalebar = 100 µm. Image taken on a Zeiss EVO 15LS analytical scanning electron microscope (SEM), Imaging suite, NHM London. (C) BSE image of a type D spinel channel texture running through olivine clast. Spinel forms a linear texture. spinel (white) + clinopyroxene (grey) + olivine (dark grey) clast from TS 72415,53. Scalebar = 100 µm. Image taken on a Jeol JXA8100 Superprobe, Department of Earth and Planetary Sciences, Birkbeck College.

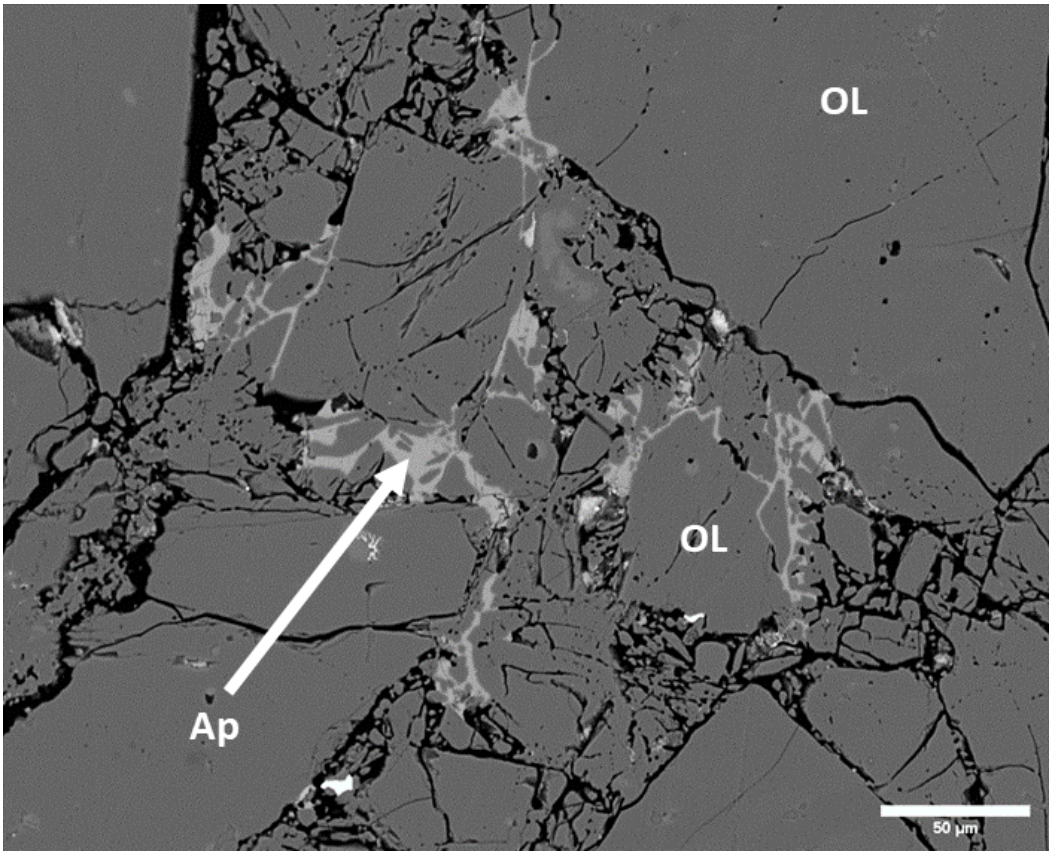

Figure 5.24. BSE image of apatite (light grey) inside large olivine clasts. Scalebar = 50 µm. Image taken on a Jeol JXA8100 Superprobe, Department of Earth and Planetary Sciences, Birkbeck College.

5.4 Micro-CT analysis.

The 3D textures of the lunar dunite samples 72415,4 and 72417,9003 were investigated using micro-CT analysis. Micro-CT data was collected at the Natural History Museum, London on a Zeiss Xradia Versa 520 is a high-resolution micro-CT scanner. Due to the extremely small size (~2 mm diameter) and the priceless nature of the samples, they were not cored but scanned without any preparation. Samples were placed in plastic bags and packed to secure restrict movement during collection rotation and placed inside a plastic tube and mounted on the sample stage of the instrument. Typical data collection parameters for collection were a source setting of 88 kV and 88 µA, exposure time of 7s, LE1 source filter and a pixel size of 1.9248 µm. For the 3D and 2D slice images were processed using both the Avizo and ORS Dragonfly 3D visualization software suites. Each dunite sample is composed of several small angular fragments. Typical size of samples analysed is shown in Figure 5.25 A and B. As EMPA analysis had revealed an uneven distribution of spinel throughout the sample, only the larger fragments were selected for analysis because they are more representative and more likely to contain spinel symplectites.

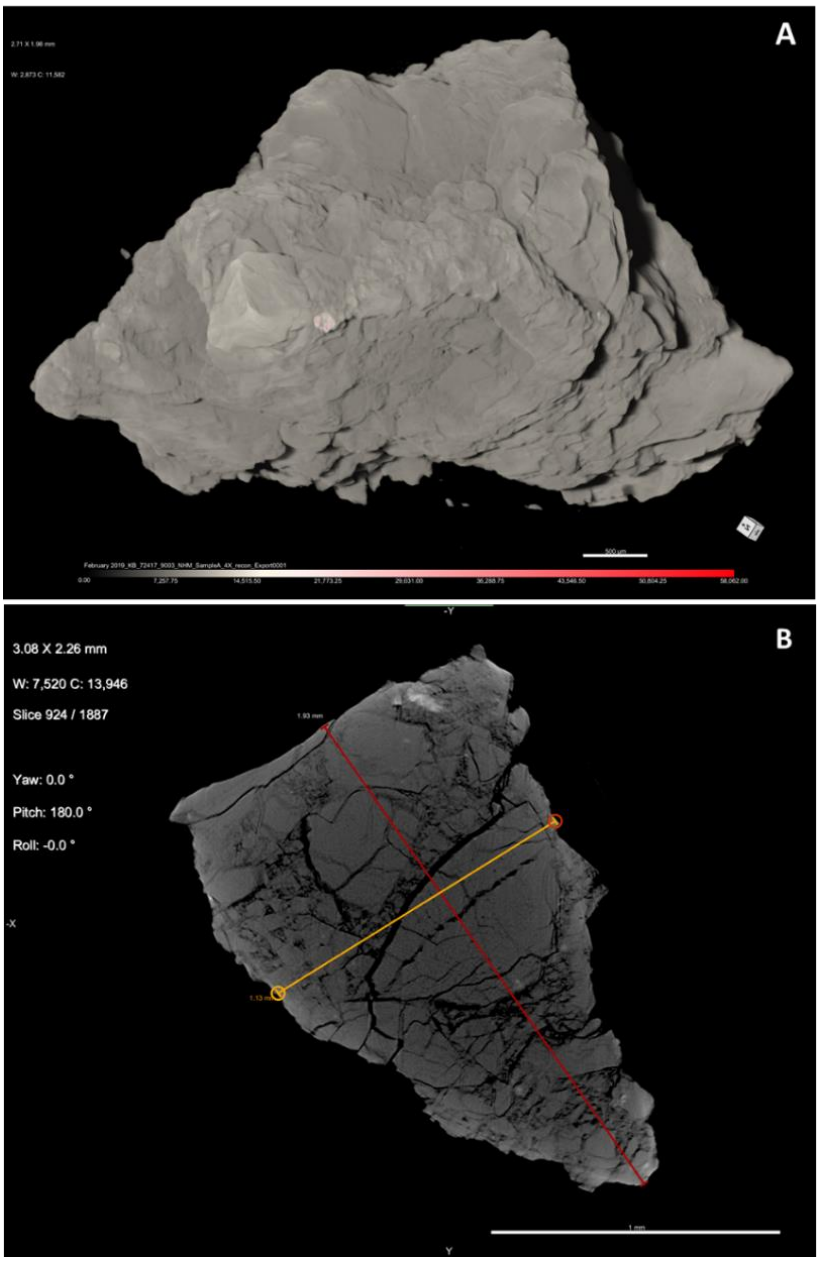

Figure 5.25. Image of a fragment of lunar dunite 72117, 9003: (A) solid, (B) 2D slice. Dimensions 1.93 x 1.13 x 2.64 mm. Slice thickness 0.0014 mm. Scale 1 mm. Images processed using Dragonfly CT software (Object Research Systems (ORS) inc. Ver. 2020.1)

Micro-CT analysis confirmed that spinel occurs in several different textural types of varying size, shape and mineral associations within the dunite fragments. These include:

Type A spinel-pyroxene clusters which are single grains with randomly orientated elliptical (~ 0.3 mm) intergrowths of highly vermicular spinel within pyroxenes (cpx>>opx). In these clusters, individual spinel branches are in contact with each other and thus the spinel forms a single crystal. Individual spinel-pyroxene clusters generally have rounded edges but can have angular margins indicating that the cluster has been fractured.

Type B spinel/anorthite/Fe metal/olivine clusters which are large highly complex intergrowths with a less vermicular and blocky spinel. In these clusters, multiple individual branches of spinel are visible throughout the cluster. Individual spinel branches are elongate and form linear features which display a weak parallel orientation. These linear spinels often terminate in highly elliptical and very flat plate-like structures which when viewed together form an elliptical complex. These anorthite-rich clusters do not show any textural evidence for fracturing.

Type C tiny spinel-pyroxene inclusions are present inside olivine grains but cannot be easily imaged in 3D by CT scanning because of their small size. However, 2D slice images show small specks of high-density spinel inclusions randomly distributed in olivine grains.

Type D tiny spinel/pyroxene/olivine reaction rims. These are 75 µm in average diameter, and only occur on the edges of olivine grains. These are also difficult to analyse in 3D by CT but can be identified in 2D slices.

5.4.1 Type A Spinel-pyroxene clusters

Type A spinel-pyroxene clusters have been identified in fragments of sample 72417,9003. Figure 5.26 shows a 3D rendered image of this texture. Spinel forms a highly complex structure, elliptical in shape with a strong vermicular texture. Dimensions of the complex structure are 0.28 x 0.14 x 0.29 mm. Individual spinel branches are in contact with one another, thus forming a single grain. The length of the branches is ~50 µm. Branches are not uniform in thickness. Larger branches are ~10 µm in width (Fig. 5.27). A low-density phase is visible between the spinel branches; this is interpreted as pyroxene, as seen in the BSE image in figure 5.17. Spinel is wholly contained with the cluster and there is no olivine associated with the clusters. In one example, seen in the 3D and 2D slice image (Fig. 5.27), there is a straight edge which implies that this grain has been fractured.

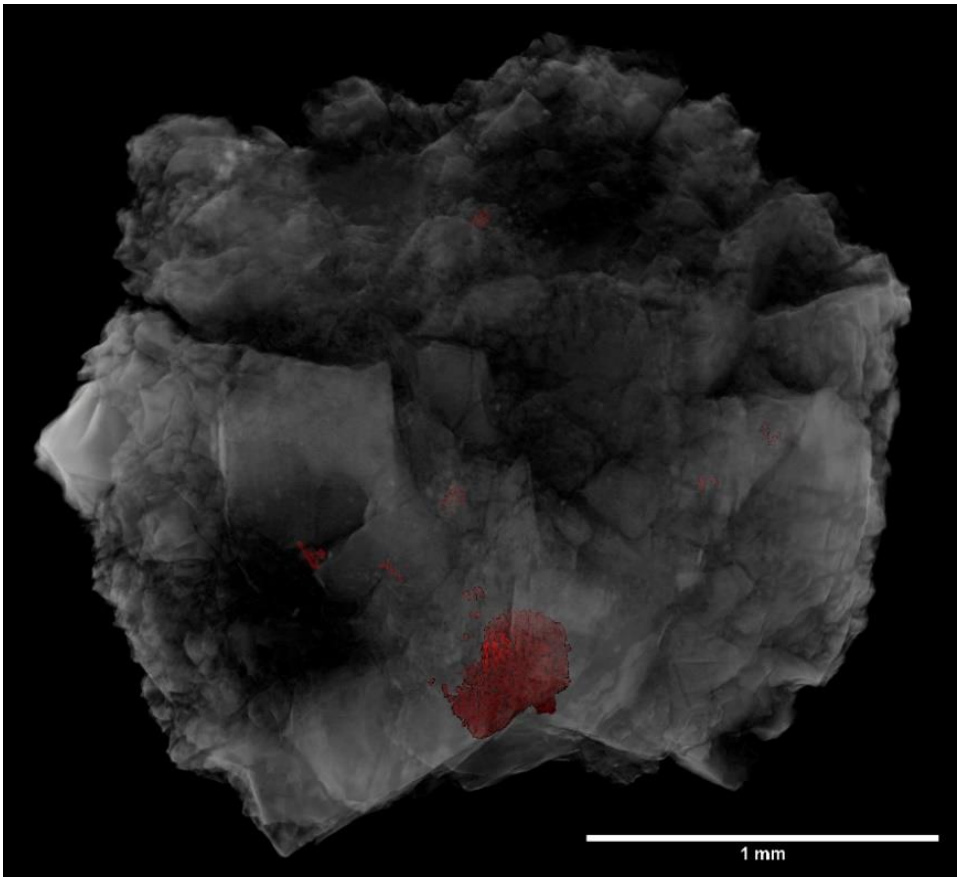

Figure 5.26. 3D rendered image of an individual Type A spinel-pyroxene cluster in lunar dunite sample 72417,9009. Scalebar 1mm. Image processed using Avizo software suite.

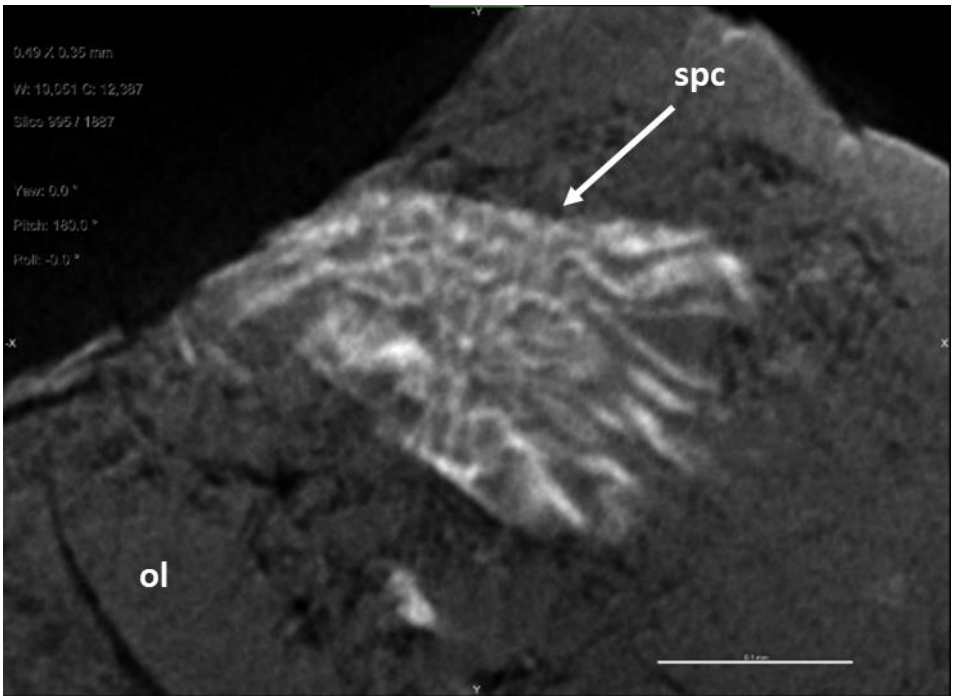

Figure 5.27. 2D slice image in grayscale highlighting a Type A spinel-pyroxene cluster in 72417,9003. Scalebar 0.1 mm. Images processed using Dragonfly CT software (Object Research Systems (ORS) inc. Ver. 2020.1).

5.4.2 Type B Spinel/anorthite/Fe Metal/olivine clusters

Type B Spinel/anorthite/ Fe Metal/olivine clusters are found in fragments of sample 72415,4 (Fig. 5.28) forming large complex clusters ca. 1.5 mm in length. The whole clusters are generally elliptical in shape with dimensions of 2.37 x 2.43 x 3.21 mm. Spinel is less vermicular than in the Type A spinel-pyroxene clusters and appears to display a blockier texture. It forms numerous elongate features with various lengths with the larger features ~ 0.4 mm in length and 0.06 mm width. Several elongated spinels lie in a near parallel orientation showing some degree of alignment. Spinel branches are connected, thus forming a single grain. However, several satellite spinel structures surround the large spinel. These smaller complexes are considered to form part of the larger spinel.

In 2D slice image (Fig. 5.28), spinel forms blocky blebs concentrated in a small region of the cluster. Spinel blebs range in size from 20 to 80 µm. Finer spinel grains are also visible randomly distributed amongst the larger spinel blebs. Spinel is not confined to a single grain but appears in a highly fractured section of the lunar dunite sample and is strongly associated with two silicate phases which are interpreted has olivine and anorthite (as seen in the BSE images of this texture (Fig. 5.21A). When individual slices are viewed through the volumetric stack, the blebs are clearly the cross-section of the elongate spinels described above. Larger olivine fragments reveal that spinel (and the low-density phase which is probably anorthite) form an olivine + spinel + low density silicate (anorthite) structure. 2D images also show a high-density phase forming generally circular blebs within the complex structure. The 3D volume shows that several large high density spherical blebs exist with a number of blebs terminating at the end of spinel channels. This phase has been interpreted as Fe Metal (Fig. 5.28C).

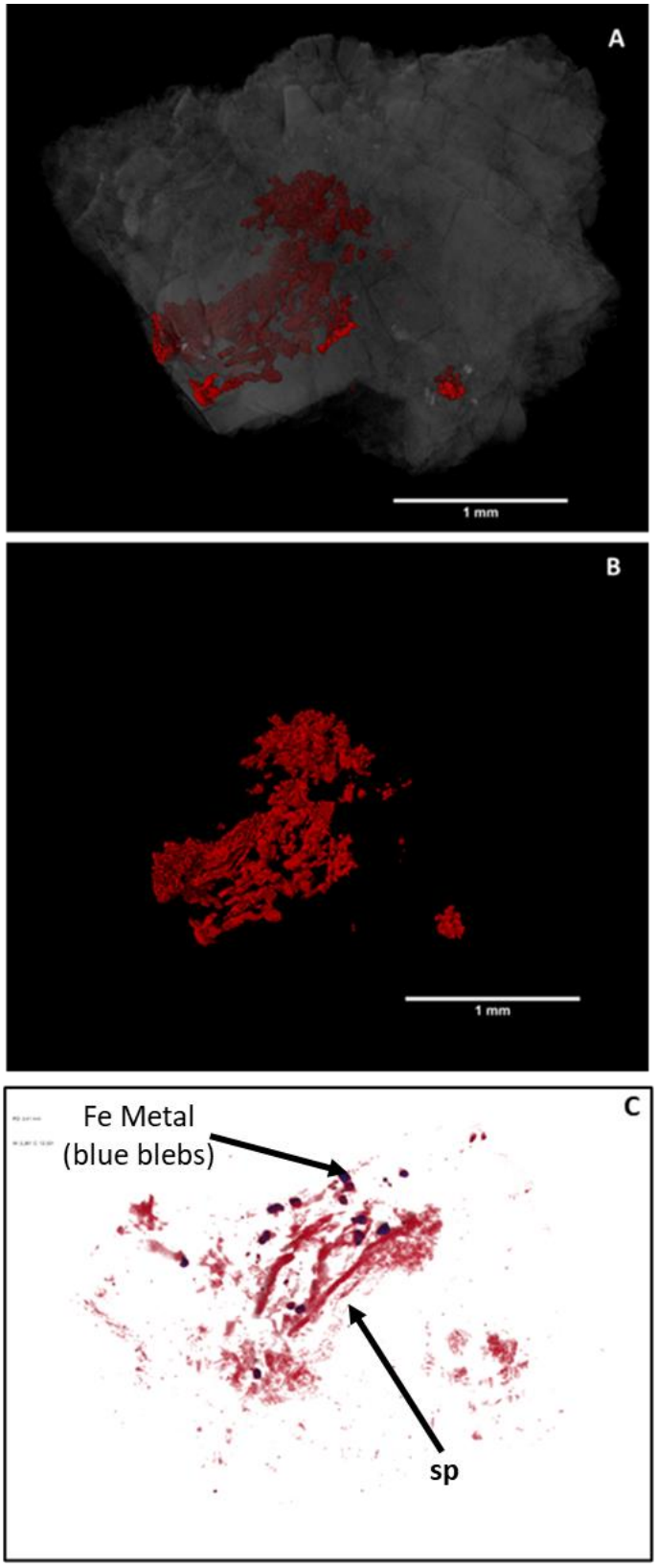

Figure 5.28. (A) 3D rendered image of a Type B spinel-anorthite-olivine structure in lunar dunite 72415,4. Scalebar 1 mm. (B) 3D rendered image of spinel in a single cluster, with silicate phases removed. Scalebar 1 mm. (C) 3D rendered image of type complex structure with Fe Metal (blue) blebs within spinel (red) channels. Image processed using Dragonfly CT software (Object Research Systems (ORS) inc. Ver. 2020.

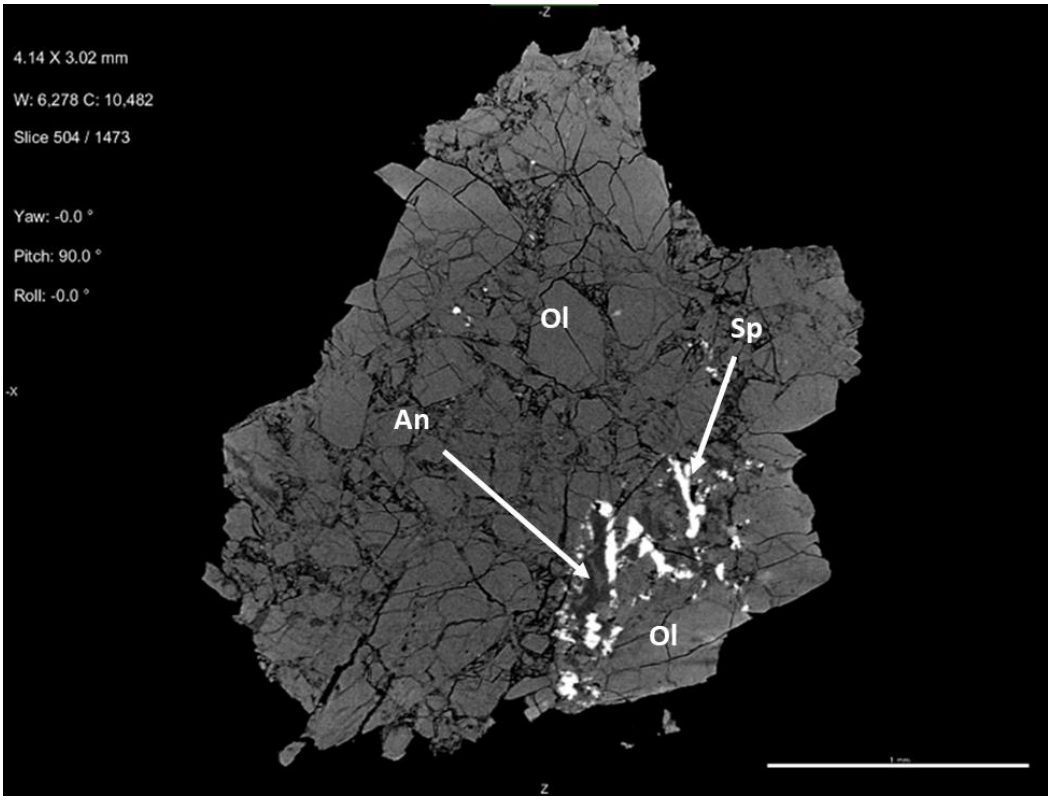

Figure 5.29. 2D slice image of a Type B spinel + olivine + anorthite cluster in lunar dunite 72415,4. Scalebar 1 mm. Bright mineral is spinel. Dark grey mineral is anorthite. Images processed using Dragonfly CT software (Object Research Systems (ORS) inc. Ver. 2020.

A second spinel-anorthite-olivine texture is also visible in the 3D volume. Spinel forms an elongate feature running through a large olivine grain. Spinel consists of fine blocky blebs with a generally uniform size. The structure overall shape is that of a flat narrow-tapered channel (Fig. 5.29). This structure is also associated with the low-density silicate phase (anorthite). Dimensions are 0.72 mm x 0.08 mm x 0.27 mm. This spinel filament has been interpreted not has an isolated vein but as part of the type B complex structure (Fig. 5.28C and Fig. 5.30).

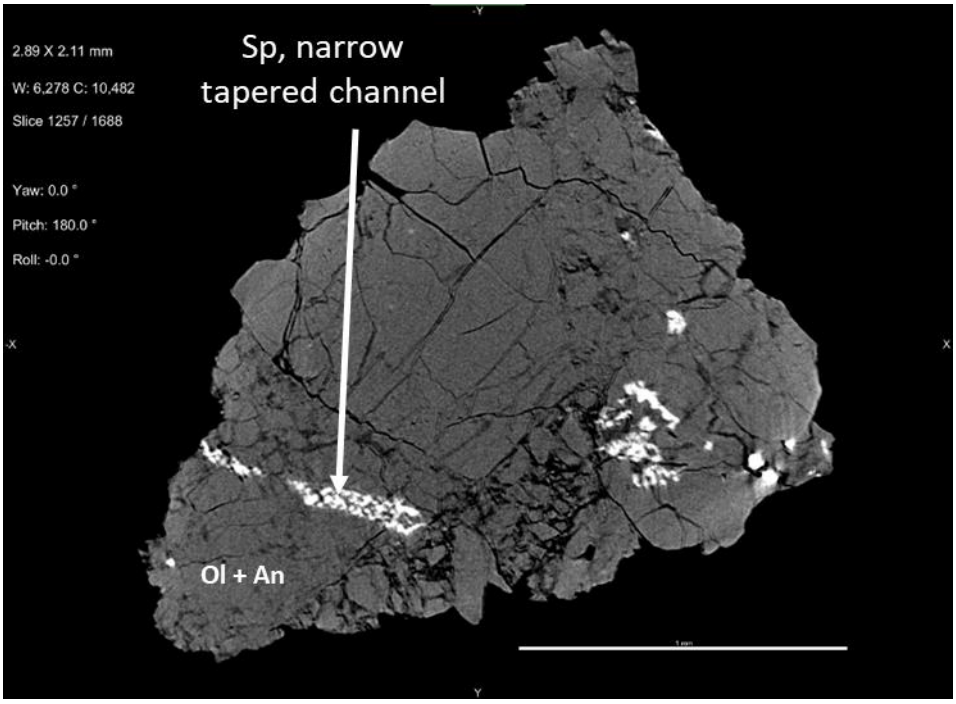

Figure 5.30. 2D slice image of a narrow-tapered channel of spinel + olivine + anorthite structure in lunar dunite 72415,4. Scalebar 1 mm. Images processed using Dragonfly CT software (Object Research Systems (ORS) inc. Ver. 2020.1).

Spinel in 72415,4 also forms a large (>1 mm length) complex spinel/anorthite/olivine structure (Fig. 5.31 and Fig. 5.32). Spinel forms multiple channels varying in length with the larger channels ~ 0.3 mm in length and 0.1 mm width. Spinel is more concentrated and less dispersed compared with the texture in the spinel-anorthite-olivine structure shown in Figure 5.28. Spinel channels display a degree of alignment. Spinel branches are connected, thus forming a single grain. The general shape of the whole complex structure is elliptical. Spinel is less vermicular and appears to display a blocky texture. Dimensions of the complex structure are 2.59 x 2.65 x 3.83 mm. Individual slices through the volumetric stack show that the spinel blebs are isolated within an olivine grain which also forms an olivine + spinel + low density silicate structure.

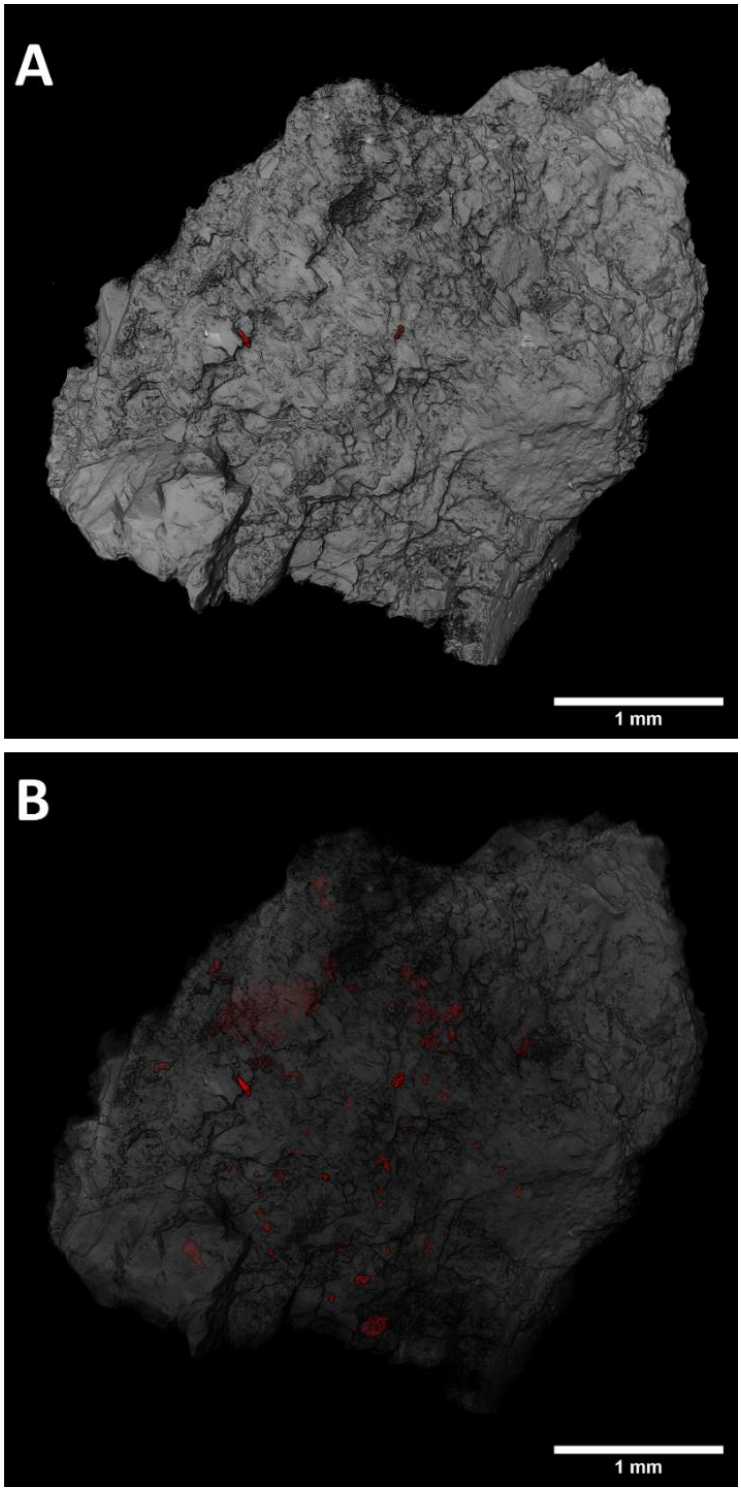

Figure 5.31. (A) 3D rendered image of Sample 72415,4, Solid. Scalebar 1mm. (B) 3D rendered image of Sample 72415,4. Silicate phase set to semi-transparent. Spinel phase highlighted in red. Scalebar 1 mm. Images processed using Avizo software suite.

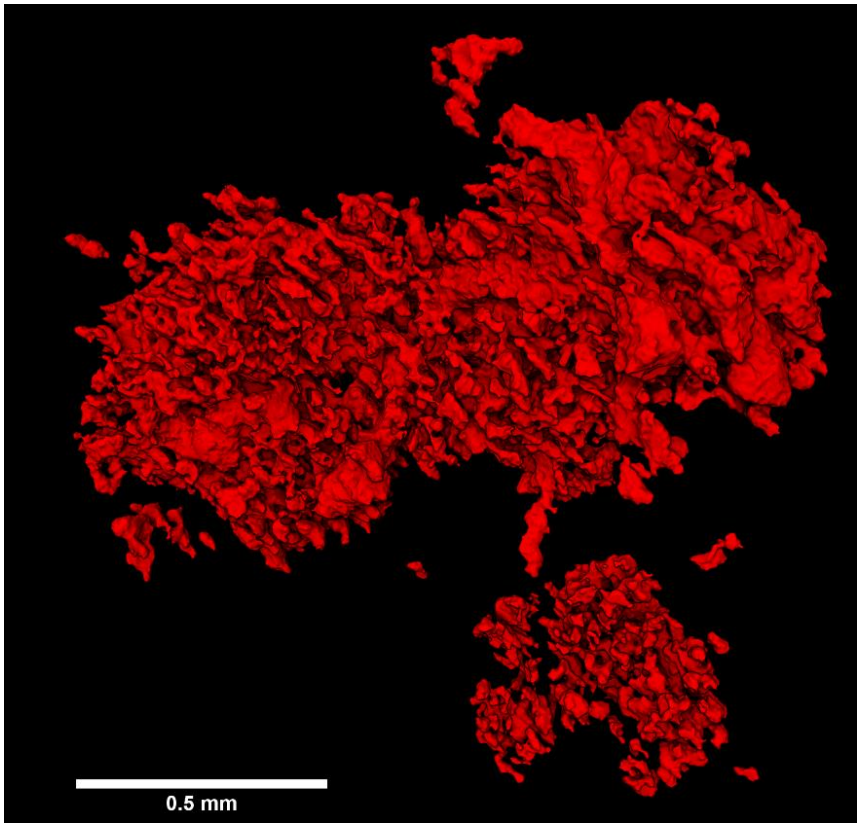

Figure 5.32. 3D rendered image of a type B of a spinel texture in a spinel-anorthite olivine structure in lunar dunite 72415,4. Scalebar 0.5 mm. Images processed using Avizo software suite.

5.4.3 Type C, Microsymplectites and Type D spinel textural types.

Type C spinel-pyroxene microsymplectites and type D spinel textures are found in olivine grains of sample TS 72415,53 (Fig. 5.22 and Fig. 5.33). These textures are difficult to render in the 3D volume, but analysis of the 2D individual slice images of 72415 and 72417 the spinel microsymplectites can be resolved i.e., showing has bright elliptical specks within an olivine clast. Type C textures appear on large olivine clasts randomly distributed with no appearance of lineation or alignment. However, the 2D images do show that certain grains do show higher concentrations of microsymplectites where other regions and clasts remain devoid of this texture. The Z dimension of these structures is ~ 25 µm. This confirms that the microsymplectites are circular to elliptical in shape and exist has isolated inclusions within olivine grains.

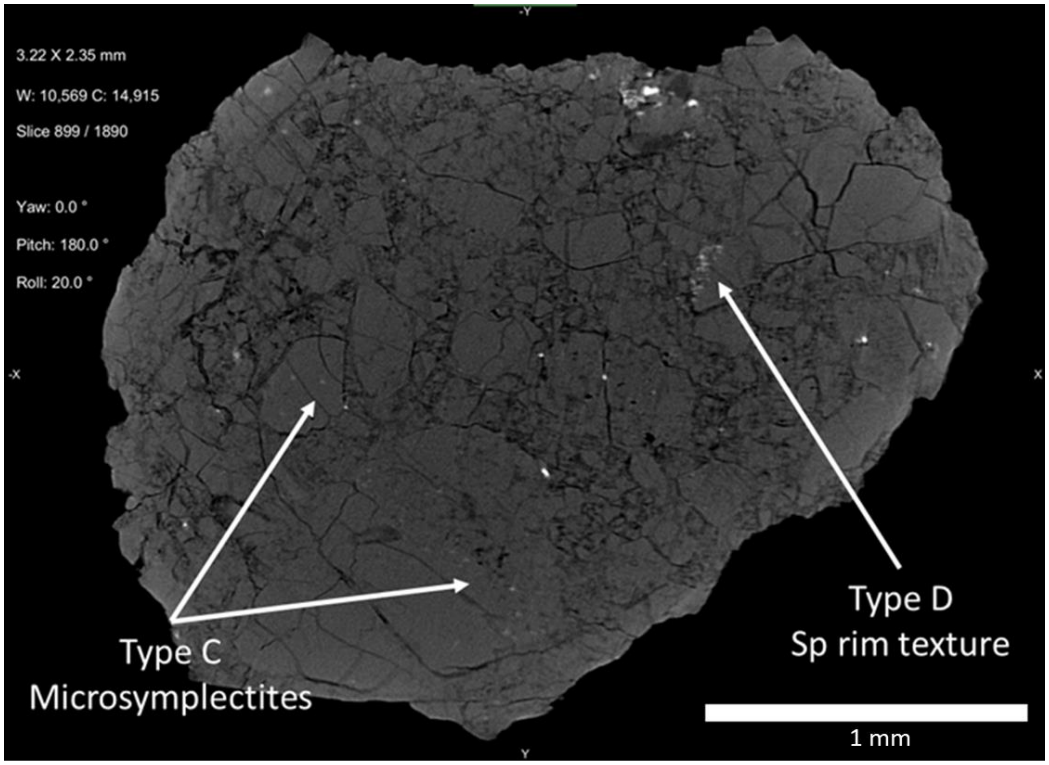

Figure 5.33. 2D slice image of a spinel Type C (microsymplectite) textures and type D spinel rim texture in lunar dunite 72417,9003. Scalebar 1 mm. Images processed using Dragonfly CT software (Object Research Systems (ORS) inc. Ver. 2020.1). Due to extreme small size of Type C and type D spinel textures and difficulty in fully resolving these textures, resolution is low.

Type D rim textures are also difficult to resolve in the 3D volume due to their small size, i.e. <75 µm. They form flattened elliptical channels and blebs on isolated rims of olivine clasts (Fig. 5.33). However, through the Avizo magic wand processing tool manual assignment of grey scale intensities, these small structures on isolated olivine rims can be segmented. The 3D structures show these to be confined to extreme rims of olivine grains. Examples of type D rim textures are shown in the 3D rendered imagine in Figure 5.34 A and B.

2D slice images of sample 72417,9003 have revealed several linear spinel channels. The images show that these channels are generally straight and can be seen bisecting olivine grains. Large linear spinel channels are also associated with semi-circular symplectite blebs (Figures 5.35 and 5.23C).

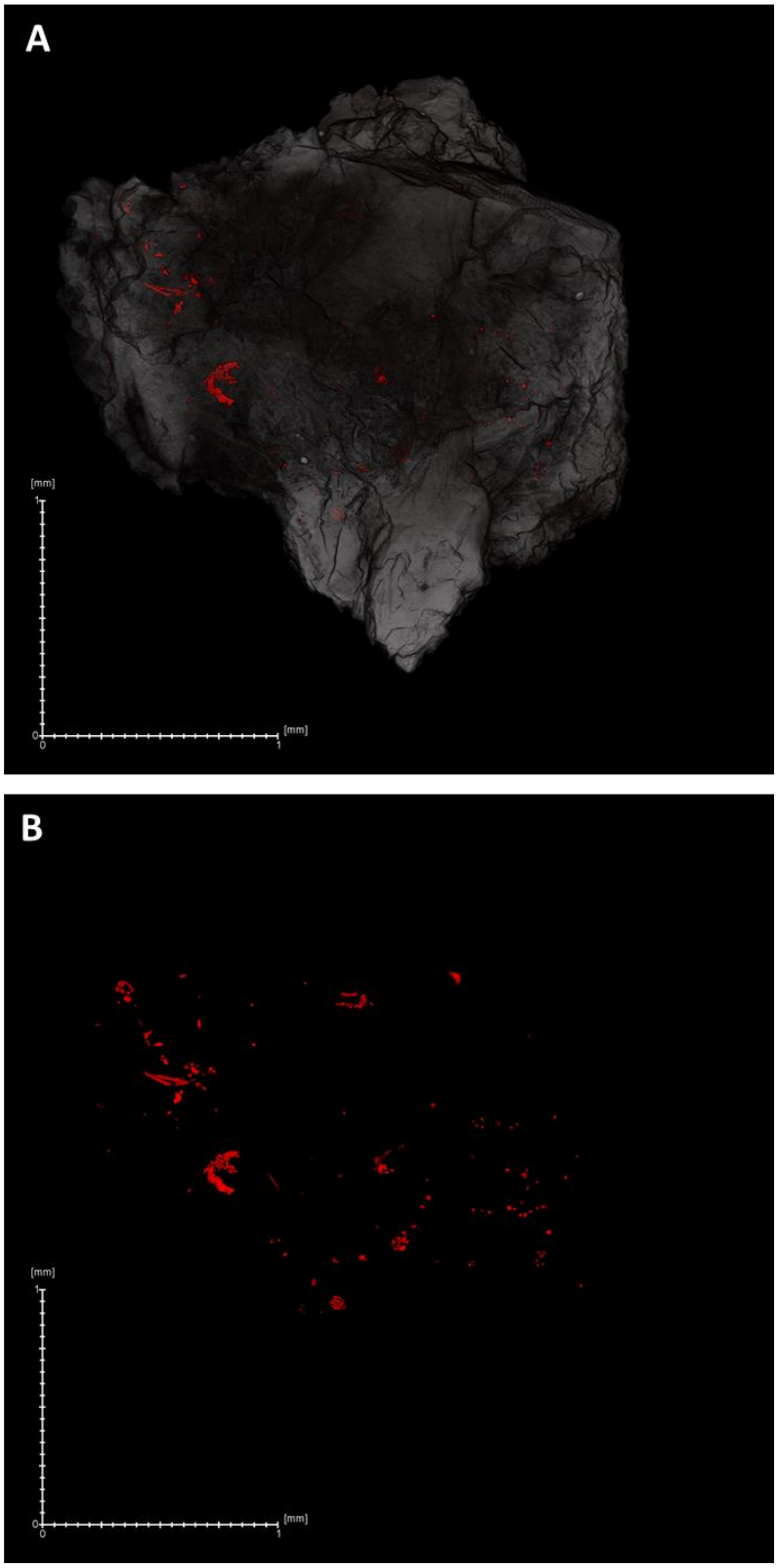

Figure 5.34. (A) 3D rendered in of a spinel (red) type D texture on an isolated rim of an olivine clast in lunar dunite 72417,9003. Silicate phase (grey) set to semi-transparent. Scalebar 1 mm. (B) 3D rendered in of a spinel type D texture (red) on an isolated rim of an olivine clast in lunar dunite 72417,9003. Silicate phase removed. Scalebar 1 mm. Images processed using Avizo software suite.

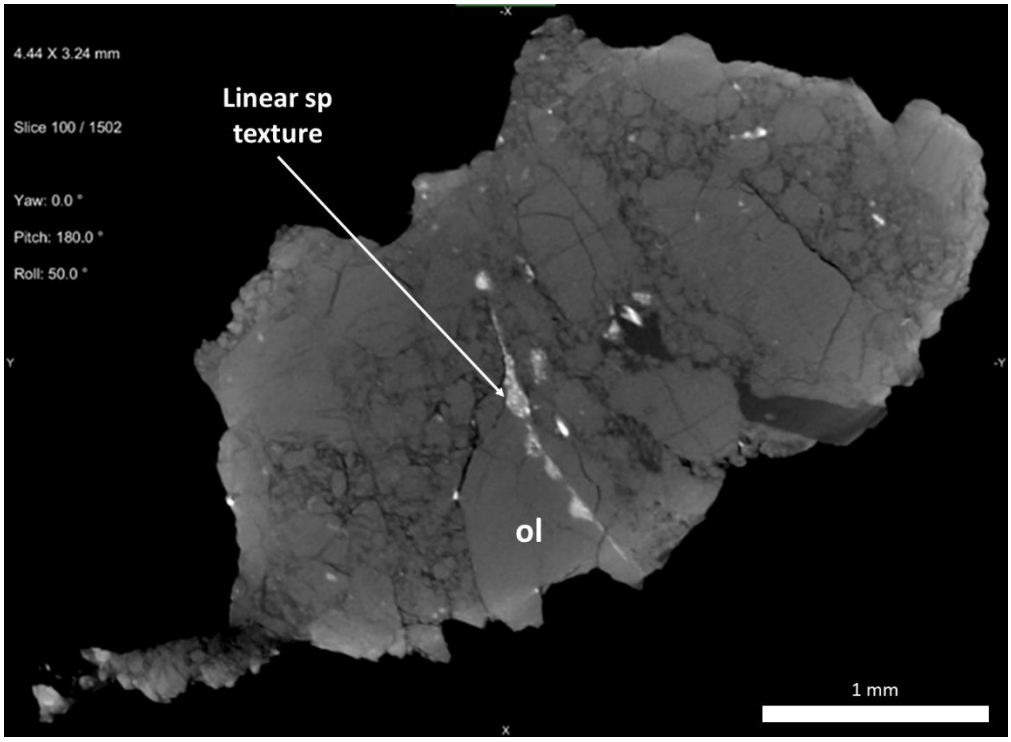

Figure 5.35. Type D linear spinel texture (white). Sample 72417,9003. Scale 1mm. Images processed using Dragonfly CT software (Object Research Systems (ORS) inc. Ver. 2020.1).

5.4.4 Unknown structure.

A completely new large unfractured high density structure with many individual elongate branches forms linear channel-like features (Fig. 5.36). These features often terminate at plate-like structures. Such structures have only been seen in the CT scans. 2D slice images show this structure forms within a large olivine grain (Fig. 5.37). The bright (high attenuating, dense phase) is notably brighter when compared with the greyscale intensities for the type A – D spinel textures. In the 3D volume, the intensity of the unknown structure is similar to Fe metal. We have interpreted this as a melt texture, but this requires further investigation to confirm whether it is spinel or possibly troilite and its study is ongoing.

This texture shows no signs of fracturing, thus making it younger than all Type A-D spinel textures and most likely related to shock melting.

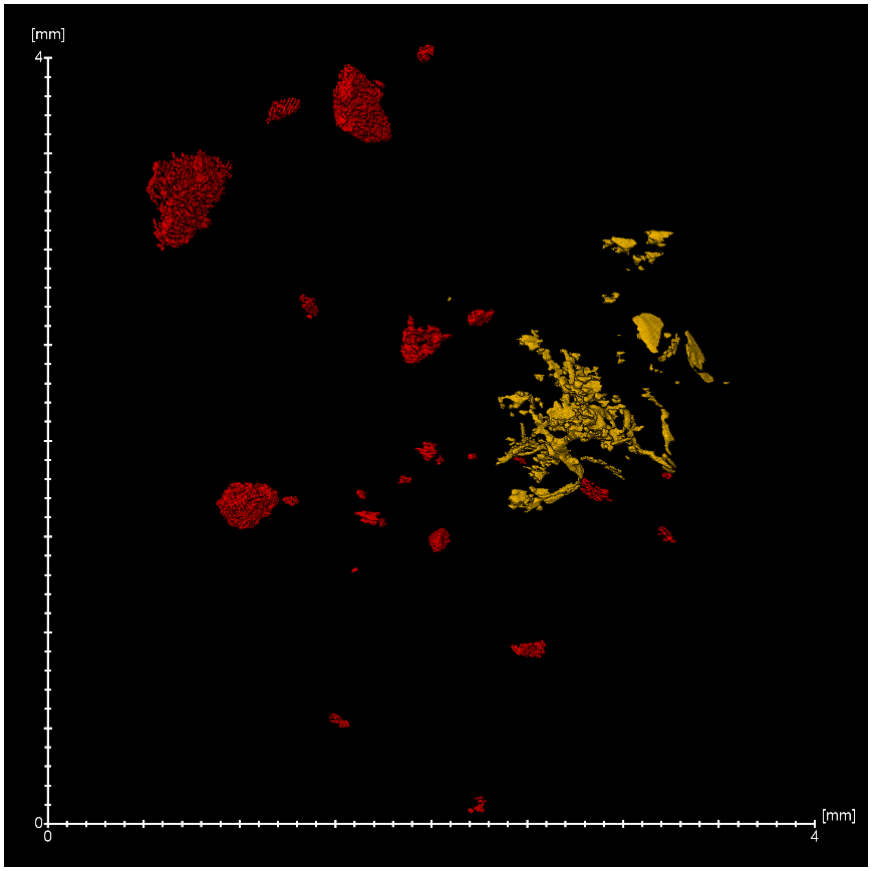

Figure 5.36. 3D rendered image of an unknown texture (yellow) in 72417,9003, fragment C. Ellipsoidal shaped structures are spinel type-A spinel-pyroxene clusters. Scalebar 4mm.

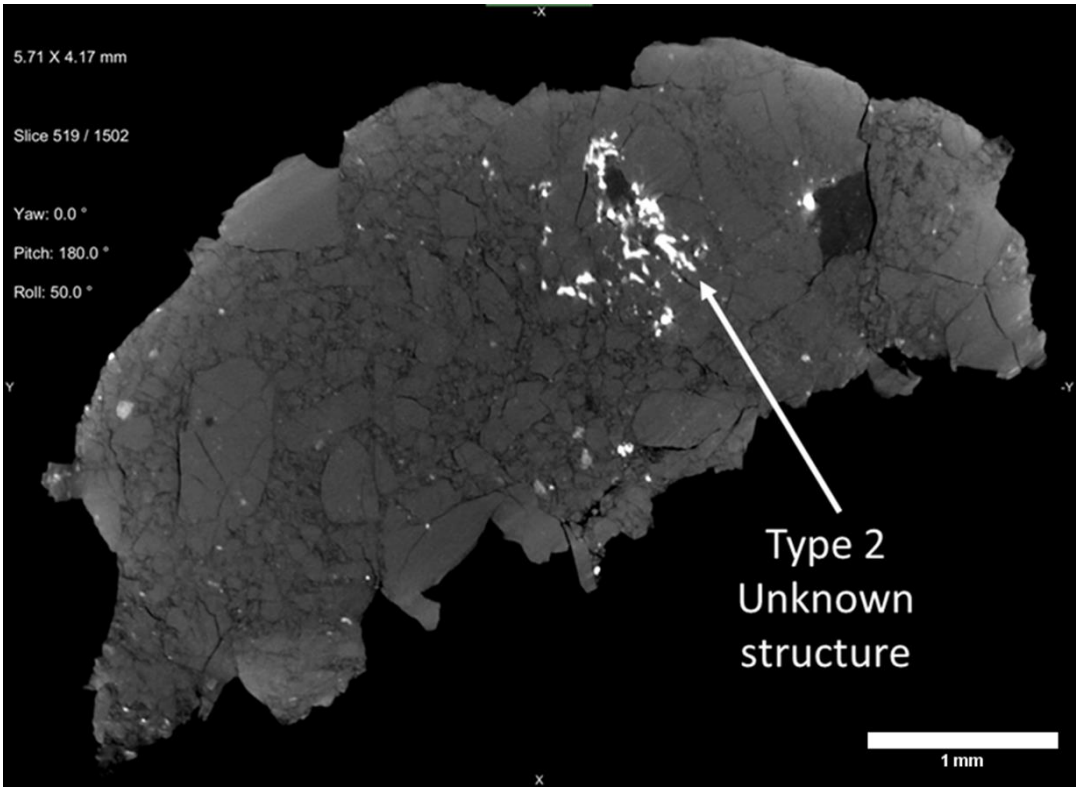

Figure 5.37. 2D slice image of olivine + unknown Type 2 structure in 72417,9003, fragment C. Scalebar 1 mm. Images processed using Dragonfly CT software (Object Research Systems (ORS) inc. Ver. 2020.1).

5.5 Electron microprobe results

Representative microprobe results of minerals in lunar dunite TS72415,53 is shown in Tables 5.3. They are similar to previous studies (Albee et al., 1974; Dymek et al., 1975). We will consider the mineral compositions found in the different types of symplectite separately.

5.5.1 Spinel Type A – Spinel-pyroxene cluster (spinel + diopside ± enstatite ± Fe metal)

In Type A symplectites, Mg#s for olivine is 87.8-88.7 (Table 5.3). Orthopyroxenes are enstatite containing 0.0-0.7 wt% Al_2O_3 and 0.3-1.1 wt% CaO, with Mg#s of 87.9-88.8, similar to that of olivine. Clinopyroxenes are diopside containing 1.3 wt% Al_2O_3 and 18.4-23.2 wt% CaO. Their Mg#s are higher than those of olivine and orthopyroxene and ranges from 91.9 to 92.6. Spinels compositions are more varied with Cr#s = 65-71 and Mg# = 48-54. Their compositional variations are: 49.9-51.5 wt% Cr_2O_3, 16.6-18.2 wt% Al_2O_3, 10.1-11.6 wt% MgO and 17.9-19.7 wt% FeO. Fe metal contains 61.9 wt% Fe, 34.4 wt% Ni and 2.8 wt% Co.

5.5.2 Spinel Type B – Spinel anorthite olivine cluster (spinel + anorthite ± diopside ± enstatite ± Fe metal + olivine).

The range of Mg# for olivine in Type B is 87.5-87.8 (Table 5.3), narrower than in the Type A spinel-pyroxene clusters. Orthopyroxenes are enstatite and contains 0.3 wt% CaO, with Mg#s of 87.8-88.8, higher than that of olivine. Anorthite is $An_{97.4}Ab_{2.6}$ and contains 19.9 wt% CaO and 0.3 wt % Na_2O. Spinel Cr#s range from 51.4 to 59.9 and Mg# = 51.9-59.5. Spinel contains 20.8-26.4 wt% Al_2O_3, 41.9-46.4 wt% Cr_2O_3, 10.5-13.6 wt% MgO and 16.5-16.9 wt% FeO.

5.5.3 Spinel Type C micro-symplectites

Spinel Type C micro-symplectites spinel-pyroxene inclusions (spinel + anorthite ± diopside ± enstatite) are closely associated with olivine. Mg# for olivine is similar to Types A and B and is 87.5 (Table 5.3). Orthopyroxene is enstatite and contains 1.3 wt% Al_2O_3 and 1 wt% CaO. Orthopyroxene Mg# is 88, similar to that of olivine. Clinopyroxene is diopside with 45.2 wt% SiO_2, 25.7 wt% Al_2O_3 and 17.2 wt% CaO. Clinopyroxene Mg# is higher than both olivine and orthopyroxene at 90.4. Spinel Cr#s range from 69 to 72 and Mg# = 51.0-53.0. Al_2O_3 contents in spinel are 13.0-13.4 wt%, Cr_2O_3 is 46.5-51.4 wt%, MgO is 10.4-12.1 wt% and FeO is 18.6-20 wt%.

5.5.4 Spinel Type D

Spinel Type D is composed of spinel-pyroxene intergrowths (spinel ± diopside ± anorthite), closely associated with olivine. They form on isolated rims of olivine clasts with individual grains displaying a blocky texture with elliptical grains <16 µm in the longest axis or has a long linear channel /vein running through an olivine grain.

5.5.4.1 Spinel-pyroxene-olivine lobate rim texture (spinel + diopside + olivine) closely associated with olivine (Fig. 5.23A).

Mg# for olivine is similar to Types A, B and C and is 87.9 (Table 5.3). Clinopyroxene is diopside with 1.2 wt% Al_2O_3 and 23.21 wt% CaO. Clinopyroxene Mg# is higher than both olivine and orthopyroxene at 91.4. Spinel Cr#s range from 66.2 to 67.7 and Mg# = 50.3-53.1. Al_2O_3 contents in spinel are 16.7-17.6 wt%, Cr_2O_3 is 51.5-52.2 wt%, MgO is 10.8-11.3 wt% and FeO is 17.8-18.9 wt%.

5.5.4.2 Spinel-olivine rim texture (spinel + diopside + olivine) (Fig. 5.23B)

There is a minor variation in Mg# for intergrowth olivine and the larger olivine clast. Mg#s are 88.4 and 87.9, respectively. Clinopyroxene is diopside with 1.3 wt% Al_2O_3 and 22.6 wt% CaO. Clinopyroxene Mg# is higher than both olivine and orthopyroxene at 91.5. Spinel Cr#s range from

68.4 to 73.9 and Mg# is 47.5. Al_2O_3 contents in spinel is 14.8 wt%, Cr_2O_3 is 54.2 wt%, MgO is 9.7-10.2 wt% and FeO is 19.3-20.3 wt%.

5.5.4.3 Spinel linear channel/vein (Fig. 5.23C)

Mg# for olivine is similar to Types A, B and C and is 87.4. Spinel Cr#s is 71 and Mg# number is 51. Al_2O_3 contents in spinel is 13.6 wt%, Cr_2O_3 is 49.3wt%, MgO is 11.3 wt% and FeO is 19.3 wt%.

5.5.3 Apatite

Apatite contains 56.0 wt% CaO and 37.0 wt% P_2O_5. Olivine associated with apatite is similar to olivine throughout the sample with a Mg# of 87.6.

Table 5.3. Representative probe analysis (EDS) of lunar dunite in sample 72415,53 (wt%).

Structure	soi	Mineral	SiO_2	FeO	MnO	MgO	Total	Mg#	No.
A	5	ol	40.23	11.67	0.02	47.42	99.34	87.87	3
A	5	Min	40.23	11.33	0.02	46.98	98.90	87.87	
A	5	Max	40.57	11.33	0.02	46.98	98.90	88.08	
A	5	SD	0.30	0.37		0.56	0.41	0.35	
A	G	ol clu	40.42	10.90	0.06	47.87	99.24	88.68	2
A	G	Min	40.33	10.33	0.01	47.57	99.01	88.09	
A	G	Max	40.51	11.46	0.11	48.16	99.47	89.26	
A	G	SD	0.13	0.80	0.07	0.42	0.33	0.82	
A	G	ol	40.22	11.86	0.09	47.79	99.96	87.78	3
A	G	Min	40.00	11.80	0.06	47.66	99.76	87.65	
A	G	Max	40.53	11.97	0.11	47.85	100.26	87.85	
A	G	SD	0.28	0.10	0.03	0.11	0.27	0.11	
B	4	ol	40.05	12.20	0.13	47.72	100.06	87.46	3
B	4	min	39.30	11.82		47.19	98.88	87.15	
B	4	max	40.60	12.61	0.23	48.00	98.88	87.15	
B	4	SD	0.67	0.40	0.14	0.46	1.04	0.36	
C	10	ol	40.25	12.18	0.11	47.66	100.23	87.46	6
C	10	Min	39.86	11.81	0.07	47.40	99.71	86.93	
C	10	Max	40.96	12.80	0.18	47.84	100.72	87.82	
C	10	SD	0.46	0.34	0.04	0.19	0.41	0.30	
D (lob)	3	ol	40.25	11.81	0.13	47.89	100.08	87.85	3
D (lob)	3	min	39.54	11.80	0.01	47.34	98.79	87.73	
D (lob)	3	max	40.61	11.82	0.30	48.33	101.02	87.93	
D (lob)	3	SD	0.54	0.01	0.12	0.43	1.15	0.12	
D(ch)	6	ol	40.31	12.19	0.12	47.64	100.22	87.44	3
D(ch)	6	Min	40.12	11.97	0.07	47.59	99.89	87.12	
D(ch)	6	Max	40.45	12.56	0.17	47.67	100.75	87.63	
D(ch)	6	SD	0.17	0.32	0.07	0.04	0.47	0.28	
D(ch	6	ol	40.06	11.66	0.09	47.78	99.70	87.96	3
D(ch)	6	Min	39.90	11.34	0.06	47.46	99.52	87.72	
D(ch)	6	Max	40.25	11.84	0.11	48.16	100.01	88.24	
D(ch)	6	SD	0.18	0.28	0.03	0.35	0.27	0.26	
D(Rim)	H	ol_ch	40.09	11.18	0.29	47.92	99.71	88.42	3
D(Rim)	H	Min	39.97	10.96	0.12	47.71	99.20	88.11	
D(Rim)	H	Max	40.21	11.52	0.38	48.16	100.06	88.58	
D(Rim)	H	SD	0.12	0.30	0.15	0.23	0.45	0.27	

Structure	soi	Mineral	SiO_2	TiO_2	Al_2O_3	Cr_2O_3	FeO	MnO	MgO	Total	Mg#	Cr#
A	14	sp		0.73	16.90	51.46	19.39	1.13	10.11	99.71	48.17	67.14
A	14	Min		0.49	16.39	50.94	18.94	0.81	9.86	99.09	46.95	66.74
A	14	Max		0.89	17.27	51.86	19.86	1.35	10.45	100.63	49.56	67.58
A	14	SD		0.17	0.40	0.41	0.51	0.23	0.26	0.75	1.24	0.45
A	14	ion	Si	Ti	Al	Cr	Fe(iii)	Fe(ii)	Mn	Mg	Total	No.
A	14	Formula	0.00	0.02	0.63	1.30	0.03	0.51	0.03	0.48	3.0	4

Structure	soi	Mineral	SiO_2	TiO_2	Al_2O_3	Cr_2O_3	FeO	MnO	MgO	Total	Mg#	Cr#
B	4	sp			26.39	41.68	16.49	0.75	13.60	98.91	59.51	51.45
B	4	Min			22.43	39.30	15.80	0.48	12.51	98.01	58.53	54.03
B	4	Max			28.45	45.75	17.27	0.91	14.31	99.90	59.63	51.89
B	4	SD			3.43	3.54	0.74	0.24	0.96	0.95	2.71	5.43
B	4	Ion			Al	Cr	Fe(iii)	Fe(ii)	Mn	Mg	Total	No.
B	4	Formula			0.94	1.00	0.05	0.36	0.02	0.62	3.0	3

Structure	soi	Mineral	SiO_2	TiO_2	Al_2O_3	Cr_2O_3	FeO	MnO	MgO	Total	Mg#	Cr#
C	2	sp	5.12	0.59	13.56	49.42	19.34	1.07	11.29	100.38	50.95	70.96
C	4	Min	3.49	0.46	13.03	46.52	18.58	0.78	10.49	99.49	49.13	68.99
C	3	Max	7.85	0.84	14.03	51.39	20.01	1.46	12.10	101.40	52.62	72.07
C	5	SD	2.03	0.17	0.45	2.13	0.59	0.29	0.70	0.86	1.44	1.38
C	6	sp	2.92	0.47	11.71	51.12	19.67	1.21	13.45	100.55	54.93	74.54
C	6	Ion	Si	Ti	Al	Cr	Fe(iii)	Fe(ii)	Mn	Mg	Total	No.
C	6	Formula	0.09	0.01	0.44	1.28	0.08	0.44	0.03	0.63	3.0	3

Structure	soi	Mineral	SiO_2	TiO_2	Al_2O_3	Cr_2O_3	FeO	MnO	MgO	Total	Mg#	Cr#
D (ch)	6	sp	5.12	0.59	13.56	49.42	19.34	1.07	11.29	100.38	50.95	70.96
D (ch)	6	Min	3.49	0.46	13.03	46.52	18.58	0.78	10.49	99.49	49.13	68.99
D (ch)	6	Max	7.85	0.84	14.03	51.39	20.01	1.46	12.10	101.40	52.62	72.07
D (ch)	6	SD	2.03	0.17	0.45	2.13	0.59	0.29	0.70	0.86	1.44	1.38
D (ch)	6	Ion	Si	Ti	Al	Cr	Fe(iii)	Fe(ii)	Mn	Mg	Total	No.
D (ch)	6	Formula	0.16	0.01	0.51	1.24	0.00	0.51	0.03	0.53	3.0	4

Structure	soi	Mineral	SiO_2	TiO_2	Al_2O_3	Cr_2O_3	FeO	MnO	MgO	Total	Mg#	Cr#
D (lob)	3	sp	-	-	17.06	51.89	18.37	1.15	10.99	99.46	51.60	67.11
D (lob)	3	min	-	-	16.70	51.45	17.77	0.80	10.78	99.29	50.31	66.16
D (lob)	3	max	-	-	17.65	52.17	18.98	1.35	11.30	99.66	53.13	67.70
D (lob)	3	SD	-	-	0.52	0.39	0.61	0.30	0.28	0.19	1.42	0.83
D (lob)	3	Ion	-	-	Al	Cr	Fe(iii)	Fe(ii)	Mn	Mg	Total	no.
D (lob)	3	Formula	-	-	0.64	1.31	0.05	0.45	0.03	0.52	3.0	3

Structure	soi	Mineral	SiO_2	TiO_2	Al_2O_3	Cr_2O_3	FeO	MnO	MgO	Total	Mg#	Cr#
D(rim)	H	Sp	-	-	14.85	54.16	19.61	1.22	9.94	99.77	47.46	70.98
D(rim)	H	Min	-	-	13.23	52.19	19.33	1.12	9.68	99.18	45.99	68.39
D(rim)	H	Max	-	-	16.18	55.84	20.26	1.33	10.15	100.86	48.35	73.90
D(rim)	H	SD	-	-	1.27	1.50	0.43	0.09	0.21	0.74	1.03	2.31
D(rim)	H	Ion	Si	Ti	Al	Cr	Fe(iii)	Fe(ii)	Mn	Mg	Total	No.
D(rim)	H	Formula	-	-	0.57	1.39	0.05	0.49	0.03	0.48	3	3

Structure	soi	Mineral	SiO_2	TiO_2	Al_2O_3	Cr_2O_3	FeO	Mn	MgO	CaO	Na_2O	Total	Mg#	Wo	En	Fs	No.
A	G	cpx	53.30	0.28	1.30	1.03	2.65	0.25	18.48	22.87	-	100.50	92.56	45.10	50.71	4.19	3
A	G	Min	53.15	0.23	1.24	0.90	2.51	0.19	18.30	22.58	-	100.22	92.33	-	-	-	-
A	G	Max	53.55	0.32	1.42	1.14	2.72	0.30	18.69	23.22	-	100.65	92.99	-	-	-	-
A	G	SD	0.22	0.05	0.10	0.12	0.12	0.08	0.20	0.32	-	0.22	0.37	-	-	-	-
A	G	Ion															
A	G	Formula															
C	10	cpx	50.98	0.36	1.61	2.22	3.67	0.15	19.52	20.82	-	99.31	90.45	40.87	53.32	5.80	8
C	10	Min	46.67	0.06	0.95	0.97	2.99	0.06	17.49	15.37	-	97.83	87.62	-	-	-	-
C	10	Max	53.44	0.54	2.64	6.03	5.31	0.37	22.12	23.15	-	100.75	91.88	-	-	-	-
C	10	SD	2.16	0.16	0.69	1.98	0.83	0.11	1.80	2.59	-	1.26	1.65	-	-	-	-
C	10	Ion															
C	10	Formula															
D_lob	3	cpx	53.04	0.12	1.19	0.84	3.02	0.32	18.07	23.21	0.08	99.71	91.43	45.56	49.35	5.09	3
D_lob	3	min	52.88	0.01	1.04	0.65	2.80	0.28	17.97	22.94	0.05	99.55	91.96	-	-	-	-
D_lob	3	max	53.14	0.25	1.32	1.00	3.19	0.36	18.13	23.56	0.11	99.86	91.02	-	-	-	-
D_lob	3	sd	0.12	0.10	0.14	0.15	0.19	0.06	0.07	0.26	0.03	0.13	0.49	-	-	-	-
D_lob	3	Ion															
D_lob	3	Formula															
D_Ch	6 inc	cpx	50.13	0.24	0.93	0.51	4.75	0.15	26.07	17.42	0.14	100.29	90.72	30.35	63.21	6.44	3
D_Ch	6 inc	Min	49.76	0.19	0.83	0.44	4.43	0.11	25.48	16.75	0.08	100.14	90.15	-	-	-	-
D_Ch	6 inc	Max	50.80	0.30	1.06	0.63	5.16	0.18	26.49	17.85	0.20	100.46	91.34	-	-	-	-
D_Ch	6 inc	SD	0.58	0.06	0.12	0.10	0.37	0.05	0.52	0.59	0.06	0.16	0.60	-	-	-	-
D_Ch	6 inc	Ion															
D_Ch	6 inc	Formula															
D(Rim)	H	cpx	53.10	0.23	1.31	0.99	3.03	-	18.31	22.58	-	99.64	91.51	44.76	50.49	4.75	3
D(Rim)	H	Min	52.96	0.11	1.19	0.82	2.77	-	17.80	21.78	-	98.50	90.69	-	-	-	-
D(Rim)	H	Max	53.38	0.35	1.40	1.28	3.48	-	19.02	23.17	-	100.52	91.97	-	-	-	-
D(Rim)	H	SD	0.24	0.12	0.11	0.25	0.39	-	0.64	0.72	-	1.04	0.71	-	-	-	-
D(Rim)	H	Ion	Si	Ti	Al	Cr	Fe(ii)	Mn	Mg	Ca	Na	Total		-	-	-	-
D(Rim)	H	Formula	1.94	0.01	0.06	0.03	0.09	0.00	1.00	0.88	0.00	4.00		-	-	-	-

Structure	soi	Mineral	SiO_2	TiO_2	Al_2O_3	Cr_2O_3	FeO	Mn	MgO	CaO	Na_2O	Total	Mg#	Wo	En	Fs	No.
A	5	opx	39.73	0.05		0.23	11.66	0.16	47.39	0.29	0.07	99.60	87.87	0.39	88.60	11.00	3
A	5	min	39.61	0.03		0.20	11.25	0.04	47.16	0.11	0.04	99.26	87.55				
A	5	Max	39.92	0.06		0.27	12.05	0.27	47.55	0.49	0.09	99.97	88.26				
A	5	SD	0.17	0.02		0.04	0.40	0.12	0.20	0.19	0.03	0.36	0.36				
C	10	opx	54.54	0.17	1.34	2.28	7.77	0.12	32.15	1.96	0.06	100.31	88.06	3.70	84.71	11.59	9
C	10	Min	49.60	0.06	0.83	0.65	6.88	0.03	30.18	0.87	0.01	99.20	85.75				
C	10	Max	57.43	0.27	2.52	7.47	9.19	0.21	33.23	7.24	0.11	101.75	89.36				
C	10	SD	2.26	0.07	0.56	2.18	0.69	0.07	0.97	2.12	0.03	0.98	1.00				

Structure	soi	Mineral	SiO_2	Al_2O_3	FeO	MgO	CaO	Na_2O	Total	An	Ab	Or	No.
B	4	An	42.22	36.76	0.34	0.14	19.86	0.29	99.61	97.4	2.6	0.0	3.00
B	4	min	41.95	36.51	0.06	0.10	19.70	0.24	99.28				
B	4	max	42.48	36.90	0.50	0.17	19.97	0.37	100.12				
B	4	SD	0.27	0.21	0.25	0.04	0.14	0.07	0.45				
B	4	Ions	Si	Ti	Al	Fe(ii)	Ca	Na	Total				
B	4	Formula	7.9	0.0	8.1	0.1	4.0	0.1	20.1				
B	D	An	42.3	35.5	0.7	1.6	19.0	0.3	99.4	96.9	3.1	0.0	3.0
B	D	Min	42.0	34.6	0.5	0.2	18.0	0.2	99.1				
B	D	Max	42.6	36.2	1.1	3.8	19.7	0.4	100.0				
B	D	SD	0.3	0.8	0.3	1.9	0.9	0.1	0.5				
B	D	Ions	Si	Ti	Al	Fe(ii)	Ca	Na	Total	no.			
B	D	F	8.03	0.00	7.93	0.12	3.86	0.13	20.1	3.0			
Ol-An	G	An	43.54	35.80	0.55	0.33	18.66	0.53	99.40	94.54	5.46	0.00	3
Ol-An	G	min	43.34	35.72	0.47	0.29	18.50	0.45	99.20				
Ol-An	G	max	43.79	35.97	0.64	0.35	18.90	0.59	99.59				
Ol-An	G	SD	0.23	0.14	0.09	0.03	0.21	0.07	0.20				
Ol-An	G	Ions	Si	Al	Fe(ii)	Ca	Na	Total	no.				
Ol-An	G	F	8.16	7.85	0.10	3.69	0.21	20.0	3.00				

Structure	soi	Mineral	SiO_2	FeO	MgO	CaO	P_2O_5	Total	No.
ol-Ap	F	Ap	0.28	0.25	0.03	53.74	35.17	92.59	3.00
ol-Ap	F	min	0.28	0.25	0.03	53.74	35.17	92.59	
ol-Ap	F	Max	1.67	0.68	2.07	55.67	36.89	94.25	
ol-Ap	F	SD	0.61	0.19	0.93	1.01	0.81	0.77	

Structure	soi	Mineral	Fe	Ni	Co	Total	no.
A	5	Fe metal	61.69	34.42	2.82	99.34	3
A	5	min	61.48	34.12	2.58	98.78	
A	5	Max	62.08	34.78	3.09	99.71	
A	5	SD	0.28	0.27	0.21	0.39	

Arai (1987) showed that, for terrestrial mantle rocks, the values of Mg# in olivine and Cr# in spinel are concentrated in a narrow band and thus can constrain the origin of spinel peridotites. The olivine-spinel mantle array (OSMA) shows the compositional differences between spinel peridotites from different tectonic settings on Earth. Fig. 5.38 is an OSMA diagram for the lunar dunite spinel textural types compared with examples of spinel in mantle xenoliths from Lanzarote and Massif Central (Bhanot et al., 2017). Terrestrial mantle samples lie within the OSMA, whilst coexisting olivine and spinel in the lunar dunites, including the 4 spinel textural types, plot outside the OSMA, to lower olivine Mg#s. The spinel compositions are generally higher than those of the terrestrial mantle xenoliths (Fig. 5.38).

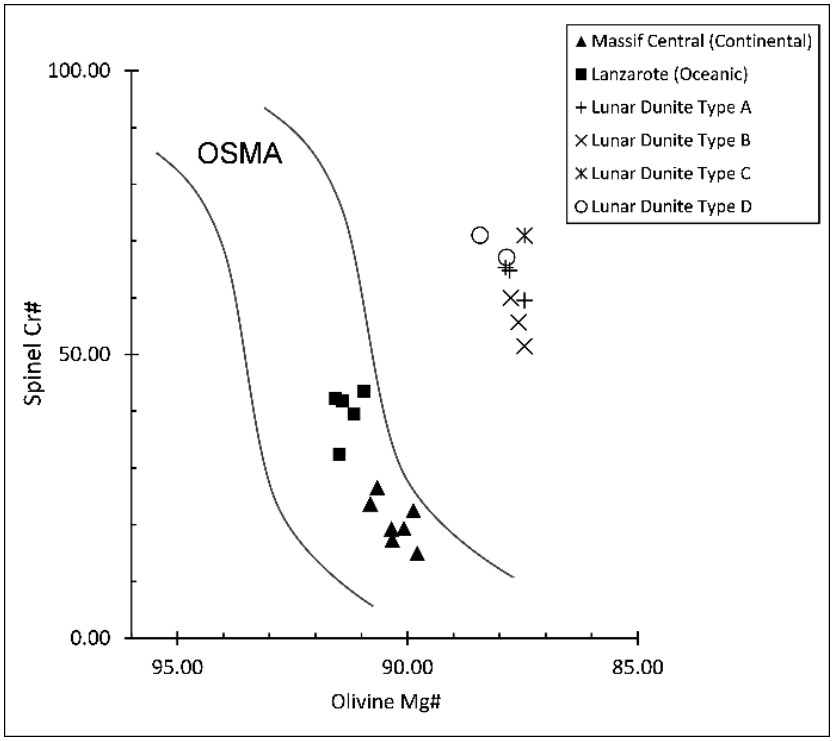

Figure 5.38. Mg# in olivine versus Cr# in spinel (OSMA), showing the compositional variation in lunar dunite 72515,53 and terrestrial spinel peridotite xenoliths from Massif Central and Lanzarote (Bhanot et al., 2017).

Enstatite compositions measured in Type A, B and C are similar showing little variation. However, diopsides in Type A, B, C and D (rim lobate texture) exhibits a range of compositions with type C spinel textural type showing the lowest Mg# and CaO content. Table 5.4 provides a summary of the spinel textural types in lunar dunite.

Table 5.4. Summary table of spinel textural types in Lunar dunite 72415,53, 72415,4 and 72417,9003.

Textural type	Mineral composition	Spinel texture	Interpretation
Type A	spinel + diopside ± enstatite ± Fe metal	Sp forms a highly complex structure, elliptical in shape with a strong vermicular texture. Not associated with olivine forming a single grain.	Spinel-pyroxene cluster: Individual clasts
Type B	spinel + anorthite ± diopside ± enstatite ± Fe metal + olivine	Sp forms elongate channels running through a large olivine grain. Randomly distributed blocky texture with larger grains concentrated in a small region of ol grain but with finer blebs distributed throughout.	Spinel-olivine cluster: Shallow origin - reaction between olivine and impact-related decompression melts
Type C	spinel + diopside ± enstatite ± anorthite	Spc inclusions closely associated with ol. Sp forms vermicular texture with narrow branches interconnected. Also associated with type d sp textural type.	Microsymplectite: Melt inclusions formed during olivine crystallisation
Type D (lobate rim texture)	spinel + diopside + olivine	Vermicular texture with long thin branches. Spinel and cpx forms a lobate rim on edge of ol clast	Spinel/olivine reaction texture: Reaction between olivine grains and decompressed melts
Type D (rim texture)	spinel + diopside + olivine	Spinel forms a blocky blebs texture on isolated rim of ol clast.	Spinel/olivine reaction texture: Reaction between olivine grains and decompressed melts and both relatively recent crack and annealed cracks
Type D (linear channel)	spinel + diopside + olivine + microsymplectites	Spinel forms vermicular texture with long thin branches. Spinel and cpx forms a lobate rim on edge of ol clast	Spinel/olivine reaction texture: Reaction between olivine grains and decompressed melts.
Type 2	spinel + Fe metal(?), Troilite(?)	Many individual elongate branches form linear channel-like features	Spinel + Fe (?), Troilite(?) Shallow origin - reaction between olivine and impact-related decompression melts(?)

5.6 Discussion

5.6.1 Lunar Dunite Spinel textures

Several previous studies have discussed the origin of symplectites in lunar dunites. Based on the observation that the symplectites commonly occur along olivine-plagioclase grain boundaries (our Type B), Albee et al. (1975) suggested that the stability pressure for olivine + plagioclase + spinel had not been exceeded, so crystallization had occurred at low pressures in the crust. They proposed that the dunites are olivine + spinel cumulates and that late stage adcumulus olivine growth was associated with crystallization of orthopyroxene, clinopyroxene, anorthite and Cr-spinel as vermicular intergrowths. Dymek et al. (1975) proposed that variations in texture and phase assemblages reflect local variations in the composition of the trapped melt.

In contrast, Albee et al. (1974) reported zones of spinel symplectites (our Type A, B) and tiny ovoid inclusions in olivine (our Type C). The intergrowths were interpreted as existing prior to excavation and the interpretation was that the lunar dunite represents a very early differentiate derived from the upper mantle, i.e., a cumulate formed during early lunar differentiation and associated gravitational settling. Bell and Mao (1975) also reported “eutectoid” intergrowths of spinel + pyroxene and occasional plagioclase (our Type A and B) and considered that the lunar dunite formed under high pressures and temperatures, and originally contained garnet because the microsymplectites (our Type C) had an idealised bulk composition of a garnet. Bell et al. (1975) proposed that the symplectite intergrowths were the result of the breakdown of garnet and diffusion of minor elements (Ca, Cr and Al). Schmitt (2016) supported the hypothesis of late overturn of magma ocean cumulates and considered that the related pressure release-initiated decomposition of a high-pressure Cr-rich garnet present in the original mantle cumulates resulting in the Cr-spinel, Ca-clinopyroxene and Mg-orthopyroxene symplectitic intergrowths (our type A-D).

Back-Scattered Electron and micro-CT images in this study have revealed that lunar dunite 72415 and 72417 displays four distinct spinel textures (Types A, B, C, D), probably formed by different processes. Before discussing each texture in turn, the general features of the lunar dunite will be discussed. All analysed olivine crystals show a narrow range of Mg#s from 87 to 88, in agreement with Dymek et al (1975). The mg# of the lunar mantle has been reported by a number of studies. Buck and Toksoz (1980) calculated it to be 70, whereas Warren (1986) proposed that it ranges from 87 to 91. However, according to Drake (1986), most estimates of the mg# of the bulk Moon are lower than that of the Earth’s upper mantle because lunar basalts are more FeO-rich than terrestrial basalts (Wanke et al., 1983). The first cumulates at the base of the LMO cumulate layer were likely to be dunites. Their mg# values would be constrained by the composition of the LMO and the depth of

crystallization. Olivine formed as early cumulates from the LMO would have high Mg#s. For example, the mg# values of olivine in equilibrium with a peridotitic LMO with mg# > 80 at pressures of 3-4 GPa are > 90 (Hess and Parmentier, 1995). The observed olivine Mg# of lunar dunite 72415 is 87-88, consistent with the rock being an early cumulate formed at depth in the lunar mantle. In terrestrial mantle xenoliths both the cpx and opx Mg# are slightly higher than coexisting olivine (Pearson et al., 2003). Type C opx and cpx Mg#'s are similar to that of olivine. However, type A and B opx Mg#'s are also similar to that of olivine but cpx Mg#'s in type A, B and D are notably higher (Table 5.5).

Based on texture and mineral chemistry of the spinels, we propose that Types A, B, C and D have different origins. Table 5.5 and Figure 5.39 shows the variation in mineral composition in the four spinel texture types. EMPA data show a variation in Cr_2O_3 content of spinel in Type A Sp + Cpx clusters and Type B Sp + An symplectite intergrowths (Tables 5.3), with spinel in the Type A clusters being more Cr-rich (Cr# = 65, compared with Cr# = 56 in Type B intergrowths) (Figure 5.38). Spinel in the microsymplectites (Type C) have a Mg# of 53 and Cr# of 74. Spinel in Type D textures have a generally lower Mg# of 47-55 and Cr# of 67-75. Both Type C and D have the highest Cr content of the spinel textures. Figure 5.38 is a plot of Cr# against Mg# for spinels from the four textural types. This plot highlights the chemical variation of spinel across the lunar dunite spinel textural types with type B having the lowest Cr# and highest mg#, whilst type A, C and D have a higher Cr# and lower Mg#. There is some overlap for type A, C and D spinels but these are distinct from type B.

Table 5.5. Table showing average compositions of minerals in the four types of spinel textures in lunar dunite 72415,53.

	Type A	Type B	Type C	Type D
Mg# in olivine	88.0	87.5	87.5	87.9
Mg# in opx	88.3	89.5	88.3	-
Mg# in cpx	92.0	92.0	88.9	90.9
Mg# in spinel	50.6	56.1	51.9	51.3
Cr# in spinel	66.2	55.7	72.5	70.9
interpretation	Decompressed garnet (spinel-pyroxene cluster)	Shallow origin - reaction between olivine and impact-related decompression melts	Pre Serenitatis event. Melt inclusions formed during olivine crystallisation	Reaction between olivine grains and decompressed melts

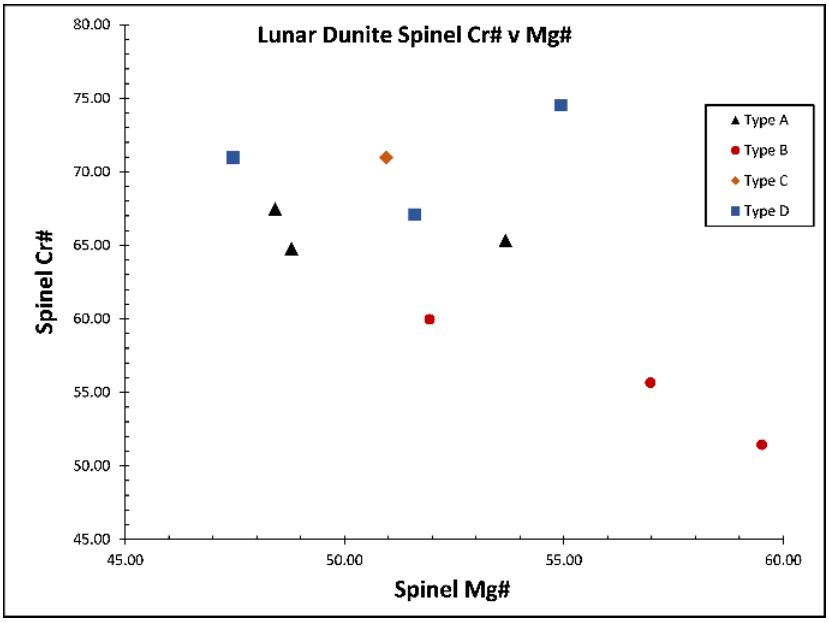

Figure 5.39. Plot of Lunar dunite spinel Mg# against spinel Cr# for all spinel textural types in lunar dunite 72415,53.

5.6.2 Type A symplectites.

BSE images, elemental maps and our probe analysis showed that several clasts were composed of complex intergrowths of spinel and pyroxene (our type A) without olivine (Figs. 5.17 and 5.20). Spinel forms narrow branches with a vermicular texture with interstitial diopside and enstatite. From the 2D and 3D images (Fig. 5.26 and 5.27), Type A symplectite textures were identified as spinel-pyroxene clusters. Spinel forms a highly complex structure, ellipsoidal in shape with a strong vermicular texture. This texture is similar to the complex structures of spinel textures in spinel-pyroxene cluster-bearing peridotites found in terrestrial mantle xenoliths from Lanzarote and the Massif Central (Bhanot et al., 2017) and other studies of mantle peridotites (Mercier and Nicolas, 1975; Basu and Macgregor, 1975). The clusters lack olivine, so pyroxene is the only other mineral phase present. The mineral assemblage thus provides another line of evidence that these spinel

symplectites are indeed spinel-pyroxene clusters brought on by the solid-state reaction of olivine and garnet due to reduction in pressure.

In the terrestrial mantle, garnet is the stable aluminous phase at pressures >13 kbar and temperatures of 1200^{O} C. It is formed by the reaction shown in equation 2 (Kushiro and Yoder, 1966), although the bulk composition of the mantle also plays a role. The boundary between spinel and garnet-bearing peridotites on Earth depends on the bulk ratio of Cr_2O_3, Fe_2O_3 and Al_2O_3, with the spinel phase assemblage extending to higher pressures with increasing Cr_2O_3 and Fe_2O_3 content (Macgregor, 1970; Basu and Macgregor, 1975).

Diopside + Enstatite + Spinel ⇌ Olivine + Garnet Equ.5.2

The Moon has no active plate tectonics, therefore mantle overturn provides the only possible mechanism for migration of garnet-bearing mantle (which would be deeper than 400 km (Fig. 5.1) into the spinel stability field and formation of the Type A spinel-pyroxene clusters. However, mantle overturn would not bring the dunite to the lunar surface but could have brought it to a position beneath the lunar Moho (at depths of >60 km). It would have remained at this depth until it was excavated by the Serentiatis impact.

5.6.3 Spinel Type B – Spinel-anorthite-olivine cluster.

BSE, elemental maps, 2D and 3D images of lunar dunite 72415 and 72417 reveal type B symplectites are complex structures between spinel + anorthite and olivine, all contained inside large olivine grains. This differs from the type A symplectites in a number of ways. The spinel in ol-sp-an structures are Cr-poor compared to the type A spinel-pyroxene clusters and forms less vermicular but blocky blebs. Seen in 2D slice images, the blocky blebs are, in fact, cross-sections of spinel which run through large olivine grains in near linear channels. There is no variation in spinel mineral chemistry within the cluster. Anorthite also forms blocky linear grains and is associated with both olivine and spinel (Fig. 5.21). 2D slices images show that distribution of spinel and anorthite is not uniform throughout the olivine grain. Individual slice images show small amounts of anorthite with spinel absent. However, spinel is always associated with both olivine and anorthite. Dymek et al (1975) reported that deformation features in the olivine grains containing ol-sp-an symplectites (our Type B) indicate that the dunite was subjected to pressures ~330 - 440 kbar, and that this occurred during the basin-forming event and excavation. They reported “irregular to linear veinlets of lath-shaped plagioclase” which are the complex ol-sp-an Type B structures identified in our 3D rendered volume and 2D slice images (Fig. 5.28). Type B symplectites have a shallower origin via interaction between olivine and impact-related decompression melts forming the ol + an + sp symplectitic

textures within olivine grains. Spinel channels and veins inside olivine grains support the view that these are melt-related textures, as opposed to the sub-solidus reaction seen in the formation of Type A spinel-pyroxene clusters.

5.6.4 Spinel Type C, D, Micro-symplectites and olivine reaction rim textures

Type C spinel micro-symplectites of spinel + anorthite ± diopside ± enstatite, closely associated with olivine and were identified in BSE images of large olivine clasts (Fig. 5.19 and 5.22), are not visible in the 3D rendered volume but can be identified in the 2D slice images which show that they are inclusions distributed throughout olivine grains (Fig 5.33). Distribution is entirely random but some large olivine grains show that certain portions of the grain are more strongly associated with the micro-symplectite inclusions whereas other regions of the same grain are devoid of these structures (Fig. 5.37). Dymek et al (1975) proposed that the inclusions represent sites in which melt inclusions were trapped within growing olivine grains. The micro-symplectites are Cr-rich, suggesting that the inclusions were originally formed of trapped mafic melt plus Cr-rich spinel crystals. BSE images do show microsymplectites heavily associated with Type C symplectites (Fig. 5.19) are therefore considered to be melt inclusions formed from trapped melt during olivine crystallisation, in agreement with Dymek et al. (1975). Based on the fact that the microsymplectites are isolated features within olivine grains and commonly found in both samples and appear to be associated with annealed cracks, we also conclude that micro-symplectite inclusions represent melt inclusions related to impact melts and partial melting prior to the Serenitatis event.

Type D reaction rims and EMPA images (Fig. 5.23A and B) show that spinel and pyroxene display a lobate texture forming a spinel-pyroxene structure. This texture is considered the product of olivine grains reacting with melt. 2D images show spinel on rim of olivine grains. Size of structure remain small and does not penetrate much beyond the olivine grain rim. Type D spinel textures are considered reaction rim textures. Similar to the type C micro-symplectite inclusions are not easily identified in the 3D rendered volume. However, cross-referencing their identification in the 2D volume, the spinel is confined to extreme edge of olivine grains whilst most of the grain edge is free of this spinel texture. Olivine clasts with reaction rim textures are cross cut by large cracks. We believe that these were formed by the interaction of impact melts or possibly decompression melts and represent textures older than the Serenitatis event.

5.6.5 Excavation of sample to surface

Data from Grail and SELENE/Kaguya missions (Miljković et al., 2015; Yamamoto et al., 2010) show high olivine abundances surrounding large (> 200 km) impact basins and proposed that at least some of this olivine originated from the lunar upper mantle. Exposure of mantle olivine could potentially have originated during the basin-forming event, in which the crust was fully excavated, and mantle material was deposited on the basin rim.

Spudis (1999) stated that the Serenitatis impact occurred into a highland region of lunar crust in which mare volcanism was already active. Due to the effect of the Imbrium ejecta and post-impact structural changes, the identification of the Serenitatis cavity is difficult. The transient crater, an ephemeral form of the evolving crater marking the transition between excavation and collapse, is an important concept in impact cratering (Fig. 5.2)**.** Numerical and laboratory experiments have shown, for small craters, that transient crater volume and diameter can be used to predict, with reasonable accuracy, maximum depth and volume of ejected material (Potter et al., 2012). Ejected material originates from an excavation cavity which as a geometry distinct from the transient crater. The excavation cavity and transient crater have the same diameter, but the depth of lunar basin excavation cavity is ~0.1 of the transient cavity diameter, or about one-third of the transient crater depth (Croft, 1980). Material from the deepest part of the cavity is likely to be the closest and last to be deposited from the ejecta blanket. Spudis (1999) estimated an excavation cavity of 600 ± 100 km for the Serenitatis basin, thus yielding an excavation depth of up to 70 km. Considering the textural evidence of the spinel-pyroxene clusters symplectites (spinel Type A) in lunar dunite 72415,52 and 72417,9003, we consider that the symplectites represent lunar mantle material formed from decompression of garnet peridotite to a depth just beneath the crust-mantle boundary, and the garnet was brought up from ~420 km depth by convective overturn and later deposited as part of the Serenitatis impact ejecta.

5.7 Conclusion

In this study, we have identified four spinel textural types in the Apollo 17 dunite via EMPA and micro-CT. Each textural type is defined by its chemical composition and relationship with olivine. Textural type A is the product of a solid-state metamorphic reaction brought on by decompression of garnet, the originally high-pressure mantle Al-phase, during lunar mantle overturn.

The Apollo 17 dunite is indeed a fragment of the lunar mantle. It was formed by crystallisation of the LMO, at depths that corresponded to the pressure of the garnet peridotite facies (22 kbar, 420 km). This part of the mantle was involved in an overturn event, which brought the garnet peridotite into a shallower part of the lunar interior. During this event, decompression caused garnet + olivine to react to form large elliptical spinel + pyroxene symplectites, identified here as Type A. This sub-solidus part of the rock's history is in agreement with that proposed by Bell et al (1975) and later endorsed by Schmitt (2016).

The other three spinel textures were formed from igneous melts. Type B ol + an + sp symplectites are interpreted as having a shallower origin because they contain plagioclase. They were formed by the interaction of shock melts and mantle olivine. Their linear features are interpreted as being formed by injection of small amounts of silicate melt into fractures in olivine crystals. This is in agreement with the origin proposed by Dymek et al (1975). Thus, they are related to the impact event which excavated the rock from the mantle to the lunar surface during the formation of the Serenitatis basin. Types C and D are much smaller than Types A and B, and have an exsolution origin, possibly as inclusions of decompression melts that cooled slowly and crystallised.

Each textural type represents a different stage in the history of the lunar dunite (Fig. 5.40) with type A being the oldest texture i.e., the transformation of garnet to a spinel-pyroxene cluster due to mantle overturn. Type C and D are considered igneous textures resulting of melt interaction with the mantle prior to the Serenitatis impact event. Type B represents the youngest spinel texture and was most likely formed from impact melts during the Serenitatis event. Figure 5.41 shows the relative ages of each textural type.

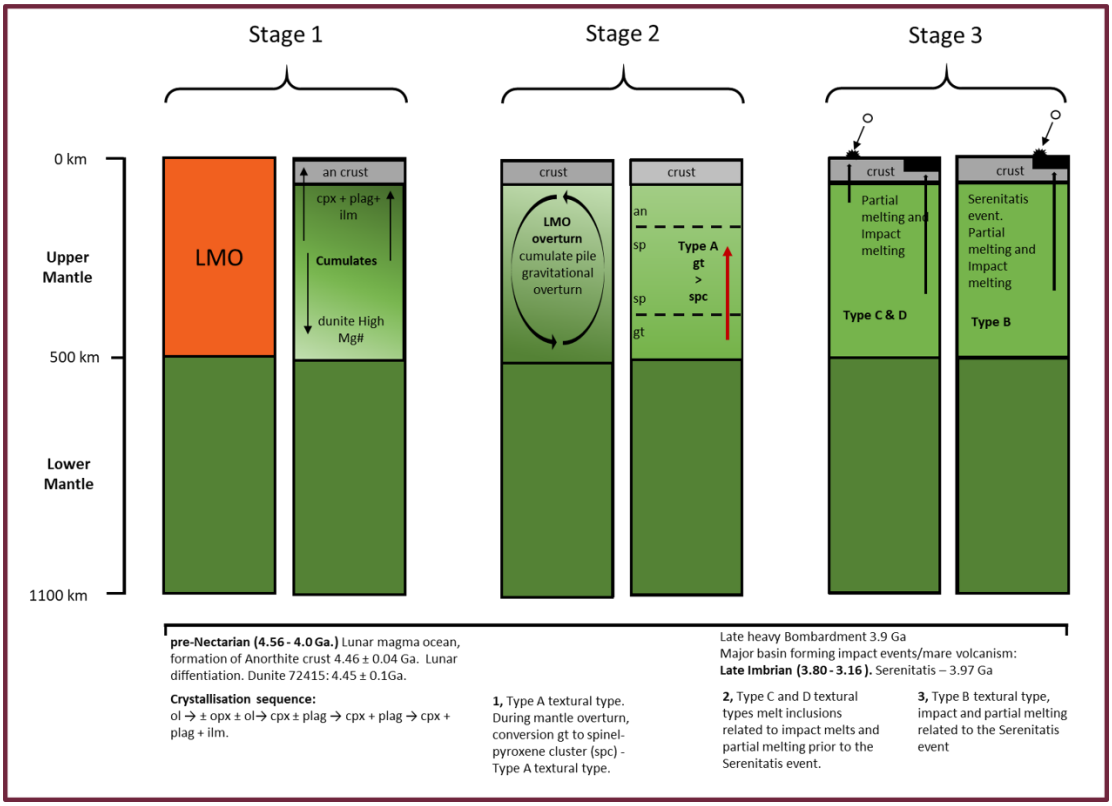

Figure 5.40. Diagram showing relative histories and ages of each spinel textural type in the lunar dunite. Stage 1: Lunar Magma Ocean formation. Stage 2: mantle overturn, leading to transformation of garnet into spinel pyroxene cluster; Stage 3: late heavy bombardment; Stage 4: Serenitatis impact event and dunite excavation.

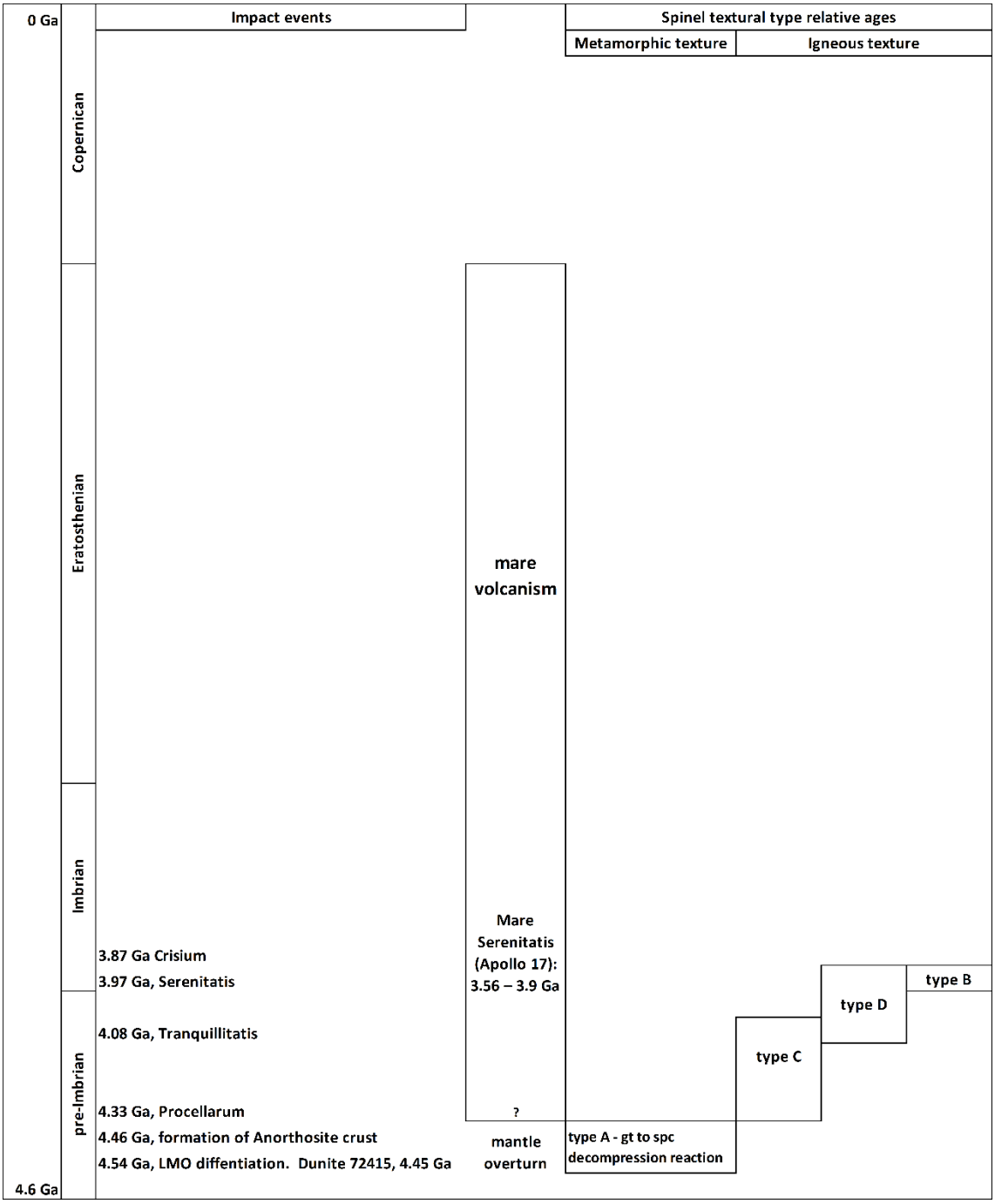

Figure 5.41. Sketch showing relative ages of spinel textural types in Lunar dunite 72415,53, 72415,4 and 72417,9003 (Wilhelms et al., 1987; Stöffler et al., 2001; Schmitt 2014).

Chapter 6

Discussion and concluding remarks.

6.1 Evolution of the study of mantle material by CT scanning

The aim of this study was to use CT scanning to investigate the textures of mantle peridotites, supplemented by electron microprobe analyses (EMPA) of the constituent phases. Textures observed in thin-section might be identified in the 3D volume, although thin-section preparation may not capture a specific texture due to uneven distribution throughout a rock sample. Alternatively micro-CT images could be used to provide data to allow for targeted sectioning of relevant structures.

Various types of mantle material were analysed, including xenoliths with different mineralogical compositions such as spinel peridotites with and without spinel-pyroxene clusters, garnet-spinel peridotites, and garnet peridotites. The samples were from different tectonic settings, including the oceanic mantle (Lanzarote), young thinned continental lithosphere (Massif Central, Calatrava), older complex lithosphere (Patagonia, Vitim), cratonic lithosphere (Kaapvaal), and the solidified magma ocean lithosphere of the Moon.

The study commenced with CT analysis of some of the simplest type of mantle material available, spinel peridotite xenoliths showing the range of deformation textures described by Mercier and Nicolas (1975). Micro-CT and EMPA studies were undertaken on samples from the Ray Pic locality in the Massif Central, to identify and record the range of textural types. This was, in effect, a “proof of concept”, to demonstrate the efficiency of Micro-CT as a technique to image spinel textures and spinel distribution in mantle rocks and to provide examples of representative textural types of spinel peridotites which could provide a reference to which textures in other xenoliths could be compared.

A single garnet peridotite xenolith was also analysed, to constrain the texture of the starting material for the spinel-pyroxene clusters and to fully understand the texture of spinel in spinel-pyroxene cluster-bearing samples. The garnet peridotite represents the initial phase of the deep lithospheric mantle prior to lithospheric thinning and the subsolidus reaction of garnet and olivine brought on by decompression.

The study proceeded with increasingly complex mantle textures. Three groups of samples from regions of thinned lithosphere were examined. These all contained spinel-pyroxene clusters which can be seen occasionally in hand specimen. The results from Lanzarote and the Massif Central were

obtained and published before those from Calatrava. Samples of Calatrava were analysed to examine how spinel-pyroxene cluster textures from a third location compared with textures seen in Massif Central and Lanzarote and to confirm that spinel-pyroxene cluster textures are indeed a distinct texture, separate from those of the standard textures observed in the samples for Ray Pic and described by Mercier and Nicolas (1975). The 3D data showed that the spinel textures from Calatrava revealed complex, ellipsoidal structures comparable with those observed in the Massif Central Northern domain and more notably Lanzarote. In my opinion this lends weight to my conclusion that spinel clusters textures formed from decompression of garnets yield these distinct textures.

The next step was the investigation of rare xenoliths in which garnet and spinel coexist and would thus represent an early stage of the reaction of gt + ol converting to a spinel-pyroxene cluster. Details of this part of the study have also been published.

Finally, the most complex sample investigated in this study was a lunar dunite returned by the Apollo 17 mission, which contained a variety of spinel symplectite textures. The sample size, fragility, small size of the spinel textures (~ 25 µm) and the priceless nature of the sample required careful consideration in terms of sample mounting for micro-CT analysis.

Obtaining EMPA data allowed for identification of mineral associations and mineral chemistry. Identifying differences in mineral chemistry was an important factor to distinguish spinel types. BSE and elemental images yielded very high-resolution images of spinel textures. Analysis of spinel textures in 2D by EMPA provided important reference images for viewing and identifying similar textures in 2D slices of the 3D CT volume.

WDS and EDS are complementary techniques for collecting EMPA data. EDS data allows for fast acquisition of all elements simultaneously but with a lower precision compared with WDS data. WDS data is more precise and with a higher Peak/Background ratio, allowing for better analysis of low concentrations. Resolution of CT slice images is less than that of BSE images. At high magnification (x1200), BSE images can yield a spatial resolution in the order of <5 µm.

Spinel, garnet and garnet-spinel peridotites were imaged using a Nikon Metrology HMX ST 225 micro-CT scanner. This scanner provides the high power (~225 kV) X-Ray source and can analyse 25 mm cores with a resolution of 11-17 µm /pixel. Sample size and shape are important factors when considering sample preparation and reducing artifacts in the CT data which negatively affect data quality. Ideal samples sizes are cores with a diameter of 25 mm. The advantage of a cylindrical sample is to provide an equal path for the X-Ray beam through the sample as it is rotated. However,

experiments were undertaken in which entire irregular-shaped spinel peridotite xenoliths from the Massif Central and Calatrava were imaged, and internal spinel structures were identified. The advantage of imaging whole rock samples would be the visualisation of any structure orientations and concentrations of large spinel structures which are potentially lost by reducing the sample to a core of < 25 mm. Beam hardening leads to differences in greyscale intensities of similar objects on the outer rim of the core to those in the central portion. This behaviour was more prevalent in the garnet and garnet-spinel peridotites from Vitim and Pali-Aike. Several data sets showed an almost complete loss of signal in the central portion of the image. To reduce the effect of beam hardening, the more intense outer portion of the data set was cropped, and analysis of the data set was carried out on the remainder.

There is a distinct difference in processing data containing Cr-rich spinel and low-Cr garnets. Spinel is easily segmented from the silicate phase from the histogram whilst the low-Cr garnet requires additional processing and analysis. Spinel peridotites segmentation was done using the Drishti software suite, whilst garnet and garnet-spinel peridotite data was analysed using the Avizo software package. Although the greyscale intensity difference between garnet and the other silicate phases is identifiable with the naked eye, segmentation through the histogram is challenging with sections of the other silicate phases being assigned to the garnet phase, yielding inaccurate texture representations. The “magic wand utility” in Avizo allowed individual regions of interest to be segmented manually in the 2D volume, thus building up a manually segmented 3D volume and a more accurate texture representation.

The lunar dunite required the most consideration to obtain CT data. They were imaged as irregular shaped fragments and were not altered in shape or size. The fact the samples could not be physically secured, leading to movement of the sample during data collection, was an extra complication. Lunar dunites were imaged using a Zeiss Xradia Versa 520 scanner, with an X-Ray cone beam coupled with optical lenses (0.4X, 4X, 20X and 40X) to gain additional magnification of a sample.

Table 6.1. Zeiss Xradia Versa 520 scanner pixel size reported and actual.

Theoretical pixel size

Objective lens magnification	FOV (mm)	Pixel Size (µm)
0.4	2	1.00
4	1	0.50
20	0.5	0.25

Pixel size for lunar dunite data

Objective lens magnification	FOV (mm)	Pixel Size (µm)
0.4	2	1.92
4	1	1.39

In comparison, the Nikon data sets for terrestrial peridotites have a pixel size ~ 12 µm (Table 6.1).

Segmentation of the lunar dunite was done using the Object Research Systems (ORS) Dragonfly software suite, used under an academic licence. The advantage of using Dragonfly is that it offers powerful 2D analysis and movie-making tools. Avizo was also used to segment data using the "magic wand utility".

The project benefited from the use of different software packages, with each offering their own advantages in data processing. Micro-CT results benefited greatly from using multiple software packages and multiple repeats in data processing. Repeated data processing allowed me to gain experience in data processing techniques and to explore how much data can be extracted from the 3D data set. Data analysis was also complemented by the use of ImageJ.

In conclusion, micro-CT scanning has been shown to produce excellent detailed 3D images of the textures of spinel and garnet in mantle peridotites. Two papers have been published using the results of micro-CT scanning of peridotites with unusual textures relating to the garnet-spinel transition in the Earth's mantle. The results will now be discussed in more detail below.

6.2 Textural varieties of spinel peridotites from Massif Central

Mantle xenoliths from Ray Pic in the southern Massif Central were analysed to identify and record the protogranular-porphyroclastic-equigranular textural groups designated by Mercier and Nicolas (1975) for spinel peridotites. This was undertaken to provide a baseline, to which results for other more complex mantle material could be compared. The results, presented in Chapter 3, show that

spinel exists as large, concentrated blebs distributed throughout the protogranular sample with a strong preferred orientation. Transition from protogranular to porphyroclastic textural types shows that spinel becomes finer-grained displaying a holly leaf texture with a weaker orientation (Fig. 6.1). The transition to equigranular types shows fine-grained spinel grains evenly distributed throughout the rock in which preferred orientation is absent. In all textural types, spinel is associated with individual olivine grains. Figure 6.1 shows examples of CT scans of each textural type described by Mercier and Nicolas (1975).

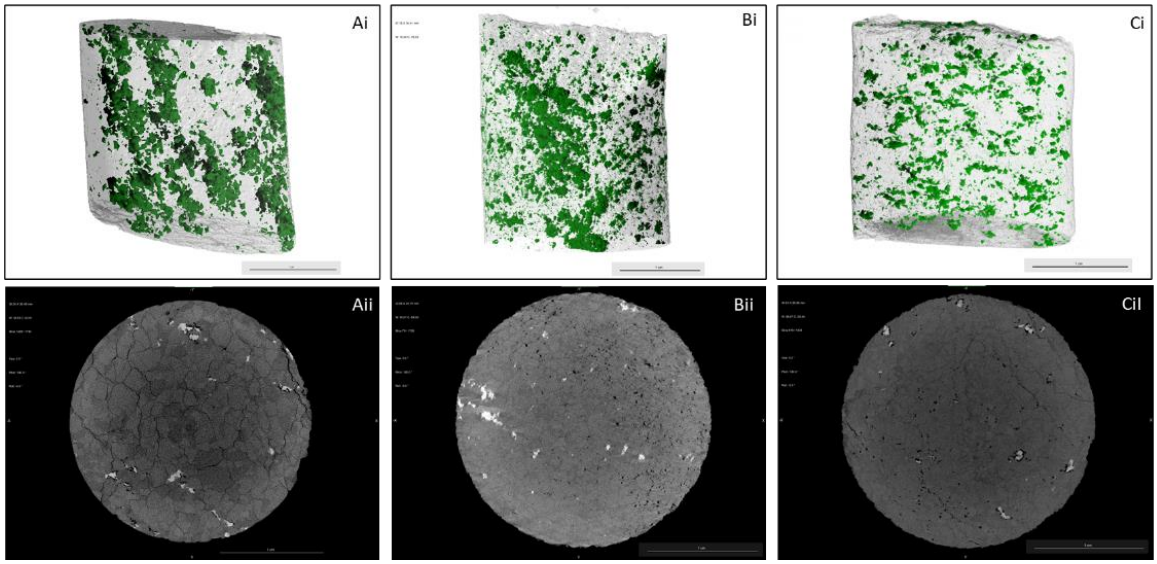

Figure 6.1. 3D rendered images of the three textural types for Ray Pic mantle xenoliths as described by Mercier and Nicolas (1975). ***A****, protogranular (i) 3D rendered image of a spinel peridotite (RP91_22). Spinel, green. Scale bar 10 mm. (ii) 2D slice image of a spinel peridotite (RP91_22). spinel, white, silicate phase dark grey. Scale bar 5 mm.* ***B****, porphyroclastic (i) 3D rendered image of a garnet peridotite (RP91_11). Spinel is green. Scale bar 10 mm. (ii) 2D slice image of a spinel peridotite (RP91_11). Spinel, white, silicate phase dark grey. Scale bar 10 mm.* ***C****, equigranular (i) 3D rendered image of a spinel peridotite (RP87_4) Spinel is green. Scale bar 10 mm. (ii) 2D slice image of a spinel peridotite (RP87_4). Spinel, white, silicate phase dark grey. Scale bar 10 mm.*

6.3 Comparison of results for xenoliths containing spinel pyroxene clusters.

Micro CT analysis of spinel-pyroxene clusters in spinel peridotites from the Massif Central and Lanzarote (Fig 6.2 A and B) revealed high-resolution images of the complex structures which are ellipsoidal in shape and often associated with a lineation. In addition, to the complex spinel structures, sites of metasomatic reactions and their relation to spinel-pyroxene clusters sites have been resolved. Analysing the textures provided evidence of the complex history of the samples. In addition, spinel-pyroxene cluster-bearing peridotites from Calatrava (Fig. 6.2C) were studied to directly compare these textures to those observed in spinel peridotites from Massif Central and Lanzarote.

3D visualisation of the spinel-pyroxene cluster structures revealed unique ellipsoidal complex structures which also showed a degree of orientation and deformation (Fig. 6.2). BSE images showed large grain size. The samples are considered part of the protogranular type of xenolith, but these concentrated spinel structures are distinct from the spinel textures observed in samples from Ray Pic and represent a unique texture representing the sub-solidus reaction of olivine and garnet under reduced pressure.

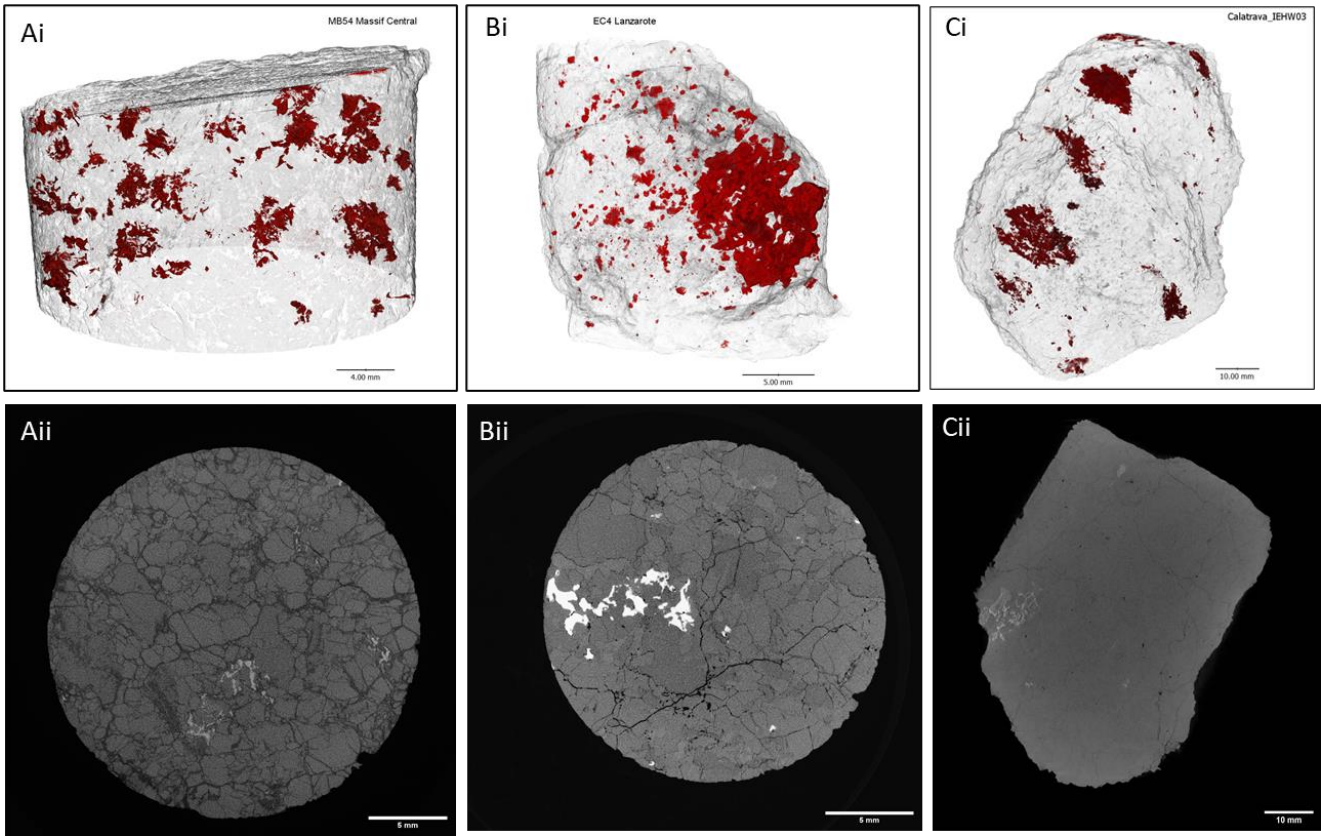

Figure 6.2. A (i) 3D rendered image of a spinel-pyroxene cluster in spinel peridotite (EC4, Lanzarote, Canary Islands). Spinel is red. Scale bar 4 mm. (ii) 2D slice image of a spinel-pyroxene cluster in a Spinel peridotite (EC4, Lanzarote, Canary Islands). B (i) 3D rendered image of a spinel-pyroxene cluster in spinel peridotite (MB54, Massif Central, France). Spinel is red. Scale bar 5 mm. (ii) 2D slice image of a spinel-pyroxene cluster in a Spinel peridotite (MB54, Massif Central, France). C (i) 3D rendered image of a spinel-pyroxene cluster in spinel peridotite (IEHW03, Calatrava, Spain). Spinel is red. Scale bar 5 mm. (ii) 2D slice image of a spinel-pyroxene cluster in a Spinel peridotite (IEHW03, Calatrava, Spain).

6.4 Results for garnet-spinel and garnet peridotite xenoliths.

Overall results have captured accurate 3D representations of the stages of the sub-solidus reaction in which the low-pressure phase of the upper mantle via lithospheric thickening and cooling converts to a spinel-pyroxene cluster. The 3D analysis of the textures when compared to typical xenolith spinel textures show that spinel-pyroxene clusters are confined to regions that have undergone lithospheric thinning. Range of volume of spinel in garnet-spinel samples implies that the conversion of spinel-pyroxene clusters to garnet is a gradual process and, with decreasing pressure, the volume of spinel increases and garnet decreases in the region of the mantle where garnet and spinel coexist. Spinel-pyroxene clusters are confined to regions that have undergone lithospheric thinning.

Micro-CT analysis of garnet peridotites from South Africa show that garnets form large individual grains which spherical to ellipsoidal in shape and measure between <4 mm in length and <3 mm in width to <2 mm in diameter and are more spherical in shape compared with the Vitim garnet peridotite xenoliths (Fig. 6.3A). Garnets are randomly and evenly distributed throughout the core

but does appear clustering of garnet grains. Spinel forms a low volume compared to garnet and exists as small blebs <1 mm and complex, vermicular structures. Spinel is largely limited to garnet-spinel clusters (Fig. 6.3B) but fine spinel grains are visible which is not associated with garnet.

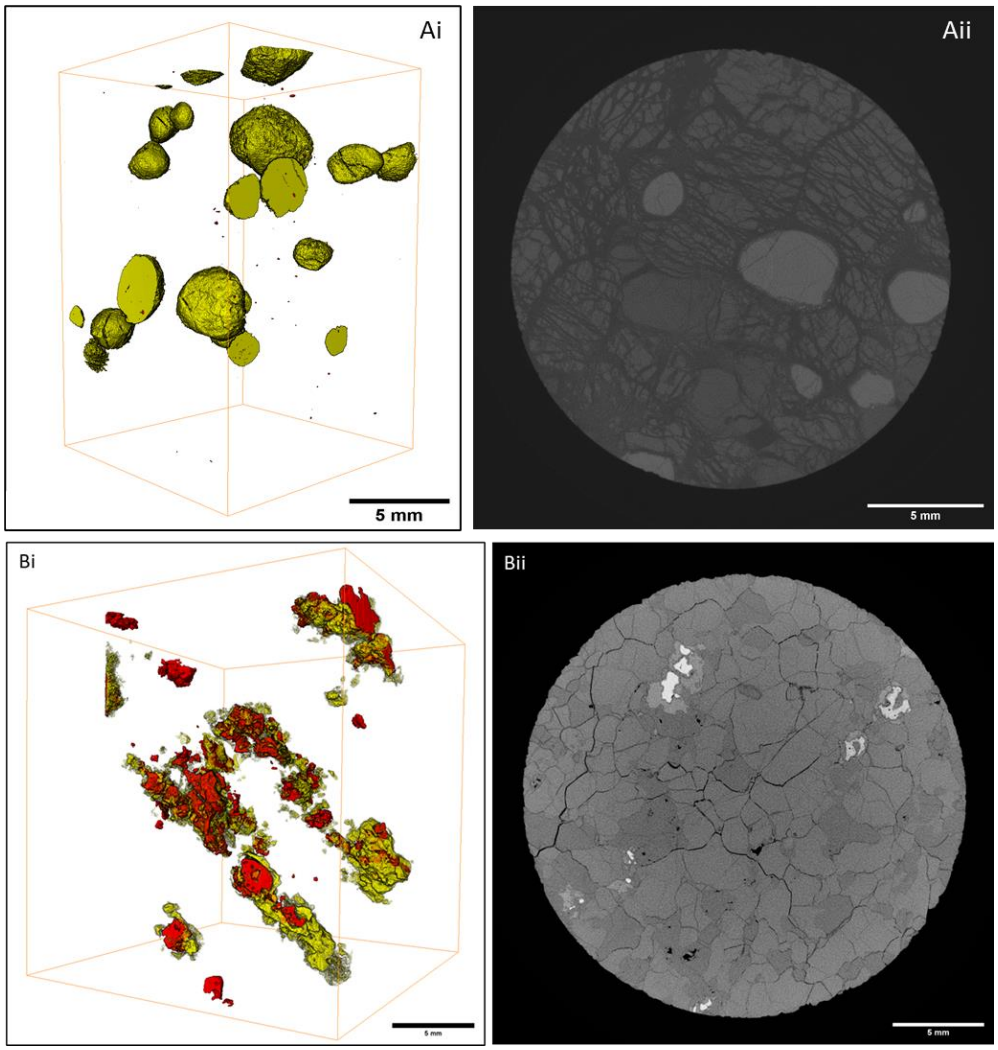

Figure 6.3. A (i) 3D rendered image of a garnet peridotite (DB1, Kaapvaal, South Africa). Garnet is yellow. Scale bar 5 mm. (ii) 2D slice image of a garnet peridotite (DB1). Garnet is light grey and silicate phase is dark grey. Scale bar 5 mm. B, (i) 3D rendered image of a garnet-spinel peridotite (PA10, Pali-Aike, South America). Garnet is yellow, Spinel is red. Scale bar 5 mm. (ii) 2D slice image of a garnet-spinel peridotite (PA10). Garnet is light grey surrounding spinel(white) and silicate phase is dark grey. Scale bar 5 mm.

Figure 6.4 is a Pressure-Temperature diagram which shows garnet-spinel peridotites from both Pali Aike and Vitim occupy a region close to the oceanic geotherm (65 mW/m^2) and show a narrow range of pressure and temperature whilst cratonic garnet peridotites from Kaapvaal plot at greater depth (~ 125 km), display a wider range in temperature and pressure in comparison to both Vitim and Pali Aike, and plot close to the continental geotherm estimated at 40 mW/m^2.

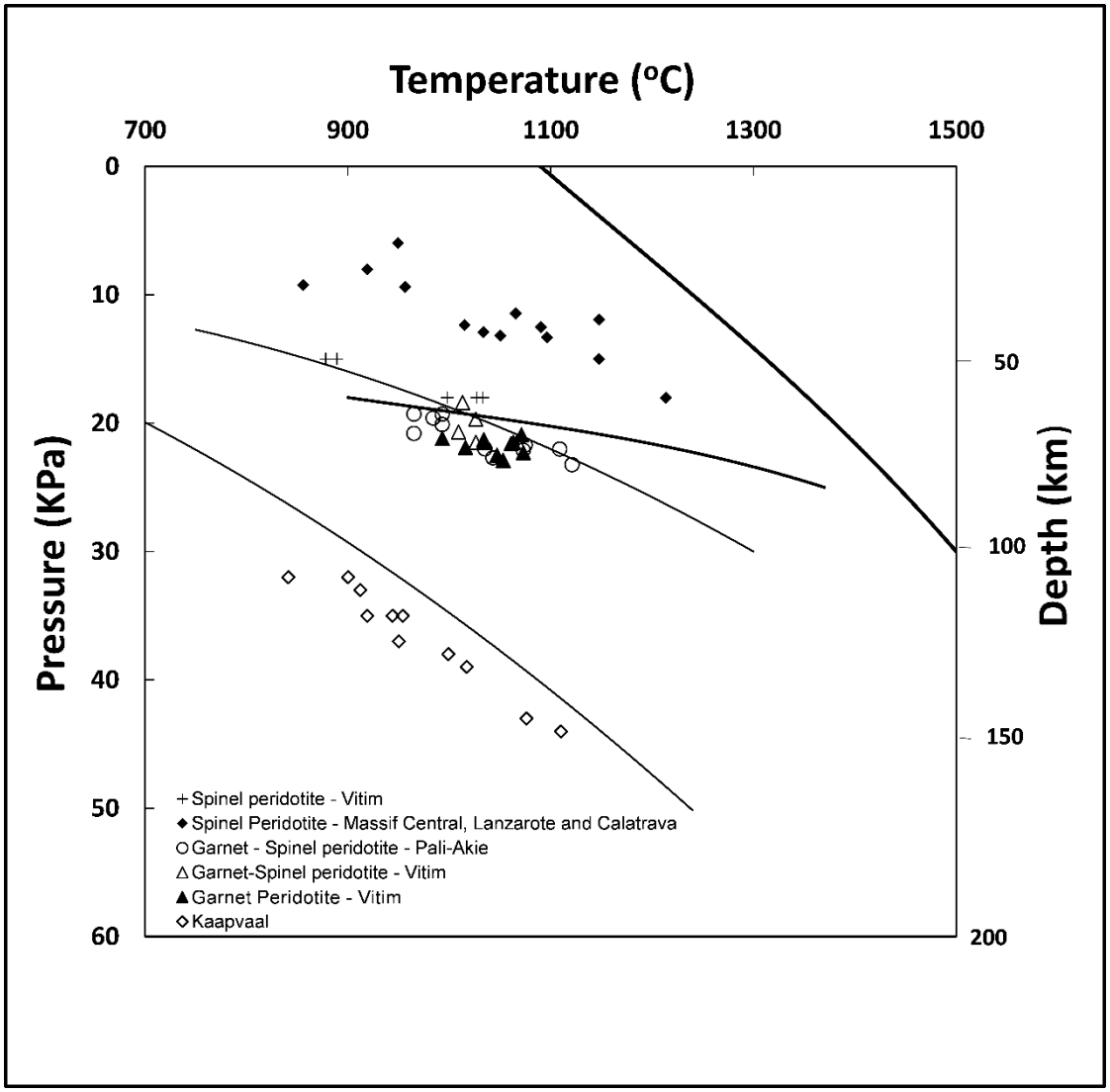

Figure 6.4. P-T diagram comparing mantle peridotites from Pali-Aike (open squares) and Vitim (open circles), spinel peridotites (Vitim, crosses) and spinel peridotites from Calatrava, Massif Central, (northern domain) and Lanzarote, solid diamonds, with cratonic mantle xenoliths (open diamonds). Data from Simon et al. (2003); Ionov et al. (2005) and Wang et al. (2008). Temperatures and pressures calculated using Brey and Köhler (1990) Ca-in-Opx thermometer, and Nickel and Green (1985) Al-in-Opx barometer. Garnet-spinel transition from Green and Ringwood (1967) is representative only, as this varies in depth according to the composition of the mantle). Temperatures and pressures calculated for Massif Central Northern domain, Lanzarote and Calatrava sp peridotites using Putirka (2008) RiMG (The Mineralogical Society of America two pyroxene spreadsheet http://www.minsocam.org/msa/rim/RiMG069/RiMG069_Ch03_two-pyroxene_P-T.xls).

6.5 Results for lunar dunite.

Study of spinel symplectite textures in lunar dunites offered the opportunity to compare these textures to terrestrial samples and determine indeed if spinel-pyroxene clusters are present and raise the possibility that decompression of dunite caused the conversion of the high-pressure garnet phase into a lower pressure spinel phase. EMPA elemental maps and data coupled with micro-CT images revealed several spinel textures. Detailed study of the spinel textures and their mineral chemistry allowed for identification of spinel mineral associations. Through this analysis, a picture was drawn showing the spinel textures having different origins and relative histories including

spinel-pyroxene clusters. Values of Mg# in olivine and Cr# in spinel constrain the origin of spinel peridotites. Spinel lherzolites and spinel harzburgites have limited ranges of Mg# in olivine and Cr# in spinel values, forming the olivine - spinel mantle array (OSMA). Comparing data for terrestrial samples and lunar dunite show that terrestrial spinel peridotites occupy distinct regions within the OSMA (Fig. 6.5). Lunar dunite values plot outside the OSMA, reflecting the difference in terrestrial and lunar mantle composition. The lunar mantle mineralogy is dominated by olivine and orthopyroxene (~80 vol%), with the remainder being composed of clinopyroxene and an aluminous phase (plagioclase, spinel or garnet (Khan et al., 2006). The Moon is generally believed to have formed from debris ejected by a large off-centre collision with the early Earth (Canup and Asphaug, 2001). This giant impact model was proposed by Hartmann and Davis, 1975; Cameron and Ward, 1976, Canup and Asphaug, 2001; Canup, 2004. The study by Khan et al (2006) states that the Moon is to a large extent made from mantle material of the impactor (~80%) and is assumed that the Earth and the impactor had already differentiated into a Fe-core and a silicate mantle. The significance of this that ejecta from both the Earth and impactor mantle would be low in Fe content and could explain the lunar iron deficit when compared to that of the Earth. Studies by Taylor, 1982; Delano, 1986 have proposed the bulk lunar composition Mg# is between 75 and 84 which is lower than that of the Earth's upper mantle reported at 89 in studies by Ringwood, 1979; Palme and Nickel, 1985; Khan et al., 2006).

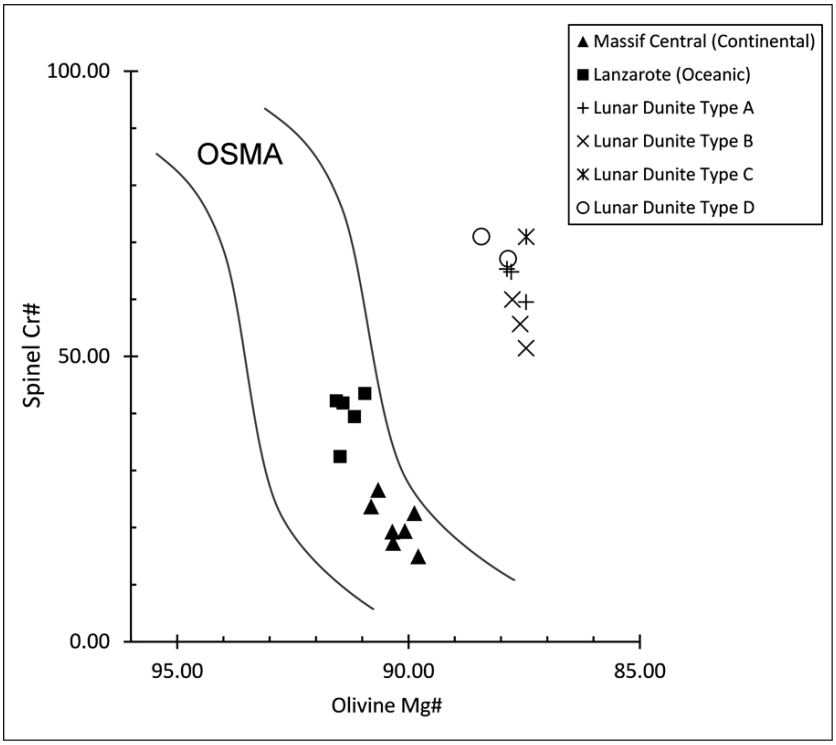

Figure 6.5. OSMA diagram showing lunar mantle compared with terrestrial mantle. Data from this study.

6.6. Conclusion.

Micro-CT analysis provides a major tool in analysis of mantle xenoliths when coupled with EMPA data. It allows for accurate analysis of the spinel textures including size, shape, and mineral association. With lithospheric thinning and as the lithospheric mantle rises, garnet peridotite undergoes a solid-state reaction transforming the garnet to a spinel-pyroxene cluster via the intermediate texture in which garnet and spinel coexist. Through combined micro-CT and EMPA analysis, we have captured the textural representation of the multiple stages for the solid-state reaction of olivine and garnet and the transition to a spinel-pyroxene cluster. Fig. 6.6 is a schematic representation of the 3D textural variations of the aluminous phase of peridotites during transformation from garnet peridotite to spinel peridotite.

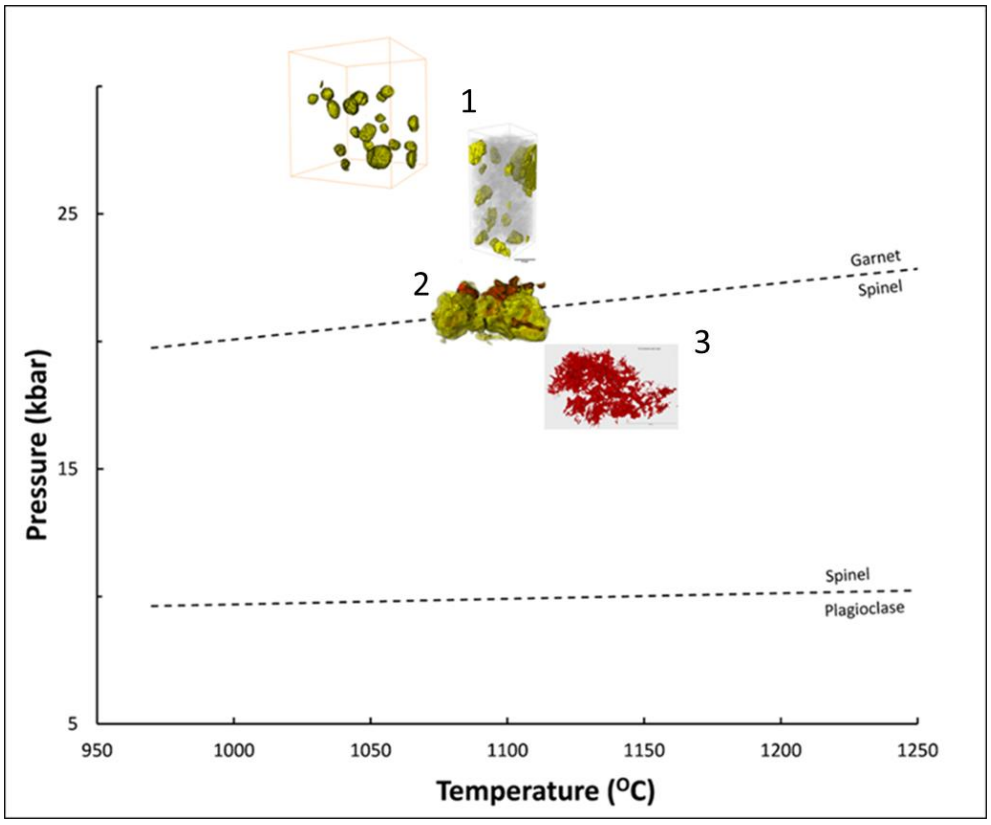

Figure 6.6. P-T diagram showing garnet and spinel stability fields. 3D images are representative textural types for conversion of garnet peridotite to a spc-bearing spinel peridotite. 1. Garnet peridotite. 2, garnet-spinel peridotite. 3, spinel-pyroxene cluster bearing spinel peridotite. Garnet is yellow and spinel is red.

Chapter 7

Continuing research

7.1 Future work.

Study of the lunar dunite has provided positive results but has raised more questions which require further investigation. Therefore, beyond this study I plan to continue researching into spinel textures on lunar dunite beginning with the study of the unknown texture using EMPA. The sample will require specialist cutting techniques yet to be fully determined. The analysis of REE in the clinopyroxenes for a garnet signature will also be pursued. Investigation into the determination of PT will also be undertaken.

The study has shown that micro-CT and EMPA are a useful tool in analysing mantle spinel textures. Further examples of the three textural types as defined by Mercier and Nicolas (1975) will be conducted from samples from Ray Pic, Massif Central, France. and obtain a clear view of the range of sp textures and with the hypothesis that the 3 textural types are not distinct in nature, but samples often show multiple textures with samples seen transitioning from one textural type to another.

Another aim beyond this project would be to continue to investigate the nature of metasomatic reactions in mantle peridotites and how these can be visualised in 3D imaging.

Analysis of the preferred crystallographic textures of olivines and spinel-pyroxene clusters using the technique of electron backscatter diffraction (EBSD) will be conducted and applied to spinel peridotites to evaluate and determine the extent of preferred orientation in peridotite samples.

A crystalline material is formed of a near flawless periodic array of atoms. When a force is applied, atoms react by moving away from their stable positions. If the force involved is small the material undergoes elastic deformation, i.e. the atoms return to their original state but if atoms move to the next stable position and when this force is not applied do not go back to their original state, the material is said to have undergone plastic deformation. Two major deformation mechanisms play important roles under upper mantle conditions (Artemieva, 2011): (1) dislocation creep and (2) diffusion creep. Dislocation creep involves the movement of dislocations within the crystalline structure of a grain brought on by high stress rates, large grain size resulting in a preferred orientation of a mineral. Diffusion creep is a solid-state process brought on by diffusion across grain boundaries or crystal lattice in a low stress regime and small grain size and does not lead to

preferred orientation of minerals and is commonly accepted that diffusion creep dominates in the upper mantle (Artemieva, 2011).

7.1.1 EBSD data

Miller indices designate crystal planes (and directions). This representation in the form of 3 integer numbers and thus represent the orientation of an atomic plane in a crystal lattice of crystal face and are defined as the reciprocals of the fractional intercepts (e.g. 1, 1/3, 2/3) which the plane makes with the crystallographic axes. Miller indices are calculated using the following procedure. Using a unit cubic cell where the x, y and z form a right-handed coordinate system. A plane can be considered as a face of a cube and which axis the plane intercepts the axis defines the miller indices, i.e. for a plane which intercepts the x axis at unit length (1) and thus being parallel to y and z axis the y and z intercepts are infinity. Taking the reciprocal of intercepts for this the plane intercepting the x axis yields 1,0,0 and the Miller indices are denoted as hkl in parenthesis and thus is identified as the (100) plane. Figure 7.1 provides examples of lattice planes and associated Miller indices.

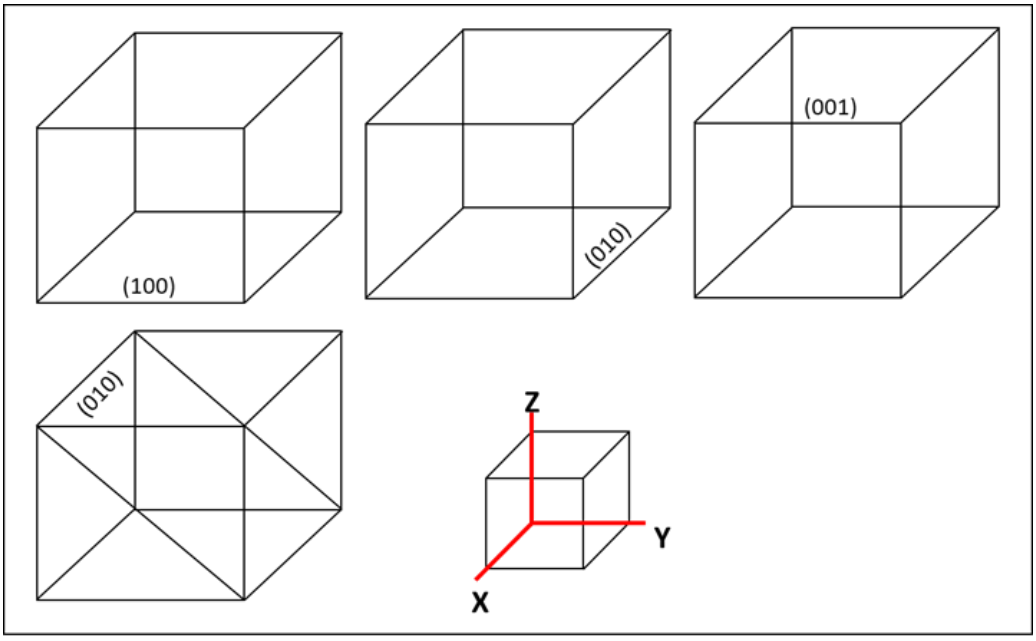

Figure 7.1. Examples of lattice planes. (Author's own image).

EBSD analysis of mineral texture (crystallographic orientation) is a pole figure. A pole figure is a map of a selected set of crystal plane normal (e.g. (100) plane normal) plotted with respect to the sample frame (sample x, y and Z). Pole figures are 2D representations of 3D orientations of specific crystallographic planes and directions within a sample and thus provide information on sample texture such as preferred crystallographic orientation and lineation. A pole figure takes a particular set of crystallographic planes then projects their position i.e., poles (or normals) projected onto a sphere and then onto a circle (stereographic projection).

An inverse pole figure plots the sample direction in the crystallographic coordinate system, i.e., instead of plotting the (100) planes in terms of the sample reference frame (x, y and z)), an inverse pole figure plots the sample frame axis with respect to major crystal directions (i.e. (100), [110] and (111). IPFs are generally used as a default scheme for orientation maps. IPF data is shown as a component utilising an RGB colouring scheme, e.g., cubic phases, red, green and blue represent planes (100), (110) or (111) parallel to the projection direction of the IPF, i.e., sample reference frame (x, y or z)). Transitional orientations are displayed as an RGB mixture.

7.1.2 Examples of EBSD analysis of mantle rocks

Falus et al (2008) investigated the microstructures and crystal preferred orientations (CPO) of upper mantle xenoliths from the lithospheric mantle beneath the SE Carpathians. Olivine and orthopyroxene revealed strong CPOs. Olivine [100] axes display single maxima aligned with the lineation implying that [100] slip was dominant, and that the [010] axes form girdles normal to the lineation with a maximum normal to the foliation, and [001] axes tend to be perpendicular to the lineation in the foliation plane or to form a girdle at high angle to the lineation. These crystal preferred orientations are characteristic of deformation by slip on [100] {0kl} systems with dominant activation of (010) planes (Falus et al., 2008).

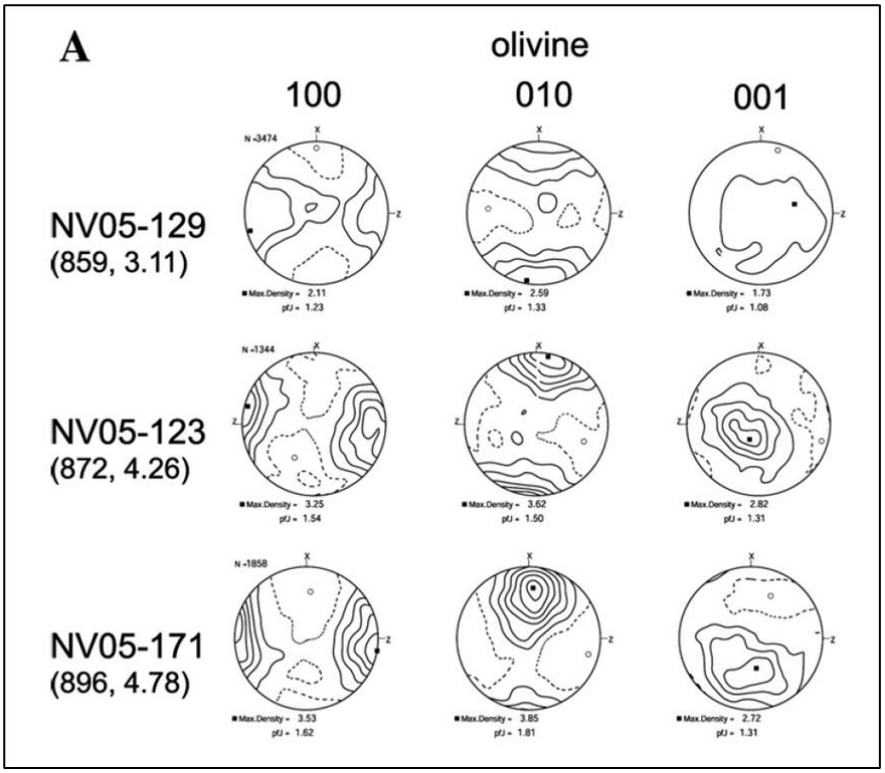

Figure 7.2. Examples of CPO of olivine in xenoliths taken from Falus et al. (2008). Lower hemisphere, equal area projection, contours at n×0.5 multiples of a uniform distribution.

A study by Tommasi et al (2004) into the microstructural and petrological analysis of mantle xenoliths from several archipelagos within the South Pacific Superswell provided evidence that the oceanic lithosphere above a mantle plume undergoes complex processes that induce significant changes in its chemical and modal composition. Crystal-preferred orientations (CPO) and hence seismic anisotropy are little affected by these processes and lherzolites and harzburgites, independent of Fe-content, show high-temperature porphyroclastic microstructures and strong olivine CPO (Tommasi et al., 2004). Lherzolites and harzburgites, regardless of composition or microstructure texture, display a strong and homogeneous olivine CPO. This CPO is characterized by a strong alignment of [100] axes close to the lineation and a girdle distribution of [010] and [001] normal to it, with weaker maxima normal and parallel to the foliation, respectively. This olivine CPO suggests deformation by dislocation creep with dominant activation of the high-temperature (010)[100] and (001)[100] slip systems (Fig. 7.3) (Tommasi et al., 2004).

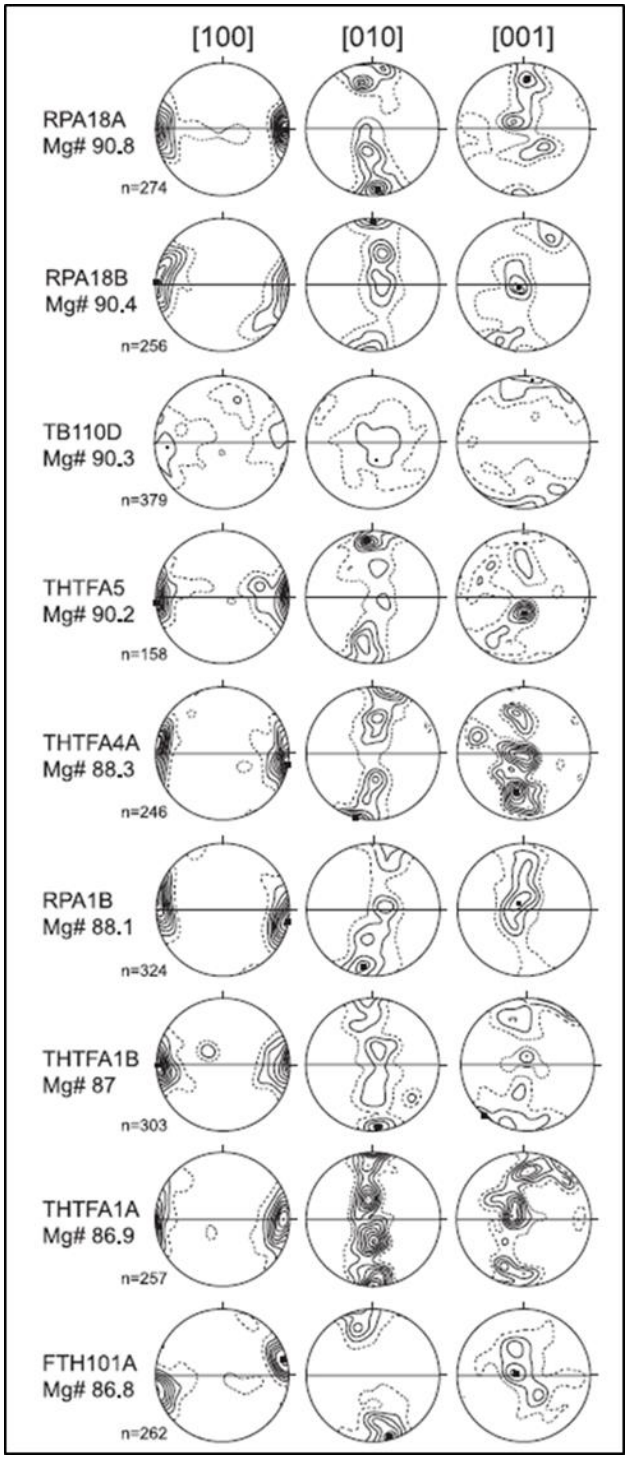

Figure 7.3. Olivine CPO displaying a strong alignment of [100] axes and a girdle distribution of [010] and [001] normal to it (Tommasi et al., 2004).

List of techniques to be used in the proposed further research include:

- EBSD. To understand how technique is applied to mantle xenoliths and investigate the orientation of spinel-pyroxene clusters with respect to olivine and non-cluster pyroxene grains. Also, to apply EBSD to the lunar dunite to investigate shock metamorphism.
- Elemental mapping. To identify mineral phases associated with metasomatic halos mantling garnet grains and spinel blebs in garnet and spinel peridotites, respectively.
- EMPA. To investigate the kelyphitic textures in garnet in Pali Aike samples.
- Micro CT. To develop better techniques to help to visualise metasomatic textures in mantle xenoliths in 3D.
- To further investigate the lunar symplectites using other imaging techniques
- LA-ICP-MS. Analysis of trace element mineral chemistry of major rock-forming minerals in mantle xenoliths and in the lunar dunite.

References

Ackerman, L., Mahlen, N., Jelĺnek, E., Medaris, G., Ulrych, J., Strnad, L., & Mihaljevič, M. 2007. Geochemistry and evolution of subcontinental lithospheric mantle in Central Europe: evidence from peridotite xenoliths of the Kozákov volcano, Czech Republic. Journal of Petrology, 48(12), 2235-2260.

Albee, A.L., Chodos, A.A., Dymek, R.F., Gancarz, A.J., Goldman, D.S., Papanastassiou, D.A. and Wasserburg, G.J., 1974. Dunite from the lunar highlands: petrography, deformational history, Rb-Sr age. Lunar and Planetary Science Conference Vol. 5, 3-4.

Albee, A.L., Dymek, R.F. and DePaolo, D.J., 1975. Spinel Symplectites: High-pressure solid-state reaction or late-stage magmatic crystallization? Lunar and Planetary Science Conference, Vol. 6, 1-3.

Anderson, D.L., 1975. On the composition of the lunar interior. Journal of Geophysical Research, 80(11), pp.1555-1557.

Aoki, K. I., & Shiba, I. 1973. Pyroxenes from lherzolite inclusions of Itinome-gata, Japan. Lithos, 6(1), 41-51.

Apollo 17 Image Library. https://www.hq.nasa.gov/alsj/a17/images17.html#MagI.

Arai, S. (1994). Characterization of spinel peridotites by olivine-spinel compositional relationships: review and interpretation. Chemical Geology, 113(3), 191-204.

Arai, S., 1987. An estimation of the least depleted spinel peridotite on the basis of olivine-spinel mantle array. Neues Jahrbuch für Mineralogie Monatshefte, 8(347), p.e354.

Arai, S., 1994. Characterization of spinel peridotites by olivine-spinel compositional relationships: review and interpretation. Chemical Geology, 113(3-4), pp.191-204.

Artemieva, I., 2011. The lithosphere: An interdisciplinary approach. Cambridge University Press.

Babuška, V., Plomerová, J., Vecsey, L., Granet, M. & Achauer, U., 2002. Seismic anisotropy of the French Massif Central and predisposition of Cenozoic rifting and volcanism by Variscan suture hidden in the mantle lithosphere. Tectonics, 21(4). 11-1–11-20.

Bailey, D.K., 1970. Volatile flux, heat focusing and the generation of magma. Geological Journal Special Issue, 2, pp.177-186.

Bailey, D.K., 1982. Mantle metasomatism—continuing chemical change within the Earth. Nature, 296 (5857), p.525.

Baker, D.R., Mancini, L., Polacci, M., Higgins, M.D., Gualda, G.A.R., Hill, R.J., and Rivers, M.L., 2012. An introduction to the application of X-ray microtomography to the three-dimensional study of igneous rocks. Lithos, 148, pp.262-276.

Basaltic Volcanism Study Project., 1981. Basaltic Volcanism on the Terrestrial Planets. Pergamon Press,Inc., New York. 1286 pp.

Basu, A.R. and MacGregor, I.D., 1976. Chromite spinels from ultramafic xenoliths. In: Chromium: its Physicochemical Behavior and Petrologic Significance (pp. 937-945). Pergamon.

Bell, P. M., and H. K. Mao, 1975. Cataclastic plutonites: Possible keys to the evolutionary history of the early moon. In: Lunar and Planetary Science Conference, vol. 6.

Bell, P.M., Mao, H.K., Roedder, E. and Weiblen, P.W., 1975. The problem of the origin of symplectites in olivine-bearing lunar rocks. Lunar and Planetary Science Conference Proceedings, Vol. 6, pp. 231-248.

Best, M.G. (2003) Igneous and metamorphic petrology. Second edition. Blackwell publishing.

Bhanot, K.K., Downes, H., Petrone, C.M. and Humphreys-Williams, E., 2017. Textures in spinel peridotite mantle xenoliths using micro-CT scanning: Examples from Canary Islands and France. Lithos, 276, 90-102.

Bhanot, K.K., Downes, H., Petrone, C.M., Humphreys-Williams, E. and Clark, B., 2020. Micro-CT investigation of garnet-spinel clusters in mantle peridotite xenoliths. Lithos, 352, p.105250.

Bianchini, G., Beccaluva, L., Bonadiman, C., Nowell, G.M., Pearson, D.G., Siena, F. and Wilson, M., 2010. Mantle metasomatism by melts of HIMU piclogite components: new insights from Fe-lherzolite xenoliths (Calatrava Volcanic District, central Spain). Geological Society, London, Special Publications, 337(1), pp.107-124.

Bjerg, E. A., Ntaflos, T., Thöni, M., Aliani, P., & Labudia, C. H. 2009. Heterogeneous lithospheric mantle beneath northern Patagonia: evidence from Prahuaniyeu garnet-and spinel-peridotites. Journal of Petrology, 50(7), 1267-1298.

Bonadiman, C., Beccaluva, L., Coltorti, M., & Siena, F. 2005. Kimberlite-like metasomatism and 'garnet signature' in spinel-peridotite xenoliths from Sal, Cape Verde Archipelago: relics of a subcontinental mantle domain within the Atlantic Oceanic lithosphere? Journal of Petrology, 46(12), 2465-2493.

Boullier, A. M., & Nicolas, A. 1975. Classification of textures and fabrics of peridotite xenoliths from South African kimberlites. Physics and Chemistry of the Earth, 9, 467-475.

Boyd, F. R. & Nixon, P. H. 1975. Origins of the ultramafic nodules from some kimberlites of northern Lesotho and the Monastery Mine, South Africa. Physics and Chemistry of the Earth, 9, 431-454.

Boyd, F. R. 1989. Compositional distinction between oceanic and cratonic lithosphere. Earth and Planetary Science Letters, 96(1-2), 15-26.

Boyd, F. R., & Nixon, P. H. 1978. Ultramafic nodules from the Kimberley pipes, South Africa. Geochimica et Cosmochimica Acta, 42(9), 13671373-13711382.

Boyd, F. R., Pokhilenko, N. P., Pearson, D. G., Mertzman, S. A., Sobolev, N. V., & Finger, L. W. 1997. Composition of the Siberian cratonic mantle: evidence from Udachnaya peridotite xenoliths. Contributions to Mineralogy and Petrology, 128(2-3), 228-246.

Boyd, F.R. and Mertzman, S.A., 1987. Composition and structure of the Kaapvaal lithosphere, southern Africa. Magmatic processes: physicochemical principles, 1, pp.3-12.

Boyd, F.R. and Nixon, P.H., 1978. Ultramafic nodules from the Kimberley pipes, South Africa. Geochimica et Cosmochimica Acta, 42(9), pp.1367-1382.

Boyd, F.R., Pearson, D.G., Nixon, P.H. and Mertzman, S.A., 1993. Low-calcium garnet harzburgites from southern Africa: their relations to craton structure and diamond crystallization. Contributions to Mineralogy and Petrology, 113(3), pp.352-366.

Brey, G.P. and Köhler, T., 1990. Geothermobarometry in four-phase lherzolites II. New thermobarometers, and practical assessment of existing thermobarometers. Journal of Petrology, 31(6), 1353-1378.

Buck, W.R. and Toksoz, M.N., 1980. The bulk composition of the Moon based on geophysical constraints. Lunar and Planetary Science Conference Proceedings, Vol. 11, pp. 2043-2058.

Cameron, A.G. and Ward, W.R., 1976, March. The origin of the Moon. In Lunar and Planetary Science Conference (Vol. 7).

Canup, R.M. and Asphaug, E., 2001. Origin of the Moon in a giant impact near the end of the Earth's formation. Nature, 412(6848), pp.708-712.

Canup, R.M., 2004. Simulations of a late lunar-forming impact. Icarus, 168(2), pp.433-456.

Cao, R.L. and Zhu, S.H., 1987. Mantle xenoliths and alkali-rich host rocks in eastern China. Mantle xenoliths (Ed P H Nixon), pp.168-180.

Carlson W D, T. Rowe T, Ketcham R A, and Colbert M W. 2003. Applications of high-resolution X-ray computed tomography in petrology, meteoritics and palaeontology. Geological Society, London, Special Publications, v. 215, p. 7-22

Carlson, R. L., & Johnson, H. P. 1994. On modeling the thermal evolution of the oceanic upper mantle: An assessment of the cooling plate model. Journal of Geophysical Research: Solid Earth, 99(B2), 3201-3214.

Carlson, W.D., 2006. Three-dimensional imaging of earth and planetary materials. Earth and Planetary Science Letters, 249(3-4), pp.133-147.

Carpenter, R. L., Edgar, A. D., & Thibault, Y. 2002. Origin of spongy textures in clinopyroxene and spinel from mantle xenoliths, Hessian Depression, Germany. Mineralogy and Petrology, 74(2-4), 149-162.

Carracedo, J. C., Day, S., Guillou, H., Rodríguez Badiola, E., Canas, J. A., & Pérez Torrado, F. J. (1998). Hotspot volcanism close to a passive continental margin: the Canary Islands. Geological Magazine, 135(05), 591-604.

Carswell, D.A., Clarke, D.B. and Mitchell, R.H., 1979. The petrology and geochemistry of ultramafic nodules from Pipe 200, northern Lesotho. The Mantle Sample: Inclusion in Kimberlites and Other Volcanics, 16, 127-144.

Carter, N.L., Raleigh, C.B. and DeCarli, P.S., 1968. Deformation of olivine in stony meteorites. Journal of Geophysical Research, 73(16), pp.5439-5461.

Clague, D. A. 1988. Petrology of ultramafic xenoliths from Loihi Seamount, Hawaii. Journal of Petrology, 29(6), 1161-1186.

Clauser, C. and Huenges, E. 1995. Thermal Conductivity of Rocks and Minerals, in Rock Physics & Phase Relations: A Handbook of Physical Constants (ed T. J. Ahrens), American Geophysical Union, Washington, D. C.

Clayton, R.N. and Mayeda, T.K., 1975. Genetic relations between the moon and meteorites. In Lunar and Planetary Science Conference Proceedings, Vol. 6, pp. 1761-1769.

Cnudde, V., Masschaele, B., Dierick, M., Vlassenbroeck, J., Van Hoorebeke, L. and Jacobs, P., 2006. Recent progress in X-ray CT as a geosciences tool. Applied Geochemistry, 21(5), pp.826-832.

Coisy, P., & Nicolas, A. 1978. Regional structure and geodynamics of the upper mantle beneath the Massif Central. Nature, 274, 429-432.

Croft, S.K., 1980. Cratering flow fields: Implications for the excavation and transient expansion stages of crater formation. Lunar and Planetary Institute Contribution 421

Dawson, J. B., & Smith, J. V. 1975. Chromite-silicate intergrowths in upper-mantle peridotites. Physics and Chemistry of the Earth, 9, 339-350.

Delano, J.W., 1986. Abundances of cobalt, nickel, and volatiles in the silicate portion of the Moon. In Origin of the Moon (pp. 231-247).

Dence, M.R., Grieve, R.A.F. and Plant, A.G., 1976, April. Apollo 17 grey breccias and crustal composition in the Serenitatis basin region. Lunar and Planetary Science Conference Proceedings, Vol. 7, pp. 1821-1832.

Douglas, B.J., Saul, S.L. and Stern, C.R., 1987. Rheology of the upper mantle beneath southernmost South America inferred from peridotite xenoliths. The Journal of Geology, 95(2), 241-253.

Downes, H., & Dupuy, C. 1987. Textural, isotopic and REE variations in spinel peridotite xenoliths, Massif Central, France. Earth and Planetary Science Letters, 82(1), 121-135.

Downes, H., Reichow, M. K., Mason, P. R. D., Beard, A. D. & Thirlwall, M. F. 2003. Mantle domains in the lithosphere beneath the French Massif Central: trace element and isotopic evidence from mantle clinopyroxenes. Chemical Geology, 200(1), 71-87.

Drake, M.J., 1986. Is lunar bulk material similar to Earth's mantle? In: Origin of the Moon (pp. 105-124).

Dymek, R.F., Albee, A.L. and Chodos, A.A., 1975. Comparative mineralogy and petrology of Apollo 17 mare basalts-Samples 70215, 71055, 74255, and 75055. Lunar and Planetary Science Conference Proceedings, Vol. 6, pp. 49-77.

Dymek, R.F., Albee, A.L. and Chodos, A.A., 1975. Comparative petrology of lunar cumulate rocks of possible primary origin-Dunite 72415, troctolite 76535, norite 78235, and anorthosite 62237. Lunar and Planetary Science Conference Proceedings, Vol. 6, pp. 301-341.

Dymek, R.F., Albee, A.L. and Chodos, A.A., 1976, April. Petrology and origin of Boulders no. 2 and no. 3, Apollo 17 Station 2. Lunar and Planetary Science Conference Proceedings, Vol. 7, pp. 2335-2378.

Elardo, S.M., Draper, D.S. and Shearer Jr, C.K., 2011. Lunar Magma Ocean crystallization revisited: Bulk composition, early cumulate mineralogy, and the source regions of the highlands Mg-suite. Geochimica et Cosmochimica Acta, 75(11), pp.3024-3045.

Elkins-Tanton, L.T., Burgess, S. and Yin, Q.Z., 2011. The lunar magma ocean: Reconciling the solidification process with lunar petrology and geochronology. Earth and Planetary Science Letters, 304(3-4), pp.326-336.

El-Rus, M. A., Neumann, E. R., & Peters, V. 2006. Serpentinization and dehydration in the upper mantle beneath Fuerteventura (eastern Canary Islands): Evidence from mantle xenoliths. Lithos, 89(1), 24-46.

Euler, L., 1775. Novi Comm. Acad. Sci. Petropol, 20, p.140.

Falus, G., Szabó, C., & Vaselli, O. 2000. Mantle upwelling within the Pannonian Basin: evidence from xenolith lithology and mineral chemistry. Terra Nova, 12(6), 295-302.

Falus, G., Tommasi, A., Ingrin, J. and Szabó, C., 2008. Deformation and seismic anisotropy of the lithospheric mantle in the southeastern Carpathians inferred from the study of mantle xenoliths. Earth and Planetary Science Letters, 272(1-2), pp.50-64.

Frost, D. J. 2008. The upper mantle and transition zone. Elements, 4(3), 171-176.

Ghosh, B., Morishita, T., & Bhatta, K. 2013. Significance of chromian spinels from the mantle sequence of the Andaman Ophiolite, India: Paleogeodynamic implications. Lithos, 164, 86-96.

Gibson, S.A., McMahon, S.C., Day, J.A. and Dawson, J.B., 2013. Highly refractory lithospheric mantle beneath the Tanzanian craton: evidence from Lashaine pre-metasomatic garnet-bearing peridotites. Journal of Petrology, 54(8), 1503-1546.

Gibson, S.A., Rooks, E.E., Day, J.A., Petrone, C.M. and Leat, P.T., 2020. The role of sub-continental mantle as both “sink” and “source” in deep Earth volatile cycles. Geochimica et Cosmochimica Acta, 275, pp.140-162.

Godard, G. and Martin, S., 2000. Petrogenesis of kelyphites in garnet peridotites: a case study from the Ulten zone, Italian Alps. Journal of Geodynamics, 30(1-2), 117-145.

Goins, N.R., Dainty, A.M. and Toksöz, M.N., 1981. Lunar seismology: The internal structure of the Moon. Journal of Geophysical Research: Solid Earth, 86(B6), pp.5061-5074.

Goins, N.R., Dainty, A.M. and Toksöz, M.N., 1981. Lunar seismology: The internal structure of the Moon. Journal of Geophysical Research: Solid Earth, 86(B6), pp.5061-5074.

Green, D.H. and Hibberson, W., 1970. The instability of plagioclase in peridotite at high pressure. Lithos, 3(3), pp.209-221.

Green, D.H. and Ringwood, A.E., 1967. The stability fields of aluminous pyroxene peridotite and garnet peridotite and their relevance in upper mantle structure. Earth and Planetary Science Letters, 3, 151-160.

Green, D.H. and Ringwood, A.E., 1970. Mineralogy of peridotitic compositions under upper mantle conditions. Physics of the Earth and Planetary Interiors, 3, pp.359-371.

Grégoire, M., Bell, D.R. and Le Roex, A.P., 2003. Garnet lherzolites from the Kaapvaal Craton (South Africa): trace element evidence for a metasomatic history. Journal of Petrology, 44(4), 629-657.

Grégoire, M., Tinguely, C., Bell, D. R., & Le Roex, A. P. 2005. Spinel lherzolite xenoliths from the Premier kimberlite (Kaapvaal craton, South Africa): nature and evolution of the shallow upper mantle beneath the Bushveld complex. Lithos, 84(3), 185-205.

Grieve, R.A.F., Robertson, P.B. and Dence, M.R., 1981. Constraints on the formation of ring impact structures, based on terrestrial data. In: Multi-ring basins: Formation and evolution (pp. 37-57).

Griffin, L.D., Elangovan, P., Mundell, A. and Hezel, D.C., 2012. Improved segmentation of meteorite micro-CT images using local histograms. Computers & Geosciences, 39, pp.129-134.

Griffin, W. L., O'Reilly, S. Y., Afonso, J. C., & Begg, G. C. 2008. The composition and evolution of lithospheric mantle: a re-evaluation and its tectonic implications. Journal of Petrology, 50(7), 1185-1204.

Grove, T.L. and Krawczynski, M.J., 2009. Lunar mare volcanism: where did the magmas come from? Elements, 5(1), pp.29-34.

Haase, I., Wählisch, M., Gläser, P., Oberst, J. and Robinson, M.S., 2019. Coordinates and maps of the Apollo 17 landing site. Earth and Space Science, 6(1), pp.59-95.

Hansteen, T. H., Andersen, T., Neumann, E. R., & Jelsma, H. 1991. Fluid and silicate glass inclusions in ultramafic and mafic xenoliths from Hierro, Canary Islands: implications for mantle metasomatism. Contributions to Mineralogy and Petrology, 107(2), 242-254.

Harte, B. 1977. Rock nomenclature with particular relation to deformation and recrystallisation textures in olivine-bearing xenoliths. The Journal of Geology, 279-288.

Hartmann, W.K. and Davis, D.R., 1975. Satellite-sized planetesimals and lunar origin. Icarus, 24(4), pp.504-515.

Hartmann, W.K. and Davis, D.R., 1975. Satellite-sized planetesimals and lunar origin. Icarus, 24(4), pp.504-515.

Hartmann, W.K. and Kuiper, G.P., 1962. Concentric structures surrounding lunar basins. CoLPL, 1, pp.51-66.

Hawkesworth, C.J., Erlank, A.J., Kempton, P.D. and Waters, F.G., 1990. Mantle metasomatism: isotope and trace-element trends in xenoliths from Kimberley, South Africa. Chemical Geology, 85(1-2), pp.19-34.

Head, J.W., 1974. Morphology and structure of the Taurus-Littrow highlands (Apollo 17): Evidence for their origin and evolution. The Moon, 9(3-4), pp.355-395.

Heiken, G.H., McKay, D.S. and Brown, R.W., 1974. Lunar deposits of possible pyroclastic origin. Geochimica et Cosmochimica Acta, 38(11), pp.1703-1718.

Heiken, G.H., Vaniman, D.T. and French, B.M., 1991. Lunar Sourcebook, a user's guide to the Moon. Cambridge University Press.

Herzberg, C.T., 1993. Lithosphere peridotites of the Kaapvaal craton. Earth and Planetary Science Letters, 120(1-2), pp.13-29.

Hess, P.C. and Parmentier, E.M., 1995. A model for the thermal and chemical evolution of the Moon's interior: Implications for the onset of mare volcanism. Earth and Planetary Science Letters, 134(3-4), pp.501-514.

Hezel, D.C., Elangovan, P., Viehmann, S., Howard, L., Abel, R.L. and Armstrong, R., 2013. Visualisation and quantification of CV chondrite petrography using micro-tomography. Geochimica et Cosmochimica Acta, 116, pp.33-40.

http://www.nist.gov/pml/data/xraycoef.

Https://astrogeology.usgs.gov/search/map/Moon/Apollo/Traverse/Apollo17/Apollo17_landing_site_map_scale15000.

Hughes, S.S., Delano, J.W. and Schmitt, R.A., 1988. Apollo 15 yellow-brown volcanic glass: Chemistry and petrogenetic relations to green volcanic glass and olivine-normative mare basalts. Geochimica et Cosmochimica Acta, 52(10), pp.2379-2391.

Huismans, R.S., Podladchikov, Y.Y. & Cloetingh, S., 2001. Transition from passive to active rifting: Relative importance of asthenospheric doming and passive extension of the lithosphere. Journal of Geophysical Research: Solid Earth, 106(B6), pp.11271-11291.

Humphreys, E. R. 2011. Carbonatite-silicate volcanism and mantle metasomatism: Case studies from Calatrava, Spain. PhD Thesis. University of Bristol.

Humphreys, E. R., & Niu, Y. 2009. On the composition of ocean island basalts (OIB): The effects of lithospheric thickness variation and mantle metasomatism. Lithos, 112(1), 118-136.

Hutchison, R., Chambers, A. L., Paul, D. K., & Harris, P. G. 1975. Chemical variation among French ultramafic xenoliths--evidence for a heterogeneous upper mantle.

Hutchison, R., Williams, C. T., Henderson, P and Reed S. J. B. 1986. New varieties of mantle xenolith from the Massif Central, France. Mineralogical Magazine, 50, 559-65.

Ionov, D., 2002. Mantle structure and rifting processes in the Baikal–Mongolia region: geophysical data and evidence from xenoliths in volcanic rocks. Tectonophysics, 351(1-2), 41-60.

Ionov, D., 2004. Chemical variations in peridotite xenoliths from Vitim, Siberia: inferences for REE and Hf behaviour in the garnet-facies upper mantle. Journal of Petrology, 45(2), 343-367.

Ionov, D.A. and Hofmann, A.W., 2007. Depth of formation of subcontinental off-craton peridotites. Earth and Planetary Science Letters, 261(3), 620-634.

Ionov, D.A., Ashchepkov, I. and Jagoutz, E., 2005. The provenance of fertile off-craton lithospheric mantle: Sr–Nd isotope and chemical composition of garnet and spinel peridotite xenoliths from Vitim, Siberia. Chemical Geology, 217(1-2), 41-75.

Ionov, D.A., Ashchepkov, I.V., Stosch, H.G., Witt-Eickschen, G. & Seck, H.A., 1993. Garnet peridotite xenoliths from the Vitim Volcanic Field, Baikal Region: the nature of the garnet-spinel peridotite transition zone in the continental mantle. Journal of Petrology, 34(6), pp.1141-1175.

Ionov, D.A., Ashchepkov, I.V., Stosch, H.G., Witt-Eickschen, G. and Seck, H.A., 1993. Garnet peridotite xenoliths from the Vitim volcanic field, Baikal region: The nature of the garnet—spinel peridotite transition zone in the continental mantle. Journal of Petrology, 34(6), pp.1141-1175.

Ionov, D.A., Doucet, L.S. and Ashchepkov, I.V., 2010. Composition of the lithospheric mantle in the Siberian craton: new constraints from fresh peridotites in the Udachnaya-East kimberlite. Journal of Petrology, 51(11), 2177-2210.

Jaupart, C., Labrosse, S. & Mareschal, J.C., 2007. 6.05- Heat Flow and Thermal Structure of the Lithosphere. Treatise on Geophysics, pp 217–251

Jenkins, D.M. and Newton, R.C., 1979. Experimental determination of the spinel peridotite to garnet peridotite inversion at 900 C and 1,000 C in the system CaO-MgO-Al2O3-SiO2, and at 900 °C with natural garnet and olivine. Contributions to Mineralogy and Petrology, 68(4), 407-419.

Jerram, D.A., Mock, A., Davis, G.R., Field, M. and Brown, R.J., 2009. 3D crystal size distributions: A case study on quantifying olivine populations in kimberlites. Lithos, 112, pp.223-235.

Jones E. M., 1995. Corrected Transcript and commentary, Apollo 17 Lunar Science Journal. https://history.nasa.gov/alsj/a17/a17.htmlhttps://history.nasa.gov/alsj/a17/a17.html.

Kempton, P.D., Lopez-Escobar, L., Hawkesworth, C.J., Pearson, D.G., Wright, D.W. and Ware, A.J., 1999. Spinel ± garnet lherzolite xenoliths from Pali Aike: Part 1. Petrography, mineral chemistry and geothermobarometry. JB Dawson volume. Proceedings of VIIth International Kimberlite Conference, pp. 403-414.

Kesson, S.E. and Ringwood, A.E., 1976. Mare basalt petrogenesis in a dynamic moon. Earth and Planetary Science Letters, 30(2), pp.155-163.

Ketcham R A and Carlson W D. 2001. Acquisition, optimization and interpretation of X-ray computed tomographic imagery: applications to the geosciences. Computers & Geosciences 27, 381–400.

Khan, A., Connolly, J.A.D., Maclennan, J. and Mosegaard, K., 2007. Joint inversion of seismic and gravity data for lunar composition and thermal state. Geophysical Journal International, 168(1), pp.243-258.

Khan, A., Maclennan, J., Taylor, S.R. and Connolly, J.A.D., 2006. Are the Earth and the Moon compositionally alike? Inferences on lunar composition and implications for lunar origin and evolution from geophysical modeling. Journal of Geophysical Research: Planets, 111(E5).

Klemme, S. and O'Neill, H.S., 2000. The near-solidus transition from garnet lherzolite to spinel lherzolite. Contributions to Mineralogy and Petrology, 138(3), 237-248.

Kruth J P, M. Bartscher M. Carmignato Schmitt R, De Chiffre L, Weckenmann A. 2011. Computed tomography for dimensional metrology. CIRP Annals - Manufacturing Technology 60 821–842.

Kushiro, I. and Yoder Jr, H.S., 1966. Anorthite-forsterite and anorthite-enstatite reactions and their bearing on the basalt-eclogite transformation. Journal of Petrology, 7(3), 337-362.

Landis E N, Keane D T. 2010. X-ray microtomography. Materials Characterization. 61. 1305 – 1316.

Laul, J.C. and Schmitt, R.A., 1975. Dunite 72417-A chemical study and interpretation. In Lunar and Planetary Science Conference Proceedings, Vol. 6, pp. 1231-1254.

Lenoir, X., Garrido, C. J., Bodinier, J. L., & Dautria, J. M. 2000. Contrasting lithospheric mantle domains beneath the Massif Central (France) revealed by geochemistry of peridotite xenoliths. Earth and Planetary Science Letters, 181(3), 359-375.

Limaye, A. 2012. Drishti: a volume exploration and presentation tool. In SPIE Optical Engineering+ Applications (pp. 85060X-85060X). International Society for Optics and Photonics.

Longhi, J., 2006. Petrogenesis of picritic mare magmas: constraints on the extent of early lunar differentiation. Geochimica et Cosmochimica Acta, 70(24), pp.5919-5934.

López-Ruiz, J., Cebriá, J.M., Doblas, M., Oyarzun, R., Hoyos, M. and Martín, C., 1993. Cenozoic intra-plate volcanism related to extensional tectonics at Calatrava, central Iberia. Journal of the Geological Society, 150(5), pp.915-922.

Luhr, J. F., & Aranda-Gómez, J. J. 1997. Mexican peridotite xenoliths and tectonic terranes: correlations among vent location, texture, temperature, pressure, and oxygen fugacity. Journal of Petrology, 38(8), 1075-1112.

Macgregor, I.D., 1970. The effect of CaO, Cr2O3, Fe2O3 and Al2O3 on the stability of spinel and garnet peridotites. Physics of the Earth and Planetary Interiors, 3, pp.372-377.

Macgregor, I.D., 1974. The System MgO-Al2O3-SiO2: Solubility of Al2O3 in Enstatite for Spinel and Garnet Peridotite Compositions. American Mineralogist, 59(1-2), pp.110-119.

Mackin, J.H., 1969. Origin of lunar maria. Geological Society of America Bulletin, 80(5), pp.735-748.

Magnarini, G., Mitchell, T., Grindrod, P. and Goren, L., 2021. Longitudinal Ridges in Long Runout Landslides: on the Applicability of High-Speed Granular Flow Mechanisms (No. EGU21-4822). Copernicus Meetings.

Maitland, T. and Sitzman, S., 2007. Electron backscatter diffraction (EBSD) technique and materials characterization examples (Vol. 14, p. 522). Berlin: Springer.

McDonough, W. F. & Rudnick, R. L. 1998. Mineralogy and composition of the upper mantle. Reviews in Mineralogy, 37, 139-164.

McDonough, W.S., 1990. Constraints on the composition of the continental lithospheric mantle. Earth and Planetary Science Letters, 101(1), pp.1-18.

McGregor, I.D., 1974. The System MgO-Al2O3-SiO2: Solubility of Al2O3 in Enstatite for Spinel and Garnet Peridotite Compositions. American Mineralogist, 59(1-2), pp.110-119.

McKenzie, D. P. 1967. Some remarks on heat flow and gravity anomalies. Journal of Geophysical Research, 72(24), 6261-6273.

McKenzie, D., 1978. Some remarks on the development of sedimentary basins. Earth and Planetary Science Letters, 40(1), pp.25-32.

McKenzie, D., Jackson, J., & Priestley, K. 2005. Thermal structure of oceanic and continental lithosphere. Earth and Planetary Science Letters, 233(3), 337-349.

Melosh, H.J., Freed, A.M., Johnson, B.C., Blair, D.M., Andrews-Hanna, J.C., Neumann, G.A., Phillips, R.J., Smith, D.E., Solomon, S.C., Wieczorek, M.A. and Zuber, M.T., 2013. The origin of lunar mascon basins. Science, 340(6140), pp.1552-1555

Melosh, H.J., Freed, A.M., Johnson, B.C., Blair, D.M., Andrews-Hanna, J.C., Neumann, G.A., Phillips, R.J., Smith, D.E., Solomon, S.C., Wieczorek, M.A. and Zuber, M.T., 2013. The origin of lunar mascon basins. Science, 340(6140), pp.1552-1555

Mercier, J.C. and Nicolas, A., 1975. Textures and fabrics of upper-mantle peridotites as illustrated by xenoliths from basalts. Journal of Petrology, 16(1), pp.454-487.

Meyer, C. 2012. Lunar Sample Compendium. http://www-curator.jsc.nasa.gov/

Miljković, K., Wieczorek, M.A., Collins, G.S., Solomon, S.C., Smith, D.E. and Zuber, M.T., 2015. Excavation of the lunar mantle by basin-forming impact events on the Moon. Earth and Planetary Science Letters, 409, pp.243-251.

Morgan, W.J., 1971. Convection plumes in the lower mantle. Nature, 230(5288), pp.42-43.

Morishita, T., & Arai, S. 2003. Evolution of spinel–pyroxene symplectite in spinel–lherzolites from the Horoman Complex, Japan. Contributions to Mineralogy and Petrology, 144(5), 509-522.

MuCalcTool. http://www.ctlab.geo.utexas.edu/software.

Muller, P.M. and Sjogren, W.L., 1968. Mascons: Lunar mass concentrations. Science, 161(3842), pp.680-684.

Muncaster R. 1985. A-Level Physics. 2nd Edition. Stanley Thomas Publishers.

Murav'yeva, N.S., Polyakov, A.I. and Senin, V.G., 1985. Physicochemical conditions and mechanism of formation of garnet-spinel lherzolite from the Vitim Plateau, Baikal rift zone. Doklady Akademii Nauk SSSR, 283, 1458-1462.

Nascimento-Dias, B.L., Araujo, O.M.O., Machado, A.S., Oliveira, D.F., Anjos, M.J., Lopes, R.T. and Assis, J.T., 2019. Analysis of two meteorite fragments (lunar and martian) using X-Ray microfluorescence and X-Ray computed microtomography techniques. Applied Radiation and Isotopes, 152, pp.156-161.

Neal, C.R., 2001. Interior of the Moon: The presence of garnet in the primitive deep lunar mantle. Journal of Geophysical Research: Planets, 106(E11), pp.27865-27885.

Neumann, E. R. 1991. Ultramafic and mafic xenoliths from Hierro, Canary Islands: evidence for melt infiltration in the upper mantle. Contributions to Mineralogy and Petrology, 106(2), 236-252.

Neumann, E. R., & Wulff-Pedersen, E. 1997. The origin of highly silicic glass in mantle xenoliths from the Canary Islands. Journal of Petrology, 38(11), 1513-1539.

Neumann, E. R., Wulff-Pedersen, E., Johnsen, K., Andersen, T., & Krogh, E. 1995. Petrogenesis of spinel harzburgite and dunite suite xenoliths from Lanzarote, eastern Canary Islands: implications for the upper mantle. Lithos, 35(1-2), 83-107.

Neumann, E. R., Wulff-Pedersen, E., Pearson, N. J., & Spencer, E. A. 2002. Mantle xenoliths from Tenerife (Canary Islands): evidence for reactions between mantle peridotites and silicic carbonatite melts inducing Ca metasomatism. Journal of Petrology, 43(5), 825-857.

Neumann, G.A., Zuber, M.T., Wieczorek, M.A., Head, J.W., Baker, D.M., Solomon, S.C., Smith, D.E., Lemoine, F.G., Mazarico, E., Sabaka, T.J. and Goossens, S.J., 2015. Lunar impact basins revealed by Gravity Recovery and Interior Laboratory measurements. Science advances, 1(9), p.e1500852.

Nickel, K.G. and Green, D.H., 1985. Empirical geothermobarometry for garnet peridotites and implications for the nature of the lithosphere, kimberlites and diamonds. Earth and Planetary Science Letters, 73(1), 158-170.

Nicolas, A., Lucazeau, F., & Bayer, R. 1987. Peridotite xenoliths in Massif Central basalts, France: textural and geophysical evidence for asthenospheric diapirism. Mantle Xenoliths (Ed. P H Nixon), 563-574.

Nishikawa, S. and Kikuchi, S., 1928. Diffraction of cathode rays by calcite. Nature, 122(3080), p.726.

O'Reilly, S.Y. and Griffin, W.L., 2013. Mantle metasomatism. In Metasomatism and the chemical transformation of rock (pp. 471-533). Springer, Berlin, Heidelberg.

Obata, M. 1976. The solubility of Al2O3 in orthopyroxenes in spinel and plagioclase peridotites and spinel pyroxenite. American Mineralogist, 61(7-8), 804-816.

Obata, M., & Morten, L. 1987. Transformation of spinel lherzolite to garnet lherzolite in ultramafic lenses of the Austridic crystalline complex, Northern Italy. Journal of Petrology, 28(3), 599-623.

Obata, M., & Ozawa, K. 2011. Topotaxic relationships between spinel and pyroxene in kelyphite after garnet in mantle-derived peridotites and their implications to reaction mechanism and kinetics. Mineralogy and Petrology, 101(3-4), 217-224.

Odashima, N., Morishita, T., Ozawa, K., Nagahara, H., Tsuchiyama, A., & Nagashima, R. 2007. Formation and deformation mechanisms of pyroxene-spinel symplectite in an ascending mantle, the Horoman peridotite complex, Japan: An EBSD (electron backscatter diffraction) study. Journal of Mineralogical and Petrological Sciences, 103(1), 1-15.

O'Hara, M.J., Richardson, S.W. and Wilson, G., 1971. Garnet-peridotite stability and occurrence in crust and mantle. Contributions to Mineralogy and Petrology, 32(1), pp.48-68.

O'Reilly, S.Y. and Griffin, W.L., 1988. Mantle metasomatism beneath western Victoria, Australia: I. Metasomatic processes in Cr-diopside lherzolites. Geochimica et Cosmochimica Acta, 52(2), pp.433-447.

Palme, H. and Nickel, K.G., 1985. CaAl ratio and composition of the Earth's upper mantle. Geochimica et Cosmochimica Acta, 49(10), pp.2123-2132.

Papanastassiou, D.A. and Wasserburg, G.J., 1975. Rb-Sr study of a lunar dunite and evidence for early lunar differentiates. Lunar and Planetary Science Conference Proceedings, Vol. 6, pp. 1467-1489.

Parsons, B., & Sclater, J. G. 1977. An analysis of the variation of ocean floor bathymetry and heat flow with age. Journal of geophysical research, 82(5), 803-827.

Patkó, L., Créon, L., Kovács, Z., Liptai, N., Rosenberg, E. and Szabó, C., 2020. Three-dimensional distribution of glass and vesicles in metasomatized xenoliths: A micro-CT case study from Nógrád–Gömör Volcanic Field (Northern Pannonian Basin). Geologica carpathica, 71(5), pp.418-423.

Pearson, D. G., Canil, D., & Shirey, S. B. 2003. Mantle samples included in volcanic rocks: xenoliths and diamonds. Treatise on Geochemistry, 2, 171-275.

Perkins, D. and Anthony, E.Y., 2011. The evolution of spinel lherzolite xenoliths and the nature of the mantle at Kilbourne Hole, New Mexico. Contributions to Mineralogy and Petrology, 162(6), pp.1139-1157.

Petit, C., Koulakov, I. and Deverchère, J., 1998. Velocity structure around the Baikal rift zone from teleseismic and local earthquake traveltimes and geodynamic implications. Tectonophysics, 296(1-2), 125-144.

Pike, J. N., & Schwarzman, E. C. 1977. Classification of textures in ultramafic xenoliths. The Journal of Geology, 85 (1) 49-61.

Potter, R.W.K., Kring, D.A., Collins, G.S., Kiefer, W.S. and McGovern, P.J., 2012. Estimating transient crater size using the crustal annular bulge: Insights from numerical modeling of lunar basin-scale impacts. Geophysical Research Letters, 39(18)

Potts, P.J., Bowles, J.F., Reed, S.J. and Cave, R. eds., 2012. Microprobe techniques in the earth sciences (Vol. 6). Springer Science & Business Media.

Prior, D.J., Boyle, A.P., Brenker, F., Cheadle, M.C., Day, A., Lopez, G., Peruzzo, L., Potts, G.J., Reddy, S., Spiess, R. and Timms, N.E., 1999. The application of electron backscatter diffraction and orientation contrast imaging in the SEM to textural problems in rocks. American Mineralogist, 84(11-12), pp.1741-1759.

Pritchard, M.E. and Stevenson, D.J., 2000. Thermal aspects of a lunar origin by giant impact. Origin of the Earth and Moon, 1, pp.179-196.

Puelles, P., Ábalos, B., Ibarguchi, J.G., Sarrionandia, F., Carracedo, M. and Fernández-Armas, S., 2016. Petrofabric and seismic properties of lithospheric mantle xenoliths from the Calatrava volcanic field (Central Spain). Tectonophysics, 683, pp.200-215. Ramakrishna K, Muralidhar, and P Munshi K. 2006. Beam-hardening in simulated X-ray tomography. NDT & E International, 39, Pp 449–457.

Rampone, E., Vissers, R. L. M., Poggio, M., Scambelluri, M., & Zanetti, A. 2009. Melt migration and intrusion during exhumation of the Alboran lithosphere: the Tallante mantle xenolith record (Betic Cordillera, SE Spain). Journal of Petrology, egp061.

Reed, S.J.B., 1993. Electron microprobe analysis, 2nd Edition. Cambridge University Press.

Reed, S.J.B., 2005. Electron microprobe analysis and scanning electron microscopy in geology. Cambridge University Press.

Reid, A. M., & Dawson, J. B. 1972. Olivine-garnet reaction in peridotites from Tanzania. Lithos, 5(2), 115-124.

Reid, A.M., Donaldson, C.H., Brown, R.W., Ridley, W.I. and Dawson, J.B., 1975. Mineral chemistry of peridotite xenoliths from the Lashaine volcano, Tanzania. In Physics and Chemistry of the Earth, 525-543. Pergamon.

Ringwood, A. E. (1979), Origin of the Earth and Moon, Springer, New York.

Robinson, J.A.C. and Wood, B.J., 1998. The depth of the spinel to garnet transition at the peridotite solidus. Earth and Planetary Science Letters, 164(1-2), 277-284.

Ross, J. V. 1983. The nature and rheology of the Cordilleran upper mantle of British Columbia: inferences from peridotite xenoliths. Tectonophysics, 100(1), 321-357.

Ryder G. 1981 The Apollo 17 highlands: The South Massif soils. Lunar and Planetary Science Conference, Vol. 12, pp. 918-920.

Ryder, G. and Wood, J.A., 1977. Serenitatis and Imbrium impact melts-Implications for large-scale layering in the lunar crust. Lunar and Planetary Science Conference Proceedings, Vol. 8, pp. 655-668.

Ryder, G., 1991. Lunar ferroan anorthosites and mare basalt sources: The mixed connection. Geophysical Research Letters, 18(11), pp.2065-2068.

Ryder, G., 1992. Chemical variation and zoning of olivine in lunar dunite 72415-Near-surface accumulation. Lunar and Planetary Science Conference Proceedings, Vol. 22, pp. 373-380.

Ryder, G., Stoeser, D.B., Marvin, U.B., Bower, J.F. and Wood, J.A., 1975. Boulder 1, Station 2, Apollo 17: petrology and petrogenesis. The Moon, 14(3-4), pp.327-357.

Schindelin, J., Arganda-Carreras, I., Frise, E., Kaynig, V., Longair, M., Pietzsch, T., ... & Tinevez, J. Y. 2012. Fiji: an open-source platform for biological-image analysis. Nature methods, 9(7), 676-682.

Schmitt, H.H., 1973. Apollo 17 report on the valley of Taurus-Littrow. Science, 182(4113), pp.681-690.

Schmitt, H.H., 2014. Apollo 17: new insights from the synthesis and integration of field notes, photo-documentation, and analytical data. Lunar and Planetary Science Conference (Abstract # 1777), p.2732.

Schmitt, H.H., 2016. Symplectites in Dunite 72415 and Troctolite 76535 Indicate Mantle Overturn Beneath Lunar Near-Side. Lunar and Planetary Science Conference (Abstract # 1903), p.2339.

Secchiari, A., Montanini, A., Bosch, D., Macera, P. and Cluzel, D., 2019. Origin of the spinel-pyroxene symplectites in the harzburgites from the New Caledonia Peridotite. Ofioliti, 44(1), pp.31-42.

Seibert J A 2004. X-Ray Imaging Physics for Nuclear Medicine Technologists. Part 1: Basic Principles of X-Ray Production. J. Nucl. Med. Technol. vol. 32 no. 3, 139-147.

Sengör, A.M. & Burke, K., 1978. Relative timing of rifting and volcanism on Earth and its tectonic implications. Geophysical Research Letters, 5(6), pp.419-421.

Shaw, C. S., Heidelbach, F., & Dingwell, D. B. 2006. The origin of reaction textures in mantle peridotite xenoliths from Sal Island, Cape Verde: the case for “metasomatism” by the host lava. Contributions to Mineralogy and Petrology, 151(6), 681-697.

Shearer, C.K. and Papike, J.J., 1999. Magmatic evolution of the Moon. American Mineralogist, 84(10), pp.1469-1494.

Shoemaker, E.M., 1977. Why study impact craters. In Impact and explosion cratering: Planetary and terrestrial implications, pp. 1-10.

Siena, F., Beccaluva, L., Coltorti, M., Marchesi, S., & Morra, V. 1991. Ridge to hot-spot evolution of the Atlantic lithospheric mantle: evidence from Lanzarote peridotite xenoliths (Canary Islands). Journal of Petrology, (2), 271-290.

Simon, N.S., Irvine, G.J., Davies, G.R., Pearson, D.G. and Carlson, R.W., 2003. The origin of garnet and clinopyroxene in "depleted" Kaapvaal peridotites. Lithos, 71(2-4), 289-322.

Simonds, C.H., Phinney, W.C. and Warner, J.L., 1974. Petrography and classification of Apollo 17 non-mare rocks with emphasis on samples from the Station 6 boulder. Proceedings of the Fifth Lunar Conference, volume 1, pp 337-353.

Skewes, M.A. and Stern, C.R., 1979. Petrology and geochemistry of alkali basalts and ultramafic inclusions from the Pali-Aike volcanic field in southern Chile and the origin of the Patagonian plateau lavas. Journal of Volcanology and Geothermal Research, 6(1-2), 3-25.

Smith D. 1977. The Origin and Interpretation of Spinel-Pyroxene Clusters in Peridotite. The Journal of Geology. 85, 476-482.

Smith J. V., Anderson A. T., Newton R. C., Olsen E. J. and Wyllie P. J., 1970. A petrologic model for the Moon based on petrogenesis, experimental petrology, and physical properties. J. Geol. 78, 381–405.

Snee, L.W. and Ahrens, T.J., 1975. Shock-induced deformation features in terrestrial peridot and lunar dunite. Lunar and Planetary Science Conference Proceedings, Vol. 6, pp. 833-842.

Snyder, G.A., Taylor, L.A. and Neal, C.R., 1992. A chemical model for generating the sources of mare basalts: Combined equilibrium and fractional crystallization of the lunar magmasphere. Geochimica et Cosmochimica Acta, 56(10), pp.3809-3823.

Solomon, S.C. and Head, J.W., 1980. Lunar mascon basins: Lava filling, tectonics, and evolution of the lithosphere. Reviews of Geophysics, 18(1), pp.107-141.

Spudis, P.D. and Ryder, G., 1981. Apollo 17 impact melts and their relation to the Serenitatis basin. In: Multi-ring basins: Formation and evolution (pp. 133-148).

Spudis, P.D., 1993. The Geology of Multi-Ring Impact Basins. Cambridge University Press, New York. 277 pp.

Spudis, P.D., Hawke, B.R.A.Y. and Lucey, P.G., 1993. Geology and deposits of the Serenitatis basin. Lunar and Planetary Science Conference, Vol. 24, 1341-1342.

Spudis, P.D., Wilhelms, D.E. and Robinson, M.S., 2011. The Sculptured Hills of the Taurus Highlands: Implications for the relative age of Serenitatis, basin chronologies and the cratering history of the Moon. Journal of Geophysical Research: Planets, 116(E12).

Stern, C.R., Kilian, R., Olker, B., Hauri, E.H. and Kyser, T.K., 1999. Evidence from mantle xenoliths for relatively thin (< 100 km) continental lithosphere below the Phanerozoic crust of southernmost South America. In: Developments in Geotectonics, 24, 217-235.

Stöffler, D. and Ryder, G., 2001. Stratigraphy and isotope ages of lunar geologic units: Chronological standard for the inner solar system. In: Chronology and Evolution of Mars (pp. 9-54). Springer, Dordrecht.

Streckeisen, A. (1974). Classification and nomenclature of plutonic rocks recommendations of the IUGS subcommission on the systematics of igneous rocks. Geologische Rundschau, 63(2), 773-786.

Suhr, G. 1993. Evaluation of upper mantle microstructures in the Table Mountain massif (Bay of Islands ophiolite). Journal of Structural Geology, 15(11), 1273-1292.

Tabor, F. A., Tabor, B. E. & Downes, H. 2010. Quantitative characterization of textures in mantle spinel peridotite xenoliths. Geological Society, London, Special Publications, 337(1), 195-211.

Tan, Y., Kiekens, K., Welkenhuyzen, F., Angel, J., De Chiffre, L., Kruth, J.P. and Dewulf, W., 2014. Simulation-aided investigation of beam hardening induced errors in CT dimensional metrology. Measurement Science and Technology, 25(6), p.064014.

Taylor, S.R. and Jakeš, P., 1974. The geochemical evolution of the Moon. Proceedings of the Fifth Lunar Conference, volume 2, pp 1287-1305.

Taylor, S.R., 1982. Planetary science: A lunar perspective (Vol. 3303). Houston: Lunar and Planetary Institute.

Team, A.F.G.I., 1973. Geologic exploration of Taurus-Littrow: Apollo 17 landing site. Science, 182(4113), pp.672-680.

Tommasi, A., Godard, M., Coromina, G., Dautria, J.M. and Barsczus, H., 2004. Seismic anisotropy and compositionally induced velocity anomalies in the lithosphere above mantle plumes: a petrological and microstructural study of mantle xenoliths from French Polynesia. Earth and Planetary Science Letters, 227(3-4), pp.539-556.

Tonks, W.B. and Melosh, H.J., 1993. Magma ocean formation due to giant impacts. Journal of Geophysical Research: Planets, 98(E3), pp.5319-5333.

Villaseca, C., Ancochea, E., Orejana, D. and Jeffries, T.E., 2010. Composition and evolution of the lithospheric mantle in central Spain: inferences from peridotite xenoliths from the Cenozoic Calatrava volcanic field. Geological Society, London, Special Publications, 337(1), pp.125-151.

Wallace, R. C. 1975. Mineralogy and petrology of xenoliths in a diatreme from South Westland, New Zealand. Contributions to Mineralogy and Petrology, 49(3), 191-199.

Wang, J., Hattori, K.H., Li, J. and Stern, C.R., 2008. Oxidation state of Paleozoic subcontinental lithospheric mantle below the Pali Aike volcanic field in southernmost Patagonia. Lithos, 105(1-2), 98-110.

Wanke, H., Dreibus, G., Palme, H., Rammensee, W. and Weckwerth, G., 1983. Geochemical evidence for the formation of the Moon from material of the Earth's mantle. Lunar and Planetary Science Conference, Vol. 14, pp. 818-819.

Warren, P.H., 1985. The magma ocean concept and lunar evolution. Annual Review of Earth and Planetary Sciences, 13(1), pp.201-240.

Warren, P.H., 1986. The bulk-Moon MgO/FeO ratio: A highlands perspective. In: Origin of the Moon (p. 279).

Werling, F., & Altherr, R. 1997. Thermal evolution of the lithosphere beneath the French Massif Central as deduced from geothermobarometry on mantle xenoliths. Tectonophysics, 275(1), 119-141.

White, R.S., 1988. The Earth's crust and lithosphere. Journal of Petrology, (1), pp.1-10.

Wieczorek, M.A. and Phillips, R.J., 2000. The “Procellarum KREEP Terrane”: Implications for mare volcanism and lunar evolution. Journal of Geophysical Research: Planets, 105(E8), pp.20417-20430.

Wieczorek, M.A., 2009. The interior structure of the moon: What does geophysics have to say? Elements, 5(1), pp.35-40.

Wieczorek, M.A., Jolliff, B.L., Khan, A., Pritchard, M.E., Weiss, B.P., Williams, J.G., Hood, L.L., Righter, K., Neal, C.R., Shearer, C.K. and McCallum, I.S., 2006. The constitution and structure of the lunar interior. Reviews in Mineralogy and Geochemistry, 60(1), pp.221-364.

Wilhelms, D.E. and McCauley, J.F., 1971. Geologic map of the near side of the Moon. Washington, DC: US Geological Survey.

Wilhelms, D.E., John, F. and Trask, N.J., 1987. The geologic history of the Moon. United States Geological Survey Professional Paper, No. 1348.

Wilson, J.T., 1963. A possible origin of the Hawaiian Islands. Canadian Journal of Physics, 41(6), pp.863-870.

Wilson, M., & Downes, H. 1991. Tertiary-Quaternary extension-related alkaline magmatism in western and central Europe. Journal of Petrology, 32(4), 811-849.

Wilson, M., 1993. Magmatism and the geodynamics of basin formation. Sedimentary Geology, 86(1-2), pp.5-29.

Witt, G. & Seck, H.A., 1987. Temperature history of sheared mantle xenoliths from the West Eifel, West Germany: evidence for mantle diapirism beneath the Rhenish Massif. Journal of Petrology, 28(3), pp.475-493.

Witt-Eickschen, G., & Kramm, U. 1997. Mantle upwelling and metasomatism beneath Central Europe: geochemical and isotopic constraints from mantle xenoliths from the Rhön (Germany). Journal of Petrology, 38(4), 479-493.

Wolfe E.W., Bailey N.G., Lucchitta B. K., Muehlberger W. R., Scott D.H., Sutton R.L., Wiltshire H G. 1981. The geologic investigation of the Taurus-Littrow valley; Apollo 17 landing site. United States Geological Survey Professional Paper ISSN 0096-0446; USA

Wolfe, E.W., Lucchitta, B.K., Reed, V.S., Ulrich, G.E. and Sanchez, A.G., 1975. Geology of the Taurus-Littrow valley floor. Lunar and Planetary Science Conference Proceedings, Vol. 6, pp. 2463-2482.

Wood J. A., Dickey, Jr., J. S., Marvin U. B. and Powell B. N. 1970. Lunar anorthosites and a geophysical model of the Moon. Proc. Apollo 11 Lunar Sci. Conf., 965–988.

Wood, B.J., Walter, M.J. and Wade, J., 2006. Accretion of the Earth and segregation of its core. Nature, 441(7095), pp.825-833.

Wood, J.A., 1975. Lunar petrogenesis in a well-stirred magma ocean. Lunar and Planetary Science Conference Proceedings Vol. 6, pp. 1087-1102.

Wyllie, P.J., 1981. Plate tectonics and magma genesis. Geologische Rundschau, 70(1), pp.128-153.

Xu, Y., Menzies, M. A., Vroon, P., Mercier, J. C., & Lin, C. 1998. Texture–temperature–geochemistry relationships in the upper mantle as revealed from spinel peridotite xenoliths from Wangqing, NE China. Journal of Petrology, 39(3), 469-493.

Yamamoto, S., Nakamura, R., Matsunaga, T., Ogawa, Y., Ishihara, Y., Morota, T., Hirata, N., Ohtake, M., Hiroi, T., Yokota, Y. and Haruyama, J., 2010. Possible mantle origin of olivine around lunar impact basins detected by SELENE. Nature Geoscience, 3(8), pp.533-536.

Zangana, N. A., Downes, H., Thirlwall, M. F., & Hegner, E. 1997. Relationship between deformation, equilibration temperatures, REE and radiogenic isotopes in mantle xenoliths (Ray Pic, Massif Central, France): an example of plume-lithosphere interaction? Contributions to Mineralogy and Petrology, 127(1-2), 187-203.

Zhang, J. and Herzberg, C., 1994. Melting experiments on anhydrous peridotite KLB-1 from 5.0 to 22.5 GPa. Journal of Geophysical Research: Solid Earth, 99(B9), pp.17729-17742.

Ziegler, P.A., 1992. European Cenozoic rift system. Tectonophysics, 208(1-3), pp.91-111.

Zuber, M.T., Smith, D.E., Lemoine, F.G. and Neumann, G.A., 1994. The shape and internal structure of the Moon from the Clementine mission. Science, 266(5192), pp.1839-1843.

Appendix

Movies of 3D rendered volumes are available to view on YouTube channel Krishan Bhanot. Link to the channel is listed below.

https://www.youtube.com/channel/UCiR0Gr0pJpJExY7LXN5DNjg

Supplementary tables - Massif Central, Lanzarote and Calatrava. Olivine

Sample	location	site	Mineral	SiO2	FeO	MnO	NiO	MgO	Total	Mg#	no.
12548	Cal	nc	ol core	40.78	10.09	0.16	0.37	48.46	99.84	89.54	12
12548	Cal	nc	Min	40.26	9.38	0.03	0.07	47.23	98.09	88.87	-
12548	Cal	nc	Max	41.60	10.88	0.43	0.68	49.13	101.39	90.12	-
12548	Cal	nc	σ	0.40	0.41	0.12	0.21	0.56	1.08	0.37	-
6	Cal	nc	ol core	40.39	11.24	0.20	0.34	47.89	100.01	88.37	10
6	Cal	nc	Min	39.92	10.76	0.06	0.07	47.55	99.15	88.07	-
6	Cal	nc	Max	40.88	11.57	0.49	0.63	48.39	101.17	88.77	-
6	Cal	nc	σ	0.26	0.25	0.12	0.21	0.26	0.58	0.23	-
5	Cal	nc	ol core	41.09	10.00	0.16	0.23	48.87	100.31	89.71	13
5	Cal	nc	Min	40.69	9.49	0.00	0.01	48.13	99.12	89.22	-
5	Cal	nc	Max	41.75	10.60	0.43	0.52	49.52	101.14	90.18	-
5	Cal	nc	σ	0.34	0.32	0.11	0.15	0.41	0.73	0.28	
3	Cal	nc	ol core	40.80	8.35	0.15	0.45	49.93	99.66	91.42	8
3	Cal	nc	Min	40.51	8.02	0.04	0.21	49.39	98.43	90.86	-
3	Cal	nc	Max	41.24	8.86	0.24	0.76	50.82	100.68	91.73	-
3	Cal	nc	σ	0.24	0.23	0.07	0.16	0.44	0.75	0.25	
EC3	Lanz	halo	ol core	40.74	7.94	0.12	0.41	49.85	99.06	91.79	6
EC3	Lanz	halo	Min	40.32	7.60	0.09	0.38	49.00	98.31	91.39	-
EC3	Lanz	halo	Max	41.37	8.23	0.13	0.45	50.73	100.65	92.11	-
EC3	Lanz	halo	σ	0.38	0.25	0.02	0.03	0.55	0.94	0.26	-
EC3	Lanz	nhalo	ol core	41.06	8.44	0.13	0.41	50.42	100.46	91.41	11
EC3	Lanz	nhalo	Min	40.15	8.28	0.11	0.39	49.89	99.32	91.25	-
EC3	Lanz	nhalo	Max	41.97	8.53	0.14	0.42	51.15	101.71	91.56	-
EC3	Lanz	nhalo	σ	0.57	0.08	0.01	0.01	0.46	0.76	0.12	-
EC4	Lanz	nc	ol core	41.11	8.83	0.17	0.35	50.11	100.56	91.01	7
EC4	Lanz	nc	Min	40.93	8.46	0.03	0.15	49.76	100.03	90.75	-
EC4	Lanz	nc	Max	41.42	9.06	0.34	0.55	50.63	101.25	91.36	-
EC4	Lanz	nc	σ	0.19	0.26	0.12	0.14	0.29	0.43	0.25	-
EC5	Lanz	Halo	ol core	40.48	8.79	0.37	0.16	49.71	99.50	90.98	9
EC5	Lanz	Halo	Min	39.75	8.35	0.32	0.14	48.67	98.46	90.07	-
EC5	Lanz	Halo	Max	41.47	9.56	0.40	0.17	50.38	100.72	91.49	-
EC5	Lanz	Halo	σ	0.61	0.44	0.02	0.01	0.59	0.79	0.50	-
EC5	Lanz	nHalo	ol core	40.61	10.43	0.36	0.17	48.67	100.24	89.27	19
EC5	Lanz	nHalo	Min	39.53	8.83	0.33	0.14	46.88	97.82	88.48	-
EC5	Lanz	nHalo	Max	40.97	11.07	0.39	0.20	49.89	101.17	90.91	-
EC5	Lanz	nHalo	σ	0.31	0.74	0.02	0.02	0.70	0.77	0.79	
EC6	Lanz	nc	ol core	40.76	8.63	-	0.33	49.85	99.64	91.15	6
EC6	Lanz	nc	min	40.43	8.22	-	0.15	49.44	98.68	90.91	-
EC6	Lanz	nc	max	41.09	8.86	-	0.47	50.55	100.97	91.47	-
EC6	Lanz	nc	σ	0.29	0.24	-	0.12	0.41	0.84	0.19	-
EC21	Lanz	halo	ol core	40.85	7.57	0.32	0.12	51.22	100.09	92.34	3
EC21	Lanz	halo	min	40.47	7.41	0.32	0.11	50.97	99.57	92.21	-
EC21	Lanz	halo	max	41.13	7.68	0.33	0.13	51.41	100.48	92.52	-
EC21	Lanz	halo	σ	0.34	0.14	0.01	0.01	0.23	0.47	0.16	-
EC21	Lanz	nc	ol core	40.98	8.45	0.39	0.13	50.36	100.36	91.40	18
EC21	Lanz	nc	min	40.10	8.08	0.36	0.11	49.54	99.17	91.21	-
EC21	Lanz	nc	max	41.82	8.58	0.42	0.15	50.83	101.28	91.81	-
EC21	Lanz	nc	σ	0.57	0.15	0.02	0.01	0.32	0.66	0.14	-
CH11	MCn	nc	ol core	42.45	8.61	0.13	0.43	48.38	99.99	90.92	8
CH11	MCn	nc	min	41.96	8.40	0.01	0.06	47.81	99.03	91.03	-
CH11	MCn	nc	max	42.78	8.91	0.19	0.58	48.84	100.78	91.15	-
CH11	MCn	nc	σ	0.30	0.18	0.07	0.16	0.32	0.62	0.17	-
MB1	MCn	spc	ol core	40.44	9.64	0.14	0.39	47.89	98.51	89.86	9
MB1	MCn	spc	min	36.58	9.35	0.03	0.22	42.34	88.99	88.74	-
MB1	MCn	spc	max	41.49	9.95	0.22	0.49	49.12	100.45	90.34	-
MB1	MCn	spc	σ	1.50	0.19	0.06	0.09	2.11	3.61	0.47	-
MB9	MCn	nc	ol core	41.07	7.49	-	1.78	49.70	100.04	97.79	12
MB9	MCn	nc	min	40.38	0.03	-	0.18	49.16	98.90	89.11	-
MB9	MCn	nc	max	41.72	9.15	-	8.89	50.15	100.91	99.75	-
MB9	MCn	nc	σ	0.37	3.47	-	3.28	0.35	0.69	3.99	-

Sample	location	site	Mineral	SiO2	FeO	MnO	NiO	MgO	Total	Mg#	no.
MB63B	MCn	nc	ol core	42.52	8.49	0.16	0.31	48.69	100.11	91.09	11
MB63B	MCn	nc	min	41.52	8.32	0.09	0.10	47.79	98.09	90.83	-
MB63B	MCn	nc	max	43.09	8.67	0.23	0.56	49.42	101.52	91.34	-
MB63B	MCn	nc	σ	0.52	0.12	0.04	0.13	0.59	1.15	0.15	-
MB64	MCn	nc	ol core	42.28	9.49	0.11	0.45	48.09	100.42	90.03	11
MB64	MCn	nc	min	41.43	9.23	0.01	0.26	47.50	98.88	89.79	-
MB64	MCn	nc	max	42.71	9.78	0.21	0.60	48.43	101.15	90.24	-
MB64	MCn	nc	σ	0.40	0.15	0.05	0.11	0.31	0.74	0.15	-
RP87-6	MCs	nc	ol core	40.86	9.82	0.16	-	48.50	99.33	89.80	8
RP87-6	MCs	nc	min	40.21	9.64	0.14	-	47.86	98.55	89.85	-
RP87-6	MCs	nc	max	41.35	9.94	0.19	-	49.48	99.96	89.87	-
RP87-6	MCs	nc	σ	0.40	0.11	0.02	-	0.76	0.49	0.19	-
RP91-22	MCs	nc	ol core	40.60	9.25	0.13	0.38	49.04	99.40	90.43	11
RP91-22	MCs	nc	min	40.15	9.18	0.11	0.34	48.36	98.40	90.19	-
RP91-22	MCs	nc	max	41.25	9.38	0.16	0.40	49.63	99.96	90.56	-
RP91-22	MCs	nc	σ	0.33	0.06	0.02	0.02	0.44	0.49	0.11	-

Supplementary tables - Massif Central, Lanzarote and Calatrava. Orthopyroxene

Sample	location	site	Mineral	SiO2	TiO2	Al2O3	Cr2O3	FeO	MnO	MgO	CaO	Na2O	Total	Mg#	Wo	En	Fs	Si	Ti	Al	Cr	Fe(ii)	Mn	Mg	Ca	Na	Total	no.
12548	Cal	spc	opx core	54.83	-	3.95	0.36	6.51	0.30	33.21	0.63	0.07	99.70	90.10	1.2	88.6	10.2	1.9	0.0	0.2	0.0	0.2	0.0	1.7	0.0	0.0	4.0	9
12548	Cal	spc	Min	51.62	-	2.82	0.10	6.01	0.12	32.03	0.45	0.00	98.78	89.60	-	-	-	-	-	-	-	-	-	-	-	-	-	-
12548	Cal	spc	Max	55.84	-	8.35	0.95	6.90	0.44	33.72	0.80	0.17	100.70	90.80	-	-	-	-	-	-	-	-	-	-	-	-	-	-
12548	Cal	spc	σ	1.25	-	1.70	0.28	0.32	0.13	0.54	0.11	0.06	0.79	0.45	-	-	-	-	-	-	-	-	-	-	-	-	-	-
12548	Cal	spc	opx core	54.82	-	3.85	0.29	6.90	0.19	32.70	0.62	0.06	99.44	89.41	1.2	88.1	10.7	1.9	0.0	0.2	0.0	0.2	0.0	1.7	0.0	0.0	4.0	3
12548	Cal	spc	Min	54.68	-	3.72	0.23	6.61	0.06	32.60	0.55	0.02	99.00	88.66	-	-	-	-	-	-	-	-	-	-	-	-	-	-
12548	Cal	spc	Max	54.90	-	4.03	0.38	7.43	0.33	32.86	0.73	0.12	99.75	89.86	-	-	-	-	-	-	-	-	-	-	-	-	-	-
12548	Cal	spc	σ	0.12	-	0.16	0.08	0.46	0.14	0.14	0.10	0.05	0.39	0.66	-	-	-	-	-	-	-	-	-	-	-	-	-	-
12548	Cal	spc	opx rim	54.82	-	3.85	0.29	6.90	0.19	32.70	0.62	0.06	99.44	89.41	1.2	88.1	10.7	1.9	0.0	0.2	0.0	0.2	0.0	1.7	0.0	0.0	4.0	3
12548	Cal	spc	Min	54.68	-	3.72	0.23	6.61	0.06	32.60	0.55	0.02	99.00	88.66	-	-	-	-	-	-	-	-	-	-	-	-	-	-
12548	Cal	spc	Max	54.90	-	4.03	0.38	7.43	0.33	32.86	0.73	0.12	99.75	89.86	-	-	-	-	-	-	-	-	-	-	-	-	-	-
12548	Cal	spc	σ	0.12	-	0.16	0.08	0.46	0.14	0.14	0.10	0.05	0.39	0.66	-	-	-	-	-	-	-	-	-	-	-	-	-	-
12548	Cal	nspc	opx core	55.14	-	4.96	0.58	6.71	0.33	32.99	0.56	-	100.96	89.76	1.1	88.3	10.6	1.9	0.0	0.2	0.0	0.2	0.0	1.7	0.0	0.0	4.0	3
12548	Cal	nspc	Min	52.79	-	3.79	0.40	6.42	0.32	32.33	0.51	-	100.79	88.77	-	-	-	-	-	-	-	-	-	-	-	-	-	-
12548	Cal	nspc	Max	56.55	-	7.09	0.75	7.29	0.33	33.59	0.64	-	101.09	90.32	-	-	-	-	-	-	-	-	-	-	-	-	-	-
12548	Cal	nspc	σ	2.05	-	1.85	0.25	0.50	0.01	0.63	0.07	-	0.15	0.85	-	-	-	-	-	-	-	-	-	-	-	-	-	-
12548	Cal	nspc	opx rim	55.52	-	3.60	0.31	6.85	0.08	33.04	0.69	-	100.07	89.58	1.3	88.3	10.4	1.9	0.0	0.1	0.0	0.2	0.0	1.7	0.0	0.0	4.0	4
12548	Cal	nspc	Min	55.19	-	3.48	0.20	6.48	0.04	32.88	0.67	-	99.65	89.26	-	-	-	-	-	-	-	-	-	-	-	-	-	-
12548	Cal	nspc	Max	55.72	-	3.77	0.44	7.12	0.12	33.20	0.72	-	100.38	90.12	-	-	-	-	-	-	-	-	-	-	-	-	-	-
12548	Cal	nspc	σ	0.23	-	0.13	0.12	0.29	0.04	0.16	0.02	-	0.32	0.41	-	-	-	-	-	-	-	-	-	-	-	-	-	-
6	Cal	spc	opx core	53.89	0.14	5.32	0.16	7.03	0.27	31.77	1.09	0.12	99.79	88.95	2.1	86.7	11.1	1.9	0.0	0.2	0.0	0.2	0.0	1.6	0.0	0.0	4.0	11
6	Cal	spc	Min	53.32	0.07	4.67	0.02	6.75	0.23	30.07	0.48	0.02	98.75	88.81	-	-	-	-	-	-	-	-	-	-	-	-	-	-
6	Cal	spc	Max	54.83	0.22	6.01	0.28	7.43	0.30	32.51	3.64	0.20	100.34	88.64	-	-	-	-	-	-	-	-	-	-	-	-	-	-
6	Cal	spc	σ	0.53	0.06	0.45	0.09	0.20	0.03	0.71	0.95	0.06	0.53	0.28	-	-	-	-	-	-	-	-	-	-	-	-	-	-
6	Cal	spc	opx core	53.32	0.08	6.30	0.25	7.18	0.14	31.65	0.80	0.10	99.81	88.71	1.6	87.1	11.3	1.8	0.0	0.3	0.0	0.2	0.0	1.6	0.0	0.0	4.0	4
6	Cal	spc	Min	52.99	0.00	6.09	0.14	6.95	0.05	31.30	0.42	0.07	99.37	88.44	-	-	-	-	-	-	-	-	-	-	-	-	-	-
6	Cal	spc	Max	53.57	0.18	6.62	0.39	7.37	0.23	32.08	1.26	0.13	100.24	89.01	-	-	-	-	-	-	-	-	-	-	-	-	-	-
6	Cal	spc	σ	0.24	0.09	0.24	0.10	0.20	0.08	0.32	0.41	0.03	0.36	0.29	-	-	-	-	-	-	-	-	-	-	-	-	-	-
6	Cal	spc	opx rim	54.62	0.21	4.81	0.12	7.13	0.21	32.58	0.55	0.11	100.35	89.06	1.1	87.9	11.1	1.9	0.0	0.2	0.0	0.2	0.0	1.7	0.0	0.0	4.0	3
6	Cal	spc	Min	54.34	0.19	4.51	0.05	6.90	0.19	32.27	0.50	0.09	99.84	88.78	-	-	-	-	-	-	-	-	-	-	-	-	-	-
6	Cal	spc	Max	54.91	0.23	5.14	0.18	7.38	0.24	32.75	0.64	0.13	100.89	89.29	-	-	-	-	-	-	-	-	-	-	-	-	-	-
6	Cal	spc	σ	0.29	0.03	0.32	0.09	0.24	0.03	0.27	0.08	0.02	0.57	0.26	-	-	-	-	-	-	-	-	-	-	-	-	-	-
5	Cal	spc	opx core	54.84	-	3.96	0.28	6.66	0.17	32.32	1.67	0.08	99.99	89.64	3.7	96.3	0.0	1.9	0.0	0.2	0.0	0.2	0.0	1.7	0.1	0.0	4.0	5
5	Cal	spc	Min	54.55	-	3.58	0.09	6.21	0.03	30.52	0.41	0.04	99.50	88.81	-	-	-	-	-	-	-	-	-	-	-	-	-	-
5	Cal	spc	Max	55.15	-	4.44	0.52	7.53	0.53	33.94	3.23	0.12	100.72	90.16	-	-	-	-	-	-	-	-	-	-	-	-	-	-
5	Cal	spc	σ	0.26	-	0.34	0.16	0.51	0.20	1.43	1.24	0.04	0.47	0.52	-	-	-	-	-	-	-	-	-	-	-	-	-	-
5	Cal	nspc	opx core	55.06	-	4.17	0.30	6.79	0.20	33.00	0.52	0.09	100.07	89.65	1.0	88.5	10.5	1.9	0.0	0.2	0.0	0.2	0.0	1.7	0.0	0.0	4.0	8
5	Cal	nspc	Min	53.29	-	3.13	0.10	6.27	0.09	32.53	0.36	0.02	99.09	89.61	-	-	-	-	-	-	-	-	-	-	-	-	-	-
5	Cal	nspc	Max	56.51	-	6.29	0.49	7.35	0.35	33.73	0.70	0.17	101.25	90.01	-	-	-	-	-	-	-	-	-	-	-	-	-	-
5	Cal	nspc	σ	1.06	-	0.97	0.15	0.37	0.10	0.47	0.11	0.05	0.83	0.22	-	-	-	-	-	-	-	-	-	-	-	-	-	-

Sample	location	site	Mineral	SiO2	TiO2	Al2O3	Cr2O3	FeO	MnO	MgO	CaO	Na2O	Total	Mg#	Wo	En	Fs	Si	Ti	Al	Cr	Fe(ii)	Mn	Mg	Ca	Na	Total	no.
3	Cal	nspc	opx core	56.00	-	2.63	0.86	5.53	0.19	33.58	1.03	0.16	99.83	91.55	2.0	89.5	8.5	1.9	0.0	0.1	0.0	0.2	0.0	1.7	0.0	0.0	4.0	8
3	Cal	nspc	min	55.09	-	2.52	0.67	5.20	0.14	33.07	0.94	0.11	98.24	91.11	-	-	-	-	-	-	-	-	-	-	-	-	-	-
3	Cal	nspc	max	56.61	-	2.80	0.98	5.83	0.24	33.83	1.10	0.25	100.94	91.99	-	-	-	-	-	-	-	-	-	-	-	-	-	-
3	Cal	nspc	σ	0.55	-	0.12	0.12	0.18	0.06	0.26	0.05	0.07	0.91	0.25	-	-	-	-	-	-	-	-	-	-	-	-	-	-
EC4	Lanz	spc	opx core	55.14	0.02	3.16	0.47	5.58	0.20	33.85	0.63	0.45	99.50	91.53	1.2	90.2	8.6	1.9	0.0	0.1	0.0	0.2	0.0	1.7	0.0	0.0	4.0	4
EC4	Lanz	spc	min	54.84	0.01	2.92	0.37	5.48	0.15	33.71	0.62	0.40	99.19	91.47	-	-	-	-	-	-	-	-	-	-	-	-	-	-
EC4	Lanz	spc	max	55.46	0.02	3.31	0.64	5.63	0.30	33.99	0.64	0.58	99.87	91.64	-	-	-	-	-	-	-	-	-	-	-	-	-	-
EC4	Lanz	spc	σ	0.27	0.01	0.18	0.11	0.07	0.07	0.12	0.01	0.09	0.36	0.08	-	-	-	-	-	-	-	-	-	-	-	-	-	-
EC4	Lanz	nc	opx core	**55.15**	0.05	3.12	0.60	5.62	0.17	33.73	0.81	0.42	99.65	91.46	1.5	89.9	8.6	1.9	0.0	0.1	0.0	0.2	0.0	1.7	0.0	0.0	4.0	5
EC4	Lanz	nc	min	**54.71**	0.03	2.87	0.48	5.34	0.10	33.32	0.61	0.35	98.81	91.31	-	-	-	-	-	-	-	-	-	-	-	-	-	-
EC4	Lanz	nc	max	**55.43**	0.09	3.38	0.82	5.76	0.30	34.04	1.09	0.50	100.37	91.75	-	-	-	-	-	-	-	-	-	-	-	-	-	-
EC4	Lanz	nc	σ	**0.27**	0.03	0.18	0.13	0.16	0.08	0.35	0.19	0.06	0.72	0.18	-	-	-	-	-	-	-	-	-	-	-	-	-	-
EC6	Lanz	spc	opx core	**55.34**	0.04	3.55	0.59	5.18	0.16	31.66	3.80	0.44	100.76	91.67	7.3	84.7	8.0	1.9	0.0	0.1	0.0	0.1	0.0	1.6	0.1	0.0	4.0	7
EC6	Lanz	spc	min	**52.94**	0.00	3.10	0.37	2.44	0.05	17.45	0.62	0.30	99.84	91.12	-	-	-	-	-	-	-	-	-	-	-	-	-	-
EC6	Lanz	spc	max	**56.79**	0.08	4.04	0.97	5.91	0.28	34.57	22.46	0.75	101.91	92.71	-	-	-	-	-	-	-	-	-	-	-	-	-	-
EC6	Lanz	spc	σ	**1.18**	0.03	0.38	0.20	1.22	0.08	6.28	8.23	0.16	0.70	0.51	-	-	-	-	-	-	-	-	-	-	-	-	-	-
EC6	Lanz	nc	opx core	54.41	-	4.17	0.91	5.63	0.13	33.48	0.80	0.46	100.00	91.38	1.5	89.9	8.6	1.9	0.0	0.2	0.0	0.2	0.0	1.7	0.0	0.0	4.0	5
EC6	Lanz	nc	min	53.46	-	3.28	0.54	5.37	0.01	32.52	0.70	0.37	98.73	91.17	-	-	-	-	-	-	-	-	-	-	-	-	-	-
EC6	Lanz	nc	max	55.49	-	5.58	1.60	5.79	0.23	34.38	1.03	0.70	101.18	91.53	-	-	-	-	-	-	-	-	-	-	-	-	-	-
EC6	Lanz	nc	σ	0.73	-	0.89	0.47	0.16	0.08	0.66	0.13	0.13	1.05	0.16	-	-	-	-	-	-	-	-	-	-	-	-	-	-
EC21	Lanz	halo	opx core	55.74	0.05	3.30	0.47	5.54	0.14	34.30	0.70	0.06	100.28	18.29	1.3	90.3	8.4	1.9	0.0	0.1	0.0	0.2	0.0	1.8	0.0	0.0	4.0	8
EC21	Lanz	halo	min	53.81	0.05	2.78	0.43	5.37	0.12	33.69	0.61	0.04	98.33	16.26	-	-	-	-	-	-	-	-	-	-	-	-	-	-
EC21	Lanz	halo	max	57.42	0.06	6.43	0.54	5.63	0.14	34.58	0.99	0.09	101.71	17.27	-	-	-	-	-	-	-	-	-	-	-	-	-	-
EC21	Lanz	halo	σ	1.46	0.00	1.27	0.04	0.08	0.01	0.29	0.12	0.02	1.41	0.51	-	-	-	-	-	-	-	-	-	-	-	-	-	-
EC21	Lanz	nc	opx core	55.74	0.05	3.30	0.47	5.54	0.14	34.30	0.70	0.06	100.28	18.29	1.3	90.3	8.4	1.9	0.0	0.1	0.0	0.2	0.0	1.8	0.0	0.0	4.0	8
EC21	Lanz	nc	min	53.81	0.05	2.78	0.43	5.37	0.12	33.69	0.61	0.04	98.33	16.26	-	-	-	-	-	-	-	-	-	-	-	-	-	-
EC21	Lanz	nc	max	57.42	0.06	6.43	0.54	5.63	0.14	34.58	0.99	0.09	101.71	17.27	-	-	-	-	-	-	-	-	-	-	-	-	-	-
EC21	Lanz	nc	σ	1.46	0.00	1.27	0.04	0.08	0.01	0.29	0.12	0.02	1.41	0.51	-	-	-	-	-	-	-	-	-	-	-	-	-	-
CH11	MCn	spc	opx core	56.34	-	3.78	0.34	5.87	0.12	32.77	0.46	0.22	99.87	90.86	0.9	89.9	9.2	1.9	0.0	0.2	0.0	0.2	0.0	1.7	0.0	0.0	4.0	13
CH11	MCn	spc	min	55.74	-	3.38	0.18	5.58		32.30	0.33	0.03	99.00	90.43	-	-	-	-	-	-	-	-	-	-	-	-	-	-
CH11	MCn	spc	max	56.95	-	4.73	0.46	6.11	0.22	33.11	0.56	0.37	100.44	91.36	-	-	-	-	-	-	-	-	-	-	-	-	-	-
CH11	MCn	spc	σ	0.39	-	0.35	0.08	0.17	0.07	0.28	0.07	0.11	0.54	0.29	-	-	-	-	-	-	-	-	-	-	-	-	-	-
CH11	MCn	nc	opx core	57.23	0.08	3.09	0.30	5.78	0.16	33.26	0.46	0.04	100.30	91.11	0.9	90.0	9.1	2.0	0.0	0.1	0.0	0.2	0.0	1.7	0.0	0.0	4.0	10
CH11	MCn	nc	min	56.83	0.02	2.82	0.12	5.62	0.06	32.82	0.41	0.00	99.59	90.88	-	-	-	-	-	-	-	-	-	-	-	-	-	-
CH11	MCn	nc	max	57.54	0.17	3.30	0.39	6.00	0.25	33.78	0.54	0.06	100.72	91.35	-	-	-	-	-	-	-	-	-	-	-	-	-	-
CH11	MCn	nc	σ	0.24	0.06	0.19	0.08	0.12	0.07	0.26	0.06	0.02	0.34	0.16	-	-	-	-	-	-	-	-	-	-	-	-	-	-
MB1	MCn	spc	opx core	54.62	0.06	4.26	0.59	6.49	0.19	33.09	0.56	0.39	100.24	90.08	1.1	88.9	10.0	1.9	0.0	0.2	0.0	0.2	0.0	1.7	0.0	0.0	4.0	9
MB1	MCn	spc	min	49.23	0.00	3.48	0.16	6.22	0.03	31.06	0.43	0.26	98.99	88.57	-	-	-	-	-	-	-	-	-	-	-	-	-	-
MB1	MCn	spc	max	55.86	0.12	8.27	2.70	7.15	0.31	33.65	0.68	0.47	101.06	90.47	-	-	-	-	-	-	-	-	-	-	-	-	-	-
MB1	MCn	spc	σ	2.06	0.04	1.52	0.79	0.28	0.09	0.80	0.09	0.06	0.70	0.59	-	-	-	-	-	-	-	-	-	-	-	-	-	-

Sample	location	site	Mineral	SiO2	TiO2	Al2O3	Cr2O3	FeO	MnO	MgO	CaO	Na2O	Total	Mg#	Wo	En	Fs	Si	Ti	Al	Cr	Fe(ii)	Mn	Mg	Ca	Na	Total	no.
MB1	MCn	nc	opx core	55.12	0.09	3.86	0.33	6.40	0.15	33.08	0.79	0.40	100.20	90.21	1.5	88.7	9.8	1.9	0.0	0.2	0.0	0.2	0.0	1.7	0.0	0.0	4.0	8
MB1	MCn	nc	min	54.67	0.02	3.55	0.25	6.28	0.04	32.31	0.48	0.23	99.43	89.80	-	-	-	-	-	-	-	-	-	-	-	-	-	-
MB1	MCn	nc	max	55.57	0.26	4.16	0.41	6.54	0.28	33.54	1.97	0.48	100.86	90.44	-	-	-	-	-	-	-	-	-	-	-	-	-	-
MB1	MCn	nc	σ	0.32	0.09	0.22	0.06	0.11	0.08	0.39	0.49	0.09	0.56	0.21	-	-	-	-	-	-	-	-	-	-	-	-	-	-
MB9	MCn	spc	opx core	55.94	-	3.41	0.47	5.89	-	33.82	0.56	-	100.09	91.09	1.1	90.1	8.8	1.9	0.0	0.1	0.0	0.2	0.0	1.7	0.0	0.0	4.0	18
MB9	MCn	spc	min	55.22	-	2.71	0.32	5.58	-	33.00	0.44	-	99.06	90.67	-	-	-	-	-	-	-	-	-	-	-	-	-	-
MB9	MCn	spc	max	56.89	-	4.01	0.62	6.12	-	34.26	0.95	-	100.60	91.60	-	-	-	-	-	-	-	-	-	-	-	-	-	-
MB9	MCn	spc	σ	0.50	-	0.37	0.09	0.16	-	0.31	0.11	-	0.39	0.26	-	-	-	-	-	-	-	-	-	-	-	-	-	-
MB63B	MCn	spc	opx core	56.25	0.10	3.02	0.73	5.69	0.15	32.76	0.55	0.08	99.33	91.12	1.1	89.9	9.0	2.0	0.0	0.1	0.0	0.2	0.0	1.7	0.0	0.0	4.0	8
MB63B	MCn	spc	min	51.91	0.03	2.13	0.31	5.35	0.09	31.78	0.48	0.02	98.58	89.76	-	-	-	-	-	-	-	-	-	-	-	-	-	-
MB63B	MCn	spc	max	58.01	0.23	6.11	2.82	6.46	0.20	33.34	0.63	0.15	99.99	91.57	-	-	-	-	-	-	-	-	-	-	-	-	-	-
MB63B	MCn	spc	σ	1.82	0.07	1.26	0.85	0.34	0.03	0.48	0.06	0.05	0.48	0.57	-	-	-	-	-	-	-	-	-	-	-	-	-	-
MB63B	MCn	nc	opx core	57.10	0.06	2.65	0.49	5.59	0.17	32.92	0.84	0.07	99.88	91.30	1.6	89.5	8.8	2.0	0.0	0.1	0.0	0.2	0.0	1.7	0.0	0.0	4.0	8
MB63B	MCn	nc	min	56.57	0.01	2.48	0.34	5.42	0.03	31.54	0.43	0.02	99.02	91.08	-	-	-	-	-	-	-	-	-	-	-	-	-	-
MB63B	MCn	nc	max	57.56	0.11	2.90	0.60	5.72	0.28	33.63	2.16	0.20	100.70	91.45	-	-	-	-	-	-	-	-	-	-	-	-	-	-
MB63B	MCn	nc	σ	0.38	0.04	0.12	0.08	0.12	0.08	0.72	0.57	0.07	0.69	0.13	-	-	-	-	-	-	-	-	-	-	-	-	-	-
MB64	MCn	spc	ol core	56.15	0.07	3.48	0.44	6.15	0.21	32.50	0.74	0.04	99.73	90.40	1.5	88.8	9.8	1.9	0.0	0.1	0.0	0.2	0.0	1.7	0.0	0.0	4.0	4
MB64	MCn	spc	min	56.00	0.05	3.42	0.32	6.09	0.08	32.38	0.66	0.02	99.67	90.30	-	-	-	-	-	-	-	-	-	-	-	-	-	-
MB64	MCn	spc	max	56.34	0.08	3.54	0.55	6.20	0.29	32.63	0.85	0.05	99.84	90.49	-	-	-	-	-	-	-	-	-	-	-	-	-	-
MB64	MCn	spc	σ	0.14	0.02	0.06	0.09	0.06	0.09	0.10	0.09	0.01	0.08	0.10	-	-	-	-	-	-	-	-	-	-	-	-	-	-
MB64	MCn	nc	ol core	50.04	0.09	4.29	0.51	7.57	0.14	38.81	0.72	0.05	100.06	90.13	1.2	89.3	9.5	1.7	0.0	0.2	0.0	0.2	0.0	1.9	0.0	0.0	4.0	7
MB64	MCn	nc	min	42.06	0.03	3.88	0.23	6.04	0.09	31.54	0.04	0.01	99.18	89.86	-	-	-	-	-	-	-	-	-	-	-	-	-	-
MB64	MCn	nc	max	56.24	0.13	4.56	0.81	9.48	0.20	47.93	1.63	0.09	100.46	90.33	-	-	-	-	-	-	-	-	-	-	-	-	-	-
MB64	MCn	nc	σ	7.37	0.05	0.29	0.23	1.64	0.04	8.45	0.60	0.04	0.47	0.19	-	-	-	-	-	-	-	-	-	-	-	-	-	-
RP87-6	MCs	nc	opx core	54.30	0.06	4.15	0.27	6.30	0.14	32.73	0.88	0.08	98.90	90.26	1.7	88.5	9.8	1.9	0.0	0.2	0.0	0.2	0.0	1.7	0.0	0.0	4.0	3
RP87-6	MCs	nc	min	53.88	0.04	4.04	0.25	6.25	0.13	32.72	0.88	0.06	98.61	90.21	-	-	-	-	-	-	-	-	-	-	-	-	-	-
RP87-6	MCs	nc	max	54.84	0.09	4.29	0.29	6.34	0.16	32.74	0.88	0.11	99.31	90.32	-	-	-	-	-	-	-	-	-	-	-	-	-	-
RP87-6	MCs	nc	σ	0.49	0.03	0.12	0.02	0.04	0.02	0.01	0.00	0.02	0.36	0.06	-	-	-	-	-	-	-	-	-	-	-	-	-	-
RP91-22	MCs	nc	opx core	51.41	0.32	6.17	0.91	3.12	0.10	15.57	19.74	1.29	98.62	89.88	44.9	49.3	5.7	1.9	0.0	0.3	0.0	0.1	0.0	0.9	0.8	0.1	4.0	13
RP91-22	MCs	nc	min	50.68	0.24	5.79	0.86	3.04	0.06	15.20	19.59	1.24	97.55	89.51	-	-	-	-	-	-	-	-	-	-	-	-	-	-
RP91-22	MCs	nc	max	52.14	0.43	6.97	0.97	3.22	0.12	15.87	19.96	1.34	99.25	90.17	-	-	-	-	-	-	-	-	-	-	-	-	-	-
RP91-22	MCs	nc	σ	0.52	0.07	0.44	0.04	0.05	0.02	0.22	0.12	0.03	0.51	0.20	-	-	-	-	-	-	-	-	-	-	-	-	-	-

Supplementary tables - Massif Central, Lanzarote and Calatrava. Clinopyroxene

Sample	location	site	Mineral	SiO2	TiO2	Al2O3	Cr2O3	FeO	MnO	MgO	CaO	Na2O	Total	Mg#	Wo	En	Fs	Si	Ti	Al	Cr	Fe(ii)	Mn	Mg	Ca	Na	Total	no.
12548	Cal	spc	cpx core	51.90	-	5.60	0.69	3.20	0.13	15.75	21.41	0.87	99.50	89.77	46.6	47.7	5.6	1.9	0.0	0.2	0.0	0.1	0.0	0.9	0.8	0.1	4.0	3
12548	Cal	spc	Min	51.64	-	5.36	0.54	2.75	0.01	15.47	21.25	0.76	98.73	89.00	-	-	-	-	-	-	-	-	-	-	-	-	-	-
12548	Cal	spc	Max	52.23	-	5.77	0.93	3.56	0.33	16.16	21.80	0.95	100.30	91.00	-	-	-	-	-	-	-	-	-	-	-	-	-	-
12548	Cal	spc	σ	0.31	-	0.17	0.17	0.34	0.18	0.30	0.26	0.08	0.66	0.88	-	-	-	-	-	-	-	-	-	-	-	-	-	-
12548	Cal	spc	cpx rim	52.38	-	5.04	0.85	3.07	0.11	15.87	21.63	0.84	99.74	90.22	46.8	47.8	5.4	1.9	0.0	0.2	0.0	0.1	0.0	0.9	0.8	0.1	4.0	3
12548	Cal	spc	Min	51.58	-	4.77	0.75	2.94	0.04	15.56	21.35	0.73	99.02	89.86	-	-	-	-	-	-	-	-	-	-	-	-	-	-
12548	Cal	spc	Max	52.84	-	5.51	0.97	3.13	0.17	16.17	21.89	0.92	100.20	90.74	-	-	-	-	-	-	-	-	-	-	-	-	-	-
12548	Cal	spc	σ	0.69	-	0.41	0.11	0.11	0.09	0.31	0.27	0.10	0.63	0.47	-	-	-	-	-	-	-	-	-	-	-	-	-	-
12548	Cal	spc	cpx core	52.64	-	5.38	0.80	2.87	0.14	16.03	21.55	0.73	100.10	90.87	46.7	48.3	5.0	1.9	0.0	0.2	0.0	0.1	0.0	0.9	0.8	0.1	4.0	3
12548	Cal	spc	Min	52.23	-	5.07	0.71	2.70	0.06	15.91	21.41	0.69	98.78	90.39	-	-	-	-	-	-	-	-	-	-	-	-	-	-
12548	Cal	spc	Max	53.08	-	5.60	0.88	3.08	0.21	16.25	21.79	0.79	101.21	91.31	-	-	-	-	-	-	-	-	-	-	-	-	-	-
12548	Cal	spc	σ	0.43	-	0.28	0.09	0.19	0.11	0.19	0.21	0.05	1.23	0.46	-	-	-	-	-	-	-	-	-	-	-	-	-	-
12548	Cal	spc	cpx rim	52.88	-	4.83	0.69	2.81	0.20	16.27	21.41	0.76	99.85	91.17	46.2	48.8	5.1	1.9	0.0	0.2	0.0	0.1	0.0	0.9	0.8	0.1	4.0	3
12548	Cal	spc	Min	52.33	-	4.49	0.33	2.57	0.15	16.20	21.17	0.65	99.27	90.31	-	-	-	-	-	-	-	-	-	-	-	-	-	-
12548	Cal	spc	Max	53.34	-	5.28	0.88	3.10	0.23	16.36	21.61	0.87	100.88	91.90	-	-	-	-	-	-	-	-	-	-	-	-	-	-
12548	Cal	spc	σ	0.51	-	0.41	0.31	0.27	0.04	0.08	0.22	0.11	0.90	0.81	-	-	-	-	-	-	-	-	-	-	-	-	-	-
12548	Cal	nspc	cpx core	52.11	-	6.27	0.78	2.94	0.17	15.36	21.34	0.98	99.81	90.32	47.3	47.4	5.4	1.9	0.0	0.3	0.0	0.1	0.0	0.8	0.8	0.1	4.0	4
12548	Cal	nspc	Min	51.69	-	5.96	0.72	2.35	0.17	15.20	21.07	0.91	99.47	89.48	-	-	-	-	-	-	-	-	-	-	-	-	-	-
12548	Cal	nspc	Max	52.88	-	6.48	0.82	3.22	0.17	15.52	21.60	1.04	100.48	92.17	-	-	-	-	-	-	-	-	-	-	-	-	-	-
12548	Cal	nspc	σ	0.55	-	0.22	0.05	0.40	-	0.13	0.22	0.06	0.47	1.25	-	-	-	-	-	-	-	-	-	-	-	-	-	-
6	Cal	spc	cpx core	51.43	0.27	7.28	0.48	2.77	0.11	14.85	21.38	1.08	99.64	90.53	48.3	46.7	5.1	1.9	0.0	0.3	0.0	0.1	0.0	0.8	0.8	0.1	4.0	5
6	Cal	spc	Min	51.10	0.16	7.13	0.26	2.57	0.06	14.63	21.17	1.04	98.77	89.97	-	-	-	-	-	-	-	-	-	-	-	-	-	-
6	Cal	spc	Max	51.81	0.37	7.48	0.68	2.97	0.17	15.00	21.61	1.11	100.41	91.03	-	-	-	-	-	-	-	-	-	-	-	-	-	-
6	Cal	spc	σ	0.26	0.10	0.14	0.15	0.17	0.05	0.18	0.19	0.03	0.74	0.46	-	-	-	-	-	-	-	-	-	-	-	-	-	-
6	Cal	spc	cpx rim	52.09	0.20	5.89	0.35	3.11	0.12	15.61	21.38	0.98	99.74	89.95	46.9	47.6	5.5	1.9	0.0	0.3	0.0	0.1	0.0	0.8	0.8	0.1	4.0	3
6	Cal	spc	Min	51.50	0.08	5.47	0.25	3.01	0.12	15.54	21.19	0.89	99.27	89.70	-	-	-	-	-	-	-	-	-	-	-	-	-	-
6	Cal	spc	Max	52.43	0.27	6.12	0.41	3.18	0.12	15.70	21.56	1.03	100.10	90.23	-	-	-	-	-	-	-	-	-	-	-	-	-	-
6	Cal	spc	σ	0.51	0.11	0.37	0.09	0.09	-	0.08	0.19	0.08	0.42	0.26	-	-	-	-	-	-	-	-	-	-	-	-	-	-
6	Cal	spc	cpx inc (sp)	51.65	0.32	6.07	0.42	2.87	0.21	15.38	21.55	0.97	99.32	90.54	47.5	47.2	5.3	1.9	0.0	0.3	0.0	0.1	0.0	0.8	0.8	0.1	4.0	4
6	Cal	spc	Min	51.10	0.22	5.68	0.27	2.69	0.14	15.22	21.41	0.90	98.54	89.85	-	-	-	-	-	-	-	-	-	-	-	-	-	-
6	Cal	spc	Max	51.90	0.40	6.36	0.59	3.10	0.27	15.52	21.65	1.02	99.87	91.14	-	-	-	-	-	-	-	-	-	-	-	-	-	-
6	Cal	spc	σ	0.37	0.09	0.29	0.13	0.18	0.09	0.12	0.11	0.06	0.57	0.58	-	-	-	-	-	-	-	-	-	-	-	-	-	-
6	Cal	spc	cpx core	52.04	0.29	7.20	0.53	2.96	0.11	15.12	21.44	1.08	100.87	90.11	47.8	46.9	5.3	1.9	0.0	0.3	0.0	0.1	0.0	0.8	0.8	0.1	4.0	6
6	Cal	spc	Min	51.87	0.12	7.03	0.22	2.70	0.09	14.84	21.12	1.02	100.87	89.45	-	-	-	-	-	-	-	-	-	-	-	-	-	-
6	Cal	spc	Max	52.31	0.48	7.46	0.68	3.21	0.12	15.27	21.71	1.16	100.87	90.74	-	-	-	-	-	-	-	-	-	-	-	-	-	-
6	Cal	spc	σ	0.17	0.13	0.16	0.17	0.17	0.02	0.17	0.28	0.06	0.00	0.44	-	-	-	-	-	-	-	-	-	-	-	-	-	-
6	Cal	spc	cpx rim	53.05	0.30	5.99	0.44	2.98	0.15	15.90	21.62	0.99	101.39	90.50	46.8	47.9	5.3	1.9	0.0	0.3	0.0	0.1	0.0	0.8	0.8	0.1	4.0	4
6	Cal	spc	Min	52.34	0.12	5.68	0.37	2.69	0.06	15.48	21.48	0.96	100.79	89.91	-	-	-	-	-	-	-	-	-	-	-	-	-	-
6	Cal	spc	Max	53.53	0.37	6.54	0.58	3.20	0.21	16.12	21.94	1.01	101.84	91.44	-	-	-	-	-	-	-	-	-	-	-	-	-	-
6	Cal	spc	σ	0.56	0.12	0.39	0.10	0.21	0.08	0.28	0.22	0.02	0.51	0.66	-	-	-	-	-	-	-	-	-	-	-	-	-	-

Sample	location	site	Mineral	SiO2	TiO2	Al2O3	Cr2O3	FeO	MnO	MgO	CaO	Na2O	Total	Mg#	Wo	En	Fs	Si	Ti	Al	Cr	Fe(ii)	Mn	Mg	Ca	Na	Total	no.
5	Cal	spc	cpx core	51.78	-	5.58	0.92	3.25	0.18	15.14	21.25	1.06	99.11	89.26	47.2	46.8	5.9	1.8	0.0	0.2	0.0	0.1	0.0	0.8	0.8	0.1	3.8	11
5	Cal	spc	Min	51.14	-	5.12	0.41	2.63	0.05	14.50	20.66	0.86	98.64	88.09	-	-	-	-	-	-	-	-	-	-	-	-	-	-
5	Cal	spc	Max	52.21	-	6.14	1.34	3.78	0.51	15.69	21.60	1.19	100.97	90.93	-	-	-	-	-	-	-	-	-	-	-	-	-	-
5	Cal	spc	σ	0.41	-	0.31	0.31	0.34	0.14	0.33	0.31	0.10	0.68	0.87	-	-	-	-	-	-	-	-	-	-	-	-	-	-
5	Cal	nc	cpx core	51.87	-	6.05	1.06	3.26	0.13	15.44	21.18	1.06	100.00	89.41	46.7	47.4	5.8		1.9	0.0	0.3	0.0	0.1	0.0	0.8	0.8	0.1	4
5	Cal	nc	Min	48.01	-	5.10	0.57	2.91	0.08	15.22	19.18	0.86	99.39	87.71	-	-	-	-	-	-	-	-	-	-	-	-	-	-
5	Cal	nc	Max	53.34	-	9.87	1.80	3.92	0.19	15.69	21.75	1.34	100.97	90.49	-	-	-	-	-	-	-	-	-	-	-	-	-	-
5	Cal	nc	σ	2.00	-	1.89	0.40	0.35	0.06	0.18	0.99	0.17	0.64	0.94	-	-	-	-	-	-	-	-	-	-	-	-	-	-
3	Cal	spc	cpx core	53.52	0.22	4.22	1.84	3.04	0.19	17.02	18.70	1.33	100.03	90.89	41.6	52.7	5.6	1.9	0.0	0.2	0.1	0.1	0.0	0.9	0.7	0.1	4.0	9
3	Cal	spc	min	52.84	0.09	3.97	1.59	2.88	0.02	16.51	18.12	1.24	98.95	90.5	-	-	-	-	-	-	-	-	-	-	-	-	-	-
3	Cal	spc	max	53.99	0.36	4.43	2.09	3.21	0.35	17.63	19.08	1.45	100.89	91.4	-	-	-	-	-	-	-	-	-	-	-	-	-	-
3	Cal	spc	σ.	0.31	0.09	0.15	0.18	0.11	0.14	0.31	0.28	0.07	0.70	0.3	-	-	-	-	-	-	-	-	-	-	-	-	-	-
3	Cal	nc	mean	53.31	-	4.09	1.83	2.96	0.20	17.03	18.69	1.23	99.21	91.11	41.7	52.8	5.5	1.9	0.0	0.2	0.1	0.1	0.0	0.9	0.7	0.1	4.0	6
3	Cal	nc	min	52.26	-	3.86	1.52	2.42	0.19	16.53	18.35	1.18	97.48	89.79	-	-	-	-	-	-	-	-	-	-	-	-	-	-
3	Cal	nc	max	53.89	-	4.26	2.10	3.45	0.21	17.34	18.99	1.32	99.97	92.57	-	-	-	-	-	-	-	-	-	-	-	-	-	-
3	Cal	nc	σ.	0.55	-	0.13	0.26	0.38	0.01	0.30	0.27	0.05	0.96	1.01	-	-	-	-	-	-	-	-	-	-	-	-	-	-
EC3	Lanz	nhalo	cpx core	53.14	0.37	4.59	1.07	2.78	-	16.45	20.94	1.42	100.77	91.35	45.5	49.8	4.7	1.9	0.0	0.2	0.0	0.1	0.0	0.9	0.8	0.1	4.0	7
EC3	Lanz	nhalo	min	52.22	0.32	3.94	0.73	2.70	-	16.08	20.58	1.28	99.53	90.98	-	-	-	-	-	-	-	-	-	-	-	-	-	-
EC3	Lanz	nhalo	max	54.20	0.43	5.39	1.33	2.85	-	17.05	21.26	1.59	101.60	91.61	-	-	-	-	-	-	-	-	-	-	-	-	-	-
EC3	Lanz	nhalo	σ	0.67	0.04	0.47	0.20	0.05	-	0.33	0.25	0.09	0.77	0.21	-	-	-	-	-	-	-	-	-	-	-	-	-	-
EC3	Lanz	halo	cpx core	52.00	0.72	4.03	1.28	2.64	-	16.90	21.81	0.68	100.05	91.93	46.0	49.6	4.3	1.9	0.0	0.2	0.0	0.1	0.0	0.9	0.8	0.0	4.0	9
EC3	Lanz	halo	min	49.54	0.23	1.97	0.61	2.31	-	15.52	20.35	0.35	98.81	89.89	-	-	-	-	-	-	-	-	-	-	-	-	-	-
EC3	Lanz	halo	max	54.50	1.48	5.80	1.65	3.11	-	18.90	22.74	1.25	101.03	92.97	-	-	-	-	-	-	-	-	-	-	-	-	-	-
EC3	Lanz	halo	σ	1.61	0.38	1.11	0.41	0.26	-	0.90	0.78	0.32	0.73	0.87	-	-	-	-	-	-	-	-	-	-	-	-	-	-
EC4	Lanz	spc	cpx core	52.83	0.04	3.49	0.92	2.77	0.10	17.01	21.87	1.11	100.10	91.63	45.8	49.6	4.7	1.9	0.0	0.1	0.0	0.1	0.0	0.9	0.8	0.1	4.0	4
EC4	Lanz	spc	min	52.17	0.00	3.33	0.76	2.69	0.00	16.85	21.73	1.06	98.99	91.45	-	-	-	-	-	-	-	-	-	-	-	-	-	-
EC4	Lanz	spc	max	53.13	0.08	3.62	1.04	2.82	0.25	17.15	21.98	1.20	100.68	91.88	-	-	-	-	-	-	-	-	-	-	-	-	-	-
EC4	Lanz	spc	σ	0.45	0.04	0.13	0.15	0.06	0.13	0.14	0.11	0.06	0.76	0.18	-	-	-	-	-	-	-	-	-	-	-	-	-	-
EC4	Lanz	nc	cpx core	52.75	0.20	3.44	0.89	2.87	0.12	17.97	20.75	1.03	100.00	91.78	43.2	52.0	4.8	1.9	0.0	0.1	0.0	0.1	0.0	1.0	0.8	0.1	4.0	6
EC4	Lanz	nc	min	52.19	0.03	3.11	0.64	2.54	0.06	16.91	17.77	0.92	99.33	91.13	-	-	-	-	-	-	-	-	-	-	-	-	-	-
EC4	Lanz	nc	max	53.32	0.58	4.02	1.06	3.42	0.20	19.73	22.26	1.17	100.73	92.25	-	-	-	-	-	-	-	-	-	-	-	-	-	-
EC4	Lanz	nc	σ	0.47	0.25	0.40	0.16	0.38	0.06	1.27	2.13	0.09	0.61	0.46	-	-	-	-	-	-	-	-	-	-	-	-	-	-
EC5	Lanz	halo	cpx core	51.48	0.91	2.71	1.11	3.11	0.07	16.82	22.95	0.39	99.55	90.59	47.0	47.9	5.1	1.9	0.0	0.1	0.0	0.1	0.0	0.9	0.9	0.0	4.0	6
EC5	Lanz	halo	min	50.39	0.73	2.05	0.74	2.76	0.05	16.09	22.77	0.32	99.29	89.01	-	-	-	-	-	-	-	-	-	-	-	-	-	-
EC5	Lanz	halo	max	52.08	1.21	3.86	1.52	3.54	0.08	17.44	23.18	0.46	99.90	91.57	-	-	-	-	-	-	-	-	-	-	-	-	-	-
EC5	Lanz	halo	σ	0.66	0.17	0.67	0.34	0.28	0.01	0.50	0.16	0.06	0.21	0.94	-	-	-	-	-	-	-	-	-	-	-	-	-	-
EC5	Lanz	nhalo	cpx core	52.52	0.77	2.80	1.05	3.26	0.08	17.29	22.04	0.56	100.37	90.44	46.4	50.7	2.9	1.9	0.0	0.1	0.0	0.1	0.0	0.9	0.9	0.0	4.0	8
EC5	Lanz	nhalo	min	51.65	0.56	2.36	0.31	2.91	0.06	16.61	20.96	0.35	100.07	89.04	-	-	-	-	-	-	-	-	-	-	-	-	-	-
EC5	Lanz	nhalo	max	53.04	1.08	3.33	1.50	3.67	0.09	17.87	23.30	0.76	100.69	91.38	-	-	-	-	-	-	-	-	-	-	-	-	-	-
EC5	Lanz	nhalo	σ	0.49	0.21	0.39	0.46	0.26	0.01	0.45	1.03	0.17	0.21	0.84	-	-	-	-	-	-	-	-	-	-	-	-	-	-

Sample	location	site	Mineral	SiO2	TiO2	Al2O3	Cr2O3	FeO	MnO	MgO	CaO	Na2O	Total	Mg#	Wo	En	Fs	Si	Ti	Al	Cr	Fe(ii)	Mn	Mg	Ca	Na	Total	no.
EC6	Lanz	spc	opx core	52.91	0.10	3.45	0.86	2.54	0.10	17.16	22.56	0.75	100.40	92.34	46.5	49.3	4.2	0.4	0.2	0.7	0.3	0.7	0.0	0.3	0.4	0.4	3.5	5
EC6	Lanz	spc	min	52.36	0.02	2.90	0.67	2.42	0.01	16.85	22.07	0.67	99.69	91.92	-	-	-	-	-	-	-	-	-	-	-	-	-	-
EC6	Lanz	spc	max	53.60	0.26	4.18	1.01	2.69	0.15	17.35	22.99	0.85	101.41	92.72	-	-	-	-	-	-	-	-	-	-	-	-	-	-
EC6	Lanz	spc	σ	0.46	0.13	0.47	0.15	0.11	0.06	0.20	0.34	0.09	0.64	0.35	-	-	-	-	-	-	-	-	-	-	-	-	-	-
EC6	Lanz	nc	opx core	52.65	-	3.38	0.91	2.56	0.11	17.24	22.43	0.88	100.14	92.32	46.3	49.5	4.3	1.9	0.0	0.1	0.0	0.1	0.0	0.9	0.9	0.1	4.0	9
EC6	Lanz	nc	min	51.42	-	3.29	0.69	2.34	0.00	16.85	22.03	0.78	98.19	91.82	-	-	-	-	-	-	-	-	-	-	-	-	-	-
EC6	Lanz	nc	max	53.18	-	3.56	1.14	2.72	0.26	17.70	22.94	0.99	101.07	93.00	-	-	-	-	-	-	-	-	-	-	-	-	-	-
EC6	Lanz	nc	σ	0.59	-	0.10	0.13	0.14	0.08	0.27	0.29	0.07	0.86	0.43	-	-	-	-	-	-	-	-	-	-	-	-	-	-
EC21	Lanz	halo	cpx core	54.00	0.25	3.01	1.24	3.07	0.09	18.90	19.85	0.48	100.90	91.76	40.8	54.1	5.1	1.9	0.0	0.1	0.0	0.1	0.0	1.0	0.8	0.0	4.0	5
EC21	Lanz	halo	min	53.12	0.19	2.27	1.13	2.94	0.06	18.36	19.66	0.39	100.49	91.50	-	-	-	-	-	-	-	-	-	-	-	-	-	-
EC21	Lanz	halo	max	54.75	0.37	3.67	1.39	3.29	0.12	19.40	20.08	0.61	101.18	92.03	-	-	-	-	-	-	-	-	-	-	-	-	-	-
EC21	Lanz	halo	σ	0.58	0.07	0.51	0.12	0.13	0.02	0.42	0.18	0.10	0.27	0.37	-	-	-	-	-	-	-	-	-	-	-	-	-	-
EC21	Lanz	nc	opx core	54.00	0.25	3.01	1.24	3.07	0.09	18.90	19.85	0.48	100.90	91.76	40.8	54.1	5.1	1.9	0.0	0.1	0.0	0.1	0.0	1.0	0.8	0.0	4.0	5
EC21	Lanz	nc	min	53.12	0.19	2.27	1.13	2.94	0.06	18.36	19.66	0.39	100.49	91.50	-	-	-	-	-	-	-	-	-	-	-	-	-	-
EC21	Lanz	nc	max	54.75	0.37	3.67	1.39	3.29	0.12	19.40	20.08	0.61	101.18	92.03	-	-	-	-	-	-	-	-	-	-	-	-	-	-
EC21	Lanz	nc	σ	0.58	0.07	0.51	0.12	0.13	0.02	0.42	0.18	0.10	0.27	0.37	-	-	-	-	-	-	-	-	-	-	-	-	-	-
CH11	MCn	spc	cpx core	53.09	-	3.77	0.61	2.40	0.07	15.77	23.64	0.71	100.06	92.15	49.8	46.2	4.0	1.9	0.0	0.2	0.0	0.1	0.0	0.9	0.9	0.0	4.0	9
CH11	MCn	spc	min	52.50	-	3.66	0.54	2.24	0.00	15.62	23.29	0.59	99.56	91.62	-	-	-	-	-	-	-	-	-	-	-	-	-	-
CH11	MCn	spc	max	53.42	-	3.85	0.73	2.55	0.14	16.01	23.94	0.87	100.50	92.63	-	-	-	-	-	-	-	-	-	-	-	-	-	-
CH11	MCn	spc	σ	0.26	-	0.08	0.06	0.10	0.05	0.12	0.18	0.08	0.33	0.34	-	-	-	-	-	-	-	-	-	-	-	-	-	-
CH11	MCn	nc	cpx core	52.90	0.20	3.47	0.61	2.45	0.11	16.62	23.08	0.72	100.13	92.37	47.9	48.0	4.1	1.9	0.0	0.1	0.0	0.1	0.0	0.9	0.9	0.1	4.0	15
CH11	MCn	nc	min	52.42	0.08	3.27	0.34	2.19	0.03	16.22	20.85	0.59	99.41	91.44	-	-	-	-	-	-	-	-	-	-	-	-	-	-
CH11	MCn	nc	max	53.37	0.38	3.65	0.83	3.11	0.18	18.63	23.58	0.82	100.74	93.09	-	-	-	-	-	-	-	-	-	-	-	-	-	-
CH11	MCn	nc	σ	0.30	0.07	0.12	0.14	0.24	0.06	0.59	0.66	0.06	0.42	0.52	-	-	-	-	-	-	-	-	-	-	-	-	-	-
MB1	MCn	spc	cpx core	51.58	0.10	3.89	0.74	2.81	0.13	16.45	24.03	0.72	100.43	91.25	48.8	46.5	4.6	1.9	0.0	0.2	0.0	0.1	0.0	0.9	0.9	0.0	4.0	10
MB1	MCn	spc	min	48.47	0.03	3.12	0.51	2.61	0.00	16.26	22.91	0.53	99.51	90.00	-	-	-	-	-	-	-	-	-	-	-	-	-	-
MB1	MCn	spc	max	52.55	0.20	6.22	1.28	3.24	0.23	16.62	24.61	0.87	101.16	91.79	-	-	-	-	-	-	-	-	-	-	-	-	-	-
MB1	MCn	spc	σ	1.17	0.06	0.86	0.22	0.19	0.08	0.12	0.46	0.11	0.56	0.54	-	-	-	-	-	-	-	-	-	-	-	-	-	-
MB1	MCn	nc	cpx core	51.62	0.09	3.73	0.70	2.74	0.11	16.36	23.97	0.70	100.02	91.41	49.0	46.5	4.5	1.9	0.0	0.4	0.1	0.0	0.1	0.0	0.5	0.6	3.6	17
MB1	MCn	nc	min	51.15	0.01	3.38	0.50	2.58	0.02	16.12	23.65	0.51	99.09	90.74	-	-	-	-	-	-	-	-	-	-	-	-	-	-
MB1	MCn	nc	max	52.27	0.25	4.00	0.94	2.95	0.25	16.72	24.28	0.82	100.98	91.86	-	-	-	-	-	-	-	-	-	-	-	-	-	-
MB1	MCn	nc	σ	0.26	0.07	0.20	0.13	0.10	0.07	0.17	0.15	0.10	0.62	0.29	-	-	-	-	-	-	-	-	-	-	-	-	-	-

Sample	location	site	Mineral	SiO2	TiO2	Al2O3	Cr2O3	FeO	MnO	MgO	CaO	Na2O	Total	Mg#	Wo	En	Fs	Si	Ti	Al	Cr	Fe(ii)	Mn	Mg	Ca	Na	Total	no.
MB9	MCn	spc	cpx core	53.24	-	3.70	0.70	2.68	-	16.90	22.32	0.77	100.31	91.84	46.6	49.1	4.3	1.9	0.0	0.2	0.0	0.1	0.0	0.9	0.9	0.1	4.0	7
MB9	MCn	spc	min	52.70	-	3.49	0.48	2.43	-	16.51	21.99	0.71	99.35	91.36	-	-	-	-	-	-	-	-	-	-	-	-	-	-
MB9	MCn	spc	max	53.65	-	4.12	0.98	2.82	-	17.22	22.61	0.84	100.91	92.59	-	-	-	-	-	-	-	-	-	-	-	-	-	-

MB9	MCn	spc	σ	0.36	-	0.22	0.19	0.13	-	0.23	0.21	0.05	0.64	0.42	-	-	-	-	-	-	-	-	-	-	-	-	-	-	-	-	
MB63B	MCn	spc	cpx core	51.76	0.21	3.99	1.38	2.36	0.13	15.88	22.51	0.94	99.13	92.32	48.4	47.5	4.2	1.9	0.0	0.2	0.0	0.1	0.0	0.9	0.9	0.1	4.0	6				
MB63B	MCn	spc	min	51.46	0.14	3.74	1.19	2.14	0.02	15.67	22.23	0.88	98.80	91.67	-	-	-	-	-	-	-	-	-	-	-	-	-	-	-	-	
MB63B	MCn	spc	max	51.97	0.27	4.21	1.76	2.60	0.25	16.06	22.62	1.03	99.58	93.02	-	-	-	-	-	-	-	-	-	-	-	-	-	-	-	-	
MB63B	MCn	spc	σ	0.17	0.05	0.18	0.20	0.16	0.09	0.15	0.15	0.05	0.26	0.47	-	-	-	-	-	-	-	-	-	-	-	-	-	-	-	-	
MB63B	MCn	nc	cpx core	52.51	0.25	3.76	1.27	2.25	0.06	16.03	22.78	0.94	100.53	92.71	48.6	47.6	3.8	1.9	1.9	0.0	0.2	0.0	0.1	0.0	0.9	0.9	4.0	13				
MB63B	MCn	nc	min	51.71	0.16	3.01	0.77	2.10	0.00	15.64	22.12	0.81	98.58	92.24	-	-	-	-	-	-	-	-	-	-	-	-	-	-	-	-	
MB63B	MCn	nc	max	53.55	0.40	4.13	1.58	2.39	0.20	16.71	23.37	1.08	101.02	93.21	-	-	-	-	-	-	-	-	-	-	-	-	-	-	-	-	
MB63B	MCn	nc	σ	0.55	0.07	0.29	0.23	0.08	0.06	0.29	0.30	0.08	0.80	0.26	-	-	-	-	-	-	-	-	-	-	-	-	-	-	-	-	
MB64	MCn	spc	cpx core	52.04	0.13	4.34	0.76	2.90	0.11	16.75	22.35	0.61	99.95	91.16	46.6	48.6	4.9	1.9	0.0	0.2	0.0	0.1	0.0	0.9	0.9	0.0	4.0	3				
MB64	MCn	spc	min	51.86	0.07	4.27	0.72	2.73	0.05	16.69	22.23	0.57	99.81	90.62	-	-	-	-	-	-	-	-	-	-	-	-	-	-	-	-	
MB64	MCn	spc	max	52.18	0.17	4.47	0.85	3.09	0.16	16.82	22.47	0.64	100.23	91.59	-	-	-	-	-	-	-	-	-	-	-	-	-	-	-	-	
MB64	MCn	spc	σ	0.16	0.05	0.11	0.08	0.18	0.08	0.07	0.12	0.04	0.24	0.50	-	-	-	-	-	-	-	-	-	-	-	-	-	-	-	-	
MB64	MCn	nc	ol core	52.14	0.07	4.34	0.72	2.95	0.07	16.61	22.45	0.60	99.96	90.94	46.9	48.2	4.9	1.9	0.0	0.2	0.0	0.1	0.0	0.9	0.9	0.0	4.0	7				
MB64	MCn	nc	min	51.45	0.02	4.24	0.67	2.73	0.01	16.49	22.30	0.56	98.82	90.44	-	-	-	-	-	-	-	-	-	-	-	-	-	-	-	-	
MB64	MCn	nc	max	52.54	0.13	4.43	0.79	3.12	0.21	16.77	22.55	0.65	100.59	91.50	-	-	-	-	-	-	-	-	-	-	-	-	-	-	-	-	
MB64	MCn	nc	σ	0.38	0.04	0.08	0.04	0.14	0.07	0.11	0.09	0.03	0.61	0.38	-	-	-	-	-	-	-	-	-	-	-	-	-	-	-	-	
RP87-6	MCs	nc	cpx core	51.8	0.3	6.2	0.7	3.3	0.1	15.8	20.0	1.1	99.3	89.4	45.2	49.5	5.4	1.9	0.0	0.3	0.0	0.1	0.0	0.9	0.8	0.1	4.0	7				
RP87-6	MCs	nc	min	51.1	0.2	5.0	0.5	3.2	0.1	15.2	19.7	1.1	98.9	88.9	-	-	-	-	-	-	-	-	-	-	-	-	-	-	-	-	
RP87-6	MCs	nc	max	52.5	0.5	7.3	0.8	3.4	0.1	16.4	20.1	1.2	99.9	89.8	-	-	-	-	-	-	-	-	-	-	-	-	-	-	-	-	
RP87-6	MCs	nc	σ	0.5	0.1	1.0	0.2	0.1	0.0	0.5	0.1	0.1	0.4	0.4	-	-	-	-	-	-	-	-	-	-	-	-	-	-	-	-	
RP91-22	MCs	nc	cpx core	54.8	0.1	4.0	0.4	6.0	0.1	32.7	0.8	0.1	99.0	90.7	1.5	89.1	9.3	1.9	0.0	0.2	0.0	0.2	0.0	1.7	0.0	0.0	4.0	10				
RP91-22	MCs	nc	min	53.5	0.0	3.7	0.3	5.9	0.1	32.1	0.6	0.1	97.3	90.6	-	-	-	-	-	-	-	-	-	-	-	-	-	-	-	-	
RP91-22	MCs	nc	max	55.8	0.1	4.4	0.4	6.0	0.2	33.3	0.9	0.2	100.0	91.0	-	-	-	-	-	-	-	-	-	-	-	-	-	-	-	-	
RP91-22	MCs	nc	σ	0.7	0.0	0.3	0.0	0.0	0.0	0.4	0.1	0.0	0.8	0.1	-	-	-	-	-	-	-	-	-	-	-	-	-	-	-	-	

Supplementary tables - Massif Central, Lanzarote and Calatrava. Spinel

Sample	location	site	Mineral	SiO2	TiO2	Al2O3	Cr2O3	Fe2O3	FeO	MnO	NiO	MgO	Total	Mg#	Cr#	Al	Cr	Fe(iii)	Fe(ii)	Mn	Mg	Total	no.
12548	Cal	spc	sp	-	-	56.35	10.10	2.98	9.42	0.19	-	20.37	99.38	83.42	10.74	1.7	0.2	0.1	0.2	0.0	0.8	3.0	7
12548	Cal	spc	Min	-	-	55.57	9.74	1.76	8.93	0.08	-	19.77	98.16	82.24	10.39	-	-	-	-	-	-	-	-
12548	Cal	spc	Max	-	-	56.68	10.56	3.96	9.97	0.40	-	20.96	100.28	84.94	11.11	-	-	-	-	-	-	-	-
12548	Cal	spc	σ	-	-	0.39	0.30	0.70	0.39	0.12	-	0.43	0.88	0.87	0.28	-	-	-	-	-	-	-	-
6	Cal	spc	sp	-	-	63.18	3.59	2.43	8.84	0.21	-	21.46	99.71	79.38	3.67	1.9	0.1	0.0	0.2	0.0	0.8	3.0	3
6	Cal	spc	Min	-	-	63.11	3.48	2.27	8.44	0.13	-	21.19	99.55	78.71	3.57	-	-	-	-	-	-	-	-
6	Cal	spc	Max	-	-	63.25	3.70	2.70	9.19	0.31	-	21.71	99.80	80.30	3.78	-	-	-	-	-	-	-	-
6	Cal	spc	σ	-	-	0.07	0.11	0.23	0.38	0.09	-	0.26	0.14	0.83	0.11	-	-	-	-	-	-	-	-
5	Cal	spc	Mean	-	-	54.83	10.38	4.21	9.72	0.31	-	19.86	99.31	75.29	11.27	1.70	0.22	0.08	0.21	0.01	0.78	3.00	12
5	Cal	spc	Min	-	-	53.90	9.25	3.37	9.17	0.00	-	19.26	98.41	73.81	10.03	-	-	-	-	-	-	-	-
5	Cal	spc	Max	-	-	55.64	10.98	5.10	10.41	0.75	-	20.38	101.32	76.11	11.92	-	-	-	-	-	-	-	-
5	Cal	spc	σ	-	-	0.54	0.56	0.53	0.39	0.22	-	0.32	0.79	0.72	0.59	-	-	-	-	-	-	-	-
3	Cal	spc	sp	-	-	36.69	6.93	-	14.94	-	-	16.24	100.79	65.98	51.57	0.9	1.0	0.1	0.3		0.7	3.0	4
3	Cal	spc	Min	-	-	26.48	41.93	-	13.92	-	-	16.10	98.74	64.81	51.22	-	-	-	-	-	-	-	-
3	Cal	spc	Max	-	-	26.83	42.74	-	15.69	-	-	16.46	101.82	67.34	51.79	-	-	-	-	-	-	-	-
3	Cal	spc	σ	-	-	0.14	0.43	-	0.85	-	-	0.16	1.39	1.30	0.26	-	-	-	-	-	-	-	-
EC3	Lanz	nhalo	sp core	-	0.51	31.37	34.18	5.13	11.12	0.15	-	16.95	99.40	74.89	42.23	1.08	0.79	0.11	0.27	0.00	0.74	3.00	9
EC3	Lanz	nhalo	min	-	0.51	28.82	33.10	4.69	10.47	0.11	-	15.91	15.91	72.65	40.72	-	-	-	-	-	-	-	-
EC3	Lanz	nhalo	max	-	0.54	32.33	36.31	5.18	12.31	0.19	-	17.50	17.50	76.26	45.80	-	-	-	-	-	-	-	-
EC3	Lanz	nhalo	σ	-	0.01	1.08	0.96	0.16	0.62	0.03	-	0.52	0.52	1.13	1.52	-	-	-	-	-	-	-	-
EC3	Lanz	nhalo	sp rim	0.61	1.00	25.04	39.49	4.30	12.19	0.15	-	16.23	99.00	67.19	51.41	0.89	0.93	0.06	0.34	0.00	0.71	3.00	10.00
EC3	Lanz	nhalo	sp rim	0.10	0.88	24.00	36.69	2.84	11.08	0.13	-	15.85	98.34	65.45	47.39	-	-	-	-	-	-	-	-
EC3	Lanz	nhalo	sp rim	1.23	1.15	27.32	42.01	5.28	13.66	0.17	-	16.64	100.61	68.93	53.98	-	-	-	-	-	-	-	-
EC3	Lanz	nhalo	sp rim	0.39	0.08	1.12	1.72	0.79	0.87	0.01	-	0.30	0.67	1.26	2.17	-	-	-	-	-	-	-	-
EC5	Lanz	halo	sp core	0.19	1.64	18.49	8.39	41.52	14.94	0.24	0.22	13.80	98.99	42.39	23.55	0.7	1.0	0.2	0.4	0.0	0.6	3.0	4
EC5	Lanz	halo	min	0.10	1.46	14.00	7.25	36.70	14.27	0.19	0.19	12.89	98.53	38.33	21.30	-	-	-	-	-	-	-	-
EC5	Lanz	halo	max	0.36	1.73	22.13	8.93	47.92	15.39	0.29	0.25	14.53	99.53	45.69	25.78	-	-	-	-	-	-	-	-
EC5	Lanz	halo	σ	0.12	0.13	3.36	0.77	4.68	0.50	0.04	0.03	0.70	0.41	3.05	1.83	-	-	-	-	-	-	-	-
EC5	Lanz	nhalo	sp core	0.05	1.32	17.14	8.88	43.90	14.44	0.20	-	13.83	99.76	41.88	25.80	0.6	1.1	0.2	0.4	0.0	0.6	3.0	5
EC5	Lanz	nhalo	min	0.04	1.30	16.95	8.78	43.77	14.01	0.19	-	13.65	99.42	41.48	25.57	-	-	-	-	-	-	-	-
EC5	Lanz	nhalo	max	0.05	1.33	17.33	8.98	44.04	14.60	0.21	-	14.14	99.98	42.74	26.04	-	-	-	-	-	-	-	-
EC5	Lanz	nhalo	σ	0.00	0.01	0.16	0.07	0.11	0.25	0.01	-	0.20	0.24	0.51	0.17	-	-	-	-	-	-	-	-
EC4	Lanz	spc	sp core	0.26	0.00	30.44	34.99	6.41	11.52	0.24	-	16.68	0.00	67.36	43.54	1.0	0.8	0.1	0.3	0.0	0.7	3.0	7
EC4	Lanz	spc	min	0.18	0.00	30.18	34.22	6.08	11.11	0.08	-	16.51	0.00	66.40	42.63	-	-	-	-	-	-	-	-
EC4	Lanz	spc	max	0.37	0.00	30.88	35.70	6.85	12.15	0.40	-	16.85	0.00	67.94	44.04	-	-	-	-	-	-	-	-
EC4	Lanz	spc	σ	0.08	0.00	0.22	0.52	0.24	0.36	0.13	-	0.12	0.00	0.56	0.49	-	-	-	-	-	-	-	-
EC4	Lanz	spc	sp rim	0.26	0.45	28.86	37.24	5.78	10.96	0.33	-	17.22	101.10	69.35	46.40	1.0	0.9	0.1	0.3	0.0	0.7	3.0	5
EC4	Lanz	spc	min	0.17	0.24	26.01	35.17	5.37	10.66	0.18	-	16.58	100.73	69.32	47.56	-	-	-	-	-	-	-	-
EC4	Lanz	spc	max	0.33	0.63	30.68	40.39	6.15	11.26	0.50	-	17.63	101.42	69.15	46.90	-	-	-	-	-	-	-	-
EC4	Lanz	spc	σ	0.08	0.17	2.10	2.30	0.33	0.27	0.12	-	0.47	0.29	66.62	42.39	-	-	-	-	-	-	-	-

Sample	location	site	Mineral	SiO2	TiO2	Al2O3	Cr2O3	Fe2O3	FeO	MnO	NiO	MgO	Total	Mg#	Cr#	Al	Cr	Fe(iii)	Fe(ii)	Mn	Mg	Total	no.
EC6	Lanz	spc	sp core	-	-	33.02	31.82	6.24	10.96	-	-	17.17	99.21	68.96	39.26	1.13	0.73	0.14	0.26		0.74	3.00	6
EC6	Lanz	spc	min	-	-	32.60	31.35	5.83	10.69	-	-	17.00	98.68	68.26	38.54	-	-	-	-	-	-	-	-
EC6	Lanz	spc	max	-	-	33.54	32.42	6.69	11.46	-	-	17.29	99.84	69.50	39.90	-	-	-	-	-	-	-	-
EC6	Lanz	spc	σ	-	-	0.40	0.35	0.34	0.28	-	-	0.11	0.45	0.42	0.47	-	-	-	-	-	-	-	-
EC21	Lanz	halo	sp core	0.05	0.12	38.06	27.28	4.88	10.04	0.28	0.13	17.98	98.82	72.38	32.47	1.27	0.61	0.10	0.24	0.00	0.76	3.00	7
EC21	Lanz	halo	min	0.04	0.10	37.33	26.07	4.70	9.58	0.26	0.12	17.71	98.53	71.22	30.92	-	-	-	-	-	-	-	-
EC21	Lanz	halo	max	0.06	0.14	39.07	28.49	5.00	10.64	0.29	0.15	18.29	99.25	73.37	33.86	-	-	-	-	-	-	-	-
EC21	Lanz	halo	σ	0.01	0.02	0.58	0.81	0.10	0.38	0.01	0.01	0.22	0.26	0.80	0.97	-	-	-	-	-	-	-	-
EC21	Lanz	halo	sp rim	0.32	0.24	29.87	37.32	3.65	10.07	0.18	0.14	17.46	99.26	72.63	45.60	1.01	0.88	0.06	0.27	0.00	0.75	3.00	5
EC21	Lanz	halo	min	0.08	0.22	27.69	34.69	2.71	9.52	0.17	0.12	16.87	98.11	71.46	42.73	-	-	-	-	-	-	-	-
EC21	Lanz	halo	max	0.90	0.26	31.25	38.96	4.17	10.71	0.20	0.16	18.49	101.88	74.43	48.56	-	-	-	-	-	-	-	-
EC21	Lanz	halo	σ	0.33	0.02	1.49	1.62	0.58	0.44	0.01	0.01	0.63	1.60	1.17	2.12	-	-	-	-	-	-	-	-
CH11	MCn	spc	sp core	-	-	51.45	16.00	2.11	11.17	0.23	-	19.22	100.18	73.86	17.26	1.61	0.34	0.06	0.23	0.01	0.76	3.00	10
CH11	MCn	spc	min	-	-	50.30	15.49	0.90	10.62	0.10	-	18.85	99.00	72.96	16.50	-	-	-	-	-	-	-	-
CH11	MCn	spc	max	-	-	52.58	16.34	3.47	11.58	0.39	-	19.48	101.11	75.44	17.73	-	-	-	-	-	-	-	-
CH11	MCn	spc	σ	-	-	0.71	0.28	0.79	0.36	0.09	-	0.19	0.61	0.75	0.34	-	-	-	-	-	-	-	-
MB1	MCn	spc	sp core	0.28	-	45.13	19.80	4.73	11.30	0.19	-	18.21	99.64	70.74	22.74	1.46	0.43	0.10	0.26	0.00	0.74	3.00	5
MB1	MCn	spc	min	0.16	-	44.60	19.10	3.69	5.60	0.09	-	18.02	98.72	69.87	21.78	-	-	-	-	-	-	-	-
MB1	MCn	spc	max	0.40	-	46.03	20.34	10.86	12.35	0.31	-	18.48	100.56	75.84	23.37	-	-	-	-	-	-	-	-
MB1	MCn	spc	σ	0.10	-	0.56	0.46	3.00	2.80	0.10	-	0.17	0.70	2.50	0.61	-	-	-	-	-	-	-	-
MB9	MCn	spc	sp core	-	-	45.83	20.99	3.69	10.81	0.00	-	19.06	100.46	73.15	23.51	1.46	0.45	0.09	0.23	0.00	0.77	3.00	17
MB9	MCn	spc	min	-	-	44.61	19.25	3.91	9.73	0.00	-	18.74	99.30	73.05	21.64	-	-	-	-	-	-	-	-
MB9	MCn	spc	max	-	-	46.83	22.04	5.21	10.51	0.00	-	19.31	101.33	74.57	24.89	-	-	-	-	-	-	-	-
MB9	MCn	spc	σ	-	-	0.77	0.74	0.33	0.22	-	-	0.17	0.61	0.42	0.90	-	-	-	-	-	-	-	-
MB63B	MCn	spc	sp core	-	-	38.94	29.17	2.16	12.25	-	0.09	16.75	99.35	69.30	33.44	1.30	0.65	0.00	0.05	0.29	0.00	0.71	4
MB63B	MCn	spc	min	-	-	38.00	28.54	1.88	11.98	-	0.00	16.40	98.37	68.75	33.06	-	-	-	-	-	-	-	-
MB63B	MCn	spc	max	-	-	39.51	29.68	2.32	12.42	-	0.14	17.14	100.27	70.18	34.38	-	-	-	-	-	-	-	-
MB63B	MCn	spc	σ	-	-	0.71	0.48	0.19	0.19	-	0.07	0.35	1.03	0.62	0.63	-	-	-	-	-	-	-	-
MB64	MCn	spc	sp core	-	-	50.52	17.11	1.50	10.84	0.09	-	18.75	100.00	75.50	18.51	1.60	0.36	0.03	0.24	0.00	0.75	3.00	4
MB64	MCn	spc	min	-	-	50.52	17.11	1.46	10.50	0.00	-	18.75	99.64	74.75	18.26	-	-	-	-	-	-	-	-
MB64	MCn	spc	max	-	-	51.37	17.56	2.32	11.29	0.27	-	19.37	100.53	76.68	18.91	-	-	-	-	-	-	-	-
MB64	MCn	spc	σ	-	-	0.39	0.19	0.38	0.34	0.11	-	0.27	0.43	0.83	0.26	-	-	-	-	-	-	-	-
RP87-6	MCs	-	sp core	0.20	0.10	55.57	11.72	2.04	10.00	0.12	-	20.28	100.04	76.79	12.40	1.70	0.24	0.04	0.22	0.00	0.79	3.00	6
RP87-6	MCs	-	min	0.09	0.08	54.92	11.45	1.86	9.82	0.11	-	20.16	98.96	76.52	12.27	-	-	-	-	-	-	-	-
RP87-6	MCs	-	max	0.33	0.11	55.85	11.89	2.11	10.19	0.15	-	20.51	100.46	77.26	12.53	-	-	-	-	-	-	-	-
RP87-6	MCs	-	σ	0.10	0.01	0.33	0.16	0.09	0.15	0.01	-	0.15	0.55	0.31	0.10	-	-	-	-	-	-	-	-
RP91-22	MCs	-	sp core	0.16	0.10	52.83	14.59	2.02	9.80	0.13	-	20.00	99.62	76.91	15.63	1.64	0.30	0.04	0.22	0.00	0.79	3.00	7
RP91-22	MCs	-	min	0.01	0.06	52.02	14.02	1.66	8.80	0.10	-	19.90	98.21	76.25	15.29	-	-	-	-	-	-	-	-
RP91-22	MCs	-	max	0.25	0.12	53.24	14.95	2.65	10.30	0.14	-	20.30	100.43	78.36	16.02	-	-	-	-	-	-	-	-
RP91-22	MCs	-	σ	0.10	0.02	0.42	0.36	0.34	0.51	0.01	-	0.14	0.77	0.74	0.29	-	-	-	-	-	-	-	-

Supplementary tables - Massif Central, Lanzarote and Calatrava. Amphibole

Sample	Location	Site	Mineral	SiO2	Al2O3	Cr2O3	FeO	MgO	CaO	Na2O	Total	Mg#	Si	Ti	Al	Cr	Fe(ii)	Mn	Mg	Ca	Na	Total	no.
12548	Cal	spc	amph	43.10	15.18	1.19	4.43	17.94	11.00	3.13	95.97	87.83	6	0.0	2.6	0.1	0.5	0.0	3.9	1.7	0.9	16.0	3
12548	Cal	spc	Min	43.09	14.94	1.15	4.35	17.82	10.84	3.00	95.53	87.68	-	-	-	-	-	-	-	-	-	-	-
12548	Cal	spc	Max	43.10	15.45	1.26	4.54	18.12	11.09	3.26	96.56	87.99	-	-	-	-	-	-	-	-	-	-	-
12548	Cal	spc	σ	0.01	0.26	0.06	0.10	0.16	0.14	0.13	0.53	0.16	-	-	-	-	-	-	-	-	-	-	-
5	Cal	spc	amph	42.27	14.41	0.78	4.85	17.17	10.84	2.82	93.14	86.33	6	0.0	2.5	0.1	0.6	0.0	3.8	1.7	0.8	16.0	3
5	Cal	spc	Min	41.94	14.25	0.61	4.47	16.85	10.75	2.72	92.65	84.95	-	-	-	-	-	-	-	-	-	-	-
5	Cal	spc	Max	42.57	14.67	1.03	5.32	17.37	10.90	2.87	93.79	87.33	-	-	-	-	-	-	-	-	-	-	-
5	Cal	spc	σ	0.32	0.23	0.22	0.43	0.28	0.08	0.09	0.59	1.23	-	-	-	-	-	-	-	-	-	-	-

Supplementary tables - Massif Central, Lanzarote and Calatrava. Glass

Sample	Location	Site	Mineral	SiO2	TiO2	Al2O3	FeO	MnO	MgO	CaO	Na2O	K2O	Total	Mg#	Na2O + K20	No.
EC3	Lanz	Halo	Glass	52.94	1.71	17.39	4.53	-	5.58	10.31	4.19	1.38	98.03	68.69	5.57	11
EC3	Lanz	Halo	Min	51.51	1.53	17.08	3.52	-	4.11	6.91	3.76	1.21	97.06	67.48	4.97	-
EC3	Lanz	Halo	Max	60.70	1.83	17.88	5.09	-	6.00	11.13	4.47	1.86	100.80	70.74	6.18	-
EC3	Lanz	Halo	σ	2.59	0.08	0.30	0.41	-	0.53	1.18	0.23	0.17	0.98	1.19	0.33	-
EC5	Lanz	Halo	Glass	49.57	2.74	16.31	6.77	-	4.76	11.44	4.43	1.57	97.96	55.54	5.99	18
EC5	Lanz	Halo	min	47.19	2.63	15.43	6.39	-	3.90	10.39	4.11	1.44	96.50	50.77	5.57	-
EC5	Lanz	Halo	max	50.46	2.86	19.10	8.22	-	5.31	12.10	4.88	1.79	99.02	58.55	6.67	-
EC5	Lanz	Halo	σ	0.85	0.07	0.89	0.40	-	0.37	0.55	0.19	0.10	0.51	2.20	0.29	-
EC21	Lanz	halo	Glass	54.73	0.48	18.47	3.88	0.08	5.72	10.92	3.33	0.54	98.14	72.45	3.87	3
EC21	Lanz	halo	min	54.04	0.46	18.03	3.81	0.07	5.70	10.86	3.23	0.51	97.74	72.21	3.74	-
EC21	Lanz	halo	max	55.22	0.49	18.85	3.91	0.09	5.75	10.95	3.44	0.57	98.71	72.76	4.01	-
EC21	Lanz	halo	σ	0.61	0.02	0.41	0.06	0.01	0.03	0.05	0.11	0.03	0.51	0.28	0.14	-

Supplementary tables. BCR

Comment	No.	SiO2	TiO2	Al2O3	Cr2O3	FeO	MnO	MgO	CaO	Na2O	K2O	Total
BCR2	1	55.20	2.24	13.56	0.02	12.64	0.20	3.60	7.10	2.07	1.82	98.44
BCR2	2	54.86	2.02	13.20	0.00	12.68	0.23	3.58	7.08	1.99	1.79	97.44
BCR2	3	55.20	13.56	2.24	0.02	12.64	0.20	3.60	7.10	2.07	-	96.62
BCR2	4	54.86	13.20	2.02	0.00	12.68	0.23	3.58	7.08	1.99	-	95.65

Supplementary tables - Pali-Aike, South Africa, Vitim and BCR. Olivine

Sample	location	Type	Mineral	SiO2	FeO	MnO	NiO	MgO	Total	Mg#	no.
PA10	PA	gt-sp	ol core	40.75	10.40	0.12	0.38	47.76	99.41	89.11	14
PA10	PA	gt-sp	Min	39.67	10.20	0.10	0.34	47.43	98.32	88.96	
PA10	PA	gt-sp	Max	41.31	10.59	0.15	0.44	48.04	100.22	89.28	
PA10	PA	gt-sp	σ	0.40	0.11	0.02	0.02	0.18	0.42	0.09	
PA10	PA	gt-sp	ol inc	40.79	10.44	0.13	0.39	47.36	99.11	88.99	5
PA10	PA	gt-sp	Min	40.69	10.38	0.11	0.36	46.97	98.84	88.85	
PA10	PA	gt-sp	Max	40.90	10.51	0.14	0.43	47.62	99.26	89.10	
PA10	PA	gt-sp	σ	0.08	0.06	0.01	0.03	0.24	0.16	0.09	
PA13	PA	gt-sp	ol core	40.81	10.71	0.15	0.43	47.88	99.98	88.79	7
PA13	PA	gt-sp	Min	40.48	10.21	0.08	0.28	46.57	98.44	88.76	
PA13	PA	gt-sp	Max	41.27	11.08	0.27	0.53	48.87	101.42	88.81	
PA13	PA	gt-sp	σ	0.30	0.31	0.09	0.08	0.85	1.20	0.02	
PA13	PA	gt-sp	ol inc	40.03	10.65	0.12	0.38	47.07	98.37	88.74	2
PA13	PA	gt-sp	Min	39.74	10.57	0.11	0.35	46.99	98.07	88.64	
PA13	PA	gt-sp	Max	40.31	10.73	0.12	0.40	47.15	98.68	88.83	
PA13	PA	gt-sp	σ	0.41	0.11	0.00	0.03	0.11	0.43	0.13	
PA16	PA	gt-sp	ol core	40.70	10.03	-	0.44	48.85	100.02	89.67	4
PA16	PA	gt-sp	Min	40.58	9.85	-	0.27	48.39	99.75	89.53	
PA16	PA	gt-sp	Max	40.8	10.2	-	0.6	49.2	100.3	89.9	
PA16	PA	gt-sp	σ	0.1	0.2	-	0.2	0.3	0.2	0.2	
PA16	PA	gt-sp	ol inc	40.60	9.71	0.13	0.46	48.84	99.74	89.97	3
PA16	PA	gt-sp	Min	40.47	40.47	9.45	0.05	0.27	48.77	89.62	
PA16	PA	gt-sp	Max	40.74	40.74	10.11	0.25	0.59	48.97	90.20	
PA16	PA	gt-sp	σ	0.14	0.14	0.35	0.10	0.17	0.11	0.31	
PA18	PA	gt	ol core	41.10	10.85	0.13	0.42	47.82	100.37	88.71	6
PA18	PA	gt	Min	40.89	10.78	0.12	0.39	47.11	99.76	88.49	
PA18	PA	gt	Max	41.24	10.92	0.16	0.44	48.18	100.86	88.79	
PA18	PA	gt	σ	0.12	0.05	0.02	0.02	0.39	0.39	0.11	
PA18	PA	gt	ol inc	40.65	10.81	0.14	0.41	47.44	99.44	88.66	3
PA18	PA	gt	Min	40.16	10.73	0.14	0.40	47.09	98.71	88.60	
PA18	PA	gt	Max	41.32	10.88	0.15	0.42	48.03	100.79	88.72	
PA18	PA	gt	σ	0.60	0.08	0.01	0.01	0.52	1.17	0.06	
DB1	SA	gt	gt core	41.25	5.75	0.11	0.42	52.91	100.39	94.26	11
DB1	SA	gt	Min	40.85	5.59	0.05	0.29	52.37	99.56	94.16	
DB1	SA	gt	Max	41.61	5.96	0.24	0.46	53.96	101.81	94.43	
DB1	SA	gt	σ	0.26	0.09	0.07	0.06	0.45	0.62	0.08	
313116	VI	gt-sp	ol core	40.83	9.56	0.13	0.35	48.72	99.60	90.08	12
313116	VI	gt-sp	Min	40.07	9.48	0.11	0.33	48.48	98.81	89.97	
313116	VI	gt-sp	Max	41.44	9.67	0.16	0.39	48.98	100.33	90.15	
313116	VI	gt-sp	σ	0.39	0.05	0.01	0.02	0.15	0.42	0.05	

Sample	location	Type	Mineral	SiO2	FeO	MnO	NiO	MgO	Total	Mg#	no.
1278	VI	gt-sp	ol core	40.23	10.25	0.58	0.09	48.91	99.95	89.48	6
1278	VI	gt-sp	Min	39.85	10.02	0.31	0.04	48.73	99.63	89.29	
1278	VI	gt-sp	Max	40.59	10.44	0.89	0.22	49.08	100.32	89.68	
1278	VI	gt-sp	σ	0.30	0.16	0.24	0.07	0.14	0.25	0.16	
1278	VI	gt-sp	ol inc	40.29	9.90	0.33	0.19	49.10	99.81	89.84	3
1278	VI	gt-sp	Min	40.20	9.64	0.29	0.03	48.85	99.34	89.59	
1278	VI	gt-sp	Max	40.34	10.20	0.39	0.34	49.26	100.42	90.03	
1278	VI	gt-sp	σ	0.06	0.23	0.04	0.13	0.18	0.45	0.18	
3131280a	VI	gt	ol core	41.26	10.18	0.14	0.41	48.58	100.56	89.48	14
3131280a	VI	gt	Min	40.72	9.86	0.01	0.16	47.84	99.37	89.24	
3131280a	VI	gt	Max	41.87	10.50	0.40	0.60	48.86	101.36	89.80	
3131280a	VI	gt	σ	0.31	0.21	0.10	0.14	0.27	0.61	0.18	
48	VI	gt	ol core	40.59	9.70	0.13	0.36	48.45	99.22	89.90	4
48	VI	gt	Min	39.71	9.70	0.12	0.36	47.99	97.87	89.82	
48	VI	gt	Max	41.16	9.78	0.14	0.39	48.70	99.76	89.99	
48	VI	gt	σ	0.62	0.06	0.01	0.03	0.32	0.90	0.08	
48	VI	gt	ol inc (gt)	41.23	10.05	0.12	0.39	48.86	100.64	89.75	2
48	VI	gt	Min	40.76	10.00	0.12	0.37	48.56	99.94	89.66	
48	VI	gt	Max	41.69	10.10	0.12	0.41	49.17	101.35	89.75	
48	VI	gt	σ	0.66	0.07	0.00	0.03	0.43	0.99	0.07	
1204	VI	gt	ol core	40.52	9.62	0.10	0.39	49.35	99.97	90.14	18
1240	VI	gt	Min	39.85	9.16	0.00	0.04	48.94	98.99	89.75	
1240	VI	gt	Max	41.01	10.11	0.20	0.64	49.74	101.18	90.59	
1240	VI	gt	σ	0.27	0.25	0.07	0.15	0.27	0.58	0.23	
3131270	VI	gt	ol core	41.00	8.80	-	-	50.33	100.54	91.07	15
3131270	VI	gt	Min	40.40	8.57	-	-	49.35	98.80	90.91	
3131270	VI	gt	Max	41.82	9.07	-	-	50.90	101.92	91.32	
3131270	VI	gt	σ	0.39	0.12	-	-	0.48	0.98	0.09	
313532	VI	gt	ol core	40.70	9.44	0.10	0.37	48.90	99.50	90.23	9
313532	VI	gt	Min	40.05	9.15	0.05	0.30	47.89	98.30	89.93	
313532	VI	gt	Max	41.44	9.68	0.17	0.44	49.36	100.79	90.44	
313532	VI	gt	σ	0.44	0.18	0.04	0.04	0.51	0.86	0.17	

Supplementary tables - Pali-Aike, South Africa, Vitim and BCR. Orthopyroxene

Sample	location	site	Mineral	SiO2	TiO2	Al2O3	Cr2O3	FeO	MnO	MgO	CaO	Na2O	Total	Mg#	Wo	En	Fs	Si	Ti	Al	Cr	Fe(ii)	Mn	Mg	Ca	Na	Total	no.
PA10	PA	gt-sp	opx core	55.17	0.15	3.80	0.41	6.55	0.12	31.88	0.69	0.09	98.87	89.67	1.4	88.2	10.4	1.9	0.0	0.2	0.0	0.2	0.0	1.7	0.0	0.0	4.0	9
PA10	PA	gt-sp	Min	54.43	0.08	3.56	0.34	6.47	0.10	31.52	0.63	0.07	97.96	89.55	-	-	-	-	-	-	-	-	-	-	-	-	-	-
PA10	PA	gt-sp	Max	55.63	0.22	4.18	0.45	6.62	0.16	32.27	0.73	0.11	99.70	89.78	-	-	-	-	-	-	-	-	-	-	-	-	-	-
PA10	PA	gt-sp	σ	0.51	0.04	0.23	0.04	0.05	0.02	0.23	0.04	0.01	0.65	0.08	-	-	-	-	-	-	-	-	-	-	-	-	-	-
PA13	PA	gt-sp	opx core	55.00	0.35	3.55	0.61	6.76	0.04	32.71	0.79	0.15	100.09	89.61	1.5	88.2	10.3	1.9	0.0	0.1	0.0	0.2	0.0	1.7	0.0	0.0	4.0	6
PA13	PA	gt-sp	Min	54.81	0.28	3.36	0.59	6.30	0.03	32.34	0.77	0.13	99.62	89.14	-	-	-	-	-	-	-	-	-	-	-	-	-	-
PA13	PA	gt-sp	Max	55.15	0.47	3.74	0.63	7.02	0.04	33.01	0.81	0.17	100.09	90.27	-	-	-	-	-	-	-	-	-	-	-	-	-	-
PA13	PA	gt-sp	σ	0.16	0.10	0.17	0.02	0.36	0.01	0.31	0.02	0.02	0.17	0.59	-	-	-	-	-	-	-	-	-	-	-	-	-	-
PA16	PA	gt-sp	opx core	55.0	0.1	3.3	0.6	6.3	0.2	33.4	0.7	0.1	99.7	90.4	1.3	89.1	9.7	1.9	0.0	0.1	0.0	0.2	0.0	1.7	0.0	0.0	4.0	6
PA16	PA	gt-sp	Min	54.3	0.0	3.1	0.5	5.8	0.0	32.9	0.6	0.1	98.6	90.0	-	-	-	-	-	-	-	-	-	-	-	-	-	-
PA16	PA	gt-sp	Max	55.9	0.2	3.5	0.6	6.6	0.4	34.1	0.7	0.2	101.5	90.9	-	-	-	-	-	-	-	-	-	-	-	-	-	-
PA16	PA	gt-sp	σ	0.6	0.1	0.1	0.1	0.2	0.1	0.5	0.0	0.0	1.2	0.3	-	-	-	-	-	-	-	-	-	-	-	-	-	-
PA18	PA	gt	opx core	55.26	0.26	3.56	0.50	6.87	0.13	32.02	0.79	0.10	99.62	89.25	1.6	87.7	10.8	1.9	0.0	0.1	0.0	0.2	0.0	1.7	0.0	0.0	4.0	9
PA18	PA	gt	Min	54.54	0.23	3.47	0.46	6.73	0.11	31.76	0.75	0.08	98.37	89.04	-	-	-	-	-	-	-	-	-	-	-	-	-	-
PA18	PA	gt	Max	55.86	0.29	3.70	0.55	7.00	0.16	32.28	0.83	0.11	100.41	89.39	-	-	-	-	-	-	-	-	-	-	-	-	-	-
PA18	PA	gt	σ	0.39	0.02	0.08	0.03	0.08	0.02	0.19	0.03	0.01	0.59	0.10	-	-	-	-	-	-	-	-	-	-	-	-	-	-
DB1	SA	gt	opx core	58.21	-	0.75	0.33	3.53	-	37.15	0.42	-	100.67	94.94	0.8	94.2	5.0	2.0	0.0	0.0	0.0	0.1	0.0	1.9	0.0	0.0	4.0	14
DB1	SA	gt	Min	56.82	-	0.59	0.17	3.35	-	36.33	0.35	-	98.71	94.67	-	-	-	-	-	-	-	-	-	-	-	-	-	-
DB1	SA	gt	Max	59.01	-	1.18	0.51	3.67	-	37.74	0.52	-	102.09	95.25	-	-	-	-	-	-	-	-	-	-	-	-	-	-
DB1	SA	gt	σ	0.68	-	0.14	0.09	0.11	-	0.45	0.05	-	1.00	0.18	-	-	-	-	-	-	-	-	-	-	-	-	-	-
313116	VI	gt-sp	opx core	54.17	0.19	5.27	0.63	5.98	0.11	31.43	1.22	0.18	99.18	90.35	2.3	88.4	9.3	1.9	0.0	0.3	0.0	0.1	0.0	0.9	0.7	0.1	4.0	6
313116	VI	gt-sp	Min	53.48	0.17	5.16	0.61	5.83	0.10	31.22	1.15	0.16	98.43	90.23	-	-	-	-	-	-	-	-	-	-	-	-	-	-
313116	VI	gt-sp	Max	54.55	0.21	5.38	0.66	6.07	0.13	31.70	1.27	0.20	99.64	90.65	-	-	-	-	-	-	-	-	-	-	-	-	-	-
313116	VI	gt-sp	σ	0.37	0.01	0.09	0.02	0.08	0.01	0.19	0.04	0.01	0.41	0.15	-	-	-	-	-	-	-	-	-	-	-	-	-	-
1278	VI	gt-sp	opx core	53.71	0.31	5.22	0.61	6.46	0.25	31.91	1.26	0.17	99.86	89.80	2.5	87.3	10.3	1.9	0.0	0.2	0.0	0.2	0.0	1.6	0.0	0.0	4.0	6
1278	VI	gt-sp	Min	53.17	0.24	4.99	0.50	6.14	0.10	31.66	1.19	0.09	98.80	89.47	-	-	-	-	-	-	-	-	-	-	-	-	-	-
1278	VI	gt-sp	Max	54.11	0.41	5.47	0.68	6.72	0.34	32.10	1.36	0.25	100.36	90.27	-	-	-	-	-	-	-	-	-	-	-	-	-	-
1278	VI	gt-sp	σ	0.40	0.07	0.16	0.08	0.21	0.10	0.15	0.07	0.05	0.58	0.28	-	-	-	-	-	-	-	-	-	-	-	-	-	-
3131280a	VI	gt	opx core	55.52	0.13	3.93	0.57	6.48	0.14	32.48	0.84	0.14	100.42	89.93	1.6	88.3	10.1	1.9	0.0	0.2	0.0	0.2	0.0	1.6	0.1	0.0	4.0	18
3131280a	VI	gt	Min	55.13	0.03	3.78	0.37	6.21	0.00	32.21	0.73	0.09	99.33	89.74	-	-	-	-	-	-	-	-	-	-	-	-	-	-
3131280a	VI	gt	Max	56.14	0.20	4.01	0.66	6.65	0.29	32.69	0.94	0.20	100.94	90.26	-	-	-	-	-	-	-	-	-	-	-	-	-	-
3131280a	VI	gt	σ	0.28	0.06	0.07	0.08	0.14	0.09	0.16	0.07	0.03	0.52	0.17	-	-	-	-	-	-	-	-	-	-	-	-	-	-
48	VI	gt	opx core	53.90	0.15	5.18	0.56	5.97	0.13	31.44	1.15	0.18	98.76	90.37	2.3	88.1	9.6	1.9	0.0	0.2	0.0	0.2	0.0	1.6	0.0	0.0	4.0	3
48	VI	gt	Min	53.20	0.14	5.05	0.55	5.88	0.12	31.24	1.14	0.17	97.97	90.27	-	-	-	-	-	-	-	-	-	-	-	-	-	-
48	VI	gt	Max	54.49	0.17	5.24	0.59	6.03	0.14	31.69	1.18	0.20	99.28	90.48	-	-	-	-	-	-	-	-	-	-	-	-	-	-
48	VI	gt	σ	0.66	0.02	0.10	0.02	0.08	0.01	0.23	0.03	0.02	0.69	0.11	-	-	-	-	-	-	-	-	-	-	-	-	-	-
1204	VI	gt	opx core	55.03	0.22	3.71	0.61	6.11	0.15	**33.40**	0.89	0.12	100.25	90.69	1.7	89.0	9.3	1.9	0.0	0.2	0.0	0.2	0.0	1.7	0.0	0.0	4.0	9
1240	VI	gt	Min	54.74	0.07	3.57	0.52	5.90	0.01	**33.10**	0.79	0.05	99.52	90.51	-	-	-	-	-	-	-	-	-	-	-	-	-	-
1240	VI	gt	Max	55.54	0.30	3.90	0.69	6.31	0.31	**33.82**	1.00	0.18	100.97	90.92	-	-	-	-	-	-	-	-	-	-	-	-	-	-
1240	VI	gt	σ	0.26	0.08	0.10	0.06	0.14	0.11	**0.28**	0.06	0.04	0.51	0.16	-	-	-	-	-	-	-	-	-	-	-	-	-	-

Sample	location	site	Mineral	SiO2	TiO2	Al2O3	Cr2O3	FeO	MnO	MgO	CaO	Na2O	Total	Mg#	Wo	En	Fs	Si	Ti	Al	Cr	Fe(ii)	Mn	Mg	Ca	Na	Total	no.
3131270	VI	gt	opx core	55.61	0.10	4.27	0.59	5.57	0.10	33.61	0.96	0.11	100.90	91.49	1.8	89.7	8.5	1.9	0.0	0.2	0.0	0.2	0.0	**1.7**	0.0	0.0	4.0	10
3131270	VI	gt	Min	54.95	0.04	3.97	0.43	5.26	-0.02	33.20	0.84	0.05	100.00	91.04	-	-	-	-	-	-	-	-	-	-	-	-	-	-
3131270	VI	gt	Max	56.11	0.15	4.51	0.73	5.91	0.24	33.89	1.06	0.17	101.70	91.84	-	-	-	-	-	-	-	-	-	-	-	-	-	-
3131270	VI	gt	σ	0.36	0.04	0.18	0.09	0.17	0.07	0.25	0.07	0.06	0.59	0.28	-	-	-	-	-	-	-	-	-	-	-	-	-	-
313532	VI	gt	opx core	54.75	0.21	3.97	0.51	5.94	0.17	32.49	0.81	0.16	99.02	90.69	1.5	90.0	8.4	1.9	0.0	0.2	0.0	0.2	0.0	1.7	0.0	0.0	4.00	5
313532	VI	gt	Min	54.09	0.15	3.88	0.46	5.73	0.08	32.18	0.76	0.11	98.26	90.30	-	-	-	-	-	-	-	-	-	-	-	-	-	-
313532	VI	gt	Max	55.60	0.32	4.10	0.55	6.16	0.27	32.91	0.89	0.23	99.85	91.03	-	-	-	-	-	-	-	-	-	-	-	-	-	-
313532	VI	gt	σ	0.76	0.07	0.10	0.04	0.19	0.08	0.30	0.05	0.05	0.70	0.28	-	-	-	-	-	-	-	-	-	-	-	-	-	-

Supplementary tables - Pali-Aike, South Africa, Vitim and BCR. Clinopyroxene

Sample	location	type	Mineral	SiO2	TiO2	Al2O3	Cr2O3	FeO	MnO	MgO	CaO	Na2O	Total	Mg#	Wo	En	Fs	Si	Ti	Al	Cr	Fe(ii)	Mn	Mg	Ca	Na	Total	no.
PA10	PA	gt-sp	cpx core	51.63	0.85	5.63	0.97	3.23	0.08	15.18	19.78	1.36	98.71	89.34	45.5	48.6	5.9	1.9	0.0	0.2	0.0	0.1	0.0	0.8	0.8	0.1	4.0	3
PA10	PA	gt-sp	Min	50.67	0.83	5.57	0.96	3.17	0.07	15.16	19.77	1.35	97.77	89.20	-	-	-	-	-	-	-	-	-	-	-	-	-	-
PA10	PA	gt-sp	Max	52.27	0.87	5.68	0.98	3.28	0.09	15.21	19.81	1.38	99.36	89.50	-	-	-	-	-	-	-	-	-	-	-	-	-	-
PA10	PA	gt-sp	σ	0.84	0.02	0.06	0.01	0.05	0.01	0.02	0.02	0.02	0.83	0.15	-	-	-	-	-	-	-	-	-	-	-	-	-	-
PA13	PA	gt-sp	cpx core	49.35	0.51	9.78	0.40	3.98	0.19	15.79	18.26	0.63	98.91	87.61	36.0	56.3	7.7	1.9	0.0	0.3	0.0	0.1	0.0	1.0	0.6	0.0	4.0	3
PA13	PA	gt-sp	Min	48.21	0.27	6.42	0.34	3.79	0.18	14.36	16.57	0.51	98.39	87.00	-	-	-	-	-	-	-	-	-	-	-	-	-	-
PA13	PA	gt-sp	Max	51.16	0.70	11.47	0.45	4.32	0.20	18.60	19.14	0.71	99.29	88.47	-	-	-	-	-	-	-	-	-	-	-	-	-	-
PA13	PA	gt-sp	σ	1.58	0.22	2.91	0.06	0.30	0.01	2.43	1.46	0.11	0.47	0.81	-	-	-	-	-	-	-	-	-	-	-	-	-	-
PA16	PA	gt-sp	cpx core	52.44	5.22	0.41	1.15	3.10	0.23	15.33	19.49	1.52	98.89	89.82	44.9	49.1	6.1	2.0	0.1	0.0	0.0	0.1	0.0	0.9	0.8	0.1	4.0	4
PA16	PA	gt-sp	Min	51.99	4.97	0.34	1.08	3.03	0.17	15.00	19.32	1.48	98.31	89.68	-	-	-	-	-	-	-	-	-	-	-	-	-	-
PA16	PA	gt-sp	Max	53.28	5.52	0.50	1.22	3.19	0.28	15.56	19.61	1.55	100.10	89.95	-	-	-	-	-	-	-	-	-	-	-	-	-	-
PA16	PA	gt-sp	σ	0.58	0.24	0.07	0.06	0.08	0.06	0.27	0.13	0.03	0.82	0.11	-	-	-	-	-	-	-	-	-	-	-	-	-	-
PA16	PA	gt-sp	cpx inc (sp)	52.15	4.91	0.42	1.47	3.23	0.18	15.94	20.37	1.22	99.90	89.80	45.0	49.0	5.9	1.9	0.1	0.0	0.0	0.1	0.0	0.9	0.8	0.1	4.0	5
PA16	PA	gt-sp	Min	51.16	4.57	0.15	1.08	3.03	0.05	15.53	19.32	0.92	98.55	88.83	-	-	-	-	-	-	-	-	-	-	-	-	-	-
PA16	PA	gt-sp	Max	53.28	5.29	0.76	1.89	3.72	0.28	16.60	21.18	1.55	100.53	90.40	-	-	-	-	-	-	-	-	-	-	-	-	-	-
PA16	PA	gt-sp	σ	0.77	0.29	0.22	0.37	0.28	0.09	0.44	0.87	0.28	0.80	0.62	-	-	-	-	-	-	-	-	-	-	-	-	-	-
PA18	PA	gt	cpx core	50.18	0.97	5.27	1.11	3.55	0.11	15.49	19.59	1.24	99.02	88.60	44.5	49.0	6.5	1.9	0.0	0.2	0.0	0.1	0.0	0.9	0.8	0.1	4.0	4
PA18	PA	gt	Min	45.85	0.94	5.24	1.10	3.50	0.10	15.48	19.51	1.21	98.33	88.37	-	-	-	-	-	-	-	-	-	-	-	-	-	-
PA18	PA	gt	Max	52.65	1.01	5.31	1.12	3.63	0.12	15.52	19.64	1.27	100.04	88.74	-	-	-	-	-	-	-	-	-	-	-	-	-	-
PA18	PA	gt	σ	2.98	0.03	0.03	0.01	0.06	0.01	0.02	0.06	0.02	0.74	0.16	-	-	-	-	-	-	-	-	-	-	-	-	-	-
313116	VI	gt-sp	cpx core	51.62	0.42	6.74	1.15	3.46	0.10	16.47	17.13	1.42	98.51	89.45	40.0	53.5	6.5	1.9	0.0	0.3	0.0	0.1	0.0	0.9	0.7	0.1	4.0	2.0
313116	VI	gt-sp	Min	50.99	0.41	6.72	1.12	3.45	0.09	16.41	17.12	1.41	97.93	89.37	-	-	-	-	-	-	-	-	-	-	-	-	-	-
313116	VI	gt-sp	Max	52.25	0.44	6.77	1.18	3.48	0.11	16.53	17.13	1.42	99.09	89.53	-	-	-	-	-	-	-	-	-	-	-	-	-	-
313116	VI	gt-sp	σ	0.89	0.02	0.03	0.04	0.02	0.02	0.09	0.01	0.01	0.82	0.12	-	-	-	-	-	-	-	-	-	-	-	-	-	-
1278	VI	gt-sp	cpx core	51.01	0.90	6.88	1.19	3.96	0.30	16.87	17.39	1.50	99.79	88.37	39.4	53.1	7.5	1.8	0.0	0.3	0.0	0.1	0.0	0.9	0.7	0.1	4.0	3.0
1278	VI	gt-sp	Min	50.67	0.66	6.67	0.96	3.73	0.30	16.35	17.30	1.46	99.41	87.86	-	-	-	-	-	-	-	-	-	-	-	-	-	-
1278	VI	gt-sp	Max	51.51	1.07	7.05	1.46	4.19	0.30	17.25	17.50	1.55	100.20	89.18	-	-	-	-	-	-	-	-	-	-	-	-	-	-
1278	VI	gt-sp	σ	0.44	0.21	0.19	0.25	0.23	-	0.47	0.10	0.05	0.40	0.72	-	-	-	-	-	-	-	-	-	-	-	-	-	-
3131280a	VI	gt	cpx core	53.27	0.60	5.91	1.27	3.21	0.13	15.46	18.56	1.71	100.14	89.56	43.5	50.4	6.1	1.9	0.0	0.3	0.0	0.1	0.0	0.8	0.7	0.1	4.0	18.0
3131280a	VI	gt	Min	0.47	0.47	1.10	1.10	0.02	0.02	15.04	1.65	1.65	98.71	88.89	-	-	-	-	-	-	-	-	-	-	-	-	-	-
3131280a	VI	gt	Max	53.93	0.71	6.18	1.60	3.43	0.31	15.77	18.84	1.82	101.05	90.18	-	-	-	-	-	-	-	-	-	-	-	-	-	-
3131280a	VI	gt	σ	0.36	0.07	0.14	0.10	0.12	0.08	0.14	0.17	0.05	0.54	0.36	-	-	-	-	-	-	-	-	-	-	-	-	-	-
48	VI	gt	cpx core	51.40	0.75	5.59	1.19	3.48	0.10	16.26	19.28	0.97	99.08	89.32	43.1	50.6	6.3	1.9	0.0	0.2	0.0	0.1	0.0	0.9	0.8	0.1	4.0	6.0
48	VI	gt	Min	50.27	0.51	4.76	1.14	2.97	0.07	15.68	18.59	0.45	97.82	87.84	-	-	-	-	-	-	-	-	-	-	-	-	-	-
48	VI	gt	Max	52.54	1.14	6.29	1.27	4.11	0.14	17.13	20.04	1.43	100.60	90.48	-	-	-	-	-	-	-	-	-	-	-	-	-	-
48	VI	gt	σ	0.80	0.28	0.56	0.05	0.51	0.03	0.58	0.65	0.50	1.07	1.09	-	-	-	-	-	-	-	-	-	-	-	-	-	-
1204	VI	gt	cpx core	52.5	0.5	5.6	1.2	3.0	0.1	16.1	19.2	1.5	99.7	90.5	43.5	50.9	5.6	1.9	0.0	0.2	0.0	0.1	0.0	0.9	0.7	0.1	4.0	9.0
1240	VI	gt	Min	51.9	0.3	5.5	0.9	2.8	0.0	15.8	19.0	1.4	99.0	89.6	-	-	-	-	-	-	-	-	-	-	-	-	-	-
1240	VI	gt	Max	53.1	0.7	5.7	1.5	3.3	0.2	16.6	19.5	1.5	100.4	91.2	-	-	-	-	-	-	-	-	-	-	-	-	-	-
1240	VI	gt	σ	0.4	0.1	0.1	0.2	0.2	0.1	0.2	0.2	0.0	0.5	0.5	-	-	-	-	-	-	-	-	-	-	-	-	-	-

Sample	location	type	Mineral	SiO2	TiO2	Al2O3	Cr2O3	FeO	MnO	MgO	CaO	Na2O	Total	Mg#	Wo	En	Fs	Si	Ti	Al	Cr	Fe(ii)	Mn	Mg	Ca	Na	Total	no.
3131270	VI	gt	cpx core	52.93	0.34	5.76	1.37	3.14	0.11	16.70	18.44	1.34	100.03	90.46	41.7	52.6	5.8	1.9	0.0	0.2	0.0	0.1	0.0	0.9	0.7	0.1	4.0	19.0
3131270	VI	gt	Min	51.10	0.21	4.23	1.13	2.79	0.06	16.10	17.34	0.53	98.32	85.72	-	-	-	-	-	-	-	-	-	-	-	-	-	-
3131270	VI	gt	Max	54.22	0.49	6.61	1.71	4.78	0.18	17.52	20.42	1.60	101.32	91.69	-	-	-	-	-	-	-	-	-	-	-	-	-	-
3131270	VI	gt	σ	0.79	0.08	0.58	0.14	0.42	0.06	0.33	0.91	0.34	1.00	1.22	-	-	-	-	-	-	-	-	-	-	-	-	-	-
313532	VI	gt	cpx core	51.9	0.5	5.8	1.2	3.1	0.1	15.4	19.2	**1.4**	98.4	90.0	44.5	49.8	5.7	1.9	0.0	0.2	0.0	0.1	0.0	0.8	0.8	0.1	4.0	6.0
313532	VI	gt	Min	51.1	0.4	4.4	1.1	2.8	0.0	15.0	18.6	**0.5**	97.9	87.8	-	-	-	-	-	-	-	-	-	-	-	-	-	-
313532	VI	gt	Max	53.1	0.9	6.1	1.4	3.7	0.1	15.7	21.2	**1.6**	99.9	90.8	-	-	-	-	-	-	-	-	-	-	-	-	-	-
313532	VI	gt	σ	0.6	0.2	0.7	0.1	0.3	0.0	0.3	1.0	**0.4**	0.8	1.1	-	-	-	-	-	-	-	-	-	-	-	-	-	-

Supplementary tables - Pali-Aike, South Africa, Vitim and BCR. Spinel

Sample	location	type	Mineral	TiO2	Al2O3	Cr2O3	Fe2O3	FeO	MnO	MgO	Total	Mg#	Cr#	Ti	Al	Cr	Fe(iii)	Fe(ii)	Mn	Mg	Total	no.
PA10	PA	gt-sp	sp core	-	46.36	19.81	4.31	11.05	0.14	18.38	100.06	71.60	22.28	-	1.5	0.4	0.1	0.3	0.0	0.7	3.0	6
PA10	PA	gt-sp	Min	-	44.85	18.30	3.86	10.55	0.13	18.06	98.79	70.71	20.57	-	-	-	-	-	-	-	-	-
PA10	PA	gt-sp	Max	-	48.01	21.24	4.58	11.37	0.18	18.70	101.19	72.66	24.11	-	-	-	-	-	-	-	-	-
PA10	PA	gt-sp	σ	-	1.26	1.44	0.30	0.30	0.02	0.27		0.81	1.71	-	-	-	-	-	-	-	-	-
PA13	PA	gt-sp	sp core	-	36.14	27.19	7.31	11.62	0.37	16.61	99.24	66.50	33.54	-	1.22	0.62	0.16	0.28	0.01	0.71	3.00	7
PA13	PA	gt-sp	Min	-	35.20	26.61	6.31	11.00	0.16	16.36	98.46	65.39	32.63	-	-	-	-	-	-	-	-	-
PA13	PA	gt-sp	Max	-	37.22	28.14	7.95	12.59	0.86	16.77	99.94	67.44	34.91	-	-	-	-	-	-	-	-	-
PA13	PA	gt-sp	σ	-	0.76	0.51	0.54	0.62	0.26	0.14	0.54	0.78	0.75	-	-	-	-	-	-	-	-	-
PA16	PA	gt-sp	sp core	0.43	39.79	26.54	3.70	11.65	0.27	17.45	99.84	70.01	30.91	0.01	1.32	0.59	0.08	0.27	0.01	0.73	3.00	4
PA16	PA	gt-sp	Min	0.28	39.37	26.33	3.17	11.24	0.11	17.33	99.04	69.54	30.75	-	-	-	-	-	-	-	-	-
PA16	PA	gt-sp	Max	0.57	40.20	26.73	4.82	12.12	0.44	17.65	100.35	70.21	31.11	-	-	-	-	-	-	-	-	-
PA16	PA	gt-sp	σ	0.10	0.39	0.15	0.65	0.31	0.12	0.13	0.49	0.27	0.13	-	-	-	-	-	-	-	-	-
313116	VI	gt-sp	sp core	-	48.31	18.48	3.39	9.11	0.14	19.66	99.09	76.72	20.42	-	1.54	0.39	0.07	0.21	0.00	0.79	3.00	3
313116	VI	gt-sp	Min	-	48.25	18.36	3.12	9.01	0.14	19.49	98.84	76.47	20.33	-	-	-	-	-	-	-	-	-
313116	VI	gt-sp	Max	-	48.39	18.58	3.53	9.29	0.14	19.81	99.46	76.91	20.48	-	-	-	-	-	-	-	-	-
313116	VI	gt-sp	σ	-	0.07	0.12	0.23	0.15	0.00	0.16	0.33	0.22	0.08	-	-	-	-	-	-	-	-	-
1278	VI	gt-sp	sp core	0.53	47.15	17.23	6.03	8.53	0.33	20.29	100.08	76.29	19.69	0.01	1.49	0.37	0.12	0.19	0.01	0.81	3.00	3
1278	VI	gt-sp	Min	0.51	46.79	16.95	5.58	8.24	0.31	20.13	98.58	75.96	19.21	-	-	-	-	-	-	-	-	-
1278	VI	gt-sp	Max	0.56	47.82	17.72	6.42	8.67	0.36	20.51	101.29	76.94	20.24	-	-	-	-	-	-	-	-	-
1278	VI	gt-sp	σ	0.03	0.58	0.43	0.42	0.25	0.03	0.20	1.38	0.56	0.52	-	-	-	-	-	-	-	-	-

Supplementary tables - Pali-Aike, South Africa, Vitim and BCR. Garnet

Sample	location	Type	Mineral	SiO2	TiO2	Al2O3	Cr2O3	FeO	MnO	MgO	CaO	-	Total	Mg#	Cr#	Alm	And	Gro	Pyr	Spe	Uva	Si	Ti	Al	Cr	Fe2+	Mn	Mg	Ca	Total	no.
PA10	PA	gt-sp	gt core	42.13	0.24	23.01	1.19	7.99	0.33	20.04	5.09	-	100.02	81.72	3.36	15.5	0.2	9.5	70.9	0.7	3.2	3.0	0.0	1.9	0.1	0.5	0.0	2.1	0.4	8.0	3
PA10	PA	gt-sp	Min	42.00	0.22	22.69	1.13	7.88	0.32	19.88	5.05	-	99.55	81.64	3.18	-	-	-	-	-	-	-	-	-	-	-	-	-	-	-	-
PA10	PA	gt-sp	Max	42.38	0.27	23.18	1.27	8.09	0.33	20.19	5.12	-	100.83	81.81	3.55	-	-	-	-	-	-	-	-	-	-	-	-	-	-	-	-
PA10	PA	gt-sp	σ	0.21	0.03	0.27	0.07	0.11	0.00	0.16	0.03	-	0.70	0.12	0.26	-	-	-	-	-	-	-	-	-	-	-	-	-	-	-	-
PA10	PA	gt-sp	gt rim	49.22	0.17	13.03	0.91	8.15	0.38	26.67	1.64	-	100.16	85.36	4.47	0.0	2.7	0.0	92.9	0.0	4.4	3.4	0.0	1.1	0.0	0.5	0.0	2.8	0.1	8.0	3
PA10	PA	gt-sp	Min	47.45	0.14	9.95	0.83	8.09	0.34	25.92	1.35	-	99.96	85.10	3.95	-	-	-	-	-	-	-	-	-	-	-	-	-	-	-	-
PA10	PA	gt-sp	Max	51.00	0.21	16.10	0.99	8.21	0.42	27.42	1.92	-	100.37	85.61	5.30	-	-	-	-	-	-	-	-	-	-	-	-	-	-	-	-
PA10	PA	gt-sp	σ	1.78	0.03	3.07	0.08	0.06	0.04	0.75	0.28	-	0.21	0.26	0.68	-	-	-	-	-	-	-	-	-	-	-	-	-	-	-	-
PA10	PA	gt-sp	gt core	42.58	0.24	23.18	1.34	8.14	0.33	20.04	5.11	0.02	100.97	81.45	3.74	16.2	0.0	9.3	70.3	0.6	3.6	3.0	0.0	1.9	0.1	0.5	0.0	2.1	0.4	8.0	3
PA10	PA	gt-sp	Min	42.51	0.21	23.11	1.29	8.04	0.31	20.00	5.09	-	100.89	81.26	3.58	-	-	-	-	-	-	-	-	-	-	-	-	-	-	-	-
PA10	PA	gt-sp	Max	42.69	0.26	23.29	1.41	8.23	0.35	20.12	5.12	0.04	101.06	81.60	3.92	-	-	-	-	-	-	-	-	-	-	-	-	-	-	-	-
PA10	PA	gt-sp	σ	0.09	0.03	0.10	0.06	0.10	0.02	0.06	0.02	0.02	0.08	0.18	0.17	-	-	-	-	-	-	-	-	-	-	-	-	-	-	-	-
PA13	PA	gt-sp	gt core	41.83	0.35	22.71	1.43	8.33	0.32	19.79	4.99	0.03	99.76	80.90	3.39	16.1	0.2	8.5	70.5	0.6	4.1	3.0	0.0	1.9	0.1	0.5	0.0	2.1	0.4	8.0	9
PA13	PA	gt-sp	Min	41.17	0.32	22.52	1.17	8.15	0.30	19.54	4.88	0.01	98.89	80.55	2.73	-	-	-	-	-	-	-	-	-	-	-	-	-	-	-	-
PA13	PA	gt-sp	Max	42.50	0.39	22.92	1.52	8.55	0.34	19.97	5.11	0.04	100.58	81.38	3.62	-	-	-	-	-	-	-	-	-	-	-	-	-	-	-	-
PA13	PA	gt-sp	σ	0.40	0.02	0.13	0.12	0.13	0.01	0.14	0.08	0.01	0.54	0.29	0.31	-	-	-	-	-	-	-	-	-	-	-	-	-	-	-	-
PA16	PA	gt-sp	gt core	41.92		22.83	1.35	7.89	0.43	20.53	4.95	-	99.90	82.26	3.82	13.5	1.4	7.5	73.0	0.9	3.8	3.0	0.0	1.9	0.1	0.4	0.0	2.2	0.4	8.0	5
PA16	PA	gt-sp	Min	41.58		22.59	1.18	7.68	0.27	20.13	4.74	-	99.13	81.68	3.32	-	-	-	-	-	-	-	-	-	-	-	-	-	-	-	-
PA16	PA	gt-sp	Max	42.11		23.04	1.68	8.19	0.62	20.92	5.06	-	100.76	82.92	4.69	-	-	-	-	-	-	-	-	-	-	-	-	-	-	-	-
PA16	PA	gt-sp	σ	0.20		0.17	0.22	0.19	0.14	0.28	0.13	-	0.64	0.47	0.60	-	-	-	-	-	-	-	-	-	-	-	-	-	-	-	-
PA16	PA	gt-sp	gt rim	49.27	0.08	10.64	1.30	8.25	0.54	27.51	1.74	-	99.32	85.59	7.56	0.0	1.6	0.0	91.0	0.0	7.5	3.4	0.0	0.9	0.1	0.0	0.0	2.8	0.1	7.4	5
PA16	PA	gt-sp	Min	45.86	0.01	6.07	1.07	7.98	0.29	25.96	1.34	-	98.64	85.29	6.12	-	-	-	-	-	-	-	-	-	-	-	-	-	-	-	-
PA16	PA	gt-sp	Max	52.48	0.13	15.53	1.59	8.55	0.77	28.88	2.30	-	100.13	85.90	10.57	-	-	-	-	-	-	-	-	-	-	-	-	-	-	-	-
PA16	PA	gt-sp	σ	2.86	0.05	4.13	0.22	0.22	0.22	1.25	0.40	-	0.65	0.26	1.84	-	-	-	-	-	-	-	-	-	-	-	-	-	-	-	-
PA18	PA	gt	gt core	41.73	0.28	23.34	1.27	8.22	0.32	20.29	5.09	0.03	100.58	81.48	3.51	13.8	0.6	8.8	72.5	0.7	3.6	3.0	0.0	1.9	0.1	0.5	0.0	2.1	0.4	8.0	3
PA18	PA	gt	Min	40.44	0.27	23.14	1.23	8.20	0.29	20.21	5.03	0.02	99.71	81.46	3.44	-	-	-	-	-	-	-	-	-	-	-	-	-	-	-	-
PA18	PA	gt	Max	42.38	0.30	23.62	1.29	8.24	0.36	20.38	5.14	0.03	101.12	81.51	3.59	-	-	-	-	-	-	-	-	-	-	-	-	-	-	-	-
PA18	PA	gt	σ	1.12	0.02	0.25	0.03	0.02	0.04	0.09	0.06	0.01	0.76	0.03	0.07	-	-	-	-	-	-	-	-	-	-	-	-	-	-	-	-
DB1	SA	gt	gt core	42.42		21.47	4.03	5.30	0.29	23.15	3.66	-	100.32	88.62	11.18	7.6	0.0	0.0	82.4	0.6	9.4	3.0	0.0	1.8	0.2	0.3	0.0	2.4	0.3	8.0	7
DB1	SA	gt	Min	41.99		21.23	3.90	5.20	0.21	22.94	3.55	-	99.53	88.39	10.89	-	-	-	-	-	-	-	-	-	-	-	-	-	-	-	-
DB1	SA	gt	Max	42.97		21.94	4.31	5.40	0.44	23.36	3.75	-	101.67	88.77	11.64	-	-	-	-	-	-	-	-	-	-	-	-	-	-	-	-
DB1	SA	gt	σ	0.35		0.24	0.15	0.07	0.09	0.15	0.07	-	0.67	0.14	0.31	-	-	-	-	-	-	-	-	-	-	-	-	-	-	-	-
116	VI	gt-sp	gt core	42.74	0.24	23.14	1.47	6.62	0.26	20.85	5.06	0.03	100.40	84.87	4.07	13.5	0.0	8.7	73.2	0.5	4.1	3.0	0.0	1.9	0.1	0.4	0.0	2.2	0.4	8.0	8
116	VI	gt-sp	Min	42.34	0.21	22.86	1.20	6.48	0.24	20.41	4.82	0.00	99.89	84.74	3.33	-	-	-	-	-	-	-	-	-	-	-	-	-	-	-	-
116	VI	gt-sp	Max	43.14	0.26	23.45	1.63	6.74	0.30	21.19	5.39	0.12	100.85	85.01	4.54	-	-	-	-	-	-	-	-	-	-	-	-	-	-	-	-
116	VI	gt-sp	σ	0.28	0.02	0.22	0.17	0.08	0.02	0.28	0.19	0.04	0.36	0.08	0.47	-	-	-	-	-	-	-	-	-	-	-	-	-	-	-	-

Sample	location	Type	Mineral	SiO2	TiO2	Al2O3	Cr2O3	FeO	MnO	MgO	CaO	Na2O	Total	Mg#	Cr#	Alm	And	Gro	Pyr	Spe	Uva	Si	Ti	Al	Cr	Fe2+	Mn	Mg	Ca	Total	no.
1278	VI	gt-sp	gt core	42.74	0.24	23.14	1.47	6.62	0.26	20.85	5.06	0.03	100.40	84.87	4.07	13.5	0.0	8.7	73.2	0.5	4.1	3.0	0.0	1.9	0.1	0.4	0.0	2.2	0.4	8.0	8
1278	VI	gt-sp	Min	42.34	0.21	22.86	1.20	6.48	0.24	20.41	4.82	-	99.89	84.74	3.33	-	-	-	-	-	-	-	-	-	-	-	-	-	-	-	-
1278	VI	gt-sp	Max	43.14	0.26	23.45	1.63	6.74	0.30	21.19	5.39	0.12	100.85	85.01	4.54	-	-	-	-	-	-	-	-	-	-	-	-	-	-	-	-
1278	VI	gt-sp	σ	0.28	0.02	0.22	0.17	0.08	0.02	0.28	0.19	0.04	0.36	0.08	0.47	-	-	-	-	-	-	-	-	-	-	-	-	-	-	-	-
1278	VI	gt-sp	gt core	42.00	0.33	22.26	1.34	7.32	0.29	21.63	4.93	-	100.08	84.05	3.87	10.1	3.6	5.2	76.8	0.6	3.8	3.0	0.0	1.9	0.1	0.4	0.0	2.3	0.4	7.9	10
1278	VI	gt-sp	Min	41.75	0.19	21.78	1.18	7.02	0.07	21.21	4.62	-	99.79	83.18	3.51	-	-	-	-	-	-	-	-	-	-	-	-	-	-	-	-
1278	VI	gt-sp	Max	42.54	0.61	22.69	1.58	7.82	0.50	21.93	5.19	-	100.58	84.63	4.55	-	-	-	-	-	-	-	-	-	-	-	-	-	-	-	-
1278	VI	gt-sp	σ	0.25	0.14	0.25	0.12	0.26	0.12	0.22	0.17	-	0.26	0.47	0.34	-	-	-	-	-	-	-	-	-	-	-	-	-	-	-	-
3131280a	VI	gt	gt core	42.18	0.20	22.63	1.31	7.68	0.36	20.47	4.80	0.06	99.66	82.61	3.74	17.4	0.0	57.9	1.7	18.5	4.5	3.0	0.0	1.9	0.1	0.4	0.0	2.2	0.4	8.0	14
3131280a	VI	gt	Min	41.64	0.09	22.30	1.10	7.42	0.19	20.25	4.68	0.01	98.51	82.09	3.15	-	-	-	-	-	-	-	-	-	-	-	-	-	-	-	-
3131280a	VI	gt	Max	42.56	0.30	22.95	1.49	8.01	0.45	20.73	5.02	0.11	100.45	83.10	4.27	-	-	-	-	-	-	-	-	-	-	-	-	-	-	-	-
3131280a	VI	gt	σ	0.28	0.06	0.17	0.12	0.18	0.07	0.14	0.09	0.04	0.56	0.29	0.33	-	-	-	-	-	-	-	-	-	-	-	-	-	-	-	-
48	VI	gt	gt core	42.18	0.19	23.58	1.08	6.87	0.29	20.62	4.99	0.02	99.84	84.24	2.99	13.9	0.0	9.7	72.9	0.6	3.0	3.0	0.0	2.0	0.1	0.4	0.0	2.2	0.4	8.0	5.00
48	VI	gt	Min	41.70	0.17	23.40	1.06	6.76	0.26	20.20	4.78	0.02	99.19	84.16	2.91	-	-	-	-	-	-	-	-	-	-	-	-	-	-	-	-
48	VI	gt	Max	42.58	0.23	23.73	1.10	7.03	0.31	20.95	5.42	0.03	100.51	84.38	3.03	-	-	-	-	-	-	-	-	-	-	-	-	-	-	-	-
48	VI	gt	σ	0.41	0.02	0.12	0.02	0.12	0.02	0.30	0.28	-	0.54	0.09	0.05	-	-	-	-	-	-	-	-	-	-	-	-	-	-	-	-
1240	VI	gt	gt core	42.23	0.14	22.39	1.24	7.25	0.39	21.74	5.08	-	100.42	84.23	3.58	9.6	4.0	5.4	76.7	0.8	3.5	3.0	0.0	1.9	0.1	0.4	0.0	2.3	0.4	8.0	4.00
1240	VI	gt	Min	41.92	0.09	22.26	1.17	7.04	0.35	21.70	4.95	-	99.90	84.03	3.39	-	-	-	-	-	-	-	-	-	-	-	-	-	-	-	-
1240	VI	gt	Max	42.52	0.19	22.47	1.28	7.36	0.42	21.78	5.22	-	100.90	84.65	3.71	-	-	-	-	-	-	-	-	-	-	-	-	-	-	-	-
1240	VI	gt	σ	0.31	0.05	0.09	0.05	0.14	0.03	0.03	0.12	-	0.46	0.28	0.14	-	-	-	-	-	-	-	-	-	-	-	-	-	-	-	-
3131270	VI	gt	gt core	42.09	-	23.18	1.44	6.49	0.30	21.28	4.75	-	99.52	85.39	3.99	11.9	0.1	8.0	75.4	0.6	4.1	3.0	0.0	2.0	0.1	0.4	0.0	2.2	0.4	8.0	7.00
3131270	VI	gt	Min	41.73	-	22.95	1.33	6.27	0.21	20.93	4.66	-	98.51	84.80	3.69	-	-	-	-	-	-	-	-	-	-	-	-	-	-	-	-
3131270	VI	gt	Max	42.51	-	23.39	1.55	6.83	0.41	21.75	4.82	-	100.89	85.81	4.26	-	-	-	-	-	-	-	-	-	-	-	-	-	-	-	-
3131270	VI	gt	σ	0.31	-	0.17	0.07	0.19	0.08	0.27	0.06	-	0.77	0.35	0.17	-	-	-	-	-	-	-	-	-	-	-	-	-	-	-	-
313532	VI	gt	gt core	42.78	0.18	23.49	1.14	7.14	0.30	20.70	4.85	-	100.59	83.79	3.15	14.6	0.0	9.0	72.5	0.6	3.2	3.0	0.0	1.9	0.1	0.4	0.0	2.2	0.4	8.0	3
313532	VI	gt	Min	42.45	0.17	23.44	1.10	6.99	0.23	20.58	4.81	-	100.26	83.21	3.06	-	-	-	-	-	-	-	-	-	-	-	-	-	-	-	-
313532	VI	gt	Max	42.97	0.20	23.59	1.16	7.40	0.36	20.93	4.91	-	101.10	84.23	3.20	-	-	-	-	-	-	-	-	-	-	-	-	-	-	-	-
313532	VI	gt	σ	0.29	0.02	0.09	0.03	0.23	0.07	0.19	0.05	-	0.45	0.52	0.08	-	-	-	-	-	-	-	-	-	-	-	-	-	-	-	-

Supplementary tables - Pali-Aike, South Africa, Vitim and BCR. BCR

Comment	No.	SiO2	TiO2	Al2O3	Cr2O3	FeO	MnO	NiO	MgO	CaO	Na2O	K2O	Total
BCR2	1	55.20	2.24	13.56	0.02	12.64	0.20	-	3.60	7.10	2.07	1.82	98.44
BCR2	2	54.86	2.02	13.20	0.00	12.68	0.23	-	3.58	7.08	1.99	1.79	97.44
BCR2	3	55.20	13.56	2.24	0.02	12.64	0.20	-	3.60	7.10	2.07	-	96.62
BCR2	4	54.86	13.20	2.02	0.00	12.68	0.23	-	3.58	7.08	1.99	-	95.65
BCR2	5	54.95	2.23	13.56	0.00	12.27	0.22	0.00	3.46	7.31	3.09	2.02	99.21

Supplementary tables - Lunar Dunite 72415 53. Olivine

Sp type	Mineral	site	soi	SiO2	FeO	MnO	MgO	Total	Mg#	no.
A	ol	clast	soi 5	40.23	11.67	0.02	47.42	99.34	87.87	3
A	ol	clast	min	40.23	11.33	0.02	46.98	98.90	87.87	-
A	ol	clast	max	40.57	11.33	0.02	46.98	98.90	88.08	-
A	ol	clast	σ	0.30	0.37	-	0.56	0.41	0.35	-
A	ol	clast	soi g	40.22	11.86	0.09	47.79	99.96	87.78	3
A	ol	clast	min	40.00	11.80	0.06	47.66	99.76	87.65	-
A	ol	clast	max	40.53	11.97	0.11	47.85	100.26	87.85	-
A	ol	clast	σ	0.28	0.10	0.03	0.11	0.27	0.11	-
B	ol	clu	soi 4	40.05	12.20	0.13	47.72	100.06	87.46	3
B	ol	clu	min	39.30	11.82	0.03	47.19	98.88	87.15	-
B	ol	clu	max	40.60	12.61	0.23	48.00	98.88	87.15	-
B	ol	clu	SD	0.67	0.40	0.14	0.46	1.04	0.36	-
B	ol	clu	soi b	40.34	11.82	0.12	47.52	99.79	87.75	3
B	ol	clu	min	40.17	11.63	0.10	47.38	99.32	87.67	-
B	ol	clu	max	40.61	11.95	0.13	47.71	100.37	87.91	-
B	ol	clu	σ	0.24	0.17	0.02	0.17	0.55	0.14	-
C	ol	clast	soi 10	40.25	12.18	0.11	47.66	100.19	87.46	3
C	ol	clu	min	39.86	11.81	0.07	47.40	99.69	86.93	-
C	ol	clu	max	40.96	12.80	0.18	47.84	100.70	87.82	-
C	ol	clu	σ	0.46	0.34	0.04	0.19	0.41	0.30	-
D(ch)	ol	clast	soi 6	40.31	12.19	0.12	47.64	100.40	87.44	3
D(ch)	ol	clast	min	40.12	11.97	0.07	47.59	100.06	87.12	-
D(ch)	ol	clast	max	40.45	12.56	0.17	47.67	100.91	87.63	-
D(ch)	ol	clast	σ	0.17	0.32	0.07	0.04	0.45	0.28	-
D(lob)	ol	clu	soi 3	40.25	11.81	0.13	47.89	100.08	87.85	3
D(lob)	ol	clu	min	39.54	11.80	0.01	47.34	98.79	87.73	-
D(lob)	ol	clu	max	40.61	11.82	0.30	48.33	101.02	87.93	-
D(lob)	ol	clu	σ	0.54	0.01	0.12	0.43	1.00	0.10	-
D(rim)	ol	clu	soi h	40.06	11.66	0.09	47.78	99.70	87.96	3
D(rim)	ol	clu	min	39.90	11.34	0.06	47.46	99.52	87.72	-
D(rim)	ol	clu	max	40.25	11.84	0.11	48.16	100.01	88.24	-
D(rim)	ol	clu	σ	0.18	0.28	0.03	0.35	0.27	0.26	-
D(rim)	ol	clast	soi h	40.09	11.18	0.29	47.92	99.71	88.42	3
D(rim)	ol	clu	min	39.97	10.96	0.12	47.71	99.20	88.11	-
D(rim)	ol	clu	max	40.21	11.52	0.38	48.16	100.06	88.58	-
D(rim)	ol	clu	σ	0.12	0.30	0.15	0.23	0.45	0.27	-

Supplementary tables - Lunar Dunite 72415_53. Spinel

Sp type	Mineral	site	SiO2	TiO2	Al2O3	Cr2O3	Fe2O3	FeO	MnO	MgO	Total	Mg#	Cr#	Si	Ti	Al	Cr	Fe(iii)	Fe(ii)	Mn	Mg	Total	No.
A	sp	soi 5	-	0.00	18.00	50.57	2.21	15.88	0.99	11.61	99.27	55.09	65.33	0.0	0.0	0.7	1.3	0.1	0.4	0.0	0.6	3.0	3
A	sp	min	-	0.00	17.44	49.88	1.92	14.57	0.82	11.04	98.69	52.82	64.52	-	-	-	-	-	-	-	-	-	-
A	sp	max	-	0.00	18.40	51.87	2.51	16.71	1.27	12.24	100.25	58.15	66.61	-	-	-	-	-	-	-	-	-	-
A	sp	σ	-	0.00	0.50	1.12	0.30	1.15	0.24	0.60	0.85	2.76	1.13	-	-	-	-	-	-	-	-	-	-
A	sp	soi 14	-	0.73	16.90	51.46	0.75	18.71	1.13	10.11	99.78	48.60	67.14	0.0	0.0	0.6	1.3	0.0	0.5	0.0	0.5	3.0	3
A	sp	min	-	0.89	17.27	51.86	1.27	18.93	1.35	10.45	100.69	49.88	67.58	-	-	-	-	-	-	-	-	-	-
A	sp	max	-	0.49	16.39	50.94	0.14	18.46	0.81	9.86	99.11	47.54	66.74	-	-	-	-	-	-	-	-	-	-
A	sp	σ	-	0.17	0.40	0.41	0.51	0.20	0.23	0.26	0.75	1.03	0.45	-	-	-	-	-	-	-	-	-	-
A	sp	soi g	-	0.81	18.20	49.95	1.09	18.71	0.88	10.53	100.18	49.43	64.80	0.0	0.0	0.7	1.3	0.0	0.5	0.0	0.5	3.0	3
A	sp	min	-	0.69	17.20	48.95	0.81	18.51	0.66	10.47	99.91	49.06	63.75	-	-	-	-	-	-	-	-	-	-
A	sp	max	-	0.91	18.80	51.61	1.24	18.83	1.06	10.59	100.54	49.86	66.81	-	-	-	-	-	-	-	-	-	-
A	sp	σ	-	0.11	0.87	1.45	0.25	0.18	0.20	0.06	0.33	0.40	1.74	-	-	-	-	-	-	-	-	-	-
B	sp	soi 4	-	-	26.39	41.68	2.37	14.36	0.75	13.60	99.15	61.11	51.45	0.0	0.0	0.9	1.0	0.1	0.4	0.0	0.6	3.0	3
B	sp	min	-	-	22.43	39.30	1.91	13.74	0.48	12.51	98.20	57.82	48.10	-	-	-	-	-	-	-	-	-	-
B	sp	max	-	-	28.45	45.75	2.96	15.26	0.91	14.31	100.20	62.86	57.78	-	-	-	-	-	-	-	-	-	-
B	sp	σ	-	-	3.43	3.54	0.54	0.80	0.24	0.96	1.00	2.81	5.43	-	-	-	-	-	-	-	-	-	-
B	sp	soi b	-	1.52	20.79	46.39	0.62	18.22	1.04	11.40	99.99	52.34	59.96	0.0	0.0	0.8	1.1	0.0	0.5	0.0	0.5	3.0	5
B	sp	min	-	1.81	22.75	49.19	0.90	18.57	1.35	11.84	100.64	53.76	64.45	-	-	-	-	-	-	-	-	-	-
B	sp	max	-	1.23	18.20	43.96	0.30	17.91	0.77	10.42	99.29	49.70	56.45	-	-	-	-	-	-	-	-	-	-
B	sp	σ	-	0.21	1.81	1.97	0.26	0.26	0.21	0.59	0.64	1.61	3.12	-	-	-	-	-	-	-	-	-	-
C	sp	soi 10	5.12	0.59	13.56	49.42	0.00	19.34	1.07	11.29	100.38	50.98	70.98	0.2	0.0	0.5	1.2	0.0	0.5	0.0	0.5	3.0	4
C	sp	min	7.85	0.84	14.03	51.39	0.00	20.01	1.46	12.10	101.40	52.62	72.07	-	-	-	-	-	-	-	-	-	-
C	sp	max	3.49	0.46	13.03	46.52	0.00	18.58	0.78	10.49	99.49	49.13	68.99	-	-	-	-	-	-	-	-	-	-
C	sp	σ	2.03	0.17	0.45	2.13	0.00	0.59	0.29	0.70	0.86	1.44	1.38	-	-	-	-	-	-	-	-	-	-
D	sp	soi 3	0.10	0.37	17.06	51.89	1.66	16.88	1.15	10.99	100.09	52.63	67.11	0.0	0.0	0.6	1.3	0.0	0.5	0.0	0.5	3.0	3
D	sp	min	0.06	0.20	16.70	51.45	1.03	16.03	0.80	10.78	99.82	50.93	66.16	-	-	-	-	-	-	-	-	-	-
D	sp	max	0.14	0.60	17.65	52.17	2.01	18.05	1.35	11.30	100.45	54.37	67.70	-	-	-	-	-	-	-	-	-	-
D	sp	σ	0.04	0.21	0.52	0.39	0.54	1.05	0.30	0.28	0.33	1.72	0.83	-	-	-	-	-	-	-	-	-	-
D	sp	soi 6	2.92	0.47	11.71	51.12	3.42	16.59	1.21	13.45	100.89	56.93	74.54	0.1	0.0	0.4	1.3	0.1	0.4	0.0	0.6	3.0	3
D	sp	min	1.37	0.45	10.75	49.31	3.21	15.99	1.13	11.81	99.80	54.71	75.47	-	-	-	-	-	-	-	-	-	-
D	sp	max	5.34	0.49	12.33	52.60	3.63	17.14	1.26	16.08	102.36	60.42	74.11	-	-	-	-	-	-	-	-	-	-
D	sp	σ	2.12	0.02	0.85	1.67	0.21	0.58	0.07	2.30	1.32	85.85	56.99	-	-	-	-	-	-	-	-	-	-

Sp type	Mineral	site	SiO2	TiO2	Al2O3	Cr2O3	Fe2O3	FeO	MnO	MgO	Total	Mg#	Cr#	Si	Ti	Al	Cr	Fe(iii)	Fe(ii)	Mn	Mg	Total	No.
D	sp	soi h	0.00	0.00	14.85	54.16	1.85	17.95	1.22	9.94	99.96	48.54	70.98	0.0	0.0	0.6	1.4	0.0	0.5	0.0	0.5	3.0	4
D	sp	min	0.00	0.00	13.23	52.19	1.65	17.53	1.12	9.68	99.38	46.92	68.39	-	-	-	-	-	-	-	-	-	-
D	sp	max	0.00	0.00	16.18	55.84	2.00	18.78	1.33	10.15	101.02	49.54	73.90	-	-	-	-	-	-	-	-	-	-
D	sp	σ	0.00	0.00	1.27	1.50	0.15	0.56	0.09	0.21	0.73	1.15	2.31	-	-	-	-	-	-	-	-	-	-

Supplementary tables - Lunar Dunite 72415_53. Pyroxene

Sp type	Mineral	site	SiO2	TiO2	Al2O3	Cr2O3	FeO	MnO	MgO	CaO	Na2O	Total	Mg#	Wo	En	Fs	Si	Ti	Al	Cr	Fe(ii)	Mn	Mg	Ca	Na	Total	no.
A	cpx	soi g	53.30	0.28	1.30	1.03	2.65	0.25	18.48	22.87	0.10	99.44	92.56	45.0	50.6	4.4	1.9	0.0	0.1	0.0	0.1	0.0	1.0	0.9	0.0	4.0	3
A	cpx	min	53.15	0.23	1.24	0.90	2.51	0.19	18.30	22.58	0.10	99.44	92.33	-	-	-	-	-	-	-	-	-	-	-	-	-	-
A	cpx	max	53.55	0.32	1.42	1.14	2.72	0.30	18.69	23.22	0.13	99.49	92.99	-	-	-	-	-	-	-	-	-	-	-	-	-	-
A	cpx	σ	0.22	0.05	0.10	0.12	0.12	0.08	0.20	0.32	0.05	0.22	0.37	-	-	-	-	-	-	-	-	-	-	-	-	-	-
A	cpx	soi 5	53.03	0.28	1.33	0.95	2.71	0.12	17.86	23.05	0.10	99.12	92.16	46.0	49.6	4.4	1.9	0.0	0.1	0.0	0.1	0.0	1.0	0.9	0.0	2.0	3
A	cpx	min	52.83	0.26	1.27	0.95	2.71	0.11	17.86	23.05	0.10	99.12	92.16	-	-	-	-	-	-	-	-	-	-	-	-	-	-
A	cpx	max	52.83	0.26	1.27	0.99	2.71	0.11	18.06	23.13	0.13	99.12	92.24	-	-	-	-	-	-	-	-	-	-	-	-	-	-
A	cpx	σ	0.29	0.14	0.06	0.16	0.02	0.12	0.25	0.18	0.05	0.32	0.07	-	-	-	-	-	-	-	-	-	-	-	-	-	-
C	cpx	soi 10	50.98	0.36	1.61	2.22	3.67	0.15	19.52	20.82	0.11	99.42	90.45	40.87	53.32	5.80	1.86	0.01	0.07	0.06	0.11	0.00	1.06	0.81	0.01	4.00	7
C	cpx	min	46.67	0.06	0.95	0.97	2.99	0.06	17.49	15.37	0.03	97.90	87.62	-	-	-	-	-	-	-	-	-	-	-	-	-	-
C	cpx	max	53.44	0.54	2.64	6.03	5.31	0.37	22.12	23.15	0.19	100.82	91.88	-	-	-	-	-	-	-	-	-	-	-	-	-	-
C	cpx	σ	2.16	0.16	0.69	1.98	0.83	0.11	1.80	2.59	0.06	1.23	1.65	-	-	-	-	-	-	-	-	-	-	-	-	-	-
D	cpx	soi h	53.10	0.23	1.31	0.99	3.03	-	18.31	22.58	-	99.76	91.51	44.79	50.53	4.68	1.93	0.01	0.06	0.03	0.09	0.00	0.99	0.88	0.01	4.00	3.00
D	cpx	min	52.96	0.11	1.19	0.82	2.77	-	17.80	21.78	-	98.85	90.69	-	-	-	-	-	-	-	-	-	-	-	-	-	-
D	cpx	max	53.38	0.35	1.40	1.28	3.48	-	19.02	23.17	-	100.52	91.97	-	-	-	-	-	-	-	-	-	-	-	-	-	-
D	cpx	σ	0.24	0.12	0.11	0.25	0.39	-	0.64	0.72	-	0.85	0.71	-	-	-	-	-	-	-	-	-	-	-	-	-	-
C	opx	soi 10	54.54	0.17	1.34	2.28	7.77	0.12	32.15	1.96	0.06	100.31	88.06	3.7	84.7	11.6	1.9	0.0	0.1	0.1	0.2	0.0	1.7	0.1	0.0	4.0	9
C	opx	min	49.60	0.06	0.83	0.65	6.88	0.03	30.18	0.87	0.01	99.20	85.75	-	-	-	-	-	-	-	-	-	-	-	-	-	-
C	opx	max	57.43	0.27	2.52	7.47	9.19	0.21	33.23	7.24	0.11	101.75	89.36	-	-	-	-	-	-	-	-	-	-	-	-	-	-
C	opx	σ	2.26	0.07	0.56	2.18	0.69	0.07	0.97	2.12	0.03	0.98	1.00	-	-	-	-	-	-	-	-	-	-	-	-	-	-

Supplementary tables - Lunar Dunite 72415_53. Plagioclase

Sp type	Mineral	Site	Soi	Si	Al	Cr	Fe	Mg	Ca	Na	Total	Mg#	An	Ab	Or	No.
B	An	clast	soi 5	43.39	35.38	0.23	0.30	0.73	19.43	0.51	99.97	81.52	95.44	4.56	0.00	4
B	An	clast	min	42.76	33.00	0.08	0.04	0.10	19.01	0.34	98.91	47.12	-	-	-	-
B	An	clast	max	44.37	36.73	0.33	0.62	2.44	19.87	0.69	100.72	87.52	-	-	-	-
B	An	clast	σ	0.70	1.74	0.11	0.27	1.14	0.35	0.16	0.77	17.83	-	-	-	-
C	An	clast	soi 10	45.15	25.72	-	2.03	8.97	17.19	0.22	99.27	88.76	97.79	2.21	0.00	3.0
C	An	clast	min	44.30	21.69	-	1.29	7.20	15.20	0.17	98.47	88.21	-	-	-	-
C	An	clast	max	46.13	28.81	-	3.06	12.85	18.11	0.24	100.01	90.87	-	-	-	-
C	An	clast	σ	0.88	3.36	-	0.76	2.67	1.34	0.03	0.65	1.31	-	-	-	-

Supplementary tables - Lunar Dunite 72415_53. Fe Metal and Apatite

Sp type	Mineral	site	SiO2	Al2O3	Fe	Ni	Co	V	Total
A	Fe metal	soi 5	0.08	0.24	61.69	34.42	2.82	0.10	99.34
A	Fe metal	min	0.07	0.19	61.48	34.12	2.58	0.06	98.78
A	Fe metal	max	0.09	0.28	62.08	34.78	3.09	0.13	99.71
A	Fe metal	σ	0.01	0.05	0.34	0.33	0.26	0.05	0.48

Sp type	Mineral	site	Si	Al	Fe	Ni	Mg	Ca	Na	P	Total
A	Ap	soi f	0.87	0.12	0.55	0.13	0.69	55.20	0.04	36.46	93.97
A	Ap	min	0.28	0.01	0.25	0.02	0.03	53.74	0.00	35.17	92.50
A	Ap	max	1.67	0.37	0.75	0.38	2.07	56.06	0.14	37.04	94.58
A	Ap	σ	0.51	0.17	0.16	0.12	0.71	0.70	0.05	0.66	0.67

1EHW02, Calatrava. PPL image

1EHW02, Calatrava. XPL image

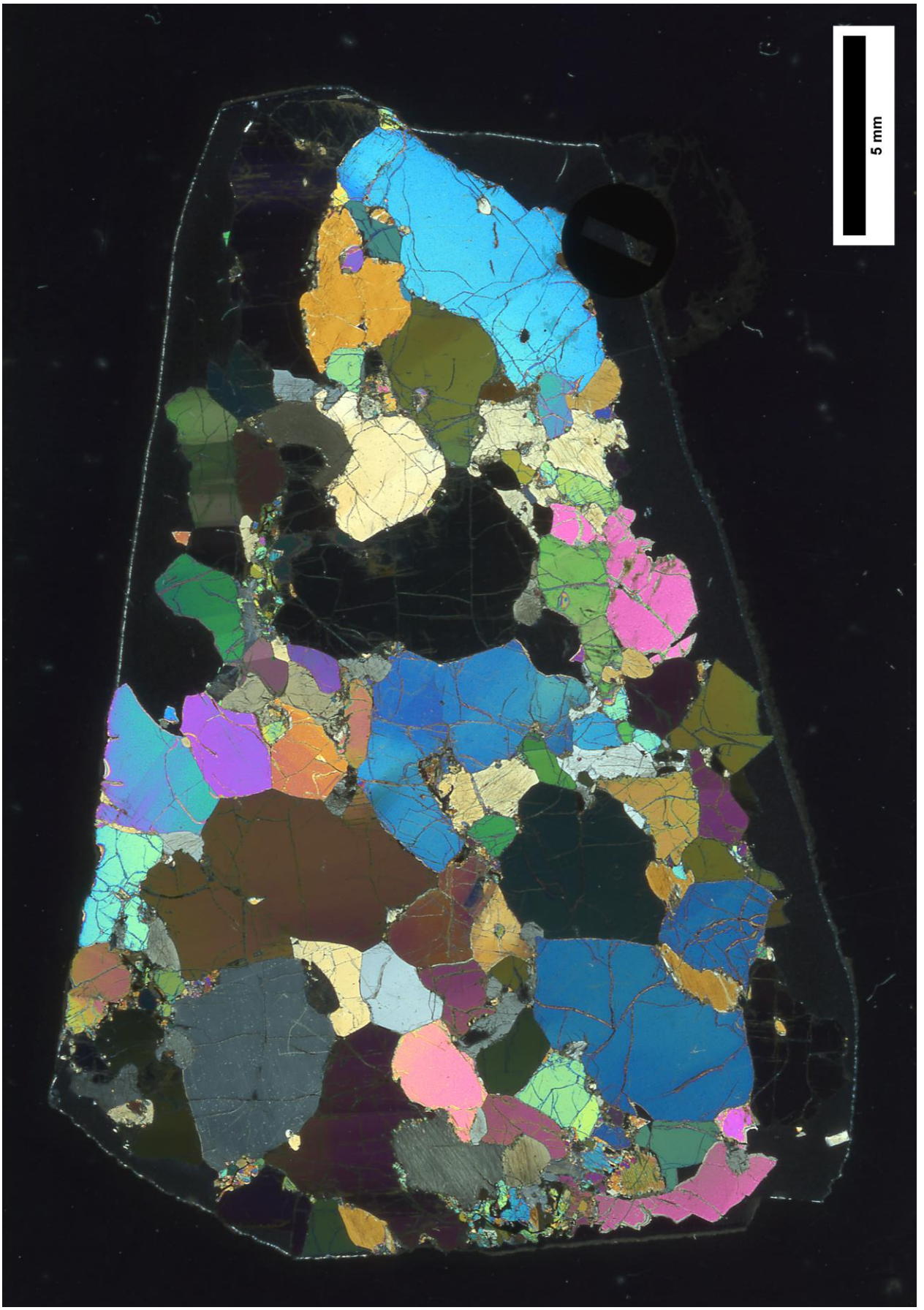

PA 31, Pali Aike, garnet spinel peridotite. Metasomatic halo elemental map.

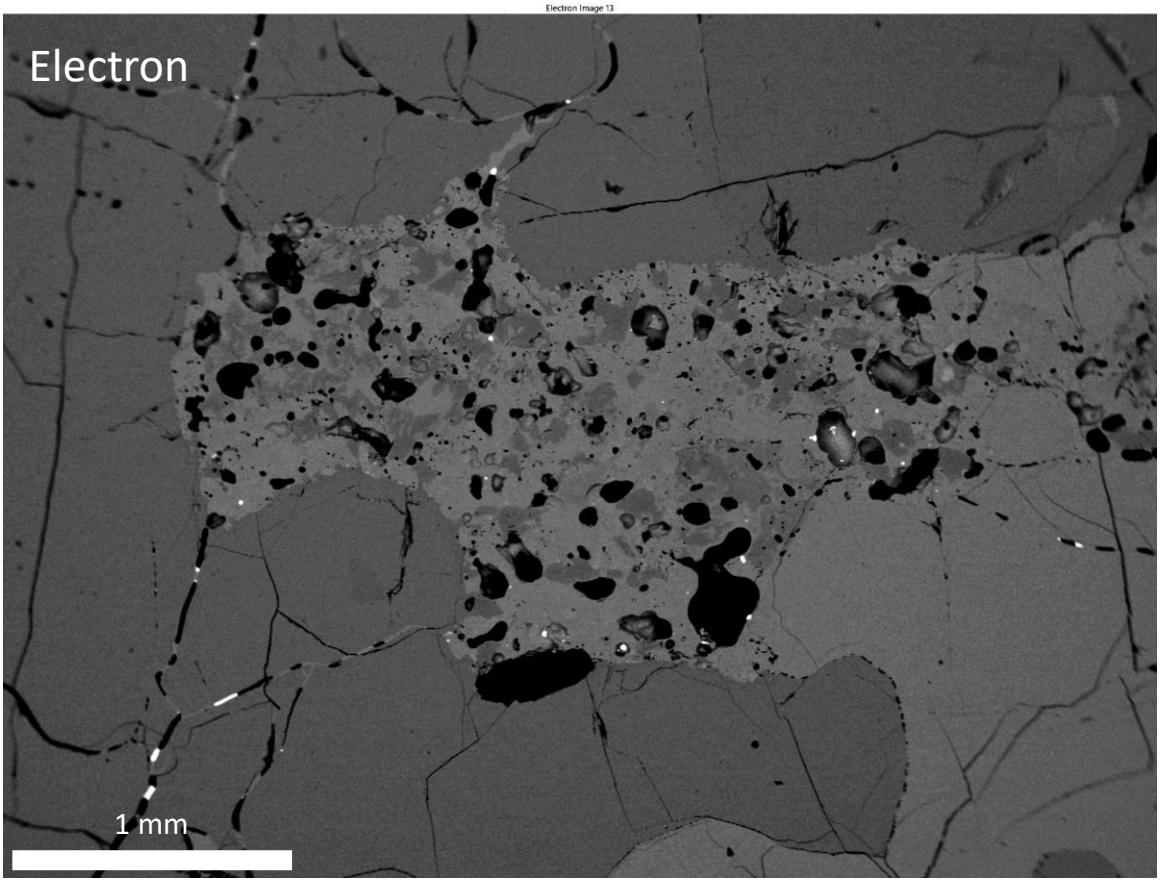

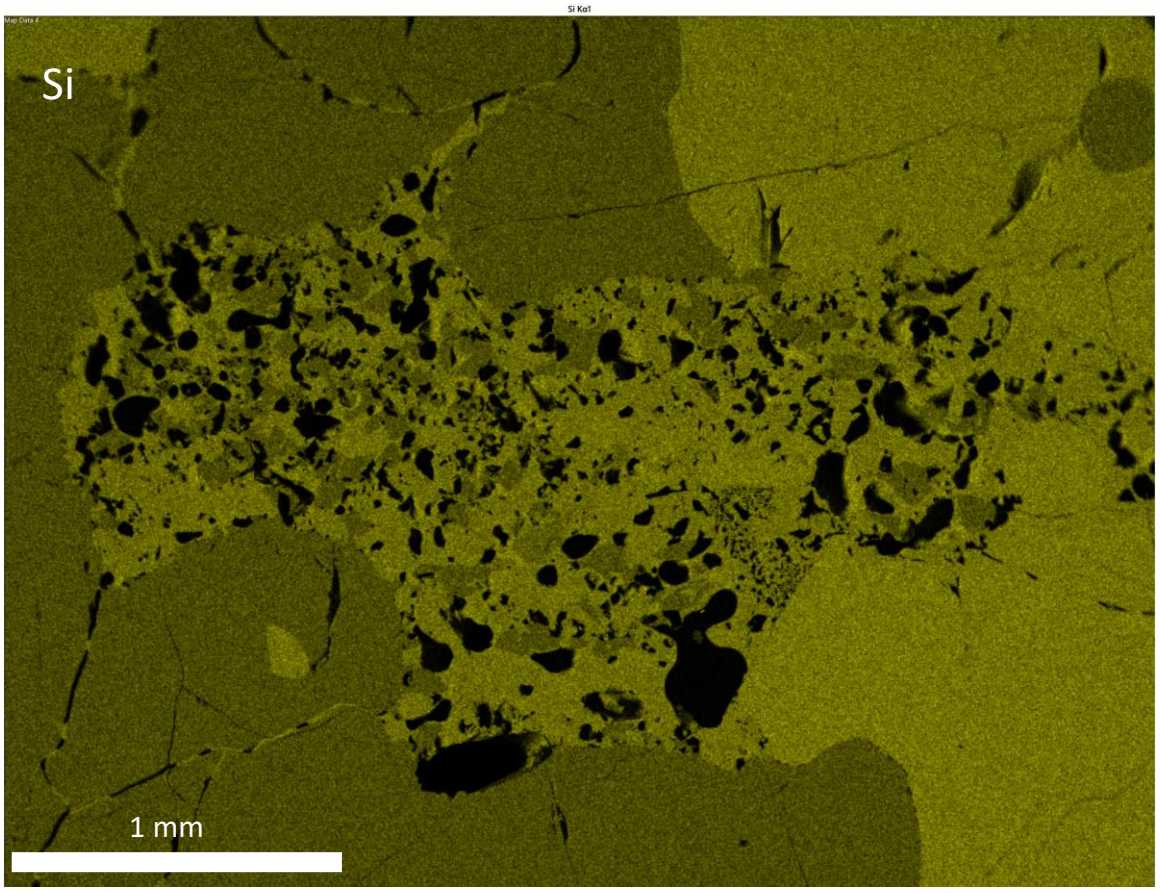

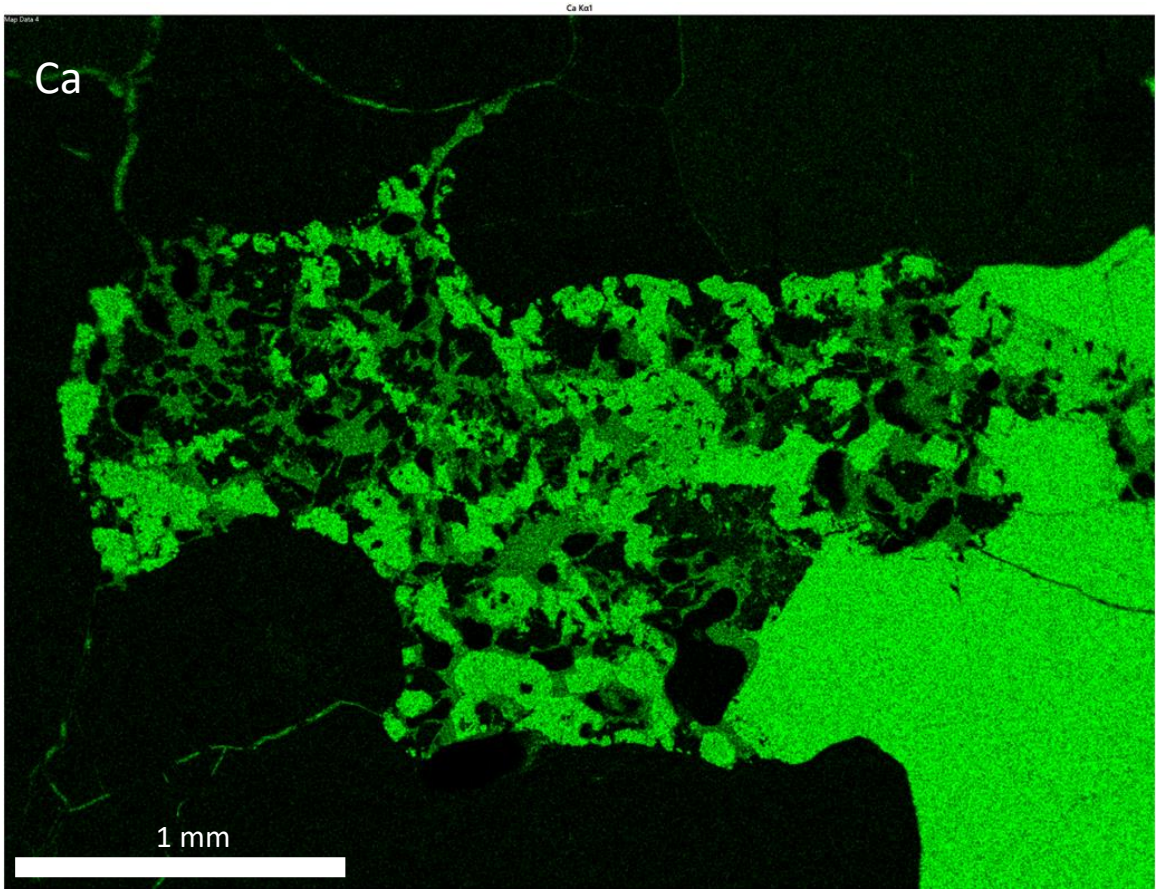
Ca Kα1
Ca
1 mm

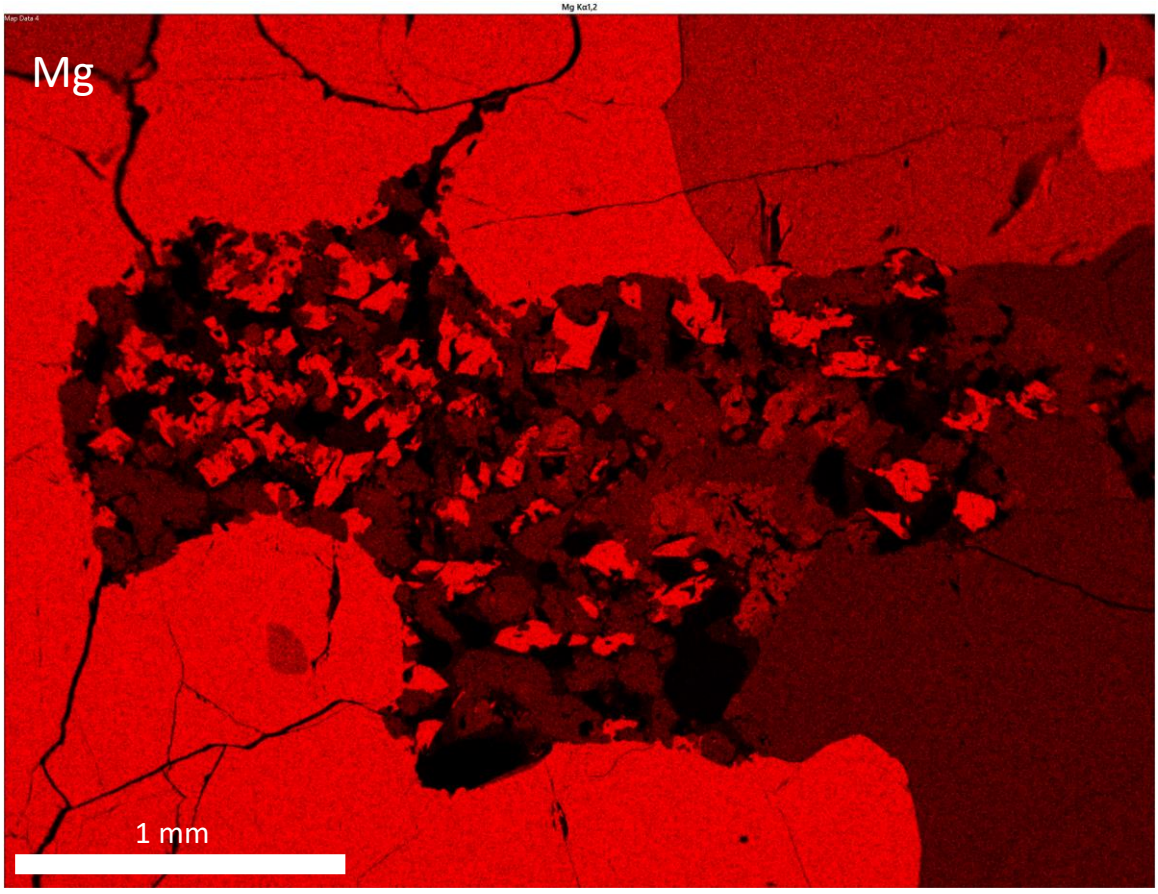
Mg Kα1,2
Mg
1 mm

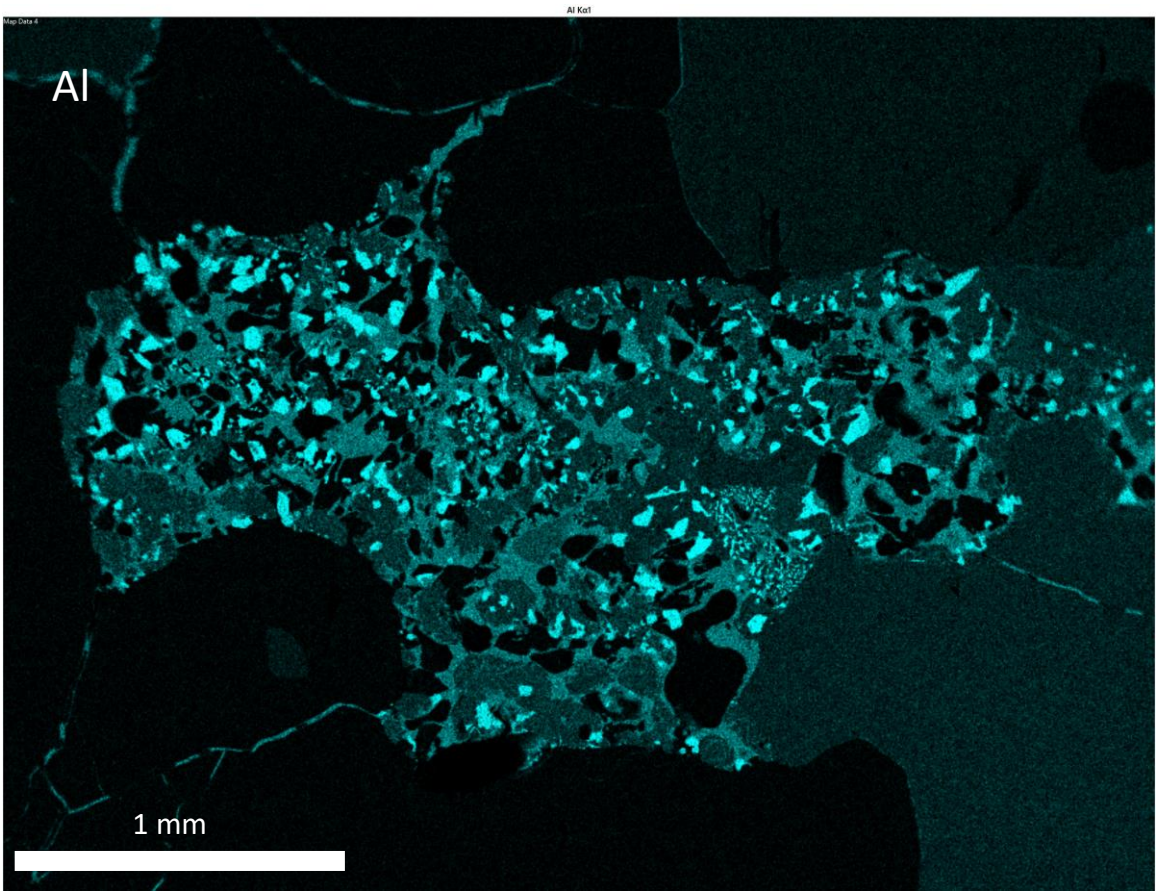
Al Kα1
Map Data 4
Al
1 mm

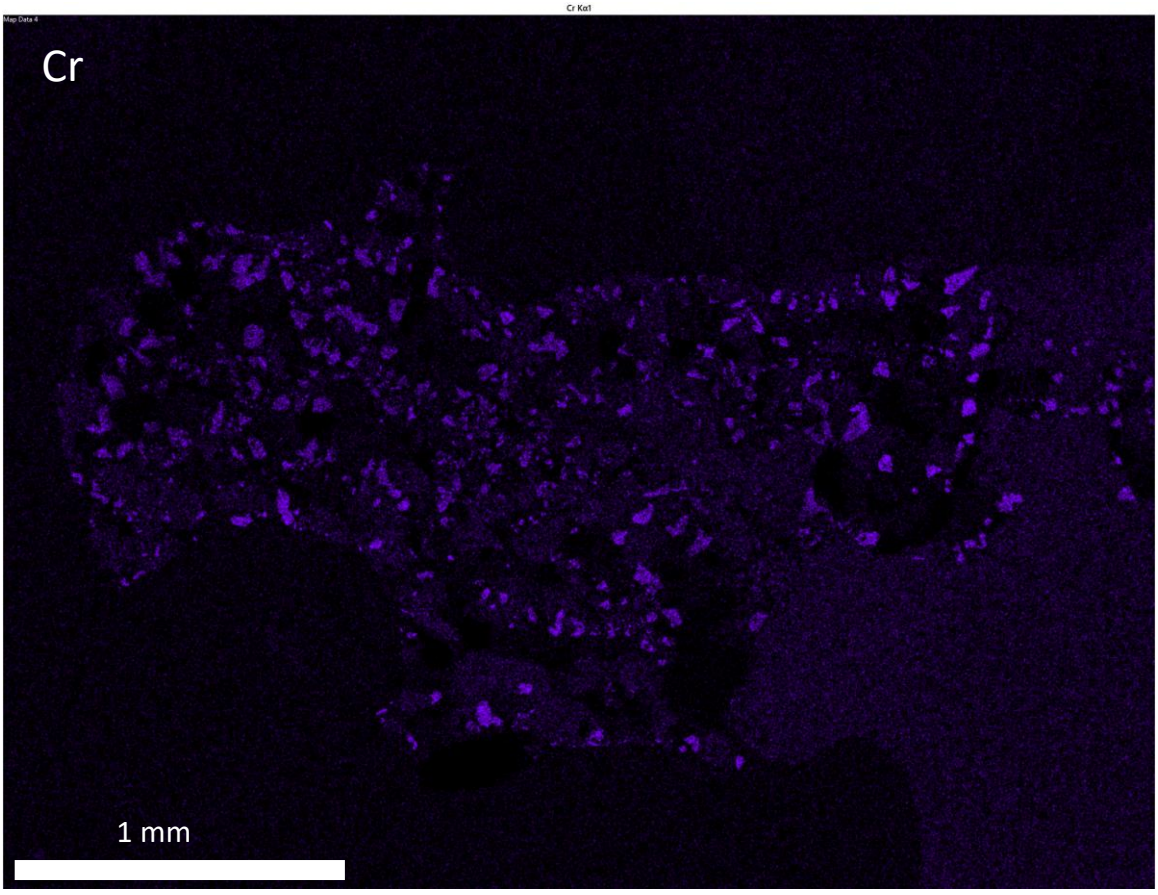
Cr Kα1
Map Data 4
Cr
1 mm